

AD-A173 682

PROCEEDINGS OF THE ARMY SCIENCE CONFERENCE (15TH) HELD
IN WEST POINT NEW. (U) DEPUTY CHIEF OF STAFF FOR
RESEARCH DEVELOPMENT AND ACQUISITIO.. J SAMU ET AL.

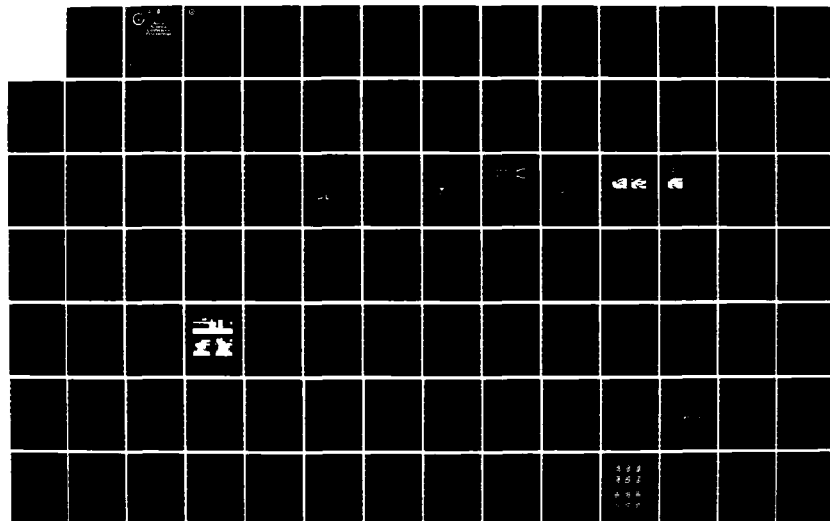
1/1

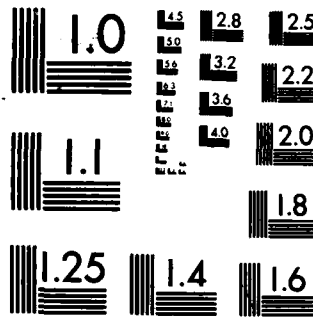
UNCLASSIFIED

20 JUN 86

F/G 5/2

NL





MICROCOPY RESOLUTION TEST CHART
NATIONAL BUREAU OF STANDARDS-1963-A

AD-A173 682



DTIC
ELECTE
OCT 28 1986
S D
D

14

Army Science Conference Proceedings

17-19 June 1986

Volume IV

Principal Authors S through Z

**This document has been approved for public
release and sale; its distribution is unlimited.**

FILE COPY

**Deputy Chief of Staff for Research,
Development & Acquisition
Department of the Army**

86



DEPARTMENT OF THE ARMY
OFFICE OF THE DEPUTY CHIEF OF STAFF
FOR RESEARCH, DEVELOPMENT, AND ACQUISITION
WASHINGTON, DC 20310-0600

REPLY TO
ATTENTION OF


DAMA-ARR

20 June 1986

SUBJECT: Proceedings of the 1986 Army Science Conference

SEE DISTRIBUTION

1. The 15th in a series of Army Science Conferences was held at the United States Military Academy, 17-19 June 1986. The conference presented a cross section of the many significant scientific and engineering programs carried out by the Department of the Army. Additionally, it provided an opportunity for Department of the Army civilian and military scientists and engineers to present the results of their research and development efforts before a distinguished and critical audience.
2. These Proceedings of the 1986 Army Science Conference are a compilation of all papers presented at the conference and the supplemental papers that were submitted. The Proceedings consist of five volumes, four of which are unclassified (Volumes I through IV). Volume V contains limited distribution and classified papers.
3. Our purpose for soliciting these papers was to:
 - a. Stimulate the involvement of scientific and engineering talent within the Department of the Army.
 - b. Demonstrate Army competence in research and development.
 - c. Provide a forum wherein Army personnel can demonstrate the full scope and depth of their current projects.
 - d. Promote the interchange of ideas among members of the Army scientific and engineering community.
4. The information contained in these volumes will be of benefit to those who attended the conference and to others interested in Army research and development. It is requested that these Proceedings be placed in technical libraries where they will be available for reference.


LOUIS C. WAGNER, JR.
Lieutenant General, GS
Deputy Chief of Staff for
Research, Development
and Acquisition



/ Codes

nd/or

Special

list

A-1

DISTRIBUTION:

Office of the Secretary of Defense, Strategic Defense Initiative Orgn, ATTN:
IST, Wash, DC 20301-7100

Office of the Under Secretary of Defense for Research and Engineering, Wash, DC
20301-3010

Office of the Under Secretary of Defense for Research and Advanced Technology,
Wash, DC 20301-3080

Office of the Assistant Secretary of the Army (RD&A), Wash, DC 20310-0103

HQDA, Assistant Chief of Staff for Intelligence, ATTN: DAMI-ZS, Wash, DC
20310-1001

U.S. Army Foreign Science and Technology Center, ATTN: AMXST-OC,
Charlottesville, VA 22901-5396

HQDA, Deputy Chief of Staff for Logistics, ATTN: DALO-ZD, Wash, DC 20310-0500

HQDA, Deputy Chief of Staff for Operations & Plans, ATTN: DAMO-ZD, Wash, DC
20310-3200

HQDA, Deputy Chief of Staff for Personnel, ATTN: DAPE-PSR, Wash, DC 20310-0300

HQDA, Deputy Chief of Staff for Research, Development and Acquisition,
ATTN: DAMA-ARR, Wash, DC 20310-0632

Combat Support Systems Directorate, ATTN: DAMA-CSZ, Wash, DC 20310-0601

Materiel Plans & Programs Directorate, ATTN: DAMA-PPF, Wash, DC 20310-0600

Weapons Systems Directorate, ATTN: DAMA-WSZ, Wash, DC 20310-0600

Office of the Chief of Engineers, ATTN: DAEN-RDZ, Wash, DC 20314-1000

Office of the Surgeon General, ATTN: DASG-RDZ, Wash, DC 20310-2300

COMMANDERS/DIRECTORS:

US Army Strategic Defense Command, P. O. Box 1500, Huntsville, AL 35807-3801

US Army Information Systems Engineering Command, Ft. Belvoir, VA 22060-5456

US Army Concepts Analysis Agency, 8120 Woodmont Avenue, Bethesda, MD
20814-2797

US Army Forces Command, Ft. McPherson, GA 30330-6000

US Army Logistics Center, ATTN: ATCL-M, Ft. Lee, VA 23801-6000

US Army Missile Command, ATTN: AMSMI-RD, Redstone Arsenal, AL 35898-5248

US Army Materiel Command, ATTN: AMCLD, 5001 Eisenhower Avenue, Alexandria,
VA 22333-0001

US Army Materiel Systems Analysis Activity, ATTN: AMXSY-D, APG, MD
21005-5071

US Army Armament, Munitions & Chemical Cmd, ATTN: AMSMC-CG, Rock Island, IL
61299-6000

US Army Armament R&D Center, ATTN: SMCAR-TD, Dover, NJ 07801-5001

Fire Support Armaments Center, ATTN: SMCAR-FS, Dover, NJ 07801-5001

Armament Engineering Directorate, ATTN: SMCAR-AE, Dover, NJ 07801-5001

Close Combat Armaments Center, ATTN: SMCAR-CC, Dover, NJ 07801-5001

Chief, Benet Weapons Lab, Watervliet Arsenal, Watervliet, NY 12189-4050

Chemical R&D Center, ATTN: SMCCR-TD, APG, MD 21010-5423

US Army Aviation Systems Cmd, ATTN: AMSAV-GTD, 4300 Goodfellow Blvd., St.
Louis, MO 63120-1798

USARTA, Ames Research Center, ATTN: SAVRT-D, Moffett Field, CA 94035-1099

USARTA, Aeroflightdynamics Dir., ATTN: SAVRT-AF, Moffett Field, CA
94035-1099

USARTA, Aviation Applied Technology Dir., ATTN: SAVRT-TY, Ft. Eustis, VA
23604-5577

USARTA, Propulsion Dir., ATTN: SAVRT-PN, 21000 Brook Park Rd., Cleveland,
OH 44135-3127

USARTA, Aerostructures Dir., ATTN: SAVRT-SD, Hampton, VA 23665-5225
 Aviation Engineering Flight Activity, ATTN: SAVTE-C, Edwards AFB, CA 93523-5000
 Avionics R&D Activity, ATTN: SAVAA-G, Ft. Monmouth, NJ 07703-5401
 US Army Communications-Electronics Cmd, ATTN: AMSEL-TDD, Ft. Monmouth, NJ 07703-5001
 Night Vision and Electro-Optics Lab, ATTN: AMSEL-NV-D, Ft. Belvoir, VA 22060-5166
 Signals Warfare Lab, ATTN: AMSEL-SW-D, Vint Hill Farms Station, Warrenton, VA 22186-5100
 Electronics Warfare TSTA Ctr, ATTN: AMSEL-EW-D, Ft. Monmouth, NJ 07703-5303
 US Army Laboratory Command, ATTN: AMSLC-CG, 2800 Powder Mill Road, Adelphi, MD 20783-1145
 US Army Ballistic Research Lab, ATTN: SLCBR-OD, APG, MD 21005-5006
 Atmospheric Sciences Laboratory, ATTN: SLCAS-DD, WSMR, NM 88002-5501
 Electronics Technology & Devices Lab, ATTN: SLCET-D, Ft. Monmouth, NJ 07703-5302
 Vulnerability Assessment Lab, ATTN: SLCEW-M-D, WSMR, NM 88002-5513
 Harry Diamond Laboratories, ATTN: SLCHD-D, Adelphi, MD 20783-1197
 Human Engineering Lab, ATTN: SLCHE-D, Aberdeen Proving Ground, MD 21005-5001
 Materials and Technology Lab, ATTN: SLCMT-D, Watertown, MA 02172-0001
 US Army Research Office, ATTN: SLCRO-D, Rsch Triangle Park, NC 27709-2211
 US Army Research, Development & Standardization Group (Europe), Box 65, FPO New York 09510
 US Army Tank-Automotive Command, ATTN: AMSTA-CR, Warren, MI 48397-5000
 Tank-Automotive Systems Lab, ATTN: AMSTA-R, Warren, MI 48397-5000
 Tank-Automotive Concepts Lab, ATTN: AMSTA-Z, Warren, MI 48397-5000
 US Army Test & Evaluation Command, ATTN: AMSTE-TD, APG, MD 21005-5055
 Aberdeen Proving Ground, ATTN: STEAP-OC, APG, MD 21005-5001
 Dugway Proving Ground, ATTN: STEDP-CO, Dugway, UT 84022-5000
 Electronic Proving Ground, ATTN: STEEP-DO, Ft. Huachuca, AZ 85613-7110
 Aviation Development Test Activity, ATTN: STEBG-CO, Ft. Rucker, AL 36362-5276
 Combat Systems Test Activity, ATTN: STECS-CO, APG, MD 21005-5059
 White Sands Missile Range, ATTN: STEWS-CG, WSMR, NM 88002-5000
 US Army Troop Support Cmd, ATTN: AMSTR-G, 4300 Goodfellow Blvd., St. Louis, MO 63120-1798
 Belvoir R&D Center, ATTN: STRBE-ZT, Ft. Belvoir, VA 22060-5606
 Natick R&D Center, ATTN: STRNC-T, Natick, MA 01760-5000
 US Army Corps of Engineers
 Cold Regions Rsch & Engineering Lab, ATTN: CRREL-TD, Hanover, NH 03755-1290
 Construction Engineering Rsch Lab, ATTN: CERL-ZT, Champaign, IL 61820-1305
 Engineer Topographic Laboratories, ATTN: ETL-TD, Ft. Belvoir, VA 22060-5546
 Waterways Experiment Station, ATTN: WESTV, P.O. Box 631, Vicksburg, MS 39180-0631
 US Army Medical R&D Command, ATTN: SGRD-ZA, Ft. Detrick, Frederick, MD 21701-5012
 Aeromedical Research Lab, ATTN: SGRD-UAC, Ft. Rucker, AL 36362-5000
 Institute of Dental Research, WRAMC, ATTN: SGRD-UDZ, Wash, DC 20307-5300
 Inst of Surgical Research, ATTN: SGRD-USZ, Ft. Sam Houston, TX 78234-6200

Letterman Army Inst of Rsch, ATTN: SGRD-ULZ, Presidio of San Francisco,
CA 94129-6800

Medical Bioengineering R&D Lab, ATTN: SGRD-UBZ, Frederick, MD 21701-5010

Medical Rsch Inst of Chemical Defense, ATTN: SGRD-UV-ZA, APG, MD 21010-5425

Medical Rsch Inst of Environmental Medicine, ATTN: SGRD-UEZ, Natick, MA
01760-5007

Medical Rsch Inst of Infectious Diseases, ATTN: SGRD-UIZ-A, Frederick, MD
21701-5011

Walter Reed Army Inst of Research, ATTN: SGRD-UWZ, Washington, DC 20307-5100

US Army Health Services Command, Ft. Sam Houston, TX 78234-6000

US Army Environmental Hygiene Agency, ATTN: HSHB-Z, APG, MD 21010-5422

US Army Research Institute for the Behavioral and Social Sciences, ATTN:

PERI-BR, 5001 Eisenhower Avenue, Alexandria, VA 22333-5600

ARI Field Unit, ATTN: PERI-IJ, PO Box 2086, Ft. Benning, GA 31905-0686

ARI Field Unit, ATTN: PERI-SB, PO Box 6057, Ft. Bliss, TX 79906-0057

ARI Field Unit, ATTN: PERI-SH, HQ TCATA, Ft. Hood, TX 76544-5065

ARI Field Unit, ATTN: PERI-IK, Steele Hall, Ft. Knox, KY 40121-5620

ARI Field Unit, ATTN: PERI-SL, PO Box 290, Ft. Leavenworth, KS 66048-0290

ARI Field Unit, ATTN: PERI-IR, Ft. Rucker, AL 36362-5000

ARI Field Unit, ATTN: PERI-IO, PO Box 5787, Presidio of Monterey, CA
93944-5011

US Army Training and Doctrine Command, ATTN: ATCG, Fort Monroe, VA 23651-5000

TRADOC Research Analysis Center, WSMR, NM 88002-5502

Training Technology Agency, ATTN: ATTG-D, Ft. Monroe, VA 23651-5000

COMMANDANTS:

US Army Air Defense School, ATTN: ATSA-CG, Ft. Bliss, TX 79916-5000

US Army Armor School, ATTN: ATSB-CG, Ft. Knox, KY 40121-5000

US Army Transportation and Aviation Logistics School, ATTN: ATSG-CG, Ft.
Eustis, VA 23604-5361

US Army Chemical School, ATTN: ATZN-CG, Ft. McClellan, AL 36205-5020

US Army Engineer School, ATTN: ATZA-CG, Ft. Belvoir, VA 22060-5331

US Army Field Artillery School, ATTN: ATSF-CG, Ft. Sill, OK 73503-5600

US Army Infantry School, ATTN: ATSH-CG, Ft. Benning, GA 31905-5007

US Army Intelligence Center and School, ATTN: ATSI-CG, Ft. Huachuca, AZ
85613-7000

US Army Logistics Center, ATTN: ATCL-CG, Ft. Lee, VA 23801-6000

US Army Ordnance Center and School, ATTN: ATSL-CG, APG, MD 21005-5201

US Army Signal Center, ATTN: ATZH-CG, Ft. Gordon, GA 30905-5000

US Army Soldier Support Center, ATTN: ATZI-CG, Ft. Harrison, IN 46216-5000

SUPERINTENDENT:

US Military Academy, ATTN: Technical Library, West Point, NY 10996-1799

COPIES FURNISHED:

DOD

Defense Advanced Research Projects Agency, 1400 Wilson Blvd., Arlington, VA
22209-2308

Defense Technical Information Center, Cameron Station, Alexandria, VA
22304-6145

US Army

US Army Information Systems Engineering Support Activity, Ft. Huachuca, AZ
85613-5300

US Army Field Office, HQ AFSC/SDOA, Andrews AFB, MD 20331

US Army Inst for Research in Management Information & Computer Sciences,
115 O'Keefe Bldg., Georgia Inst of Technology, Atlanta, GA 30332-0800

US Navy

Naval Air Systems Command, Code AIR-93-D, 1411 Jefferson Davis Hwy., Wash, DC
20361-3000

Naval Research Lab, ATTN: Director of Research, Wash, DC 20375-5000

Office of Naval Research, Code 10, 800 North Quincy Street, Arlington, VA
22217-5000

HQ US Marine Corps, Code RD-1, Washington, DC 20380-0001

US Air Force

Air Force Systems Command, ATTN: Deputy Chief of Staff for Science and Tech,
Andrews AFB, MD 20334-5000

Air Force Office of Scientific Research, ATTN: Tech Director, Bolling AFB,
Wash, DC 20332-6448

Lawrence Livermore National Lab, ATTN: L-191, P.O. Box 808, Univ of
California, Livermore, CA 94550

Los Alamos National Lab, ATTN: Dir for Energy, Res & Tech, Los Alamos, NM
87545

NASA HQS, ATTN: Suite 7237, 400 Maryland Avenue, SW, Wash, DC 20546

National Science Foundation, 1800 G Street, NW, Wash, DC 20550

United Nations Library, ATTN: Acquisiton Section, Room L-138A, NY, NY 10017

PROCEEDINGS
OF THE
1986 ARMY SCIENCE CONFERENCE

UNITED STATES MILITARY ACADEMY
WEST POINT, NEW YORK
17-19 JUNE 1986

VOLUME IV
Principal Authors S through Z

TABLE OF CONTENTS
PROCEEDINGS OF THE 1986 ARMY SCIENCE CONFERENCE

<u>Author</u>	<u>Title</u>	<u>Vol</u>	<u>Page</u>
Abele, Gunars	The Effects of Cold Environment on Rapid Runway Repairs	I	1
Adams, George F. Page, Michael J.	Thermochemistry of Boron Compounds	I	11
Alexander, Millard H.	See Melius, Carl F.	III	25
Alster, Jack	See Sollott, Gilbert P.	IV	173
Alving, Carl R.	See Owens, Roberta R.	III	163
Anderson, Jeffrey W.	The Army's Warrior Spirit	I	31
Andre, Richard G.	See Golenda, Claudia F.	I	327
Ashley, Paul R. Davis, Jack H.	Amorphous Silicon Liquid Crystal Spatial Light Modulator	I	45
Askew, Eldon W.	See Cucinell, Samuel A.	I	235
AuCoin, Thomas R.	See Ross, Raymond L.	III	311
AuCoin, Thomas R.	See Shappirio, Joel R.	IV	95
Avara, Elton P.	Comparison of Estimates of Average Transmission	V	1
Bacastow, Todd S.	See Guth, Peter L.	I	371
Bagwell, Thomas H. Jr.	Use of Streaming Current as a Method for Automatic Polyelectrolyte Dosage Control	I	53
Ballou, W. Ripley	See Hockmeyer, Wayne T.	II	27
Banderet, Louis E.	See Munro, Ilse	III	85
Bandy, John T. Smith, Edgar D.	A Practical Field Laundry Wastewater Recycling System	I	63
Barber, Teddy L.	See Measure, Edward M.	V	87
Barrett, Ann	See Briggs, Jack	I	81
Beatrice, Edwin S.	See Penetar, David M.	III	183

<u>Author</u>	<u>Title</u>	<u>Vol</u>	<u>Page</u>
Beaudoin, Richard	See Hockmeyer, Wayne T.	II	27
Behar, Isaac	See Simmons, Ronald	IV	127
Behncke, Robert	See Coe, Mark W.	I	217
Beichler, Glenn P. Lawler, Charles R.	Decoys, A Tool for Survival	V	15
Bergman, Werner	See Fedele, Paul D.	I	279
Bissett, Frank H.	See Cornell, John H.	I	225
Boobar, Lewis R.	See Sardelis, Michael R.	IV	33
Bosco, Charles D. Reitmeyer, Randolph Ferraglio, Robert	The "Science of Design" Opens the Door to Rapid and Affordable Electronic Systems Development and Life Cycle Management	I	71
Boucher, Lisa J.	See Little, James S.	II	271
Boucher, Lisa J.	See Ray, Radharaman	III	221
Bovino, Lawrence J.	See Weiner, Maurice	IV	291
Boy, J. H.	See Stephenson, L. D.	IV	189
Briggs, Jack Dunne, C. Patrick Graham, Maryann Risvik, Einar Cardello, Armand Barrett, Ann Taub, Irwin	A Calorically Dense Ration for the 21st Century	I	81
Britan, Ronnie G.	See White, James L.	IV	335
Brooks, Larry W.	Effects of Summarized and Expanded Test on Readers' Content and Structural Knowledge	I	97
Broomfield, Clarence A.	See Little, James S.	II	271
Broomfield, Clarence A.	See Ray, Radharaman	III	221
Bryant, George Hynes, Thomas Swab, Jeffrey J.	Continuous Intrusive Temperature Sensor for Molten Metals Process Control	I	111
Bryk, Darryl C.	See Rose, Douglas N.	III	283

<u>Author</u>	<u>Title</u>	<u>Vol</u>	<u>Page</u>
Burden, Henry S.	See Jamison, Keith A.	II	95
Burke, Terence	See Weiner, Maurice	IV	291
Butler, Chalmers M.	See Schwering, Felix K.	IV	81
Canonico, Peter G. Gibbs, Paul H. Huggins, John W. Linden, Carol D. MacDonald, Carolyn McKee, Kelly T. Meegan, James Morrill, John Oland, Dwayne D. Peters, C. J. Reed, Lauren V.	Ribavirin Prophylaxis of Sandfly Fever - Sicilian Infection in Human Volunteers	I	127
Cardello, Armand	See Briggs, Jack	I	81
Carlson, Dawn	See Schnakenberg, David D.	IV	69
Celmins, Aivars K.	A New Crater Size Model Derived by Fuzzy Data Analysis	I	141
Cespedes, Ernesto R. Cress, Daniel H.	Analysis of Passive Imaging Concepts for Remote Minefield Detection Application	V	31
Chang, Lang-Mann	Diagnostic Ignition Studies in Support of the Development of Advanced 105-mm and 120-mm Tank Ammunition	I	155
Chen, P.C.T.	A New Method of Predicting Residual Stresses in Autofrettaged Gun Barrels	I	171
Chin, T. N.	Self-Induced Nonlinear Optical Effects and Device Concepts for Ocular Protection	I	185
Choi, Chang Sun	See Prask, Henry J.	III	207
Chu, Shih-Chi	Nonlinear Behavior of Weapon Structural Materials	I	201
Claybaugh, John R.	See Cucinell, Samuel A.	I	235
Clay, Wallace H.	See Kayser, Lyle D.	II	141

<u>Author</u>	<u>Title</u>	<u>Vol</u>	<u>Page</u>
Coe, Mark W. Riggins, Robert E. Behncke, Robert	Innovative Systems Concepts for Integrated Training Management	I	217
Collett, Marc S.	See Dalrymple, Joel M.	I	249
Conrad, Raymond W.	See Patterson, Stanley P.	III	173
Cornell, John H. Cullen, John Richard, Gretchen C. Stapler, John T. Bissett, Frank H.	Synthesis and Evaluation of Reactive Polymers for Chemical Protection	I	225
Cress, Daniel H.	See Cespedes, Ernesto R.	V	31
Cucinell, Samuel A. Askew, Eldon W. Claybaugh, John R.	Influence of Rations on the Physical Performance of Troops at High Altitude	I	235
Cullen, John	See Cornell, John H.	I	225
Curtis, John O.	See Scoggins, Randy K.	V	157
Dagdigian, Paul J.	See Melius, Carl F.	III	25
Dalrymple, Joel M. Morrill, John C. Smith, Jonathan F. Collett, Marc S.	Evaluation of a Recombinant Vaccinia Virus Vaccine Candidate for Rift Valley Fever	I	249
D'Amico, William P.Jr.	See Kayser, Lyle D.	II	141
D'Amico, William P.Jr.	See Nusca, Michael J.	III	111
Davio, Stephen R.	See Martin, Dale G.	III	1
Davis, Edward G. Mioduszewski, Robert J.	Chemical Computer Man: Chemical Agent Response Simulation	I	263
Davis, Jack H.	See Ashley, Paul R.	I	45
Dekanski, Deborah A.	See Ross, Raymond L.	III	299
Dekanski, Deborah A.	See Ross, Raymond L.	III	311
Deponai, John M., III	See Snellen, James E.	IV	143
Diggs, Carter L.	See Hockmeyer, Wayne T.	II	27
Ditillo, John T.	See Kroutil, Robert T.	V	71

<u>Author</u>	<u>Title</u>	<u>Vol</u>	<u>Page</u>
Dixon, Samuel	See Ross, Raymond L.	III	311
Duncan, Louis D.	Transmittance Models for Broadband Systems	V	47
Dunne, C. Patrick	See Briggs, Jack	I	81
Durst, H. Dupont	See Landis, Wayne G.	II	217
Eckart, Donald W.	See Gualtieri, John G.	I	357
Escarsega, Dawn	See Rodriguez, Gumersindo	III	251
Fallesen, Jon J.	See Kurtz, Gary L.	II	183
Fedele, Paul D. Bergman, Werner McCallen, Rose Sutton, Steven	Hydrodynamically Induced Aerosol Transport Through Clothing	I	279
Ferraglio, Robert	See Bosco, Charles D.	I	71
Feuer, Henry	See Rodriguez, Gumersindo	III	251
Finnegan, John J.	See Shappirio, Joel R.	IV	95
Flanigan, Dennis F.	See Kroutil, Robert T.	V	71
Fox, Donald C.	See Shappirio, Joel R.	IV	95
Fox-Talbot, Mary K.	See Little, James S.	II	271
Francesconi, Ralph	See Schnakenberg, David D.	IV	69
Friar, Glenn S.	See Jones, Donald E.	II	125
Gallo, Benedict J.	See Walker, John E.	V	251
Gatza, Paul	See Rodriguez, Gumersindo	III	251
Gerhart, Grant R. Thomas, David J. Martin, Gary L. Gonda, Terry G.	Concept Vehicle Thermal Image Simulation	I	295
Gibbs, Paul H.	See Canonico, Peter G.	I	127
Gilbert, Everett E.	See Sollott, Gilbert P.	IV	173
Goehring, Dwight J. Hart, Roland J.	The Simulated Annealing Algorithm Applied to Scheduling of Army Unit Training	I	311

<u>Author</u>	<u>Title</u>	<u>Vol</u>	<u>Page</u>
Golenda, Claudia F. Wirtz, Robert A. Andre, Richard G.	An <u>In Vivo</u> Bioassay as a Primary Screen for Nerve Agent Antidotes	I	327
Gonda, Terry G.	See Gerhart, Grant R.	I	295
Graham, Maryann	See Briggs, Jack	I	81
Gray, Wayne D. Mutter, Sharon A. Swartz, Merryanna L. Pspotka, Joseph	Novice to Expert: Implications for Artificial Intelligence Systems	I	341
Gregory, Don A.	See Johnson, John L.	II	111
Gualtieri, John G. Eckart, Donald W.	Electrode Diffusion and its Suppression in Alpha-Quartz	I	357
Gupta, Raj K.	See Rutledge, Louis C.	III	343
Guth, Peter L. Ressler, Eugene K. Bacastow, Todd S.	Computerized Terrain Analysis for the Field: Technology and Software Deployable Today	I	371
Hagman, Joseph D. Hayes, John F.	Learning Cooperatively Can Be More Effective Than Learning Alone	II	1
Harper, Bruce G. Midgley, Leonora P. Resnick, I. Gary Landis, Wayne G.	Scale-Up Production and Purification of Diisopropylfluoroptosphatase from <u>Tetrahymena Thermophila</u>	II	17
Harper, Bruce G.	See Landis, Wayne G.	II	217
Hart, Roland J.	See Goehring, Dwight J.	I	311
Hawkins, George S.	See Reifenrath, William G.	III	235
Hayes, John F.	See Hagman, Joseph D.	II	1
Heath, Linda S.	See Shappirio, Joel R.	IV	95
Hockmeyer, Wayne T. Young, James F. Ballou, W. Ripley Wirtz, Robert A. Schneider, Imogene Miller, Louis H. Beaudoin, Richard Diggs, Carter L.	Development of a Genetically Engineered Malaria Vaccine for Man	II	27
Hockmeyer, Wayne T.	See Owens, Roberta R.	III	163

<u>Author</u>	<u>Title</u>	<u>Vol</u>	<u>Page</u>
Hock, V. F.	See Stephenson, L. D.	IV	189
Hoenig, Stuart A.	See Yalamanchili, Rao	IV	361
Hollinger, Jeffrey O. Schmitz, John P.	A Synthetic Bone Repair Material	II	39
Holter, John J.	See Seiders, Barbara A. B.	V	189
Homan, Clarke G. Scholz, W.	Superconducting Augmented Rail Gun (SARG)	II	55
Hsu, Chen C. Pistritto, Joseph V.	Catalytic Air Purification for Collective Protection	II	67
Hubbard, Roger W.	See Schnakenberg, David D.	IV	69
Huggins, John W.	See Canonico, Peter G.	I	127
Hynes, Thomas	See Bryant, George	I	111
Iafrate, Gerald J.	See Ross, Raymond L.	III	299
Iyer, Sury	Radiation Casting of Energetic Material Formulations with Binders	II	81
Jamison, Keith A. Powell, John D. Marquez-Reines, Miguel Burden, Henry S.	Results from Railgun Plasma - Armature Investigations	II	95
Johnson, Bruce D.	See Weisman, Idelle M.	IV	303
Johnson, John L. Gregory, Don A.	Adaptive Phased Array Radar, Artificial Neural Networks, and Optics	II	111
Johnson, Richard	See Schnakenberg, David D.	IV	69
Jones, Donald E. Friar, Glenn S.	Development of an Experimental Manipulator Arm for Applications in the Close Combat Mission Area	II	125
Jourdan, Mark R. Sullivan, Garrett J.	Hydrologic Forecasting in the Tactical Environment	V	57
Kayser, Lyle D. Clay, Wallace H. D'Amico, William P., Jr.	Surface Pressure Measurements on a 155mm Projectile in Free-Flight at Transonic Speeds	II	141
Klein, Joel M.	Modeling the Spread of Liquid Droplets on Non-Ideal Surfaces	II	155

<u>Author</u>	<u>Title</u>	<u>Vol</u>	<u>Page</u>
Knox, Francis S.	See Simmons, Ronald	IV	127
Koza, Walter	See Ward, Janet E.	IV	265
Krishnamurthy, Thaiya Szafraniec, Linda Sarver, Emory W.	Structural Investigations and Analysis of Fresh Water Blue-Green Algal (Microcystis Aeruginosa and Anabena-Flos-Aquae) Hepatotoxic Peptides by Tandem Mass Spectrometric Techniques	II	169
Kroutil, Robert T. Ditillo, John T. Flanigan, Dennis F.	An Autonomous Background Compensation Algorithm for Stand-Off Chemical Agent Detection	V	71
Kurtz, Gary L. Fallesen, Jon J.	Display and Control Research to Enhance Performance of Short-Range Air Defense (SHORAD) Fire Unit Personnel	II	183
Kwiatkowski, Joseph H.	See Shappirio, Joel R.	IV	95
Lakhani, Hyder	Enlisted Manpower Costs of the Bradley Fighting Vehicle and the M113: An Application of a Prototype Army Manpower Cost (AMCOS) Model	II	199
Landis, Wayne G. Durst, H. Dupont Savage, Russell E.Jr. Harper, Bruce G.	The Tetrahymena-DFPases: Elucidation, Characteristics, Therapeutic Potential, and Utility as Non-Corrosive Decontaminants	II	217
Landis, Wayne G.	See Harper, Bruce G.	II	17
Lane, Gerald R.	See Leighty, Robert D.	II	243
Langley, William H.	See Lorton, Lewis	II	285
Lawler, Charles R.	See Beichler, Glenn P.	V	15
Lee, Claire H.	See Silverman, Gerald J.	V	205
Leibrecht, Bruce C. Patterson, James H.Jr.	Controlling Impulse Noise Hazards: Programmatic Model for Developing Validated Exposure Standards	II	233
Leighty, Robert D. Lane, Gerald R.	Developing Technologies for Army Autonomous Land Vehicles	II	243
Leipertz, Donald F.	See White, James L.	IV	335
Lengsfeld, Byron H.III	Application of Theoretically Computed Vibrational Spectra to the Remote Sensing of Chemical Agents and the Study of Energetic Compounds	II	259

<u>Author</u>	<u>Title</u>	<u>Vol</u>	<u>Page</u>
Leonard, Joseph M.	See Seiders, Barbara A. B.	V	189
Linden, Carol D.	See Canonico, Peter G.	I	127
Little, James S. Broomfield, Clarence A. Fox-Taibot, Mary K. Boucher, Lisa J.	A Potential Nerve Agent Decontaminant from Mammalian Liver	II	271
Lorton, Lewis Langley, William H.	Computer Assisted Postmortem Identification	II	285
Lovelace, Donald E. Sims, S. Richard F.	The Analysis of Shaped Charge Jet Flash Radiographs Using Image Processing Techniques	II	301
Lowell, George H. Smith, Lynette F. Seid, Robert C. Zollinger, Wendell D.	A Small Synthetic Peptide Bound via its Hydrophobic Foot to Meningococcal Outer Membrane Proteins Becomes a Highly Immunogenic Vaccine	II	313
Lukes, George E.	Automated Screening of Reconnaissance Imagery	II	329
Lussier, Adrien R.	See Munro, Ilse	III	85
Luteran, Thomas	See Seiders, Barbara A. B.	V	189
Lux, Robert A.	See Ross, Raymond L.	III	299
Lux, Robert A.	See Ross, Raymond L.	III	311
Lux, Robert A.	See Shappirio, Joel R.	IV	95
MacDonald, Carolyn	See Canonico, Peter G.	I	127
Manavalli, Shekhar	See Willingham, Reginald A.	IV	349
Marquez-Reines, Miguel	See Jamison, Keith A.	II	95
Martin, Dale G. Parker, Gerald W. Davio, Stephen R.	Medical Defense Against Saxitoxin	III	1
Martin, Gary L.	See Gerhart, Grant R.	I	295
McCallen, Rose	See Fedele, Paul D.	I	279
McDonald, Joseph K.	Wide Spectral Range Laser Research	III	15
McKee, Kelly T.	See Canonico, Peter G.	I	127

<u>Author</u>	<u>Title</u>	<u>Vol</u>	<u>Page</u>
McLachlan, Anthony D.	See Meyer, Fred P.	V	101
Measure Edward M. Yee, Young P. Barber, Teddy L.	Artillery Meteorology Without the Balloon	V	87
Meegan, James	See Canonico, Peter G.	I	127
Melius, Carl F. Thorne, Larry R. Dagdigian, Paul J. Alexander, Millard H. Miziolek, Andrzej W.	Gas Phase Combustion Chemistry of Nitramine Propellants	III	25
Mescall, John F. Tracy, Carl	Improved Modeling of Fracture in Ceramic Armors	III	41
Meyer, Fred P. Walck, James C. McLachlan, Anthony D.	Hardening of High Silica Content Optical Glasses to Infra-Red Laser Radiation	V	101
Midgley, Leonora P.	See Harper, Bruce G.	II	17
Milham, Merrill E.	CW Agent Detection by Lidar Returns from Ensembles of Optically Large Particles	III	55
Miller, Lewis D.	Nonlinear Mechanics of Granular Media: A Practical Application of Soliton Dynamics?	III	71
Miller, Louis H.	See Hockmeyer, Wayne T.	II	27
Mioduszewski, Robert J.	See Davis, Edward G.	I	263
Mitchell, Glen W.	See Simmons, Ronald	IV	127
Miziolek, Andrzej W.	See Melius, Carl F.	III	25
Moerkirk, Robert P.	See Ross, Raymond L.	III	299
Morrill, John C.	See Canonico, Peter G.	I	127
Morrill, John C.	See Dalrymple, Joel M.	I	249
Munro, Ilse Rauch, Terry M. Tharion, William Banderet, Louis E. Lussier, Adrien R. Shukitt, Barbara	Factors Limiting Endurance of Armor, Artillery and Infantry Units Under Simulated NBC Conditions	III	85

<u>Author</u>	<u>Title</u>	<u>Vol</u>	<u>Page</u>
Mutter, Sharon A.	See Gray, Wayne D.	I	341
Nauman, Robert K.	See Olenick, John G.	III	127
Nunes, John	Predicting Tensile Failure Stresses in Metal Matrix Composites	III	97
Nusca, Michael J. D'Amico, William P.Jr.	Parametric Study of Low Reynolds Number Precessing/Spinning Incompressible Flows	III	111
Oland, Dwayne D.	See Canonico, Peter G.	I	127
Olenick, John G. Wolff, Ruth Nauman, Robert K.	Nonvariant Nature, Cellular Localization and Protective Potential of a Membrane Fraction from <u>Trypanosoma rhodesiense</u>	III	127
O'Neill, Timothy R. Scott, Brad D.	"Dazzle" Camouflage and Tracking Performance	III	139
Owens, Frank J.	Computer Molecular Synthesis of Energetic Molecules	III	151
Owens, Roberta R. Wirtz, Robert A. Hockmeyer, Wayne T. Alving, Carl R.	Liposomes as Carriers for a Malaria Peptide Vaccine: Developmental Aspects	III	163
Page, Michael J.	See Adams, George F.	I	11
Parker, Gerald W.	See Martin, Dale G.	III	1
Patil, Ashok S.	Multispectral Camouflage Materials	V	119
Patterson, James H.Jr.	See Leibrecht, Bruce C.	II	233
Patterson, Stanley P. Conrad, Raymond W. Russell, Stephen D.	Scintillation Smoothing of Pulsed and CW, Visible Laser Beams	III	173
Penetar, David M. Beatrice, Edwin S.	Effects of Atropine and 2-PAM Cl on Human Pursuit Tracking Performance	III	183
Peters, C. J.	See Canonico, Peter G.	I	127
Pistritto, Joseph V.	See Hsu, Chen C.	II	67
Powanda, Michael C.	See Reifenrath, William G.	III	235
Powell, John D.	See Jamison, Keith A.	II	95

<u>Author</u>	<u>Title</u>	<u>Vol</u>	<u>Page</u>
Prakash, Anand	Rebatron: A Compact Accelerator for Producing High Energy, Ultra-High Current Electron Beams	III	193
Prask, Henry J. Choi, Chang S.	The Nondestructive Determination of Residual Stresses in Armament-System Components	III	207
Previte, Joseph J.	See Silverman, Gerald J.	V	205
Pсотka, Joseph	See Gray, Wayne D.	I	341
Puri, Narindra N.	See Schwering, Feliz K.	IV	81
Rauch, Terry M.	See Munro, Ilse	III	85
Ray, Radharaman Boucher, Lisa J. Broomfield, Clarence A.	Specific Soman Hydrolyzing Enzyme in a Clonal Neuronal Cell Culture: Possible Application in Soman Detection, Decontamination, Prophylaxis and Therapy	III	221
Reed, Lauren V.	See Canonico, Peter G.	I	127
Reifenrath, William G. Waring, Paul P. Hawkins, George S. Powanda, Michael C.	Semi-Automated System for Testing the Efficacy of Nerve Agent Protection/Decontamination Formulations	III	235
Reifenrath, William G.	See Rutledge, Louis C.	III	343
Reitmeyer, Randolph	See Bosco, Charles D.	I	71
Resnick, I. Gary	See Harper, Bruce G.	II	17
Ressler, Eugene K.	See Guth, Peter L.	I	371
Richard, Gretchen C.	See Cornell, John H.	I	225
Richmond, Paul	Land Mine Use in Winter	V	133
Riggins, Robert E.	See Coe, Mark W.	I	217
Rigsbee, J. M.	See Stephenson, L. D.	IV	189
Rinker, Jack N.	See Satterwhite, Melvin B.	IV	41
Risvik, Einar	See Briggs, Jack	I	81
Roach, Lisa K.	See Schall, James E.	IV	57
Robbins, Frederick M.	See Walker, John E.	V	251

<u>Author</u>	<u>Title</u>	<u>Vol</u>	<u>Page</u>
Robertson, Donald H.	Rapid Monitoring of Materials Penetration by Toxins and Chemical Surrogates	V	149
Rodriguez, Gumersindo Touchet, Paul Gatza, Paul Teets, Alan Escarsega, Dawn Feuer, Henry	Development of Elastomeric Tank Pad Compounds with Improved Service Life	III	251
Rohde, Frederick W. Jr.	Radar Descriptors for the Classification of Terrain Features	III	267
Rose, Douglas N. Bryk, Darryl C.	Photoacoustic Microscopy - Thermal Wave Probing	III	283
Ross, Raymond L. Lux, Robert A. Dekanski, Deborah A. Iafrate, Gerald J. Moerkirk, Robert P.	Ballistic-Launched Advanced Millimetric Oscillators	III	299
Ross, Raymond L. Winter, John J. Lux, Robert A. Dixon, Samuel Dekanski, Deborah A. AuCoin, Thomas R.	The Zero-Bias Depletion Diode: A Promising New Subharmonic Mixer	III	311
Roy, Gerald G.	See Silverman, Gerald J.	V	205
Rumsey, Michael G.	Work Sample and Job Knowledge Measures: Interchangeable or Complementary?	III	327
Russell, Stephen D.	See Patterson, Stanley P.	III	173
Rutledge, Louis C. Reifenrath, William G. Gupta, Raj K.	Sustained-Release Formulations of the U.S. Army Insect Repellent	III	343
Sahu, Jubaraj	Computational Investigation of Base Flow in the Presence of a Centered Propulsive Jet	IV	1
Sandmeyer, Richard S.	Optimum Aiming of Artillery Indirect Fire	IV	17
Sandus, Oscar	See Sollott, Gilbert P.	IV	173
Sardelis, Michael R. Boobar, Lewis R.	Pesticide Dispersal Unit (PDU), Multicapability, Helicopter Slung	IV	33

<u>Author</u>	<u>Title</u>	<u>Vol</u>	<u>Page</u>
Sarver, Emory W.	See Krishnamurthy, Thaiya	II	169
Satterwhite, Melvin B. Rinker, Jack N.	Effect of Shadows on the Reflectance Spectra of Vegetation and their Digital Classification,	IV	41
Savage, Robert O.	See Shappirio, Joel R.	IV	95
Savage, Russell E. Jr.	See Landis, Wayne G.	II	217
Sawyers, Michael	See Schnakenberg, David D.	IV	69
Schall, James E., Jr. Roach, Lisa K.	Chemical Munition Effects Analysis in Support of Targeting Manual Development	IV	57
Schick, Milton J.	See Yalamanchili, Rao	IV	361
Schnakenberg, David D. Carlson, Dawn Sawyers, Michael Vogel, James A. Johnson, Richard Szlyk, Patricia C. Francesconi, Ralph Hubbard, Roger W.	Nutritional Evaluation of a New Combat Field Feeding System for the Army.	IV	69
Schmitz, John P.	See Hollinger, Jeffrey O.	II	39
Schneider, Imogene	See Hockmeyer, Wayne T.	II	27
Scholz, Wilfred	See Homan, C. G.	II	55
Schwering, Felix K. Puri, Narindra N. Butler, Chalmers M.	Modified Diakoptic Theory of Antennas	IV	81
Scoggins, Randy K. Curtis, John O.	Thermal Camouflage for Fixed Installations	V	157
Scott, Brad D.	See O'Neill, Timothy R.	III	139
Scott, P. A.	See Stephenson, L. D.	IV	189
Seagraves, Mary Ann	Target Acquisition Intelligence Techniques	V	173
Seiders, Barbara A.B. Holter, John J. Leonard, Joseph M. Luteran, Thomas	Technology for the Soldier: Visualizing Penetrants	V	189

<u>Author</u>	<u>Title</u>	<u>Vol</u>	<u>Page</u>
Seid, Robert C.	See Lowell, George H.	II	313
Shappirio, Joel R. Finnegan, John J. Lux, Robert A. Kwiatkowski, Joseph H. Fox, Donald C. Heath, Linda S. Wade, Melvin J. Savage, Robert O. AuCoin, Thomas R.	New Metallization Technologies for Advanced Military Micro- electronics.	IV	95
Shukitt, Barbara	See Munro, Ilse	III	85
Siering, George D.	See Simmons, Ronald	IV	127
Silber, Leo Tauber, Arthur Wilber, William	Hexagonal Ferrites for Millimeter-Wave Control Devices	IV	111
Silverman, Gerald J. Roy, Gerald G., Jr. Woodbury, Charles T. Lee, Claire H. Previte, Joseph J.	Environmental Stability and Detoxification of Staphylococcal Enterotoxin A and Botulinum Neurotoxin A	V	205
Simmons, Ronald R. Knox, Francis Siering, George Behar, Isaac Mitchell, Glenn	Effects of Chemical Defense Antidotes on Aviator Performance	IV	127
Sims, S. Richard F.	See Lovelace, Donald E.	II	301
Singler, Robert E.	See Willingham, Reginald A.	IV	349
Skudera, William J. Jr.	Real Time Transition Detection Method for BPSK Signals in the Presence of Narrow Band Interference	V	215
Slagg, Norman	See Sollott, Gilbert P.	IV	173
Smith, Edgar D.	See Bandy, John T.	I	63
Smith, Jonathan F.	See Dalrymple, Joel M.	I	249
Smith, Lynette F.	See Lowell, George H.	II	313
Smith, William J.	See Walker, John E.	V	251
Snellen, James E. Deponai, John M. III	The MALOS Combat Engineer Simulation Environment	IV	143

<u>Author</u>	<u>Title</u>	<u>Vol</u>	<u>Page</u>
Soicher, Haim	Variability of Transionospheric Signal Time Delay at High Latitudes	IV	159
Sollott, Gilbert P. Alster, Jack Gilbert, Everett E. Sandus, Oscar Slagg, Norman	Synthesis of More Powerful Explosives	IV	173
Stapler, John T.	See Cornell, John H.	I	225
Stephenson, L. D. Hock, V. F. Boy, J. H. Scott, P. A. Rigsbee, J. M.	Ion-Plated Conductive Ceramic and Metal/Ceramic Composite Coatings	IV	189
Sturek, Walter B.	See Weinacht, Paul	IV	275
Sullivan, Garrett J.	See Jourdan, Mark R.	V	57
Sutton, Steven	See Fedele, Paul D.	I	279
Swab, Jeffrey J.	See Bryant, George	I	111
Swartz, Merryanna L.	See Gray, Wayne D.	I	341
Szafraniec, Linda	See Krishnamurthy, Thaiya	II	169
Szlyk, Patricia C.	See Schnakenberg, David D.	IV	69
Tauber, Arthur	See Silber, Leo	IV	111
Taub, Irwin A.	See Briggs, Jack	I	81
Teets, Alan	See Rodriguez, Gumersindo	III	251
Tharion, William J.	See Munro, Ilse	III	85
Thomas, David J.	See Gerhart, Grant R.	I	295
Thompson, Edward F.	Sea State Prediction for Military and Civil Works Applications	IV	205
Thorne, Larry R.	See Melius, Carl F.	III	25
Touchet, Paul	See Rodriguez, Gumersindo	III	251
Tracy, Carl	See Mescall, John F.	III	41
Trevino, S. F. Tsai, D. H.	The Simulation of Condensed Matter Chemistry and Detonation.	IV	219

<u>Author</u>	<u>Title</u>	<u>Vol</u>	<u>Page</u>
Tsai, D. H.	See Trevino, S. F.	IV	219
Turetsky, Abraham L.	Novel Infrared Chaff	V	229
Viechnicki, Dennis J.	Factors Controlling the Ballistic Behavior of Armor Ceramics	IV	233
Vogel, James A.	See Schnakenberg, David D.	IV	69
Wade, Melvin J.	See Shappirio, Joel R.	IV	95
Wade, Melvin J.	See Weiner, Maurice	IV	291
Walck, James C.	See Meyer, Fred P.	V	101
Walker, John E.	Use of Spin Labeled Organophosphonates in the Measurement, Binding and Detoxifying Properties of CBW Protecting Substances Attached to Fabrics	V	241
Walker, John E. Robbins, Frederick M. Smith, William J. Gallo, Benedict J.	Enzymes from Microbial Sources with Activities Against G-Agents	V	251
Walton, W. Scott	Dynamic Response of Armor Plate to Non-Penetrating Projectile Impact	IV	249
Ward, Janet E. Koza, Walter	Hi-Tech Fibers for Improved Ballistic Protection	IV	265
Waring, Paul P.	See Reifenrath, William G.	III	235
Weinacht, Paul Sturek, Walter B.	Simulation of the Supersonic Flow About Finned Projectiles	IV	275
Weiner, Maurice Bovino, Lawrence J. Burke, Terence Youmans, Robert J. Wade, Melvin J.	Optically Activated Switch Technology	IV	291
Weisman, Idelle M. Zeballos, R. Jorge Johnson, Bruce D.	Acute Strenuous Exercise at a Simulated Altitude of 2300M (7500 ft.) Compared to Sea Level in Individuals with Sick Cell Trait (SCT): A Controlled Study in Basic Trainees	IV	303
Wells, Francine S.	Acoustic Birefringence Measurements in Rolled 5083 Aluminum Plate	IV	319

<u>Author</u>	<u>Title</u>	<u>Vol</u>	<u>Page</u>
White, James L. Leipertz, Donald F. Britan, Ronnie G.	The Army's Key Operational Capabilities Analysis of C3 Contribution	IV	335
Wilber, William	See Silber, Leo	IV	111
Willingham, Reginald A. Singler, Robert E. Manavalli, Shekhar	Liquid Crystalline Side Chain Polymers as Potential Detection Agents for Chemical Defense	IV	349
Winter, John J.	See Ross, Raymond L.	III	311
Wirtz, Robert A.	See Golenda, Claudia F.	I	327
Wirtz, Robert A.	See Hockmeyer, Wayne T.	II	27
Wirtz, Robert A.	See Owens, Roberta R.	III	163
Wolff, Ruth	See Olenick, John G.	III	127
Woodbury, Charles T.	See Silverman, Gerald J.	V	205
Yalamanchili, Rao Hoenig, Stuart A. Schick, Milton J.	Cooling of Weapons by Electrostatic Phenomena	IV	361
Yee, Young P.	See Measure, Edward M.	V	87
Youmans, Robert J.	See Weiner, Maurice	IV	291
Young, James F.	See Hockmeyer, Wayne T.	II	27
Zeballos, R. Jorge	See Weisman, Idelle M.	IV	303
Zollinger, Wendell D.	See Lowell, George H.	II	313

SAHU

COMPUTATIONAL INVESTIGATION OF BASE FLOW IN THE PRESENCE OF A CENTERED PROPULSIVE JET

JUBARAJ SAHU, DR.*
US ARMY BALLISTIC RESEARCH LABORATORY
ABERDEEN PROVING GROUND, MARYLAND 21005-5066

I. INTRODUCTION

The flow field in the base region of a jet-propelled tactical missile or a rocket-assisted artillery projectile is complex. The aerodynamic drag associated with afterbody configurations is influenced both by the afterbody geometry and by the interaction of the exhaust jet with the external flow. The under expanded propulsive jet can strongly affect the base pressure distribution and the afterbody flow field. For large jet to free stream pressure ratios, the interaction of the exhaust jet with the external flow can be large enough to induce extensive afterbody flow separation. This can, of course, seriously affect the control effectiveness of any control surface located in that region. For over a decade, experimental efforts and the component approach of Korst (1) have provided valuable insight into this flow problem. The flow field under consideration is complicated due to strong viscous/inviscid interaction and regions of flow separation. The component approach has its serious limitations for three-dimensional configurations and similar procedures are extremely difficult to apply at transonic speeds (2).

Recent advances in numerical algorithms and the advent of supercomputers have made numerical modeling of the Navier-Stokes equations a reality. As computational speed has sharply increased, the computing costs have sharply dropped. This trend in technology makes the direct solution of Navier-Stokes equations more attractive. The Navier-Stokes computational technique models the strong interactions involved between the viscous-inviscid flow regimes in a fully coupled manner and does not contain the empiricism found in the component approach. Some empiricism does enter into the Navier-Stokes solutions through turbulence modeling which is an area of further computational and experimental research.

SAHU

As part of a continued research effort at the Aerodynamics Research Branch of the Ballistic Research Laboratory, computational capabilities have been developed to predict the aerodynamic behavior of artillery shell. Recently, Sahu et al (3) have developed a new predictive capability for complete numerical simulation of the flowfield about a projectile or a missile including the base region. The thin-layer Navier-Stokes equations are used in conjunction with a unique flow field segmentation procedure that facilitated the modification of the computer code. The capability of the code has been extended further to include computation of the base flow in the presence of a centered propulsive jet (4). This paper describes the recent computational investigation of the effect of an exhaust jet on the base pressure and the base region flow field at both transonic and supersonic speeds using the numerical procedure of Reference 3. Additionally, the grids in the base region were adapted to the free shear layer as solutions developed. Solutions were obtained using the Cray 1S computer and are compared with experimental data.

II. GOVERNING EQUATIONS

The set of equations which govern fluid motion are the Navier-Stokes equations. This set of highly non-linear partial differential equations have proven extremely difficult to solve in their entirety. In most instances, approximations had to be made before a solution could be attempted. For example, the well known boundary-layer equations are derived by applying approximations to the Navier-Stokes equations. The present solution technique also makes use of an approximation. The Navier-Stokes equations solved here make use of the thin-layer approximation. That is, viscous terms are neglected in both the longitudinal and circumferential directions. The viscous terms are retained, however, in a direction nearly normal to the surface where large flow field gradients exist. This formulation retains the momentum equations in all three coordinate directions. The retention of the three momentum equations allows for the computation of separated flow and thus differs significantly from boundary layer assumptions.

The equations solved here are written in a generalized coordinate system. This allows a wide variety of body shapes to be computed using the same basic numerical technique. The notation for the physical and transformed coordinate systems are shown in Figure 1. The azimuthal invariant or generalized axisymmetric, transformed, thin-layer Navier-Stokes equations, written in non-dimensional, strong conservation law form (5) are

SAHU

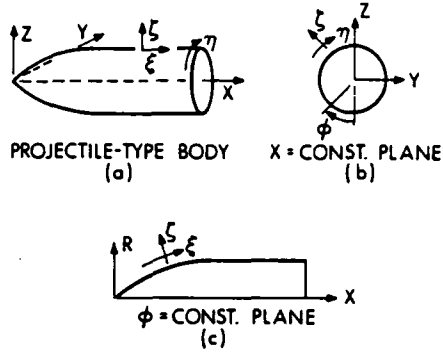


Figure 1. Axisymmetric Body and Coordinate System

$$\partial_{\tau} \hat{q} = \partial_{\xi} \hat{E} + \partial_{\zeta} \hat{G} + \hat{H} = \text{Re}^{-1} \partial_{\zeta} \hat{S} \quad (1)$$

where $\xi = \xi(x, y, z, t)$ is the longitudinal coordinate

$\eta = \eta(y, z, t)$ is the circumferential coordinate

$\zeta = \zeta(x, y, z, t)$ is the near coordinate

$\tau = t$ is the time

and

$$\hat{q} = J^{-1} \begin{bmatrix} \rho \\ \rho u \\ \rho v \\ \rho w \\ e \end{bmatrix},$$

$$\hat{E} = J^{-1} \begin{bmatrix} \rho U \\ \rho u U + \xi_x p \\ \rho v U + \xi_y p \\ \rho w U + \xi_z p \\ (e+p)U - \xi_t p \end{bmatrix},$$

$$\hat{G} = J^{-1} \begin{bmatrix} \rho w \\ \rho u w + \zeta_x p \\ \rho v w + \zeta_y p \\ \rho w w + \zeta_z p \\ (e+p)w - \zeta_t p \end{bmatrix},$$

$$\hat{H} = J^{-1} \begin{bmatrix} 0 \\ 0 \\ \rho V [R_{\xi} (U - \xi_t) + R_{\zeta} (W - \zeta_t)] \\ -\rho V R (V - \eta_t) - p/R \\ 0 \end{bmatrix}$$

The matrix \hat{S} , contains all the viscous terms.

The velocities

$$\begin{aligned} U &= \xi_t + \xi_x u + \xi_y v + \xi_z w \\ V &= \eta_t + \eta_x u + \eta_y v + \eta_z w \\ W &= \zeta_t + \zeta_x u + \zeta_y v + \zeta_z w \end{aligned} \quad (2)$$

represent the contravariant velocities. The non-dimensional velocities (U , V and W) are those components in the direction of the transformed coordinates ξ , η and ζ , respectively. The Cartesian velocity components (u , v , w) together with the density (ρ) and total energy per unit volume (e) are retained as the dependent variables. The local pressure, p , is determined using the relation

$$p = (\gamma - 1)(e - .5\rho(u^2 + v^2 + w^2)). \quad (3)$$

The velocities are non-dimensionalized by the free stream speed of sound a_∞ , the density by ρ_∞ , and the total energy by $\rho_\infty a_\infty^2$. The additional parameters appearing in equation (1) are: (a) coefficient of thermal conductivity, κ ; (b) dynamic viscosity, μ ; (c) Reynolds number based on body diameter, Re ; (d) Prandtl number, Pr ; (e) λ which, based on Stokes hypothesis, is $-2/3 \mu$.

In Equation (1), axisymmetric flow assumptions have been made which result in the source term, \hat{H} . The details of how this is obtained can be found in Reference 5 and are not discussed here. Equation (1) contains only two spatial derivatives. However, it retains all three momentum equations and allows a degree of generality over the standard axisymmetric equations. In particular, the circumferential velocity is not assumed to be zero thus allowing computations for spinning projectiles to be accomplished.

III. NUMERICAL METHOD

a. Computational Algorithm

The thin-layer Navier-Stokes equations are solved using an implicit approximate factorization finite difference scheme in delta form (6). An implicit method was chosen because, for viscous flow problems, it permits a time step much greater than that allowed by explicit schemes. The Beam-Warming implicit algorithm has been used in various applications (3-7) for the equations in general curvilinear coordinates. The algorithm can be first- or second-order accurate in time and second- or fourth-order accurate in space. The equations are factored (spatially split) which reduces the solution process to one-dimensional problems at a given time level. Central difference operators are employed and the algorithm produces block tridiagonal systems for each space coordinate. The main computational work is contained in the solution of these block tridiagonal systems of equations. Although time-dependent calculations

are made, the transient flow is not of primary interest at the present time. The steady flow is the desired result which is obtained in a time asymptotic fashion.

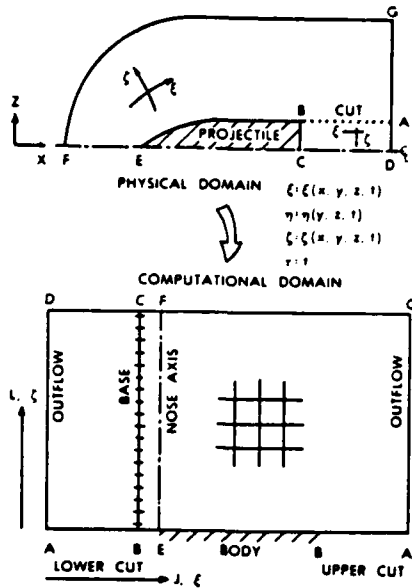


Figure 2. Schematic Illustration of Flow Field Segmentation

b. Flow Field Segmentation

In order to simulate a projectile including the base, we have used two adjoining grids. However, this has been accomplished by a unique flow field segmentation procedure. As described below, our segmentation process allows the existing implicit finite difference algorithm to be applied to two grids by making modifications only in the treatment of the boundary conditions and the internal structure of the block tridiagonal matrix.

Figure 2 is a schematic illustration of the flow field segmentation used to compute the entire projectile flow field that includes the base flow. It shows how the two grids ABCD and AEFG in the physical plane are transformed into a single segmented grid in the computational domain. An important advantage of this segmentation procedure lies in the

preservation of the sharp corner at the base, which allows easy blending of the computational meshes between the regions ABCD and AEFG. No approximation of the actual sharp corner at the base is made. Thus, realistic representation of the base is inherent in the current procedure. The cross-hatched region represents the projectile. The line BC is the projectile base and the region ABCD is the base or wake region. The line AB is a computational cut through the physical base region that acts as a repetitive boundary in the computational domain.

c. Boundary Conditions

The no slip boundary condition for viscous flow is enforced by setting the contravariant velocities to zero, i.e., $U = V = W = 0$ on the projectile surface. The flowfield in the immediate near-wake region has been considered to be weakly viscous and inviscid boundary conditions are used at the base. The viscous terms near the projectile surface and across the shear layer are considered to be the most dominant and have been retained within the thin-layer approximation used here. This

approximation neglects the viscous terms normal to the base that are believed to be less significant. The recirculation region, which has a predominant effect on the base pressure, is in part set up by the viscously dominated shear layer. Additionally, at the corner of the base, the boundary conditions are double valued and depend on the direction from which the corner is approached. Approaching it in the streamwise direction (EB), the no-slip boundary condition is used; approaching it in the radial direction (along the base, CB), the inviscid boundary condition procedure is used.

Along the computational cut (line AB), the flow variables above and below the cut are simply averaged to determine the boundary conditions on the cut. On the centerline of the wake region (line CD), a symmetry condition is imposed. Freestream conditions are used at the outer boundary (FG of Figure 2). Simple extrapolation for all of the flow variables is used at the downstream boundary (lines AD and AG). A combination of extrapolation and symmetry is used on the nose axis (line EF). At the jet exit, boundary conditions are used which are based on the nozzle exit Mach number, stagnation temperature and pressure. The velocity components are linearly interpolated from the centerline of symmetry to the nozzle height at the exit, i.e., conical flow at the jet exit has been assumed.

d. Turbulence Model

For the computation of turbulent flows a turbulence model must be supplied. In the present calculations, a two layer algebraic eddy viscosity model by Baldwin and Lomax (8) is used. In their two layer model the inner region follows the Prandtl-Van Driest formulation. Their outer formulation can be used in wakes as well as in attached and separated boundary layers. In both the inner and outer formulations the distribution of vorticity is used to determine length scales thereby avoiding the necessity of finding the outer edge of the boundary layer (or wake). A few other minor modifications are made in the model which are included in Reference 3. The algebraic eddy viscosity model may not be strictly valid for all wake flow situations. More realistic or complex turbulence models must be considered which is a subject for future study.

IV. RESULTS

a. Transonic Flow ($M = 1.343$)

One means of establishing the accuracy of a numerical scheme is through comparisons with available experimental data. The model used for

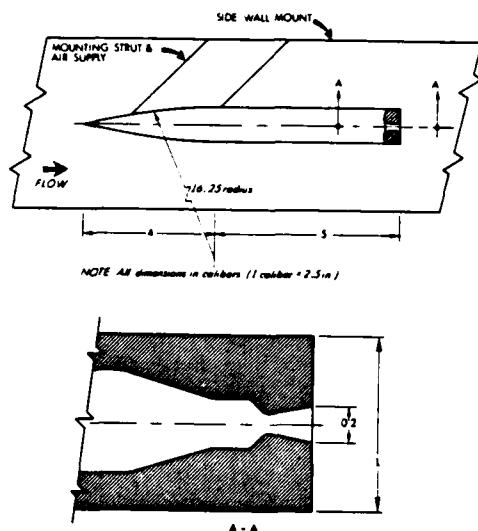


Figure 3. MICOM Base Flow Model Mounted in the Wind Tunnel

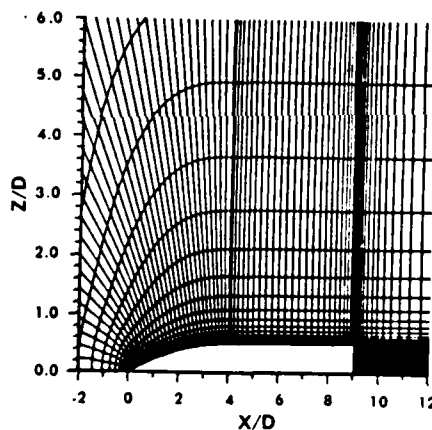


Figure 4. Expanded View of the Grid in the Vicinity of the Model

surface. Additional grid clustering is used in the longitudinal direction near the nose-cylinder junction and at the base where appreciable changes in the flow variables are expected.

Figure 5 shows the Mach number contours in the near wake flow field. The flow expands rapidly at the blunt base which is followed by the recompression shock downstream of the base. The free shear layer as well as the jet shear layer in the base region can be seen clearly. It

the experiment and computational study is shown in Figure 3. It consists of a 4-caliber tangent-ogive nose and a 5-caliber cylindrical afterbody. The base diameter is 1-caliber and the nozzle exit diameter is 0.2 caliber.

The experimental model was side-wall mounted in AEDC Wind Tunnel (9) 1-T as shown in Figure 3a; additional details of the nozzle and base are shown in Figure 3b. The free stream Mach number is 1.343 and the jet exit Mach number is 2.7. The exhaust jet static pressure is 2.15 times the free stream static pressure and the conical nozzle half angle is 10° . Detailed experimental measurements for this shape and these conditions have been made by Walker (9) of the Missile Command (MICOM).

One of the first steps in performing a computation is the generation of a computational grid. An expanded view of the grid near the model is shown in Figure 4. The grid consists of 109 points in the longitudinal direction with 25 points in the base region and 40 points in the radial direction. The computational domain extended to little more than a body length in front, about 3 body lengths in the radial direction and about 2 body lengths behind the base of the missile. The clustering of grid points near the body surface is required in order to resolve the viscous boundary layer near the body

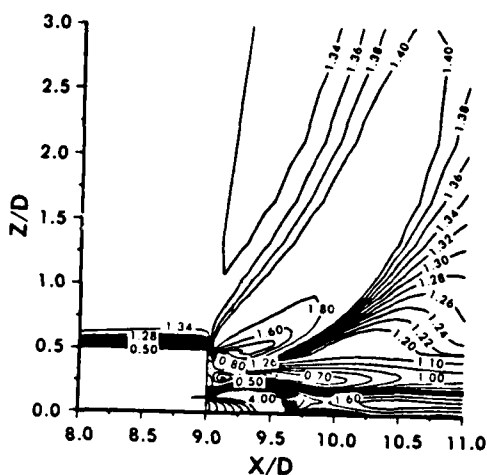


Figure 5. Mach Contours,
 $M_\infty = 1.343$, $\alpha = 0$

MICOM BASE FLOW WITH JET
 $M = 14$, $\alpha = 0$

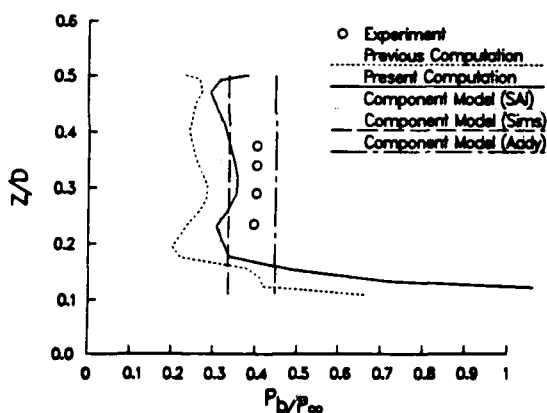


Figure 6. Variation of Base Pressure Along
the Base, $M_\infty = 1.343$, $\alpha = 0$

also indicates the presence of a Mach disk about .75 caliber downstream of the base which agrees very well with the location observed experimentally (9).

The effect of the centered jet on the base pressure is of primary interest. Figure 6 shows the pressure distribution along the base. The computed base pressure is compared with experiment and component model predictions. The present computational result has been obtained using a CRAY 1S computer and an improved version of the code which includes the recent advances made in the computational algorithm. This present result shows a marked improvement over our previous numerical result. Additionally, the present numerical result does as good or better than the component model prediction (based on Reference 1) which have been developed for over a decade. The average level of base pressure from the present computation is $P_b/P_\infty = .365$.

b. Supersonic Flow ($M = 2.0$)

All the computations for this case were made at $M_\infty = 2.0$, $\alpha = 0$ and for jet a exit Mach number of 2.5. Solutions were obtained for various jet-to-free-

stream pressure ratios, $P_j/P_\infty = 1, 3$ and 9. The model geometry used in this study comprised of a 2-caliber 14° half-angle conical nose, 6-caliber cylindrical mid-section and a 1-caliber 8° boattail. The nozzle exit diameter is 0.6 calibers. Detailed experimental measurements for this shape and the same flow conditions have been made by Agrell, et al (10). Figure 7 shows a schematic illustration of the base flow for the jet-on condition and its associated nomenclature.

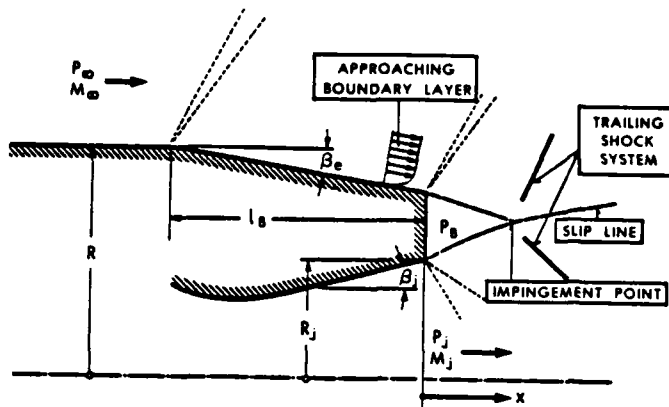
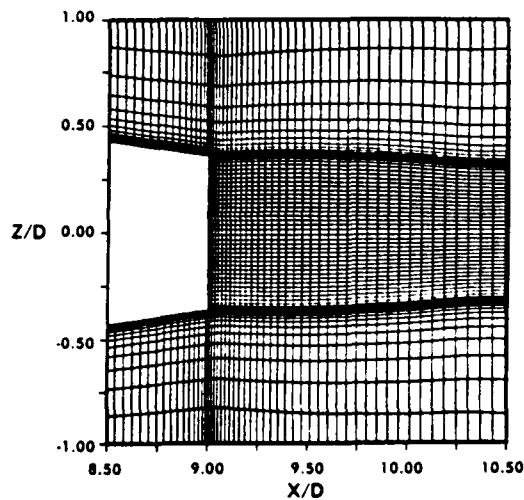


Figure 7. Schematics of the Afterbody Flow With Jet

Figure 8. Computational Grid in the Base Region,
 $P_j/P_\infty = 1.0$

When computations over the entire model are made, only a limited number of grid points can be used in the base region. One way to eliminate this restriction is to use known data given by experiment or otherwise at a station upstream of the base and then compute the flow field in the isolated base region only. This, of course, allows a large number of grid points to be used in the base region. This is ideally suited for the numerical

computations of base region flow field at supersonic velocities. Solutions can be obtained for the forebody with the space-marching, parabolized Navier-Stokes (PNS) code (11). In the present study, the PNS code was used to generate a solution at a station 1.5 calibers upstream of the base and this solution was then used as an upstream boundary condition for the computation of the base region flow field by the unsteady base flow code.

Figures 8-10 show the expanded view of the computational grids in the base region for various jet pressures, $P_j/P_\infty = 1, 3$ and 9 respectively. These grids

are shown for both upper and lower halves for clarity; however, computations are made only for the upper half plane for axisymmetric flow. Additionally, these grids were adapted to the free shear layer as the solutions developed using a procedure described in Reference 3. This is done in an attempt to place the grid points where large gradients in the flow variables exist. Each of these grids consisted of 200 points in the longitudinal direction with 80 points located in the base region and 50 points in the normal direction.

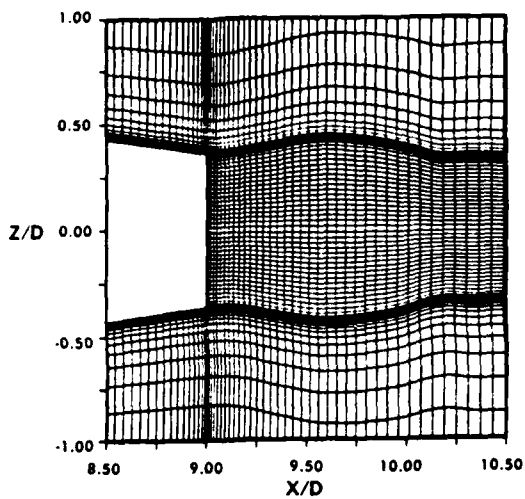


Figure 9. Computational Grid in the Base Region,
 $P_j/P_\infty = 3.0$

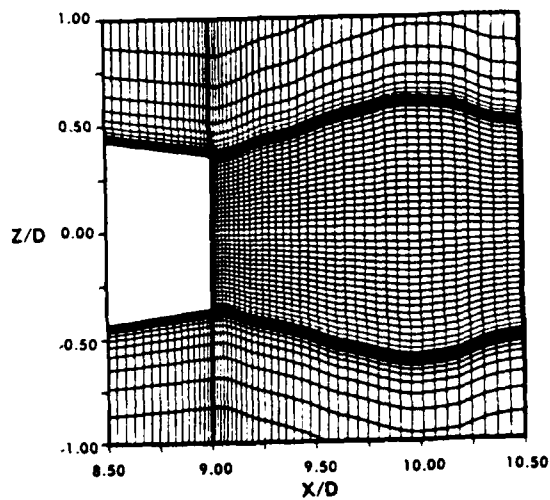


Figure 10. Computational Grid in the Base Region,
 $P_j/P_\infty = 9.0$

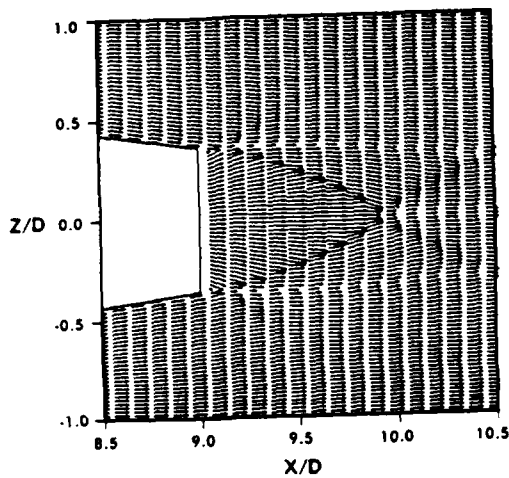


Figure 11a. Velocity Vectors in the Base Region,
 $M_\infty = 2.0, M_j = 2.5, P_j/P_\infty = 1.0$

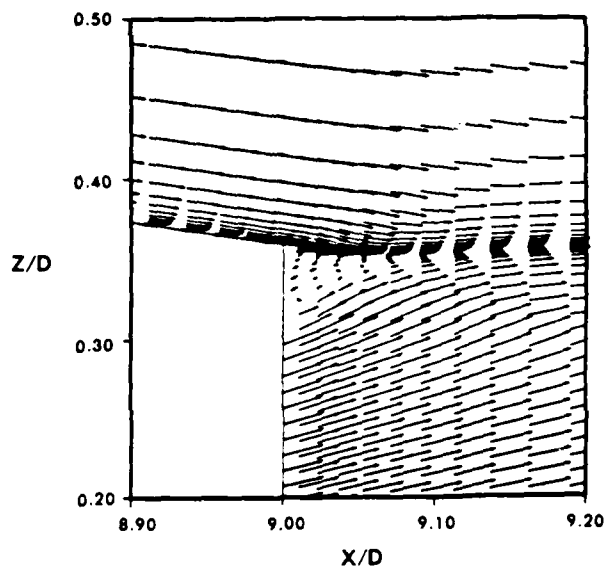


Figure 11b. Velocity Vectors Expanded Near the Base Corner,
 $M_\infty = 2.0, M_j = 2.5, P_j/P_\infty = 1.0$

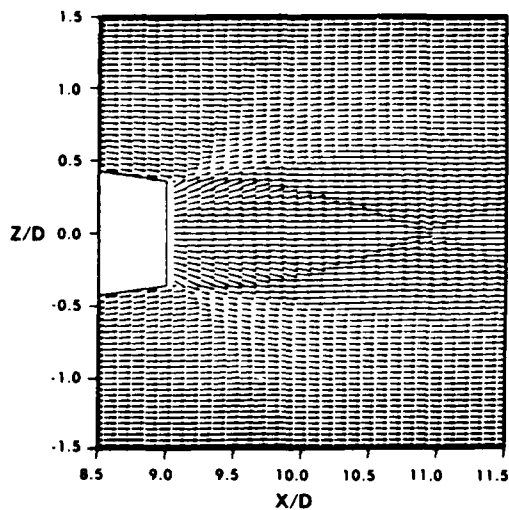


Figure 12. Velocity Vectors in the Base Region,
 $M_\infty = 2.0$, $M_j = 2.5$, $P_j/P_\infty = 3.0$

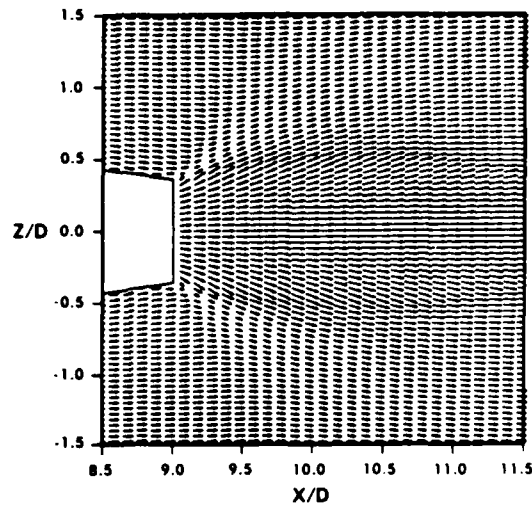


Figure 13a. Velocity Vectors in the Base Region,
 $M_\infty = 2.0$, $M_j = 2.5$, $P_j/P_\infty = 9.0$

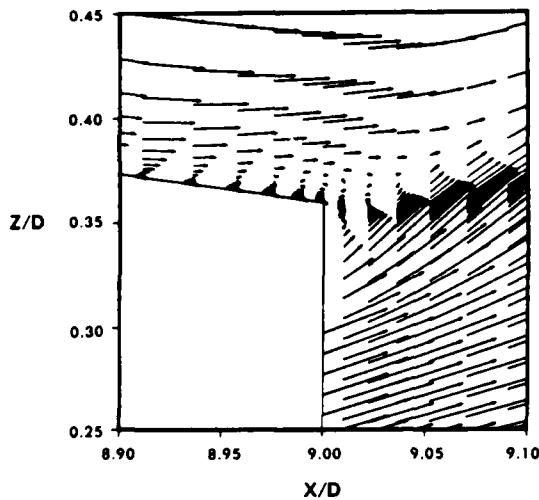


Figure 13b. Velocity Vectors Expanded Near the Base Corner,
 $M_\infty = 2.0$, $M_j = 2.5$, $P_j/P_\infty = 9.0$

The effect of the centered propulsive jet on the base region flow field is shown in Figures 11-13 for $P_j/P_\infty = 1, 3$ and 9 , respectively. Figure 11a shows the velocity vectors in the near wake for a pressure ratio of 1 . It shows the shock structure in the base region flow field and indicates the presence of a small recirculation region. This small separation bubble is a region of counter clockwise recirculating flow and can be seen clearly near the base corner as shown in Figure 11b. Similar features can be seen for the pressure ratio, $P_j/P_\infty = 3$ as shown in Figure 12. In both

Figures 11 and 12, one can observe the oblique compression shock wave at the end of the afterbody and the barrel shock inside the plume indicated by the turning of the velocity vectors. Figure 13a shows the velocity vectors for the high pressure ratio case of $P_j/P_\infty = 9$. The shape of the plume is clearly shown. An expanded view of the flow field near the end of the afterbody and the base corner is shown in Figure 13b.

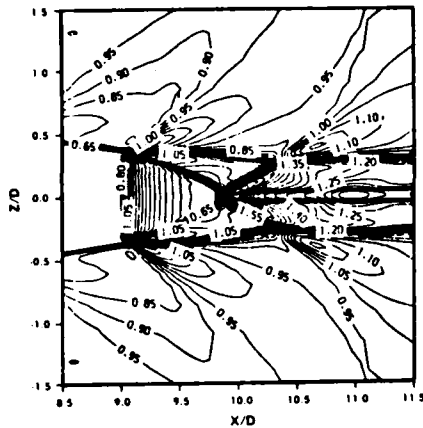


Figure 14. Computed Density Contours;
Experimental Schlieren Photograph,
 $M_\infty = 2.0$, $M_j = 2.5$, $P_j/P_\infty = 1.0$

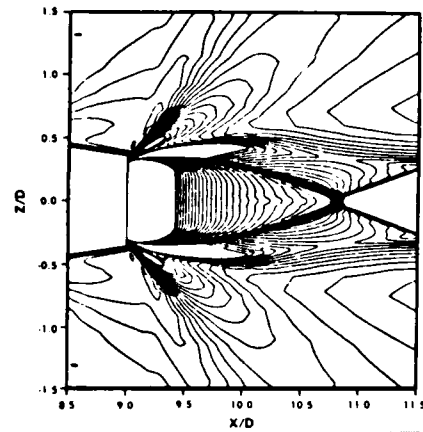


Figure 15. Computed Density Contours;
Experimental Schlieren Photograph,
 $M_\infty = 2.0$, $M_j = 2.5$, $P_j/P_\infty = 3.0$

This figure shows an extensive region of flow separation upstream of the base corner. The small separation bubble seen downstream of the base corner for the lower pressure ratio case is virtually eliminated. The separation bubble upstream of the base corner is confined to the boundary layer on the afterbody. Additionally, the compression shock wave seen at the end of the afterbody with the lower jet pressure has now moved further upstream of the base corner with the high jet exit pressure.

The next three Figures 14-16 show the comparisons of the computed density contours and the experimental Schlieren pictures for jet-on cases, $P_j/P_\infty = 1, 3$ and 9 , respectively. These Schlieren photographs are for the same geometry and flow conditions obtained from the experimental study of Agrell, et al (10). Figure 14 shows the results for the jet pressure ratio of 1. The flow features of interest are the oblique shock at the end of the afterbody, the trailing shock system inside the plume and the slip line that emanates from the nozzle lip and defines the jet boundary. The trailing shock inside the plume closes about $1/2$ cali-

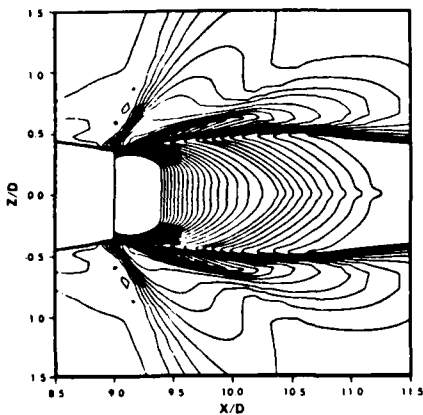


Figure 16. Computed Density Contours;
Experimental Schlieren Photograph,
 $M_\infty = 2.0$, $M_j = 2.5$, $P_j/P_\infty = 9.0$

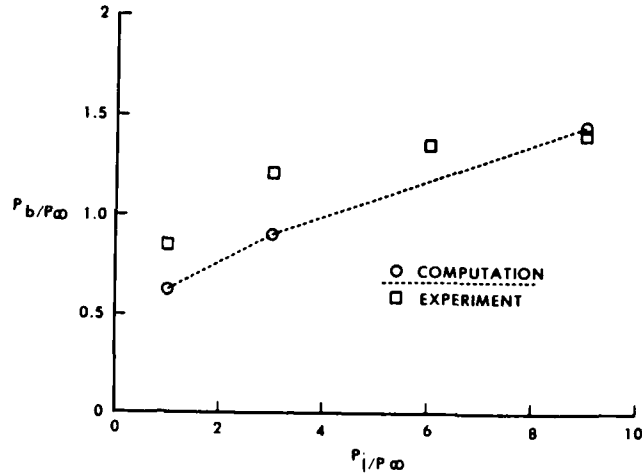


Figure 17. Variation of Base Pressure with Jet Pressure,
 $M_\infty = 2.0$, $\alpha = 0$

ber downstream of the exit plane and results in a Mach reflection. As the jet-to-free-stream pressure ratio is increased to 3.0, the trailing shocks inside the plume cross each other about 2-calibers downstream of the base (see Figure 15). Other features are similar to the case of pressure ratio one. Details of the flow features in the base region are changed as the jet exit pressure ratio is increased to 9.

The trailing shock system seen with the lower pressure ratios are not observed in both the computations and experiment (see Figure 16). For this higher jet pressure ratio, one can observe a lambda shock near the base corner which induces a separation region on the afterbody just upstream of the base corner. The agreement between the computed and the experimentally observed flow features is excellent for all jet-on conditions.

Quantitatively, one is interested in how the complex flow field in the base region affects the base pressure. The centered jet affects the base region flow field considerably and, thus, has a strong effect on the base pressure. The effect of the jet on the base pressure for various jet to free stream pressure ratios is shown in Figure 17. The trend of increasing base pressure with increasing jet pressure seen experimentally is clearly predicted by the numerical solutions. Good agreement is found at the high pressure ratio. Some disagreement, however, is observed at the lower pressure ratios.

As previously mentioned, the solution is marched in time until a steady state result is obtained. A typical converged solution required approximately 1400-1600 time steps which resulted in about an hour of CPU time on CRAY 1S. The present computations have not taken full advantage of the vector capability of the CRAY computer. With full vectorization, it is anticipated that the computation time can be reduced to 20 minutes. With the advent of even faster machines such as CRAY X-MP and CRAY 2, the eventual computational time can potentially be reduced to ten minutes or less.

V. CONCLUDING REMARKS

The research effort presented in this paper is part of an overall program to develop a sophisticated predictive capability for projectile aerodynamics. A new computational capability has been developed to compute the base region flow field at transonic and supersonic speeds using a unique flow field segmentation procedure. A computational study has been made for transonic flow over a cylindrical missile afterbody and supersonic flow over a boattailed afterbody in the presence of a centered propulsive jet. Increased grid resolution with faster computational speed was obtained by performing the computations on a CRAY 1S computer.

Various jet pressures were considered to study the effect of the jet on the base region flow field and on the base pressure. The grids in the base region were adapted to the free shear layer as the solutions developed. Qualitative features of the base region flow field such as the recirculation region, complex shock structures and plume shape seen experimentally were very well observed in the computed results. The effect of the jet on the base pressure has been predicted and compares favorably with experiment. The accuracy of these numerical predictions should improve further as turbulence modeling improves. This technique can also be easily extended to three dimensional flow situations where other technique such as component modeling may fail.

The present results indicate that the thin-layer Navier-Stokes computational technique has the potential of providing the capability to accurately predict the base region flow fields of projectiles and missiles at transonic and supersonic speeds.

REFERENCES

1. Korst, H.H., "A Theory for Base Pressures in Transonic and Supersonic Flow," Journal of Applied Mechanics, December 1956.

SAHU

2. Chow, W.L., "The Effect of Boattailing of a Projectile in Transonic Flow," Proceedings of the Third Symposium on Numerical and Physical Aspects of Aerodynamic Flows, Long Beach California, June 1985.
3. Sahu, J., Nietubicz, C.J. and Steger, J.L., "Navier-Stokes Computations of Projectile Base Flow with and without Base Injection," AIAA Journal, Vol. 23, No. 9, September 1985, pp. 1348-1355.
4. Sahu, J. and Nietubicz, C.J., "Numerical Computation of Base Flow for a Missile in the Presence of a Centered Jet," AIAA Paper No. 84-0527, January 1984.
5. Nietubicz, C.J., Pulliam, T.H. and Steger, J.L., "Numerical Solution of the Azimuthal-Invariant Thin-Layer Navier-Stokes Equations," AIAA Journal, Vol. 18, No. 12, December 1980, pp 1411-1412.
6. Beam, R. and Warming, R.F., "An Implicit Factored Scheme for the Compressible Navier-Stokes Equations," AIAA Paper No. 77-645.
7. Pulliam, T.H. and Steger, J.L., "On Implicit Finite-Difference Simulations of Three-Dimensional Flow," AIAA Journal, Vol. 18, No. 2, February 1980, pp. 159-167.
8. Baldwin, B.S. and Lomax, H., "Thin-Layer Approximation and Algebraic Model for Separated Turbulent Flows," AIAA Paper No. 78-257, 1978.
9. Petrie, H.L. and Walker, B.J., "Comparison of Experiment and Computation for a Missile Base Region Flowfield with a Centered Propulsive Jet," AIAA Paper No. 85-1618, July 1985.
10. Agrell, J and White, R.A., "An Experimental Investigation of Supersonic Axisymmetric Flow Over Boattails Containing a Centered Propulsive Jet," FFA Technical Note AU-913, 1974.
11. Schiff, L.B. and Steger, J.L., "Numerical Simulation of Steady Supersonic Viscous Flow," AIAA Journal, Vol. 18, No. 12, December 1980, pp. 1421-1430.

SANDMEYER

OPTIMUM AIMING OF ARTILLERY INDIRECT FIRE

*Richard S. Sandmeyer, Mr.
U.S. Army Materiel Systems Analysis Activity
Aberdeen Proving Ground, Maryland 21005-5071

I. Introduction

A number of procedures have been proposed for selecting patterns of aimpoints for field artillery pieces when delivering indirect fire with conventional, unguided munitions against an area target. The present author was inspired to do original research on this subject after studying both the US Army Battery Computer System (BCS) and the Russian Fendrikov-Yakovlev[2] aiming algorithms. One finding was that both algorithms are suboptimal in terms of expected casualty production; the BCS algorithm is sometimes quite poor. (See examples.)

This paper outlines a method for selecting optimal patterns of aimpoints. It includes some examples (using fictitious, unclassified data) comparing expected casualties produced using optimal aimpoints to those produced using BCS generated aimpoints. A significant increase in artillery effectiveness (casualty production) results from optimal aimpoint patterns.

The mathematical techniques (Gibb's method, surface fitting, steepest descent, etc.) used in this paper certainly did not originate with the author; however, the author believes that their application to selecting optimal aimpoints for indirect artillery fire is original.

II. Statement of Problem

The lethality of an artillery round is represented by its probability of kill function. Let $P_k(x,y)$ be the probability that a target element located at coordinates (x,y) in the ground plane is killed (or damaged to some specified level) by a round bursting at or (for air bursts) above the origin. (The term target is used in this paper to mean a set of target elements [such as personnel, tanks, trucks, etc.] distributed over an area

small enough to be attacked by conventional artillery fire. This paper assumes a homogeneous target; that is, all target elements are of the same type.) The method of this paper applies to any of the common forms of the P_K function with varying computational efficiency.

Conventional unguided artillery fire is plagued by delivery errors which are grouped into two classes: those that are repeated by all rounds fired on a given occasion (mean point of impact or MPI errors) and those that vary from round to round (precision errors). Delivery errors of each type are treated by resolving them into range (y-axis) and deflection (x-axis) components and defining a joint probability density function for these two components. Let $h(x,y)$ and $g(x,y)$ be respectively the joint probability density functions (pdf) for the MPI and precision error distributions.

Next, let $t(x,y)$ be the target density at the point (x,y) in the ground plane. t is normalized so that

$$\int_{-\infty}^{\infty} \int_{-\infty}^{\infty} t(x,y) dx dy = 1. \quad (II.1)$$

With this definition, integrating t over any subregion of the ground plane gives the fraction of the target in that region. (Using t so normalized means that the expected casualties will actually be expected fractional casualties; that is, the expected fraction of the target elements killed.) One can represent a very general layout of target elements by appropriate choice of t ; however, the most common form (because of computational considerations) of t is a positive constant value for points inside a rectangle and zero for points outside.

Next suppose that (a_i, b_i) for $i=1, 2, \dots, N_r$ are the aimpoints for N_r rounds delivered with precision errors according to joint pdf g and MPI errors according to joint pdf h . Let w_i, z_i be the precision errors in deflection and range respectively for the i th round and let (u, v) be the MPI errors in deflection and range respectively on this occasion; thus, the round aimed at (a_i, b_i) will burst at $(a_i + w_i + u, b_i + z_i + v)$ because of the errors.

The quantities defined above are now combined to obtain the mathematical formula for expected fractional casualties E (derivation in [8] and [9]):

$$E = \int_{-\infty}^{\infty} \int_{-\infty}^{\infty} \int_{-\infty}^{\infty} \int_{-\infty}^{\infty} t(x,y) \left(1 - \prod_{i=1}^{N_r} \left\{ 1 - \int_{-\infty}^{\infty} \int_{-\infty}^{\infty} P_K(x - a_i - w_i - u, y - b_i - z_i - v) g(w_i, z_i) dw_i dz_i \right\} h(u,v) du dv \right) dx dy \quad (II.2)$$

SANDMEYER

To simplify notation, define:

$$t^*(x,y) = \int_{-\infty}^{\infty} \int_{-\infty}^{\infty} t(x+u, y+v) h(u,v) du dv \quad (II.3)$$

$$P_K^*(x,y) = \int_{-\infty}^{\infty} \int_{-\infty}^{\infty} P_K(x-w, y-z) g(w,z) dw dz \quad (II.4)$$

with these definitions, (II.2) can be rewritten as:

$$E = \int_{-\infty}^{\infty} \int_{-\infty}^{\infty} t^*(x,y) \left(1 - \prod_{i=1}^{N_r} \{1 - P_K^*(x-a_i, y-b_i)\} \right) dx dy \quad (II.5)$$

The problem then is to choose aimpoint coordinates (a_i, b_i) for $i = 1, 2, \dots, N_r$ which maximize E subject to the constraints imposed by specifying the round P_K function, delivery error distribution pdfs g and h , target density function t , and the number of rounds N_r .

III. Solution

The selection of optimal aimpoints proceeds in three phases: First, the problem constraints are relaxed to allow the application of Gibb's method from calculus of variations to obtain an optimal munition density surface and an associated non-trivial upper bound on the expected fractional casualties that can be obtained with any aiming policy subject to the imposed constraints. Second, a surface fit determines how many rounds to fire at each of a set of closely spaced potential aimpoints in order to best approximate the optimal munition density surface; this fit can be done either in the Chebyshev norm via integer linear programming or by obtaining a least squares fit. Third, the aimpoints obtained by phase two are used as initial values in a steepest descent algorithm to converge to the optimal aimpoints.

In order to apply the method of this paper, it is sufficient that (1) the convolution of P_K and g be a continuous, non-negative function not identically equal to zero, (2) the convolution of t and h be a continuous, non-negative function not identically equal to zero, and (3) the expression for E in (II.5) have continuous first partial derivatives with respect to the a_i s and b_i s. The first two phases of the method can be applied to give "near optimal" aimpoints even if only (1) and (2) are satisfied.

A. Calculus of Variations

SANDMEYER

The problem is to maximize E as defined in (II.5). To apply Gibb's method, define:

$$\begin{aligned} f(x,y) &= -\ln \left(\prod_{i=1}^{N_r} \{1-P_K^*(x-a_i, y-b_i)\} \right) \\ &= -\sum_{i=1}^{N_r} \ln \{1-P_K^*(x-a_i, y-b_i)\} \end{aligned} \quad (III.1)$$

Then (II.5) can be re-written as:

$$E(f) = \int_{-\infty}^{\infty} \int_{-\infty}^{\infty} t^*(x,y) (1-\exp\{-f(x,y)\}) dx dy \quad (III.2)$$

Unfortunately, it is not easy to choose f to maximize $E(f)$ if (III.1) must be satisfied; however, if one integrates both sides of (III.1) to obtain:

$$\int_{-\infty}^{\infty} \int_{-\infty}^{\infty} f(x,y) dx dy = - \sum_{i=1}^{N_r} \int_{-\infty}^{\infty} \int_{-\infty}^{\infty} \ln \{1-P_K^*(x-a_i, y-b_i)\} dx dy \quad (III.3)$$

and requires only that f satisfy the resulting equation (and be continuous and non-negative), then the problem is comparatively straightforward to solve.

$$- \int_{-\infty}^{\infty} \int_{-\infty}^{\infty} \ln \{1-P_K^*(x-a_i, y-b_i)\} dx dy \quad (III.4)$$

is translation invariant; that is, its value is independent of (a_i, b_i) . If that value is denoted as R , then the right hand side of (III.3) can be written as $N_r \cdot R$.

Thus the problem is to find the non-negative, continuous function f^* which maximizes $E(f)$ as defined by (III.2) subject to the constraint (III.3). Gibb's method from calculus of variations can be applied to solve this problem; there is not space to include the steps here but they are in [6] and [8]. It suffices to note that a solution exists and that it is of the form:

$$f^*(x,y) = \begin{cases} \ln t^*(x,y) - \ln Q & \text{when } t^*(x,y) > Q \\ 0 & \text{otherwise} \end{cases} \quad (III.5)$$

where Q is defined implicitly by substituting f^* in the constraint equation (III.3) to obtain:

$$\int_{-\infty}^{\infty} \int_{-\infty}^{\infty} \{\ln t^*(x,y) - \ln Q\}^+ dx dy = N_r \cdot R \quad (III.6)$$

(Q is then evaluated using a numerical root-finding algorithm.)

Since any function f satisfying (III.1) also satisfies (III.3) (but not vice versa), it follows that f^* is the optimal function over a larger class of functions than originally desired; hence, $E(f^*)$ is a usually unattainable, non-trivial upper bound on $E(f)$ for any f satisfying (III.1), and $z=f^*(x,y)$ defines the optimal munition density surface to which fits shall be made to approximate f^* .

B. Surface Fitting

The next phase in obtaining optimal aimpoints is to fit the contributions of N_r individual rounds to the optimal munition density surface defined by $z=f^*(x,y)$.

In the previous sections, aimpoints were not required to be distinct; however, it is now notationally convenient to consolidate identical aimpoints. Without loss of generality, let (a_j, b_j) for $j=1,2,\dots,N'$ be distinct aimpoint coordinates and let c_j be the multiplicity of the j th aimpoint (i.e., the number of rounds to be aimed at it.) Clearly, c_j must be a non-negative integer, and the c_j s must sum to N_r .

Now suppose that there existed aimpoints such that f^* actually satisfied (III.1). Using the new notation, one would then have:

$$f^*(x,y) = -\sum_{j=1}^{N'} c_j \ln\{1-P_K^*(x-a_j, y-b_j)\} \quad (\text{III.7})$$

If (III.7) held for some choice of a_j, b_j , and c_j for $j=1,2,\dots,N'$, then that would define the optimal aiming pattern and the upper bound on expected fractional casualties would actually be attained; however, this rarely happens. So the second phase of the method is to restrict aimpoints to a specified set $\{(a_j, b_j) \text{ for } j=1,2,\dots,N_p\}$ of potential aimpoints and to find c_j values which then provide the best fit in some sense to the optimal munition density surface. If this set of potential aimpoints is chosen so as to be closely spaced throughout the support of f^* (limited only by computer memory and processing time), then the resulting fit will be very good. (The c_j value found by the surface fit is the number of rounds to be fired at the j th potential aimpoint to obtain an approximation to the optimal munition density surface. A c_j value of zero indicates that the j th potential aimpoint is not used.)

To simplify notation, define:

$$q_j(x,y) = -\ln\{1-P_K^*(x-a_j, y-b_j)\} \quad (\text{III.8})$$

then (III.7) becomes:

$$f^*(x,y) = \sum_{j=1}^{N_p} c_j q_j(x,y) \quad (\text{III.9})$$

It is computationally most efficient to make the fit on a discrete, finite set of fit points $\{(d_i, r_i) \text{ for } i=1,2,\dots,M_e\}$ chosen to form a pattern of points closely spaced over the support of the function f^* .

Thus the problem now is to find c_j which provide a best fit in some sense for the set of equations:

$$f^*(d_i, r_i) = \sum_{j=1}^{N_p} c_j q_j(d_i, r_i) \quad (\text{III.10})$$

where $i=1,2,\dots,M_e$ (j now runs over all potential aimpoints).

This can be put into matrix notation by defining:

A to be the M_e by N_p matrix whose ij th element (A_{ij}) is $q_j(d_i, r_i)$,

C to be the N_p -vector whose j th element (C_j) is the (unknown) c_j value, and

B to be the M_e -vector whose i th element (B_i) is $f^*(d_i, r_i)$.

The problem then becomes: Find the N_p -vector C which provides the best fit for the equation $A \cdot C = B$ (or equivalently minimizes $A \cdot C - B$) in some sense. Two approaches have been used here with about equal success.

1. Mixed Integer Linear Programming to Minimize the Chebyshev Norm of the Vector $A \cdot C - B$.

Define ϵ to be the Chebyshev norm of the M_e -vector $A \cdot C - B$:

$$\epsilon = \max_i \left| \sum_{j=1}^{N_p} A_{ij} C_j - B_i \right| \quad (\text{III.11})$$

Now one would like to choose C_j values to minimize ϵ . At first glance that may appear difficult, however, (III.11) implies

$$-\epsilon < \sum_{j=1}^{N_p} A_{ij} C_j - B_i < \epsilon \quad (\text{III.12})$$

for every i . If one renames ϵ to be c_0 , and regards it as one more unknown variable, then the problem becomes[3]:

minimize c_0

subject to the constraint set:

$c_j > 0$ for $j=0,1,2,\dots,N_p$,

SANDMEYER

c_0 real,

c_j integer for $j=1,2,\dots,N_p$,

$$c_0 + \sum_{j=1}^{N_p} A_{ij} c_j > B_i \text{ for } i=1, 2, \dots, M_e,$$

$$c_0 - \sum_{j=1}^{N_p} A_{ij} c_j > -B_i \text{ for } i=1, 2, \dots, M_e, \text{ and}$$

$$\sum_{j=1}^{N_p} c_j = N_r$$

This is now simply a mixed-integer linear programming problem which can be solved for the c_j s using the branch-and-bound technique [5] available in many linear programming computer packages [1].

2. Non-Negative Least Squares Fit Followed by Forcing the Results to Be Integers

The less elegant method from a theoretical standpoint is to find c_j values such that $A \cdot C = B$ is fit as well as possible in the sense of least squares while requiring that the c_j be non-negative and sum to N_r [4]. The least squares fit technique does not result in integer values for the c_j ; however, one can modify the resulting c_j to obtain integer values.

A simple rounding off is not acceptable because of the constraint that the c_j s sum to N_r ; therefore, to make integers of the c_j s, first order them by decreasing fractional part, truncate them, and then, in order, add one to as many as possible until they total N_r .

Although this second approach is much less elegant than the mixed-integer linear programming approach, it is much faster computationally and gives results that (according to experience) are just as good.

C. Steepest Descent Technique

Having found an optimal munition density surface in phase one and a fit of individual rounds to it in phase two, one now has a set of points at which to aim the rounds. These points are used as initial values in applying the steepest descent algorithm to $-E$ to converge to a minimum (E as in (II.5)). Of course, minimizing $-E$ is equivalent to maximizing E .

SANDMEYER

The steepest descent method is included in many computer software libraries and is documented in textbooks [7] so an exposition is unnecessary here. One merely writes a computer program which evaluates $-E$ as a function of the $2N_F$ variables a_j, b_j (as in (II.5)) and then initiates the steepest descent algorithm using as initial values the aimpoints obtained by the surface fit of phase two (with each of the phase two aimpoints included according to its multiplicity as an aimpoint.)

There are three reasons why this three phase solution process is superior to simply finding optimal aimpoints by omitting phases one and two and just starting the steepest descent algorithm with arbitrary initial a^i and b^i values and letting it converge:

First, it is more computationally efficient than starting from an arbitrary set of initial aimpoints which would often require more iterations of the steepest descent technique than starting from the "near" optimal aimpoints obtained in phase two.

Second, by omitting the first phase, one would not have the upper bound $E(f^*)$ against which to measure optimality. By having this upper bound, one can stop (or not even begin) the steepest descent algorithm when aimpoints have been found that produce a value of E within some tolerance of the upper bound. In fact, when this tolerance is set to .025, most cases will not even require the steepest descent technique; that is, the aimpoints produced by phase two achieve casualties greater than .975 of the upper bound without even using the expensive, time-consuming steepest descent technique.

Third, one cannot rule out the possibility that the steepest descent technique might converge to some local extreme point different from the global one. By using the near optimal set of initial aimpoints from the phase two surface fit, one reduces that possibility. (One can never completely guarantee that for some sufficiently pathological P_k and t functions the steepest descent algorithm will not converge to a non-global extreme point.)

Application of this three phase method has produced, in all cases examined, aimpoint patterns whose expected fractional casualties are within a few percent of the theoretical upper bound and which are superior to expected fractional casualties produced by either the BCS or the Fendrikov-Yakovlev aimpoint patterns.

IV. Examples

SANDMEYER

Three examples of artillery fire missions are included to compare the expected fractional casualties produced using the Battery Computer System (BCS) aimpoint patterns to those produced by the optimal aimpoint pattern process (OPT) described in this paper.

The examples use fictitious, unclassified data. However, the data were chosen to exhibit the range of phenomena that can occur. In some cases the OPT aimpoints produce results far superior to the BCS aimpoints whereas in other cases the superiority is very small indeed; however, in no case has BCS ever performed better than OPT. A plot is included of the results for each example, and there is a page summarizing the data used in the examples.

With four weapons firing against a target with dimensions as in example 1, BCS would select four aimpoints as in figure 1a and fire one-fourth of the N_r rounds at each aimpoint. OPT would select its aimpoints differently depending on the value of N_r . Figure 1b shows the pattern of aimpoints used by OPT with 12 rounds. As one can see from figure 1c which gives the expected fractional casualties for each aiming policy (OPT and BCS) as a function of the number of rounds fired, OPT is only slightly better than BCS in this case. The curve labeled UB is the theoretical upper bound on expected fractional casualties which could only be attained by a perfect fit to the optimal munition density surface. Note that the OPT curve is quite close to the UB curve.

For a target with dimensions as in example 2 and with six weapons, BCS would select aimpoints as in the figure 2a and fire one-sixth of its rounds at each aimpoint. For the same target, OPT would select its aimpoints as in figure 2b when $N_r=12$. In this case, the OPT curve is noticeably above (better than) the BCS curve, and the OPT curve is now indistinguishable from the UB curve.

Finally, for a target as in case 3 and with six weapons, BCS would aim in a row as in figure 3a with one-sixth of N_r rounds fired at each aimpoint. For the same case, OPT would choose aimpoints as in figure 3b for $N_r=12$ rounds. In this case, the OPT curve is far above (superior to) the BCS curve, and again the OPT curve is indistinguishable from the UB curve.

There are three fundamental reasons why the BCS curves are suboptimal: (1) BCS concentrates all rounds on four or six aimpoints resulting in overkill in some parts of the target and little damage in others, (2) BCS does not take into account delivery errors in its selection of aimpoints (thus there is often no spreading of aimpoints along the axis of largest error in order to insure that at least some rounds land on target), and (3) BCS does not take into account the P_k function of the round in spacing the aimpoints. In fact the only things BCS does take into account in selecting aimpoints are the number of weapons firing and the target dimensions.

SANDMEYER

In fairness, it must be remembered that the artillery commander could decide to exercise judgement and use an alternative aiming technique in cases where BCS aimpoints are deemed inappropriate. Also doctrine calls for breaking very large targets into several small ones so the BCS would not recommend that a four weapon fire unit attack a 400m by 600m target with only four aimpoints. However, even making these concessions to BCS, it remains true that BCS would make the aiming recommendations in the examples here and, unless the commander intervened to spread the aimpoints out some in range, it would achieve very suboptimal effects in example 3.

V. Practicality of Optimal Aimpoint Patterns

The real advantages that BCS enjoys over the optimal aiming process described here are (1) it does not require that a weapon shift aimpoints between rounds as OPT frequently does, and (2) it requires much less time to calculate the aimpoint coordinates. The optimal aiming process requires typically two minutes of computer time on a Control Data Corporation CYBER 76 mainframe computer; it would require much more time on a BCS.

Thus it appears that the optimal aiming process will be of practical value only when very high speed integrated circuits and massive exploitation of parallel processing are incorporated into future artillery computers to bring the computation time down to a few seconds.

The other problem of shifting aimpoints between rounds is not so serious provided the sequence of gun (or rocket launcher) settings necessary for the optimal aiming pattern can be rapidly executed by each gun. That should be possible with digital gun displays and a good communications link between a fast artillery computer and the individual guns.

This author recommends that the next generation of artillery computers incorporate an optimal aiming algorithm, or if the computing power is not adequate, then at least an improvement on the BCS aiming pattern algorithm to account better for delivery errors, overkill, and lethality of the round being fired.

In summary, indirect fire with conventional, unguided artillery can be made significantly more effective by optimal aiming. However, full application of optimal aimpoints will have to wait for much faster artillery computers. Hence, this is a clear case where technology now on the horizon can be applied to increase the field artillery soldier's combat effectiveness. In the meantime, the optimal aiming procedure outlined here provides a benchmark against which to compare other aiming policies such as that in the current BCS.

Data for Examples

In all three case, the P_K function was the Carleton damage function thus:

$$P_K = \frac{A_L}{2\pi S_1 S_2} \exp \left\{ -\frac{1}{2} \left[\left(\frac{x}{S_1} \right)^2 + \left(\frac{y}{S_2} \right)^2 \right] \right\}$$

where A_L is the lethal area or mean area of effects of the round and S_1 and S_2 are pseudo-standard deviations which determine the spread of the damage in deflection and range respectively.

P_K function:	example 1	example 2	example 3
A_L (m ²)	1200	350	200
S_1 (m)	69.1	17.8	25.2
S_2 (m)	13.8	4.5	4.2

The delivery error distributions (both MPI and Precision) were bivariate normal with mean point (0,0) and no correlation between deflection and range.

Delivery Errors:	example 1	example 2	example 3
MPI error			
std dev defl (m)	20	30	20
std dev range (m)	100	140	100
Precision error			
std dev defl (m)	2	8	4
std dev range (m)	40	20	12
Target Location Error (absorbed into MPI error before applying the optimum aimpoint procedure)			
CEP (m)	150	75	50

In all cases, the target is a rectangle centered at (0,0). The resulting target density function is equal to zero for points outside the rectangle and equal to the reciprocal of the area of the rectangle for points inside the rectangle.

Target Dimensions:	example 1	example 2	example 3
deflection (m)	200	150	150
range (m)	100	75	10
Number of weapons:	example 1	example 2	example 3
	4	6	6

SANDMEYER

EXAMPLE 1

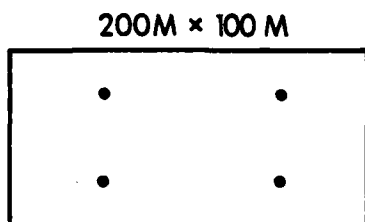


Figure 1a. BCS Aimpoints

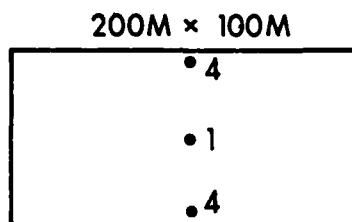
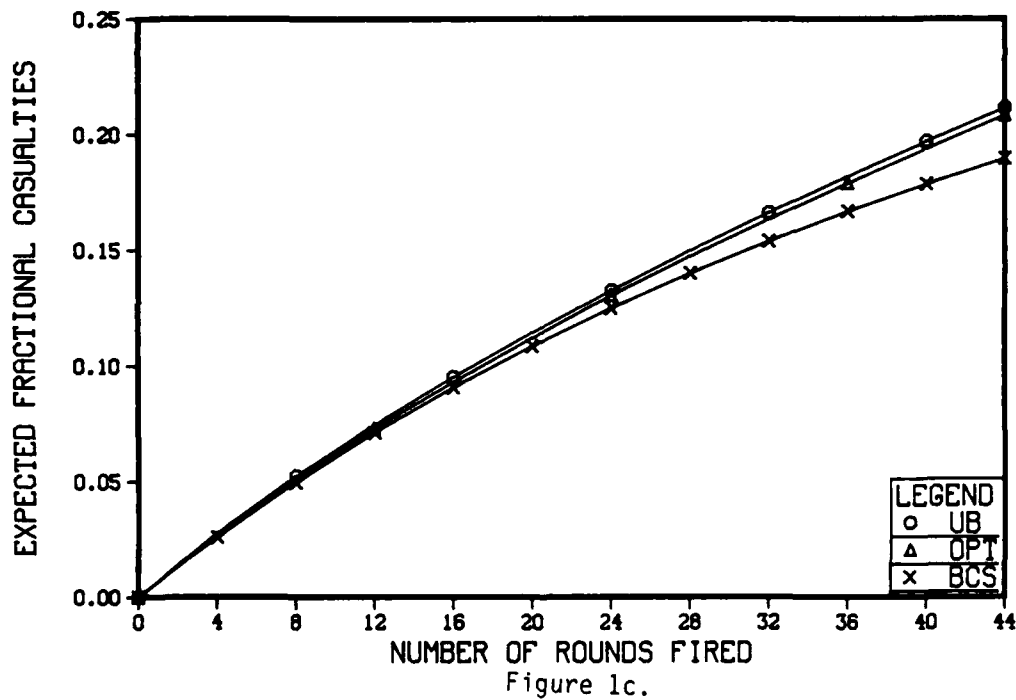


Figure 1b. OPT Aimpoints with multiplicities, $N_r=12$

ARTILLERY AIMING PATTERN EFFECTIVENESS 200 M BY 100 M RECTANGULAR TARGET -- 4 WEAPONS FIRING



EXAMPLE 2

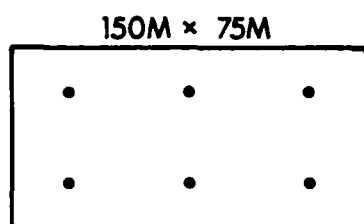


Figure 2a. BCS Aimpoints

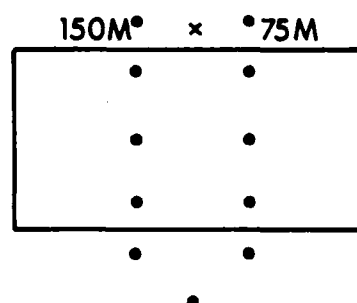
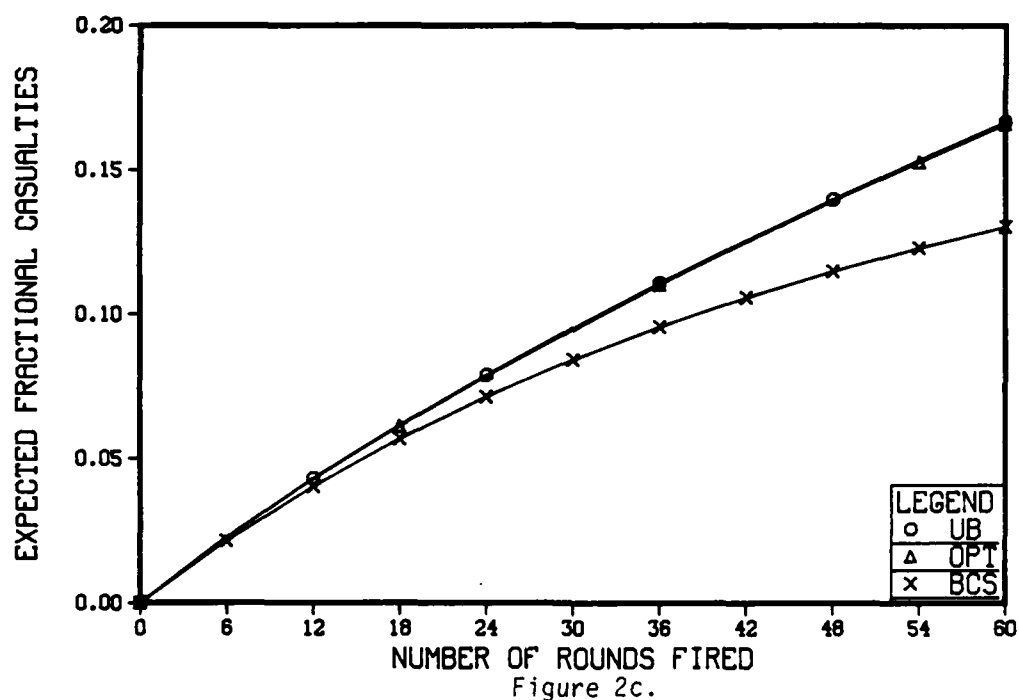


Figure 2b. OPT Aimpoints for $N_r=12$

ARTILLERY AIMING PATTERN EFFECTIVENESS
150 M BY 75 M RECTANGULAR TARGET -- 6 WEAPONS FIRING



SANDMEYER

EXAMPLE 3



Figure 3a. BCS Aimpoints

Figure 3b. OPT Aimpoints
for $N_r=12$

ARTILLERY AIMING PATTERN EFFECTIVENESS 150 M BY 10 M RECTANGULAR TARGET -- 6 WEAPONS FIRING

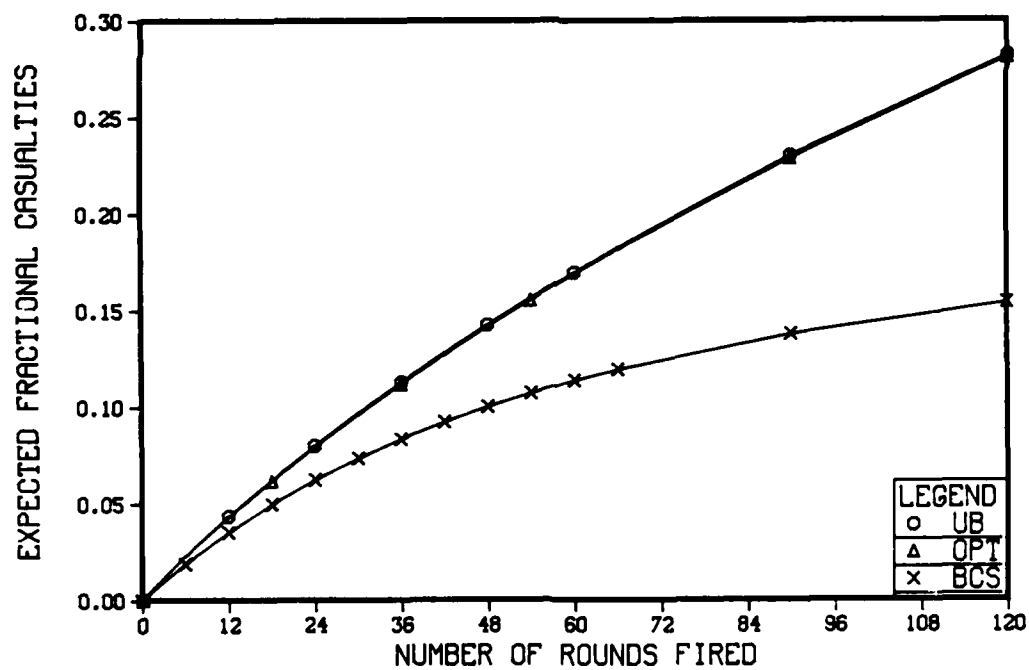


Figure 3c.

SANDMEYER

BIBLIOGRAPHY

1. APEX-IV REFERENCE MANUAL, Control Data Corporation, 1982-83, unclassified
2. Fendrikov, N.M., and V.I. Yakovlev, Methods for Calculating Combat Effectiveness of Armament, original Russian book translated into English by US Department of Commerce, National Technical Information Service, JPRS-56631, July 1972, unclassified
3. Franklin, Joel, "Mathematical Methods of Economics", The American Mathematical Monthly, Vol 90, No. 4, April 1983, unclassified
4. Lawson, C.L., and R.J. Hanson, Solving Least Squares Problems, Prentice-Hall, 1974, unclassified
5. Hillier, F.J., and G.J. Lieberman, Operations Research, Holden-Day, third edition, 1980, unclassified
6. Koopman, Bernard O., "Search and Its Optimization", The American Mathematical Monthly, Vol 86, No. 7, August-September 1979, unclassified
7. Luenberger, David G., Linear and Nonlinear Programming, Addison-Wesley, second edition, 1984, unclassified
8. Sandmeyer, Richard S., Optimum Aiming of Artillery Indirect Fire: Part I -- Statement of Problem and an Upper Bound on Effectiveness, US Army Materiel Systems Analysis Activity, Interim Note G-150, (now in final preparation for publication), unclassified
9. Snow, Roger, and Margaret Ryan, A Simplified Weapons Evaluation Model, The RAND Corporation, RM-5677-1-PR, 1970, unclassified

SARDELIS & BOOBAR

PESTICIDE DISPERSAL UNIT (PDU), MULTICAPABILITY,
HELICOPTER SLUNG (U)

* MICHAEL R. SARDELIS, SGT
LEWIS R. BOOBAR, CPT
US ARMY MEDICAL BIOENGINEERING RESEARCH AND
DEVELOPMENT LABORATORY
FORT DETRICK, FREDERICK, MD 21701-5010

INTRODUCTION

Preventive medicine units and installations have a requirement to aerielly disperse both liquid and solid pesticides to control arthropod disease vectors and pest insects. The helicopter mounted pesticide sprayer currently in the Army's inventory is no longer suitable for military use because it is incompatible with new models of helicopters, it is unable to disperse solid pesticides, and creates the possibility of pesticide contamination to aircraft and crew. To materially improve the Army's technical capability, a program was initiated at the US Army Medical Bioengineering Research and Development Laboratory (USAMBRDL) to develop and type classify two helicopter slung units, one with liquid, and the other with solid dispersal capability. In 1983, the USAMBRDL developed a Pesticide Dispersal Unit (PDU), Multicapability, Helicopter Slung, which is capable of dispersing both solid and liquid pesticides.

A preliminary test using the prototype PDU was conducted at Yuma Proving Ground, AZ, where extensive flooding of the Colorado River had created an ideal habitat for the propagation of Culex tarsalis, the predominant local vector of Western Equine Encephalitis (WEE). Mosquito populations were successfully suppressed by applying solid pesticide to larval habitat and liquid pesticide to control flying adults. Positive results from this field test proved that the PDU as the only unit within the Department of Defense able to aerielly apply pesticides using four different application modes; high volume (HV), low volume (LV), ultra low volume (ULV), and solid. This report will address the PDU's capability and versatility in controlling target insects under various conditions.

METHODS AND MATERIALS

TEST ITEM DESIGN AND OPERATIONAL CHARACTERISTICS. The PDU (Figure 1) is attached to any helicopter's cargo hook using a 1.8 m (6 ft), Federal Aviation Administration (FAA) certified, nylon strap. The pesticide container is a streamline, 570 l (.7 cu m), fiberglass hopper with dorsal fin for flight stability. The self-contained PDU is powered by a ten horsepower gasoline engine and is electrically independent of the helicopter. Controls enable the operator inside the helicopter to start and stop the engine, to activate the dispersal valves, and to determine when the pesticide container (hopper) is empty.

When configured for liquid dispersal, the PDU is capable of dispensing liquid pesticide in HV (>37.2 l/ha), LV (9.3-37.2 l/ha), and ULV (<9.3 l/ha). A 9 m boom with a total of 34 sites for hydraulic nozzles is available for HV and LV application (A). Two, hydraulically powered rotary nozzles mounted on a 2.3 m boom are used for ULV application (B). In the solid configuration (C), two chutes with hydraulically actuated gates are installed. A metering plate in each chute controls flow rate. Solid material is funneled into a 42.5 cm diameter, hydraulically powered slinger for dispersal.

Additional physical and operational characteristics of the PDU are shown in Table 1.

FIELD TESTING (FT). FT was conducted to estimate the PDU's operational effectiveness in three unique sites.

Philippines (PI). An outbreak of dengue hemorrhagic fever around the Subic Bay Naval Base, and Clark Air Base served as an opportunity to evaluate the effectiveness of ULV aerial applications in urban areas. The cities of Olongapo and San Miguel, PI, were chosen as the test sites. Olongapo was sprayed in the early morning of September 24, and San Miguel was sprayed in the early morning of September 25, and the early evening of September 27, 1984. The PDU was calibrated to disperse 0.58 l/ha of technical grade (91%) malathion through 20 microns (μ), porous, plastic sleeves. Navy CH-3 (Sea King) and CH-46 (Sea Knight) helicopters served as spray aircraft. The helicopters flew at 102 kph (55 knots), while maintaining an altitude of 45 m above ground level (AGL). Twenty mosquito cages, each containing 15 unsexed *Aedes aegypti*, were placed randomly throughout the test sites in exposed areas and under eaves of buildings 15 min prior to the spraying. Caged mosquitoes were also placed outside the spray area to serve as controls. Sentinel mosquito mortality was measured 24 hrs after treatment. Comparisons between caged mosquito mortality in the treatment and control sites, and between cage locations in the test

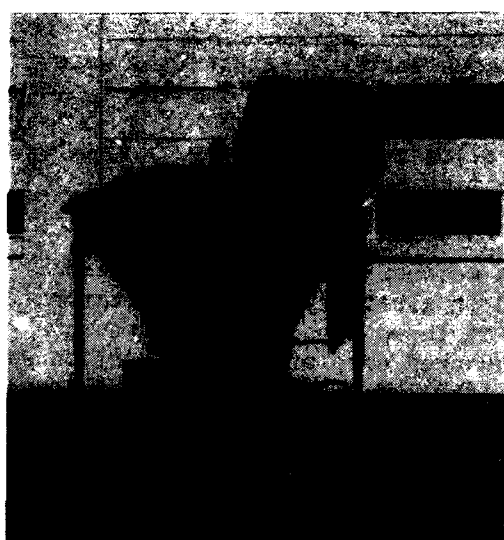


Figure 1. The Pesticide Dispersal Unit (PDU), Multicapability, Helicopter Slung: A) high and low volume configuration; B) ultra low volume (ULV) configuration; and C) solid configuration.

Table 1. Physical and operational characteristics of the PDU.

<u>Characteristic</u>	<u>Measurement</u>
Empty Weight:	
Liquid configuration	
High and low volume	169 kg (373 lbs)
Ultra low volume	164 kg (360 lbs)
Solid configuration	143 kg (315 lbs)
Dimensions:	
Length	148 cm (58 in)
Width of bucket	130 cm (51 in)
Height	
Top of bucket	152 cm (60 in)
Top of fin	205 cm (80 in)
1	
Swath width:	
High and low volume mode	91 m (300 ft)
Ultra low volume mode	61 m (200 ft)
Solid mode	61 m (200 ft)
2	
Reliability:	97%

¹Test materials were water and diatomaceous earth. Swath widths were determined with the helicopter flying 30 m above ground level.

²Reliability was determined using the following equation: $e^{-t/\theta}$ (where t = average mission time, and θ = mean time between failures.)

site were analyzed using the Chi square method. Spray droplets were collected on Teflon coated slides held in a battery operated rotator (2 slides/rotator) 1.2 m above the ground at three randomly selected locations in the treatment area. One hundred droplets/slide/location were measured, and the volume mean diameter (VMD), the diameter that divides the droplet output into two equal portions by volume, was calculated (1).

Panama. The PDU was used to determine if ULV aerially sprayed pesticide was capable of penetrating the canopy of Neotropical forest and thereby, effectively controlling mosquitoes. Approximately 40 ha of the Mojanga Forest, described by Chaniotis (2), were sprayed in the early morning and late evening of April 10, 1984. The PDU was operated in the ULV configuration with 20 μ , porous, plastic sleeves installed in the rotary nozzles. The PDU was calibrated to disperse 0.58 l/ha of technical

grade (91%) malathion. The helicopter, a UH-1 (Huey), flew at 93 kph (50 knots) forward air speed 7 m above the canopy, or approximately 45 m AGL. World Health Organization (WHO) standard exposure tubes containing Culex pipiens quinquefasciatus (sentinel mosquito cages), 20 female adults/cage, were placed randomly in the test site 1 hr prior to spraying. Sentinel cages were also placed in a control site located upwind and adjacent to the test site. Mosquito mortality was measured 24 hrs after treatment. Comparisons between mortality in the treatment and control site were made using the Chi square method. Spray droplets were collected and VMD's determined as in the Philippine's study.

Fort A.P. Hill, VA. The PDU was used to evaluate the effectiveness of aerially applied solid pesticide to suppress ticks, vectors of Rocky Mountain Spotted Fever, at the 1985 National Scout Jamboree on May 20, 1985 (3). This method had not been previously used for tick control. The PDU was calibrated to disperse 4.5 kg/ha of the granular pesticide Diazinon® 14 G to 560 ha of tick habitat bordering the campsites and activity areas to be used by the Scouts. The spray aircraft, a UH-1 flew at 74 kph (40 knots), 30 m AGL. Pretreatment surveys were conducted May 12-15, and posttreatment surveys were conducted June 4-10, 1985, using the method described by Grothaus et al (4). Tick densities were recorded 2 hr after trap placement. Comparisons between mean number of ticks per trap before and after aerial application were made using Student's t test.

RESULTS AND DISCUSSION

Olongapo and San Miguel, Philippines. The mortality of caged mosquitoes after aerial spray of urban test sites is presented in Table 2. Statistical analysis showed a significant difference between the mortality in the treated versus control sites, while mortality between cages in different locations throughout the treatment area showed no significant difference ($P < 0.05$). This homogeneity in mortality of sentinel mosquitoes in open areas and in protected areas under eaves of buildings confirms that drift of droplets is a factor in obtaining effective control from ULV aerial application of pesticides.

Mojinga Forest, Panama. Mortality of sentinel mosquitoes in the treatment site was 78% as compared to 40% in the control site. Mortality was significantly different using Chi square ($P < 0.05$). The VMD of the droplets penetrating the forest canopy was determined to be 34.5 μ . Mosquito mortality and droplet measurement indicate that ULV aerially sprayed pesticides are capable of penetrating Neotropical forests. Further aerial spray tests are necessary in this environment to further refine application methodologies, and subsequently improve target insect mortality.

Table 2. Percent mortality of sentinel mosquitoes after ULV aerial application of malathion (91%) in two urban test sites in the Philippines.

Site	Spray	VMD (μ)	Percent mortality*		χ^2
			Treatment	Control	
Olongapo	1	40.8	83	10	65.7
San Miguel	1	31.2	85	10	90.1
	2	34.6	88	14	74.0

*Treatments significantly different from controls using Chi square. (N = 15 for treatment, N = 3 for control and $P < 0.05$).

Fort A.P. Hill, VA. Mean tick densities ($\bar{X} \pm SE$) from pretreatment (60.2 ± 10.1) and posttreatment (13.5 ± 1.9) surveys were found to be significantly different by Student's t test ($N = 51$, $P < 0.05$). This data demonstrated that aerial application of granular pesticide is a feasible alternative to conventional method of tick control. This is especially evident in the large and relatively inaccessible areas that characterized this test site.

Posttreatment surveys detected pesticide at 35 of 51 locations in the test area. Measurements of the accumulated material in collection containers showed the mean application rate to be 3.6 kg/ha.

CONCLUSIONS

The PDU's design, operation and performance features exceed all military requirements. Through optimal use of lightweight materials, the PDU's weight has been reduced. The ability to apply pesticides in HV, LV, ULV, and granular modes is a unique feature. Mission times are lowered due to the PDU being a slung load. This is especially vital when aircraft availability is at a premium. Maintenance, training requirements, and cost are minimized by incorporating liquid and solid capabilities into a single unit.

SARDELIS & BOOBAR

Field tests with the PDU have shown it to be a versatile and reliable tool for the control of arthropod disease vectors. ULV aerial applications in urban areas and Neotropical forests were demonstrated to be effective. The first effort ever to control tick populations by aerial application of granular pesticide was successful. Integration of the PDU into the military system will greatly enhance the overall ability of preventive medicine units and installations to conduct effective pest management programs.

ACKNOWLEDGEMENTS

The authors express their appreciation to the Preventive Medicine Activity, USA MEDDAC, Panama; the Occupational and Preventive Medicine Department, US Naval Hospital, Subic Bay, Republic of the Philippines; and the US Army Environmental Hygiene Agency, Fort Meade, MD, for their assistance with the field testing. We also thank Mr. James Shankle for invaluable technical expertise and Ms. Sara Mizzoni for excellent secretarial support.

REFERENCES

1. Akesson, N. B. and W. E. Yates. 1982. The use of aircraft for mosquito control. Amer. Mosq. Control Assoc. Bull. No. 1.
2. Chaniotis, B. N. 1983. Improved trapping of phlebotomine sandflies (Diptera: Psychodidae) in light traps supplemented with dry ice in a Neotropical rain forest. J. Med. Entomol. 20:222-223.
3. Neidhardt, K. 1986. Tick surveillance and control. Proceedings Department of Defense Operational and Research Pest Management Workshop (In-Press).
4. Grothaus, R. H., J. R. Haskins, J. T. Reed. 1976. Simplified carbon dioxide collection techniques for the recovery of live ticks (Acarina) J. Med. Entomol. 12:702.

SATTERWHITE & RINKER

EFFECT OF SHADOWS ON THE REFLECTANCE SPECTRA
OF VEGETATION AND THEIR DIGITAL CLASSIFICATION

MELVIN B. SATTERWHITE*

JACK N. RINKER

U.S. ARMY ENGINEER TOPOGRAPHIC LABORATORIES
FT. BELVOIR, VA 22060-5546

Change in solar altitude and azimuth can substantially alter the reflectance spectra of the vegetation-soil mosaic. Aside from atmospheric considerations, solar irradiance varies in quality and quantity with solar altitude which varies diurnally, seasonally, and with latitude. Some direct results from change in solar altitude are alterations of the percentages of shaded and sunlit vegetation in the plant canopy, as well as the percentages of shaded and sunlit vegetation and soil in the vegetation-soil mosaic. Although the relations between solar altitude, solar azimuth, and solar time are well documented in standard astronomical tables and algorithms, the relations between solar altitude, plant canopy structure, shadow patterns, and reflectance changes have not been developed.

The shadow effect has two levels; a general level concerned with the percentages of sunlit and shaded vegetation and soil in the vegetation-soil mosaic, and a detailed level concerned with the percentages of sunlit and shaded vegetation within the plant canopy. The general level describes the percentages of sunlit and shaded vegetation and soil using the various factors of the plant canopy/radiometer/illumination model. These computations assume an opaque plant canopy and uniform soil surface conditions (2). The detail level is difficult to model because the canopy has a number of variables that are poorly defined. First, the numbers of each of the component parts, i.e., leaves, stems, and branches, can vary between the canopies of the same species and between different plant species. There is variation in the surface structure of each part, i.e., the leaf surface can be smooth, crenulated, wrinkled, waxy, or hairy; each of which has its own diffuse and specular scattering properties and each can introduce a fine shadow detail within the surface. There is

SATTERWHITE & RINKER

variation in the size, shape, and arrangement of the components parts, which alters the shadow structure as well as the volume scattering properties of the canopy. There is variation in the spectral reflectance and transmittance properties of the different surfaces and materials, i.e., leaf, twig, or stem; young leaf or old leaf; and topmost leaf or bottommost leaf. Finally, all of these factors can vary as a function of species, plant vigor, and geographic location.

Other things being equal, the light reflected from a sunlit or a shaded area in the plant canopy depends on the characteristics of the light illuminating the area and the reflectance, transmittance, and absorptance characteristics of the material. Shaded areas can be illuminated directly by skylight or by the sunlight and skylight that are transmitted through translucent materials or scattered from surfaces outside of the canopy. Some plant parts, particularly woody stems and branches, are opaque and their shadows are illuminated by light scattered from adjacent surfaces. Other plant parts, such as leaves, can be opaque in one spectral region and translucent in another, and contribute at least a small component of transmitted light to their shadows in addition to any scattered light.

Objective.

To determine if there are reliable relations between the reflectance spectra of semiarid plant canopies and solar altitude that can be used for modeling and to support digital analysis procedures of multi-spectral imagery.

Materials and Procedures.

Spectral measurements were made of selected plant canopies at six field study sites in Arizona and Nevada. Four semiarid shrubs, 30 to 80 cm tall, were measured: bursage, Ambrosia dumosa; greasewood, Sarcobatus vermiculatus; sagebrush, Artemisia tridentata; and shadscale, Atriplex confertifolia. Two herbaceous plant covers, 40 to 80 cm tall, were also measured: legume-grass, Thermopsis montana and Poa sp.; and alfalfa, Medicago sp. The plants selected were uniform in height and leaf cover, and were not flowering. All plants appeared vigorous and did not exhibit obvious plant stress.

SATTERWHITE & RINKER

The spectra of the Halon reference standard, sunlit vegetation, and shaded vegetation were measured using a scanning spectroradiometer with a 15 degree field of view. The spectra were measured over the 360nm to 1100nm region in 10nm bandpasses, between 0730 and 1400 true solar time. The plant canopy and the Halon were viewed vertically by the spectroradiometer. The plant surface in the radiometer's field of view (FOV) was the "same" except for the changes in the sunlit and shaded portions of the canopy caused by changes in solar altitude. Spectra were also taken of shaded plant canopies, i.e., all of the plant canopy in the radiometer's FOV, was within the shadow of an opaque object.

The vegetation spectra (V_x) were normalized to a Halon reference standard (H_x) using equation 1. The reflectance value (RV) was calculated for each 10nm bandpass (i) over the 360nm to 1100nm spectrum. The spectra of the Halon reference were taken within 5 minutes of the time (x) that the vegetation spectra were taken.

$$RV_x(i) = [V_x(i)/H_x(i)] * [H_m(i)/H_x(i)] * 100\% \quad \text{Equation 1.}$$

where: V_x = vegetation radiance value at time "x"
 H_x = Halon radiance at time "x" + 5 minutes,
 H_m = maximum Halon radiance in a 10nm bandpass
for the sample set.

The canopy's mean reflectances in Landsat Thematic Mapper band 1 (450-520nm), band 2 (520-600nm), band 3 (630-690nm), and band 4 (760-900nm) were calculated for each reflectance spectrum. The relations between solar altitude and the species mean reflectance in each Thematic Mapper bandpass were computed using regression analysis.

The near infrared (NIR)/Red and Normalized Difference Vegetation Index ratios were calculated from equations 2 and 3, using the mean reflectance values in Thematic Mapper band 3 and band 4.

$$\text{NIR/Red Ratio} = \text{Band 4} / \text{Band 3} \quad \text{Equation 2.}$$

$$\frac{\text{Normalized Difference Vegetation Index (NDVI) Ratio}}{= (\text{Band 4} - \text{Band 3}) / (\text{Band 4} + \text{Band 3})} \quad \text{Equation 3.}$$

Results.

The reflectance spectra of bursage, greasewood, sagebrush, shadscale, legume-grass, and alfalfa are shown in Figures 1, 2, 3, 4, 5, and 6. The reflectances of the sunlit canopies increased directly with solar altitude, although each sunlit canopy contained some shaded areas. The magnitude of the reflectance contrast between sunlit and shaded portions of the canopy is shown by comparing the spectra of the shaded canopy to the sunlit canopy spectra.

In the visible region, the canopy reflectances of the alfalfa and legume-grass did not show a strong direct relation to solar altitude. A slight increase, 1-4 percent (absolute basis), in visible reflectance was found, which is probably transmitted energy that was reflected from the lower surfaces. The reflectances of bursage, greasewood, sagebrush, and shadscale were strongly and directly related to solar altitude. The visible reflectance increased 4-11 percent, primarily from the high reflectance contrast between sunlit and shaded leaves and the increased percentage of sunlit leaves. Some of the increased reflectance could be due to transmitted energy that is reflected from lower surfaces, but this would be a small percentage.

In the NIR region, reflectances of the vegetation types varied directly with solar altitude, except the legume-grass. The alfalfa's reflectance increased 30 percent (relative basis) as solar altitude increased from 30 to 70 degrees. The relative increase of the other plant's reflectance was smaller: bursage, 26 percent; greasewood, 26 percent; sagebrush, 10 percent; and shadscale, 20 percent. The legume-grass did not increase over its sample period. Statistical analysis shows that the reflectance differences in the visible region were not significantly different at the 95% level of confidence. In the NIR region significant differences were found for bursage spectra taken before 0950 true solar time and for the other vegetation types for spectra taken before 0900 true solar time.

The direct relations between the mean reflectances in a Thematic Mapper band and solar altitude are described by the regression curves (solid lines) in Figure 7. The number associated with a species identifies the appropriate regression curve, bursage (#1); greasewood (#2); sagebrush (#3); shadscale (#4); legume-grass (#5); and alfalfa (#6). Each regression curve has an R square value >0.96 , except for

the legume-grass curve, which had R square values >0.70 . The legume-grass canopy was sampled between 1000 and 1300, which was not adequate for predicting canopy reflectance spectra for the early morning.

The NIR/Red and NDVI ratios associated with each species are presented in Figure 8. The species numbers are the same as those used in Figure 7. The lengths of the vertical lines indicate the range of the ratio values and the horizontal lines indicate the maximum, minimum, and mean ratio values for each vegetation type. The ratios varied as the visible and NIR reflectance contrast for the canopy varied with solar altitude. Close inspection of the spectral curves in Figures 1 to 4 shows that the relative reflectance of these plants increased slightly more in the visible region than in the NIR region over the sample period.

These ratios grouped vegetation into one of three groups;

- a) green colored species, legume-grass (#5) and alfalfa (#6), that have the highest ratio values;
- b) greenish-gray, bursage (#1) and yellow-green greasewood (#2), that have intermediate ratios, and
- c) gray colored species, sagebrush (#3) and shadscale (#4), that have the lowest ratios.

Discussion.

The shadows in the vegetation-soil mosaic result from the interaction of many parameters of the plant canopy/radiometer/illumination model. Some parameters, such as plant growth, changed slowly while other parameters changed rapidly, e.g., solar altitude. The rapidly changing parameters are more of an immediate concern, because they, in part, affect the spectral characteristics of the vegetation-soil mosaic in remotely sensed imagery acquired over a short time.

The plant canopy spectra show substantial differences within the same vegetation type, as well as between the six vegetation types. These differences result from solar altitude effects and from the reflectance, transmittance, and absorptance characteristics of the plant canopy. The visible reflectance spectra of alfalfa and legume-grass, which have

strong absorptances and low transmittances were seldom affected by changing highlight/shadow ratios caused by solar altitude changes. Alfalfa has high absorptance in the visible region and its reflectance varied only slightly, although the solar altitude ranged from 42 to 74 degrees. The plants that have less absorptance and high reflectance contrast between sunlit and shaded leaves, have strong direct reflectance-solar altitude relations. For example, the visible and the NIR reflectance spectra of sagebrush and shadscale increase directly with solar altitude, which decreased the shaded areas of the canopy surface.

In the NIR region, the leaf's reflectance and transmittance properties are important because they influence the amount of energy going into and reflecting from the shaded areas of the plant canopy. The transmitted energy on reaching the shaded leaf layer is reflected, absorbed, or transmitted according to the properties of the leaf. The NIR reflectance contrast between the fully sunlit green leaf and the first shaded green leaf can be about 30 percent, assuming 50 percent reflectance and 40 percent transmittance. As the solar altitude increases, the percentage of sunlit leaves will increase and change the percentages of the shaded leaves categorized as second, third, and fourth leaf layers in the plant canopy, and concurrently the canopy reflectance will increase.

The bursage, greasewood, sagebrush, shadscale, and alfalfa spectra show high reflectance contrasts between the sunlit and shaded canopies, despite two conditions that tend to reduce the reflectance contrast. First, the size of the shadow cast on the plant canopy was only slightly larger than the radiometer's FOV when the shaded canopy spectra were measured, and some scattered sunlight may have been included in the NIR reflectance spectra for these plants. This is suspected because of relatively high levels of infrared that show in the spectra of the shaded canopy for some plants. Second, all "sunlit" canopies are a mosaic of sunlit and shaded surfaces, all of which were viewed by the radiometer. Even so, the NIR reflectance spectra of the sunlit and shaded canopies show that any shadows in the canopy will lower the NIR reflectance from that expected for a fully sunlit canopy.

The reflectance-solar altitude relations for the 6 vegetation types were summarized by the mean reflectances in the four Thematic Mapper bandpasses. In the visible bands, the reflectances of the green colored species increased 1-4

percent (absolute basis) and those for the gray colored species increased 4-11 percent. This is attributed to the absorptance of the leaves and the reflectance contrast between the sunlit and shaded portions of the plant canopy. Because of their higher visible reflectance, the gray plants varied substantially more with solar altitude than did the reflectance of the green plants. The visible reflectance for gray species increased from 50-70 percent (relative basis) which was near the levels expected from change in shadow length, i.e., about 79 percent; $[\tan(70 \text{ degrees}) - \tan(30 \text{ degrees})] / \tan(70 \text{ degrees})$. The reflectance of the green canopies increased very little because of their high absorptance in the visible region.

In the NIR region, the canopy reflectances of all plants varied directly with solar altitude. As the solar altitude changed from 30 to 70 degrees, the relative NIR reflectance of bursage increased about 57 percent (relative basis), greasewood, 26 percent; big sagebrush, 39 percent; shadscale, 53 percent; and alfalfa, 46 percent. The relative NIR reflectance increases were slightly smaller than those found in the visible region, because leaf transmittance in the NIR region, and subsequent reflectance from lower surfaces reduces the reflectance contrast between sunlit and shaded leaves.

The effects of solar altitude on the NIR/Red and NDVI ratios resulted from the shadow effects on the visible and NIR reflectance. For the green canopies, legume-grass and alfalfa, the NIR/Red ratios varied substantially, because of the direct relation between NIR reflectance and solar altitude, which increased the red to near infrared reflectance contrast. The NIR/Red ratio varied slightly for the other vegetation types because the visible and NIR reflectances were about equally affected by changes in the shaded areas of the canopy. The NDVI ratio varied little for the green vegetation because of the low and almost constant visible reflectance. This reduced the NDVI ratio to essentially a NIR/NIR ratio. The NDVI ratios for the gray vegetation varied much more because of the visible and NIR reflectance changes associated with increased solar altitude. This varied the numerator and denominator of the NDVI ratio, causing it to vary inversely with solar altitude. These effects are important because the ratios have been highly correlated with various plant growth parameters (1, 5, 7, and 8).

The canopy reflectance differences associated with changes in solar altitude can substantially affect the use of multi-

date, multispectral imagery for monitoring the vegetation-soil mosaic at a given geographic location, or for monitoring a vegetation type in different latitudes. Monitoring the same area over several months should show reflectance differences in the vegetation-soil mosaic. Assigning levels of importance to these differences could be a difficult problem. Some of these differences will be associated with solar altitude effects on in-canopy shadows, which will vary the canopy reflectance. Other differences will be associated with change in percent ground cover, biomass or leaf area of the vegetation-soil mosaic (6 and 7). For example, the differences in the TM-4 band brightness values for alfalfa could suggest a doubling of the leaf area of the plant canopy, not the change in solar altitude that varied the percentages of sunlit and shaded vegetation in the sensor's FOV. Band ratios can remove some of the solar altitude effects but the ratio selected is dependent on the vegetation being considered. The NDVI ratio for green vegetation was slightly affected by shadowing, while the NIR/Red ratio was substantially affected. For the gray colored plants, the NIR/Red ratio was affected less than was the NDVI ratio. Whether a ratio for a specific vegetation type was affected depended on the plant's reflectance, absorptance, and transmittance characteristics in the visible-near infrared region.

Conclusions.

The visible-near infrared reflectance of the plant canopy varied directly with solar altitude, which affected the in-canopy shadows. In the spectral regions where plants had low reflectance contrast between sunlit and shaded canopies, the canopy reflectance differences were small as solar altitude decreased the in-canopy shadowed area. Vegetation types with large reflectance contrast between sunlit and shaded canopies had large reflectance differences.

NIR/Red and NDVI ratios varied with solar altitude and were affected by the reflectance contrast between sunlit and shaded vegetation. These ratios can be used to monitor vegetative change, but the diurnal, seasonal, and latitudinal effects of solar altitude on vegetation spectra must address reflectance differences associated with different colored vegetation. The ratios differentiated three vegetation groups for which the ratio values varied from high to low

SATTERWHITE & RINKER

green colored vegetation,
greenish-gray and yellowish-green colored vegetation,
gray colored vegetation.

Canopy reflectance differences were significant between the true solar noon spectra and those taken before 0930. Spectra taken after this time varied from the true solar noon spectra, but these differences became smaller as the spectra were taken closer to true solar noon.

References.

1. Daughtry, C.S.T., M.E. Bauer, D.W. Crecelius, and M.M. Hixson. 1980. Effects of management practices on reflectance of spring wheat canopies. *Agronomy Journal* 72:1055-1060.
2. Jackson, R.J., R.J. Reginato, P.J. Pinter, Jr., and S. B. Idso. 1979. Plant canopy information extraction from composite scene reflectance of row crops. *Applied Optics* 18:3775-3782.
3. Kollenkark, J.C., V.C. Vanderbilt, C.S.T. Daughtry, and M.E. Bauer. 1982. Influence of solar illumination angle on soybean canopy reflectance. *Applied Optics* 21:1179-1184.
4. Ranson, K.J., C.S.T. Daughtry, L.L. Biehl, and M.E. Bauer. 1985. Sun-view angle effects on reflectance factors of corn canopies. *Remote Sensing of Environment* 18:147-161.
5. Satterwhite, M.B., J.P. Henley, and M. Treiber. 1982. Vegetative cover effects on soil spectral reflectance. U.S. Army Engineer Topographic Laboratories, Research Institute, Ft. Belvoir, VA. 22060. ETL-0284.
6. Satterwhite, M.B. 1984. Discriminating vegetation and soils using Landsat MSS and Thematic Mapper bands and band ratios. *ACSM-ASP Technical Papers* 2:479-490. Washington, D.C. 11-16 March.
7. Tucker, C.T. 1979. Red and photographic infrared linear combinations for monitoring vegetation. *Remote Sensing of Environment* 8:127-150.
8. Wiegand, C.L., A.J. Richardson, and E.T. Kanemasu. 1979. Leaf area index estimates for wheat from LANDSAT and their implications for evapotranspiration and crop modeling. *Agronomy Journal* 71:336-342.

SATTERWHITE & RINKER

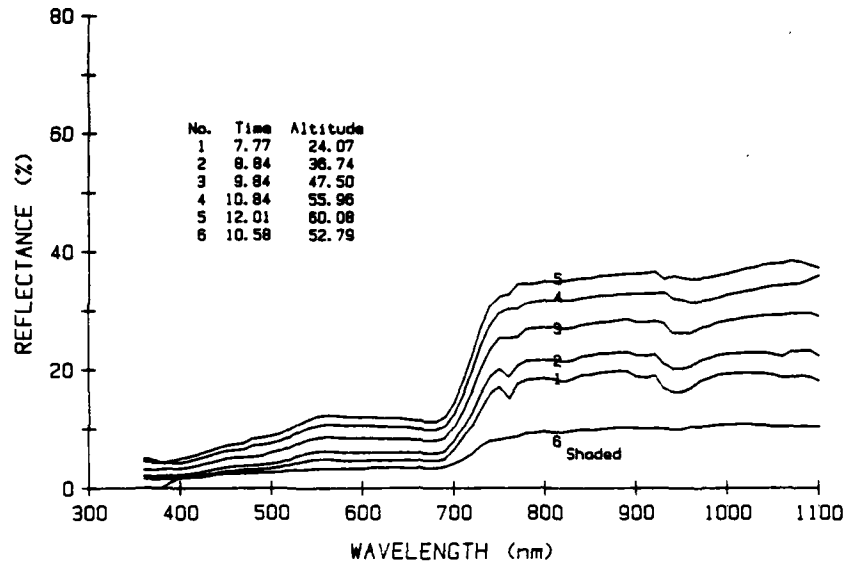


Figure 1. Reflectance Spectra of Sunlit and Shaded Bursage Canopies.

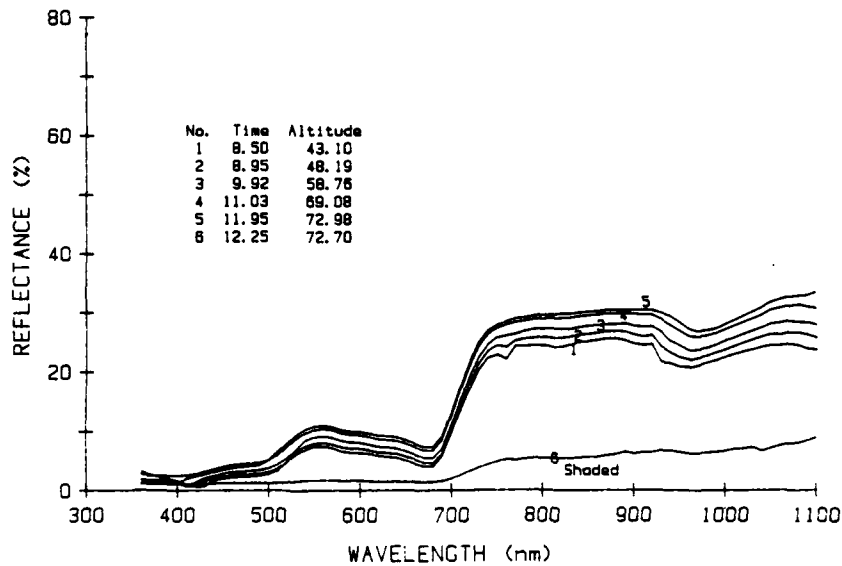


Figure 2. Reflectance Spectra of Sunlit and Shaded Greasewood Canopies

SATTERWHITE & RINKER

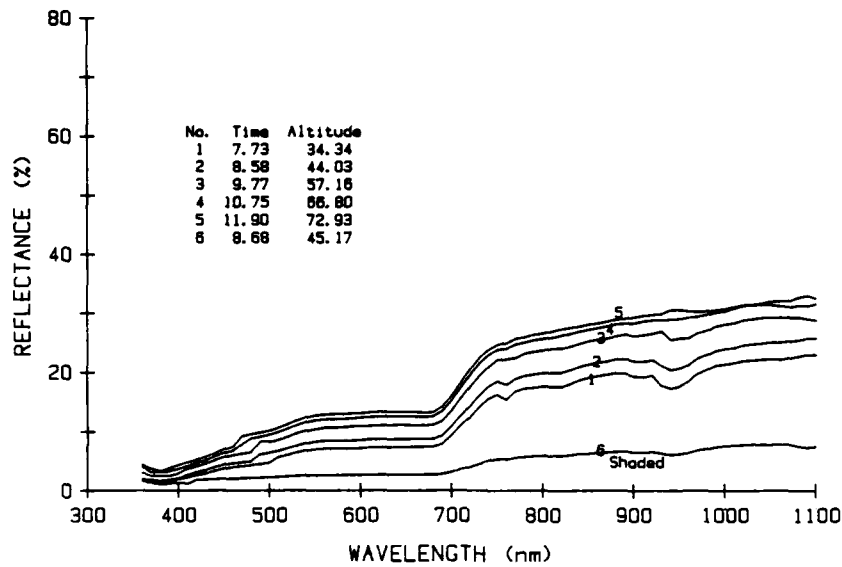


Figure 3. Reflectance Spectra of Sunlit and Shaded Big Sagebrush Canopies.

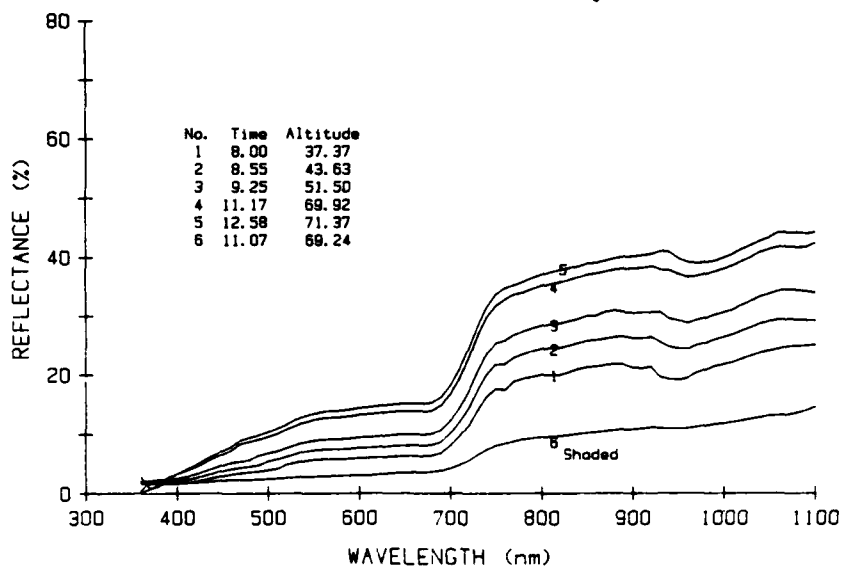


Figure 4. Reflectance Spectra of Sunlit and Shaded Shadscale Canopies.

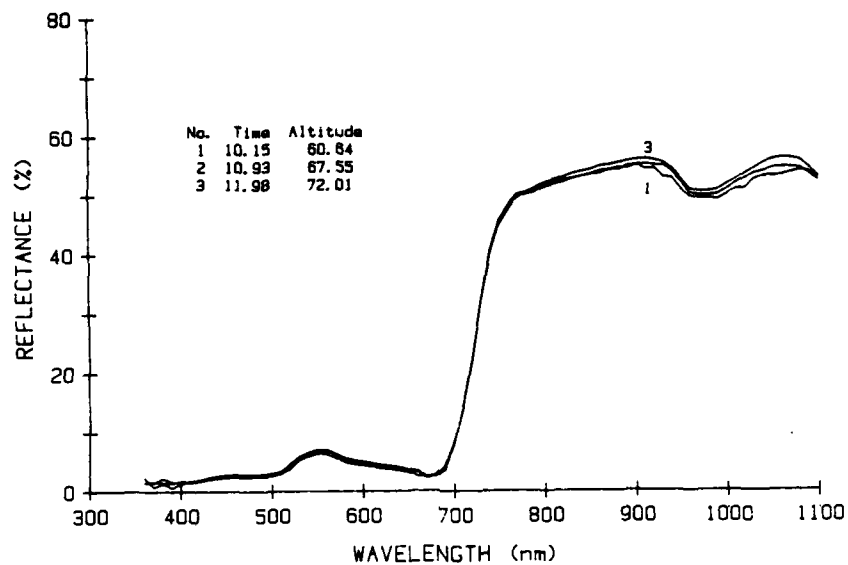


Figure 5. Reflectance Spectra of Sunlit Legume-Grass Canopy

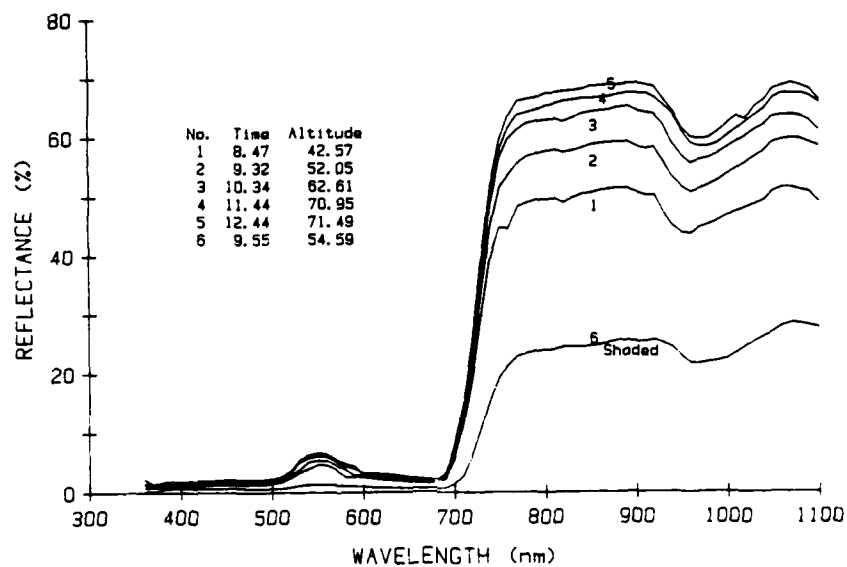


Figure 6. Reflectance Spectra of Sunlit and Shaded Alfalfa Canopies.

SATTERWHITE & RINKER

Bursage	(1)	$Y(X) = 5.036 - (0.163 \cdot X) + (0.0037 \cdot X^2)$	$R^2 = 0.982$
Greasewood	(2)	$Y(X) = 4.281 - (0.093 \cdot X) + (0.0014 \cdot X^2)$	$R^2 = 0.991$
Sagebrush	(3)	$Y(X) = 1.131 + (0.096 \cdot X) + (0.0002 \cdot X^2)$	$R^2 = 0.997$
Shadscale	(4)	$Y(X) = -1.486 + (0.137 \cdot X) + (0.0002 \cdot X^2)$	$R^2 = 0.995$
Legume-grass	(5)	$Y(X) = 25.237 - (0.722 \cdot X) + (0.0058 \cdot X^2)$	$R^2 = 0.755$
Alfalfa	(6)	$Y(X) = -0.498 + (0.058 \cdot X) - (0.0003 \cdot X^2)$	$R^2 = 0.978$

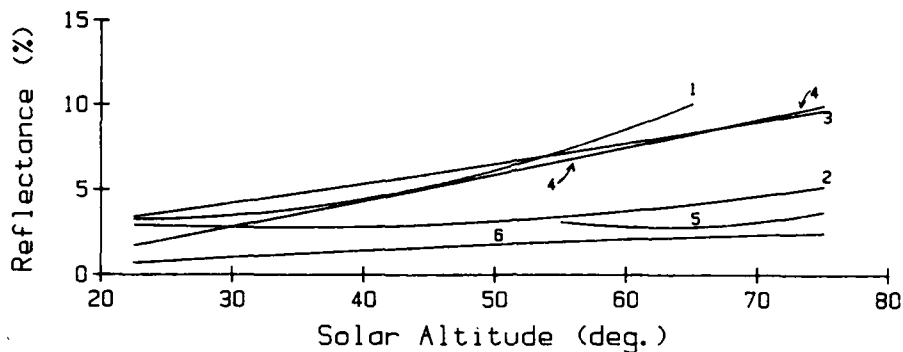


Figure 7a. Relation between Solar Altitude and Canopy Reflectance in Landsat TM BAND 1 (450-520nm)

Bursage	(1)	$Y(X) = 5.986 - (0.165 \cdot X) + (0.0044 \cdot X^2)$	$R^2 = 0.983$
Greasewood	(2)	$Y(X) = 4.418 + (0.018 \cdot X) + (0.0008 \cdot X^2)$	$R^2 = 0.994$
Sagebrush	(3)	$Y(X) = 0.472 + (0.201 \cdot X) - (0.0005 \cdot X^2)$	$R^2 = 0.997$
Shadscale	(4)	$Y(X) = -1.425 + (0.185 \cdot X) + (0.0003 \cdot X^2)$	$R^2 = 0.994$
Legume-grass	(5)	$Y(X) = 35.836 - (0.985 \cdot X) + (0.0079 \cdot X^2)$	$R^2 = 0.744$
Alfalfa	(6)	$Y(X) = -3.983 + (0.235 \cdot X) - (0.0015 \cdot X^2)$	$R^2 = 0.973$

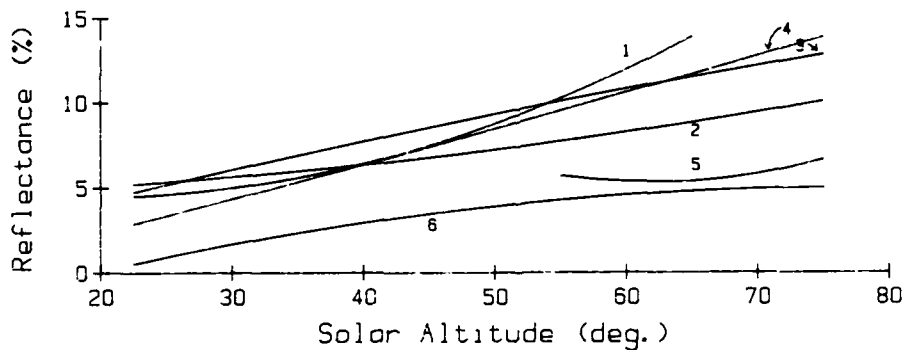


Figure 7b. Relation between Solar Altitude and Canopy Reflectance in Landsat TM BAND 2 (520-600nm)

SATTERWHITE & RINKER

Bursage	(1)	$Y(X) = 5.821 - (0.150 \cdot X) + (0.0042 \cdot X^2)$	$R^2 = 0.984$
Greasewood	(2)	$Y(X) = 3.661 - (0.013 \cdot X) + (0.0010 \cdot X^2)$	$R^2 = 0.996$
Sagebrush	(3)	$Y(X) = 0.393 + (0.225 \cdot X) - (0.0006 \cdot X^2)$	$R^2 = 0.996$
Shadscale	(4)	$Y(X) = -1.347 + (0.200 \cdot X) + (0.0004 \cdot X^2)$	$R^2 = 0.993$
Legume-grass	(5)	$Y(X) = 24.311 - (0.694 \cdot X) + (0.0057 \cdot X^2)$	$R^2 = 0.723$
Alfalfa	(6)	$Y(X) = -0.977 + (0.083 \cdot X) - (0.0005 \cdot X^2)$	$R^2 = 0.975$

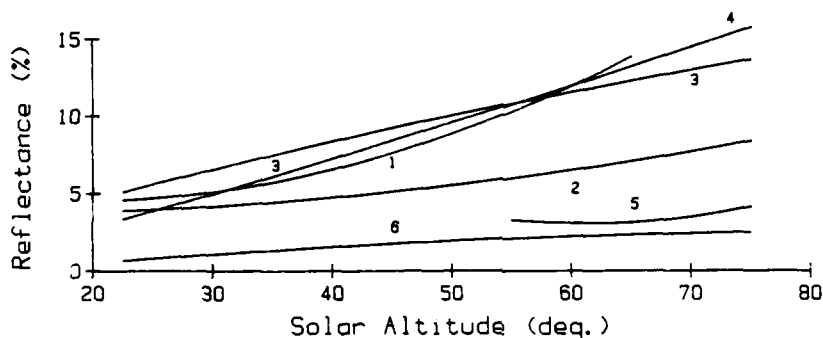


Figure 7c. Relation between Solar Altitude and Canopy Reflectance in Landsat TM BAND 3 (630-690nm)

Bursage	(1)	$Y(X) = 20.195 - (0.306 \cdot X) + (0.0095 \cdot X^2)$	$R^2 = 0.984$
Greasewood	(2)	$Y(X) = 11.886 + (0.385 \cdot X) - (0.0020 \cdot X^2)$	$R^2 = 0.968$
Sagebrush	(3)	$Y(X) = 2.551 + (0.542 \cdot X) - (0.0028 \cdot X^2)$	$R^2 = 0.989$
Shadscale	(4)	$Y(X) = -3.399 + (0.754 \cdot X) - (0.0026 \cdot X^2)$	$R^2 = 0.993$
Legume-grass	(5)	$Y(X) = 209.750 - (4.812 \cdot X) + (0.0366 \cdot X^2)$	$R^2 = 0.233$
Alfalfa	(6)	$Y(X) = -11.571 + (1.914 \cdot X) - (0.0114 \cdot X^2)$	$R^2 = 0.980$

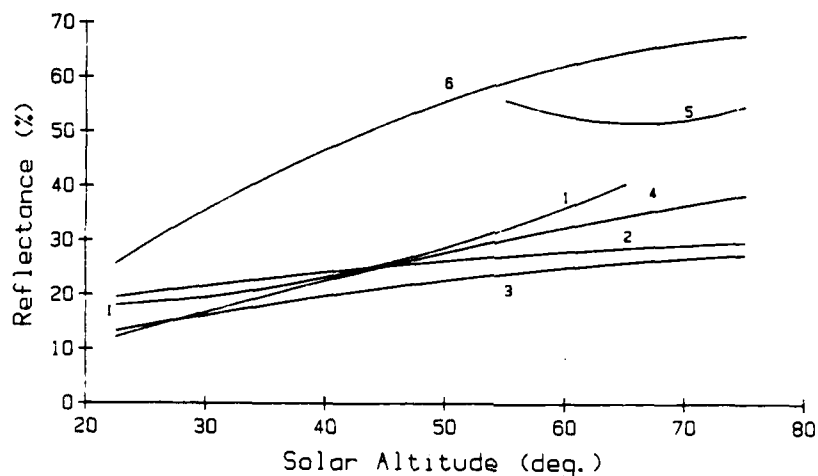


Figure 7d. Relation between Solar Altitude and Canopy Reflectance in Landsat TM BAND 4 (760-900nm)

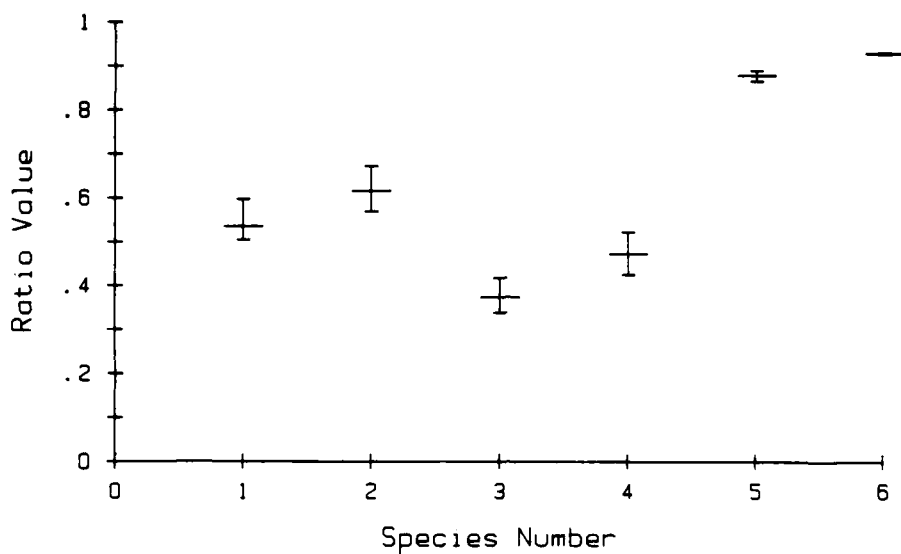


Figure 8b. Normalized Difference Vegetation Index for Vegetation Types

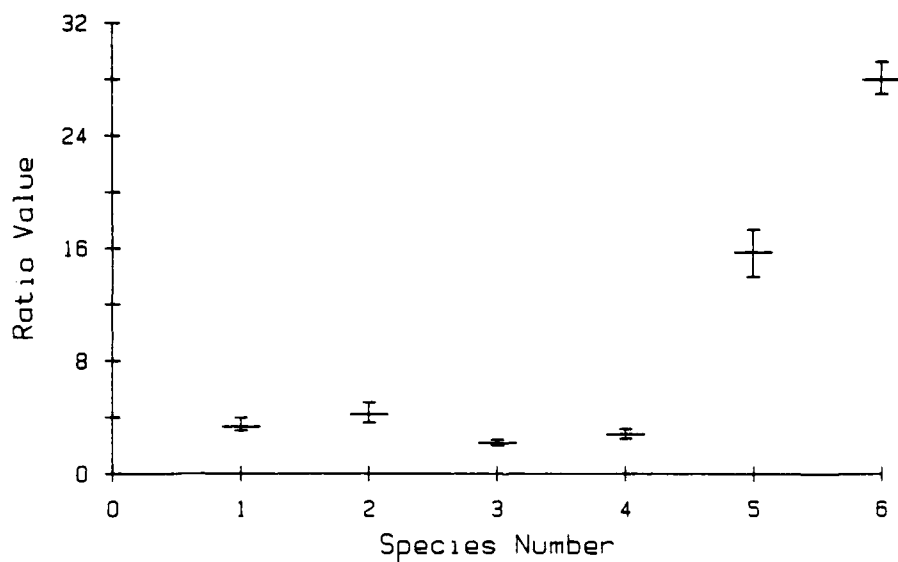


Figure 8a. NIR/Red Ratio for Vegetation Types

SCHALL & ROACH

CHEMICAL MUNITION EFFECTS ANALYSIS
IN SUPPORT OF TARGETING MANUAL DEVELOPMENT

*JAMES E. SCHALL, JR., MR.
LISA K. ROACH, MRS.
USA BALLISTIC RESEARCH LABORATORY
ABERDEEN PROVING GROUND, MD 21005-5066

A critical need exists for current, updated targeting manuals for use by the military planners. As a result of this need, an effort is currently underway to generate new data to be used in updating both the Joint Munitions Effectiveness Manuals (JMEMs) and the Army published FM 3-10B series (Employment of Chemical Agents). Studies recently conducted by the U.S. Army Ballistic Research Laboratory (BRL) for the Chemical Working Group (CWG) of the Joint Technical Coordinating Group for Munitions Effectiveness (JTCG/ME) have demonstrated the applicability of the BRL-developed Army Unit Resiliency Analysis (AURA) methodology as the primary tool to support the development of the new manuals. These BRL studies assessed the effectiveness of various chemical threats against selected Soviet targets. The results of this effort will form the basis of a revised FM 3-10-2 manual and a field circular for target analysts. This paper will present the preliminary results of the study, focusing on the types of targets analyzed and the effects of chemical munitions on personnel and unit operations. Some attention will be given to the development of chemical lethal footprints for a number of chemical agents.

Results of previous BRL studies have shown that the major effects of chemical weapon employment are personnel degradation due to the use of chemical protective clothing and equipment and casualties resulting from heat stress. In the previous employment manuals, these factors were not considered. Furthermore, previous studies have been limited to a "lethal dose" (step function) approach due to a lack of knowledge on the physiological response of humans to intermediate (less-than-lethal) chemical doses; in addition, the structure of the available analytical tools did not permit the inclusion of this data. AURA, however, has a unique capability to address these factors. AURA is an event sequenced, one-sided combat simulation methodology which is composed of a number of highly detailed models from the various technical communities interfaced into a large, time-dependent, event playing and optimization routine.

The interfaces are varied, involving such diverse kill probabilities as lethal footprints for conventional munitions, log normal kill probabilities for nuclear effects and toxic chemical dispersions and evaporations. Additionally, AURA takes into account degradation due to MOPP, reliability and target acquisition probabilities. The optimization is a dedicated, non-linear routine which models the reallocation of assets in order to minimize the choke points in the optimal functional path. Additionally, the methodology allows for the detailed modelling of the functional structure of military units.

Figure 1 is a schematic representation of AURA. The upper inputs are provided by the Army's technical community; the lower inputs are obtained from the Training & Doctrine Command (TRADOC) and the Intelligence community. The methodology is mature and has been institutionalized within both the Army Materiel Command (AMC) and TRADOC, providing for the first time, a common tool for both the developer and user.

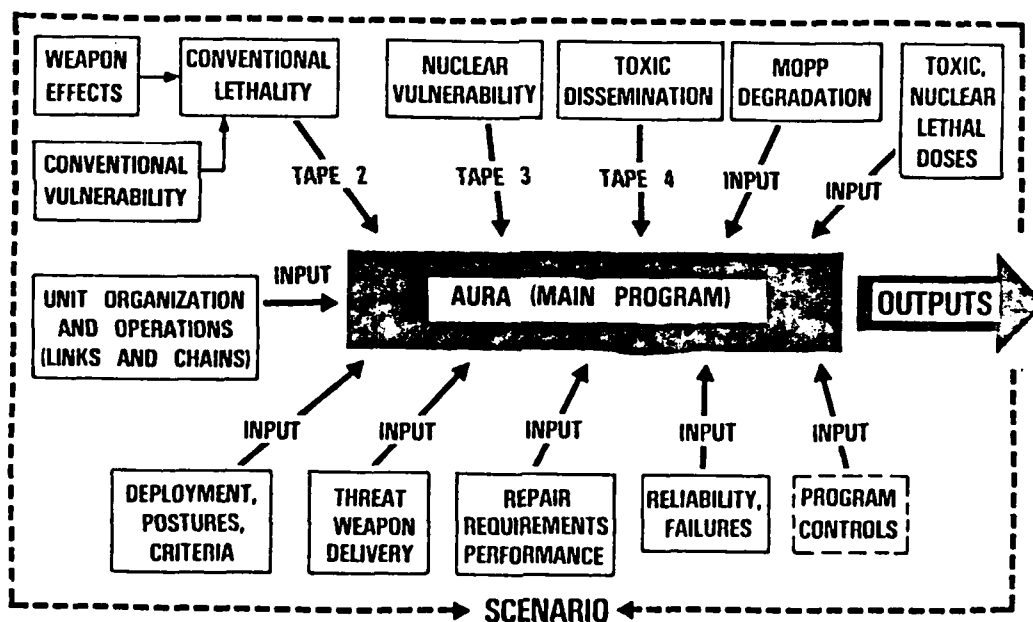


Figure 1. Schematic Representation of the AURA Methodology

SCHALL & ROACH

Typical outputs from AURA are:

Time Dependent:

- . Quantitative Unit Effectiveness
- . Personnel and Materiel Losses
- . Task Performance and Degradation
- . Reason for Degradation (Achilles' Heel)
- . Most Effective Methods of Mission Accomplishment
- . Sensitivity Analyses

AURA has also been demonstrated as a useful tool for:

- . Examining TO & Es
- . Comparing Results of Changes in Unit Doctrine
- . Measuring Materiel Development/Hardening Benefits
- . Evaluating Weapon/Weapon Employment Effectiveness
- . Providing Realistic, Verifiable Residual Combat Capability
Input Data for Broader Scale Simulations

Of particular importance to the Chemical Munition Effectiveness Analysis were the Toxic Dissemination and Military Oriented Protective Posture (MOPP) Toxic Dose subroutines.

The dissemination effects of chemical munitions on a unit are markedly different from those effects which result from attack by conventional munitions. The U.S. Army Chemical Research and Development Center (CRDC) has developed a methodology, NUSSE3 (Non-Uniform Simple Surface Evaporation), for simulating the dispersal of a given agent, by a specified delivery system along with the various other parameters which have an effect on the chemical dispersal (i.e., meteorological conditions, height of weapon bursts, etc.). NUSSE3 is run at the BRL using input data from CRDC, while the outputs are reformatted by an automated preprocessor for use in AURA.

In simulating the dispersal of a given chemical agent over a target area, NUSSE3 determines droplet sizes and corresponding evaporation times, along with a variety of additional information. NUSSE3 simulates the chemical cloud descending on the target area, eventually settling on the ground. The output evaporation times are a result of two important assumptions: 1) the surface considered is Canadian grassland (other surface types are also available); and 2) once the droplet has settled on the grass, a percentage of the droplet is absorbed by the ground.

Until recently, vulnerability/lethality studies have been based on "go-no go" measures expressed as dosage levels below which no effect is assumed. Such criteria have the probability of underestimating weapon

effects on targets. Improved understanding and ability to analyze "less-than-lethal" chemical effects have made possible the development of data which can be used by comprehensive combat models and also improve our understanding of true weapons effects. Nerve agents such as GB and VX interfere with the ability of the central nervous system to control voluntary and involuntary muscular responses. After agent entry, rapid degradation is followed by some recovery in non-lethal cases and death in lethal ones. Figure 2 shows the GB dosage from one 155mm round. The contours reflect 0.1, 0.5, 1.0 and 5.0 times the level of a lethal dose, with 0.1 being the outer contour. It is obvious from this figure that a large portion of the area has been affected by less than a lethal dose.

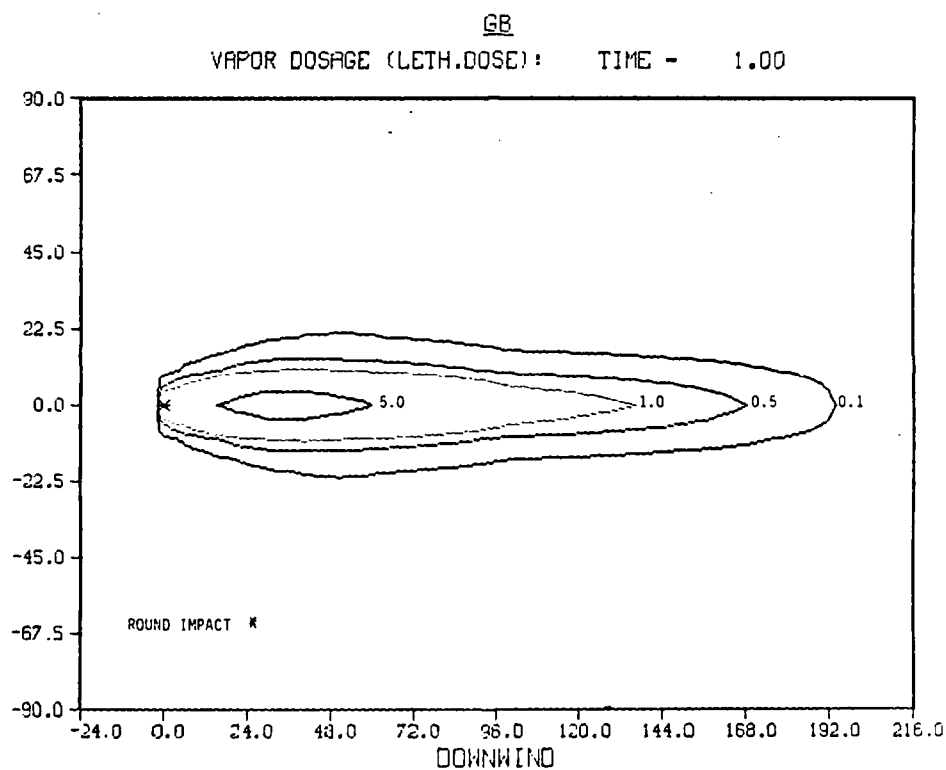


Figure 2. Dosage Patterns Created by One 155mm GB Round at One Minute after Detonation

SCHALL & ROACH

Low level (less than lethal) effects of chemical agents have been included in AURA under the auspices of the BRL mission program with assistance from the Toxicology Branch, Chemical Research and Development Center. This significant advancement allows us to examine decontamination techniques and requirements, protective systems such as overpressure in vehicles and protective clothing, and the effectiveness of agents as incapacitants.

Early in the process of determining the effects of chemical munitions on military units, it became apparent that the major effect of such weapons against well prepared, well equipped troops is not casualty production. Rather, the dominating effects are indirect, that is, the effects of protective measures taken. The donning of (MOPP) results in several adverse phenomena such as decreased agility, heat stress, and fatigue due to the encumbrance of the equipment. For this reason, a BRL algorithm was developed to predict the degradation due to protective posture. This algorithm has been refined and validated as a result of the BRL direction of the DOD funded, Dugway Proving Ground administered DO-49 chemical data project.

Through live troop tests (DO-49), performance degradation of individual soldiers in chemical protective gear is being accurately quantified. The BRL is currently the major source of such data to analysis agencies such as TRASANA, AMSAA, The Chemical School and USANCA. The field tests of soldiers and units in MOPP are incorporated in the algorithm by multiple linear regression analysis.

As stated earlier, the objective of this effort is to replace the current chemical targeting manuals. Specifically the JTOG JMEM for chemical munitions and the Army published FM 3-10B are to be replaced with FM 3-10-2. Both manuals are circa 1966, and evidence exists that the validity of the data contained therein is suspect. In addition, a field circular will be published this summer in order to expedite the use of the data in the field. FM 3-10-2 will contain data pertaining to specific targets. The first edition will address the following targets:

- . Regimental Command Post
- . Motorized Rifle Company
- . Tank Company
- . Surface-to-Air Missile Battery
- . Engineer Bridge Company
- . Portable Rocket Technical Base (PRTB)
- . BM21 Multiple Rocket Launcher Battery
- . BM27 Multiple Rocket Launcher Battery
- . 240mm Mortar Battery

SCHALL & ROACH

- . 122mm Howitzer (Towed) Battery
- . 122mm Howitzer (SP) Battery
- . 152mm Howitzer (SP) Battery
- . Target Acquisition Battery

AURA Input data was obtained through extensive coordination with the following Army agencies and the other services:

- . U.S. Army Nuclear and Chemical Agency
- . U.S. Army Intelligence Agency
- . Joint Technical Coordinating Group/Munitions Effectiveness
- . USA Chemical Center and School
- . USA Field Artillery Center and School
- . USA Chemical Research and Development Center
- . USA TRADOC Systems Analysis Agency

In order to perform the field circular analysis, generic target sizes and numbers of personnel per target had to be determined. Based on the requirements of the field circular, the US Army Chemical School calculated four target sizes versus five chemical munitions. Each generic target was assigned a radius and number of personnel dependent upon the munition used in the attack. For the 8 inch and 155 mm munitions, target radii were 100, 300, 500 and 1250 meters; the 105 mm munition was employed against target radii of 100, 200 and 300 meters. Personnel per target size were as follows: 1) 50 personnel for the 100 meter radius; 2) 200 for the 200 meter radius; 3) 450 for the 300 meter radius; and, 4) 1250 for the 500 meter radius. The number of personnel per target size was based upon the 100 meter target radius. The Chemical School estimated that 50 personnel would be deployed in an area of that size. Since a 100 meter radius is roughly equal to 31400 square meters, this allowed for a ratio of one person for every 682 square meters. In order to be consistent, the Chemical School used this ratio in determining the number of personnel deployed in the larger target radii.

Several assumptions were made prior to the start of the analysis. With regard to the chemical munitions, two agent types were employed, a persistent (VX) and a non-persistent (GB). In addition, both summer and winter weather conditions were considered. The analysis also considered the effects of the Mission Oriented Protective Posture (MOPP) on unit personnel. In the first part of the analysis, personnel were assumed to be in MOPP II (transmission factor 1.0), changing to MOPP IV (transmission factor 0.0) upon any incoming round; for VX, the time to change postures was assumed to be one minute while a thirty second masking time was used in the GB runs. The analysis also considered completely unprotected personnel.

The initial effort for the field manual involves an attack force of the Army "chemical capable" surface to surface systems, e.g., the 8", 155mm and 105mm howitzers, with currently fielded munitions. Follow on analyses will address air to surface munitions and future systems such as the Multiple Launch Rocket System (MLRS).

Figure 3 is presented as an example of the type of data generated by the AURA model and is a graphical representation of a chemical attack on an hypothetical artillery unit by a howitzer platoon. Depicted is unit effectiveness versus time as a result of attack by the non-persistent nerve agent GB. In AURA, a unit's effectiveness is "graded" based upon its ability to perform a quantified mission(s). The artillery unit examined here had an initial capability to fire 98 rounds in three minutes. An effectiveness of 50 percent indicates that the unit can fire only 49 rounds in three minutes, or could fire 98 rounds in six minutes. At time zero, the unit is 100 percent effective; after attack, effectiveness drops to 40 percent as a result of casualties and the degradation associated with the donning of MOPP IV. As the agent evaporates MOPP gear is removed, and the unit reconstitutes, effectiveness rising to 50 percent. For a persistent agent such as VX the drop in effectiveness to 40 percent would continue for hours instead of minutes as the soldiers must remain in complete protective ensemble until either natural or contrived decontamination occurs. As personnel who have received sub-lethal doses recover, the unit effectiveness gradually increases until it reaches approximately 70 percent, the best it will ever achieve without replacement of personnel and/or equipment.

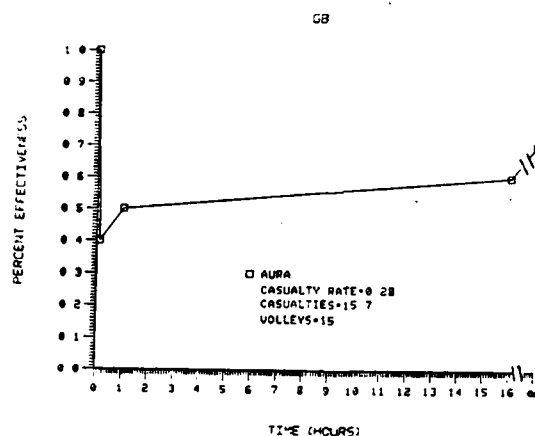


Figure 3. Unit Effectiveness as a Result of Attack by GB.

SCHALL & ROACH

Figures 4 and 5 contain the same information as Figure 3, in the proposed tabular format for FM 3-10-2. Figure 4 is the heading for the table, containing information of interest to the target analyst/commander. Figure 5 is the body of the table and shows the results previously depicted graphically. In this table, casualties are divided into levels of severity. 'TH' indicates a threshold casualty and represents those personnel who have received less than 20 percent of a lethal dose. Symptoms associated with this level are myosis, tightness of chest and headache. Personnel receiving greater than 20 percent but less than 60 percent of a lethal dose are referred to as moderate (MD) casualties; symptoms related to this group include nausea, cramps, vomiting and diarrhea. Finally, personnel receiving greater than 60 percent of a lethal dose are termed severe (SV) casualties. Symptoms linked with this level include severe tremors, acute weakness and ataxia.

TARGET/DELIVERY/MET CONDITIONS	
TARGET	
Type	122 mm SP Howitzer Battery
Size	100 m X 200 m (56 personnel)
Capability	98 Rounds - 3 Minutes
Protective Posture	MOPP II to MOPP IV - 30 Sec.
Location (Range)	10 -15 Kms.
DELIVERY SYSTEM	
Munition	M109A1 SP Howitzer Plt.
Agent	GB
Persistence	12.6 Minutes
Fuzing	PD
Delivery Parameters	TLE 75 Meters
MET CONDITIONS/ TERRAIN TYPE	
Temp	15 Degrees Celsius
Humidity	50 %
WDSPD	2.5 m/sec
Terrain	Grassy
Stability Category	Neutral

Figure 4. Heading for Proposed Tabular Format for Field Manual 3-10-2 Tables

# of Volleys	Severity	Casualties	Effectiveness				TLE		
		Percent	Time				50	100	500
			5	60	960	XXX			
15	TH	6							
	MD	6	0.4	0.5	0.6	0.7			
	SV	6							
	Total	28							

Figure 5. Effects (Tabular) of 155mm GB Munition vs A Soviet 122mm Howitzer Battery

Figure 6 contains an example of the proposed tables for the field circular (which will contain generic targets). The field circular will also contain agent/weapon "footprints" similar to that depicted in Figure 2, and chapters on degradation due to protective posture and resultant heat stress casualties.

The tables displayed in Figure 6 reflect the percent casualties for a particular target (radius) given the threat employed. The threat is listed across the top of the table in terms of the number of firing platoons and number of volleys fired. The percent casualties data is provided for both protected (MOPP IV) and unprotected personnel under summer and winter weather conditions (as listed in the first two rows). The data is further broken down into two time periods - five minutes and ultimate (representing the final time period considered); these times are contained in the third row. For example, selecting a platoon firing four volleys, one can expect 11 percent casualties in the summer if personnel are protected (target T2, r=300m).

SCHALL & ROACH

			T1 R=100m											
Platoons			1			2			4			6		
Volleys			1	2	4	1	2	4	1	2	4	1	2	4
P R O T E C T E D	Summer	5 min	14	28	52	28	52	76	52	76	92	60	86	96
		Ultimate	14	28	52	28	52	76	52	76	92	60	86	96
	Winter	5 min	10	20	40	20	38	66	38	66	86	54	78	92
		Ultimate	10	20	40	20	38	66	38	66	86	54	78	92
U N P R O T	Summer	5 min	48	70	90	70	90	98	90	98	100	96	100	100
		Ultimate	76	92	96	92	96	98	96	98	100	98	100	100
	Winter	5 min	44	64	88	66	88	98	88	98	100	94	98	100
		Ultimate	66	86	96	82	96	98	96	98	100	96	98	100

			T2 R=100m											
Platoons			1			2			4			6		
Volleys			1	2	4	1	2	4	1	2	4	1	2	4
P R O T E C T E D	Summer	5 min	3	6	11	6	11	21	11	21	37	16	30	47
		Ultimate	3	6	11	6	11	21	11	21	37	16	30	47
	Winter	5 min	2	4	7	4	7	15	7	15	28	11	22	38
		Ultimate	2	4	7	4	7	15	7	15	28	11	22	38
U N P R O T	Summer	5 min	16	26	36	29	36	42	36	42	46	39	44	48
		Ultimate	42	62	74	66	73	79	73	79	82	76	80	83
	Winter	5 min	13	22	32	24	31	38	31	38	44	35	41	46
		Ultimate	30	49	62	51	61	69	61	69	74	65	72	80

Figure 6. Proposed Tabular Format for the Field Circular

			T3 R=500m											
Platoons			1			2			4			6		
Volleys			1	2	4	1	2	4	1	2	4	1	2	4
P R O T E C T E D	Summer	5 min	<1	1	2	1	1	3	1	3	6	2	4	9
		Ultimate	<1	1	2	1	1	3	1	3	6	2	4	9
	Winter	5 min	<1	1	1	1	1	2	1	2	4	2	3	7
		Ultimate	<1	1	1	1	1	2	1	2	4	2	3	7
U N P R O T E C T E D	Summer	5 min	4	8	13	8	13	17	13	17	20	15	18	20
		Ultimate	25	35	43	34	43	48	43	48	51	45	49	52
	Winter	5 min	3	6	8	6	8	11	8	11	13	10	12	14
		Ultimate	16	24	31	24	31	35	31	35	39	33	37	46

Figure 6. (Continued) Proposed Tabular Format for the Field Circular

In summary, a series of analyses are being conducted to assess the effectiveness of chemical agents against a number of military targets. Specifically, these targets include:

- . Regimental Command Post
- . Motorized Rifle Company
- . Tank Company
- . Surface-to-Air Missile Battery
- . Engineer Bridge Company
- . Portable Rocket Technical Base (PRTB)
- . BM21 Multiple Rocket Launcher Battery
- . BM27 Multiple Rocket Launcher Battery
- . 240mm Mortar Battery
- . 122mm Howitzer (Towed) Battery
- . 122mm Howitzer (SP) Battery
- . 152mm Howitzer (SP) Battery
- . Target Acquisition Battery

The data resulting from these analyses will be used in the development of the new FM 3-10 series of manuals. Additional analyses, evaluating at least six more specific targets, will be conducted next year. Finally, in order to expedite the use of this data in the field, the U.S. Army Chemical Center and School will publish a field circular for target analysts this summer.

SCHNAKENBERG, CARLSON, SAWYERS, VOGEL, JOHNSON, SZLYK, FRANCESCONI & HUBBARD

NUTRITIONAL EVALUATION OF A NEW COMBAT
FIELD FEEDING SYSTEM FOR THE ARMY(U)

*DAVID D. SCHNAKENBERG, COL, DAWN CARLSON, MAJ, MICHAEL SAWYERS, CPT,
JAMES A. VOGEL, DR., RICHARD JOHNSON, DR., PATRICIA C. SZLYK, DR.,
RALPH FRANCESCONI, DR. AND ROGER W. HUBBARD, DR.
US Army Research Institute of Environmental Medicine
Natick, Massachusetts 01760-5007

The most comprehensive test and evaluation ever of a Combat Field Feeding System (CFFS) was conducted with approximately 1650 soldiers from the 25th Infantry Division engaged in field training exercises at Pohakuloa Training Area (PTA), Hawaii during a seven week period beginning in August 1985. The purpose of this Vice Chief of Staff, Army (VCSA) directed test was to determine if the innovative food technologies employed in the proposed new CFFS will significantly reduce the combat food service requirement for labor (cooks), water, fuel, food preparation time and increase the mobility, flexibility and responsiveness of combat field feeding operations. Furthermore, the VCSA specifically directed that the test design evaluate the nutritional and bio-medical effects of prolonged (6-7 consecutive weeks) consumption of the new T (tray pack) ration meals as compared to the standard B and A rations. The US Army Combat Developments Experimentation Center (CDEC) was tasked to conduct the Force Development Test and Experimentation (FDTE) in collaboration with the US Army Research Institute of Environmental Medicine (USARIEM). CDEC was responsible for testing organizational and operational issues and USARIEM was responsible for testing and evaluation of nutritional and bio-medical issues. The scope of this paper will be limited to a presentation and discussion of the nutritional and biomedical data.

The nutritional and bio-medical issues addressed in this study were as follows:

- a. Nutrient Consumption
- b. Energy Balance
- c. Hydration Status
- d. Nutritional Status
- e. Food Related Health Disorders
- f. Muscle Strength and Eye-hand Coordination

To evaluate these issues, forty volunteer test subjects from each of six

SCHNAKENBERG, CARLSON, SAWYERS, VOGEL, JOHNSON, SZLYK, FRANCESCONI & HUBBARD

test units participating in the CFFS FDTE were briefed on all data collection procedures. Baseline (pre) biomedical measurements were taken before breakfast at Schofield Barracks 4-6 days prior to deployment of the units to PTA. The measurements included demographics, height, weight, and body composition. Urine analyses included specific gravity, osmolality, creatinine, sodium, potassium and chloride. Blood analyses included hematocrit, hemoglobin, total protein, sodium, potassium, magnesium, and biochemical indices of vitamin A, vitamin C, thiamin, folic acid and iron status. Blood lipid analyses included triglycerides, total cholesterol and high density lipoprotein (HDL) and low density lipoprotein (LDL) cholesterol. The incidence of gastrointestinal symptoms was assessed with the USARIEM Environmental Symptoms Questionnaire and by monitoring sick call logs. Muscular performance was assessed by measurement of handgrip force and endurance, maximal upright pull force and maximal lift capacity. Eye-hand coordination was assessed by an arm-hand steadiness test and a ball-pipe test. Essentially all of these measures were repeated at the beginning (T+1), middle (T+20) and end (T+44) of the 44-day FDTE at PTA.

Total daily food and water consumption data were obtained on 16 days of the 44-day FDTE using a combination of observation, interview and self-reporting diary techniques. Nutrient composition and food consumption data were combined to compute nutrient consumption. To facilitate rapid data reduction, essentially all of the approximately one million nutrition and biomedical data points were entered into a computerized data base and verified on site. The details of all the methodologies and procedures used were described previously (1).

During the FDTE, the test units consumed differing mixes of T-, B-, or A-rations and Meal Ready to Eat (MRE) rations according to the schedule at Table 1.

TABLE 1. RATION SCHEDULE

Test Group	Unit	Test Day			
		1-3	4-7	8-21	22-44
1T	Artillery Btry	3 MRE	1T/2 MRE	1T/2 MRE	1T/2 MRE
1TF	DISCOM (females)	3 MRE	1T/2 MRE	1T/2 MRE	1T/2 MRE
2T	Artillery Btry	3 MRE	1T/2 MRE	2T/1 MRE	2T/1 MRE
2TE	Artillery Btry	3 MRE	1T/2 MRE	2T/1 MRE	2T/1 MRE (enhanced)
2B	Engineer Co.	3 MRE	2B/1 MRE	2B/1 MRE	2B/1 MRE
2A	Artillery Btry	3 MRE	2A/1 MRE	2A/1 MRE	2A/1 MRE

SCHNAKENBERG, CARLSON, SAWYERS, VOGEL, JOHNSON, SZLYK, FRANCESCONI & HUBBARD

The MRE has replaced the Meal Combat Individual (MCI or "C" ration) as the individual packaged ration. The A-ration meals were prepared from perishable (requiring refrigeration) and non-perishable ingredients according to a 14-day menu cycle on a Mobile Kitchen Trailer (MKT). The B-ration meals were prepared from solely non-perishable ingredients according to a 10-day menu cycle. The T-ration is a developmental ration which yields considerable manpower savings because it eliminates the need for food preparation from ingredients. Thermostabilized entree, starch, vegetable and certain dessert items are bulk packaged (12-25 servings) in rectangular metal containers (tray packs) which also serve as a heating pan and serving tray. The T-ration also includes spreads, beverage powders, and condiments. The T-ration meals were served according to a 14-day menu cycle. The menus of test group 2TE were enhanced by modifying or supplementing the T-ration menus with B-and A-ration components beginning on day T+22. Unitized T-rations were issued to the units with sufficient quantities of tray packs, spreads, beverage powders, condiments and disposable dinnerware for a given menu to serve 72 soldiers. Canned bread was served to all ration groups on days T+4 through T+14. A Hawaiian National Guard bakery unit prepared field bread for all units beginning on day T+15. No other sources of food were available during the FDTE.

All test units were engaged in meaningful training throughout the FDTE. The artillery units participated in numerous FTXs and the DISCOM supported these DVARTY activities. The Engineer Company built roads and completed several construction projects. The temperature at PTA in August and September was mild (average high and low temperatures were 68°F and 48°F respectively). Measurable rainfall occurred on only one day during the FDTE. The average elevation at PTA is 6000 ft.

The average daily nutrient intakes for each test group were compared with the Military Recommended Dietary Allowances (MRDAs) for male and female (Group 1TF) personnel as published in AR 40-25(2). These data and MRDAs are graphically displayed in Figures 1 and 2. Group means for a specific nutrient with unlike superscripts significantly differ at the $p < 0.05$ level by the Student Newman Kuels procedure.

The average daily energy intakes of all groups except 2A were below the MRDA range of 2800-3600 Kcal/day and 2000-2800 Kcal/day for moderately active males and females, respectively. Group 2A consumed more ($p < 0.05$) energy (3047 Kcal/day) than any of the other male groups which averaged 2700 Kcal/day. Energy intakes averaged only 2445 Kcal/day from the 3669 Kcal available during the first three days of the FDTE when all groups were consuming three MREs per day. These results were consistent with those of a previous prolonged (35 day) feeding test at PTA (3) and confirm that troops fed solely three MREs per day do not consume sufficient quantities of food to meet the demands of even moderate levels of energy expenditure. Further analyses indicated that all male groups continued to

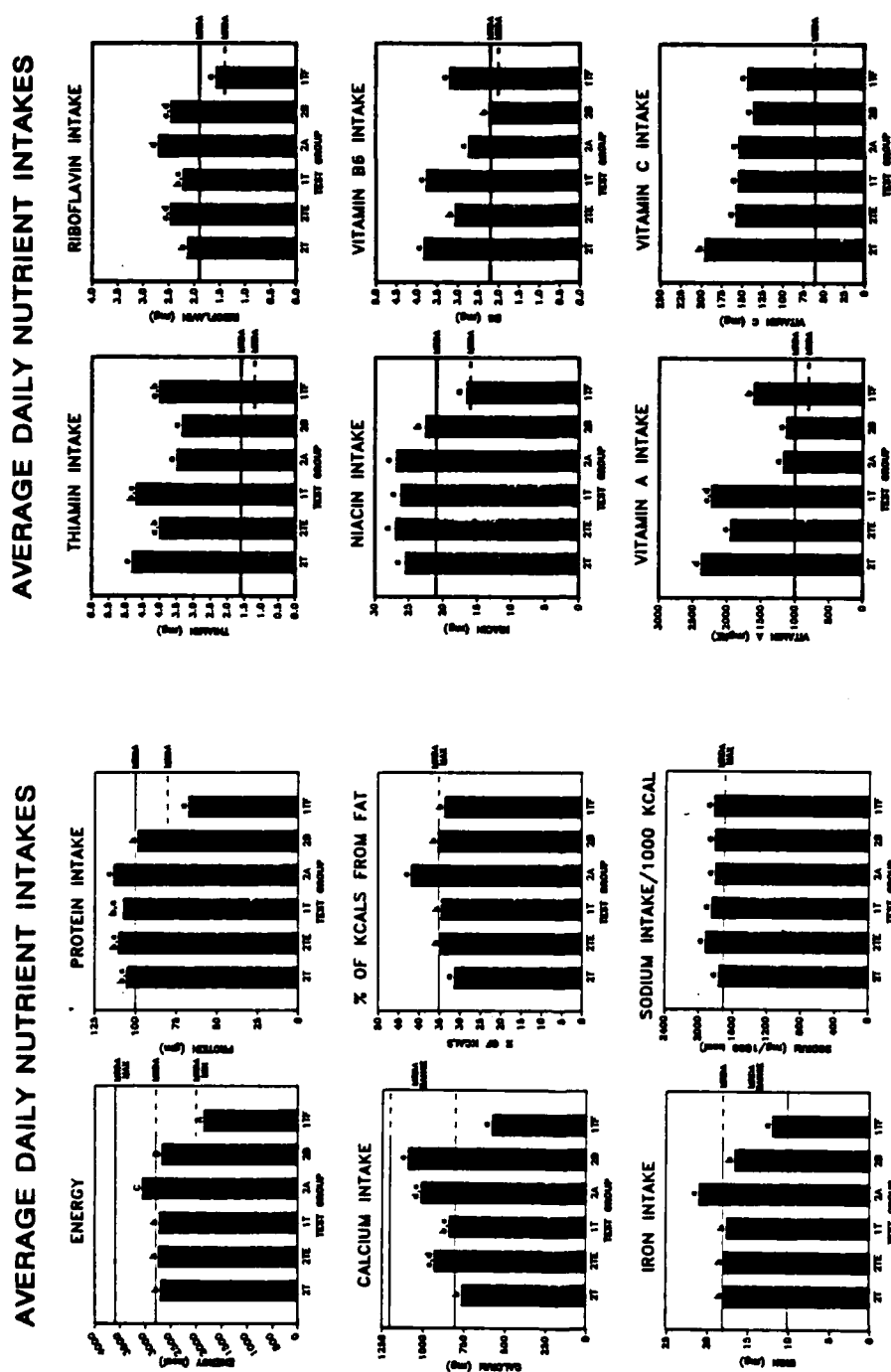


Fig. 1

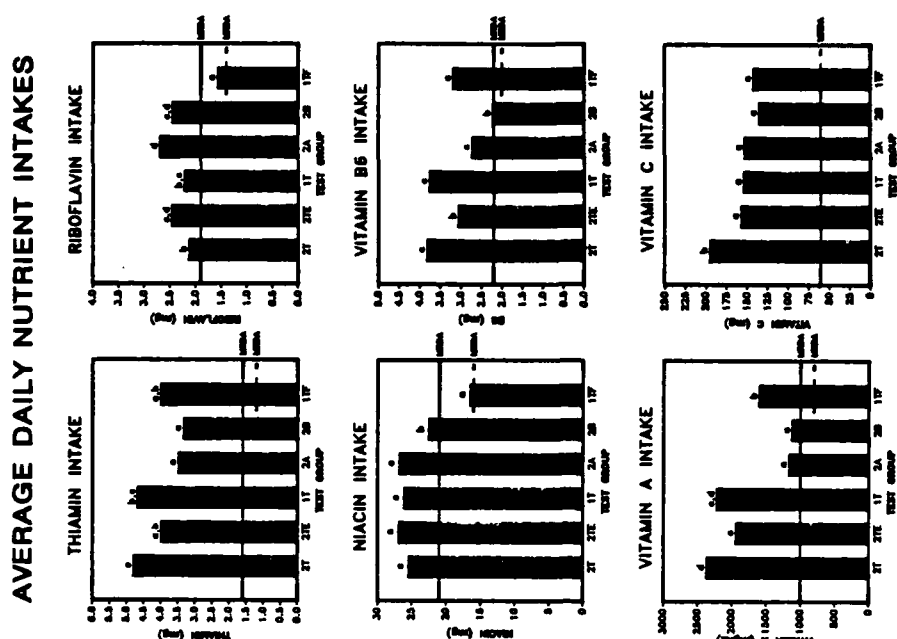


Fig. 2

SCHNAKENBERG, CARLSON, SAWYERS, VOGEL, JOHNSON, SZLYK, FRANCESCONI & HUBBARD

consume only approximately two-thirds of the calories available in the one or two MRE portion of their respective ration mixes.

Average calorie consumptions at breakfast meals were similar for T-(871 Kcal), B-(765 Kcal) and A-(958 Kcal) ration menus. However, calorie consumptions at T-ration dinner meals were much lower (986 Kcal) than at B-ration (1246 Kcal) or A-ration (1501 Kcal) meals. A comparison of the calories available and actually consumed at T- and A-ration dinner meals (Table 2) identifies menu factors contributing to the differing calorie consumptions. T-ration entrees and canned fruits (used as desserts) were

TABLE 2. CALORIES AVAILABLE AND CONSUMED AT T-RATION AND A-RATION DINNER MEALS

	T-Ration		A-Ration	
	Calories Available (Kcal)	Calories Consumed (%)	Calories Available (Kcal)	Calories Consumed (%)
Entrees	245	91	398	108
Starches	250	70	172	54
Vegetables	43	62	102	65
Fruits/Pudding	114	74	90	31
Desserts	-	-	271	90
Salads	-	-	59	58
Dressings	-	-	153	65
Gravies	-	-	20	84
Breads	256	64	250	61
Spreads	337	5	29	65
Beverage Base	108	86	108	96
Milk	-	-	149	76
Cocoa Powder	119	13	-	-
Condiments	34	23	34	6
Total	1506		1835	

well accepted but contained fewer calories per serving than A-ration entrees and baked desserts. The T-ration included spreads (MRE peanut butter, cheese spread) to increase caloric content but only 5 percent of the available calories from these spreads were actually consumed. Further analyses indicates that the soldiers liked and ate a high percentage of

SCHNAKENBERG, CARLSON, SAWYERS, VOGEL, JOHNSON, SZLYK, FRANCESCONI & HUBBARD

these same spreads with their MRE meals but did not want them with the T-ration meal.

Protein intakes (Fig 1) were adequate for males and the marginally low (67 gm) protein intake for the female group is not of concern because the protein MRDA is approximately twice the requirement level to reflect the usual protein consumption patterns of Americans. The OTSG recommendation is that dietary fat calories should not exceed 35 percent of the total energy intake. The fat intake of Group 2A (42% fat calories) exceeded that recommendation and was greater ($p < 0.05$) than all other groups. The lowest fat intake was observed in Group 2T (31% fat calories). The A-ration menu included whole milk, butter, salad dressings, gravies and high fat desserts such as cakes. The T-ration contains less fat because there was less fat in the entrees and the desserts were mostly canned fruits.

Calcium intakes (Fig 1) of the 1TF (female) and 2T groups were below the MRDA of 800 mg/day. The low calcium intakes (577 mg/day) by females on the 1T/2 MRE diet may not be adequate to maintain bone health and may lead to a greater risk for development of osteoporotic disease. Recent research (4) indicates that women who consumed milk frequently during their teens and 20s had greater bone density at age 40 than infrequent milk drinkers. Because of a lack of refrigeration, the T-ration menu does not provide dairy products, such as milk, which are the primary sources of calcium in the diet. Females consuming 2T ration and 1 MRE meals per day would be predicted to have even lower calcium consumptions than observed in this study.

Iron intakes were adequate for the male groups. The iron intake of the female Group 1TF (12 mg/day) is considered adequate because of the high bioavailability of iron in the CFFS rations. The OTSG has recommended an upper limit of 1700 mg sodium per 1000 Kcal. As shown in Figure 1, all ration groups exceeded that goal by approximately 10 percent. Further analyses indicates that approximately 6% of the daily sodium consumption was derived from added salt (salt packets).

Average daily vitamin intakes are shown in Figure 2. All ration groups met or exceeded the MRDA for thiamin, riboflavin, niacin, vitamin B₆, vitamin A and vitamin C.

All ration groups were able to maintain body weights within the energy balance criterion of ± 3 percent of initial body weight. Group 2A had the lowest incidence (8%) and Group 2B had the highest incidence (35%) of individual soldiers with weight losses exceeding 5 percent of initial body weight (Figure 3).

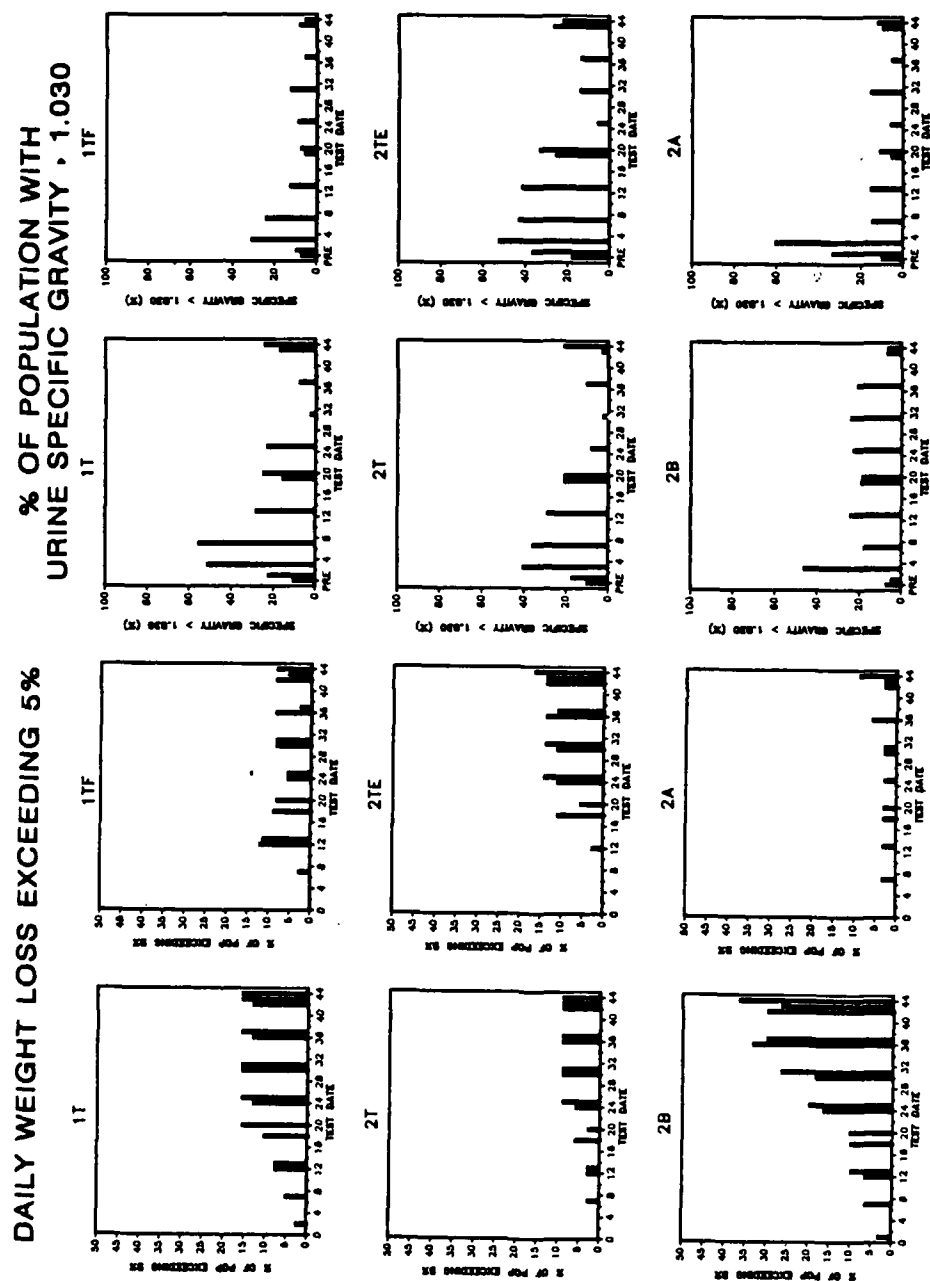


Fig. 3

Fig. 4

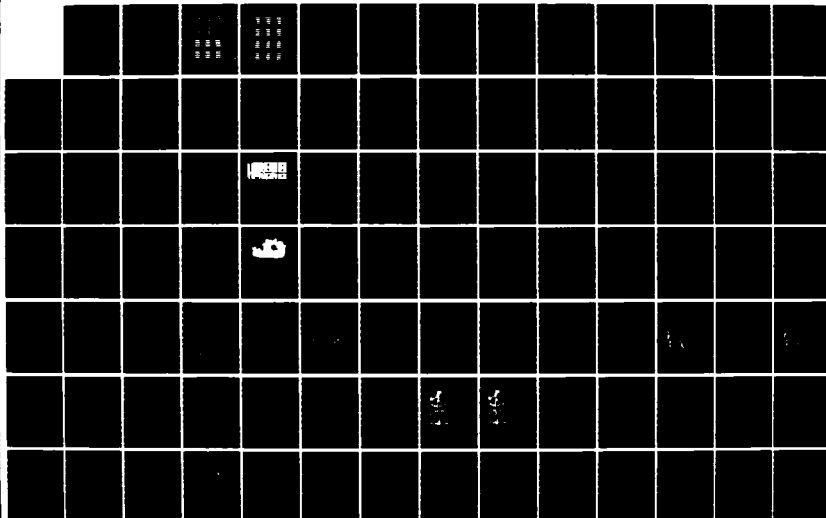
AO-A173 682

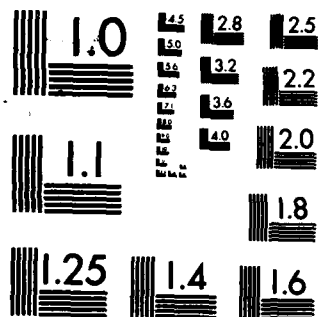
PROCEEDINGS OF THE ARMY SCIENCE CONFERENCE (15TH) HELD
IN WEST POINT NEW. (U) DEPUTY CHIEF OF STAFF FOR
RESEARCH DEVELOPMENT AND ACQUISITIO.. J SAHU ET AL.
28 JUN 86 F/G 5/2

2/4

UNCLASSIFIED

NL





MICROCOPY RESOLUTION TEST CHART
NATIONAL BUREAU OF STANDARDS-1963-A

SCHNAKENBERG, CARLSON, SAWYERS, VOGEL, JOHNSON, SZLYK, FRANCESCONI & HUBBARD

All ration groups were able to maintain their hydration status within the criterion that the average urine specific gravities of a unit should not exceed 1.030. Although acute dehydration was not a problem, there were indications that individual soldiers were not always optimally hydrated as shown in Figure 4. At Schofield Barracks (pre), only 6-18 percent of the individuals had concentrated urines (S.G. > 1.030). However, a very high incidence (40-60%) of concentrated urines occurred on day T+3 when all test groups had consumed three MREs per day. A ration effect was observed thereafter when the incidence of concentrated urines for Group 2A and 2B rapidly returned to baseline levels whereas the groups fed T-rations did not. The unitized T-ration provided only one 7 oz. paper cup per diner. Frequently, the cups developed leaks discouraging consumption of a second beverage. Recorded beverage consumption was less at T-ration meals than at A- or B-ration meals. Milk in one-half pint cartons was available with A- and B-ration meals and thus contributed additional fluids.

Biochemical assessment indicated that all ration groups were able to maintain their vitamin A, folic acid, and iron status. The serum total cholesterol values (Mean \pm SD) are shown in Figure 5. For age groups 19-29, a National Institute of Health Expert Group recently proposed that serum total cholesterol values less than 200 mg/dl are associated with low risk of coronary heart disease (CHD) whereas values greater than 220 mg/dl are associated with increasing risk of CHD. The distribution of the test groups according to these criteria are shown in Figure 6. By Chi-Square test, a significant ($p < 0.05$) shift in distributions occurred in Group 2A where the percentage of the population at low risk of CHD decreased from 72 percent at pre to 34 percent at day T+44. The high density lipoprotein (HDL) cholesterol levels (Mean \pm SD) are shown in Figure 7.

It is generally agreed that high HDL values are associated with a lower risk of CHD and that HDLs will rise with increased physical (aerobic) activity such as running several times per week. The observed general decline in HDL values in all groups may have been due to the abrupt reduction of running activity during the FDTE at PTA compared to the usual unit organized and self-paced physical training program at Schofield Barracks. Some authorities suggest that the ratio of total cholesterol to HDL is a more sensitive risk indicator of CHD and that cholesterol: HDL ratios greater than 5.0 for males and 4.4 for females may be associated with an increased risk of CHD. The distribution of these ratios is shown in Figure 8. The incidence of high ratios in Group 2A rose ($p < 0.02$) from 7 percent prior to deployment (pre) to 32 percent at T+44.

As noted earlier, Group 2A (fed two A rations and one MRE) consumed 42 percent of their calories from fat. Furthermore, Group 2A consumed

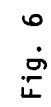


Fig. 5

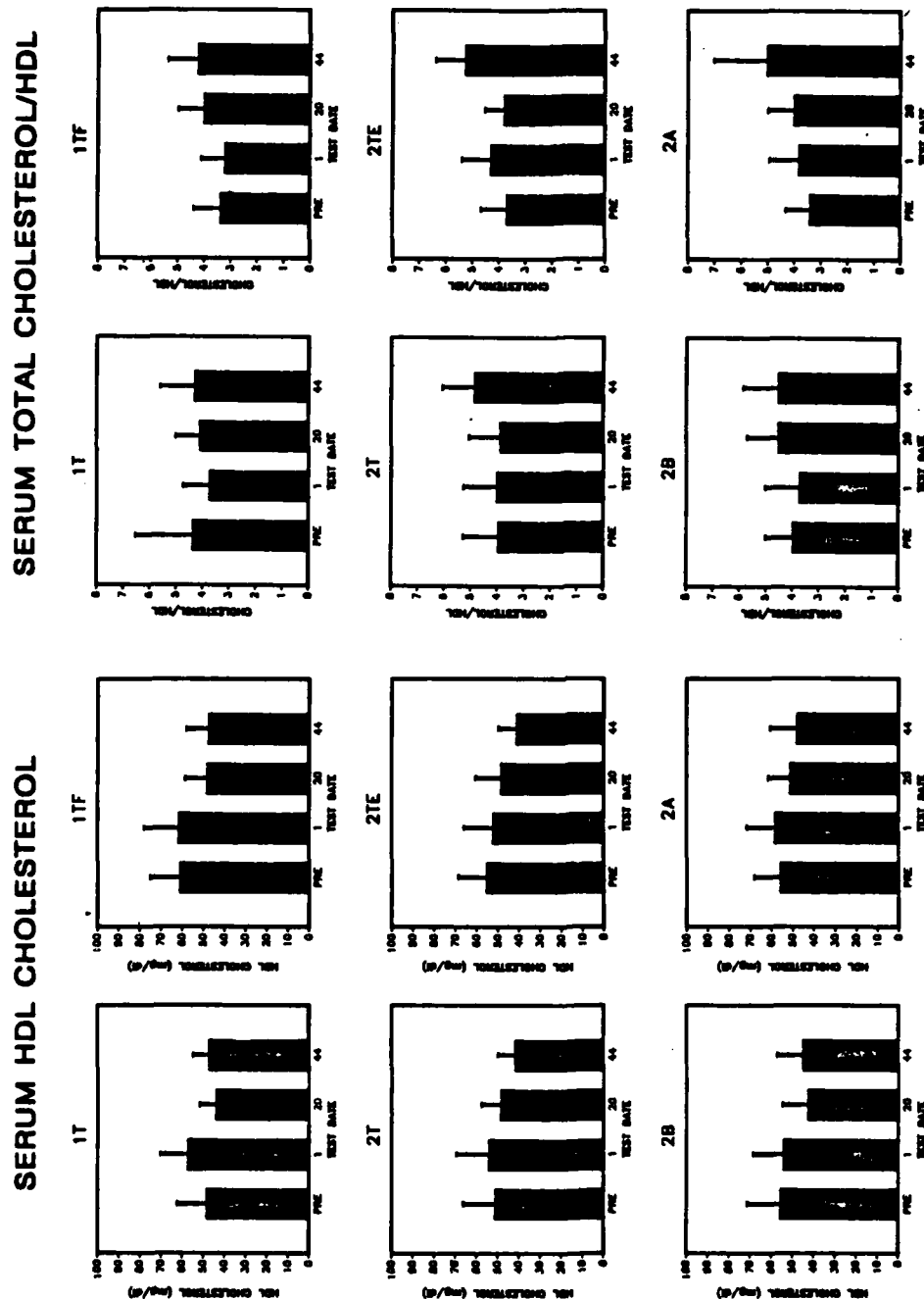


Fig. 7

Fig. 8

SCHNAKENBERG, CARLSON, SAWYERS, VOGEL, JOHNSON, SZLYK, FRANCESCONI & HUBBARD

770 mg cholesterol per day. All other groups had fat intakes less than 35 percent and their cholesterol intakes were below 300 mg/day. Most of the cholesterol was consumed at the A-ration breakfast meal (563 mg/meal) because eggs were served at every meal and were selected by most individuals. These data suggest that the excessive fat and cholesterol content of the A-ration meals combined with the decreased running activity at PTA may have contributed to the rise in serum total cholesterol, decrease in HDL and increase in cholesterol: HDL ratio observed in Group 2A. Such shifts in lipid profile are undesirable and, if continued for prolonged periods, will contribute to an increased risk of CHD.

The body composition data indicated that muscle mass was maintained in all groups and that any body weight losses were due primarily to losses of body fat. Body composition and energy consumption data were used to calculate estimated energy expenditures for the various test groups during the FDTE. The male groups expended approximately 3000 Kcal/day compared to approximately 2050 Kcal/day for the females. These energy expenditures are equivalent to a low to moderate level of physical activity.

The incidence of food related health disorders was very low throughout the FDTE. There were 1.6 days lost per 1000 man days for sick call due to gastrointestinal distress compared to 25.6 days lost per 1000 man days for sick call due to non-gastrointestinal distress. Self reported gastrointestinal complaints were lowest for Group 2A.

There was no evidence in any of the four muscle strength/endurance measurements and two eye-hand coordination tests of any decrement as a result of dietary treatment over time.

In summary, soldiers fed CFFS rations consumed sufficient calories to maintain energy balance for light to moderate physical activity (3000 Kcal) for extended periods. Protein, vitamin and iron intakes were adequate for all rations. The T-ration meals consumed contained much less fat and cholesterol than A-rations which provided too much fat and cholesterol. Seven continuous weeks of 2A rations and one MRE per day caused an undesirable rise in blood lipids. The T-ration menus will require modification to assure adequate calcium intakes, especially for female personnel. Consumption at T-ration meals can be increased and waste reduced by providing more of the calories as entrees and desserts and eliminating or reducing MRE spreads with T-ration meals. Some problems with adequate consumption of the MRE, certain T-ration components and fluids were identified for improvement and further field evaluation. Decreased aerobic (running) training activity during extended field training exercises may contribute to an undesirable decrease in serum high density lipoprotein (HDL) cholesterol.

SCHNAKENBERG, CARLSON, SAWYERS, VOGEL, JOHNSON, SZLYK, FRANCESCONI & HUBBARD

REFERENCES

1. _____. Combat Field Feeding System -- Force Development Test and Experimentation Test Report. US Army Combat Developments Experimentation Center, Ft. Ord, CA, and US Army Research Institute of Environmental Medicine, Natick, MA, Report No. CDEC-TR-85-006A, January, 1986.
2. _____. Nutritional Allowances, Standards and Education. Army Regulation 40-25, Headquarters, Department of the Army, Washington, DC, 15 May 1985.
3. Hirsch, E., H.L. Meiselman, R.D. Popper, G. Smits, B. Jezior, I. Lichton, N. Wenkam, J. Burt, M. Fox, S. McNutt, M.N. Thiele and O. Divige. The Effects of Prolonged Feeding of Meal, Ready to Eat (MRE) Operational Rations. US Army Natick Research and Development Center, Natick, MA Technical Report No. Natick/TR-85/035, October, 1984.
4. Sandler, R.B., C.W. Slemenda, R.E. LaPorte, J.A. Cauley, M.M. Schramm, M.L. Barrese and A.M. Kriska. Postmenopausal bone density and milk consumption in childhood and adolescence. Amer. J. Clin. Nutr. 42:270, 1985.

MODIFIED DIAKOPTIC THEORY OF ANTENNAS

*FELIX K. SCHWERING, DR. AND NARINDRA N. PURI, DR.
US Army CECOM, FORT MONMOUTH, NJ 07703-5202
CHALMERS M. BUTLER, DR.
Clemson University, Clemson, SC 29634-0915

I. INTRODUCTION

Low profile, survivable HF and VHF communication antennas are, by necessity, electrically small. As a consequence, these antennas tend to exhibit poor efficiency and narrow bandwidth. However, the performance of these antennas can be substantially improved by the utilization of multi-element radiating structures of complex configuration [1] which in a sense combine the tuning and matching networks with the radiating elements of the antenna. Such antenna structures, however, are difficult to analyze. The diakoptic theory of antennas, suggested recently by Goubau, et al [2], takes a new approach to this problem. It is designed to reduce the computational burden and to lead to a physically transparent network representation of multi-element antennas. But, in part, the theory is unconventional. The purpose of the present paper is to present a modified version of this theory which employs conventional antenna analysis methods only and which may facilitate understanding of the diakoptic method. Before discussion of the modified version, a short review of the original diakoptic theory appears useful here.

According to the original theory, the composite antenna structure is broken up (diakopted) into individual structure elements. As a simple example, Fig. 1 shows a disk loaded dipole which may be thought to consist of four structure elements, i.e., the two antenna arms and the top and bottom disks. The excitation of each element is ascribed to two causes: (a) the currents entering the element at its terminals, i.e., at its junctions with adjacent elements or the source, and (b) the fields due to the currents and charges on all the other elements. The first cause is referred to as "current coupling" and the second as "field coupling."

Current coupling dominates. It produces current distributions on the elements, which are determined by the size and shape of each element and the location of its terminals but are independent of the presence of

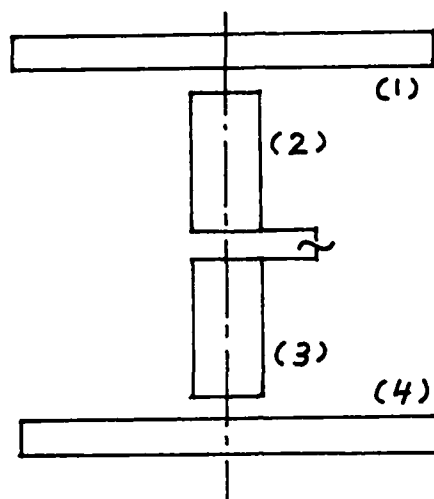


Fig. 1: Diakopted Antenna
(Disk-Loaded Dipole, in Cross Section)

all other elements. In other words, these current distributions can be calculated under isolated-element conditions (with all elements other than the considered element removed). They play a central role in the diakoptic theory and are called the "dominant" current distributions. Current coupling effects are described in terms of an "intrinsic" impedance matrix which relates the values of the retarded scalar potential at the terminals of each element to the currents entering or leaving the element at these terminals. Field coupling produces "scatter" currents on all the elements and its effect is represented by a field coupling matrix. The intrinsic and field coupling matrices are combined to arrive at the total impedance matrix of the diakopted antenna. The elements of this matrix are obtained as integrals over bi-linear expressions in the dominant and scatter current distributions and their associated charge distributions. The matrix elements in this representation have stationary properties with the consequence that computation of these elements from the dominant current distributions alone (i.e., with the scatter currents suppressed) leads to an impedance matrix that describes not only current coupling but also field coupling to first order.

In a final step, continuity of current and equality of potentials is enforced at all interconnection points, and an appropriate source condition is imposed at the feed points. This yields a system of linear equations for the junction currents of the reassembled antenna and permits one to determine the current distribution and input impedance of the antenna.

If field coupling is to be accounted for only in first order, then only the dominant current distributions must be used in the calculation of the impedance matrix, and scatter currents are neglected. Since, furthermore, the dominant currents for each structure element can be calculated under isolated-element conditions, the computational effort is greatly reduced. Numerical evaluations have shown that the first order theory yields good results even if the structure elements are chosen comparatively large [2,3]. This is expected because of the stationary properties of the impedance matrix coefficients.

The calculations of the dominant current distributions, however, introduce a conceptual complication: These current distributions are generated by impressing unit currents at the contact areas of the structure elements, which implies the assumption of hypothetical current sources with a single terminal only. Such sources violate the current continuity condition and the associated fields have to be expressed in terms of the retarded scalar and vector potentials, while Maxwell's equations cannot be applied without precautions. A consequence is that the impedance matrix, as defined here, relates the currents entering or leaving the structure elements to the values of the scalar potentials at the element terminals rather than to the voltages at the antenna ports (potential differences across terminal pairs). The current continuity condition is restored, however, for the total antenna when the structure elements are reconnected and continuity of current is enforced at all junctions.

The modified diakoptic theory suggested here eliminates this complication by a simple change in the basic approach, while otherwise it preserves most features of Goubau's original diakoptic theory. After diakopting the antenna, pairs of structure elements rather than single elements are considered as the basic building blocks of the antenna. The two elements of each pair are excited against each other so that there is no need for the assumption of one-terminal current sources. The pairs considered here are formed by adjacent elements and define the various ports of the (diakopted) antenna. Note that these pairs are overlapping. The modified theory describes the antenna by as many element pairs as it has ports, which means that most structure elements - except for end pieces - will be part of two or more pairs, depending on the branching that may occur at the elements. The antenna of Fig. 1, which has three ports, would be described by the pairs (1,2), (2,3) and (3,4).

The fields, currents and sources of the modified diakoptic theory satisfy Maxwell's equations. A second advantage is that this theory can be derived in a direct manner. The starting point is a standard impedance matrix formulation of the problem linking the port voltages and currents of the diakopted antenna. This formulation leads after only a few steps to an exact integral representation for the matrix elements in terms of suitably defined, normalized current distributions that serve as basis

functions of the diakopted antenna. This representation is rigorous. The distinction between "dominant currents" and "scatter currents" is made only as a convenience in the evaluation of the expressions for the impedance matrix elements, i.e., after the rigorous relationship between port voltages and actual port currents has been established. For the purpose of the evaluation, sound approximations are introduced in keeping with established principles and properties. The modified diakoptic theory can be "deduced" rather than "developed."

Furthermore, this theory facilitates comparison of the diakoptic method with the Method-of-Moments. But pairs of elements are more complex to analyze than is a single element, and their current distribution is more difficult to calculate, in particular, if the two elements are of different shapes.

This paper is concerned with the basic theory of the diakoptic method. Numerical examples which illustrate the usefulness of this method may be found in the papers on the original theory [2,3].

II. OUTLINE OF MODIFIED DIAKOPTIC THEORY

Similar to the original theory, the first step in the modified theory is to diakopt the antenna into individual structure elements. We assume that after diakopting, the antenna has N ports. The second step is the introduction of an impedance matrix formulation of the problem. (Consideration of element pairs will be introduced after formulation.) Thus

$$V_n = \sum_{m=1}^N Z_{nm} I_m \quad n = 1, 2, \dots, N \quad (1)$$

where V_n and I_n are the voltages and currents at the n th port and

$$Z_{nm} = \frac{V_n}{I_m} \quad \text{for } I_1, I_2, \dots, I_{m-1}, I_{m+1}, \dots, I_N = 0$$

Reciprocity requires symmetry of the impedance matrix, i.e., $Z_{nm} = Z_{mn}$.

Assume that a current of amplitude I_n is enforced at port n while all other ports are open circuited, i.e.,

$$I_m = \begin{cases} I_n & m = n \\ 0 & m \neq n \end{cases}$$

The resulting current distribution on the antenna surface S is termed $\bar{I}_n(\bar{r}_s)$ and the associated charge distribution is given by

$$q_n(\bar{r}_s) = -\frac{1}{i\omega} \bar{\nabla}_s \cdot \bar{i}_n(\bar{r}_s) \quad (3)$$

Where $\bar{\nabla}_s \cdot \bar{i}_n$ is the surface divergence of \bar{i}_n . Note that \bar{i}_n is zero at all ports, apart from the nth port where the total current is I_n :

$$\oint_{C_m} \bar{i}_n(\bar{r}_s) \cdot (\bar{n}_s(\bar{r}_s) \times d\bar{c}) = \begin{cases} I_n & m = n \\ 0 & m \neq n \end{cases} \quad (4)$$

In this equation, \bar{n}_s is the unit vector normal to the antenna surface S ; C_m is the contour curve* of port m ; and $d\bar{c}$ is the line element of C_m as indicated in Fig. 2. If the diakopted antenna has N ports, there are

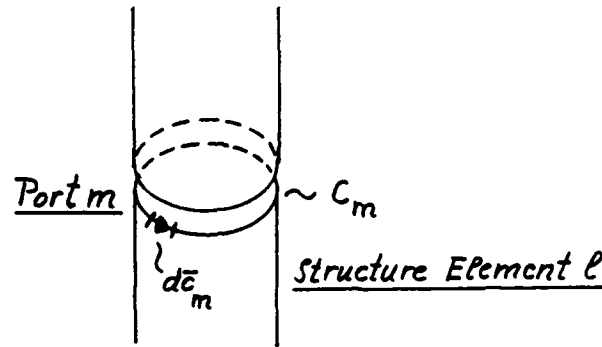


Fig. 2: Contour Curve C_m of Port m of Diakopted Antenna

N such current distributions \bar{i}_n , and the current distribution of the overall antenna can be expressed in terms of the \bar{i}_n for any arbitrary excitation (by voltage or current sources at the N ports). The normalized distributions

*Each port has two contour curves C_m ; see Fig. 2. Equation (4) holds for either curve.

$$\frac{\bar{i}_n(\bar{r}_s)}{I_n} \quad \text{and} \quad \frac{q_n(\bar{r}_s)}{Q_n} \quad (5)$$

with $Q_n = \frac{I_n}{i\omega}$

depend only on the antenna geometry and can be regarded as the basis functions of the antenna. We assume for the moment that these basis functions are known and proceed to express the matrix coefficients Z_{nm} in terms of these functions.

The current distribution \bar{i}_n causes the electric field strength

$$\bar{E}_n(\bar{r}_p) = -i\omega \bar{A}_n(\bar{r}_p) - \nabla_p \Phi_n(\bar{r}_p) \quad (6a)$$

where

$$\bar{A}_n(\bar{r}_p) = \frac{\mu_0}{4\pi} \iint_S \bar{i}_n(\bar{r}_s) \frac{e^{-ikr_{sp}}}{r_{sp}} dS \quad (6b)$$

$$\Phi_n(\bar{r}_p) = \frac{1}{4\pi\epsilon_0} \iint_S q_n(\bar{r}_s) \frac{e^{-ikr_{sp}}}{r_{sp}} dS \quad (6c)$$

\bar{A}_n and Φ_n are the retarded vector and scalar potentials associated with \bar{i}_n and q_n , respectively; \bar{r}_s is any point on the antenna surface S ; \bar{r}_p is the point of observation and $r_{sp} = |\bar{r}_p - \bar{r}_s|$.

\bar{E}_n satisfies the boundary condition $(\bar{E}_n)_{\text{tang}} = \bar{0}$ on all metal surfaces of the antenna while $\bar{i}_n = \bar{0}$ at all ports except for the n th port. Hence, the scalar product $\bar{E}_m \cdot \bar{i}_n$ is different from zero only at the n th port, and it is easily verified with Eqs. (1) and (4) that

$$-\frac{1}{I_n I_m} \iint_S \bar{E}_m \cdot \bar{i}_n dS = Z_{nm} \quad (7a)$$

This representation of Z_{nm} is stationary about the true currents \bar{i}_n, \bar{i}_m . Harrington [4] has shown that a first order error in these currents will produce only a second order error in Z_{nm} ; the proof as it applies to the present problem is sketched in Ref. [6]. Using Eqs. (6) in Eq. (7a) we obtain the desired representation of Z_{nm} in terms of the current and charge distributions \bar{i}_n and q_n :

$$Z_{nm} = \frac{i\omega\mu_0}{4\pi} \iint_S \iint_S \left\{ \frac{\bar{i}_n(\bar{r}_s) \cdot \bar{i}_m(\bar{r}_s)}{I_n I_m} - \frac{1}{k^2} \frac{q_n(\bar{r}_s) q_m(\bar{r}_s)}{Q_n Q_m} \right\} \frac{e^{-ikr_{ss'}}}{r_{ss'}} dS dS' \quad (7b)$$

We have used here the relation

$$r_{ss'} = |\bar{r}_s - \bar{r}_{s'}|$$

$$\iint_S \bar{i}_n \cdot \bar{\nabla} \Phi_m dS = i\omega \iint_S q_n \Phi_m dS \quad (7c)$$

which follows from Gauss' Theorem. The symmetry of the impedance matrix is obvious from Eq. (7b).

The expression for Z_{nm} is rigorous. Up to this point, it has been assumed that the functions $\bar{i}_n(\bar{r}_s)$ and $q_n(\bar{r}_s)$ are the exact current and charge distributions of the diakopted antenna. However, because of the stationary properties of representation (7b), no significant loss in accuracy will occur when the exact distributions are replaced by appropriate close approximations. A useful, easy-to-calculate approximation is obtained from the following consideration. If all structure elements of the antenna have dimensions sufficiently below their first resonance, then \bar{i}_n will be of significant magnitude only on the two elements meeting at port n , while it is very small on the remaining elements where often it can be neglected. (Recall that \bar{i}_n is the current distribution that obtains when all ports are open except for port n which is driven by I_n .)

Moreover, the distribution of \bar{i}_n on the two driven elements should be close to that existing under isolated conditions, i.e., when all other

elements are removed. Thus, \bar{I}_n may be approximated by this isolated-case current distribution on the pair of driven elements and by zero on all other elements.

These approximate current distributions and the associated charge distributions will be denoted by \bar{I}_n^d , q_n^d in the following. Their use as basis functions introduces into the modified theory the consideration of element pairs as the basic building blocks of the antenna as was mentioned in Section I. The pairs considered here are formed by adjacent elements which meet at the ports of the diakopted antenna. There is one such pair for each port, which also means that these pairs overlap and that most structure elements - apart from end pieces - are part of two or more pairs. They are part of more than two pairs when branching occurs and a given element terminates into more than two ports. In general, the number of pairs to which a structure element belongs is equal to the number of ports to which it branches out. In the case of the antenna of Fig. 1, no branching occurs; the antenna has three ports and is characterized by the pairs (1,2), (2,3), and (3,4).

The \bar{I}_n^d are the equivalents of the dominant current distributions of the original theory (and the difference currents $\bar{I}_n - \bar{I}_n^d$ are the equivalents of the (total) scatter currents). But while the dominant currents of the original theory are associated with single structure elements and require hypothetical one-terminal current sources for their excitation, the currents \bar{I}_n^d defined here are associated with element pairs and are excited by conventional two-terminal current sources satisfying the current continuity condition. Calculation of the \bar{I}_n^d and their use in Eq. (7b), to compute the impedance matrix coefficients Z_{nm} , constitutes the first order* modified diakoptic theory. The stationary properties of representation (7b) should ensure good accuracy.

If needed, the accuracy of the current distributions can be improved by calculating them in a higher order approximation, i.e., by the consideration of scatter currents in addition to the dominant currents. Values

*Since, in calculating the \bar{I}_n^d , isolated element-pair conditions are assumed and interaction with other element pairs is neglected, these current distributions are zero order approximations as far as field coupling is concerned. However, the stationary representation (7b) for the Z_{nm} takes field coupling into account in higher order than do the current and charge distributions which appear in this equation. If the zero order distributions \bar{I}_n^d and q_n^d are used here, the values obtained for the Z_{nm} will include field coupling in first order.

for \bar{I}_n different from zero will then be obtained on all structure elements of the antenna. A procedure which allows one to determine current correction terms in an iterative fashion has recently been developed. We restrict ourselves here to a brief discussion of its main features and refer to a forthcoming paper [6] for a detailed presentation of the method.

A particular advantage of this method is that, at each iteration step, the correction terms for \bar{I}_n associated with the various structure elements can be calculated separately. They are determined by integral equations that are decoupled and can be solved on an element-by-element basis. In physical terms, calculation of these higher order current corrections involves the solution of the standard scatterer problem for each individual structure element with the incident field (describing field coupling to the other elements) determined in the previous iteration step and therefore known at this stage. Hence, from iteration to iteration, the basic integral equation for each structure element remains the same with only the forcing term varying. The procedure avoids the need for computation, storage and inversion of large matrices, and calculation of the current distributions \bar{I}_n in higher order accuracy should not be a computationally demanding task.

When the impedance matrix coefficients are known, the currents I_n at the antenna ports are found from Eqs. (1) by imposing the condition that $V_n = 0$ for all n , except for the input port of the overall antenna ($n=\tilde{n}$) where V_n is equated to the driving voltage U . Impedance loading of the antenna ports could be easily handled in this final step as well.* With the currents I_n determined, the current distribution $\bar{I}_A(\bar{r}_s)$ of the reassembled antenna and its input impedance Z_A are obtained as

$$\bar{I}_A(\bar{r}_s) = \sum_{n=1}^N \bar{I}_n(\bar{r}_s) \quad (8a)$$

$$Z_A = \frac{U}{I_{\tilde{n}}} \quad (8b)$$

*For a structure driven at several ports, the appropriate V_n 's are replaced in Eq. (1) by the known driving voltages. In the general case that port n is driven by a voltage source U_n and loaded with an impedance Z_n we have $V_n = U_n - Z_n I_n$.

where the \bar{i}_n on the right side of Eq. (8a) may be interpreted as the products of the n port currents I_n and the normalized current distributions $\bar{i}_n(\vec{r}_s)/I_n$ which depend on the antenna geometry only.

III. COMPARISON OF DIAKOPTIC THEORY WITH METHOD-OF-MOMENTS

The matrix formulation of the antenna problem in terms of Eqs. (1) and (7b) is formally identical with the system of equations which is obtained if one applies the Galerkin version of the Method-Of-Moments (MOM) [5] to the E-field integral equation formulation of the problem while using the current distributions $\bar{i}_n(\vec{r}_s)$ as the basis and weighting functions. It is of no consequence here whether the exact or the approximate current distributions are employed for this purpose; as long as one uses the same functions in the diakoptic theory and the MOM, an identical set of equations will result.

Generally speaking, there is, however, the following difference between the two methods: In the MOM, the basis and weighting functions are, in principle, arbitrary and are usually chosen to have a simple profile. In the diakoptic theory, these basis functions are adapted to the problem at hand. They are obtained by solving an integral equation. Typically, the approximate current distributions \bar{i}_n^d are employed since they can be handled numerically with relative ease. The integral equation which is solved to find \bar{i}_n^d enforces the boundary condition $\bar{E}_{\text{tang}} = \bar{0}$ for the pair of structure elements driven by the port current I_n under isolated case conditions. In other words, \bar{i}_n^d is determined such that it satisfies $\bar{E}_{\text{tang}} = \bar{0}$ exactly on the element pair excited by the dominant effect of current coupling. Consequently, the structure elements can be chosen comparatively large* and the number of basis functions needed to obtain good accuracy is comparatively small which means that the resulting matrix size is small. It is hoped that a conceptually transparent network representation of multielement antennas will eventually evolve from the diakoptic method.

A second point concerns the computational effort involved in the MOM and the diakoptic method. The MOM, in the following referred to as Method A, usually employs a large number of basis functions of simple profile and, accordingly, subdivides the antenna surface into many electrically small subdomains. The antenna problem is solved by the computation of a single large matrix and the evaluation of the corresponding linear system of equations. The diakoptic theory, Method B, uses relatively few structure elements (which, however, are chosen sufficiently small to operate

*The size of the structure elements is limited however, by the condition that each individual element should operate below its first resonance.

below their first resonance) and breaks the procedure up into several steps. First, the integral equations for the \bar{I}_n^d are solved, typically by the use of a MOM approach, i.e., by setting up and solving a set of N matrix equations (N : number of ports); the matrices involved are of comparatively small size and describe the element pairs of diakopted antenna under isolated case conditions. This is followed by the computation of the $N \times N$ element impedance matrix (7b) and the determination of the port currents I_n . For the antenna problems of interest here, the matrix elements are usually given in the form of multiple integrals and the matrix fill time exceeds the matrix inversion time. If the Galerkin version of the MOM is employed, the number of matrix elements that have to be computed* is $\frac{1}{2}S(S+1)$ for Method A and $2NM(M+1) + \frac{1}{2}N(N+1)$ (total number including \bar{I}_n^d matrices) for Method B, where S is the number of basis functions used in Method A, and M is the number of subdivisions of individual structure elements employed in the computation of the \bar{I}_n^d in Method B; M is assumed here to be the same for each element. With L denoting the number of structure elements of the diakopted antenna, it is obvious that $S = L \cdot M$ if both methods use the same subdomain structure of the antenna surface, i.e., if the same basis functions and subdomains which are employed by Method A to formulate the matrix representation of the overall antenna problem are also used by Method B, on an element pair basis, to formulate the matrix equations determining the \bar{I}_n^d . For complex antennas S , N , M , L are sizeable numbers, and L is close to N . The above expressions for the number of matrix elements indicate that, in this case, the diakoptic method can reduce the computation time by a factor of $N/4$. Further significant improvements will result if accurate closed form approximations can be determined for the \bar{I}_n^d . This should be possible in cases where the structure element pairs are of particularly simple configuration; alternatively data tables may be employed. Numerical examples discussed in [2] have assumed a triangular profile for the dominant current distributions on the structure elements of a thin dipole antenna. The computational effort has been minimal in this case while comparison with exact data has shown good accuracy of the results obtained.

A third difference between the two methods is apparent in the way in which accuracy is improved, if necessary. In the MOM, the number of basis functions and the matrix size are increased to enhance accuracy which, in a subdomain representation of an unknown function, means that the antenna surface subdivision is increased. In the diakoptic theory, the number of ports, hence, the number and size of structure elements

*Symmetries of the antenna configuration may be utilized to reduce the matrix size but are not considered at this point. Usually they would reduce the computational effort involved in the two methods by the same factor.

would not change typically, and improvements would be achieved by the addition of higher order correction terms* to the current distributions \bar{I}_n^d such that each basis function satisfies the boundary condition $\bar{E}_{\text{tang}} = \bar{0}$ not only on its pair of driven elements (current-coupled elements) but, with increasing accuracy, on the remaining structure elements as well (with the ports resulting from diakopting open-circuited). The iterative procedure of Ref [6], which was briefly discussed in the preceding section, should permit one to determine these current correction terms in a numerically efficient and systematic manner. Of course, in the diakoptic theory, one has the liberty in many structures to increase the number of ports and elements if such is desired to increase accuracy.

IV. CONCLUSIONS

Apart from the simple change that the modified theory considers pairs of structure elements instead of single elements as the basic building blocks of the diakopted antenna, it preserves most features of the original theory developed by Goubau. The modified theory has the advantage that it maintains current continuity at every step and remains fully within the framework of Maxwell's equations. Formulation of the theory is rigorous and conceptually straightforward; approximations are introduced only after exact equations have been formulated. Furthermore, this theory facilitates relating the diakoptic method to the Method-of-Moments. A disadvantage is that pairs of elements are somewhat more difficult to analyze than single elements so that calculation of the "dominant" current distributions is computationally more complex, in particular, if the two elements do not have the same shape.

*As opposed to the zero order currents \bar{I}_n^d which are different from zero on element pairs only, the higher order current corrections (scatter currents) have values different from zero on all structure elements of the diakopted antenna.

References:

- [1] G. Goubau and F. Schwing, Proceedings of the ECOM-ARO Workshop on Electrically Small Antennas, Fort Monmouth, NJ, pp. 63-67, Oct 1976.
- [2] G. Goubau, N. N. Puri and F. Schwing, Diakoptic Theory of Multi-element Antennas, IEEE Transactions on Antennas and Prop., Vol. AP-30, pp. 16-26, Jan 1982.
- [3] A. Stavridis, Mathematical Modeling of Multielement Antennas, Ph.D. Dissertation, Rutgers University, May 1982.
- [4] R. F. Harrington, Time Harmonic Electromagnetic Fields, McGraw-Hill, New York, 1961.
- [5] R. F. Harrington, Field Computation by Moment Methods, Macmillan, New York, 1968.
- [6] F. K. Schwing, N. N. Puri and C. M. Butler, Modified Diakoptic Theory of Antennas, accepted for publication in IEEE Transactions on Antennas and Propagation.

SHAPPIRIO, FINNEGAN, LUX, KWIATKOWSKI, FOX, HEATH, WADE, SAVAGE, AU COIN

NEW METALLIZATION TECHNOLOGIES FOR ADVANCED MILITARY MICROELECTRONICS

*JOEL R. SHAPPIRIO, DR., JOHN J. FINNEGAN, MR., ROBERT A. LUX., DR.,
JOSEPH H. KWIATKOWSKI, MR., DONALD C. FOX, MR., LINDA S. HEATH, MS.,
MELVIN J. WADE, MR., ROBERT O. SAVAGE, MR., AND THOMAS R. AU COIN, MR.
US ARMY ELECTRONICS TECHNOLOGY AND DEVICES LABORATORY (LABCOM)
FORT MONMOUTH, NEW JERSEY 07703-5302

INTRODUCTION

Future military requirements for real-time information acquisition and processing in tactical EW, DC³I and smart munitions establish a critical need for ultralarge-scale superhigh-speed integrated circuits and microelectronics. The number of process technologies which must be invoked to achieve this integration is large, including ion implantation, diffusion, film depositions of both dielectric and metallization, lithography, oxidation, and etching. Not only must each individual process step be optimized to its state-of-the-art limits, but each must be integrated with the others in order to successfully achieve an operational IC. The consequences of this integration have been to dramatically increase the number of components per chip, while simultaneously decreasing the minimum feature size which must be patterned.

The metallization employed in the fabrication of such circuits is as profoundly influenced by device geometry downscaling as any of the other process steps. With increased integration, not only are the lateral dimensions of the metallic circuit elements reduced, but so also are the vertical dimensions of the electrically active regions of the device components. This dimensional shrinkage has two important implications:

1. With the reduction in lateral dimensions, smaller design rules have tended to result in reduced linewidth without a concomitant reduction in interconnect length (1). For a constant interconnect length, reduction in the RC time constant is most readily achieved by a reduction in the sheet resistivity of the metal interconnect (2), thus, the choice of connector material can have a dramatic effect. Sinha (3) shows that for a given acceptable delay, the interconnect may be an order of magnitude longer if a silicide (TaSi₂) rather than polysilicon is employed, simply because of the difference in sheet resistivities between the two compounds.
2. The reduction in vertical dimension imposes severe constraints on the

extent of permissible interaction between metal and semiconductor. At the extreme, this interaction may locally penetrate throughout the electrically active junction region; junction shorting in aluminum contacts to silicon is the classic example (4).

The evolution of an extremely diverse assortment of metallization systems and structures for Schottky and ohmic contacts, and for interconnection metallurgy, has essentially been driven in response to the added constraints placed on the metallization by this geometry downscaling. Implicit in these sometimes complex multilevel metallization structures is the need for identification of new metallization materials with improved contact characteristics, as well as for the creation, through metal deposition, of barrier layers which will permit each individual metal film to perform its intended function while maintaining its integrity during subsequent device operation.

In this paper, details of the synthesis and properties of an entirely new class of contact metals are presented, their remarkable effectiveness as diffusion barriers when used to separate silicon from second level aluminum metallization are demonstrated, and finally results are described employing diboride diffusion barriers to achieve extremely stable ohmic contacts to n-type GaAs. These are the thinnest ohmic metallization yet achieved, and with the lowest specific contact resistivity yet reported.

DIBORIDE METALLIZATION FOR Si TECHNOLOGY

Diboride Synthesis

Thin films of ZrB_2 and TiB_2 up to 800 nm in thickness were deposited by r.f. diode sputtering onto silicon, thermal SiO_2 on silicon, and on beryllium foil substrates. The TiB_2 or ZrB_2 sputtering targets used were vacuum hot pressed to yield densities of approximately 80% and 92% of the bulk values respectively. The best films obtained, as determined by conductivity and Auger depth profiling, were sputtered using an r.f. power of 800 W and a negative bias of 75-80 V. Under these conditions, the sputter rate was $10-15\text{ nm min}^{-1}$; thicknesses were measured using a stylus instrument on chemically etched steps.

Annealing experiments, performed in an attempt to optimize the properties of the as-deposited films, included conventional furnace anneals and rapid annealing experiments using a commercial microprocessor-controlled high intensity source of incoherent visible light having two banks of quartz-tungsten-halogen lamps directed at the sample through a quartz reaction chamber containing flowing high purity argon. The properties of as-deposited, annealed and aluminized films were evaluated by a variety of characterization techniques, including conventional four-point probe resistivity measurements, Auger electron spectroscopy (AES),

Rutherford backscattering spectroscopy (RBS), X-ray diffractometry (XRD), transmission electron microscopy (TEM) and scanning electron microscopy.

Diboride Properties

As-deposited films of both TiB_2 and ZrB_2 are reflective, hard, show good adhesion characteristics to both silicon and SiO_2 on silicon substrates and can be wet chemically etched in 80% H_2O_2 or hot 50% HNO_3 for TiB_2 and ZrB_2 respectively; preliminary plasma etching of annealed ZrB_2 films using NF_3 gas gave an etch rate of 18nm min^{-1} . The compositions of the as-deposited films were estimated from AES measurements using the relative elemental sensitivity factors due to Davis et al(5). They suggest that the as-deposited films are boron deficient (Fig. 1(a)) and that they may contain up to 6 wt.%O and 12 wt.%O for ZrB_2 and TiB_2 respectively. RBS data from samples sputtered onto beryllium substrates show similar levels of oxygen contamination but indicate that as-deposited ZrB_2 and TiB_2 are stoichiometric.

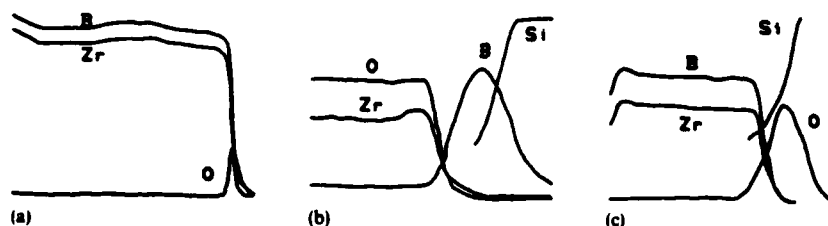


Fig. 1. AES depth profiles of ZrB_2 thin films: (a) as deposited onto silicon (deposition time, 50 min; r.f. power, 500W); (b) on silicon after a conventional furnace anneal in argon at 1000°C for 1 h; (c) on a SiO_2/Si substrate after a rapid pulse anneal in argon at 1050°C for 100s. The film-substrate interface is to the right in each profile.

Four-point probe sheet resistance measurements were made on all as-deposited ZrB_2 and TiB_2 thin films to evaluate the effect of variation in the sputtering parameters on the quality of the films produced. In general, an applied substrate bias, a high r.f. power, a high argon throughput at low sputtering pressure and a thorough target pre-clean and chamber clean-up all favor lower sheet resistances. The lowest sheet resistances obtained to date for these as-deposited films are $3\Omega/\square$ and $5\Omega/\square$ for ZrB_2 and TiB_2 respectively. The best measured resistivities for TiB_2 films fail to approach those reported for the bulk material as closely as do those for ZrB_2 . This may relate to the poorer quality of the TiB_2 sputtering target, which, with its higher porosity, precludes the elimination of contaminant species even with extensive presputter target clean-up.

Conventional furnace heat treatments were performed in flowing N_2 argon or N_2 - H_2 mixtures at a flow rate of $200 \text{ cm}^3 \text{ min}^{-1}$ and at temperatures of up to 1000°C for 1 h. In all cases the samples failed to survive such treatments, suffering marked losses in reflectivity and becoming crazed, cracked, multicolored and discontinuous with corresponding drastic increases in sheet resistance. Auger depth profiles showed a strong tendency for both ZrB_2 and TiB_2 films to pick up oxygen from the furnace ambient and become ZrO_2 or TiO_2 as confirmed by XRD, with the concomitant migration of boron to the film-substrate interface (Fig. 1(b)). Oxygen levels in as-deposited films were insufficient to account for the concentrations observed in the films after conventional (equilibrium) furnace anneal experiments.

Successful recrystallization was accomplished using the previously described halogen lamp rapid anneal system. Samples were heated in flowing argon to a maximum temperature of 1150°C for times of up to 200s. The resultant annealed films retain their initial reflectivity and yield XRD patterns identical with those reported in the powder diffraction file for the corresponding bulk hexagonal ZrB_2 and TiB_2 ; no other phases were evident in the XRD pattern. TEM reveals an increase in the grain size to 80-100 nm, and AES (Fig. 1 (c)) and RBS data indicate that diffusion of boron and oxidation of the films, as observed in conventional furnace annealing, were avoided.

In general, the lowest annealed sheet resistances, about $1\Omega/\square$, are observed in the films with the highest as-deposited conductivity. This sheet resistance was obtained using 60 s anneals at 100% applied power, corresponding to 1150°C ; a roughly tenfold drop in resistance is thus observed from the as-deposited to the annealed film. The diboride thickness was 250-300 nm, leading to an estimate of the film resistivity for annealed ZrB_2 of between 25 and $30 \mu\Omega\text{cm}$. Such values are thus seen to compare very favorably with the annealed resistivities of the typical transition metal silicides.

In Table 1 are summarized the as-deposited and rapidly annealed thin film resistivity data obtained in this study, together with representative thin film disilicide data of Murarka et al(6), the bulk resistivity data of Nicolet(7) and the bulk melting point data for the disilicides due to Poate et al(8) and for the diborides due to Muetterties(9).

The stability of ZrB_2 against aluminum has been evaluated in thin film couples to temperatures of 625°C for up to 2 h in flowing N_2 by RBS and AES depth profiling methods. RBS spectra, taken at 1.8 MeV using helium, indicated only limited reaction between the ZrB_2 and the overlying aluminum metallization at 625°C (Fig. 2); at temperatures of 600°C and below, no reaction has been observed. The corresponding AES depth profile (Fig. 3) for a sample run at the same temperature showed some evidence of

Table 1. COMPARISON OF BULK AND THIN FILM RESISTIVITY AND MELTING POINT DATA FOR SOME REPRESENTATIVE DISILICIDES AND DIBORIDES

Material	Resistivity ($\mu\Omega\text{cm}$)			Melting point (C) ^a
	Bulk ^b	Thin film ^c		
		As deposited	Annealed	
Silicides ^d				
TiSi ₂	16.7-123	440	25	1540
TaSi ₂	8.5-46	500	51-55	2200
MoSi ₂	21	750	100	2050
WSi ₂	16-38	1250	70	2165
NbSi ₂	6.3	300	120	1950
Borides ^e				
ZrB ₂	7-38	250	25	3245
TiB ₂	9-28	500	150	2980

^a Silicide data from ref. 14; diboride data from ref. 15

^b Bulk resistivities from ref. 13

^c Thin film silicide data from ref. 12; thin film boride data this work

^d Prepared from a co-sputtered target

^e Prepared from a sintered target

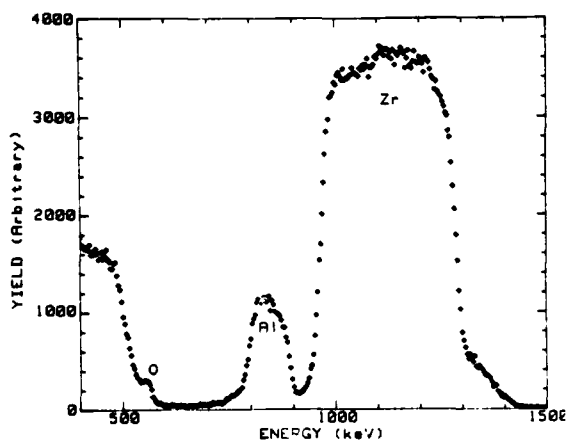


Fig. 2. RBS spectrum of 100 nm aluminum on ZrB₂ heat treated in N₂ at 625C for 2 h showing limited interaction.

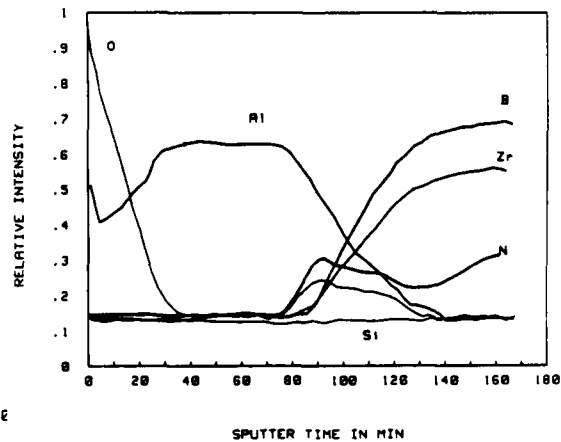


Fig. 3. AES depth profile of 400 nm aluminum on ZrB₂ heat treated at 625C in flowing N₂ for 2 h showing limited interaction.

limited diffusion of zirconium, and perhaps boron, into the aluminum; assuming equivalent sputter rates for aluminum and ZrB_2 , this diffusion region is estimated to be less than 80nm in width. Furthermore, the zirconium trace in this depth profile does not suggest compound formation, and we have been unable to see evidence for such compound formation by either RBS or XRD study; the XRD was performed both on samples with the aluminum overlayer intact and on samples where the aluminum was removed by immersion in an NaOH solution.

This observed stability of ZrB_2 against aluminum to temperatures of 625C is in marked contrast with the behavior of most metal silicides (10, 11,12), which show the initiation of compound formation (usually ternaries of the metal, silicon and aluminum) at temperatures higher than 400-450C, and which therefore require the interposition of a diffusion barrier such as Ti-W between the silicide and the overlying aluminum in order to stabilize the contact. Thus the prediction of Nicolet (7) that the borides should form attractive candidates for effective diffusion barriers is confirmed; indeed, the diborides have been observed (13) to have the highest stability in contact with aluminum of any of the related interstitial transition metal nitride and carbide compounds so far studied.

APPLICATION OF BORIDE DIFFUSION BARRIERS TO GaAs TECHNOLOGY

Overview of GaAs Ohmic Contacts

A wide variety of metallization schemes have been investigated to provide reliable ohmic contacts to III-V semiconductors in general, and to n-type GaAs specifically. The principle of these contacts is to produce a highly doped region at the surface of the GaAs in order to achieve a low contact resistance between the semiconductor and the contact metal (14). For n-type GaAs this is accomplished by choosing a metal composition which will alloy with the GaAs, and where one constituent of the metallization becomes a donor atom. The most widely studied and the most commonly applied ohmic metallization consists of the eutectic Au-Ge alloy (88% Au) usually in combination with a Ni layer designed to minimize ball-up during subsequent alloying as well as to assist in the decomposition of the GaAs. Alloying of the metallization layers is required at temperatures in the range 400-500C for times ranging from seconds to several minutes to obtain contact resistivities on the order of $10^{-6} \Omega cm^2$. Numerous studies (15) have established that the resultant contact is laterally and vertically nonhomogeneous. In addition, the thick Au overlayer normally deposited above the Ni/Ge/Au metallization in order to facilitate later device contacting provides a large reservoir of reactive material that contributes both to the increasing depth of the contact region by further in-migration of gold, as well as to contact instability during subsequent device processing and operation. Total penetration depth of such alloyed contacts may reach 200 nm. Such a depth is unacceptably high

for ohmic contacts in emerging GaAs field-effect transistor (FET) and high electron mobility transistor (HEMT) structures which may require contact depths less than 50-100 nm. In this section, we report studies on the use of ZrB_2 and TiB_2 diffusion barriers between Ni/Ge/Au ohmic contact metallization and overlying thick Au in order to evaluate their effectiveness in stabilizing ohmic contacts by limiting the in-diffusion of gold (16,17).

Experimental Synthesis of New Ohmic Contact Structures

GaAs wafers employed for this study were 560 μm thick n-type Si-doped (100) orientation with a carrier concentration of $1-2 \times 10^{18}/cm^3$. Prior to Ni/Ge/Au ohmic metal deposition, the wafers were washed with detergent, degreased sequentially in boiling electronic grade acetone, trichlorethylene, methanol, and acetone for 1 min each, etched in NH_4OH to remove native oxide, and then blown dry in N_2 . Before metallization, the samples were patterned for specific contact resistivity measurements.

Two different metallization schemes were employed. In order to evaluate specific contact resistivity for ohmic metallizations, Ni/Ge/Au were sequentially e-beam evaporated in a deposition chamber prepumped to 5×10^{-8} Torr, with the Ni in contact to the GaAs and the Au the final metal deposited. Total thickness of the ohmic metallization ranged from 25-100 nm; Au amounted to 85 wt. %, Ge 10%, and Ni 5% of the total metallization and the ratio of Au/Ge was selected to coincide with the eutectic alloy composition. Diffusion barrier layers of e-beam TiB_2 or sputtered ZrB_2 , 50-100 nm in thickness were next deposited. TiB_2 was evaporated in the same chamber and in the same pumpdown as the ohmic contact metals and was followed by the deposition of 200 nm of gold without breaking vacuum.

In the second metallization scheme, designed to compare a conventional ohmic contact with one employing a TiB_2 diffusion barrier, a total thickness of ~ 100 nm of ohmic metallization was deposited in the sequence Ni (5nm), Ge (30nm) and Au (60nm). Then two types of contact layers were deposited, consisting of 50nm each of either Ni or TiB_2 . Finally each sample received 200nm of Au for layer contacting and measurement.

Two techniques (Fig 4) were employed to alloy the ohmic metallization, comprising either a strip heater under flowing forming gas, or under flowing N_2 in an optical annealing system employing quartz-halogen lamps. Temperature was measured by a thermocouple bonded to either a silicon support wafer (optical system), or to the ceramic heating block (strip heater).

Contact resistance was measured by a modification of the method of Cox and Strack (18). Resistance was measured between five pairs of circular contacts ranging from 3 to 50 μm diam. with contact-to-contact spacing

of 200 μ m deposited on 560 μ m thick n-3aAs. For this geometry, where the substrate thickness and contact spacing are large compared to the contact radius, and the spacing is not large compared to the thickness, the measured resistance is given by (19)

$$R_{\text{meas}} = \rho/2a + 2r_c/\pi a^2, \quad (1)$$

$$\pi a^2 R_{\text{meas}}/2 = \pi \rho a/4 + r_c, \quad (2)$$

where a is the contact radius, ρ is the substrate resistivity, and r_c is the specific contact resistivity. The term $\rho/2a$ in Eq. (1) is an approximation to the spreading resistance in the GaAs. A numerical calculation of the spreading resistance using the method of Berkowitz and Lux(20) indicates the error of the approximation is 5% for the 50 μ m contacts and less than 1% for all others.

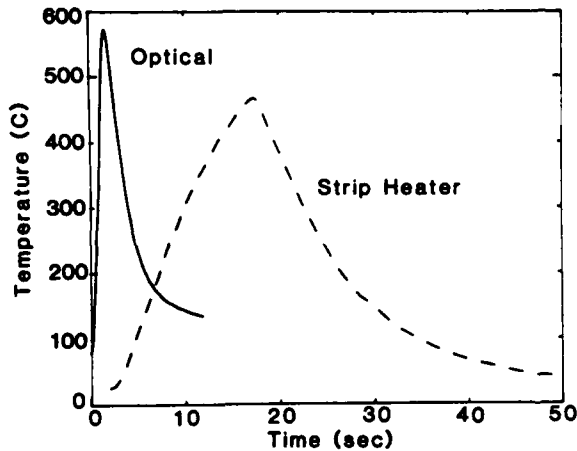


Fig. 4 Time-temperature profiles used to alloy ohmic contacts.

From Eq. (2), a plot of half the measured resistance times the contact area versus diameter then gives a straight line, with the y-intercept being the contact resistivity, as in Fig. 5. The major source of error is the accurate measurement of the diameter of the contact windows. To explore the effect of this error, we have artificially changed the value of all window diameters by $\pm 1\mu$ m, or changed only the smallest window by the same amount, leaving all others fixed. The resultant recomputed contact resistivities varied at most by $\pm 1 \times 10^{-7} \Omega \text{cm}^2$. In measuring the resistance, separate voltage and current probes were placed on the contacts to eliminate the effect of probe resistance.

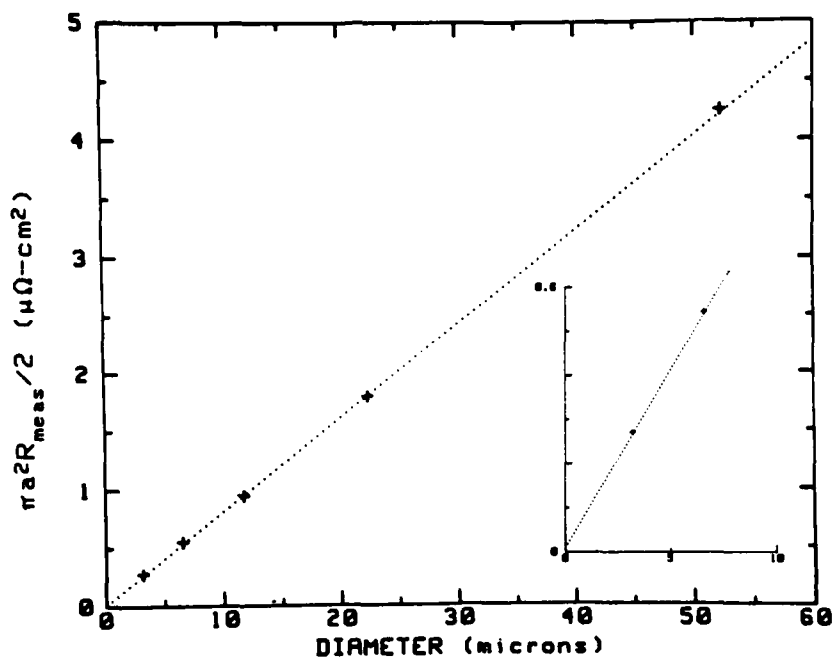


Fig. 5. Typical plot of data in the form of Eq. (2) which is used to obtain the contact resistivity. The straight line is a least-squares fit to the data. The insert is an expansion of the plot near the origin.

Specific Contact Resistivity

Measurement of contact resistivity was made for four thicknesses of Ni/Ge/Au metallization of 25, 50, 75, and 100 nm, covered with 50 nm TiB₂ and 200 nm Au. Three alloying cycles were used consisting of a ramp up to maximum temperature and an immediate ramp down. The results of these measurements are shown in Table II.

For several combinations of alloying temperature and film thickness, the results did not fall on a straight line, thus precluding the determination of the contact resistivity. Two types of failures were observed: (1) failure of most or all of the 3 and 6 μm contacts to form ohmic contacts, and (2) anomalously high resistance in the 3 and 6 μm contacts, well off the line extrapolated from the other contacts. Type (2) failures may be the result of incomplete removal of the resist from the contact openings.

Table II CONTACT RESISTIVITY ($\mu\Omega\text{cm}^2$) OF THE OHMIC CONTACTS

As-deposited layer thicknesses (nm)	417C	Peak temperature 438C	455C
25	0.1	(2)	(2)
50	0.5	(2)	(2)
75	(1)	0.2	(1)
100	(1)	0.1	0.1

The results of alloying TiB_2 barrier layer samples in the optical system are shown in Figure 6. The minimum in contact resistivity over a limited temperature range is typical of previously reported results with Ge/Au/Ni contacts, however the temperature of the minimum, about 600C, is higher than the 400-450C reported for alloying times of 30 sec to 3 minutes (14). It is not known if these differences represent an actual temperature difference on the samples or result from measuring the temperatures at the sample carrier, as is typical in both optical and strip heater systems. The minimum contact resistivities are approximately the same as previously obtained for the same thickness Ge/Au/Ni metal for longer, lower temperature alloying in a strip heater (16).

Although samples containing the 50nm Ni/200nm Au cap layers were observed to be ohmic (linear I-V characteristic) after either optical or strip heater alloying, we were unable to obtain a specific contact resistivity by the technique used above. The plot of measured resistance times contact area vs. diameter either was not a straight line or produced a line with slope unrelated to the resistivity or the carrier concentration of the substrate. The failure of this technique indicates that the conventional Ge/Au/Ni contact is not well modeled by a thin layer of high resistivity material which is independent of contact size, under the metal.

Contact Aging

The deterioration of Ni/Ge/Au Ohmic contacts under long term thermal stress has been reported by Marlow et al (21). To investigate this effect a group of contact patterns consisting of 100 nm of Ni/Ge/Au capped by 50 nm TiB_2 and 200 nm Au were alloyed in both strip-heater and optical systems. The contacts were then annealed up to 180 h at 350C with periodic measurements of contact resistivity. The results, shown in Fig. 7, indicate a rapid deterioration of the contact resistivity after 3.5h followed by a longer period of slowly increasing contact resistivity as was seen by Macksey (22). The contact resistivity at 180 h did not exceed

$1.5 \times 10^{-6} \Omega \text{cm}^2$. This performance is attributed to the effectiveness of the diboride layer in blocking in-migration of Au and out-migration of Ga.

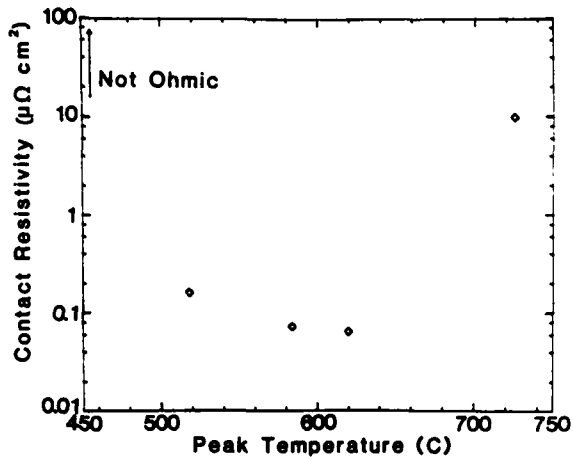


Fig. 6 Average r_c versus alloying temperature in optical system for TiB_2 barrier sample.

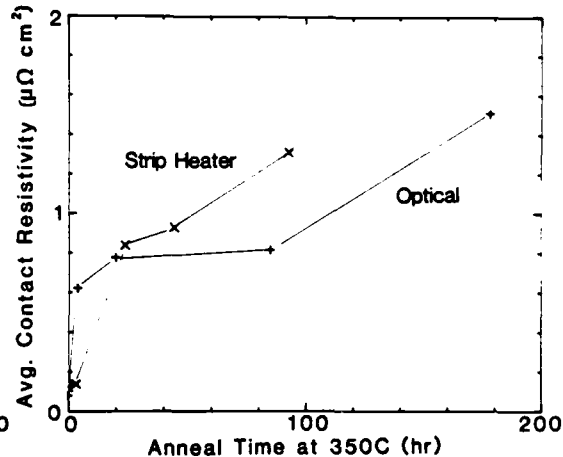


Fig. 7 Variation of r_c data with aging time for optically (+) and strip heater (x) alloyed samples.

Essentially no difference was observed in the aging characteristics for optically or resistively alloyed contacts. In contrast, Lee et al.(23) compared e-beam (100nsec pulse) and thermally alloyed AuGe/Pt ohmic contacts to n-GaAs; although they found a lower specific contact resistivity for the e-beamed contacts, on aging at 250°C, such contacts degraded more rapidly than their thermally alloyed counterparts.

Barrier Effectiveness

The efficiency of the diboride thin film diffusion barrier in preventing Au in-migration to the evolving ohmic metallization can be estimated from the Auger data shown in Figs. 8 and 9. Figure 8 is an AES sputter depth profile through 200 nm of Au over 50 nm of TiB_2 e-beam evaporated onto GaAs and heat treated for 3.5 h at 500°C. Figure 9 shows an AES profile through 200 nm Au over 100 nm of rf-diode sputtered ZrB_2 over 100 nm total thickness of Ni/Ge/Au on GaAs and alloyed at 450°C for 2 min. In the case of the TiB_2 film shown in Fig. 9, the heat treatment conditions are far more severe than those typically employed in conventional GaAs ohmic contact technology where temperatures are typically below 500°C and alloy times are measured in seconds; in contrast, the conditions employed for the ZrB_2 example are generally consistent with standard processing. The important observation in both cases is clear,

namely that thin film diboride diffusion barriers are extremely effective in blocking the in-migration of Au. In the absence of such a blocking layer an already established metallization structure achieved by some preselected alloying scheme could be further modified by the supply of additional, reactive gold to that interface, during either subsequent elevated device processing temperature, or by heat generated during the operation of a high power device. Furthermore, the abruptness of the Au/ZrB₂ and Au/TiB₂ interfaces which was observed suggests strongly that even thinner diffusion barrier layers, perhaps as thin as 10 nm or less, would function effectively for this purpose. The minimum thickness required for such diboride barriers is under investigation.

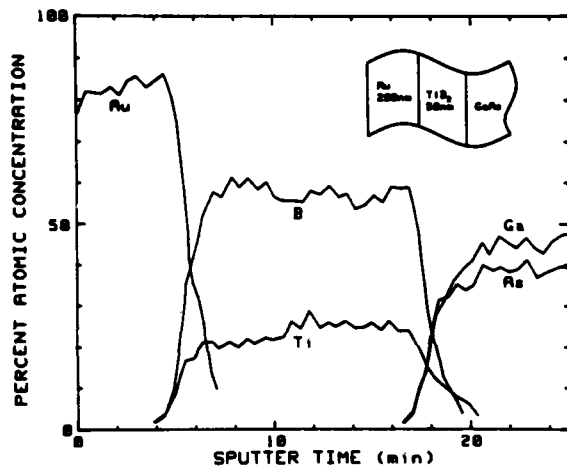


Fig. 8 Auger electron spectroscopy sputter depth profile through 200 nm of Au over 50 nm of e-beam evaporated TiB₂ aged at 500C for 3.5 h.

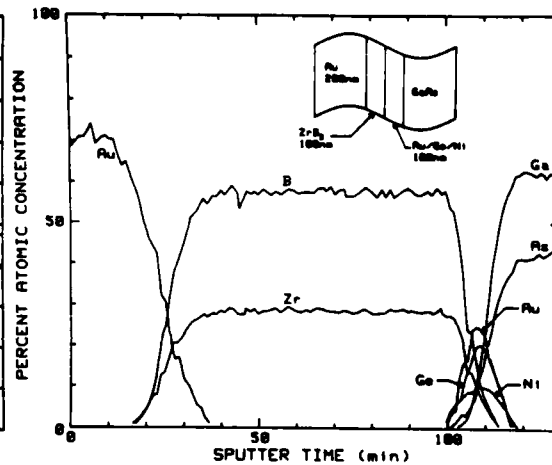


Fig. 9 Auger electron spectroscopy sputter depth profile through 200 nm of Au over rf-diode sputtered ZrB₂ over 100 nm total thickness of Ni/Ge/Au on GaAs, alloyed at 450C for 2 min.

Contact Chemistry and Morphology

Figure 10 compares the surface microstructure for the alloyed contacts of Au/Ni/Au/Ge/Ni (Fig 10b) with that of Au/TiB₂/Au/Ge/Ni (Fig 10c). Fig 10a shows the patterned nitride sample. In regions of sample 10b where the metallization is in direct contact with the GaAs substrate the films have reacted with the substrate, showing a pronounced surface roughness. In contrast, the diffusion barrier sample (Fig 12c) is smooth, and shows no evidence of a reaction involving the top metal.

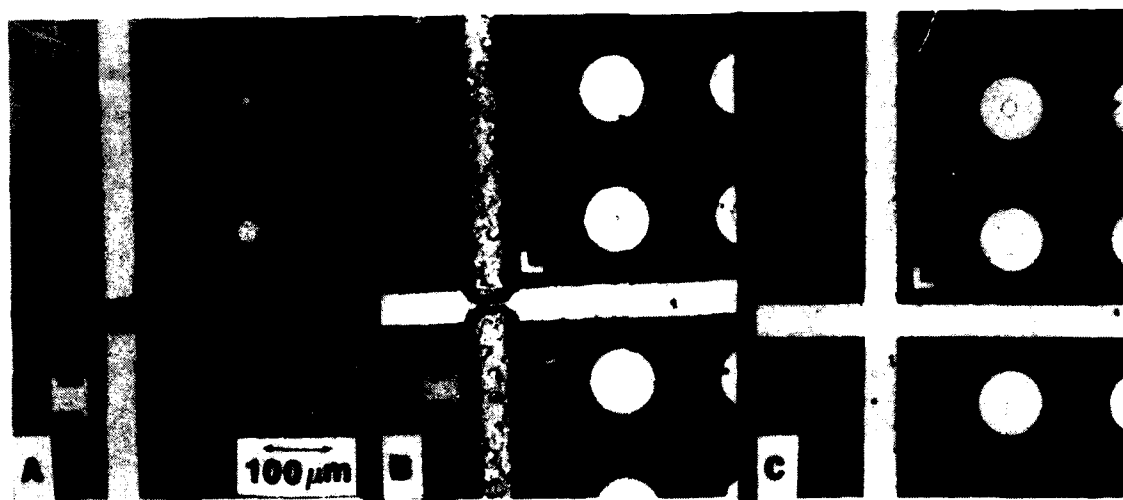


Fig. 10 Optical micrographs showing (A) patterned Si_3N_4 sample, (B) alloyed Au/Ni/Au/Ge/Ni sample and (C) alloyed sample containing a TiB_2 barrier.

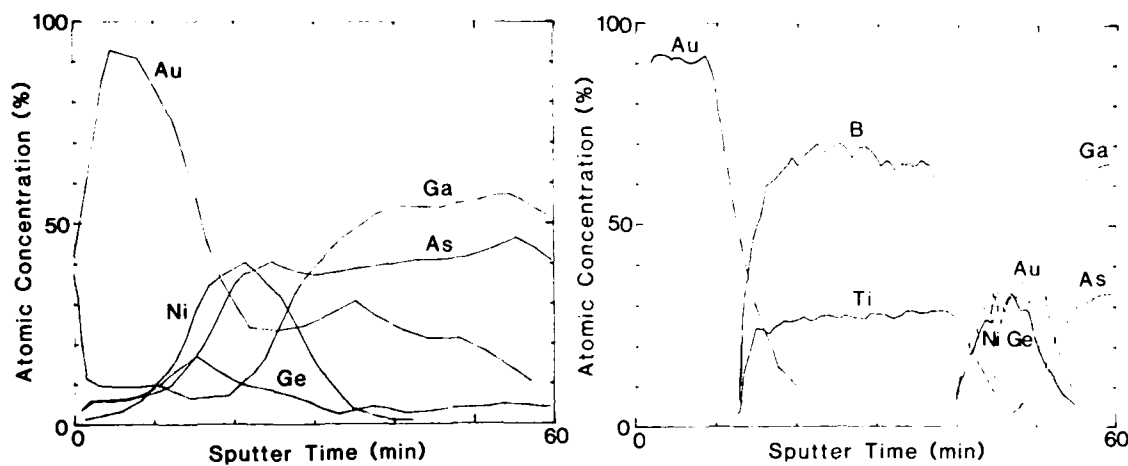


Fig. 11 AES depth profiles for (left) the Au/Ni/Au/Ge/Ni samples and (right) the $\text{Au/TiB}_2/\text{Au/Ge/Ni}$ sample, both after alloying.

Figure 11 presents Auger spectroscopy depth profiles for alloyed Ni

and alloyed diboride samples. In the Ni sample (left), there is a pronounced pileup of Ga at the gold surface, and nickel is seen to accumulate at the GaAs contact, as observed by Robinson (24). No such surface Ga is seen in the diboride sample and the reaction with the GaAs is confined to the metal under the diboride barrier (right).

CONCLUSION

A new class of metallurgical contact materials, the transition metal borides, has been described and synthesized. Their properties have been shown to fulfill all of the requirements for contacting advanced VLSI/VHSIC Si-based device structures. Their diffusion barrier characteristics demonstrate them to be the most stable materials yet reported in contacts involving second-level aluminum metallization. Finally, in contact structures for ohmic contacts to n-type GaAs, they constitute a new and fundamental building block which permits the attainment of the lowest specific contact resistivity as well as the thinnest ohmic contact metallizations yet achieved.

Implementation of these concepts into devices incorporating high conductivity, improved stability diboride contact structures will have a significant and far-reaching impact upon future Army and DOD microwave, millimeter wave and VHSIC systems for secure communications, fire control, terminal homing and high speed digital signal processing.

REFERENCES

1. A. K. Sinha, J. Vac. Sci. Tech, 19 (3), 778 (1981).
2. A. N. Saxena and D. Pramanik, Solid State Technology, 27 (12), 93, Dec. 1984.
3. A. K. Sinha, "VLSI Technology", S. M. Sze, ed., McGraw Hill, NY, 373 (1983).
4. J. M. Poate, K. N. Tu and J. W. Mayer, (Eds) "Thin Films - Interdiffusion and Reactions", John Wiley, NY, 9 (1978).
5. L. E. Davis, N. C. MacDonald, P. W. Palmberg, G. E. Riach and R. E. Weber, "Handbook of Auger Electron Spectroscopy", Physical Electronic Industries, Eden Prairie, MN, (1976).
6. S. P. Murarka, M. H. Read, C. J. Doherty and D. B. Fraser, J. Electrochem Soc., 129, 293, (1982).
7. M. A. Nicolet, Thin Solid Films, 52 415, (1978).

*SHAPPIRIO, et al

8. J. M. Poate, K. N. Tu and J. W. Mayer (Eds) "Thin Films - Interdiffusion and Reactions", John Wiley, NY, 378, (1978).
9. E. L. Muetterties, "The Chemistry of Boron and Its Compounds", John Wiley, NY, 135, (1967).
10. S. P. Murarka, J. Vac. Sci. Tech., 17 (4) 775, (1980).
11. J. L. Vossen, J. Vac. Sci. Tech., 19 (3), 761, (1981).
12. J. M. Poate, K. N. Tu and J. W. Mayer (Eds), "Thin Films - Interdiffusion and Reactions", John Wiley, NY, 362, (1978).
13. J. R. Shappirio, Solid State Technology, 28 (10) 161, (1985).
14. R. E. Williams, "Gallium Arsenide Processing Techniques", Artech House, Dedham, MA, 231, (1984).
15. N. Braslau, in "Interfaces and Contacts", MRS Symposium Proceedings, R. Ludeke, K. Rose (Eds) North Holland, NY, 393, (1982).
16. J. R. Shappirio, J. J. Finnegan, R. A. Lux, D. C. Fox, and J. H. Kwiatkowski, J. Vac. Sci. Tech, A3 (6) Nov/Dec 1985.
17. J. R. Shappirio, R. A. Lux, J. J. Finnegan, D. C. Fox and J. H. Kwiatkowski, 1985 MRS Fall Mtg., Boston, MA, Dec 1985.
18. R. H. Cox and H. Strack, Solid State Electron., 10, 1213, (1967).
19. P. Severin, in "Semiconductor Measurement Technology: Spreading Resistance Symposium", NBS Special Publication, J. Ehrstein (ed.), U.S. GPO, Washington, DC, (1974).
20. H. Berkowitz and R. Lux, J. Electrochem. Soc., 128, 1137 (1981).
21. G. S. Marlow, M. B. Das and L. Tongson, Solid State Electron., 26 259, (1983).
22. H. M. Macksey, Inst. Phys. Conf. Ser., 33b, 254, (1977).
23. C. P. Lee, B. M. Welch, J. L. Tandon, Appl. Phys. Lett., 39 (7), 556, (1981).
24. G. Y. Robinson, Solid State Electron., 18, 331, (1975).

SILBER, TAUBER, WILBER

HEXAGONAL FERRITES FOR MILLIMETER-WAVE CONTROL DEVICES (U)

LEO SILBER, DR.
ARTHUR TAUBER, DR.
*WILLIAM WILBER, DR.

US ARMY ELECTRONICS TECHNOLOGY & DEVICES LABORATORY (LABCOM)
FORT MONMOUTH, N.J. 07703-5302

Twenty-first century military assessments of battlefield requirements for surveillance, target acquisition, smart munitions, electronic warfare receivers, and squad-level tactical or secure transceivers require use of the millimeter-wave frequencies (upwards of 30 GHz) for radar and communication functions. Millimeter frequencies are the choice over optical and infrared when penetration of battlefield obscuration (smoke, dust, fog, precipitation) is critical. It is the choice over microwaves when directionality, weight and size of a system are important considerations. Finally, it may be selected because it offers a directionally oriented short propagation range with rapid attenuation, affording systems that may be used for secure communications. Magnetic control devices are essential to the proper operation of radar and communications systems. Few of these devices exist at mm frequencies and, when available often fail to meet the requirements of power, bandwidth and insertion loss specified for new and evolving systems.

Described in this account is the application of ferrites and, in particular, hexagonal ferrites to achieve such components as isolators, circulators, and tunable filters (we use the term ferrite as a generic term for insulating materials with a permanent magnetic moment, regardless of crystal structure or type of magnetic ordering). "Intellegent munitions," such as SARADM (sense and destroy armor (35 GHz)) and multiple launch rocket system (MLRS (95 GHz)) employ isolators and circulators. The state-of-the-art versions of these components employ cubic ferrites which do not meet requisite specifications.

Tunable filters are important for the front ends of frequency-agile command post radios and EW receivers. A number of communications systems have been identified: wireless intercellular communications system (WICS (56-58 GHz)); improved interassemblages command system (IICS), an upgraded WICS system; and mobile intercept resistant radio (54-58 GHz).

Cubic ferrites work quite well in tunable filters up to 40 GHz. Above this frequency, the size of the structure providing the variable magnetic field becomes prohibitively large. Hexagonal ferrites, by virtue of their large internal magnetic field, require much smaller magnetic structures.

To appreciate how hexagonal ferrites can improve the performance of millimeter-wave control devices, we must consider briefly the basis of operation of microwave ferrite devices. The reason conventional cubic ferrites are of interest at microwave or millimeter-wave frequencies is that they exhibit a resonance at a frequency determined by the static external magnetic field and, in the frequency range near this resonance, have a large and controllable permeability, which in actuality is a tensor. It is this permeability which makes possible the development of devices such as phase shifters and circulators, which operate at a frequency somewhat higher than the ferromagnetic resonance frequency (for optimum efficiency about 50 percent higher), and resonant devices such as tunable filters, ferrite-tuned oscillators, and resonance isolators which operate at the ferromagnetic resonance frequency.

To appreciate the difficulties in developing efficient ferrite devices at millimeter-wave frequencies, we need to consider the factors that determine the ferromagnetic resonance frequency and microwave permeability. The ferromagnetic resonance frequency may be written

$$\omega_0 = \gamma H_{\text{eff}}, \quad (1a)$$

$$\text{or } f_0(\text{MHz}) = 2.8 H_{\text{eff}} (\text{Oe}). \quad (1b)$$

In this equation γ is the magnetogyric ratio which, for all practical ferrites, is very close to the value indicated in Eq. (1b), 2.8 MHz/Oe. H_{eff} is the "effective" magnetic field which, in general, depends upon the static magnetic field applied to the sample, the sample shape, anisotropy field, and its saturation magnetization. At a frequency of 56 GHz, ferromagnetic resonance requires an effective field of 20 kOe. Since the magnetization of all ferrites is less than 6000 gauss, we make only a small error at millimeter-wave frequencies if we ignore shape and magnetization. Then, in a conventional cubic ferrite (including garnets), $f_0 (\text{GHz}) = 2.8 H_0 (\text{kOe})$, where H_0 is the externally applied static field. Thus, a tunable filter operating at 56 GHz requires an external static field of 20 kOe, which entails a bulky, heavy magnet.

The advantage of uniaxial hexagonal ferrites is that their symmetry permits a very large magnetocrystalline anisotropy, which manifests

itself as a "built-in" magnetic field called the anisotropy field H_A . Thus, for hexagonal ferrites,

$$f_0 = 2.8 (H_0 + H_A). \quad (1c)$$

In the simplest hexagonal ferrite ($\text{BaFe}_{12}\text{O}_{19}$), $H_A = 17$ kOe so that the applied field needed for resonance at 56 GHz in a spherical sample is reduced from 20 kOe to 3 kOe, with a corresponding reduction in device mass and bulk. In addition, by suitable chemical substitution for barium and/or iron, the anisotropy field can be varied over a wide range---from $H_A = 0$ to $H_A = 35$ kOe or more. Thus, the ferromagnetic resonance frequency can be adjusted to suit the required application up to at least 100 GHz for resonant devices, or 140GHz for off-resonance devices.

Off-resonance devices, such as circulators and phase shifters, depend upon the microwave permeability---the response of the ferrite to the oscillating millimeter-wave magnetic field. Insight into the role of the ferromagnetic resonance frequency and how hexagonal ferrites can help may be obtained by considering just the off-diagonal element of the permeability tensor. The real part may be written

$$K = \frac{\gamma^4 \pi M_s \omega}{\omega_0^2 - \omega^2}, \quad (2a)$$

where ω_0 is the ferromagnetic resonance frequency, as before, and ω is the operating frequency. Off-resonance devices are normally operated with small biasing fields, no greater than a few kilo-oersteds. Thus, at millimeter-wave frequencies, ω_0^2 is much less than ω^2 and may be neglected. The permeability then becomes

$$K = \frac{\gamma^4 \pi M_s}{\omega}. \quad (2b)$$

Clearly, operation at high frequency calls for the largest available value of saturation magnetization. The magnetization of ferrites is limited; the largest value seems to be somewhat less than 6000 gauss. This value of $4\pi M_s$ yields a maximum value of K of 0.3 at 56 GHz, and even smaller at higher frequencies. Efforts over the past 30 years to increase the magnetization of ferrites have not been successful, so we cannot increase the numerator in Eq. (2a), but reducing the denominator by increasing ω_0 is equally effective in increasing K . While this is possible in cubic ferrites through the introduction of a static field, very large static fields entailing large, bulky magnets would be required

to effect appreciable enhancement of K at millimeter frequencies (at 56 GHz, a static field of 14 kOe would be required to achieve $K = 0.7$). By using hexagonal ferrites, with their associated anisotropy field, the enhancement of K is achieved without any increase in the size of the static magnetic field or its associated magnet.

In our discussion thus far we have ignored magnetic losses in the ferrite. The magnetic losses are usually characterized by the ferromagnetic resonance linewidth ΔH . The effect of magnetic loss is best shown in the tunable ferrite filter, where the unloaded Q of a ferrite resonator is $\omega_0 / \Delta H$. In consequence, the insertion loss of a tunable filter of a given design (number of sections, width of passband) is directly proportional to ΔH . In this respect, hexagonal ferrites are inferior to the best cubic ferrites. In yttrium iron garnet, one obtains an unloaded Q of 10,000 independent of frequency (at least up to 60 GHz) whereas previous measurements on hexagonal ferrites, both in this and other laboratories, indicate that unloaded Q 's are below 1000. Because of the crucial role played by the linewidth in tunable filters, as well as in other devices, we have undertaken fundamental studies, both experimental and theoretical, to determine just what limits the linewidth in hexagonal ferrites and how the linewidth may be minimized. These results are discussed in greater detail subsequently. It appears, however, that one must pay a price for the anisotropy field that hexagonal ferrites offer in the form of increased linewidth. In barium ferrite, with $H_A = 17,000$ oersteds, it appears that the unloaded Q cannot be greater than 1500 to 2000. This implies that filters with very narrow passbands would have insertion losses that are excessive for some applications, although wider bandwidth filters or tunable oscillators may be quite practical.

For off-resonance devices, a figure of merit may be defined for each type of device, which is proportional to $4\pi M / \Delta H$, assuming that the magnetic losses at the operating frequency, which might be 50 percent to 100 percent higher than the ferromagnetic resonance frequency, are correctly given by the resonance linewidth. In cubic ferrites, it is known that this assumption is not valid; the losses at the operating frequency are usually much smaller, perhaps one-tenth as large. We may use the expression given for the figure of merit, providing we substitute for ΔH an "effective linewidth," ΔH_{eff} , which correctly describes the magnetic loss under the operating conditions. Until now, no measurements of ΔH_{eff} have been made on hexagonal ferrites at millimeter-wave frequencies. We are presently developing a spectrometer to make such measurements.

Crystal Growth

We have initiated a program of single-crystal growth to supply materials both for our fundamental studies and for the device work.

Initially, we have concentrated on materials for circulators and tunable filters at center frequencies of 37 and 58 GHz, because of a need for these devices in a number of Army systems. Recently we initiated studies of materials suitable for 94 GHz devices. Until now, since we were exploring compositions with suitable properties, all crystal-growth runs have been by multinucleation, using a flux. Now that we have chosen a few compositions for further study, we are initiating growth by top seeding and pulling. This technique should yield crystals of better chemical homogeneity, hence, narrower linewidth. We are also investigating the possibility of growing hexaferrites by metal-organic chemical vapor deposition.

For use in a tunable filter at 58 GHz, pure barium ferrite, with its anisotropy field of 17 kOe, is suitable, and it appears to have the narrowest linewidth of any hexaferrite at this frequency. We have grown single crystals of this material and we have prepared well-polished spheres that have been tested in a tunable filter. We have also used this material for fundamental studies of the origin of linewidth in hexaferrites.

For off-resonance devices at 58 GHz, or resonance or off-resonance devices at 37 GHz, a material with smaller anisotropy field is required. One also wants to keep the magnetization as large as possible. The anisotropy field in a uniaxial hexagonal ferrite is related to the magnetocrystalline anisotropy energy K_1 and the magnetization by the relation $H_A = 2K_1/M$. For barium ferrite ($\text{BaFe}_{12}\text{O}_{19}$), $K_1 = 3 \times 10^6$ ergs/cm³ at room temperature and $4\pi M = 4500$ gauss, so H_A is about 17 kOe. One would like to reduce H_A by increasing M , but there are no known metal ion substitutions which succeed in doing this. AuCoin et al. [1] tried substituting zinc and titanium for iron, hoping that zinc would increase the magnetization, as it does in cubic ferrites. In fact, since they used tetravalent titanium to charge-compensate the divalent zinc, the magnetization decreased. (Substitution of only zinc would lead to the presence of divalent iron, which would increase both dielectric and magnetic losses.) For an anisotropy field of 10 kOe, they found a saturation magnetization of 3100. We felt that substitution of a single trivalent ion might be preferable. Scandium is reputed to substitute only in one particular crystallographic site in barium ferrite---the trigonal bipyramid site [2] which is a major contributor to the crystalline anisotropy. Thus, we felt that the necessary reduction in anisotropy energy could be achieved with the least reduction in magnetization by substitution of scandium for iron. This would have the additional advantage of resulting in the least reduction of the crystalline order of the lattice and, hence, least increase in linewidth.

Figure 1 shows our results of anisotropy field and magnetization as a function of scandium substitution.

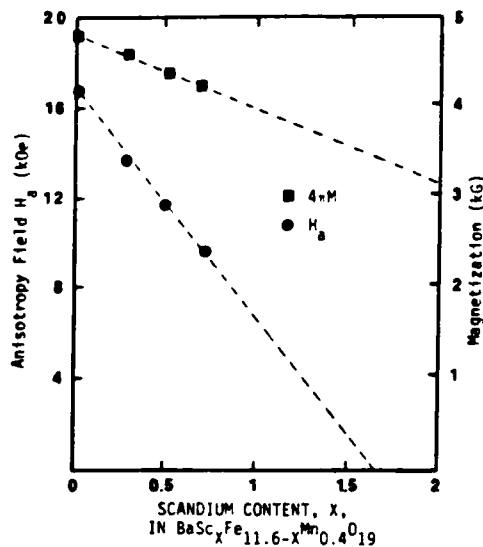


Figure 1. Magnetization and anisotropy field as a function of scandium substitution.

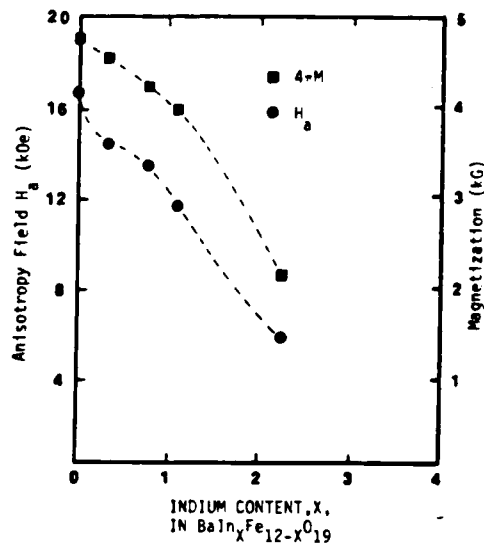


Figure 2. Magnetization and anisotropy field as a function of indium substitution.

We see that the anisotropy field and magnetization do decrease linearly with scandium substitution, as expected. For an anisotropy field of 10 kOe, we find a saturation magnetization $4\pi M = 4100$ gauss, 30 percent greater than that obtained with zinc-titanium substitution. However, since scandium is extremely expensive and in short supply (the principal source is the Soviet Union), we sought a different substituent. We had hoped that indium would also substitute preferentially in the trigonal bipyramid site. The experimental results, shown in Fig. 2, suggest that, initially, indium does go into this site, but with further substitution also goes into other sites. We see that an anisotropy field of 10 kOe can be achieved with a magnetization $4\pi M = 3500$ gauss. Ferromagnetic resonance measurements on unpolished specimens of indium-substituted hexaferrites indicate that the linewidths are reasonable. Thus, it appears that indium substitution will yield hexaferrites suitable for device applications at frequencies below 60 GHz. We are now preparing to grow larger crystals by top seeding and pulling.

Ferrites for operation at 94 GHz require a higher anisotropy field. Strontium ferrite, $\text{SmFe}_{12}\text{O}_{19}$, is a better starting material than is

barium ferrite, since it has a larger H_A . Since one does not at present know how to increase K_1 , previous workers have proceeded by reducing M by substitution of nonmagnetic aluminum for iron. The value of K_1 is almost independent of aluminum substitution, while M decreases linearly, so that H_A increases. Unfortunately, with aluminum substitutions, the curie temperature decreases and the linewidth increases. Tolksdorf [3] has reported a linewidth of 58 Oe at 88 GHz in $\text{SrAl}_{1.9}\text{Fe}_{11.1}\text{O}_{19}$, a material with $H_A = 28$ kOe and $4\pi M = 3000$. We have begun to grow such materials by multinucleation for use in circulators around 94 GHz.

Magnetic Loss Mechanisms

Because the magnetic loss in barium ferrite (hexagonal ferrites, in general) is such a critical material problem, a series of experiments has been performed to determine the fundamental sources of this loss. Once the basic mechanisms have been identified, one should be able to decrease the effect of each loss mechanism and, indeed, determine the minimum loss for a "perfect" crystal. The ferromagnetic resonance (FMR) linewidth is taken as a direct measure of the loss due to various relaxation processes and is particularly relevant to resonant devices. By measuring the linewidth over a range of temperatures and at different frequencies, one can differentiate between the linewidth contributions due to the various relaxation mechanisms because of their different temperature and frequency dependences [4]. These linewidth measurements and their interpretation are discussed at length in the following section.

The first relaxation mechanism to be examined is two-magnon scattering, or the decay of a uniform-mode magnon into a nonzero wave number magnon [5]. The magnitude of this particular relaxation process is known to scale with the bulk magnetization of the material. This is intuitively reasonable because the two-magnon scattering is initiated by discontinuities in the magnetization, such as nonmagnetic inclusions, voids, or a rough surface texture. The magnetization of barium ferrite shows an essentially linear decrease from about 50°K to nearly 600°K [6]. Accordingly, the two-magnon relaxation linewidth should decrease linearly over this same temperature range.

Experimental evidence of the two-magnon contribution was obtained by measuring the temperature dependence of ΔH for two samples of barium ferrite: sample BaF-S1 was a highly polished sphere of barium ferrite, and sample BaF-S2 was a rough-surfaced sphere (both samples prepared from crystals grown at ETDL). The linewidth for each sphere was measured from approximately 50°K up to room temperature at a frequency of 56 GHz. The results of the measurements are shown in Fig. 3 [7]. The linewidth data for samples BaF-S1 and BaF-S2 clearly differ in terms of their: 1) absolute magnitude, and 2) temperature dependence. The linewidth for the

rough-surface sample is significantly larger than ΔH for the polished sample (note the break in the vertical axis), and the slope of ΔH versus T for sample BaF-S1 is positive, while the slope for BaF-S2 is negative. Since the two samples are essentially identical except for the surface finish, the difference in ΔH is attributed to surface roughness-induced two-magnon scattering. The slope of the BaF-S2 data is consistent with this conclusion; the linewidth decreases linearly with temperature because the magnetization and, therefore, the two-magnon scattering decreases linearly with temperature.

From the above discussion, it follows that the two-magnon loss has essentially been eliminated for the highly polished sphere. The linewidth for sample BaF-S1 shows a linear increase in ΔH with temperature, and an extrapolated intercept of only 3 Oe. Similar results were found for a second polished sphere of barium ferrite measured at 56.1 GHz, as shown in Fig. 4. A least-squares straight line fit is indicated by the solid line, and fits to well within the ± 10 percent experimental uncertainty.

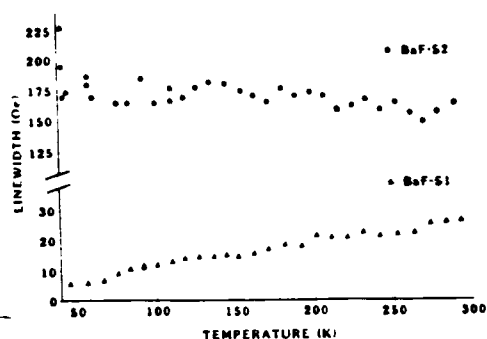


Figure 3. Linewidth as a function of temperature for a polished sphere (BaF-S1) and a rough-surface sphere (BaF-S2) of barium ferrite at 56 GHz.

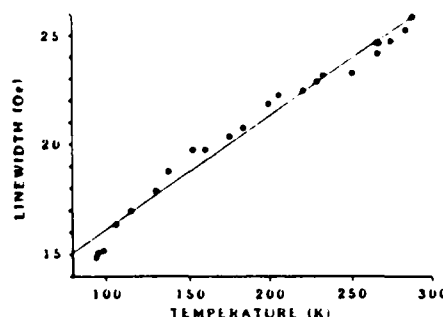


Figure 4. Linewidth as a function of temperature for pure barium ferrite at 56.1 GHz.

The results for the highly polished spheres are attributed to two scattering mechanisms which would lead to a linear ΔH temperature dependence. The first relaxation process is the confluence of a uniform-mode magnon and a phonon to form a nonzero wave number magnon. This process is referred to here as the Kasuya-LeCraw (KL) mechanism [8]. The KL relaxation mechanism is linearly dependent both on temperature and frequency. The second process is one phonon-one magnon scattering

at low wave numbers. Although this relaxation mode is thought to be unimportant in YIG, it has been proposed [9] that the phonon and magnon dispersion character for barium ferrite may allow this two-boson process to contribute significantly to the total linewidth. This second mechanism is linear in temperature and independent of frequency. The relative magnitude of these loss contributions is discussed next.

Taking into account all three of the relaxation processes discussed to this point, the total FMR linewidth may be expressed as

$$\Delta H = AfT + BT + C, \quad (3)$$

where f is the microwave frequency, and T is the temperature. The coefficient A represents the KL contribution, coefficient B is determined by the temperature-dependent, two-magnon contribution and the loss due to phonon-magnon scattering, and coefficient C is the temperature independent two-magnon loss. By measuring the temperature dependence of ΔH , one can determine the value of $Af + B$. If one repeats the same measurements at several different frequencies, the coefficients A and B can then be found. This experiment has been performed over a frequency range of 52 to 64 GHz for a well-polished sphere of barium ferrite, and the resulting coefficients are listed in the first row of Table I.

TABLE I. Linewidth Coefficients

SAMPLE	$A(\text{Oe/GHz} - ^\circ\text{K})$	$B(\text{Oe}/^\circ\text{K})$	$C(\text{Oe})$
$\text{BaFe}_{12}\text{O}_{19}$	7.3×10^{-4}	0.014	13.8
$\text{BaFe}_{11.8}\text{Mn}_{0.2}\text{O}_{19}$	3.7×10^{-4}	0.016	15.5

Notice first that, for a frequency near 60 GHz, the A and B terms result in approximately equal contributions. The magnitude of C is slightly larger than, for example, the zero-temperature intercept in Fig. 3. Apparently, there is still a rather significant two-magnon contribution to the linewidth for this particular sample, perhaps due to volume imperfections.

While the linewidth of the pure barium ferrite samples is adequately described by Eq. 3, another sample containing a small amount of manganese gives rise to a more complicated ΔH behavior. As an example, Fig. 5 linewidth as a function of temperature, at 59.4 GHz, for a barium ferrite sample with 0.2 atoms of Mn per formula unit ($\text{BaFe}_{11.8}\text{Mn}_{0.2}\text{O}_{19}$). The data indicate a distinct peak near 130°K. Following some earlier work on spinel ferrites [10], this new contribution to the linewidth is attributed to a valence-exchange relaxation mechanism involving charge

transfer between Fe^{2+} and Fe^{3+} ions. A linewidth due to this mechanism has the form

$$\Delta H \propto \frac{\omega \tau_R}{1 + \omega^2 \tau_R^2} \quad (4)$$

where ω is the microwave (or mm-wave) frequency. The relaxation time τ_R can be expressed as

$$\tau_R \propto \exp(E/kT) \quad (5)$$

where k is the Boltzmann constant and E is the energy barrier for the valence exchange.

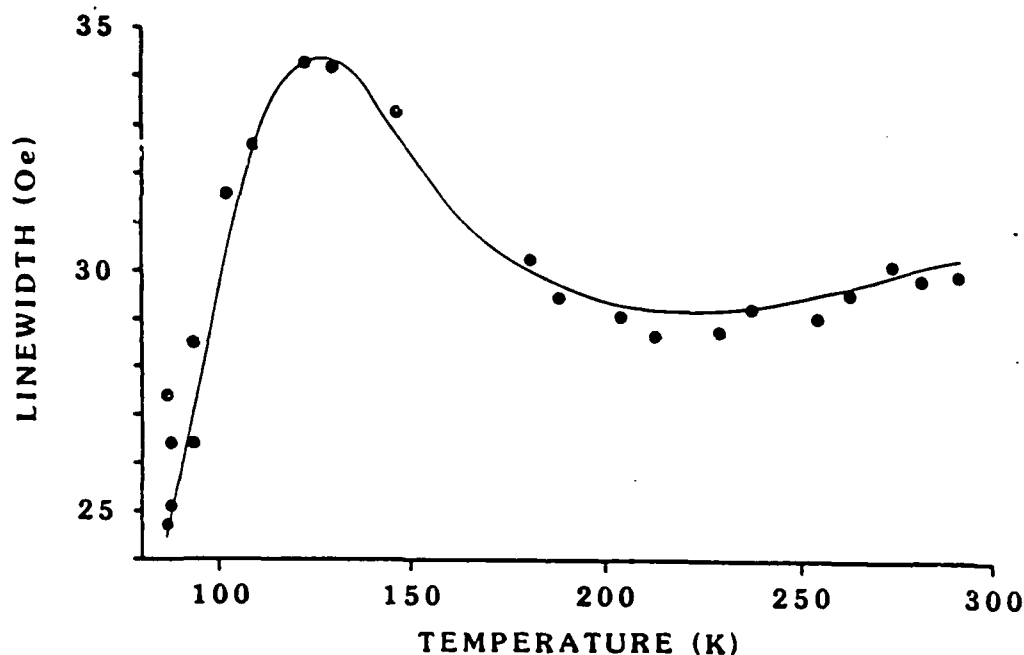


Figure 5. Linewidth as a function of temperature for Mn-substituted barium ferrite at 59.4 GHz.

A sum of the linewidth contributions represented by Eqs. (3) and (4) was fit to the data of Fig. 5, with the result shown by the solid line. The resulting A, B, and C coefficients of Eq. (3) are given in the second row of Table 1. The values of B and C are very close to those for

the pure barium ferrite sample. The value of A is somewhat lower for the Mn-substituted sample. Although part of the difference in coefficients may be due to measurement uncertainty, a decrease in A is consistent with the idea that a small amount of Mn can decrease the overall linewidth by reducing the conductivity. The energy barrier E found from the fit in Fig. 5 is approximately 0.04 eV, and is comparable to that found in earlier work on spinels [10].

In conclusion of this section, the magnetic loss for pure barium ferrite can be understood in terms of three fundamental scattering processes: 1) the KL mechanism, 2) a magnon-phonon relaxation process, and 3) two-magnon scattering associated with surface roughness and bulk imperfections. The linewidth model for the Mn-substituted sample must include an additional temperature-peak process. Although the addition of Mn leads to a decrease in the KL contribution to ΔH , an overall increase in line-width results from the valence-exchange process. Given our present understanding of the various contributions to the total line-width, it seems reasonable to estimate that the current linewidth values of 22 to 23 Oe found at 60 GHz (for the best samples) can be lowered by a factor of two for ideal materials.

Experimental Devices

It has been remarked that the large magnetocrystalline anisotropy intrinsic to hexagonal ferrites eliminates the need for excessively large applied fields and the large, bulky magnet structure associated with such fields. This point is well-illustrated in Fig. 6, which shows two single-resonator filters with 1) the large magnet structure capable of the 20 kOe fields required for YIG at 56 GHz, and 2) the significantly smaller magnet structure required for a barium ferrite-based tunable filter. While the large magnet shown in Fig. 6 has been designed for optimum efficiency, the small magnet could be decreased in size and weight from the model shown, and would provide an even greater contrast between the filters. The performance of these filters, and of hexaferrite isolators and circulators, is discussed below.

In general, a filter placed in a transmission line will allow a specifically defined frequency band to pass and will reject signals at any other frequency. In a magnetically tunable filter, a narrow passband frequency is defined by the resonance frequency of the ferrite element(s). The single-resonator filters shown in Fig. 6 consist of a magic-tee with an electrical short in one arm, the ferrite in a second arm (extended into the magnet gap), and the remaining two ports used for input and output.



Figure 6. Magnetically tunable barium ferrite (left) and YIG (right) filters with appropriate permanent magnet structures.

Three important parameters for these filters are their frequency range of operation, the bandwidth, and the insertion loss. The bandwidth (BW) can be determined from the operating frequency f_0 and the loaded Q according to

$$BW = f_0/Q_L. \quad (6)$$

The insertion loss (IL) of the filter may be expressed by

$$IL(dB) = 20 \log_{10} \left(\frac{Q_U}{Q_U + Q_E} \right), \quad (7)$$

where Q_E is the external Q , and Q_U is the unloaded Q of the ferrite sphere. The three quality factors are related by

$$\frac{1}{Q_L} = \frac{1}{Q_U} + \frac{1}{Q_E}, \quad (8)$$

and the unloaded Q , as discussed earlier, is inversely proportional to the FMR linewidth. To minimize the insertion loss in Eq. (2), one would like a very high Q_U and a relatively small Q_E . However, with Q_U limited by the ferrite linewidth, one must choose a Q_E that permits an acceptable insertion loss, while maintaining, as expressed through Eqs. (6) and (7), a usefully narrow bandwidth.

A first attempt at a single-resonator, barium ferrite-based filter used a 0.33 mm sphere of substituted barium ferrite with a linewidth of 35 Oe and an anisotropy field of 16.7 kOe obtained from Philips Laboratories, W. Germany. For a 3 dB bandwidth of 140 MHz, the measured insertion loss was 11.7 dB (10.5 dB, if calculated from the BW) at 58 GHz [12]. The same measurements for a YIG filter reveal an IL = 1.35 to 1.5 dB and BW = 40 to 70 MHz. The first attempt at a hexagonal filter was clearly inferior to the garnet-based filter, despite the reduction in required biasing field from 20 kOe to an easily obtainable 4 kOe. A second attempt at a hexagonal filter was made with a highly polished, pure barium ferrite sample grown at ETDL. The linewidth was approximately 24 Oe at 56 GHz, and resulted in an IL = 2.4 dB and BW = 220 MHz. This second model shows a marked improvement over the first attempt and compares much more favorably with the YIG filter.

A second filter design uses two ferrite spheres that couple through an iris cut between two crossed waveguides. Early attempts at utilizing barium ferrite with such a filter have shown insertion loss of approximately 4 dB with a bandwidth of 350 MHz. This compares with similar work performed at Hewlett-Packard [12] for a crossed-waveguide filter with 4.5 dB insertion loss and a 325 MHz bandwidth. The advantage to this design over the one-sphere filter is higher isolation and steep skirts to the passband; the disadvantage is a higher insertion loss. Both of the filter designs described above will obviously benefit from further reductions of the magnetic loss in hexagonal ferrites.

Resonance isolators at mm-wave frequencies are another potential application for hexagonal ferrites. The fundamental idea, as with any isolator, is to allow the flow of energy (mm-wave signal, in this case) in one direction and to highly attenuate any signal propagating in the opposite direction. Experimental devices at 35 GHz have been developed at this laboratory [13] and devices at 65 GHz have been tested at Philips, W. Germany [14]. Results in both cases indicate an insertion loss of 1.5 - 3 dB and isolation of 20-25 dB. As with the hexaferrite filters, the main advantage to the isolators is the tremendous decrease in the requisite external field.

Appropriately tailored hexagonal ferrites may also lead to highly efficient nonresonant devices. One such device currently under study is

a circulator. The basic operation of, for example, a three-port circulator is to allow a signal to propagate from one port to the next (i.e., 1→2, 2→3, 3→1) without any transmission into the third port. The first hexaferrite-based circulator to be tested employed TiZn-material as the center element. The initial tests on this device at 35 GHz give an insertion loss of 3 to 4 dB and an isolation of between 14 and 17 dB [14]. While these results are not yet sufficient for practical applications, there is significant potential for improvement. The test apparatus used for the measurements was designed for materials with significantly different magnetization and dielectric constant, which accounts for an appreciable part of the insertion loss. Work is currently underway at this laboratory to determine both the real and imaginary parts of the dielectric constants in various hexaferrites. These results will enable the design of more appropriate test structures, and will provide information on the dielectric loss critical to such devices.

Conclusions

Present and future Army systems for radar and communication will increasingly rely on millimeter-wave technology. The ferrite research program here at ETDL is engaged in the development of materials and devices to meet the needs of these high frequency systems. Cubic ferrites, which give good device operation at microwave frequencies, are not adequate at millimeter frequencies. With hexagonal ferrites, the large anisotropy field can be tailored to minimize the required applied field and thereby drastically reduce the size and weight of the associated permanent magnet structure. The unique properties of hexagonal ferrites also provide for more efficient operation of nonresonant devices.

The major problem with currently available hexagonal ferrites is the relatively high magnetic loss. A study of the ferromagnetic resonance linewidth has revealed that three fundamental scattering processes and a charge-transfer mechanism can account for the measured linewidths. By means of appropriate chemical substitution and of improved crystal growth techniques, a factor of two reduction in the magnetic loss should be possible.

To demonstrate the applications of hexagonal ferrites, experimental models of one- and two-resonator tunable filters have been developed, as well as an isolator and a circulator. Both filters have been successfully demonstrated near 60 GHz, and show promise for improved performance. Lower loss ferrites are a critical factor for this improvement. The isolator and circulator represent a relatively new focus for hexaferrite applications. From the results of preliminary tests on these devices it is believed that efficient device operation is possible with reduced size and weight.

References

1. S. Dixon, T. AuCoin & R. Savage, J. Appl. Phys. 41, 1357 (1970).
2. O. P. Aleshko-Ozhevskii, R. A. Sizov, I. I. Yamzin, and V. A. Lubimtzev, Sov. Phys. JETP 28, 425 (1969).
3. W. Tolksdorf et al, Proc. of Conference of German Society for Crystal Growth, March (1985), and private communication.
4. M. Sparks, Ferromagnetic-Relaxation Theory, (McGraw-Hill, New York, 1964).
5. M. Sparks, Phys. Rev. Lett. 8, 54 (1962).
6. H. B. G. Casimir, in Handbook of Microwave Ferrite Materials, edited by W. H. von Aulock (Academic Press, New York, 1965) p. 468.
7. L. M. Silber, E. Tsantes, and W. D. Wilber, J. Mag. Mag. Mtls. 54-57, 1141 (1986).
8. T. Kasuya and R. C. LeCraw, Phys. Rev. Lett. 6, 223 (1961).
9. E. Tsantes (private communication).
10. W. A. Yager, J. K. Galt, and F. R. Merritt, Phys. Rev 99, 1203 (1955).
11. L. M. Silber, IEEE Trans. Mag. 21, 1788 (1985).
12. D. Nicholson (private communication).
13. Work done in collaboration with R. Stern and R. Babbitt of this Laboratory.
14. M. Lemke, W. Tolksdorf, and F. Welz, IEE Colloquim on Ferrite Mtls. Devices and Appl., London (1985).

SIMMONS, KNOX, SIERING, BEHAR, AND MITCHELL

EFFECTS OF CHEMICAL DEFENSE ANTIDOTES
ON AVIATOR PERFORMANCE (U)

*RONALD SIMMONS, MR., FRANCIS KNOX, DR., GEORGE SIERING, DR.,
ISAAC BEHAR, DR., AND GLENN MITCHELL, DR.
US ARMY AEROMEDICAL RESEARCH LABORATORY
FORT RUCKER, AL 36362-5000

INTRODUCTION

Army aviation is at serious risk in chemical and biological warfare environments. Even nonlethal riot control agents such as tear gas will hamper the ability of aviators to maintain control of their aircraft. Thus, in real terms, should unprepared aviators encounter a chemical agent in aerosol form (or any form), the potential outcome is the loss of the aircrew and aircraft and the failure of the mission. While crews and passengers could conceivably don protective gear as needed inflight, it would be very difficult for aviators to neglect their flight tasks to don a chemical defense (CD) ensemble in the cockpit. Therefore, in any chemical threat situation aviators must don the CD ensemble prior to entering the cockpit. Thus, the ability of the pilot to effectively operate his aircraft while in a CD ensemble is the first requirement for operational effectiveness on the chemically contaminated battlefield.

The second key to effective operation in a chemical environment is the development of antidote and pretreatment drugs, which hopefully will allow safe return of the crew and aircraft. Three compounds, atropine sulfate, pralidoxime chloride (2 PAM-CL), and pyridostigmine, currently are under consideration as chemical warfare antidotes and pretreatment drugs. There are, however, only a few limited studies which address the ability of aviators to fly helicopters after having taken these drugs (1). Each drug has side effects which suggest 'a priori' that effective mission accomplishment or safe flight may not be possible after receiving the normal doctrinal dose of these drugs. Thus, the need to determine the performance effects of antidote and pretreatment drugs is driven by the requirement for Army aviators to survive and maintain combat effectiveness on the chemically contaminated battlefield. More specifically the question becomes, if an aviator self-injects an antidote while flying in a hostile environment, will he be able to return to a safe area of operation; and will he be able to carry out other missions before fully recovering from the antidotes?

This report briefly outlines the first phase of a systematic program using controlled, simulated flight conditions to identify and measure performance, physiological and psychological effects of one of these compounds, atropine, on aviators. Future phases will validate, with inflight combat scenarios, the results found in the simulated flight conditions described in this report.

METHODS

Subjects. The 12 subjects selected for the simulator phase of this study, were volunteer male Army aviators in good health possessing uncorrected normal vision and hearing. Each of the volunteers passed a comprehensive physical examination including a cardiac stress screen and was tested for atropine sensitivity prior to starting the project. Subject pilots were qualified and current in the Army's utility class helicopter. The mean age of the participants was 27, with a range from 21 to 32 years. The mean flight time was 667 flight hours, with a range from 184 to 3000 flight hr. Two of the subjects had in excess of 1100 hr (high time); seven had in excess of 400 flight hr (medium time); and the remaining three aviators had fewer than 400 flight hr (low time).

General approach. This simulator phase of the program was conducted totally within a controlled research environment at the US Army Aeromedical Research Laboratory. Since the subjects were required to remain within the laboratory for 6 consecutive days, full living accommodations were provided.

Research parameters used to monitor and measure the effects of the atropine were divided into three main areas of interest. First, operational performance was evaluated with instructor pilots' ratings of the subjects' ability to fly the helicopter simulator and with data retrieved from computer monitoring of the flights. Second, laboratory benchmarks of performance were collected before and after each simulator flight. These tests included a Performance Assessment Battery, Zero Input Tracking task, visual contrast sensitivity, and visual evoked response. Finally, the third area of interest included physiological and biochemical measures which were monitored and analyzed to model the drug effects on the human system. These measures included electrocardiographic data, visual accommodation, and biochemical tests on urine; the last of these will not be reported herein.

Operational flight measures. The simulated flights were conducted in the Laboratory's two degree of motion simulator which was designed and programmed to simulate the configuration and general flight dynamic characteristics of the UH-1, utility class helicopter. The simulator is linked to a real time data acquisition system (SIMUHIMS) which allows simultaneous data collection of pilot aircraft control inputs as well as aircraft dynamic response and flight status (2). The simulated flights consisted of precision

SIMMONS, KNOX, SIERING, BEHAR, & MITCHELL

'upper-air' instrument flight maneuvers and a standard instrument flight to include an instrument flight take-off, navigation/flight to a destination airport, holding at the approach outer marker, and an instrument (ILS) approach to minimums. An instructor pilot performed copilot duties and rated the subject pilots' performance on each of the flight maneuvers. The ratings were based on aircrew training manual (ATM) standards with each maneuver receiving a score from '1' (unacceptable) to '5' (perfect). A total flight score then was computed by summing the maneuver scores. A perfect flight would then be a score of 20 and any score less than 12 would have represented failure to maintain ATM standards.

Performance Assessment Battery. Psychological and psychomotor changes were evaluated by administering a computerized Performance Assessment Battery (PAB) at designated intervals. The battery is composed of standardized subtests which include self reported mood scale, feeling/tone fatigue scale, short term memory task, addition/subtraction problems, and a Wilkinson four-choice reaction task (3). The subjects' responses and reaction times were recorded for analysis.

Zero Input Tracking Apparatus. Fine motor coordination, as well as ability to respond to concurrent tasking, were measured via the Laboratory's Zero Input Tracking Apparatus (ZITA) (4). The ZITA is a one-dimensional compensatory tracking task. Acceleration and reversal rates can be manipulated by the experimenter to develop differing levels of control ability or workload demand on the subject. An additional auditory stimulus/response paradigm can be introduced to create levels of concurrent tasking. The ZITA stimuli presentations were controlled and subject responses were recorded.

Contrast Sensitivity. Contrast thresholds were obtained for sinusoidal gratings at six spatial frequencies (0.5, 1, 2, 4, 8, and 16 cycles per degree) using the Nicolet CS-2000 test system (5). Testing was conducted under two viewing conditions, dim ambient illumination and in the presence of a glare source (a high intensity fluorescent tube that surrounded the video display of the CS-2000).

Visual Evoked Potential. The final benchmark performance measures were two visual evoked potential (VEP) response paradigms which were utilized to evaluate atropine influence on central nervous system (CNS) activity. A 'checkerboard' pattern was presented on a CRT (cathode ray tube) monitor 1 m from the subject's eyes under dim ambient lighting. Six different patterns were presented ranging from 4 checks by 4 checks to 128 checks by 128 checks. (In this report the 4X4 checkerboard pattern will be referred to as Pattern 1; the 8x8-Pattern 2; 16X16-Pattern 3; 32X32-Pattern 4; 64X64-Pattern 5; and 128X128 as Pattern 6.) Pattern reversal was at one Hz and the responses were averaged for 100 stimulus presentations for each of the check patterns. Electroencephalographic (EEG) electrodes were attached to

frontal and occipital cortical scalp locations from which event-related brain potentials (ERP) could be recorded. The ERP is a transient series of voltage oscillations in the brain which can be recorded on the scalp in response to any discrete stimulus event (6). The ERP waveform can be analyzed into a series of components which are considered to represent the sequence of information processing activity related to the eliciting stimulus. The peak amplitude and latency of each component has been shown to vary as a function of the informational propriety of the eliciting event or the subject's cognitive response to the stimulus. The critical ERP components for this research project were those which should have occurred approximately 75 msec (N75) and 100 msec (P100) after the visual stimuli was presented. These responses have been linked with cortical recognition. The N75 and P100 were recorded for each of the six checkerboard patterns before and after each simulator flight.

The second VEP paradigm was based on 200 presentations of a 4X8 checkerboard during which a random 15 percent of the presentations had pattern reversal. At the occurrence of each reversal, the subject was instructed to press a button to acknowledge the change. Two critical measures were recorded from this test. The recognition components (N75 and P100) were recorded as in the prior test. Additionally, the subjects' ERPs' centralized at the parietal cortex region of the scalp were recorded and analyzed. This response which should have peaked at approximately 300 msec (P300) after the visual presentation is considered to coincide with the decision process (decision to press the button in this case) (7).

The two VEP tests were designed to determine if there were any shifts in CNS ability to recognize and make an appropriate decision in response to visual stimuli as a function of atropine. Figure 1 is an illustration of

VISUAL EVOKED POTENTIAL RESPONSE

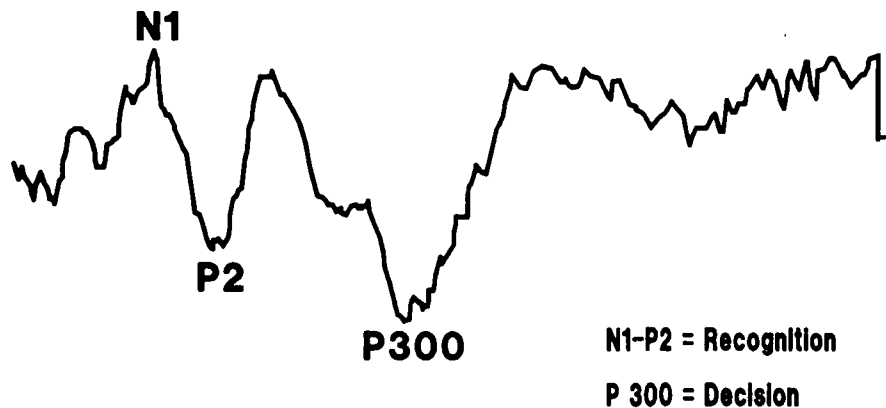


Figure 1. Three Components of VEP

the relationship of the three components from the onset of the stimulus (represented by the left edge of the graph.) 'N1' represents the N75 component, 'P2' is the P100 component, and P300 is labeled as the decision component.

Electrocardiography. Electrocardiograms were recorded from each subject using three ECG chest leads and a Holter tape recorder. During the flight in the simulator, the Holter recorder was replaced with a PDP 11/03 based data acquisition system which digitized the ECG, computed and stored each interbeat interval. The heart rate was displayed continuously on a CRT for the medical monitors. Each subject was allowed approximately 10 min for attaining baseline conditions within the cockpit prior to receiving the dose (atropine or saline).

Visual Accommodation. A Prinz Rule was used to measure the subject's accommodation at preselected intervals during the experimental day (8). With one eye patched, the subject brought a standard target containing fine print towards the unpatched eye until the print "was no longer readable." The distance between the target and the inferior orbital edge was measured from the rule. This procedure was then repeated with the opposite eye. Subjects were tested at 0, 2.5, 4.5, 6.5, 8.5, 21.5, and 24 hr after intramuscular doses of 2 and 4 mg of atropine sulfate.

Test procedure. Each subject arrived at the Laboratory on Sunday of the week he was to participate. On this day he was thoroughly briefed on all phases of the project; signed a volunteer consent form; and received a physical exam to include the cardiac stress screen and atropine sensitivity test. Additionally, each subject had the opportunity on Sunday for familiarization training on each of the performance tests to include a simulator flight to minimize any training effect during the actual data collection. Each of three drug injections (sterile isotonic saline solution, 2 mg of atropine sulfate or 4 mg of atropine sulfate) were administered intramuscularly to the subject on different test days. Nondose control days were utilized within the design after the 2- and 4-mg atropine days to ensure that previous dosages would not result in an additive effect. All of the nonflight laboratory test batteries were administered the first of each test day to establish a daily baseline of performance. At 0955 hr, on test days, the subject was injected in the right thigh muscle with one of the three possible dosages. At this time he was already seated in the helicopter simulator so the test profile would be similar to a mission scenario during which the pilot would encounter a chemical threat in a hostile environment. Performance was monitored across the entire 1-hr 40-min simulator flight to determine if flight safety would have been compromised before the pilot could return from his mission to a secure area.

After the simulator flight, each subject was administered the same laboratory tests he had completed prior to the flight. At 1440 hr, a second

simulator flight of 1 hr 40 min was performed, simulating the requirement for an aviator to be assigned other operational missions within 24 hr of atropine injection. After this flight each subject participated for the third time of the testing day in the laboratory testing sessions. Thus, each test day was comprised of three laboratory performance testing sessions and two operational flight trials.

The order of the three injections was counterbalanced between subjects to minimize nuisance variable effects. Three null hypotheses were anticipated. The first null hypothesis was that pilot performance would not be degraded as a function of the atropine injections. The second was that the overall physiological and biochemical status of healthy subjects would not be adversely affected by atropine. Finally, psychomotor, psychological, and cognitive capabilities would not be adversely affected by administration of atropine as measured by laboratory tasks, performance batteries, and subjective evaluations.

RESULTS

Operational Flight Performance. As was previously noted, the 12 subject pilots' flight experience could be divided into three groups: low-, medium-, and high-time aviators. Based on computer analysis of the flight performance and the instructor pilots' ratings of the same performance, each pilot was ranked from 1 to 12. The rankings from the instructors' ratings then were compared through a Friedman two-way analysis (nonparametric statistical procedure) to the subject pilots' rankings resulting from the computer analysis of flight performance. The results demonstrated that there was a significant agreement between the computer and instructors' scores, $\chi^2(11) = 22.05$, $P < .05$. However, this ranking did not reflect that the pilots' flight experience was correlated with overall performance. For example, one of the low-time aviators was ranked as the second best overall pilot while the highest-time pilot was ranked as number 6.

The instructor pilots' evaluations were subjected to an analysis of variance and a discriminant analysis. Analysis of variance procedures first were utilized to determine if there were any differences between the 0 mg test day and the 2 control days. The results indicated that there was no significant effect. Since there were no differences across these non-atropine days, the mean score for each individual across these days then was utilized to represent their baseline flight ability. Each subsequent flight score then was compared to this baseline to determine any changes created by the atropine injections. Analysis of variance then was utilized to determine if any significant effects in the flight performance existed as a function of the three dosages (0, 2, and 4 mg of atropine). There were significant differences found for the pilots' overall score, $F(2,69) = 4.96$, $P < .01$, across the three dosages. Of the four instrument flight maneuvers which comprised this score, statistically significant difference

across the three dosages was found for the instrument-take-off, $F(2,69) = 3.20$, $P < .05$; level flight, $F(2,69) = 4.92$, $P < .01$; and holding at the approach outermarker, $F(2,69) = 3.41$, $P < .04$. Post hoc tests (Bartlette-Box F and Tukey B) supported that there was homogeneity of the variance and that the major group differences were between the 0 mg dosage and the 4 mg dosage flights performance.

A discriminant analysis was completed, utilizing the statistically significant maneuvers and the total flight score to attempt to predict the dosage associated with each simulator flight. Overall, the analysis yielded a 55.56 percent correct grouping for the morning flights and a 69.44 percent correct grouping for the afternoon flights. Table 1 illustrates this breakdown of actual groups into the predicted group membership. Strikingly, the analysis could successfully predict 91.7 percent of the 4 mg afternoon group membership correctly.

Table 1

Actual Dose Groups	No. of Cases	Predicted Group Membership					
		Morning Flight			Afternoon Flight		
		0 mg	2 mg	4 mg	0 mg	2 mg	4 mg
0 mg	24	9 75.0%	2 16.7%	1 8.3%	7 58.3%	3 5.0%	2 16.7%
2 mg	24	3 25.0%	5 41.7%	4 33.3%	3 25.0%	7 58.3%	2 16.7%
4 mg	24	1 8.3%	5 41.7%	6 50.0%	0 0.0%	1 8.3%	11 91.7%

Heart rate. Changes in heart rate proved to be significantly different across the dosages (Fig 3). When compared to a baseline heart rate just prior to injection the initial bradycardia (decrease in rate) was significant, $F(2,93) = 10.0598$ $P < .001$ for both 2- and 4- mg trials. The peak rates (tachycardia), reached at approximately 30 min post injection, also were significantly elevated above baseline, $F(2,93) = 180.5013$ $P < .0001$ for both drug levels and there was a significant but less robust increase from 2- to 4- mg, $T(93) = 2.53$, $P < .02$.

Accommodation. The percentage of accommodative change were plotted versus time for 2- and 4-mg doses (Fig 4). Analysis of variance revealed significant differences, $F(2,84) = 13.94$, $P < .003$, between 0, 2, and 4 mg doses for percent change in accommodation during the first 6 hr.

Contrast Sensitivity. A repeated measures ANOVA was performed on the log threshold contrast measures obtained on the placebo (0 mg) days. There

were no statistically significant differences in thresholds obtained prior to saline injection and those obtained approximately 2 and 7 hr later, indicating that contrast thresholds in the absence of drug are stable over the test day, there being no consistent diurnal, practice or fatigue effect. Because of this stability, all atropine effects were evaluated against their same-day preinjection baseline thresholds. When 4 mg of atropine sulfate was injected, the contrast thresholds were significantly elevated $F(2,22) = 37.10, p < .001$ as can be seen in Figure 2 in which contrast sensitivity (reciprocal of threshold contrast) is plotted against stimulus grating spatial frequency (called the contrast sensitivity function). The thresholds at the two postinjection times do not differ from each other, thus the loss in visual sensitivity is rather long lasting. The loss in contrast sensitivity is greater at the middle and higher spatial frequencies, (significantly, as evidenced by a significant interaction between time of threshold determination and spatial frequency, $F(10,110) = 7.82, p < .0001$), where real world object recognition would be most affected. The observed losses are greater in the presence of glare than in its absence, $F(2,22) = 8.94, p < .0014$, substantiating the presence of enhanced light sensitivity. The results obtained with the 2 mg dose were qualitatively similar to those obtained with 4 mg but of considerably reduced magnitude.

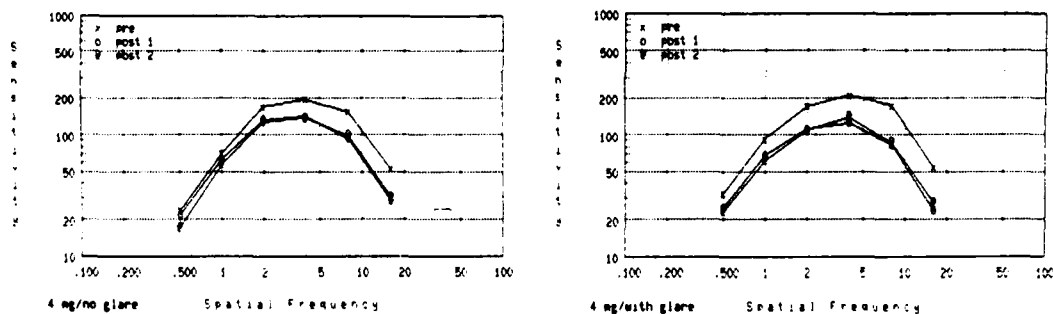


Figure 2. Effect of 4 mg Atropine on Visual Contrast Sensitivity

Visual Evoked Potential. Visual evoked responses to the checkerboard stimulus were analyzed in the same manner as the instructor pilots' evaluations. Since these VEP measures are known to be sensitive to diurnal effects, the noon measures as well as the evening measures were compared to the first test of each day. The resulting measures were the noon shift and evening shift of the N75; P100; and P300 from the morning baseline results. Analysis of variance was completed comparing these component amplitude shifts for the 0-mg test day and the 2 control days. The shifts under these conditions were not significantly different; thus, these measures could be considered to be stable across nonatropine conditions. The 'N75';

'P100'; and the 'P300' amplitude components for the three dose conditions then were subjected to the same analysis. A significant main effect was found for the shifts of the N75 component across the three dosages for pattern 2 ($P<.001$), pattern 5 ($P<.01$), and pattern 6 ($P<.03$) during both the noon and evening test sessions. The P100 peak amplitude shifts were significant for pattern 4, ($P<.05$) during both noon and evening tests, and patterns 5 and 6 ($P<.0006$) for the noon test. P300 peak amplitude shifts were significant across dosage for both noon and evening periods, $P<.05$.

Discriminant analysis was completed on those components which had been significant in the analysis of variance procedure. However, since the literature does not support any interpretive difference in the P100 and N75 and since negative and positive values would tend to nullify discrimination, only the N75 values were utilized for the analysis. Table 2 shows the results of the noon and evening classifications. The noon scores provide 77.78 percent of the cases correctly classified, while the evening scores predicted 91.67 percent correct.

Table 2

Actual Dose Groups	No. of Cases	Predicted Group Membership					
		Noon			Evening		
		0 mg	2 mg	4 mg	0 mg	2 mg	4 mg
0 mg	24	9 75.0%	3 25.0%	0 0.0%	11 91.7%	1 8.3%	0 0.0%
2 mg	24	2 16.7%	9 75.0%	1 8.3%	2 16.7%	10 83.3%	0 0.0%
4 mg	24	0 0.0%	2 16.7%	10 83.3%	0 0.0%	0 0.0%	12 100.0%

DISCUSSION

The strength of this project lies in the statistically repeatable manner in which the 12 subject pilots responded to the atropine dosages and the relative stability of the research measures utilized to identify and define the drug effects. These findings are especially noteworthy since each pilot entered into the project possessing different metabolic characteristics which impacted on the amplitude, onset, and duration of the atropine effects. Additionally, all of the subject pilots' flight aptitude differed in terms of flight experience, current flight proficiency, and general flight ability.

The pharmacodynamic effects of the atropine could be characterized as a

state of mild psychophysiological 'distress' during the morning flights immediately after injection. During this 1-hr 40-min flight, subjects exhibited elevated heart rate, blurring vision, dry mouth, and general apprehension. The aviators were more lethargic with fewer physiological changes (only visual accommodation) during their afternoon flights (5 hr post injection).

Flight behavior also was observed to be different for the two flight periods. The pilots' flight performance during the morning missions were more of active participation during which subjects under mild stress were attempting to maintain the most precise flight parameters possible. In contrast, afternoon flights became more of a passive participation; only when the aircraft was drifting away from standard parameters were corrections introduced.

The data reported in the results section support the above observations. Heart rate gave a clear picture of the atropine available in the vascular compartment. Figure 3 illustrates the response to the maximum dosage. The heart rate curve demonstrates a classic initial bradycardia followed by tachycardia. The second curve, at the bottom of Figure 3, shows a decrease in the variability of heart rate (decreased standard deviation). The mean heart rate of the subjects prior to injection was 73.4 beats per minute (BPM). This rate decreased to 64.7 BPM, then peaked at about 133 BPM approximately 30 min postinjection. By the afternoon flight, the atropine had sufficiently cleared the vascular compartment for heart

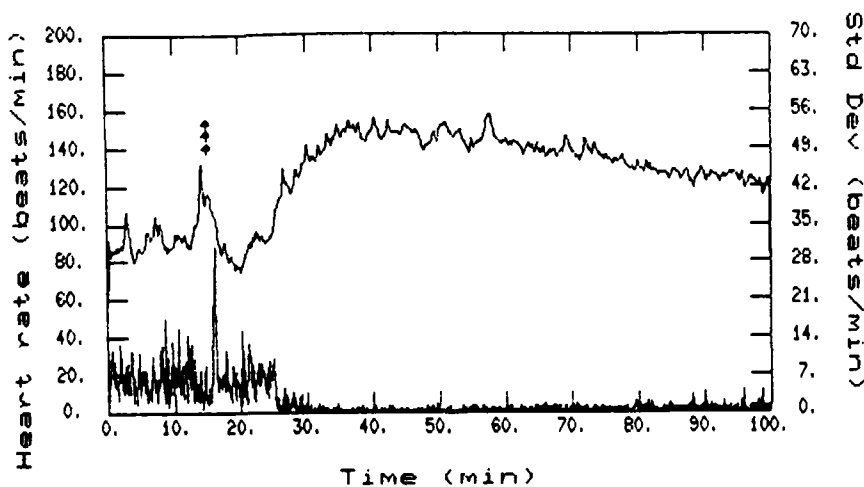


Figure 3. Effect of 4 mg Atropine on Heart rate

rate to be back to baseline. The 2 mg trials were similar to the 4 mg with the exception that the effects did not peak as high and recovery started sooner.

Visual accommodative changes which reflect the presence of atropine in the visual compartment were slower to return to normal than heart rate. The accommodation changes, as shown in Figure 4, did reflect changes across the three dose levels. The return of accommodation to normal appeared to be dose-dependent and was complete within 24 hr for 2 mg and within 36 hr for 4 mg.

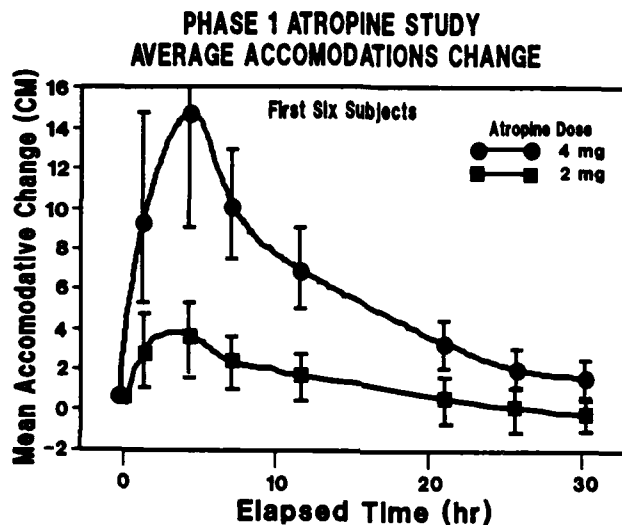


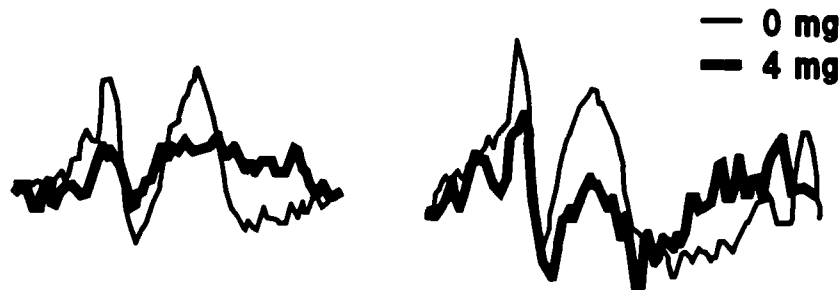
Figure 4. Visual Accommodation Curves

Both the instructor pilots' and the computer flight performance data reflected a statistically significant degradation in performance as a result of 4 mg of atropine. Neither the instructor ratings nor the computer performance analysis could successfully distinguish between the 2 mg and the 0 mg conditions. However, the statistically significant degradation in performance associated with the four milligrams were considered to not be 'operationally' significant for the simulated flight conditions that were experienced in this phase. For example, the instructors' ratings indicated that the mean overall flight score for the twelve aviators ranged from 14.2 for 0 mg to 13.2 for 2 mg and 12.6 for 4 mg during flights that occurred after initial injection. The afternoon scores ranged from 14.1 for 0 mg 13.9 for 2 mg and 12.1 for 4 mg. Since the minimum passing score under ATM standards was 12.0, the mean flight performance was above minimum safe flight standards. Individually, one aviator's morning score was below ATM standards; and four dropped below ATM standards on the afternoon of the 4-mg-dose day.

The reader is urged to interpret these results with caution. Although the aviators tested typically flew above ATM standards, implications for combat scenarios should be limited to the simulated instrument flight conditions experienced in this phase. The more stressful or demanding flight regimes expected in combat might be less tolerant of the amount of degradation observed under these ideal conditions.

The contrast sensitivity function provides an excellent indication of overall visual function, reflecting capability to readily see large, intermediate, and very small objects. It predicts more accurately than traditional acuity measures and real target acquisition performance. The magnitude of losses in contrast sensitivity observed in this study, as high as 50 percent with 4 mg of atropine, can be expected to adversely impact target acquisition and recognition of navigational landmarks, but should not prevent routine flying.

The effect of 4 mg of atropine on the ERP results are illustrated in Figure 5. The graph on the left is the worse case example and the graph on



N1-P2 COMPLEX

Figure 5. N_1 - P_2 Shifts as a Function of 4 mg Atropine

the right demonstrates the least atropine effect. The P300 component (not shown) has the same decrease in amplitude under the 4 mg dose. As the other comparisons indicated, the main statistically significant effects are observed between 4- and 0-mg trials. These data would indicate that there is some CNS degradation attributable to atropine which might be correlated with degradation in flight performance. Since flying is extremely dependent upon visual input information, any degradation to CNS activity associ-

ated with recognition or cognitive decision processes would be expected to degrade overall flight performance. This degradation could range from inability to maintain safe flight parameters to failure to visually detect targets of opportunity or threat.

Two observations on the effects of atropine which have not been included in previous discussion should be noted. During the 4-mg dose days subjects tended to have an 'activated imagination' with visual hallucinatory activity stimulated by viewing TV-monitors utilized in the contrast sensitivity test and the visual evoked response testing. This 'activated imagination' varied from perceiving undefined shadows to television programs, cartoons, and still scenes (a baby on a blanket with a parachute lying next to the blanket). Only four of the subjects did not experience this phenomenon.

The second observation involved the fourth subject to participate in this project. He was the only individual to allow the simulator to come in contact with the ground during the upper air precision maneuver (or any other maneuver). These occurred with the 4 mg atropine dosage. The first inadvertent ground contact was within the first 20 min of flight and the other was during the afternoon flight period. Both occurrences were during maneuvers which were to be flown approximately 600 ft above ground level. The subject twice failed to monitor a slow and progressive loss of altitude until ground contact was made. Thus, the pilot did not abruptly lose control of the aircraft, but rather failed to maintain proper vigilance of his aircraft instruments. Associated factors observed include lower flight time, fatigue, and relative inattention.

CONCLUSIONS

This research project was the first phase in a directed program to evaluate the effects of antidotes and pretreatment countermeasures upon aviator performance. Twelve subject pilots were injected with a sterile isotonic saline solution, 2 mg of atropine sulfate, and 4 mg of atropine sulfate during separate testing sessions. Their physiological response to the dosages were monitored as well as their operational flight performance. Additional laboratory tests were completed to evaluate their cognitive, psychophysiological, and psychomotor behavior shifts as a function of the atropine. The conclusions from this investigation can be summarized as follows:

1. The physiological status of healthy subjects was not adversely compromised by the effect of a maximum of 4 mg of atropine.
2. The 4 mg of atropine significantly affected flight performance, but 2 mg did not.
3. The flight performance decrements associated with atropine injec-

tion although, statistically significant, were not operationally significant.

4. Event related brain potential (ERP) data reflected shifts in the cognitive recognition and decision components of the subjects' EEG.

5. Visual accommodation measured by a Printz Rule could prove to be an inexpensive tool to estimate atropine dose injected and recovery from drug effect.

6. Contrast sensitivity losses ranging up to 50 percent were observed with the 4 mg dose of atropine, a magnitude that can significantly impact critical vision tasks.

Although the conclusions tend to indicate that safe flight can be performed under the influence of up to 4 mg of atropine the following cautions should be noted:

1. The magnitude of atropine induced flight performance degradation will vary with individual physiological response, flight experience, current proficiency level, and the stress/work demand of the flight.

2. This phase has not resolved the impact of additional variables such as high environmental temperatures, motion/vestibular interaction, partial sleep deprivation or high altitude flights.

3. Additionally, more investigation is required to determine if aircraft subsystems using phosphor screens could induce hallucinatory activity such as that experienced by some subjects in this study. Potential candidates could be helmet mounted night vision systems, or cockpit CRT displays.

One of the following phases of this research program will investigate the effect of atropine on inflight performance in an UH-1 utility class helicopter. The potential impact of such research is two-fold. First, some of the questions raised in this report can be addressed. Second, the research techniques used in both the simulated and inflight phases will further develop methodological approaches to evaluate other pharmaceutical compounds which might compromise safe mission completion.

REFERENCES CITED

1. Taylor, H. L., Dellinger, J. A., Richardson, B. C., Weller, M. H., Porges, S. W., Wickens, C. D., LeGrand, J. E., and Davis, J. M. 1985. The effects of atropine sulfate on aviator performance. US Army Medical Research and Development Command, Fort Detrick, Frederick, MD. Report ARL TR-85-1 and Aviation Research Laboratory, Institute of Aviation, University of Illinois at Urbana-Champaign. Contract No. DAMD-17-83-C-3150.
2. Jones, H. D. and Higdon, A. A. Jr. 1985. "UH-1 simulator data acquisition and management on the USAARL VAX-11/780." Fort Rucker, AL. Internal working document at US Army Aeromedical Research Laboratory.
3. Hamilton, B. E., Simmons, R. R., and Kimball, K. A. 1982. Psychological effects of chemical defense on ensemble imposed heat stress on Army aviators. Fort Rucker, AL: US Army Aeromedical Research Laboratory. USAARL Report No. 83-6.
4. Walker, N. K. and Fricker, C. J. 1964. Tracking tasks as indicators of stress. College Park, MD. Institute of Behavioral Research. Contract No. DA-49-193-MD-2208.
5. Bachman, W. G. and Behar, I., 1986. Effects of cyclopegia on the visual contrast sensitivity function. Fort Rucker, AL: US Army Aeromedical Research Laboratory. USAARL Report No. 86-2.
6. Israel, J. B., Wickens, C. D., Chesney, G. L., and Donchin, E. 1980. "The effect-related brain potential as an index on display-monitoring work load." Human Factors. 22(2):211-224.
7. Israel, J. B., Chesney, G. L., Wickens, C. D., and Donchin, E. 1980. "P300 and tracking difficulty: evidence for multiple resources in dual-task performance." Psychophysiology. 17(3): 259-273.
8. Meadley, D. B. 1982. "Effects of atropine sulfate and pralidoxime chloride on visual physiological, performance, subjective, and cognitive variables in man: a review." Military Science. Vol. 197, No. 2.

SNELLEN & DEPONAI

THE MALOS COMBAT ENGINEER SIMULATION ENVIRONMENT (U)

JAMES E. SNELLEN, DR.
MICROCOMPUTER SYSTEMS LABORATORY
URBANA, ILLINOIS 61801-0000
*JOHN M. DEPONAI, III, MR.
U.S. ARMY CONSTRUCTION ENGINEERING RESEARCH LABORATORY
CHAMPAIGN, ILLINOIS 61820-1305

MALOS is a PLATO-based simulated combat environment developed for the U.S. Army Engineer School (USAES). The development of MALOS was influenced by the following design considerations:

1. The simulation must run in solitaire mode using standard PLATO system hardware.
2. The combat resolution phase of the simulation must take 15 minutes or less to complete.
3. The operating characteristics of the simulation driver must be data-based rather than hard-coded to allow maximum flexibility in scenario design.
4. The simulation must provide experiential learning in how to design an effective obstacle plan.
5. Exercising the simulation should be interesting and enjoyable.

MALOS is designed to present situations that give the student experience in planning defensive works such as minefields, abatis, anti-tank ditches, and fighting positions. The MALOS environment is extendible to other aspects of land-based combat. The Obstacle Planning Simulation (OPS), a prototype demonstration scenario that runs under MALOS, has been documented (1, 2). A complete description of the MALOS Simulation Environment is being published as a two-volume set of technical reports (3, 4).

The MALOS simulation system consists of two major components: the Scenario Generation System and the Simulation Driver.

The Scenario Generation System is based on an "Instructor's Workbench" concept (5) that provides the tools necessary to create and modify a MALOS scenario in a manner independent of the software that drives the scenario. Included in the "workbench" is a standard library of data on weapons performance, engineering resources, obstacle characteristics, etc. Thus, knowledge concerning these areas is stored for the scenario designer to use as is, or to modify to meet particular needs. The Scenario Generation System consists of three components: the Map Editor, the Scenario Editor, and the Access System.

1. The Map Editor is used to create the map on which the exercise is to be run. Each new map is stored in a map library and is available to any scenario designer who might wish to use it.
2. The Scenario Editor contains a compiler for the Scenario Description Language which is used to describe the functional characteristics that the scenario will have. It includes an attack/defense plan editor that is used to define the deployment of the defensive (Blue) team and the attack plan of the attacking (Red) team. The attack/defense plan editor enables the scenario designer to define up to seven attack plans, one of which is chosen at random each time the scenario is run. Thus, students do not know in advance which attack they must defend against.
3. The Access System provides control over who may edit various scenarios and/or maps. The access system protects each scenario designer's work from unauthorized modification.

The Simulation Driver is the program that interacts directly with the students. This program runs the scenarios designed by the instructors and provides statistical data on the effectiveness of the student's obstacle plan. The Simulation Driver also provides for an "instant replay" of the battle.

SIMULATION MECHANICS

Interpreting a MALOS Map

Each cell in a MALOS map represents a piece of simple terrain (such as woods, slope, or town) or complex terrain (such as gully-woods, hill-top-town, etc.). The type of terrain at a particular location on the map can be determined by the type of graphic displayed at that point. Figure 1 shows a typical MALOS map and explains the meaning of each terrain symbol. This map display has been optimized as much as possible to take advantage of the graphic capabilities of a standard PLATO terminal.

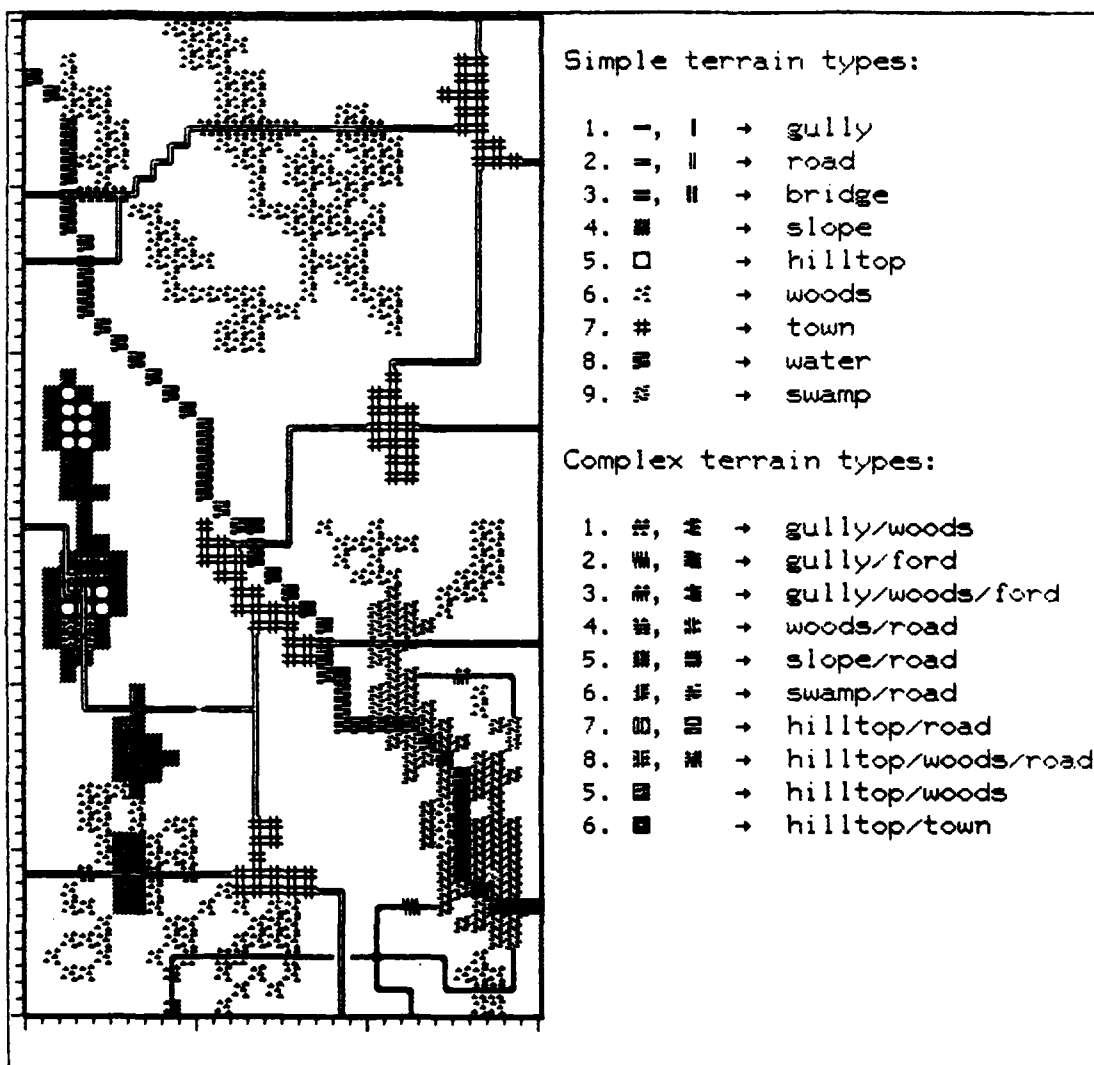


Figure 1. Example of a MALOS terrain map with terrain symbol interpretations

Line of Sight/Line of Fire (LOS/LOF)

A system of logical barriers is used to determine where terrain features will block LOS/LOF. The MALOS simulation driver recognizes three types of barriers. These barriers function as follows:

1. Class A barriers are absolute barriers that block LOS/LOF for all non-adjacent units under all conditions. Class A barriers are used to block LOS/LOF in woods and in towns located on hilltops.
2. Class B barriers block all LOS/LOF unless one or both of the units involved is on a hilltop map cell. Class B barriers are used to block LOS/LOF in ground-level woods and towns and on slopes.
3. Class C barriers are used to define the military crest of hills. LOS/LOF through a single class C barrier is not blocked. However, LOS/LOF is blocked if a second Class C barrier is encountered. In general, every hill mass is surrounded with a double ring of "C" barriers. A unit located at the military crest of a hill would have one "C" barrier between it and ground or slope level, while a unit back from the military crest would have two class C barriers between it and ground or slope level. Class C barriers have no effect if both units are located on hilltops.

If two units are in adjacent map cells, their LOS/LOF is always clear, regardless of LOS/LOF barriers.

Engineered Features

In addition to the natural terrain features, the results of combat engineer terrain modifications (minefields, anti-tank ditches, etc.) are also shown on the map. Obstacles on the map are intact at the start of the battle, but some of them may be "breached" by the time the battle is over. At the end of the battle phase, the map is updated to show which obstacles are breached and which are intact. Figure 2 shows the graphics used to represent intact and breached engineer terrain modifications.

Representation of Time

Time passes during the course of the simulation as a series of discrete increments. The amount of simulated time represented by each time increment varies, depending on the map scale selected and the speed assigned to the fastest unit in a particular scenario. For example, if a map cell is defined to be 200 meters wide and the speed of the fastest

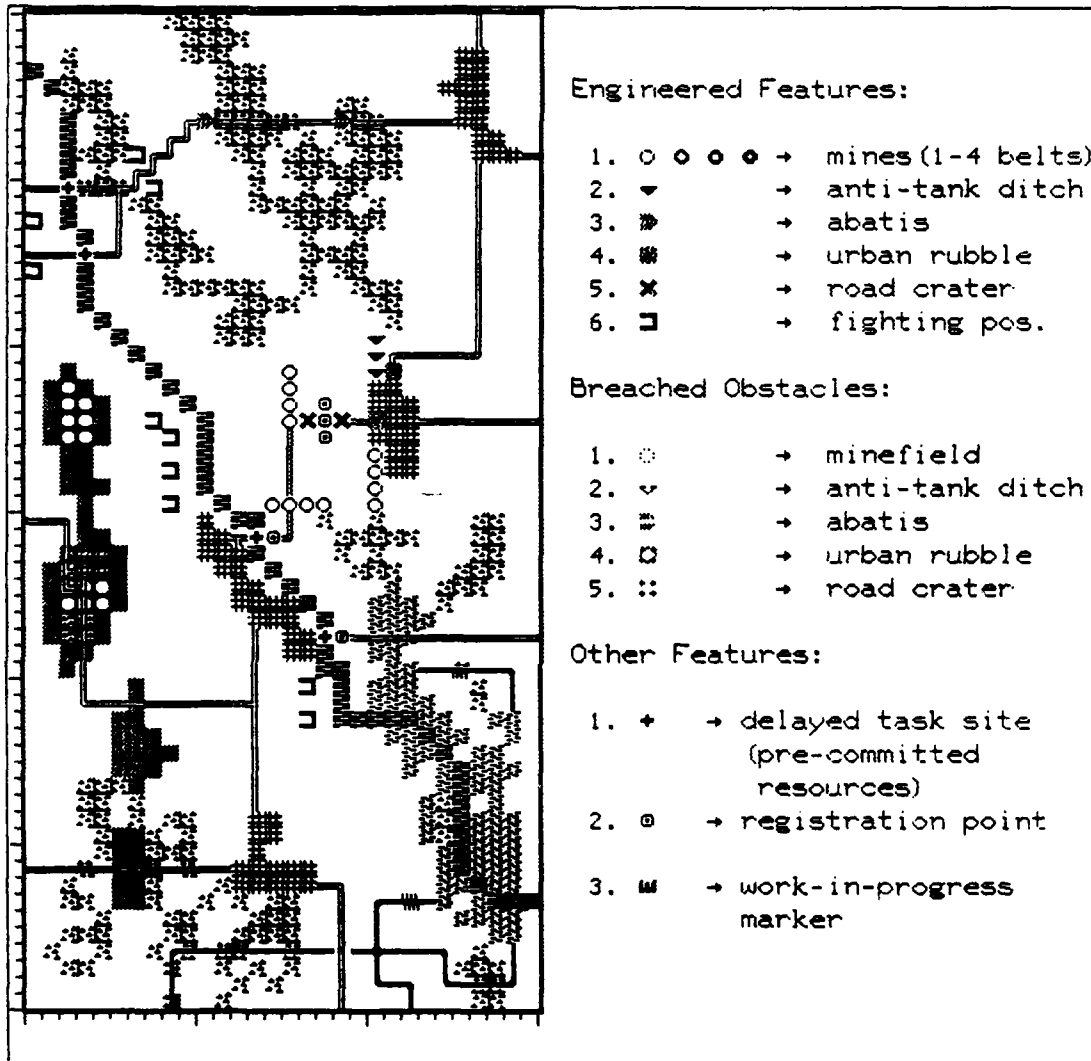


Figure 2. Definition of graphics used for engineered features

unit in a scenario is defined to be 30 kph, each time increment would correspond to 24 seconds of simulated time, because a vehicle traveling at 30 kph requires 24 seconds to traverse 200 meters. The cell width and the maximum speed are determined by the scenario designer.

Movement Factor

Time increments are grouped in a series of 12-increment "clock cycles." This facilitates the scaling of different vehicle speeds. MALOS assigns to each vehicle type a single movement factor value from a range of 0 through 12. This value determines the speed of that vehicle type relative to a maximum-speed vehicle. If a vehicle is assigned a movement factor of 12, it executes a "move impulse" in each of the 12 time increments of a clock cycle. If it is assigned a movement factor of 6, it executes 6 "move impulses" per clock cycle and thus moves half as fast as a maximum-speed vehicle. A vehicle assigned a movement factor of 0 would not move at all.

Effects of Terrain on Movement

To understand the effects of terrain on movement, it is necessary to understand the difference between "terrain" and "terrain attributes." A terrain attribute is a bit of information that describes a single functional characteristic of a map cell. The current version of MALOS models 12 terrain attributes that are grouped into three categories:

- Category 1: Three ELEVATION attributes: ground, slope, and hilltop.
- Category 2: Eight SURFACE FEATURE attributes: woods, town, swamp, gully, ford, water, clear, and bridge.
- Category 3: One SPECIAL attribute: road, which negates any extra movement costs that otherwise would be charged because of terrain attributes in the other two categories.

The terrain that a map cell represents is defined then by the cumulative effects of all the terrain attributes assigned to that map cell.

A unit moves fastest along an unobstructed road. However, the rate of travel is reduced when a unit moves cross-country. The degree to which the rate of travel is reduced varies, depending on what kind of terrain the unit is moving through. The effect of terrain on movement is further complicated by the fact that some map cells contain more than one type of terrain attribute, each of which may affect the travel rate.

In a MALOS map, there is always a basic "cost" of one "move impulse" to move through one map cell. If a unit is moving out of one map cell that contains a road into another map cell that also contains a road (i.e., along a road), only the basic movement cost is charged and the unit moves along at the rate of one movement impulse per map cell. If the unit is not moving from a road to a road, additional "cross country" movement costs due to terrain effects are charged. The additional amount charged depends on the kinds of terrain attributes in the map cells that the unit is leaving and entering.

Table 1 shows the additional movement costs associated with moving from one terrain attribute type to another. The costs are measured in number of additional "move impulses" required. Since there are 12 kinds of terrain attributes, there are $12 \times 12 = 144$ paired combinations of terrain attributes that must be considered when computing the movement cost between two adjacent map cells. A pair of terrain attributes can have one of three influences on the final movement cost calculation.

1. The terrain attribute pair may be irrelevant to the movement cost; for example, moving from ground to clear is not meaningful in terms of movement cost.
2. The terrain attribute pair may preclude movement between two map cells; for example, moving from ground to hilltop (i.e., up a cliff) is prohibited.
3. A "cross country" movement cost may be added to the basic movement cost. For example, moving from woods to woods adds an additional five "move impulses" to the basic movement cost of one "move impulse."

The total cost to move from one map cell to the next is one "move impulse" (base cost) plus the sum of the effects of all positive terrain attribute combinations of the first map cell paired with the terrain attributes of the second map cell. For example, if a unit is moving from a ground-level-woods-road cell to a ground-level-woods-gully cell, the special-case road effect is not applicable because the map cell being moved into does not contain a "road" attribute. The total movement cost is: 1 (basic cost) + 5 (for moving from woods to woods) + 3 (for moving from woods to gully) for a total of nine "move impulses" required to complete the movement. From Table 1, all other terrain attribute combinations are irrelevant and therefore contribute nothing to the movement cost.

Table 1. Additional "Move Impulses" Required Per Terrain Attribute Pairs

From\To	Ground	Slope	Hilltop	Clear	Woods	Road	Bridge	Town	Gully	Swamp	Ford	Water
Ground	-	5	X	-	-	-	-	-	-	-	-	-
Slope	-	5	4	2	3	-	-	2	3	3	3	11
Hilltop	X	3	-	-	-	-	X	-	X	X	X	X
Clear	-	3	-	1	2	-	-	1	2	2	2	11
Woods	-	5	-	2	5	-	2	2	3	3	3	11
Road	-	-	-	-	-	-	-	-	-	-	-	-
Bridge	-	-	-	1	2	-	-	-	X	-	-	-
Town	-	3	-	1	2	-	-	-	2	2	2	11
Gully	-	11	X	11	9	-	X	11	4	11	3	11
Swamp	X	X	X	X	X	-	X	X	X	X	X	X
Ford	2	5	X	2	2	-	-	2	2	2	2	11
Water	-	11	X	11	11	-	X	11	11	11	11	11

"-" means such a move is irrelevant
 "X" means such a move is prohibited

Non-Stacking of Red Team Units

The MALOS driver prevents Red units from stacking. A Red unit will never move into a map cell that is currently occupied by another Red unit. The Red unit will stop executing its movement plan until the map cell it is trying to enter is unoccupied by other Red units. A Red unit can move into any map cell occupied by a Blue unit or by a "destroyed" unit of either side. Being in a "stopped" state has negative combat implications that will be explained later.

Engineer Terrain Modifications

During the first phase of the simulation, the player may modify the map so as to degrade the ability of Red units to move and to fire at defending Blue units. This is done either by obstructing Red movement or by making friendly units more resistant to enemy fire. Obstacles are always more effective if they are covered by fire during the time that enemy units are attempting to breach them. An obstacle, such as an abatis, will delay an enemy unit longer if it is covered by fire than if it is not covered by fire. This is especially true for minefields, which not only delay longer if covered by fire, but also kill more vehicles. All obstacles have the following effects:

1. When a red unit encounters an obstacle, it is flagged as being in a "stopped" state, so it is more vulnerable to opposing fire. The degree to which a "stopped" state enhances vulnerability to opposing fire is determined by the scenario designer.
2. When a Red unit encounters an obstacle, some of the vehicles in that unit must engage in "clearing the obstacle" with the result that they cannot fire at Blue units. The number of vehicles engaged in clearing an obstacle is also defined by the scenario designer.

Minefields have the following additional capabilities:

1. Unlike other obstacles, which can only be present or absent, more than one minefield can be laid in a single map cell. Up to four levels (or belts) of mines can be laid in a single map cell.
2. In addition to the delay caused by a minefield, each belt of mines will kill some of the vehicles in a Red unit. The number of vehicles killed depends on whether the minefield is covered by fire at the time it is traversed by a Red unit. If covered by

fire, each belt of mines kills a pre-determined number of vehicles (defined by the scenario designer). If the scenario designer determines that each belt of mines kills four vehicles when covered by fire, then a four-belt minefield kills up to 16 vehicles. If the minefield is not covered by fire, only one vehicle is killed, even if the minefield is a four-belt field.

Demolishing a bridge delays an enemy advance, since it removes the means of traversing a water obstacle. Thus, the mechanics of bridge demolition are handled in a special manner. Unlike other engineering activities, bridge demolition actually changes the map database, in that the map cell that had been shown as a "bridge" is now shown as "water."

Fighting positions are terrain modifications that enhance a defending unit's resistance to enemy fire. Defensive enhancement is determined once at the start of the battle phase; after the battle begins, no more units may take advantage of existing fighting positions. Fighting positions benefit only those units that start the attack phase in a map cell containing a fighting position. Blue reserve units (discussed below), which appear automatically during the battle, derive no benefit from fighting positions.

Combat Mechanics

MALOS uses a modified "probability to hit (x) probability to kill" combat resolution scheme. To limit the processing load during combat resolution, these two probabilities for each weapon/target combination are combined into a single probability to kill for faster computation.

Each Blue or Red team unit can consist of 1 to 15 vehicles, each of which fires with its own independent "probability to kill" against a specific enemy target. Each recorded kill reduces the target unit by one vehicle so that its firepower, in turn, is reduced by that amount. All firing is considered to be done simultaneously, and reduction in firepower due to losses is reflected in the next round of fire.

MALOS distinguishes between combat vehicles and the weapons carried by those vehicles. Vehicles and weapons are defined separately in the MALOS database. It is possible for each vehicle to be assigned both a primary and a secondary weapon. This means that any set of weapons can be assigned to any vehicle by the scenario designer. Furthermore, a limited ammunition load can be assigned to the primary weapon so that MALOS can simulate the limitations of a basic load.

SNELLEN & DEPONAI

When a Blue vehicle exhausts its primary weapon ammunition supply, it automatically "retreats" to avoid being destroyed needlessly by the advancing Red units. The "retreating" Blue unit does not actually trace a movement path off the board. It is removed from the map after enduring enemy fire for one time increment after it runs out of ammunition.

Target Acquisition

During the attack phase of the simulation, each unit on the map attempts to acquire an enemy target during each time increment. The rules for acquiring a target are similar for Red and Blue vehicles, but there are some important differences. For a Red vehicle to qualify as a target, the following conditions must be met:

1. The Red vehicle must be within maximum effective fire range of the weapon carried by a Blue vehicle. "Maximum effective fire range" is the maximum range at which the firing vehicle can expect some minimum kill probability on a target. This minimum required kill probability is defined by the scenario designer.
2. There must be an unobstructed LOS/LOF between the Blue vehicle and the Red vehicle.
3. The Red vehicle must be within the area of responsibility defined for the Blue vehicle. This "area of responsibility" is defined by the scenario designer.

For a Blue vehicle to qualify as a target, the following conditions must be met:

1. The Blue vehicle must be within maximum effective fire range of the weapon carried by a Red vehicle.
2. There must be an unobstructed LOS/LOF between the Red vehicle and Blue vehicle.
3. The Blue vehicle must have fired at least once. The assumption is that defending vehicles are concealed until they open fire.

Reserve Units

The scenario designer has the option to designate a portion of the Blue team as reserve units. A reserve unit does not appear on the map at the start of the scenario and does not participate in the battle until one or both of the following conditions are met:

1. All defending units (including any reserve units that have already become active in the battle) within the reserve unit's field of responsibility have been destroyed or have retreated after exhausting the ammunition supply of their primary weapon.
2. An enemy unit comes within some minimum distance of the reserve unit. This distance is defined by the scenario designer.

RUNNING THE GAME

A MALOS scenario consists of two sequential phases. Phase I is implementation of the obstacle plan by the user. During this phase, the user has a limited number of turns to prepare the battlefield (the game map) for the enemy attack. The actual number of turns is determined randomly within some range of turns specified by the scenario designer. Figure 3 shows a typical display seen by the user during Phase I. Note that the types and amounts of resources available to the user for preparing the defensive works are listed, and balances are updated as these resources are expended. The acronyms in the task menu of Figure 3 are explained below.

mfj - "1-0-0" density minefield, laid by hand
mfg - "1-0-0" density minefield, laid by M128 mine-layer
mfa - "1-0-0" density minefield, laid by artillery
atd - Anti-tank ditch
brb - Blow bridge
rcm - Road crater
aam - Abatis
urr - Urban rubble
fp - Fighting position

During Phase II, the battle is executed by MALOS. The degree to which this phase is interactive is determined by the scenario designer. As a minimum the user may specify how many time increments are to be run before a "pause" in the simulated battle occurs. The scenario designer may also specify some tasks (such as bridge demolition or artillery-delivered mines) as having delayed execution. In this case, the user will also have the option of calling for the execution of these delayed tasks during the battle phase.

At the conclusion of the battle phase, MALOS displays a set of summary statistics as shown in Figure 4. The losses inflicted on the Red team and the contribution of the various obstacle types to these losses provide a measure of the effectiveness of the player's obstacle plan.

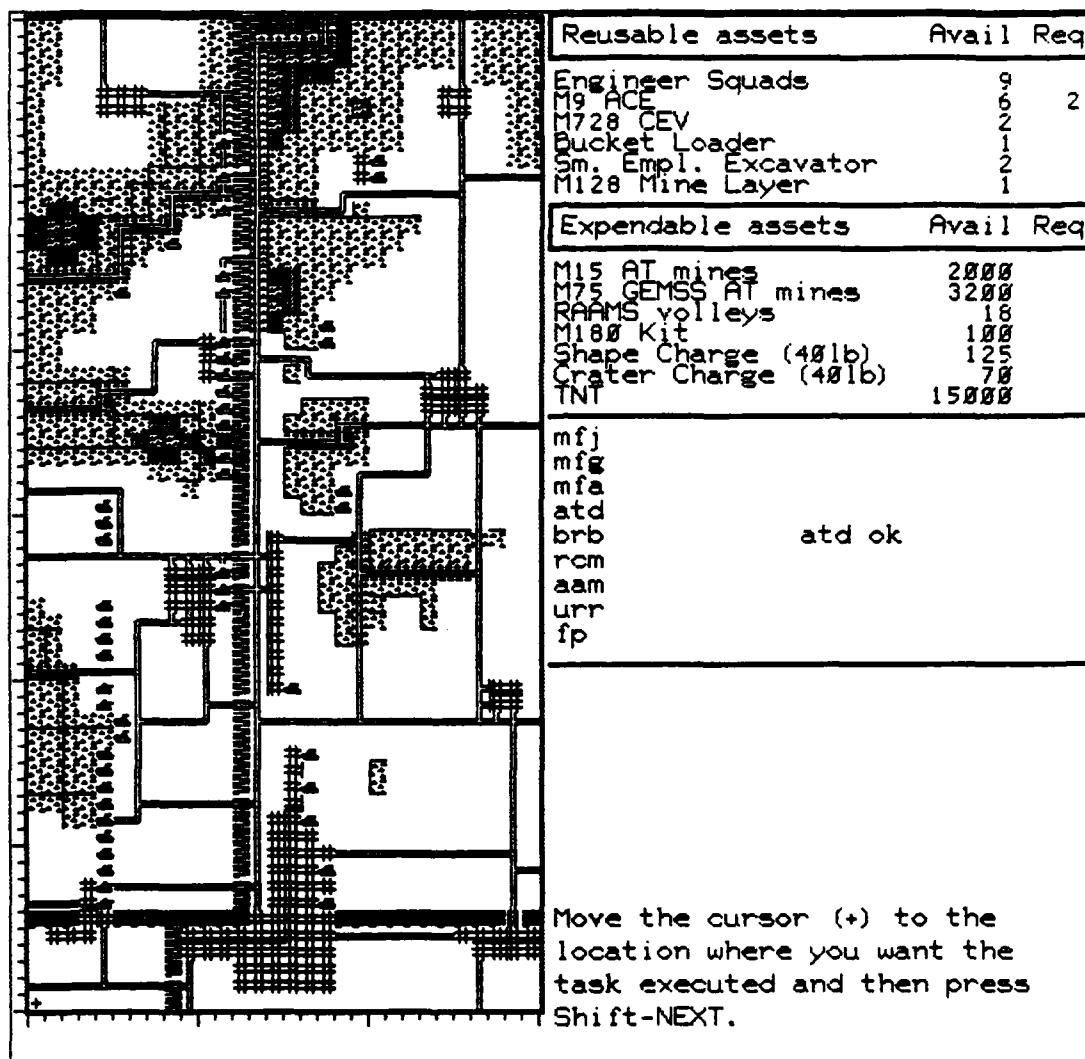


Figure 3. Example of a Phase I MALOS screen display

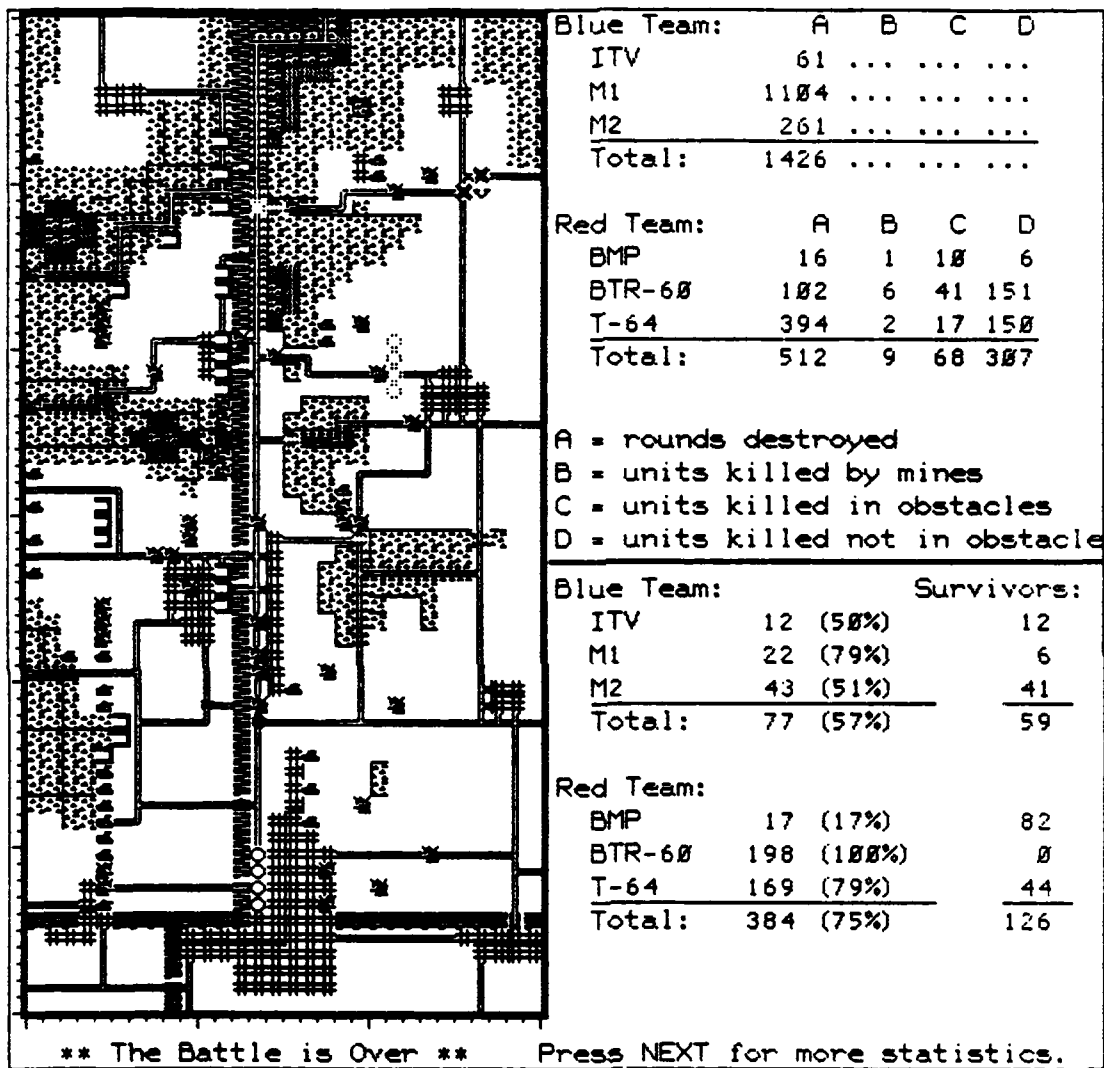


Figure 4. Example of a Phase II MALOS statistical summary

CONCLUSIONS

MALOS is an experiential learning tool to reinforce the principles of obstacle planning. It does not require the intervention of a human umpire. Once the student has conceived and implemented an obstacle plan, MALOS automatically runs a simulated battle using that plan and provides a statistical report on the combat outcomes. We believe the level of abstraction used in simulating the battle is of sufficient fidelity to make the exercise a useful learning experience.

MALOS scenarios have been designed by engineer school instructors to reinforce certain teaching points. A student can execute a simple scenario in as little as 5 minutes. Even a very complex scenario, such as the OPS Division-level attack, can be run in 15 to 30 minutes, depending on how long the student takes to implement the obstacle plan. This short cycle time makes MALOS a very useful tool for exploring several "what-if" possibilities for a given scenario within a limited time.

Currently, MALOS is installed on the U.S. Army Engineer School PLATO system where it is being tested and evaluated as an aid in teaching the principles of obstacle planning. The MALOS system, as described here, is subject to change depending on the results of that evaluation. The MALOS system is also being enhanced in cooperation with the U.S. Army Armor School to teach how to employ armor in the offense.

REFERENCES

1. Deponai, John M., III, and James E. Snellen. "Obstacle Planning Simulation (OPS): Introduction and User Instructions," Technical Report P-85/08 (ADA149468), U.S. Army Construction Engineering Research Laboratory (USA-CERL), 1985.
2. Deponai, John M., III, and James E. Snellen. "Obstacle Planning Simulation Version 1.1: Design and Performance Analyses," Technical Report P-85/10 (ADA149468), USA-CERL, 1985.
3. Snellen, James E., "The MALOS Combat Engineer Simulation Environment (Version 3.0), Volume I: Users Manual for the Scenario Generation System," Technical Report P-86/02, USA-CERL, 1986.
4. Snellen, James E., "The MALOS Combat Engineer Simulation Environment (Version 3.0), Volume II: Users Manual for Running Scenarios," Technical Report P-86/02, USA-CERL, 1986.
5. Mabry, Frank J., Microcomputer Systems Laboratory, University of Illinois (personal communication).

SOICHER

VARIABILITY OF TRANSIONOSPHERIC SIGNAL TIME DELAY
AT HIGH LATITUDES(U)

HAIM SOICHER, DR.
COMMUNICATIONS/AUTOMATIC DATA PROCESSING CENTER
US ARMY COMMUNICATIONS-ELECTRONICS COMMAND
FORT MONMOUTH, NEW JERSEY 07703-5000

INTRODUCTION

The transit time of a transionospheric signal from a satellite to a ground observer is

$$t = \int_0^S \frac{ds}{v_g} = \frac{1}{c} \int_0^S n_g ds \quad (1)$$

where ds is an element of distance along the signal's path, v_g is the group velocity of the signal, n_g is the group refractive index, c is the speed of light, and 0 and S are the observer and satellite positions, respectively. In the high-frequency approximation, the group refractive index is

$$n_g = 1 + \frac{40.3N}{f^2} \quad (2)$$

where N is the electron density per meter cubed, and f is the operating frequency in hertz. Equation (1) becomes

$$t = \frac{1}{c} \int_0^S ds + \frac{40.3}{cf^2} \int_0^S N ds \quad (3)$$

The first term in (3) represents the transit time of the signal in free space, whereas the second term represents the excess time-delay of the signal along the path. The excess time-delay is directly proportional to the total electron content (TEC) along the signal path and is inversely proportional to the frequency squared.

The Faraday polarization rotation technique has been used to obtain TEC data. A plane polarized wave propagating in the anisotropic ionosphere may be regarded as the vector sum of the ordinary and extraordinary magnetoionic components. Since the two components travel at different phase velocities, the plane of the polarization rotates continuously along the signal's path. The total rotation from a satellite signal source to observer is directly proportional to TEC. Faraday

SOICHER

rotation is a terrestrial-magnetic-field dependent phenomenon. Since its magnitude is heavily weighted near the earth, it is considered to provide electron content values at altitudes below ~ 1500 km. Signal excess time delay at higher altitudes is due to free electrons in the plasmasphere. Plasmaspheric delays have been measured to be $\sim 15\%$ of the ionospheric time delays (Soicher, 1977).

Faraday rotation observations were conducted at Anchorage (61.04°N , 149.75°W), using the signal of a geostationary satellite located at 96°W . The geographic subionospheric point (i.e. the coordinates of the point at which the signal path intersects a mean ionospheric altitude of 420km) is at 52.5°N , 135.5°W . The ionospheric characteristics observed are considered to be those of which are prevalent at the subionospheric point rather than those at the location of the receiving apparatus. The beacon frequency of the satellite was 136.38 MHz.

The receiving equipment was composed of an electronically rotated polarimeter which compares the left and right circular polarization components of the incident linear polarization on an eight element crossed yagi antenna (Hicks, 1972). The recording of the polarimeter output is done in analog form on a chart recorder. The conversion of polarization rotation to total electron content (TEC) is accomplished by standard procedures, at 15 minute intervals, taking into account the initial polarization transmission at the satellite source and antenna polarization calibration (Klobuchar, 1966).

The transmission from the satellite is continuous except for an occasional shut off of the satellite for power conservation purposes. Occasional fast polarization fluctuations, generally produced by irregularities in an environment of high ambient ionization (Lee et al, 1982), do not allow polarization tracking and hence cause data gaps.

TEC Structure

The superposed diurnal variation of TEC grouped in monthly intervals for the seasonally representative months of October, December 1976 and April, August 1977, are shown in Figures 1 (a,b,c,d) and 2 (a,b,c,d). The smoothed observed sunspot numbers were 13, 15, 22, 33 respectively, which were near the minimum of sunspot cycle 21 (12) which occurred in March 1976. The TEC values are normalized to the vertical direction, and have the unit of 10^{16} electrons m^{-2} (a TEC unit = 10^{16} electrons m^{-2}). As is well known, the data exhibit diurnal, day-to-day and seasonal variability. Figure 3 (a,b,c,d) shows the variation of the monthly average of TEC (upper curves), and the standard deviation of TEC about the monthly average (lower curves) as a function of time for the four months.

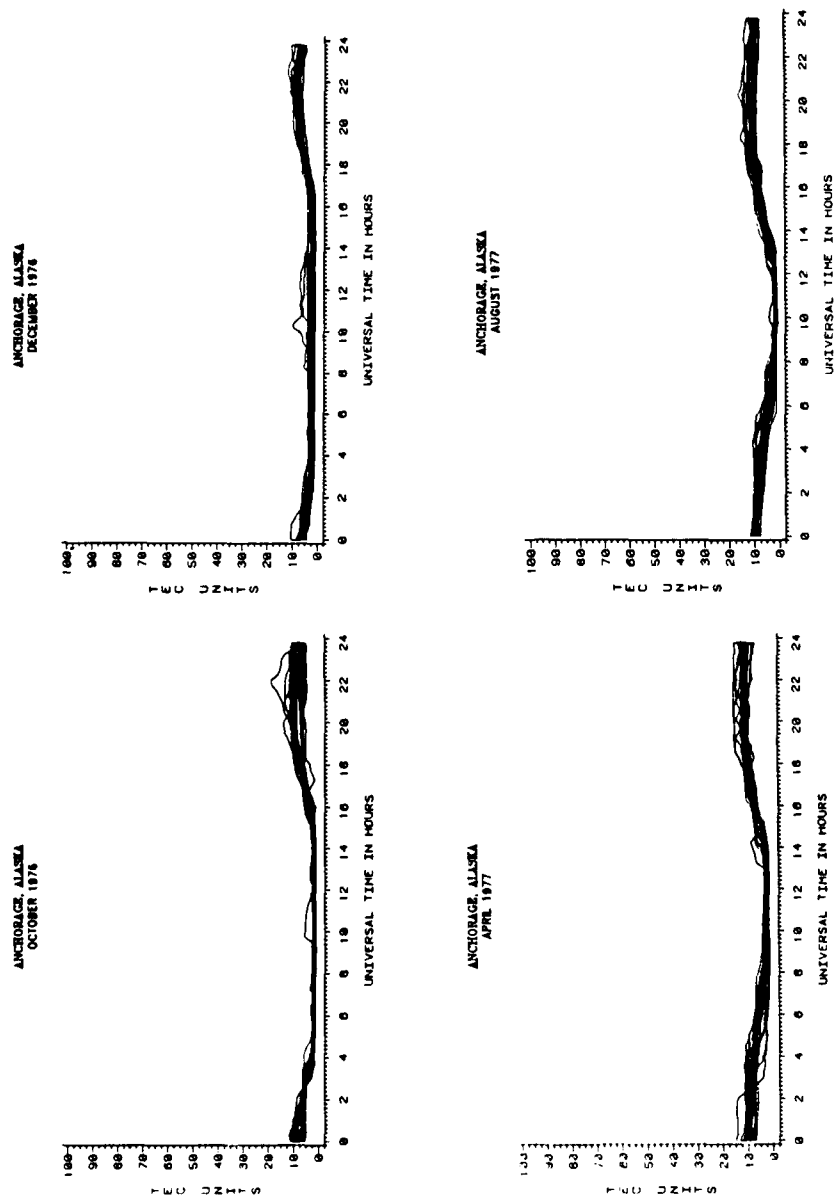


Figure 1 (a,b,c,d)

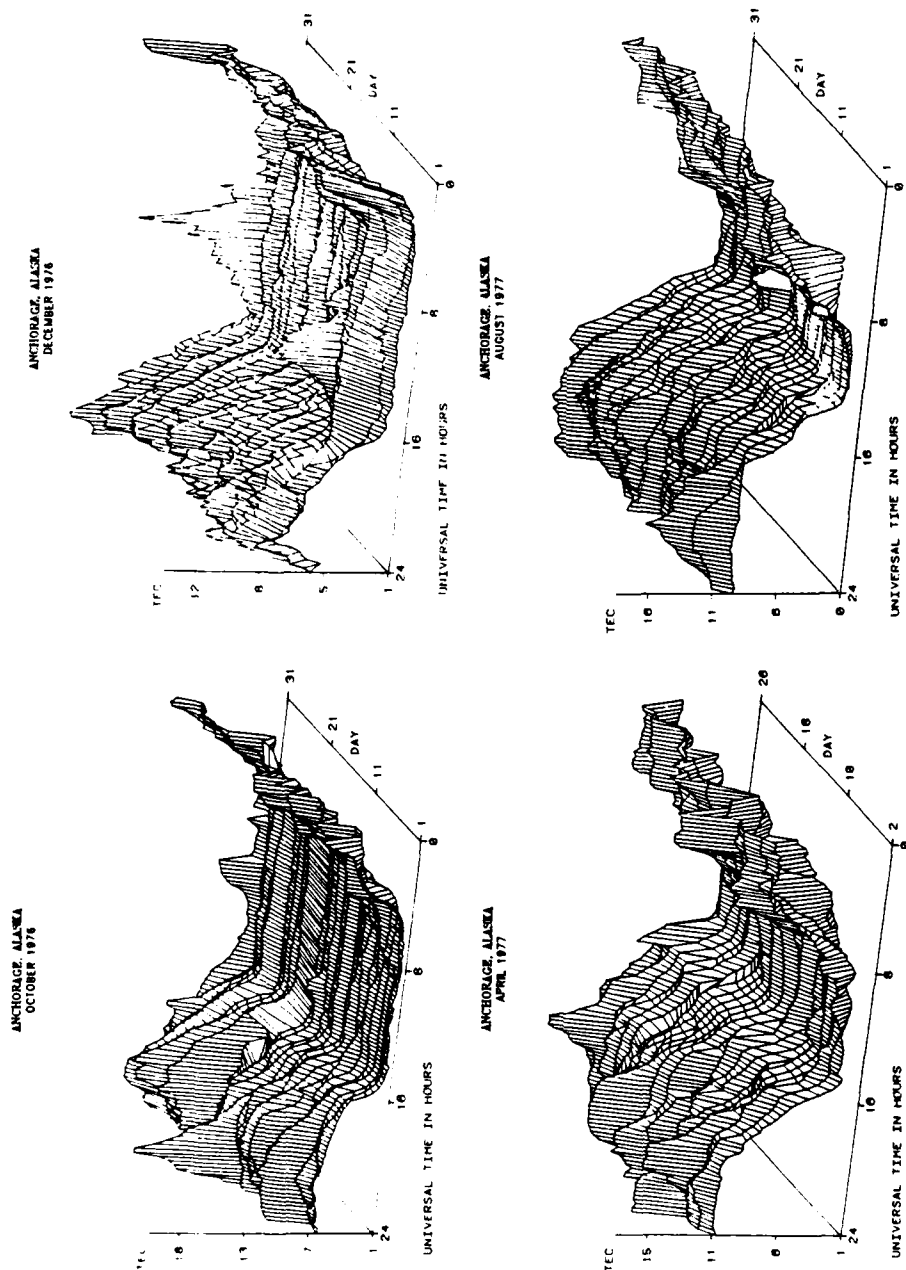


Figure 2 (a,b,c,d)

SOICHER

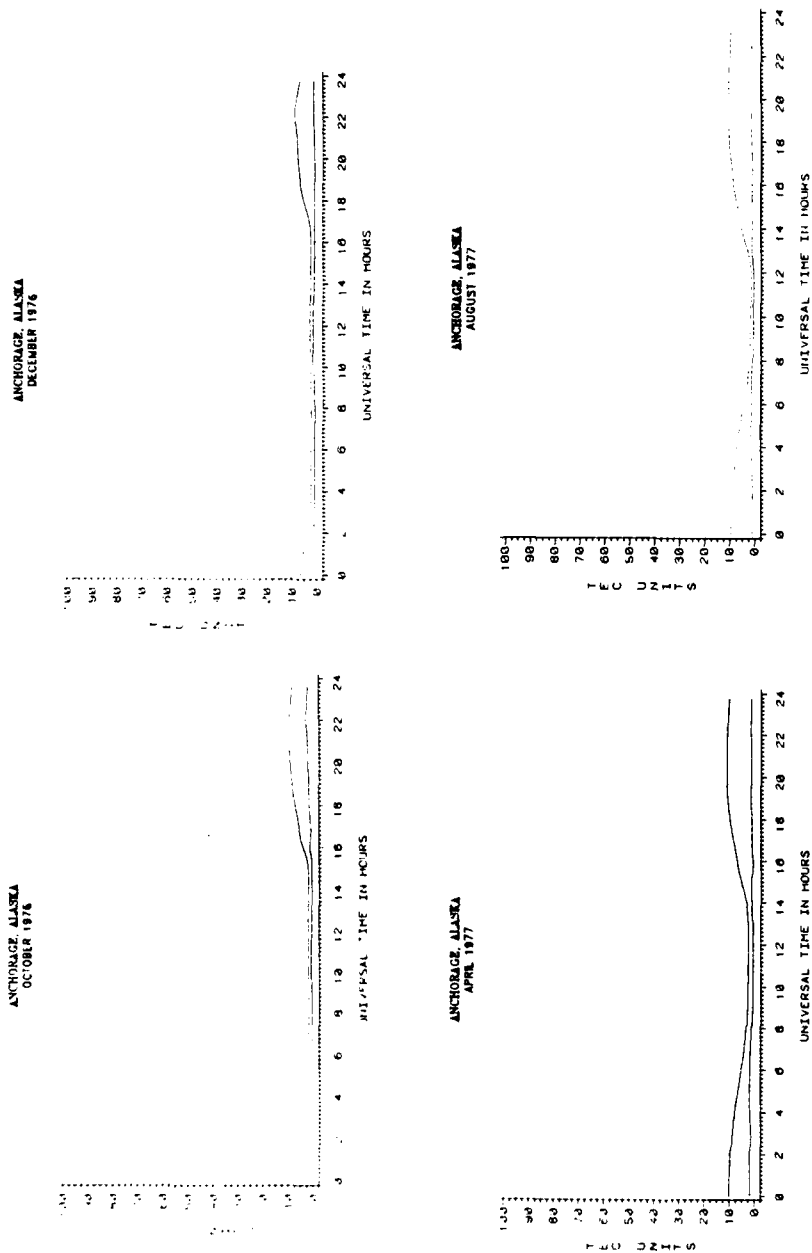


Figure 3 (a,b,c,d)

The low solar cycle epoch and the northern geographic location of the subionospheric point are exhibited by the rather low absolute values of the TEC for all reported months. The TEC never exceeded 20 TEC units, and average monthly values of TEC were always below 15 TEC units. The data exhibit diurnal, day-to-day and seasonal variability. The seasonal variation is exhibited by the time length of the post-sunset to dawn minimum TEC values indicating no illumination, and by the progressively lower average day values of the Spring (April), Summer (August), Autumn (October), and Winter (December) TEC, respectively.

The low winter values are possibly related to the mid-latitudes trough; the differences, however, were quite small (~ 1 to 3 TEC units). This is in contrast to TEC values at midlatitudes (Fort Monmouth, NJ) near solar minimum where summer TEC was higher than winter TEC and both were higher than TEC during the equinoctial periods. No seasonal variability of the day-to-day changes is exhibited by the comparable values of the standard deviation to the average TEC values as a function of time. Such ratios are plotted in Figure 4 (a,b,c,d) for the various months. For the most part, the ratio is below $\sim 25\%$ during the daytime for all reported months. During darkness, the ratio may exceed 25% and often exhibits variable periodic behavior. The daytime observations of the ratio agree with those at other locations and other times (Soicher and Gorman 1980, 1985; Soicher et al 1982, 1984).

By comparison, superposed diurnal variation, monthly average variation and the standard deviation of TEC for the latter half of August 1980, with smoothed observed sunspot number of 150 are shown in Figure 5 (a,b,d). Average maximum monthly values were about double those during the comparable period of 1977. While the standard deviation about the monthly average was higher, the daytime ratio of the standard deviation to the TEC (Figure 5c) was comparable with values of $\lesssim 25\%$.

A complementary method of assessing the day-to-day variability of TEC is to plot iso-TEC contours as a function of day-of-month and diurnal time. Such plots for the reported months near minimum solar phase are shown in Figure 6. The values of the intervals of the TEC contours are of the order of the standard deviations, so as to eliminate the appearance of normal day-to-day undulations (e.g. those due to travelling ionospheric disturbances) in these plots.

The following day-to-day features may be ascertained from the figures. For the winter data the iso-TEC contours appear to vary little throughout the month during the buildup (17-19UT) and final decay (02-04UT) phases of the diurnal variation. During the maximum phase of the diurnal variation enhanced TEC is normally maintained for a number of consecutive days. Similarly, during the predawn phase depressed TEC

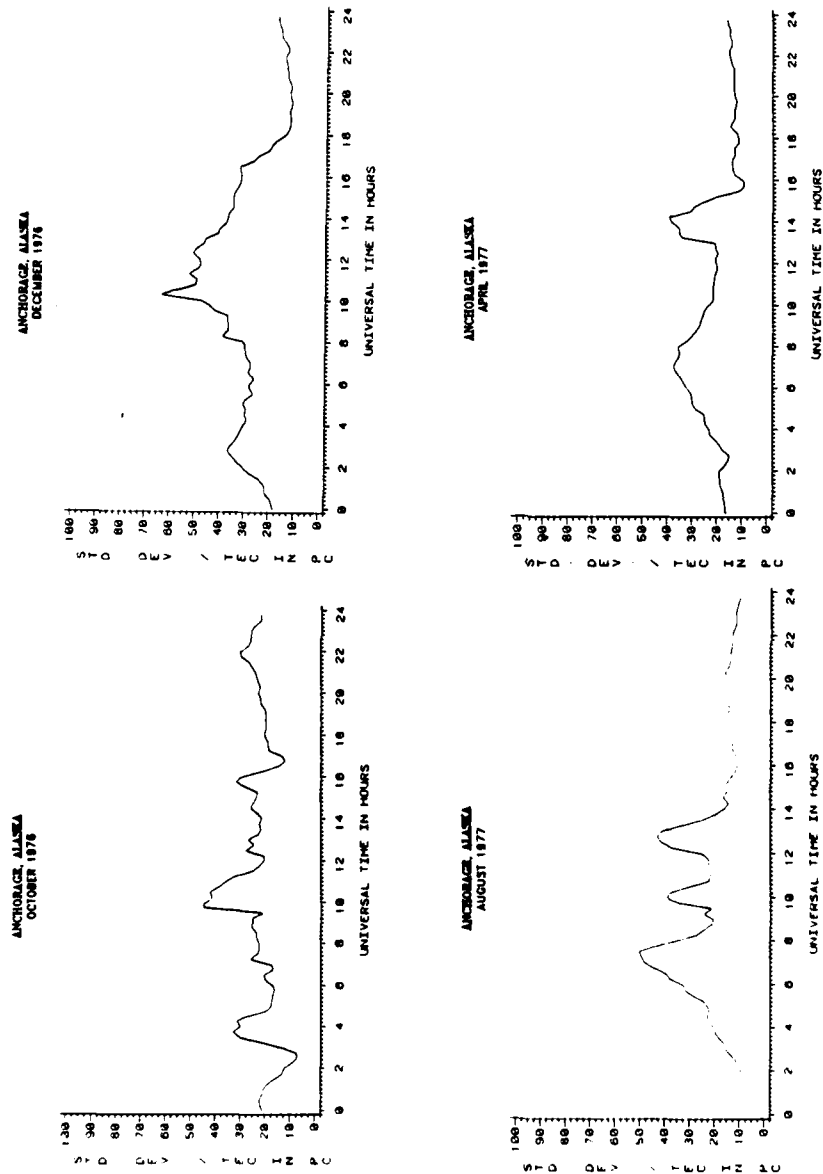
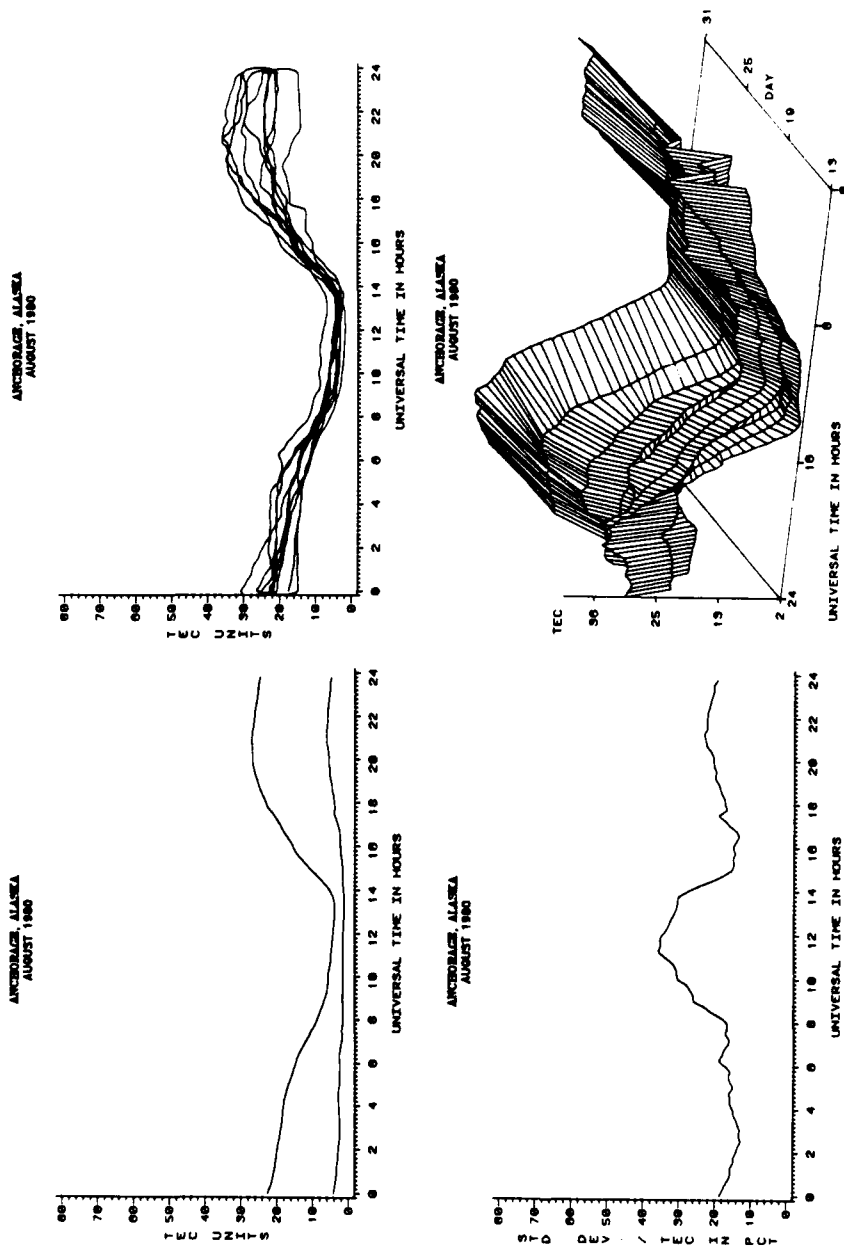


Figure 4 (a,b,c,d)

SOICHER



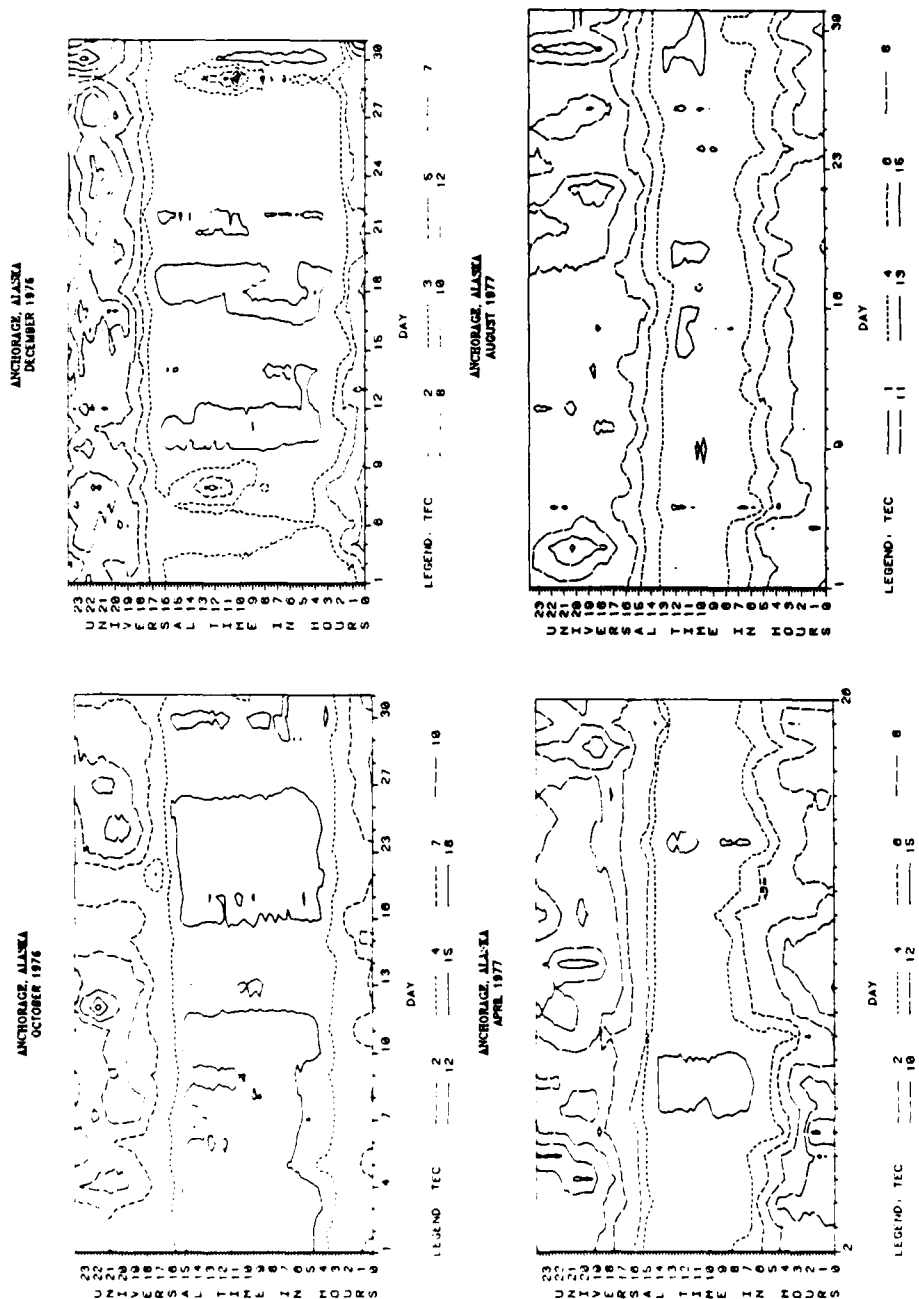


Figure 6 (a,b,c,d)

SOICHER

values are normally maintained for a number of consecutive days.

The increase in the nighttime TEC on 29 December followed by depressed values on 30 December may be associated with TEC positive phase response to sudden commencement (SC) which occurred on 28 December at 20:36 UT. No such response during daytime is observed, although enhanced values are observed on 30 December.

For the spring data the iso-TEC contours appear to vary little throughout the month during the buildup (15-17UT) and final decay (06-08UT) phases of the diurnal variation. During the maximum phase of the diurnal variation enhanced TEC may be maintained for a number of consecutive days. Similarly, during the predawn phase, depressed TEC values are normally maintained for a number of consecutive days. The low TEC values during the predawn period on 20 April may be due to SC at 0106 on the 19 April. The 6-7 April period was magnetically disturbed, and this is exhibited by the variability of content during the maximum phase of the diurnal variation.

During the summer little variation of the iso-TEC contours is observed during the decay and buildup phases of the diurnal variation. TEC enhancements/depressions during the day/night periods normally extend over few consecutive days. One-day enhancements/depressions, which do occur, are not correlated with magnetic sudden commencement. (One day enhancements near solar maximum are well correlated with sudden commencement activity on 15, 16, 17 August 1980)

During the Autumn, little variation of the iso-TEC contours is observed during the final decay and sunrise period of the diurnal variation. Enhancements/depressions of TEC during maximum/minimum phases of the diurnal variation normally occur for a number of consecutive days. One day enhancements/depressions of TEC are not associated with magnetic activity.

CONCLUSIONS

The behavior of TEC at a high latitude location during a period near the minimum phase of the current solar cycle is presented. Seasonal and day-to-day variabilities are observed.

The seasonal variability is seen in the magnitude of the absolute values of TEC maximizing in the spring, minimizing in the winter (possibly due to the mid-latitude trough) and being somewhere in between for the summer and autumn. Although absolute differences of TEC are small for the various seasons, these results are in contrast to midlatitude TEC behavior during similar periods. For all seasons the

SOICHER

day-to-day behavior of TEC appears uniform during the buildup and decay phases of the diurnal variation, although for the fall period the former is more confined to the sunrise period. The enhancements/depressions during maximum/minimum phases of the diurnal variation are maintained for a few consecutive days during all seasons, but single day enhancements/depressions are often observed. TEC enhancements during the nighttime periods in winter may be associated with positive response to sudden commencement. Similarly, TEC depressions on following nights in winter may be associated with storm behavior of TEC. No daytime TEC response, either positive or negative has been observed. During the other months magnetic activity was rather subdued. However, no single day enhancements/depressions of TEC appears correlated with magnetic activity. By contrast, single day enhancements during a period near the maximum phase of the solar cycle are correlated with magnetic sudden commencement activity.

The ratio of standard deviation to average TEC is a good indicator for day-to-day variability. For all observed periods the ratio, during the day, is normally $\leq 25\%$. The nighttime ratio is significantly higher, and it often undulates with variable periods. Since day-to-day variability is a most difficult quantity to predict, the results, which describe day-to-day patterns of behavior, have important implications to prediction improvements.

ACKNOWLEDGEMENTS

The Faraday observations were performed under the guidance of Mr. F.J. Gorman, US Army, Communications/Automatic Data Processing Center, Fort Monmouth, NJ. The analysis of the raw data and basic computations were performed under the guidance of Mr. W. Chaffee, Monmouth College, West Long Branch, New Jersey.

REFERENCES

Hicks, P.A., A low cost, all electronic Faraday rotation polarimeter, paper presented at COSPAR Symposium on the Future Application of Satellite Beacon Measurement, Comm. on Space Research, Graz, Austria, 1972.

Klobuchar, J.A., Polarization of AZ-EI mounted antenna viewing celestial objects, IEEE Trans. on Antennas and Propagation, AP-14, 650, 1966.

Lee, M.C., A. DasGupta, J.A. Klobuchar, S. Basu, S. Basu, Depolarization of VHF geostationary satellite signals near the equatorial anomaly, Radio Science, 17, 399-404, 1982.

SOICHER

Soicher, H., Ionospheric and plasmaspheric effects in satellite navigation systems, IEEE Trans. on Antennas and Propagation, AP-25, 5, 705-708, 1977.

Soicher, H., and F.J. Gorman, Variability of total electron content at temperate and high latitudes, proceedings of the COSPAR/URSI Symposium on "Scientific and Engineering uses of Satellite Radio Beacons", Warsaw, Poland, May 19-23, pp 91-98, 1980.

Soicher, H., Z. Houminer, and A. Shuval, Total electron content structure in the Middle East, Radio Science, 17, No. 6, 1623-1631, 1982.

Soicher, H., J.A. Klobuchar, P.H. Doherty, Spatial variability of total electron content in the eastern Mediterranean region, Radio Science, 19, 3, 757 - 764, 1984.

Soicher, H., F.J. Gorman, Seasonal and day-to-day variability of total electron content at midlatitudes near solar maximum, Radio Science, 20, 3, 383 - 387, 1985.

FIGURES

1. Superposed diurnal variations of total electron content (TEC) in Anchorage, Alaska for a. October 1976; b. December 1976; c. April 1977; d. August 1977.

Ordinate: 1 TEC unit - 10^{16} el m⁻²; Abscissa: time in UT.

2. Diurnal variation of total electron content (TEC) in Anchorage, Alaska as a function of day of month for: a. October 1976, b. December 1976, c. April 1977, d. August 1977.

3. Monthly average variation of total electron content (TEC) - upper curves, and the standard deviation of TEC about the monthly average - lower curves, in Anchorage, Alaska for: a. October 1976; b. December 1976; c. April 1977; d. August 1977.

4. The diurnal variation of the ratio (in percent) of the monthly standard deviation of TEC to the average TEC in Anchorage, Alaska for: a. October 1976; b. December 1976, c. April 1977; d. August 1977.

5. TEC data for Anchorage, Alaska for August 1980: a. Monthly average variation of TEC - upper curve, and the standard deviation of TEC about the monthly average - lower curve; b. Superposed diurnal variation of TEC; c. Diurnal variation of the ratio (in percent) of the monthly standard deviation to the average TEC; d. Diurnal variation of TEC as a function of day of month.

SOICHER

6. Iso-TEC contours as a function of day of month and time in UT at Anchorage, Alaska for a. October 1976; b. December 1976; c. April 1977; d. August 1977.

SOLLOTT, ALSTER, GILBERT, SANDUS, and SLAGG

SYNTHESIS OF MORE POWERFUL EXPLOSIVES (U)

*GILBERT P. SOLLOTT, DR.
JACK ALSTER, DR.
EVERETT E. GILBERT, DR.
OSCAR SANDUS, DR.
NORMAN SLAGG, DR.

ENERGETICS & WARHEADS DIVISION, ARMAMENT ENGINEERING DIRECTORATE
US ARMY ARMAMENT RESEARCH AND DEVELOPMENT CENTER, DOVER, NJ 07801-5001

INTRODUCTION

The problem of new armor becoming ever more difficult to penetrate is heightened by the fact that new, smart munitions allow only limited space for the explosive fill. Thus, if new armor is to be defeated by such munitions, it is a matter of national urgency that new explosive fills be developed having higher energies than found in the most powerful explosives currently in use.

The requirement for more powerful explosives, therefore an important part of the DoD mission, is being addressed under the Armament Engineering Directorate's research thrust bearing the title of this paper. The research consists of an aggressive program of synthesis of a new class of energetic compounds, viz. the carbocyclic polynitro cage compounds. These are molecules with compact, closed, three-dimensional cage-type skeletal frames whose faces consist of rings of carbon atoms. The program of synthesis is based on the underlying principle that the detonation pressure of an explosive increases as the square of its density (1), coupled with the fact that three-dimensional cage molecules are inherently more dense than their open-structured molecular counterparts. The density of cubane (cubane is depicted in Table 1), for example, has been calculated from x-ray data as 1.288 g/cm³, as compared to a density of only 0.93 for the isomeric (CH)₈ eight-membered, tub-shaped ring compound, cyclooctatetraene.

The previous paper on this subject (2), presented at the 1982 Army Science Conference, introduced the concept of more powerful cage explosives and reported on four "prototype" nitro cage compounds which had been synthesized under this program. These were nitro derivatives of the cubane and adamantane cage systems. Since that time, other derivatives have been synthesized en route to more highly nitrated cubanes and adamantanes. In addition, polynitro derivatives of several

other cage systems have been synthesized as part of a broad strategy to develop the methodology for achieving the polynitration of cage molecules.

The present paper is concerned with a number of target compounds of the carbocyclic cage variety whose syntheses constitute milestones on the way to optimum nitrated cage compounds (the parent cages are depicted in Table 1). The paper first discusses the theoretical calculations and their results which both support and expand the rationale for the synthesis of polynitro cage compounds. It will be seen that the calculations, which have identified the optimum polynitro cage compounds, predict detonation performances substantially higher than that of HMX, the best in-service explosive, due to a combination of (i) high crystal densities which become even higher as the number of nitro groups increases, and (ii) high strain energies which can be built into the cages, increasing as more of the faces consist of smaller-size strained rings.

Most importantly, it is likely that some of the target cage compounds will not only have high "energy density," but also low sensitivity to initiation. That the polynitrocubanes will be thermally stable compounds is supported by calculations performed by M.J.S. Dewar (University of Texas) indicating that nitro substitution on cubane, which is comprised of four-membered rings and, therefore, under considerable structural strain, will not significantly alter its thermal stability (3). Calculated heats of dissociation, moreover, have shown that any weakening of carbon-hydrogen and carbon-nitrogen bonds attributable to a nearby nitro substituent is insignificant (4). Subsequent experimental observations on the thermal behavior of over twenty cage compounds lend credence to the favorable forecast regarding thermal stability (5). The studies on thermal stability show also that, while cubane derivatives in general are thermally stable, bishomocubane and adamantane derivatives are even more stable in accordance with reduced cage strain in these molecules.

The research on polynitro cage compounds is characterized by close teamwork and many collaborative efforts involving ARDC and contractor scientists working side by side in-house, over ten university scientists, all prominent leaders in their special fields, and scientists of high renown from other government laboratories and private industry. Because of space limitations, only the more significant accomplishments thus far attained in this program will be described in this paper.

CALCULATION OF DETONATION PERFORMANCE

Thermohydrodynamic calculations were carried out to determine the theoretical number of nitro groups which, when attached to the carbo-

cyclic cages, would yield the maximum detonation performance. The equations of the Kamlet-Jacobs Simple Method (KJSM) (1) were used to calculate the Chapman-Jouguet detonation pressures. This method for the most part yields results in reasonable agreement with those provided by the more highly complex TIGER computer code (6). A significant advantage to its use is that insight into the important parameters that influence the detonation performance is gained more easily than with the TIGER code.

Both the KJSM and TIGER computations require an input of the density and heat of formation of the explosive, which includes the strain energy when strain is present in the molecule, as well as the elemental composition. Densities were calculated using the methods of Cady (7) and Stine (8), the former having a theoretical basis although incorporating an empirical packing fraction, the latter using an empirical calibrating base of over two thousand compounds. In those cases where the density of the parent cage compound or derivative is known, the methods are modified to correct for any small difference occurring between the calculated and observed densities, thus providing more accurate density values for the polynitro derivatives. Calculated densities were found to agree reasonably well with values obtained experimentally from nitro cage compounds synthesized subsequent to the calculations, confirming that the densities can be estimated with reasonable accuracy.

Heats of formation were estimated using the Arthur D. Little bond value method for calculating the heats of combustion for systems without strain (9), and strain energies were added to the estimated values as required for the strained cage systems. In those cases where strain energies were not available from the literature, they were estimated from the values known for simple ring compounds (10). Although not as accurate as the estimations of density, the estimated heats of formation do not require high accuracy for the calculations of detonation pressure, since, according to the KJSM equations (1), the detonation pressure is a very weak function of the heat of formation of the explosive.

RESULTS OF CALCULATIONS FOR MAXIMIZING DETONATION PERFORMANCE OF POLYNITRO CAGE COMPOUNDS

It can be seen from the data summarized in Table 2 that for the nitrocubanes, as the number of nitro groups is increased, detonation pressures (P_{CJ}) increase as a result of both the improving oxygen balance and increasing densities (ρ). The detonation pressure is at a maximum when all eight hydrogen atoms in cubane are replaced, producing octanitrocubane which has maximum density and is oxygen-balanced. The effect of adding nitro groups to the cubane cage is typical for carbocyclic cages of the type, $(CH)_n$. The adamantane cage, on the other

hand, consists of six CH_2 groups in addition to four CH's (see structure, Table 1), and the effect of adding nitro groups is quite different.

The data summarized in Table 3 for the nitroadamantanes show that the detonation pressure reaches a maximum at eleven nitro groups, and decreases as nitro groups continue to be added up to the maximum number of sixteen groups which, in theory, can be attached to the adamantane cage. As with cubane (Table 2), a steady (linear) increase in density and decrease in heat of formation occurs as the number of nitro groups increases. However, oxygen balance is attained at eleven nitro groups, and becomes increasingly positive as more groups are added. In the region of positive oxygen balance, therefore, the influence of density on the detonation pressure is less important than in the region of negative oxygen balance. Thus, from the standpoint of detonation performance, there is no advantage to be gained in synthesizing an adamantane containing more than eleven nitro groups. (Nevertheless, oxygen-positive adamantanes might serve as organic oxidizers.) The heats of formation of the nitroadamantanes are very negative, reflecting the relatively strain-free state of the adamantane cage; those of the nitro-cubanes are positive, pointing to the strain residing in the cubane cage.

The data listed in Table 1 show the theoretical number of nitro groups required for maximum detonation performance of the illustrated carbocyclic cage structures. It can be seen that (i) the detonation pressures for the optimum polynitro cage compounds increase as the densities increase, while (ii) the densities increase as the number of small rings making up the skeletal cages increase. Molecular strain energies reach a maximum in octanitrocubane, then decrease in hexanitro-triprismene and tetranitrotetrahedrane despite higher average C-C bond strain energies. This is the result of triprismene and tetrahedrane being small cages with fewer bonds than cubane. That tetranitrotetrahedrane shows the highest detonation pressure is in accord with the fact that it possesses the highest average C-C bond strain energy. The calculations indicate that adamantane bearing eleven nitro groups is close to HMX in detonation output, while all the other polynitro cage compounds listed in Table 1 are significantly more powerful, with some exceeding HMX by as much as 20-35%.

APPROACHES TO THE SYNTHESIS OF POLYNITRO CAGE COMPOUNDS

As discussed above, thermohydrodynamic calculations have identified the optimum polynitro cage compounds yielding maximum detonation performance for each of the hydrocarbon cage structures illustrated in Table 1. The optimum compounds thus constitute the ultimate targets for synthesis in the program to develop explosives more powerful than HMX.

A number of nitro cage compounds which are viewed as intermediate targets or milestones en route to the ultimate compounds (Table 1) have now been prepared and are reported here. All are thermally stable substances. They are but forerunners of the more highly nitrated cage compounds whose synthesis the research, both in progress and planned, is designed to achieve.

From the outset of this program, it appeared likely that direct nitration of unsubstituted hydrocarbon cage compounds would not provide a useful synthetic route to polynitro cage compounds. Various attempts to nitrate adamantane directly, for example, have reportedly produced mono- and dinitroadamantanes, and even trinitroadamantane, but at elevated temperature and pressure, and only in very low yield (11). Indirect approaches were adopted instead for the synthesis of the target compounds, consisting of (i) polysubstitution of a hydrocarbon cage, and subsequent conversion of the substituents to nitro groups (Fig. 1); (ii) synthesis (construction) of a polysubstituted hydrocarbon cage from appropriately functionalized precursors, and subsequent transformation of the substituents to nitro groups (Fig. 2). Other more direct approaches are actively being investigated, since they may prove to be viable synthetic routes to certain of the target compounds, and they will be addressed later. Consistent with the effort to develop, in an orderly manner, the chemical strategies necessary to achieve the synthesis of the ultimate targets, the number of nitro groups introduced into a cage system is being increased in a gradual and orderly fashion, thereby permitting stepwise evaluation of the effect of increasing nitro substitution on stability and explosive properties. Where it is suspected that the final step producing a particular polynitro cage compound may be hazardous, it will be performed in-house rather than in a university laboratory.

INDIRECT APPROACHES

The earliest example of this type of approach was the synthesis of 1,3,5,7-tetranitroadamantane (1a), the first cage compound containing four nitro groups (11). This was accomplished in-house starting with readily available adamantane (1), and progressing stepwise by way of tetrabromination, exchange with iodine, replacement with amide groups, hydrolysis to amino groups, and oxidation to the nitro groups. 1,4,6,9-tetranitrodiamantane (2a), the second cage compound to contain four nitro groups, was also synthesized in-house by a similar reaction sequence (12) starting with diamantane (2).

2,2-dinitroadamantane (1b), prepared in-house as the forerunner of related tetra- and hexanitroadamantanes, was obtained via adamantanone and oxime formation followed by a three-step transformation through gem-promonitro to gem-dinitro (13). Still another type of derivative syn-

AD-A173 682

PROCEEDINGS OF THE ARMY SCIENCE CONFERENCE (15TH) HELD
IN WEST POINT NEW. (U) DEPUTY CHIEF OF STAFF FOR
RESEARCH DEVELOPMENT AND ACQUISITIO.. J SAHU ET AL.

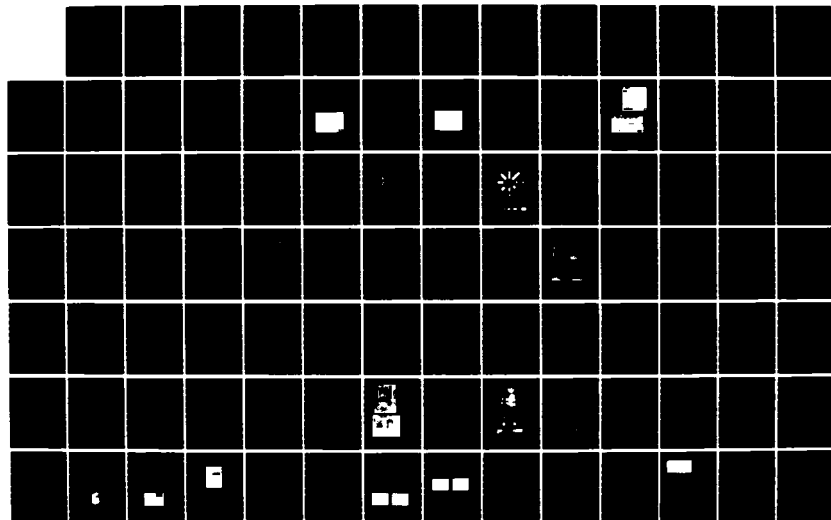
1/4

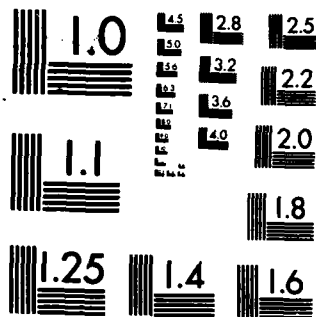
UNCLASSIFIED

20 JUN 86

F/G 5/2

NL





thesized in-house was the 1,3,5,7-tetranitrate of adamantane (1c) obtained via bromination and formation of the tetrahydroxy compound (14).

More recently, as a result of an in-house finding that polychlorinated adamantanes can be converted to their iodinated counterparts by halogen exchange, octachloroadamantane was converted to the octaiodo compound (1d) (15), a near precursor of octanitroadamantane (1e). The octachloro derivative was obtained from Professor P.v.R. Schleyer and his group (University of Erlangen-Nürnberg) who synthesized it from adamantane by photochlorination of the thermally prepared tetrachloro intermediate. Octanitroadamantane (1e) is only three nitro groups short of the optimum number predicted by the theoretical calculations (Table 1), and an effort to produce 1e using the same methodology cited above for tetranitroadamantane (1a) is currently in progress in-house. Practical syntheses for both adamantane and diamantane were pioneered much earlier by Prof. Schleyer at Princeton University (16).

Professor P.E. Eaton (University of Chicago) succeeded in preparing 1,4-dinitrocubane (3a) at an early stage of the program from the dicarboxycubane (3) in three steps involving carbamate formation, hydrochlorinolysis to the diamine, and oxidation to the nitro groups (17). His synthesis of the dicarboxycubane, reported much earlier (18), started with cyclopentanone and proceeded, in seven steps, through ethylene ketal formation and bromination, generation of the bromo diene and dimerization, cage closing with ketal hydrolyses, and finally, ring contractions producing the disubstituted cubane.

Professor G.W. Griffin (University of New Orleans) later prepared 1,4-dinitrocubane (3a) from the dicarboxycubane (3) in four steps, in a variation of the Eaton procedure (above), generating the acid chloride and isocyanate prior to the diamine. He then synthesized 1,3-dinitrocubane (4a) starting with cyclobutadiene irontricarbonyl and 2,5-dibromobenzoquinone, generating 1,3-dicarboxycubane (4) in three steps by addition, cage closing and ring contractions. The conversion of 4 to 4a was accomplished using the same procedure as for transforming 3 to 3a (19).

The diiododiamidocubane 3b ($R = iPr$) was obtained by Professor Eaton using the diisopropylamide group to promote lithium-induced "ortho"-mercuration of the cubane frame. This was an important breakthrough in that the first direct functionalization of a highly strained cage system had been achieved. Higher degrees of iodination have already been accomplished, and the synthesis of a tetranitrocubane, viz. 3c, now appears to be achievable in the near future. The probability of success is heightened by the recent extension of the synthesis of 4 to

that of 1,2,3,5-tetracarboxycubane (5), precursor of tetranitrocubane 5a, in-house by a former research associate of Prof. Griffin (20).

Other polysubstituted cubanes recently synthesized, and which are potentially useful as intermediates en route to the more highly nitro-substituted cubanes, include hexabromocubane-1,4-dicarboxylic acid (6), prepared by Prof. Griffin who achieved ring contraction of the octabrominated cage precursor. The latter had already been prepared (21) starting with hexachlorocyclopentadiene in a four-step procedure resembling the original synthesis of 3 (18). The fully substituted cubane (6) was decarboxylated to produce hexa- and octabromocubanes, possible precursors of the polynitrocubanes 6c, by replacement with hydrogen and bromine, respectively (6a and 6b). In view of the newness and highly challenging nature of the chemistry of cubane and other strained cage molecules, the above achievements in polysubstitution represent important breakthroughs in the field. Efforts to transform cubanes 6a and 6b as well as 3b and 5 to the nitro derivatives are in progress.

Professor A.P. Marchand (North Texas State University), focusing on the 1,3-bishomocubane system, prepared the 3,5,5-trinitro derivative (7a) in thirteen steps starting with cyclopentadiene and p-benzoquinone via generation of the appropriately substituted cage system 7. The final product (7a) was obtained from the oxime by stepwise conversion to gem-dinitro, and subsequent transformation of carbomethoxy to nitro by way of carbamate and amine formation (22). Trinitro derivative 7a is an important "first" from the standpoint that nitration of both secondary and tertiary carbons has been achieved in the same molecule, opening the door to higher nitration in the bishomocubane and other systems. The synthesis of 5,5,9,9-tetranitrobishomocubane (8a) was accomplished in a ten-step procedure closely paralleling the synthesis of 3, starting with cyclopentanone, but in this case generating the diene devoid of bromine to obtain the cage dione 8. Mono- then gem-dinitro groups were introduced into 8 by way of dioxime formation (23).

Similarly, the tetraphenyl cage dione 9 was generated in four steps from the appropriate phenyl-substituted cyclopentenone, and converted in four more steps to the tetranitrobishomocubane 9a with four phenyl groups attached. The latter can be transformed, in principle, to nitro groups to generate the octanitrobishomocubane. Most recently the synthesis of trishomocubane trione 10 was achieved by Prof. Marchand in a series of nine steps from the ketal of tetrabromocyclopentadiene and p-benzoquinone (24). An effort to introduce six nitro groups into 10 to produce the hexanitrotrishomocubane 10a is currently in progress.

Professor L.A. Paquette (Ohio State University), concentrating on the bishomopentaprismene system, has prepared both dinitro (11a) and

tetranitro (12a) derivatives (25). The former, which is the first known vicinal dinitro cage compound, was synthesized in ten steps from a tricyclodecatriene and p-toluenesulfonylacetylene via formation of the [4]-peristylane dione 11. The nitro groups were then introduced by way of the dioxime, and debromination of the bis-bromonitro derivative completed the cage structure. Dinitro derivative 11a, with nitro groups on adjacent carbons, has special significance in that, in fully nitrated cage systems, all (adjacent) carbons are substituted with nitro groups. Tetranitro derivative 12a was next prepared in ten steps starting with 9,10-dihydrofulvalene and an acetylenedicarboxylate, proceeding to the bishomopentaprismane dione 12, and introducing the nitro groups via dioxime formation. The synthesis of the hexanitro derivative 13a, starting with p-toluenesulfonylacetylene and the appropriate tricyclodecatriene to generate the [4]-peristylane dione 13, is currently being pursued.

An extension of the KJSM calculations (cf. Table 1) to bicyclopentane, another strained polycyclic system offering high energy-density capability, has optimized the nitro content at six groups for achieving maximum detonation output (P_{CJ} , 411 kbar; ave. C-C strain energy, 13.5 kcal/mole; density, 1.991 g/cm³; ΔH_f° , 5.27). In pursuit of this target compound, Professor K.B. Wiberg (Yale University) has recently synthesized 1,3-dinitrobicyclopentane (14a) starting with dimethyl phenylmalonate in fourteen steps generating the phenylbicyclopentanecarboxylic acid (14) as intermediate (26). The preparation of the 2,2-dinitro compound via the 2-ketone is currently in progress.

DIRECT APPROACHES

Much more limited in applicability than the indirect methods discussed above, the direct method may, nonetheless, offer a viable route, of few steps, to certain of the target compounds, particularly the polynitrocubanes. Thus, Professor R.B. King (University of Georgia) is investigating the possible tetramerization of nitroacetylenes to cubanes containing four or more nitro groups. The preparation of acetylenic derivatives of the type, $R_2NC\equiv CNO_2$ is actively being investigated to serve as candidates for the tetramerization step.

Looking to the future, the question may be raised concerning the ultimate producibility of a particular target compound of practical interest. The problem of producibility is currently being addressed by the research of Professor C.L. Hill (Emory University) among others, who is looking into producing nitrogen precursors of polynitro cage compounds in the condensed phase in a single, or few steps under low-energy conditions employing novel, true-catalytic systems.

SUMMARY AND CONCLUSIONS

Compact, three-dimensional cage compounds containing optimum numbers of nitro groups as determined in theory by thermohydrodynamic calculations, constitute a class of explosive compounds more powerful than HMX. This is a direct result of high crystal densities, particularly in combination with high strain energies built into certain of the cage systems. The synthesis of polynitro cage compounds has progressed on several fronts since the concept of more powerful cage explosives was introduced at the 1982 Army Science Conference. Nitro groups have been introduced into seven varieties of carbocyclic cage compounds, including, in descending order of molecular strain and density, cubane, bishomocubane, bishomopentaprismene, and adamantane. Twelve thermally stable derivatives containing as many as four nitro groups have been synthesized to date, serving as forerunners of more highly nitrated cage compounds which are expected to exhibit explosive properties. The syntheses of eight such potentially explosive compounds, with four to eight nitro groups, are in progress at the present time, and appear to be achievable in the near future. These compounds, in turn, are expected to lead to still more highly nitrated cage compounds nearly all of which, according to the theoretical calculations, will be significantly more powerful than HMX, exceeding its detonation output in some cases by as much as 20-35%. Both calculations and experiment predict that nitro substitution will not significantly alter the thermal stability of the hydrocarbon cage molecules, and that some of the ultimate target compounds will not only have high "energy density" but also low sensitivity to initiation. It is thus reasonable to expect that compounds less sensitive and more thermally stable, and in addition, more powerful than any explosive now in use will emerge from this program of research. With regard to the ultimate producibility of a particular target compound of practical interest, this also is being addressed by appropriate studies currently in progress. It is anticipated that "super-energetic" cage explosives will make a strong contribution to the Army mission based on their potential for increasing armor penetration by shaped charge and self-forging fragment munitions.











REFERENCES

1. M.J. Kamlet and S. Jacobs, *J. Chem. Phys.*, **48**, 23 (1968).
2. E.E. Gilbert, G.P. Sollott, J. Alster, O. Sandus, and N. Slagg, "Toward More Powerful Explosives - Polynitro Polyhedranes," Proceedings, Army Science Conference, U.S. Military Academy, West Point, NY, June 1982.
3. M.J.S. Dewar, "Quantum Chemical Calculations of Explosive Molecules," ARDC Contract No. DAAK10-84-M-2532, AMPAC Associates, 1984.
4. J.P. Ritchie, *Diss. Abstr. Int.*, **42**, 4430-B (1982).
5. D.I. Weinstein and J. Alster, "Thermal Studies of Cubane and Adamantane Derivatives," Fourth Annual Working Group Meeting on Synthesis of High Energy Density Materials, ARDC, Dover, NJ, 4-6 June 1985.

SOLLOTT, ALSTER, GILBERT, SANDUS, and SLAGG

6. M. Cowperthwaite and W.H. Zwisler, "TIGER Computer Program Documentation," Stanford Research Institute Publication No. Z-106, January 1973.
7. H.H. Cady, "Estimation of the Density of Organic Explosives from their Structural Formulas," Los Alamos Scientific Laboratory Report LA-7760-M5, August 1979.
8. J.R. Stine, "Prediction of Crystal Densities of Organic Explosives by Group Additivity," Los Alamos Scientific Laboratory Report LA-8920, August 1981.
9. Arthur D. Little, Inc., "Study of Pure Explosive Compounds, Part II, Correlation of Thermal Quantities with Explosive Properties," Office, Chief of Ordnance Contract No. W-19-020-ORD-6436, Report No. C-57625, April 2, 1947.
10. P.v.R. Schleyer, J.E. Williams, and K.R. Blanchard, J. Amer. Chem. Soc., **92**, 2377 (1970).
11. G.P. Sollott and E.E. Gilbert, J. Org. Chem., **45**, 5405 (1980), and refs. cited therein.
12. G.P. Sollott, "Polynitrodiamantanes," Working Group Meeting on Synthesis of High Density Energetic Materials, ARDC, Dover, NJ, 6-7 April 1983; G.P. Sollott and E.E. Gilbert, J. Org. Chem., submitted for publication; G.P. Sollott and E.E. Gilbert, "1,4,6,9-Tetranitrodiamantane and Process for Preparing Same," "allowed" by U.S. Patent Office for patent issuance in 1986.
13. E.E. Gilbert, unpublished results.
14. E.E. Gilbert, "1,3,5,7-Tetranitroxadamantane," U.S. Patent No. 4,476,060, Oct 9, 1984.
15. G.P. Sollott, "Polyiodinated Precursors of Polynitro Cage Compounds," Fourth Annual Working Group Meeting on Synthesis of High Energy Density Materials, ARDC, Dover, NJ, 4-6 June 1985.
16. P.v.R. Schleyer, J. Amer. Chem. Soc., **79**, 3292 (1957); T.M. Gund, V.Z. Williams, Jr., E. Osawa, and P.v.R. Schleyer, Tetrahedron Lett., 3877 (1970); T.M. Gund, E. Osawa, V.Z. Williams, Jr., and P.v.R. Schleyer, J. Org. Chem., **39**, 2979 (1974).
17. P.E. Eaton, B.K.R. Shankar, G.D. Price, J.J. Pluth, E.E. Gilbert, J. Alster, and O. Sandus, J. Org. Chem., **49**, 185 (1984).
18. P.E. Eaton and T.W. Cole, Jr., J. Amer. Chem. Soc., **86**, 962, 3157 (1964).
19. G.W. Griffin, P.P. Umrigar and C.J. Vaz, "Synthesis of 1,3- and 1,4-Dinitrocubane and Related Dinitro-Substituted Homocubanes," Working Group Meeting on Synthesis of High Density Energetic Materials," ARDC, Dover, NJ, 22-24 May 1984.
20. P.P. Umrigar, unpublished results.
21. B. Fuchs, C. Drucker, and R. Lidor, J. Org. Chem., **46**, 1479 (1981).
22. A.P. Marchand and S.C. Suri, ibid., **49**, 2041 (1984).
23. A.P. Marchand and D.S. Reddy, ibid., **49**, 4078 (1984).
24. A.P. Marchand, unpublished results.
25. L.A. Paquette, unpublished results.
26. K.B. Wiberg, J. Org. Chem., in press.

Table 1. Properties of Carbocyclic Cage Compounds with Nitro Content Optimized for Maximum Detonation Output, as Calculated by the Kamlet-Jacobs Simple Method

Parent Hydrocarbon Cage Compound	Composition of Polynitro Cage				ρ (g/cm ³)	ΔH°_f (kcal/mole)	Molecular Strain Energy		Ave. C-C Bond Strain Energy		PCJ (kcal/mole)(kbar)
	C (no.)	H (no.)	NO ₂ (no.)	(no.)			(kcal/mole)	(kcal/mole)	(kcal/mole)		
 Tetrahedrane	4	0	4	2.138	88.03	126	21.0	512			
 Triprismane	6	0	6	2.138	80.03	137	15.2	493			
 Cubane	8	0	8	2.098 ^a	81.04	157	13.1	467			
 Homocubane	9	1	9	2.094	30.08	122	9.4	453			
 1,3-Bishomocubane	10	1	11	2.092	-33.83	82.6	5.9	431			
 Bishomopentaprismane	12	2	12	2.057	-56.76	70.1	4.1	421			
 Trishomocubane	11	2	12	2.063	-75.3	57.1	3.8	419			
 Diamantane	14	5	15	2.048	-170.47	9.8	0.5	415			
 Adamantane	10	5	11	1.959	-136.69	5.6	0.5	383			
 HMX ^b	4 ^c	8	4	1.903	17.4	0	0	382			

^aModified by taking cubane as basis for calculation.^bIncluded for comparison.^cThe two-dimensional ring contains four nitrogen atoms in addition.

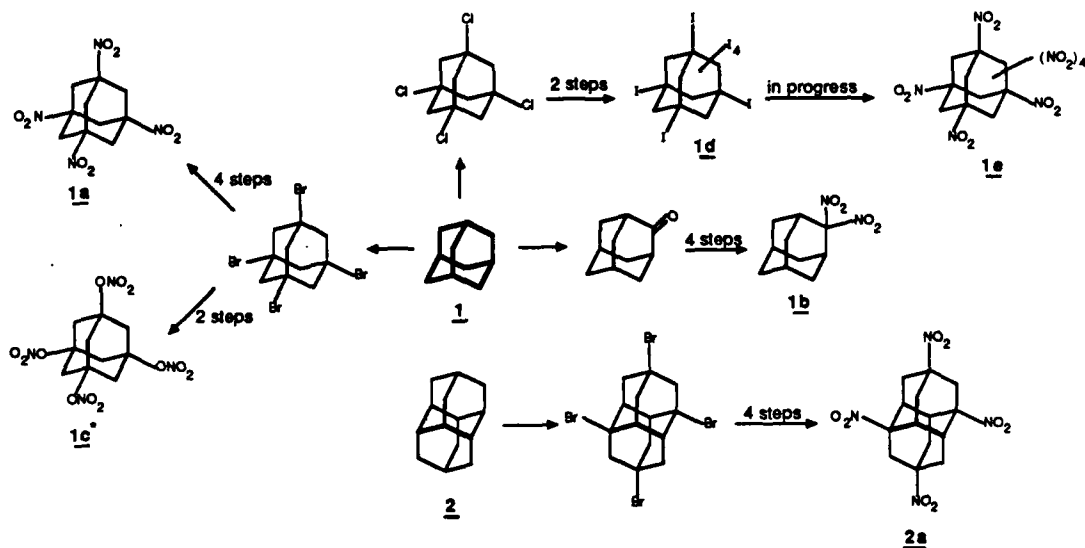
Table 2. Detonation Pressures of the Nitro Derivatives of Cubane, as Calculated by the Kamlet-Jacobs Simple Method

# of Nitro Groups	ρ (g/cm ³)	ΔH_f° (kcal/mole)	P _{CJ} (kbar)
2	1.66	132	205
3	1.78	124	270
4	1.87	115	323
5	1.94	107	368
6	2.00	98	406
7	2.06	90	439
8	2.10	81	467

Table 3. Detonation Pressures of the Nitro Derivatives of Adamantane, as Calculated by the Kamlet-Jacobs Simple Method

# of Nitro Groups	ρ (g/cm ³)	ΔH_f° (kcal/mole)	P _{CJ} (kbar)
4	1.584	-76.78	182
6	1.729	-93.90	253
8	1.838	-111.01	312
10	1.923	-128.13	361
11	1.959	-136.69	383
12	1.992	-145.25	381
13	2.022	-153.81	372
16	2.096	-179.49	342

Figure 1. Polynitro Cage Compounds via Functionalization of Hydrocarbon Cages



The nitro groups in **1c** are bonded to the cage through oxygen, producing the tetranitrate.

Figure 2. Polynitro Cage Compounds via Construction of Appropriately Substituted Hydrocarbon Cages

Cubanes

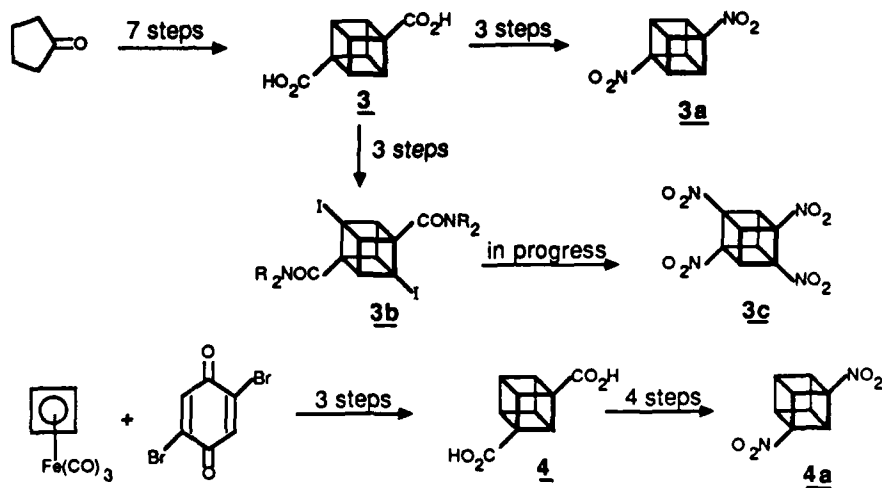
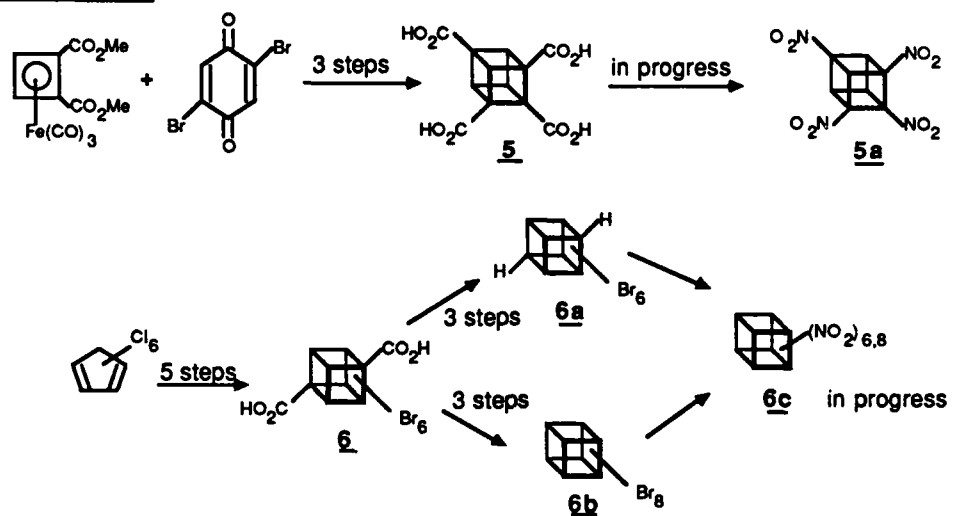


Figure 2, continued

Cubanes, continued



Bishomocubanes

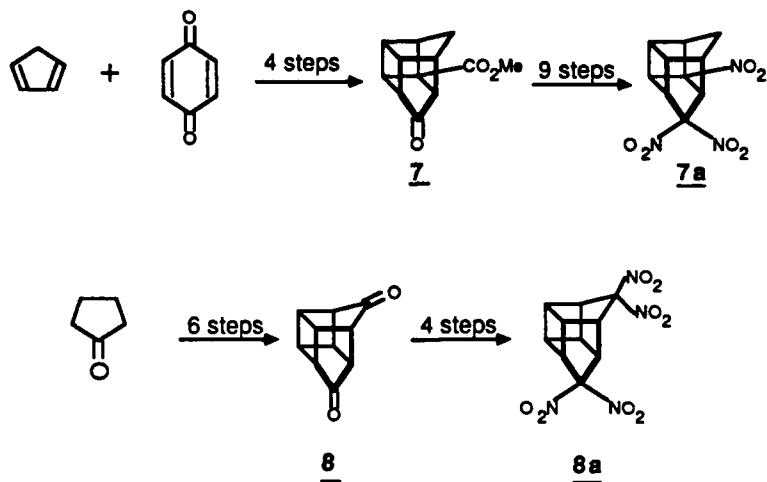
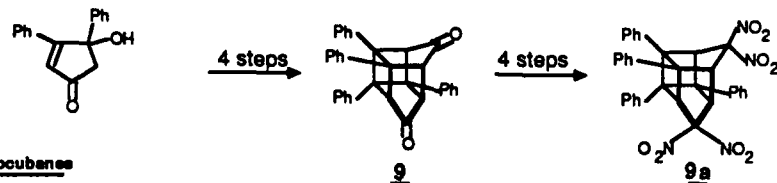
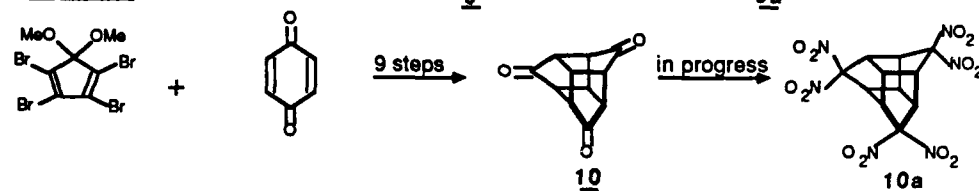


Figure 2, continued

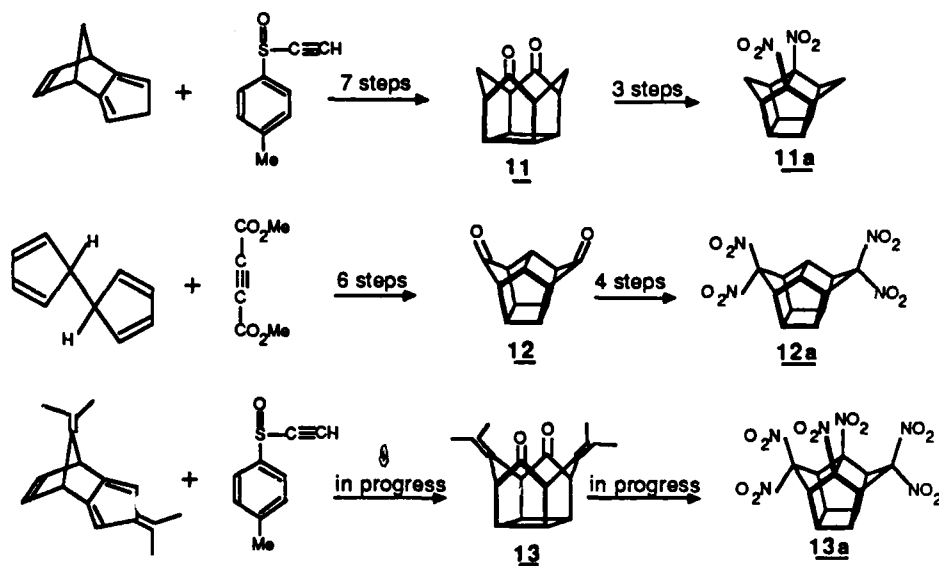
Bishomocubanes, continued



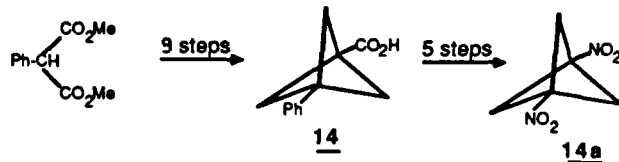
Trishomocubanes



Bishomopentaprismanes



Bicyclopentanes



Stephenson, Hock, Boy, Scott, Rigsbee

ION-PLATED CONDUCTIVE CERAMIC AND METAL/CERAMIC COMPOSITE COATINGS (U)

*L. D. STEPHENSON, DR., V. F. HOCK, MR., J. H. BOY, MR.
U. S. ARMY CONSTRUCTION ENGINEERING RESEARCH LABORATORY
CHAMPAIGN, ILLINOIS 61820-1305
P. A. SCOTT, MR., J. M. RIGSBEE, DR.
DEPARTMENT OF MATERIALS SCIENCE, UNIVERSITY OF ILLINOIS
URBANA, ILLINOIS 61801

INTRODUCTION

Ion plating is an attractive deposition technology for fabricating advanced coatings that may be useful for mitigating Army field problems such as corrosion of metallic structures, erosion and wear, and shielding for electromagnetic interference/electromagnetic pulses. Ion plating can also be applied to the development of advanced composite materials and to microelectronic packaging.

This paper provides information on ion-plating research being carried out cooperatively between the U. S. Army Construction Engineering Research Laboratory (USA-CERL) and the University of Illinois. The first topic discussed involves development of ion plated conductive oxides for ceramic anodes designed for impressed current cathodic protection systems. This is a part of a larger USA-CERL-based corrosion mitigation program (1,2). The second topic involves ion plating of metallic films onto ceramic substrates. This program investigates fundamental relationships between processing variables and the structure, chemistry, and physical properties of the resulting metal/ceramic composites. This research is oriented to the development of advanced composite materials and microelectronic packaging science. The paper will begin with a brief introduction to the ion-plating technique, including the physics behind the process and the materials science of the resulting coatings.

ION-PLATING PRINCIPLES

Ion plating, originally developed by Mattox in 1963 (3), is a plasma-aided physical vapor deposition (vacuum coating) process that incorporates the benefits of both sputter etching and ion beam mixing. Using modifications of Mattox's original ion-plating technique, it is possible to produce metal, alloy, and ceramic coatings (with minimal substrate heating)

that are fully dense, have equiaxed grain structures, and exhibit excellent coating/substrate adhesion. The superior "throwing power" of this technique allows relatively uniform coatings to be produced on exterior surfaces of even large or complex-shaped specimens. In the following paragraphs, the physics of the ion-plating technique and the materials science of the coating nucleation and growth process will be discussed. Additional discussions of this technique and its applications may be found in a review article of Mattox (4) and in the proceedings of two recent conferences on this subject (5).

In ion plating, the substrate and the coating material source are held in a chamber containing a low pressure (around 10^{-2} torr) gaseous environment. Normally, an inert gas such as argon is used for elemental metal or alloy coatings, but inert gas/reactive gas combinations can be used to produce ceramic compound coatings like TiN (6). Initially, without the coating material source operative, the substrate is biased to a high negative potential (around 2 to 5 kV), thus creating an abnormal, cold cathode glow discharge (7) between the substrate (cathode) and ground. Inert gas ions, created by ionization within the glow discharge region, are accelerated toward the cathode and strike the substrate with average kinetic energies sufficient to sputter atoms from the substrate surface (8). This sputter-etching process is a particularly critical step in ion plating since it produces a very reactive (4) and atomically clean surface (9). The as-sputtered surface is free of any oxide film and contains a high density of sputter-induced defects such as vacancy clusters, dislocation loops, and micro-ledges (10,11). The sputter-cleaned substrate surface is ideal from a coating formation perspective since it contains a high density of very active coating nucleation sites (12,13).

Once the substrate surface has been thoroughly cleaned, evaporation of the coating material is begun in conjunction with the continued glow discharge sputtering. Coating material evaporation is typically done using conventional resistance heating for low-melting-point coating materials or electron beam heating for high-melting-point materials. Of the neutral evaporated atoms, only a small percentage (usually <1%) are ionized through interaction with the metastable inert gas ions (14) and are accelerated toward the substrate by the high cathode potential. For those atoms that are ionized, very few reach the substrate with the full energy of the discharge, since the gas pressure during ion plating is high and the mean free path of the ionized evaporant and argon ions is much less (about 5 mm at 10^{-2} torr) than the cathode dark space to cathode distance (14). Each accelerating ion therefore has a high probability of undergoing multiple collisions (with corresponding momentum transfer and change in direction) with neutral evaporant atoms. Theoretical calculations (14) and experimental measurements (15) by Teer have shown that the average energy of the ions and neutral atoms deposited at the substrate surface is

typically less than 100 eV. Under typical ion-plating conditions, about 90% of the beam energy is carried by neutral atoms, which have acquired their energies through collisions with the accelerated ions. The rate of coating deposition is given by the difference in the rate at which atoms arrive at the substrate surface and the rate at which atoms are sputtered from the substrate surface and can be controlled by controlling the rate of evaporation from the coating material source. The relatively simple experimental setup required for ion plating makes it possible to plate large parts or batches of smaller parts simply by scaling up the vacuum system and the power supplies.

In ion plating, the multiple scattering and momentum transfer between ionized and neutral atoms have a three-fold benefit on the properties of the resulting coating. First, because both the ionized and neutral atoms arrive at the substrate surface with high average kinetic energies, the impacting particles can implant up to several atom layers deep in the substrate surface (16). The transfer of kinetic energy between an individual impacting particle and those substrate surface atoms very close to the impact site causes extensive localized mixing to occur and is equivalent to very briefly and locally heating the first few atom layers at the substrate surface to a temperature sufficient to cause melting. This ion-enhanced mixing between the depositing and substrate atoms creates a very complete and strong pseudodiffusion bond at the coating/substrate interface and is responsible for the excellent adhesive characteristics of ion-plated coatings. The approximately 100X adhesion improvement for Cu films on cordierite ceramic substrates discussed in this paper is a prime example of the excellent adhesion of ion-plated coatings. The graded coating/substrate interface caused by the pseudodiffusion effect produces a gradual transition from the substrate chemistry/microstructure to the coating chemistry/microstructure and serves to minimize stress concentration at the interface due to either externally applied stresses or stresses generated by differences in thermal expansion coefficients. Although a graded coating/substrate interface can normally be created by diffusion during a conventional annealing cycle (17), ion plating offers the advantages of (a) minimal substrate heating and hence minimal alteration of any temperature-sensitive substrate mechanical property and (b) the ability to create by pseudodiffusion a graded interface, even between materials that exhibit very limited mutual solid solubilities and low diffusivities.

The second benefit of depositing high average kinetic energy ionized and neutral evaporant atoms concerns the effect of the energized particles on the coating microstructure. Recent results have shown that raising the average kinetic energy of the depositing ions and atoms has the same effect on the coating microstructure as raising the substrate temperature (18,19). To produce, with low kinetic energy (<0.2 eV) evaporated atoms, a fully

dense coating with an equiaxed grain structure requires heating the substrate to more than one-half the melting point of the coating (20). It has been shown for ion plating that the substrate temperature required for transition from a porous, columnar-grained coating to a fully dense, equiaxed-grained coating is much less than that required to produce a similar quality coating by a non-plasma-aided vacuum evaporation process (18,19,21). The ratio of nucleation rate/growth rate is increased during ion plating because (a) the atomically clean surface contains a high number of defects that serve as active coating nucleation sites (12,13) and (b) the depositing coating atoms can rapidly move about to form stable nuclei because their high average kinetic energies translate into high average surface diffusion mobilities.

The third primary benefit of ion plating involves the ability of this process to produce a nearly uniform coating over the entire surface, and even in sharp crevices, of a complex part (22). The extensive amount of multiple scattering that occurs during ion plating and the tendency for any scattered coating ions to follow the electric lines of force present at all points around the negatively biased substrate produces a reasonably uniform omnidirectional shower of high average kinetic energy ions and neutral atoms onto all exposed areas of the sample surfaces and produces what is clearly not a line-of-sight coating process. It is clear that the degree of scattering is related to the pressure within the chamber since this will control the mean free path of the neutral atoms and ions. Hence, chamber pressure is an important variable when ion plating complex-shaped parts.

EXPERIMENTAL PROCEDURE

Conductive Oxides

Composite ruthenium dioxide (RuO_2)-titanium dioxide (TiO_2) films and niobium-doped titanium dioxide films were deposited by reactive ion plating onto low-carbon steel and glass substrates. Niobium, titanium, and ruthenium were electron-beam-evaporated, with the evaporation rates controlled by the electron beam power and raster frequency. An Inficon Quadrex 100 residual gas analyzer was used to ensure that an oxygen-rich argon (Ar) plasma was maintained. Table 1 summarizes the ion plating process parameters.

The microstructure and elemental composition of the deposited oxide films have been studied by scanning electron microscopy equipped with x-ray energy dispersive spectrometry (SEM/EDX), Auger electron spectroscopy (AES), and x-ray diffraction. The coating cross sections were prepared by fracturing liquid-nitrogen-cooled, v-notched steel substrates. Conductivities of the oxide films were measured with the standard four-point probe technique.

Stephenson, Hock, Boy, Scott, Rigsbee

Adhesion testing involved epoxy bonding a 2-mm-diameter stub to the coating surface and measuring the load required to cause failure of either the epoxy, the coating/substrate interface, or the substrate. The nominal strength of the epoxy and the maximum load of the test device were both about 73 MPa. Failures were occasionally found that were combinations of epoxy, coating, and substrate failures.

The dissolution rates of the oxide films were determined by testing the coated anodes in a 3.5% sodium chloride solution and in ordinary tapwater. In each case, a 25-mA current (current density = 25 A/m²) was passed through the solution with the anode biased positive relative to a graphite cathode. The dissolution rates were based on an averaged amount of constituent ions in solution as determined by mass spectroscopy from Chicago Spectrographic Service Laboratory, Inc.

As-deposited film thicknesses were determined using an Alpha-Step surface profilometer as well as measurements from cross-section scanning electron micrographs (obtained from fracture specimens).

Table 1. Operating Parameters During Coating Deposition

	Nb-Ti-O	RuO ₂ -TiO ₂
Substrate bias	- 2.5 kV	- 2.5 kV
Cathode current	15 mA	200 mA
Enhancement	+ 60 V, 0.1 A	+ 60 V, 2.2 A
Ar flow rate	25 cm ³ /min	20 cm ³ /min
O ₂ flow rate	150 cm ³ /min	100 cm ³ /min
Total working chamber pressure	2.0 Pa	2.1 Pa
Source-to-substrate distance	26 cm	26 cm
Maximum substrate temperature	350°C	300°C
Power input to electron-beam	Nb: 4.5 kW Ti: 1.0 kW	Ru: 3.0 kW Ti: 1.2 kW
Deposition time	45 min	45 min

Metal/Ceramic Composites

Elemental Cu films have been deposited onto cordierite-type glass ceramic substrates using a DC ion-plating process. The metal was electron-beam-evaporated with a typical pressure of 1 Pa Ar. Prior to evaporation, the substrates were sputter-cleaned 10 minutes with an applied bias of -2000 V and 40 mA. The effective cathode area was about 180 cm². The cathode to which the substrates were affixed was water-cooled; hence, the

Stephenson, Hock, Boy, Scott, Rigsbee

bulk substrate temperature was maintained at about 20°C.

Bilayer Cr/Cu films have also been deposited on cordierite by sequential (Cr first) evaporation following the same ion-plating process described above for elemental Cu films.

Evaluation of the chemical stability of the ion-plated metal/ceramic interfaces involved annealing the films for 30 minutes at 400°C in a reducing 5% H + Ar atmosphere. The films were then adhesion-tested as previously described.

The microstructure and microchemistry of the deposited metal film, the metal/ceramic interface region, and the ceramic substrate were studied by three methods: (a) SEM examination of fractured cross sections, (b) secondary ion mass spectroscopy (SIMS) and scanning Auger sputter depth profiles in a direction normal to the coating broad face, and (c) transmission electron microscopy (TEM) imaging, microdiffraction, and EDX analyses on coating/substrate cross sections. Sample preparation for TEM examination involved developing a procedure for thinning along a direction parallel to the metal/ceramic interface. This procedure involved: (a) encapsulating thin slices of coated ceramic substrate in epoxy-filled 3-mm-diameter stainless steel tubing; (b) slicing 0.2-mm-thick discs from the tube after curing of the epoxy; (c) mechanically thinning the central portion of the disc to a thickness of 0.02 mm; and (4) ion milling until perforation occurred at the interface. Interfacial failure stress was measured by the adhesion testing technique described previously.

RESULTS AND DISCUSSION

Conductive Oxides

Nb-doped TiO_2

Composition-depth profiles of as-deposited coatings using AES revealed a uniform composition of about 3.5 at. % Nb, 30.5 at. % Ti, and 66.0 at. % oxygen upon sputtering through an estimated 0.5 micron of the ion-plated coating (Figure 1).

Figure 2 shows results of x-ray diffraction scans of the as-deposited coatings. Most of the peaks can be indexed as belonging to the rutile (TiO_2) structure, although some of the peaks are consistent with the anatase (TiO_2) structure and possibly one of the TiO phases. The broadening of these peaks indicates that the coating is likely microcrystalline. It was difficult to positively identify any of the x-ray diffraction peaks as belonging to any intermetallic oxide compound containing Ti, Nb, and O (e.g., $\text{Nb}_x\text{Ti}_{1-x}\text{O}_2$) or to one of the oxides of niobium; however, it is possible that small amounts of these phases may

actually exist in the ion plated structure. No evidence of metallic Nb or Ti was found by x-ray diffraction. On the basis of the composition and structural analysis to date, it is likely that these coatings are made up of oxides of titanium (chiefly rutile), with niobium atoms substituted in the crystal lattice. The term "niobium-doped" titanium oxide is used here, since the true nature of the structure is not yet fully established.

Figure 3 is an SEM micrograph from a fracture specimen showing the surface and cross section of the "niobium-doped" titanium dioxide film on a steel structure. The morphology can be characterized as a dense columnar structure 10 microns thick. The apparent grain size is less than 1 micron.

The resistivity of the "niobium-doped" titanium oxide coating deposited on glass slides was 0.08 ohm-cm, which is quite satisfactory for its intended application. The measured coating adhesion was found to be 51.3 MPa.

Composite anodes formed by ion plating the "niobium-doped" titanium oxide films onto niobium substrates were found to have low dissolution rates -- 0.329 g/A/yr when tested in 3.5% NaCl solutions and 0.054 g/A/yr when tested in ordinary tapwater. Thus, anodes with highly adherent, electrically conductive "niobium-doped" titanium oxide coatings produced by reactive ion plating can be used for corrosion mitigation.

Ru and Ti Mixed Oxides

Figure 4 shows an AES composition-depth profile of the as-deposited coating containing mixed oxides of Ru and Ti. After 60 minutes of sputtering, the substrate peaks appeared, indicating that the entire coating had been sputtered through and analyzed. The composition of this coating can be seen to vary with depth, forming layers that are alternately Ti-rich and Ru-rich with an average composition of about 20 at. % ruthenium, 20 at. % titanium, and 60 at. % oxygen. These results were somewhat curious, since the production of this layered structure was unintentional. An attempt was made to hold all process parameters constant during ion plating (as in the case of the "niobium-doped" titanium dioxide coatings); however, it is apparent that the evaporation rates and/or plasma characteristics actually varied during the ion plating experiments.

Figure 5 shows x-ray diffraction scan over the as-deposited coating. Analysis of this data is difficult due to very low intensities and peak broadening. The visible peaks can be indexed as belonging to either the RuO_2 structure or the rutile (TiO_2) structure. Based on the fact that the relative concentrations of Ti and Ru are essentially equal, the coating is most likely a mixed oxide of rutile and RuO_2 . The peak broadening evident in Figure 5 indicates that the structure of the coating is micro-

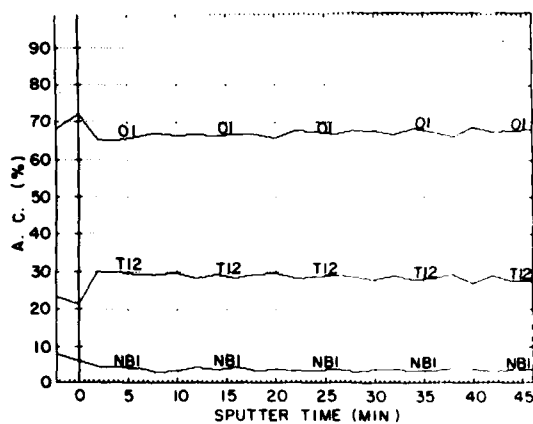


Figure 1. AES composition-depth profile of ion-plated Nb-Ti-O coating.

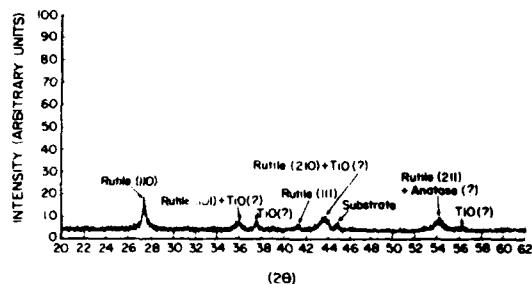


Figure 2. X-ray diffraction scan of ion-plated Nb-Ti-O coating.

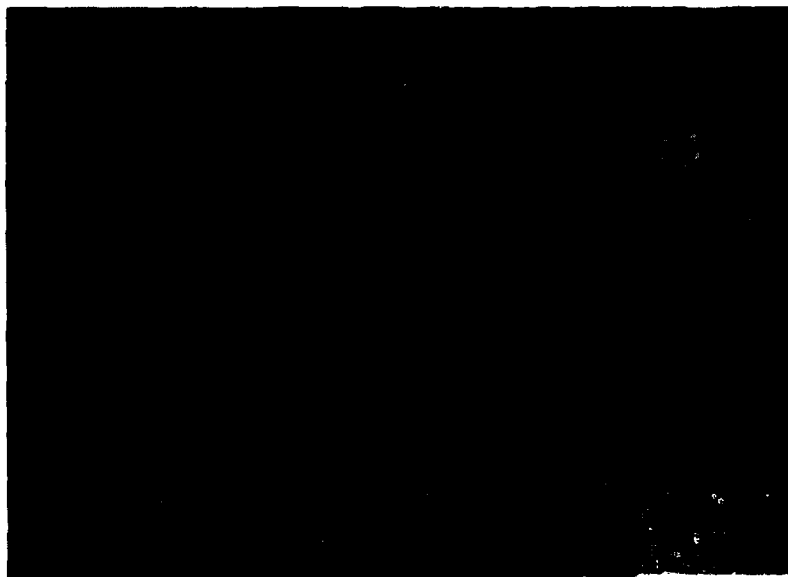


Figure 3. SEM micrograph of ion-plated Nb-Ti-O coating cross section.

crystalline. Figure 6 is an SEM micrograph from a fracture specimen showing the surface and cross section of the as-deposited $\text{RuO}_2\text{-TiO}_2$ film. The cross section indicates that the coating structure is dense and apparently columnar. It will be necessary to use AEM to determine the true nature of the apparently complex crystallographic structure and morphology of the coating. The resistivity of the $\text{RuO}_2\text{-TiO}_2$ coating on glass was 0.0018 ohm-cm. The measured coating adhesion was found to be 53.3 MPa.

Composite anodes formed by ion plating the $\text{RuO}_2\text{-TiO}_2$ film onto niobium were found to have very low dissolution rates -- 0.016 g/A/yr in 3.5% NaCl solutions, and 0.003 g/A/yr in ordinary tapwater. Anodes with $\text{RuO}_2\text{-TiO}_2$ ion-plated coatings can thus be expected to have a longer life than "niobium-doped" titanium-oxide-coated anodes. Furthermore, it has been ascertained that the mixed oxide $\text{RuO}_2\text{-TiO}_2$ coating will exhibit high conductivity over a much greater composition range (30 to 100 at. % RuO_2), as compared to the composition range of 1 to 5 at. % Nb for the "niobium-doped" titanium oxide coatings. Based on composition, it is more feasible to produce a conductive coating composed of a mixed oxide of ruthenium and titanium (23,24). However, a disadvantage of the $\text{RuO}_2\text{-TiO}_2$ coating is the high cost of the ruthenium -- about 15 times greater than the cost of niobium and titanium. Table 2 summarizes the properties of both the "niobium-doped" titanium oxide coatings and the $\text{RuO}_2\text{-TiO}_2$ coatings.

Metal/Ceramic Composites

Cu-ceramic

Evaporation of Cu onto the ceramic substrates with zero applied bias resulted in coatings with very poor adhesion. Coatings on the rougher, as-received substrates had a failure strength of about 2 MPa, while evaporated coatings on substrates metallographically polished with 0.25- μm diamond paste failed at less than 1 MPa. The slight superiority of the rougher substrate was likely due to mechanical keying of the coating in surface crevices. Figure 7 shows how the measured interfacial failure stress varies with surface roughness and applied substrate bias. For the polished substrate and an applied bias of -3000 V, the failure stress exceeded the maximum load capability of the adhesion test device (73 MPa). For this series of films, more than 80% of the tests resulted in no failure. The improvement in interfacial strength for the polished substrate is likely due to the fact that the crevices and porosity of the as-received substrate serve as stress concentration sites and promote crack initiation and propagation along the interface at low nominal applied stress levels. Secondary ion mass spectroscopy (SIMS) and Auger results indicate that the dramatically improved adhesion of the ion-plated films is due to development of a chemically graded interface region. This region results from ion-induced mixing (diffusion) and recoil implantation from the

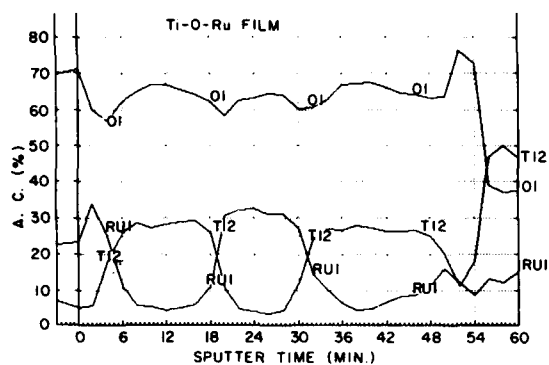


Figure 4. AES composition-depth profile of ion-plated Ru-Ti-O coating.

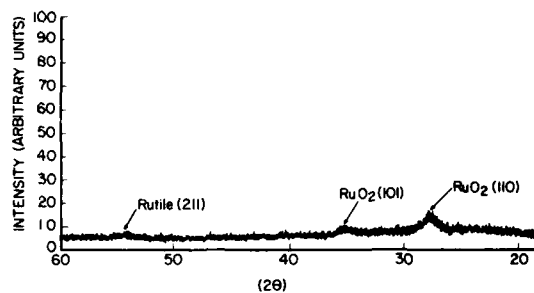


Figure 5. X-ray diffraction of ion-plated Ru-Ti-O coating.



Figure 6. SEM micrograph of ion-plated Ru-Ti-O coating.

plasma. Details of these results can be found in references 8 and 9.

Table 2. Properties of Ion-Plating Coatings

	Niobium-Doped Oxides of Titanium	Mixed Oxides of Ruthenium and Titanium
Thickness	10 μm	1.0 μm
Relative concentration of metals in oxide	90.5 at. % Ti 9.5 at. % Nb	55 at. % Ti 45 at. % Ru
Structure	Microcrystalline rutile with traces of anatase or other oxides of titanium with Nb in solution	Mixture of microcrystalline rutile and RuO_2
Morphology	Dense-Columnar	Dense-Columnar
Resistivity	0.08 $\Omega\text{ cm}$	0.0018 $\Omega\text{ cm}$
Adhesion	5.13 MPa	53.3 MPa
Dissolution rate		
Saltwater	0.329 g/A/yr*	0.016 g/A/yr
Tapwater	0.054 g/A/yr	0.003 g/A/yr

* g/A/yr represents gram/ampere/year.

Figure 8 is a bright-field TEM micrograph for an ion plated (-5000 V, 100 mA) Cu film. This figure shows several very important points. First, the Cu film is fully dense with a nearly equiaxed grain structure. The grains average about 0.2 micron in diameter and have extensive alignment of the {111} annealing twins parallel to the film growth direction. The ion bombardment during film growth has markedly altered the morphology and orientation of the Cu grains relative to those usually found for evaporated films. Second, special attention should be given to the region of the Cu film directly in contact with the light contrast ceramic substrate. This region (about 100 nm thick) shows a distinctly different grain structure from the remainder of the Cu layer. Third, note the approximately 25-nm-thick zone between the Cu and ceramic layers. This region is amorphous, and apparently plays a major role in the improved film adhesion. These last two regions are direct structural evidence of the chemically graded

Stephenson, Hock, Boy, Scott, Rigsbee

interface region detected by SIMS and Auger analysis. EDX microchemical analyses of the near-interface metal and ceramic regions further support the graded interface concept, since extensive chemical mixing was evident. It is apparent from these results that cross-section STEM-EDX analysis offers some advantages over surface-sensitive chemical analysis techniques for thin film interfacial structure/chemistry studies. Further discussion of this work can be found in references 25 and 26.

Cu-Cr-Ceramic

A series of multi-layer films was produced, in which a thin Cr deposit served as an intermediate layer between the Cu and ceramic. The presence of Cr -- an element much more reactive with O than is Cu -- should help in bonding the Cu to the ceramic. Since the thickness of a deposited film may be critical to adhesion characteristics, the intermediate Cr layer thickness was chosen as a process variable. Table 3 shows the adhesion pull test values obtained. The main modes of failure are substrate- and epoxy-related. Many samples did not fail upon twice loading to our maximum stress capability (76 MPa). This is true even after annealing samples in inert and reducing gas atmospheres to temperatures near 400°C. This demonstrates the stability of the Cr/ceramic and Cr/Cu interface.

Cross-section transmission electron microscopy of the Cr/ceramic interface reveals a layered reaction zone. Figure 9 shows a TEM micrograph of a coating cross section. This is evidence of a chemically graded interface produced by the energetic bombardment of the ion-plating process. TEM analysis of the Cr/Cu interface reveals a very fine structure (see Figure 9) that also appears to be structurally and chemically graded. The Cu structure grows directly from the top of the Cr columns. The Cr/Cu and the Cr/ceramic interfacial regions shown here are responsible for the excellent adhesion characteristics of these multilayer films.

CONCLUSIONS

This research has shown that reactive ion plating is a viable process for producing conductive metal oxide coatings that exhibit superior corrosion mitigation properties. Nb-Ti-O and Ru-Ti-O systems have each been successfully ion-plated, and each coating type has low resistivity, good adherence, and low dissolution rates. These coatings are being further investigated to determine their long-term applicability as ceramic anodes for corrosion mitigation applications.

Ion plating Cu onto a magnesia-alumina-silica ceramic substrate resulted in greatly improved adhesion (i.e., strength of the metal/ceramic interface) relative to evaporation. Detailed microstructural and microchemical studies have revealed that a chemically and structurally

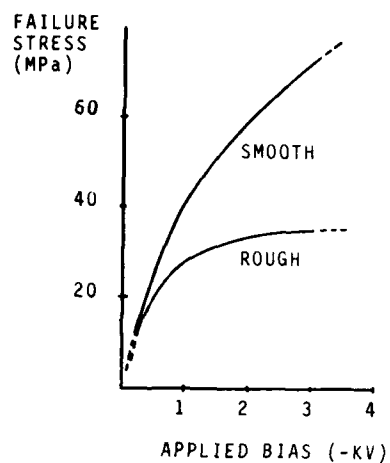


Figure 7. The dependence of failure stress on applied substrate bias during evaporation.

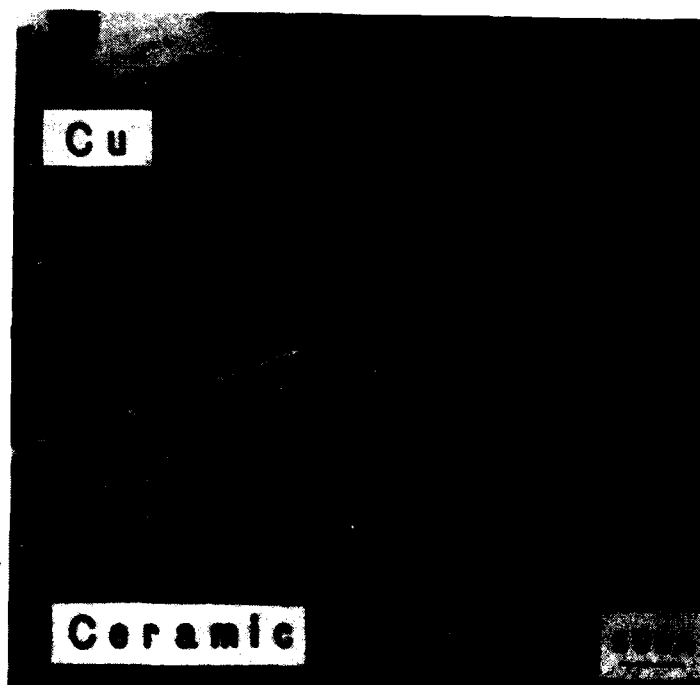


Figure 8. TEM micrograph of the Cu/ceramic interface.



Figure 9. Cross-section TEM micrograph of the Cr/Cu and Cr/ceramic interfaces.

graded interface is produced by ion plating. The nucleation and growth processes within the growing film are also altered by the effect of the ion and energetic neutral atom bombardment. Ion plating of a reactive metal such as Cr onto the cordierite ceramic substrate improves the stability of the coating/substrate interface when exposure to hydrogen-containing environments is required.

Table 3. Adhesion Data

Sample	Condition	Cr/Ceramic Interfacial Failures (MPa)	Ceramic Fractures (MPa)	Epoxy Failures (MPa)	No Failures*
Cr-Cu-2	As plated	None	67.35	38.02	1
	Ar-10% H ₂ HT Ar only HT	None	75.6	43.12	3
		None	39.45	48.22	1
				6.90	
				29.32	
Cr-Cu-3	As plated	None	None	37.12	5
	Ar-10% H ₂ HT Ar only HT	None	78.22	45.90	3
		None	75.45	None	
		None	13.05	19.05	2
			74.85	17.25	
Cr-Cu-4	As plated	7.94	None	75.98	2
	Ar-10% H ₂ HT Ar only HT	None	69.15	22.42	0
			71.62	61.05	
			22.65	78.08	
		None	None	78.60	4
				69.22	
				64.88	

* Samples in the no failure column are loaded twice to our maximum stress capability (76 MPa).

REFERENCES

1. A. Kumar, E. G. Segal, and J. Bukowski, "Ceramic Coated Anodes for Corrosion Protection," *Materials Protection* 23, 6, 24-28 (1984).
2. E. G. Segal, A. Kumar, and M. Olson, "Ceramic Anodes for Cathodic Protection," *Proc. Army Science Conference* (1984).
3. D. M. Mattox, *J. Applied Physics* 34, 2493 (1963).
4. D. M. Mattox, *J. Vac. Sci. Tech.* 10, 47 (1973).

Stephenson, Hock, Boy, Scott, Rigsbee

5. Ion Plating and Allied Techniques, 1979, and Ion and Plasma Assisted Techniques, 1985, CEP Consultants, Edinburgh, U.K.
6. A. Matthews and D. G. Teer, *ibid.*
7. J. R. Acton and J. D. Swift, Cold Cathode Discharge Tubes, London, Heywood, 1963.
8. G. Wehner, Science and Tech. 81, No. 32, 32 (1968).
9. H. D. Hagstrum and C. D'Amico, J. Applied Physics 31, 715 (1960).
10. H. E. Farnsworth and K. Hayek, Surface Science 8, 35 (1967).
11. E. V. Kornelsen, Can. J. Phys. 48, 2812 (1970).
12. K. L. Chopra, J. Applied Physics 37, 2249 (1969).
13. P. E. Bovey, Vacuum 19, 497 (1969).
14. D. G. Teer, J. Adhesion 8, 289 (1977).
15. D. G. Teer, B. L. Delcea, and A. J. Kirkham, J. Adhesion 8, 171 (1976).
16. G. Carter, J. Vac. Sci. and Tech. 7, January (1970).
17. L. I. Maissel and G. Reinhard, Handbook of Thin Film Technology, p. 4, 1970.
18. D. G. Teer and B. L. Delcea, Thin Solid Films 54, 295 (1978).
19. M. Lardon, R. Buhl, H. Signer, H. K. Pulker and E. Moll, *ibid.*, 317.
20. B. A. Movchan and A. V. Demchishin, Fiz. Metall. Metalloved 28, 653 (1969).
21. D. M. Mattox and G. J. Kominiak, J. Vac. Sci. Tech. 9, 528 (1972).
22. D. M. Mattox, Trans. SAE, 2175 (1969).
23. P. H. Duvigneaud and A. Coussement, J. Solid State Chem. 52, 22 (1984).
24. T. Sakata and E. Fromm, Z. Anorg. Allg. Chem 398, 129 (1973).
25. J. M. Rigsbee, P. A. Scott, R. K. Knipe, C. P. Ju, and V. F. Hock, "Ion Plated Metal/Ceramic Interfaces", Vacuum, in press.
26. J. M. Rigsbee, P. A. Scott, R. K. Knipe, C. P. Ju, and V. F. Hock, "Structure, Chemistry, and Adhesion of Ion Plated Metal/Ceramic Interfaces", pp. 206-211 in Proc. of Int. Conf. on Ion and Plasma Assisted Techniques, edited by H. Oechsner, CEP Consultants Ltd., Edinburgh, U.K. (1985).

ACKNOWLEDGEMENTS

Support of portions of this research by the U.S. Army Research Office under contract DAAG-29-83-K-0151 is gratefully acknowledged. The Center for Microanalysis of Materials in the University of Illinois Materials Research Laboratory, which is supported by DOE under contract DE-AC02-76ER01198, was used for all materials characterization. C. Loxton, N. Finnegan and J. Baker are gratefully acknowledged for their advice in this work. Dr. R. Quattrone and Dr. A. Kumar (CERL), Dr. Rothwarf (U.S. Army Research, Development and Standardization Group, U.K.) and Dr. M. DiLullo (NATO Scientific Affairs Division, Belgium) are also gratefully acknowledged for their encouragement.

THOMPSON

Sea State Prediction for Military and Civil Works Applications (U)

EDWARD F. THOMPSON, DR.
USAE Waterways Experiment Station
Vicksburg, Mississippi 39180-0631

INTRODUCTION

June 6, 1944, D-Day, remains one of the great days in U.S. military history. Allied troops stormed the beaches of Normandy, France, and established a beachhead in western Europe from which victory was ultimately achieved in World War II. One ingredient in the Allied success was a newly developed method for predicting wave conditions in the landing area before Operation Overlord was irreversibly launched. Thus, the Allied command was able to avoid some disastrous scenarios which accompany a landing operation in which sea states exceed tolerable levels.

Methods for accurately predicting sea states are as critical to today's Army as they were 42 years ago in both military and civil works activities. Tremendous advances in this technology have occurred during the last four decades. Progress during the past decade has been especially significant, fueled by technological leaps in computing and ocean instrumentation. The U.S. Army Engineer Waterways Experiment Station's Coastal Engineering Research Center (CERC), formerly the Beach Erosion Board, played a lead role in developing coastal information for D-Day, and CERC continues in the forefront of coastal engineering research today.

The objective of this paper is to introduce the advanced sea state prediction models which have been developed at CERC and to highlight their areas of application.

PHYSICAL PROCESSES

The waves comprising a sea state have been generated by the wind. The waves are progressive, i.e., moving across the water and often traveling away from the storm by which they were generated. Waves arriving along U.S. ocean coasts have often originated in storms hundreds of miles out to sea.

THOMPSON

Strong wind events transfer energy to water surface waves at rates which cannot be effectively absorbed. Excess energy input to the water surface is dissipated primarily by wave breaking or whitecapping.

Another essential process in the evolution of wind waves is the nonlinear transfer of energy among various frequencies in the spectrum of sea surface energy. This process accounts for the gradual shift of spectral energy to lower frequencies during wave growth.

Currents may affect the direction and energy of waves. In severe cases, a current can induce wave breaking, creating hazardous wave conditions in the current area but reduced wave conditions on the lee side of the current. The Gulf Stream, for example, is a current which influences waves along parts of the east coast of the United States.

Waves propagating into shallow water are typically strongly affected by the bottom. Important processes include refraction, diffraction, and breaking.

MODELING OF PHYSICAL PROCESSES

A critical first step in predicting sea states is development of the wind fields to be used for driving the wave model. The CERC wind model uses atmospheric pressure fields as the basic input. Since winds are primarily a response to differentials in atmospheric pressure, wind velocities at the geostrophic level above the effects of the earth's surface can be determined (Figure 1). A boundary layer model is then used to estimate wind stress at a standard elevation of 19.5 m above the water surface. The boundary layer model incorporates available information about sea surface roughness, air-water temperature difference, and other factors which materially affect the surface wind profile.

The CERC model operates on a grid as illustrated in Figure 2. A wind velocity is specified at each grid intersection for each time-step to be run. Direct measurements of wind velocity are often available from buoys, shipboard instruments, and other sources. The measurements are used to adjust the calculated wind field after being weighted according to their proximity to the grid intersection and the quality of the measurement technique.

The CERC wind wave model is based on the assumption that the wave field can be represented by a continuous spectrum of energy over a range of spectral components in frequency-direction space. The evolution of spectral density, $E(f, \theta)$, is represented by

$$\frac{dE}{dt}(f, \theta, t) = S_{in} + S_{nl} + S_b + S_d \quad (1)$$

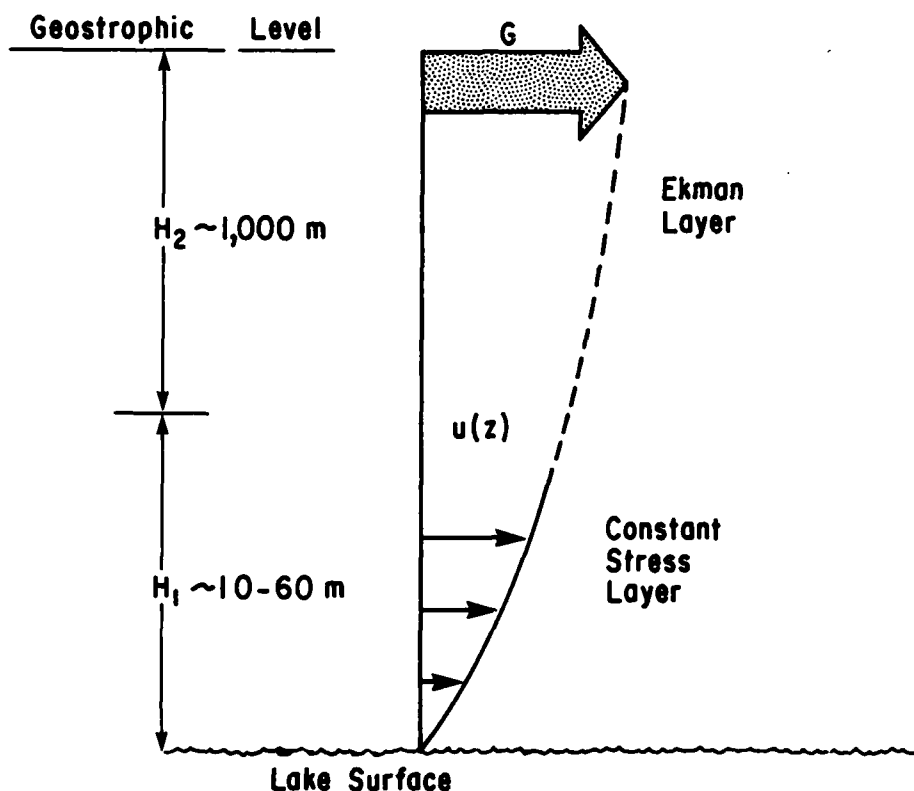


Figure 1. Idealized boundary layer over water.

where

t = time

S_{in} = energy input from the wind

S_{nl} = nonlinear energy transfer within the wave field

S_b = bottom friction

S_d = breaking and other energy dissipation within the wave field

Equation 1 provides a representation of the physical processes described in the preceding section. Parameterizations have been developed to represent the various terms on the right side of Equation 1. For example, the growth of significant wave height with fetch for various wind speeds as implemented in the model is illustrated in Figure 3.

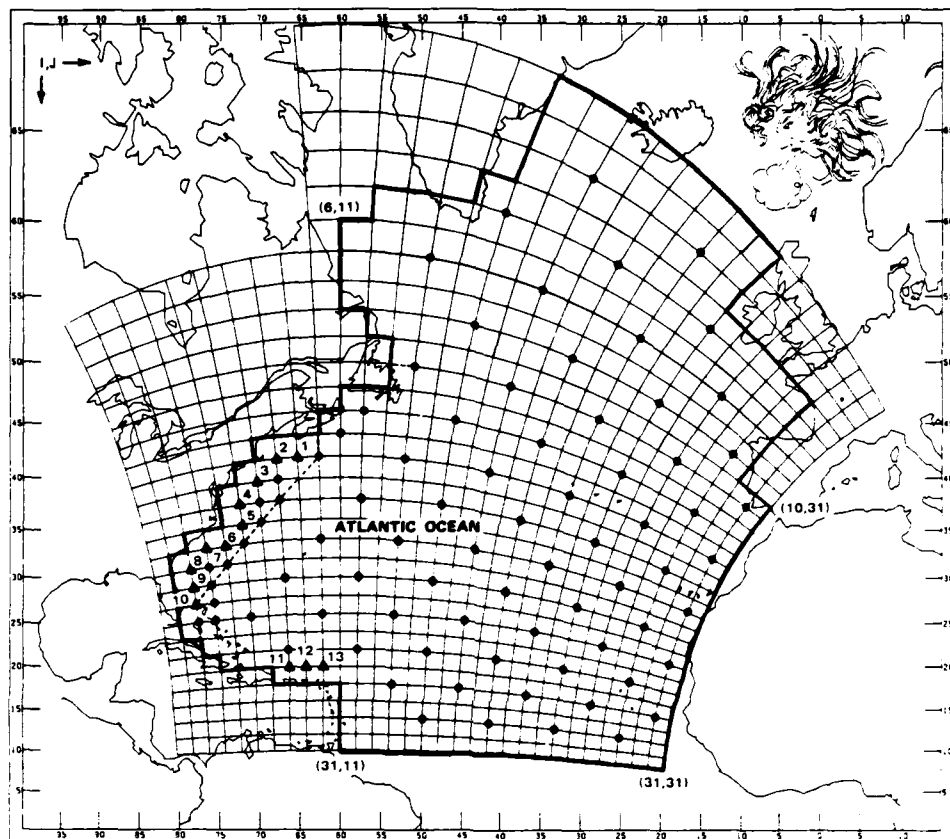


Figure 2. Grid for numerical model covering the north Atlantic Ocean.

Equation 1 is used in the model in finite difference form. Typically, 16 discrete directions and 20 frequencies are used. At each time-step, the wave energy in each frequency-direction bin at each grid intersection is adjusted in accordance with Equation 1.

VALIDATION OF MODEL

The CERC wind wave model has been run extensively to generate wind and wave data for comparison with available good quality measurements along U.S. coasts. Representative time series from the CERC model and

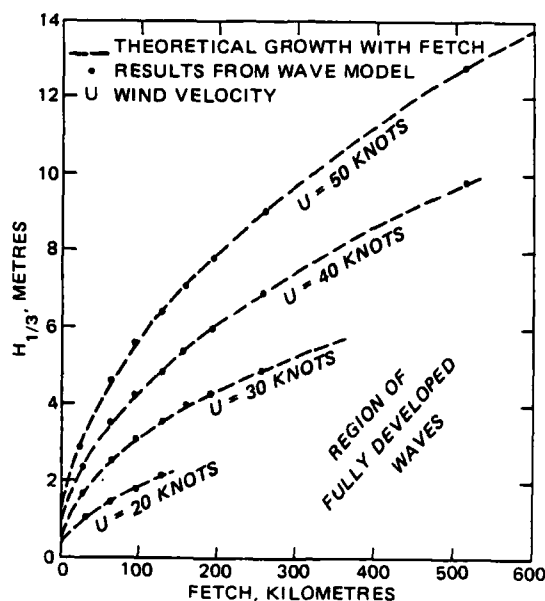


Figure 3. Growth rates from the numerical wave model compared to Hasselman's (1) growth rate.

measurements for wind speed and significant wave height are shown in Figures 4 and 5. Monthly mean and rms difference estimates between gage and hindcast wind speed values typically range between -3.0 and $+1.9$ mps and 3.1 and 5.1 mps, respectively. Similar mean and rms difference estimates for wind direction comparisons typically range between -34 and $+6$ deg and 23 and 68 deg, respectively. Comparisons over a wide range of wave conditions indicate an overall rms difference in wave height of approximately 1.0 m and no significant bias.

PRESENT APPLICATIONS

The CERC wind wave model is being systematically applied in the Wave Information Studies (WIS) to develop historical predictions, or hindcasts, of sea states along the coasts of the U.S., including the Great Lakes. The hindcasts cover the 20-year period from 1956 through 1975.

WIS is based on a three-phase approach to estimating coastal waves (Figure 6). Phase I operates on the scale of an ocean basin. Grid elements are typically 2 deg latitude by 2 deg longitude. Each time-step may be 6 hr. The grid used in Phase I of the Atlantic is represented in Figure 2. Data are archived for the grid points designated by solid symbols. Data from the points at the numbered solid triangles are used as input to Phase II.

THOMPSON

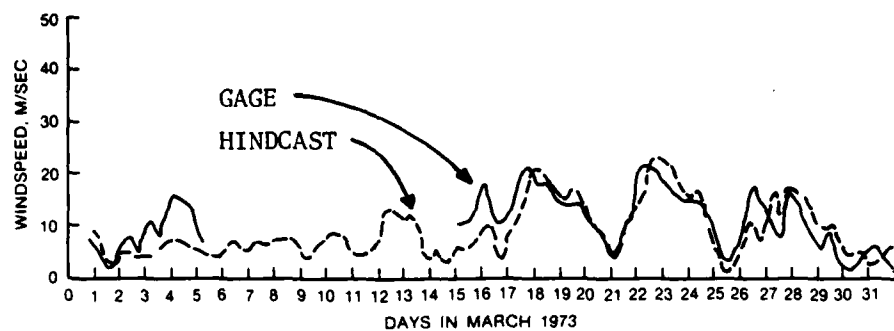


Figure 4. Wind model verification along the Atlantic coast.

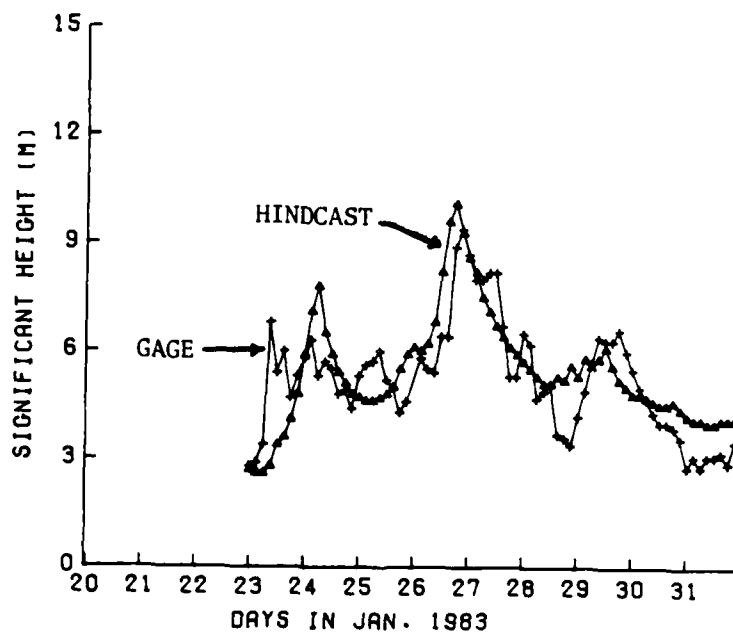


Figure 5. Wave model verification along the California coast.

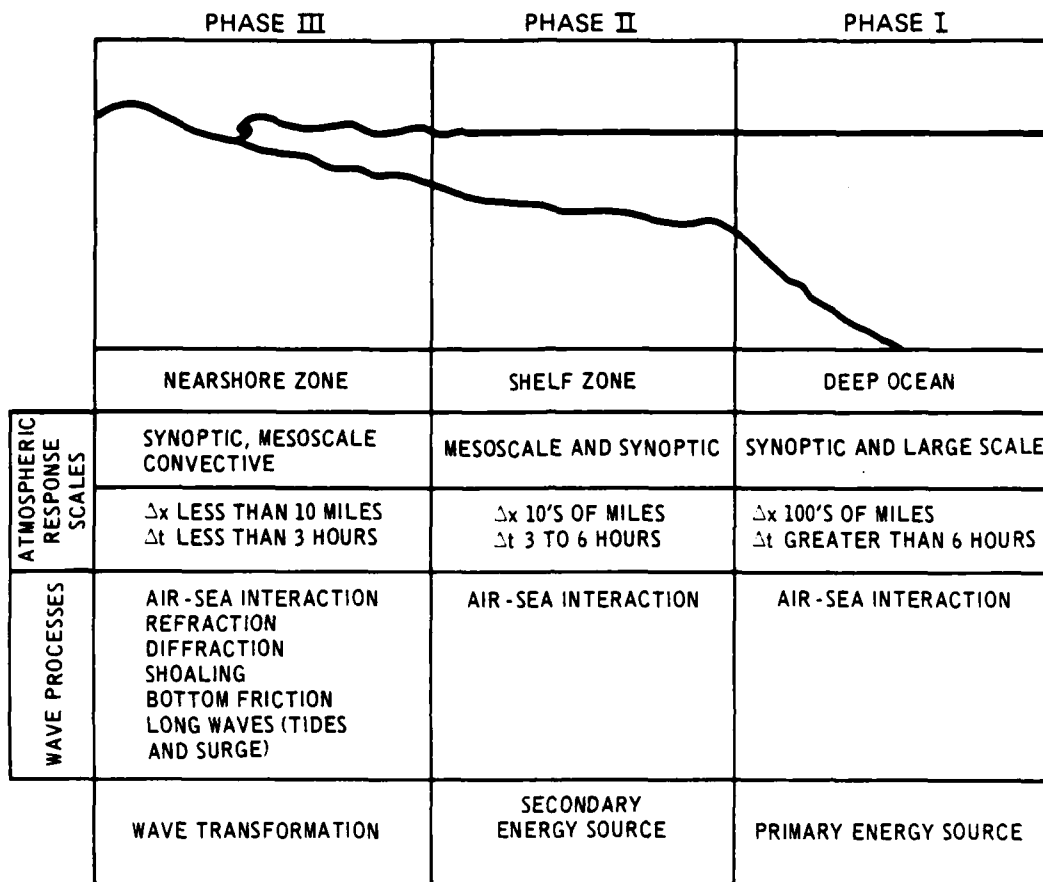


Figure 6. Summary of the three phases of WIS hindcasts.

Phase II of WIS is similar to Phase I, but a finer grid covering a smaller area is used to better resolve sheltering effects of the land mass. Phase II operates on the scale of the continental shelf and may include some shallow-water effects. The Phase II grid used along the U.S. Atlantic coast is shown in Figure 7. Grid elements are $1/2$ deg square. The time-step is 3 hr. The grid points indicated by numbered solid circles are the points at which wave information was archived for use in Phase III.

The final detailed approach to the coast or a particular project site is accomplished in Phase III which includes the strong influence of shallow water on waves approaching the coast. Simplified shallow-water

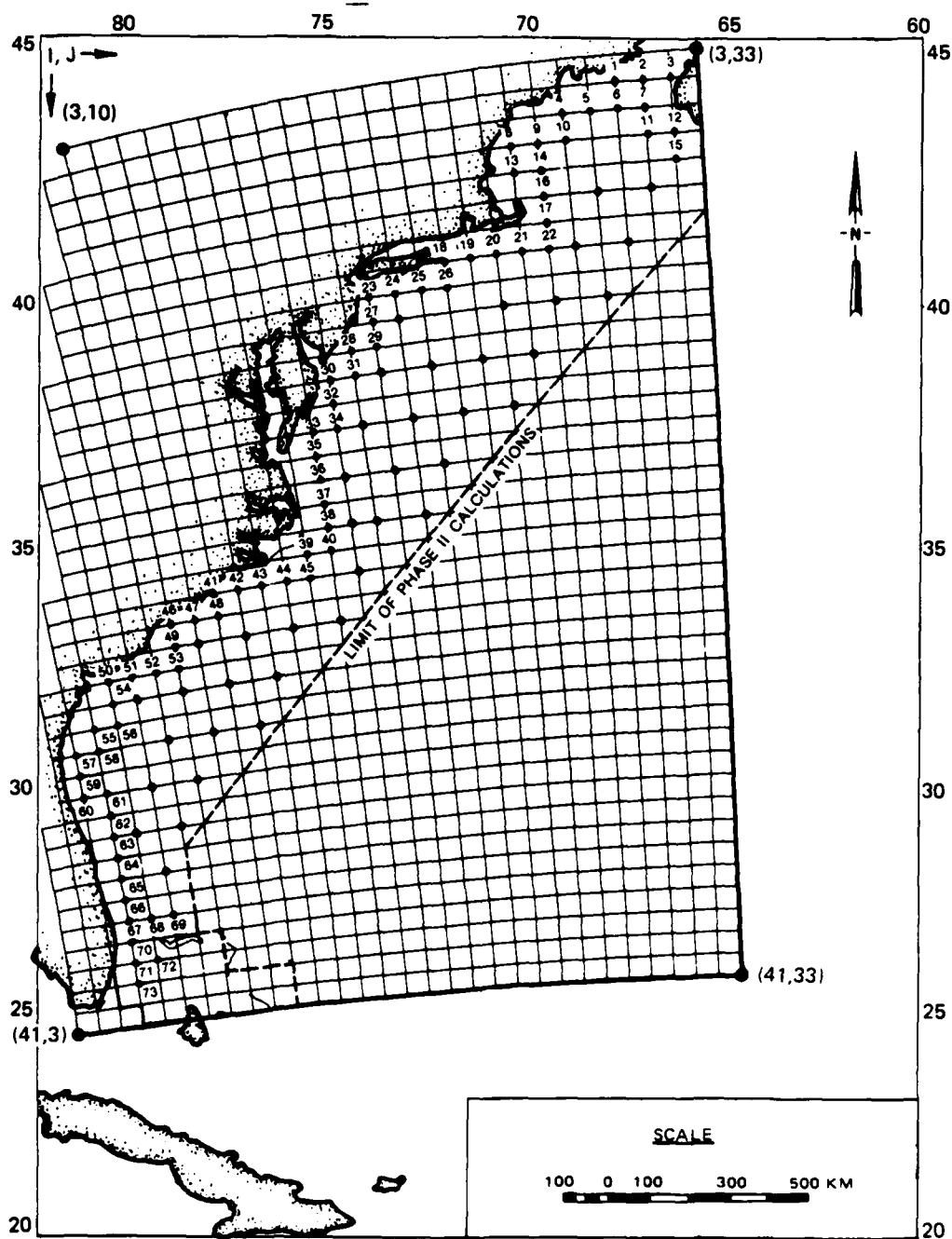


Figure 7. Grid for Phase II WIS model along the Atlantic coast.

transformation routines were used in WIS to produce wave summaries representative of 10-m water depth for coastal segments 16 km long.

An interactive data base system called the Sea State Engineering Analysis System (SEAS) has been developed to make WIS data easily available to Corps of Engineers users (Figure 8). SEAS also includes a library of routines for display and secondary calculations from the WIS data. Included is a routine for refined transformation of Phase II data to shallow water up to the point of wave breaking. The wave rose in Figure 9 illustrates the type of data available from WIS.

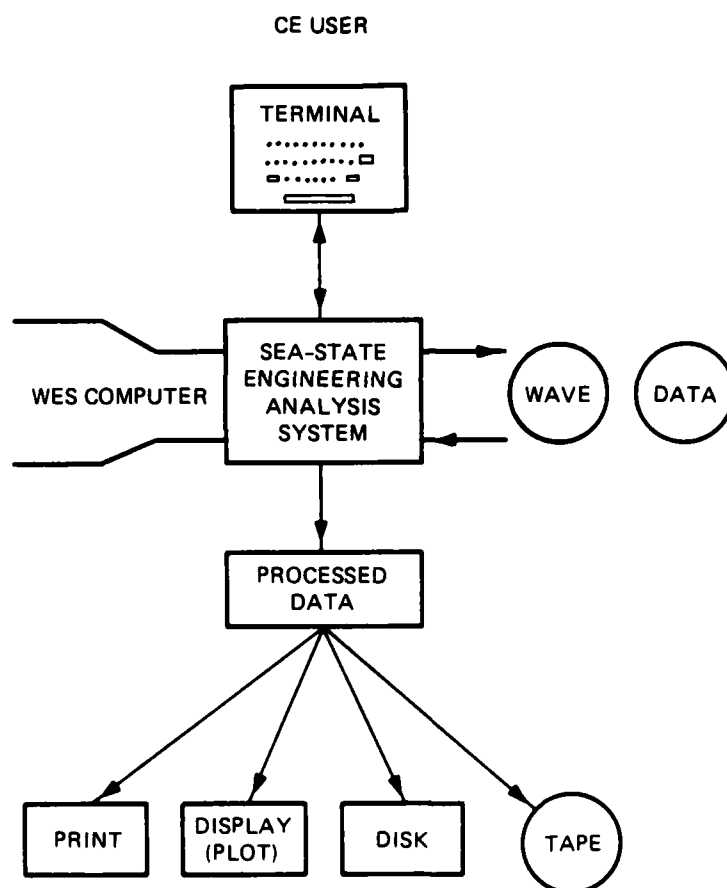


Figure 8. Schematic diagram of WIS Sea State Engineering Analysis System.

THOMPSON

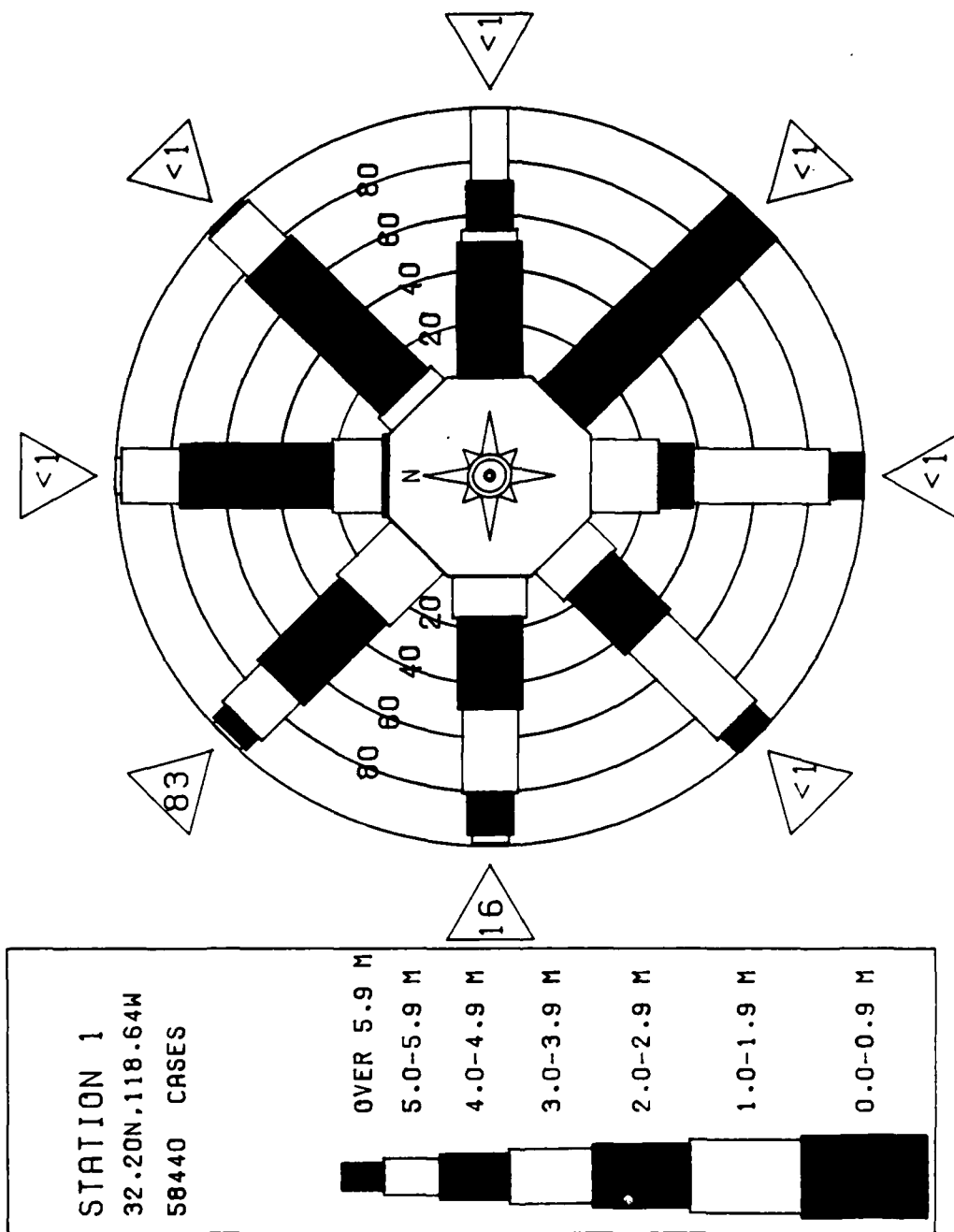


Figure 9. Example of WIS wave rose diagram.

THOMPSON

The WIS models have been developed over the last decade by a multi-disciplinary team of engineers and scientists. The models are updated as new technology becomes available from the CERC research program and the international research community. Development and implementation of the WIS models are being documented in a special series of reports listed in the reference section of this paper.

WIS has become a standard source of coastal wave data for Corps of Engineers civil works projects in the United States. WIS data are used in planning and in both functional and structural design of projects. For example, WIS estimates of extreme wave parameters as a function of return period have been used in breakwater design. WIS estimates of sea states at 3-hour intervals have been used in studies of beach profile evolution in response to nearby projects. WIS data have also been used by numerous organizations outside the Army.

POTENTIAL MILITARY APPLICATIONS

The CERC wind wave model can be an important element in the Army's military as well as civil works applications, particularly in relation to Logistics Over The Shore (LOTS) and port operations. The models can be used to develop the probability of various sea states. For example, the probability can be determined that a sea state at a given site during a given month will exceed the maximum sea state in which LOTS operations can be conducted. The models can also be adapted for use in a forecasting mode to predict sea states up to 36 hr in advance.

SUMMARY

The U. S. Army Engineer Waterways Experiment Station's Coastal Engineering Research Center has developed a series of state-of-the-art numerical models which can be used to predict sea state information. The models are being systematically applied to develop sea state estimates over a 20-yr time period for U.S. coastal areas. Summaries of the estimates are a primary source of design wave information for Corps of Engineers civil works projects. The models have a high potential for military application which has not yet been exploited.

ACKNOWLEDGMENT

The tests described and the resulting data presented herein, unless otherwise noted, were obtained from research conducted under the Coastal Program of the U.S. Army Corps of Engineers by the Coastal Engineering Research Center. The Wave Information Studies are funded under the Coastal Field Data Collection Program of the Chief of Engineers. Permission was granted by the Chief of Engineers to publish this information.

THOMPSON

REFERENCES

1. Hasselmann, K., Ross, D. B., and Sell, W., 1976. "A Parametric Wave Prediction Model," Journal of Physical Oceanography, Vol 6, pp 200-228.
2. Corson, W. D., Resio, D. T., and Vincent, C. L., 1980. "Wave Information Study for U.S. Coastlines; Surfaces Pressure Field Reconstruction for Wave Hindcasting Purposes," TR HL-80-11, Report 1.*
3. Corson, W. D., Resio, D. T., Brooks, R. M., Ebersole, B. A., Jensen, R. E., Ragsdale, D. S., and Tracy, B. A., 1981. "Atlantic Coast Hindcast, Deepwater, Significant Wave Information," WIS Report 2.
4. Corson, W. D., and Resio, D. T., 1981. "Comparisons of Hindcast and Measured Deepwater, Significant Wave Heights," WIS Report 3.
5. Resio, D. T., Vincent, C. L., and Corson, W. D., 1982. "Objective Specification of Atlantic Ocean Windfields from Historical Data," WIS Report 4.
6. Resio, D. T., 1982. "The Estimation of Wind-Wave Generation in a Discrete Spectral Model," WIS Report 5.
7. Corson, W. D., Resio, D. T., Brooks, R. M., Ebersole, B. A., Jensen R. E., Ragsdale, D. S., and Tracy, B. A., 1982. "Atlantic Coast Hindcast Phase II, Significant Wave Information," WIS Report 6.
8. Ebersole, B. A., 1982. "Atlantic Coast Water-Level Climate," WIS Report 7.
9. Jensen, R. E., 1983. "Atlantic Coast Hindcast, Shallow-Water Significant Wave Information," WIS Report 8.
10. Jensen, R. E., 1983. "Atlantic Coast Hindcast, Shallow-Water Significant Wave Information," WIS Report 9.
11. Ragsdale, D. S., 1983. "Sea State Engineering Analysis System: Users Manual," WIS Report 10.

* All Wave Information Studies reports are published by the U.S. Army Engineer Waterways Experiment Station, Coastal Engineering Research Center, Vicksburg, Mississippi.

THOMPSON

12. Tracy, B. A., 1982. "Theory and Calculation of the Nonlinear Energy Transfer Between Sea Waves in Deepwater," WIS Report 11.*
13. Resio, D. T., and Tracy, B. A., 1983. "A Numerical Model for Wind-Wave Prediction in Deepwater," WIS Report 12.
14. Brooks, R. M., and Corson, W. D., 1984. "Summary of Archived Atlantic Coast Wave Information Study, Pressure, Wind, Wave, and Water Level Data," WIS Report 13.
15. Corson, W. D., 1986. "Pacific Coast Hindcast Deepwater Wave Information," WIS Report 14.
16. Corson, W. D., and Tracy, B. A., 1985. "Atlantic Coast Hindcast, Phase II Wave Information: Additional Extremal Estimates," WIS Report 15.

* All Wave Information Studies reports are published by the U.S. Army Engineer Waterways Experiment Station, Coastal Engineering Research Center, Vicksburg, Mississippi.

TREVINO & TSAI

THE SIMULATION OF CONDENSED MATTER CHEMISTRY AND DETONATION

Dr. S. F. Trevino
SMCAR-LCE-C(D)

U. S. Army Armament, Munition and Chemical Command
Dover, NJ 07801-5001

and

Dr. D. H. TSAI
National Bureau of Standards
Gaithersburg, MD 20899

INTRODUCTION

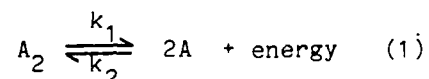
The study of reaction kinetics is a long standing effort. Much successful work has been performed for gas phase kinetics in which only a few atoms or molecules are involved in any given event. In the condensed phase where many particles participate in the dynamics the situation is less satisfactory (1). Many assumptions must be made concerning the detailed mechanisms and their effect on the kinetics due to the lack of knowledge of the very complicated trajectories executed by the many particle system. It is with the aim of providing such knowledge that the present work was initiated.

The method of molecular dynamics (MD) employs the availability of enhanced computer power to address the many body problem numerically. A system of atoms or molecules interact with each other through some potential which can be approximated by an analytic function. Various functions have been used to simulate these interactions. The specific form of the potential used here will be described below. For the purpose of discussing the method of MD it is only necessary to know that such functions exist. At each time step the force on each atom in the simulated system is obtained by summing the forces of its neighbors (which forces are obtained from the negative derivative of the potential). The classical equations of motion are then solved numerically to obtain the new positions, velocities and accelerations of all the particles in the model. This procedure is repeated for as many time steps as are required to obtain sufficient trajectories from which to calculate the properties of the material under investigation. Care must be exercised to ensure that the time step is small enough to yield accurate results. The size of the time step is determined by the highest frequency motions which the material can support (in this case the

stretching vibration of the diatomic molecule). The total number of atoms used in the simulation is typically several hundred but can be as large as 10000 according to the requirements of the problem, as in the case for the detonation wave. Various properties of the material can be "measured" as the simulation continues since the positions velocities and accelerations of the particles are known. Thus the average kinetic energy (which is proportional to the temperature), the total internal energy, the pressure, the number of reaction products, etc. can be obtained i.e., a detailed knowledge of the conditions of the sample on an atomic scale are available. This knowledge will be useful in a comparison of various theories of kinetics and detonation.

THE MODEL

The chemical reaction which we wish to simulate can be represented by the equation



Here k_1 and k_2 are respectively the forward and reverse reaction rates.

A simple function which has been found to be useful in the description of several properties of diatomic molecules is the Morse function (2). In the present study a function which describes the interaction of the atoms and is capable of producing chemical reactions is required. For this purpose a compound Morse potential V_1 and V_2 is used where

$$V_1(R) = \epsilon \{ \exp[-2a_1(R-R_1)] - 2\exp[-a_1(R-R_1)] \} \quad (2a)$$

$$\text{for } R \geq R_{\text{dis}}$$

$$V_2(R) = b_2 \epsilon \{ \exp[-a_2(R-R_2)] - 2\exp[-a_2(R-R_2)] \} + Q\epsilon \quad (2b)$$

$$\text{for } R < R_{\text{dis}}$$

Here $R = R_{ij}$ is the separation distance between atoms i and j , ϵ is the unit of energy, $R_1 = 1.0$, $a_1 = \ln 2 / 0.35$, $a_2 = \ln 2 / 0.05$ b_2 and Q are adjustable parameters to make the reaction endothermic or exothermic. Thus for example, the larger the value of Q the more exothermic the reaction will be. Fig 1. is a plot of the potential for $Q = 2$. R_{dis} is the separation distance for dissociation (this is our operational

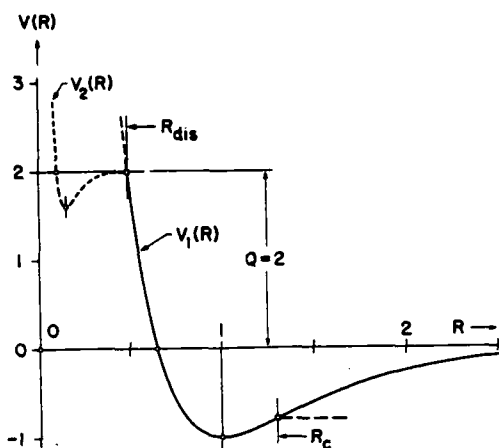


FIG. 1 The compound potential V_1 and V_2 of Eq. (1), and (2) for $Q=2$. The energy is in units of ϵ and R in units of R_1 .

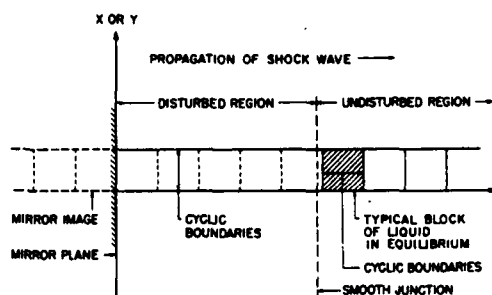


FIG. 2 A schematic representation of the model used in the simulation of the detonation wave.

definition of dissociation): When $R = R_{dis}$, $V_1 = V_2$. When $R_{ij} < R_{dis}$ atom j forms a molecule with atom i , and their interaction is given by potential V_2 . When $R_{ij} \geq R_{dis}$ the molecule ij is dissociated, and the interaction between i and j is now given by V_1 . If particle i has no neighbor closer than R_{dis} and a neighbor k at a later time finds itself at a distance from i less than R_{dis} , it interacts with i with potential V_2 and a new molecule is formed. In this manner the chemical reaction is reversible. The bond ij (when it represents a molecular bond i.e., $R_{ij} < R_{dis}$) is assumed to be saturated, this is accomplished by requiring a neighbor k to i which is closer to i than R_{dis} nevertheless to interact with i with potential V_1 .

Two qualitatively different models have been used one giving endothermic reactions and the other giving exothermic reactions by adjustment of b_2 and Q . In the investigation of the several chemical properties of the model a cube with periodic boundary conditions containing 128 diatomic molecules arranged initially with the crystal structure of solid nitrogen was used. The velocities of the atoms were distributed in a random manner with a Boltzmann distribution corresponding to an average kinetic energy per atom of $.18\epsilon$. By periodic

boundary conditions we mean the following. Each face of the cube containing the 128 molecules (whose equations of motion are solved) is in contact with another cube which contains a set of particles whose positions, velocities and accelerations are identical to those in the original cube i.e., all the cubes are periodic images of one another. These particles interact with those in the original cube through the potential given above. In this manner the model mimics an infinite material with no surfaces. The particles in the cube are heated to several temperatures and various properties determined. The results are discussed below. The heating is accomplished by scaling the velocities of all the particles by a number slightly larger than 1. (1.005).

In the second simulation the response of the system to shock loading is sought. For this purpose a closed cube can not be used since the conditions of the material in the sample is a function of how far the disturbance (the shock and detonation wave) has entered into the system. In addition a mechanism for introducing a shock wave must be included in the model. Figure 2 is a schematic representation of this model. Each of the blocks initially consists of a distribution of molecules as described in the above simulation but the blocks are joined together through periodic boundaries to form a long filament. The boundary conditions at $Z = 0$ is special and corresponds to mirror reflection. At

time $t = 0$ the velocities of all the atoms are given an additional component $-U_p$ in the Z direction so that the material next to the mirror impinges with its mirror image. This is the manner in which a continuously loaded shock is imposed on the filament. Periodic boundary conditions are imposed in the X and Y directions along the entire filament. In the Z direction periodic boundary conditions are used in a region of the material which is sufficiently removed from the disturbance that it can be considered to be in a state of initial equilibrium. This position is moved to the right as the disturbance enters the material. Thus as time proceeds, the number of atoms for which the equations of motion must be solved explicitly increases. This increase in the amount of computation is one of the factors limiting the length in time of the simulation. The largest number of atoms which has been used in this work is on the order of 14000.

RESULTS FOR EQUILIBRIUM KINETICS

The temperature dependence of the reaction rate constant k_1 is given by the Arrhenius equation:

$$k_1 = B_1 \exp(-E_1/kT), \quad (3)$$

where B_1 is a frequency factor and E_1 is the activation energy for k_1 . k_2 obeys a similar relation. The equilibrium constant $K = k_1/k_2$ is then written as:

$$K = B \exp(-\Delta E/kT), \quad (4)$$

where $B = B_1/B_2$ and $\Delta E = E_1 - E_2$. We must therefore make a series of runs at different temperatures and pressures (volumes) in order to obtain adequate data to test the results given by the model. In order to ensure equilibrium chemistry values of $Q = 0.5$ and $b_2 = 2.0$ (in Eq 2b) were used. For each run that has reached equilibrium we obtain the equilibrium rate constant in terms of the mole-fraction concentration of reaction products as

$$K_x = 4a^2/(1-a^2) \quad (5)$$

where $a = x_\infty/N$, N denotes the concentration of molecules A_2 at time zero i.e. the total number of molecules in the simulation, and x_∞ is 1/2 the concentration of reaction products at the time the material has reached chemical equilibrium. K_x has a temperature dependence similar to that given in Eq. 4.

Under the conditions of constant pressure the term $-\Delta E$ in the above equation is the change in enthalpy in the process of dissociation:

$$-\Delta E = -(\Delta \epsilon + P\Delta V) \quad (6)$$

Here $\Delta \epsilon$ is the change in the internal energy and ΔV is the change in volume associated with the process. ΔV can be shown to be given by

$$\Delta V = -kT(\delta \ln K_x / \delta P)_T \quad (7)$$

The quantities on the right hand side can be obtained from the computed data in the following way. Figure 3 presents the development of reaction products (free atoms) as a function of time for four cases in which the sample was heated from the same initial temperature by different amounts. The data labeled J was heated the most and that labeled L the least. The equilibrium values ($2x_\infty$) of the free atoms in the four cases are shown by horizontal lines. From these data the dependence of $\ln K_x$ on $\Delta \epsilon$ can be determined. The relationship turned out to be a straight line, as

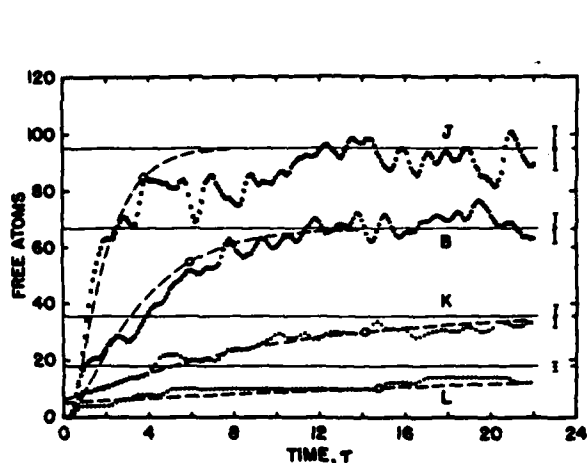


FIG. 3 The number of reaction products (free atoms) resulting after initial heating of the sample.

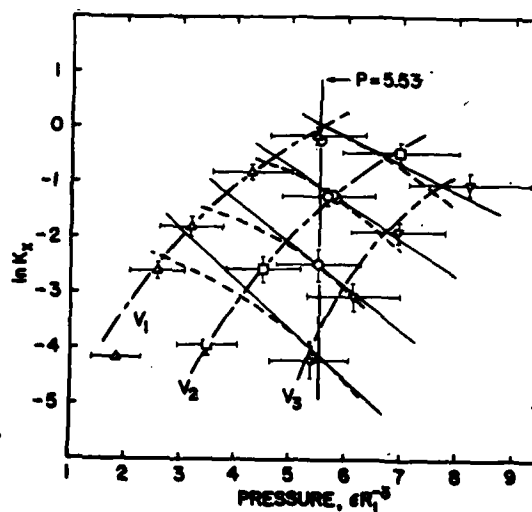


FIG. 4 A plot of $\ln K_x$ vs P for the various runs. The dashed lines are constant temp. curves and their slopes at $P=5.53$ are shown by straight lines.

kT ϵ	$(\partial \ln K_x / \partial P)_T \Delta V$ R_1^3	$P \Delta V$ ϵ	E_{PM} ϵ	E_{PA} ϵ	$\Delta \epsilon$ ϵ	ΔE ϵ
0.635	-0.50	0.328	1.814	0.216	0.449	2.05
0.498	-0.65	0.324	1.792	0.059	0.436	2.19
0.390	-0.78	0.304	1.681	-0.122	0.422	2.23
0.318	-0.90	0.286	1.582	-0.248	0.396	2.23

Average $\Delta E = 2.18 \pm 0.09$
Negative slope of $\ln K_x$ vs $1/kT = 2.21$

TABLE 1. Calculation of $\Delta E = \Delta \epsilon + P \Delta V$ for runs at constant $P=5.53eR_1^{-3}$

expected. The negative slope of the line was then equal to $-\Delta E$ by Eq. 4 under constant volume conditions. Figure 4 presents $\ln K_x$ vs pressure for all the runs which have been obtained in the present case. The derivative necessary for the calculation of ΔV has been obtained at a pressure of 5.53 (in units of eR_1^{-3}) at the four temperatures corresponding to the dashed lines. The term $\Delta \epsilon$ can be obtained by measuring the difference in the potential energy between molecules and free atoms. Table 1 presents this data and a comparison of the activation energy obtained from Eqs. 4 and 6. The agreement is satisfactory indicating that the model is capable of correctly simulating

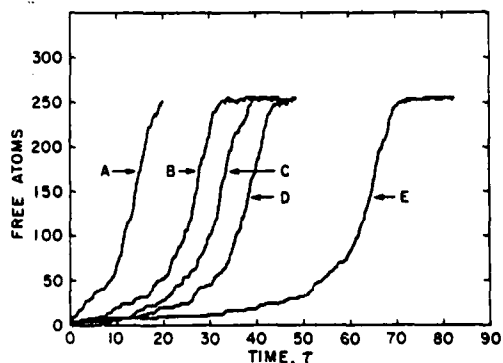


FIG. 5. The evolution of reaction products (free atoms) as a function of time for the 5 cases summarized in Table 2.

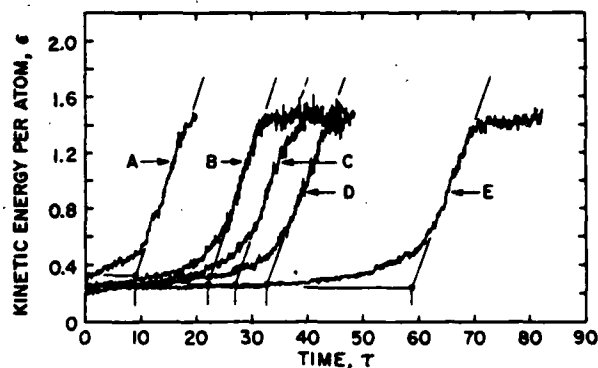


FIG. 6. The kinetic energy as a function of time for the 5 cases summarized in Table 2.

dissociation. A special note should be made of the relative contributions to the activation energy of the two terms $\Delta\epsilon$ and $P\Delta V$. In the condensed state the "cage effect" $P\Delta V$ can be quite large compared to the potential energy change. This "cage" is of course not present in the gas phase in which the reaction kinetics is completely controlled by the potential energy change. Thus condensed state chemistry is qualitatively different than gas phase chemistry.

RESULTS FOR RAPID EXOTHERMIC REACTION

In order to simulate an exothermic reaction it is only necessary to change the values of b_2 and Q in Eq. 2b to a value large enough to overcome the quenching effect of the "cage" i.e. The term $P\Delta V$ of Eq. 6. In the present work a value of $Q = 8$ and $b_2 = 0.4$ have been used. These values were chosen with the knowledge of the size of the $P\Delta V$ term from the above study. Again the sample was initially at a low temperature (0.17ϵ) and was heated by a small amount at each time step but for a different number of time steps to investigate the effects of temperature. Figure 5 presents the results of five such simulations in which the evolution of reaction products is presented as a function of time. In this figure the curve labeled A was heated initially to the highest temperature and that labeled E to the lowest temperature. The other curves were heated to intermediate values. Table 2 summarizes the conditions of the simulations. Figure 6 presents the kinetic energy (E_k) per particle for these same runs. Temperature = $2E_k/3k$ in units of ϵ/k . There are several features of these results which are worthy of notice. In all cases, for some period of time the sample produced chemical

TABLE II. Summary of conditions for the runs with the crystal in bcc structure and at constant volume of $V = 83.10 R_1^3$.^a Energies in units of ϵ per atom.

Case	E_{11} ϵ	N_{11}	ΔE_{11} ϵ	E_{1e} ϵ	E_{ke} ϵ	ΔJ	N_{fe}	τ_d
A'	3.428	0	0.01×10	3.528	0.205	1800	4	...
A	3.528	4	0.01×20	3.728	0.330	2000	252	9
B	3.428	0	0.005×40	3.628	0.267	4700	256	22.1
C	3.528	0	0.005×25	3.661	0.260	4800	256	27
D	3.528	4	0.005×20	3.628	0.263	4622	256	32.7
E	3.428	0	0.005×30	3.576	0.254	8320	256	58.8

^a E_{11} = Total energy in system before heating. N_{11} = Number of free atoms before heating. ΔE_{11} = Energy added to system per time step. E_{1e} = Total energy in system after heating. E_{ke} = Kinetic energy in system after heating. ΔJ = Number of time steps in this run. N_{fe} = Number of free atoms at end of dissociation. τ_d = Induction time

products at a slow rate. As the dissociation and the rise in the kinetic energy continued, the rate of dissociation and the rate of energy rise increase to a maximum until all of the molecules had reacted at which time both quantities stopped changing. The rise in the kinetic energy is due to the conversion of potential energy from molecules to products upon dissociation. The total internal energy of the system of course remained constant. Examination of the details of the motions of the molecules reveal several interesting effects. The first molecule to dissociate invariably was in a state in which the vibrational kinetic energy was larger than the rotational or translational kinetic energy and in fact larger than the barrier produced by the potential ($b_2 = .4$ of

Eq.2b). Molecules which dissociated late in the simulation experienced energy exchange among these degrees of freedom. In several cases a molecule spent some time in a state in which the vibrational kinetic energy was large and yet did not dissociate. The vibrational kinetic energy would redistribute itself to translational and rotational motions. However, immediately before dissociation, kinetic energy had again been transformed into vibrational energy. These observations lead to several conclusions concerning the mechanism of dissociation for our model. Firstly, dissociation is controlled by the energy residing in the motion which stretches and ruptures the bond. This is not too surprising, but it is not enough. These results show rather nicely one aspect of the "cage" effect. The idea is basically a geometric one: The surrounding molecules (and atoms) form a cage which prevents the caged molecule from breaking apart. However, the wall of the cage is not continuous. If the vibrational motion of the caged molecule is in the direction of an interstice of the wall, then it would be easier for it to break up in that direction, that is the potential barrier against dissociation is lower because there is room for the fragments.

Returning to Fig 4, we have attempted to measure a time which can be used to characterize the time to explosion by taking it to be the intersection of a horizontal line corresponding to the temperature at the

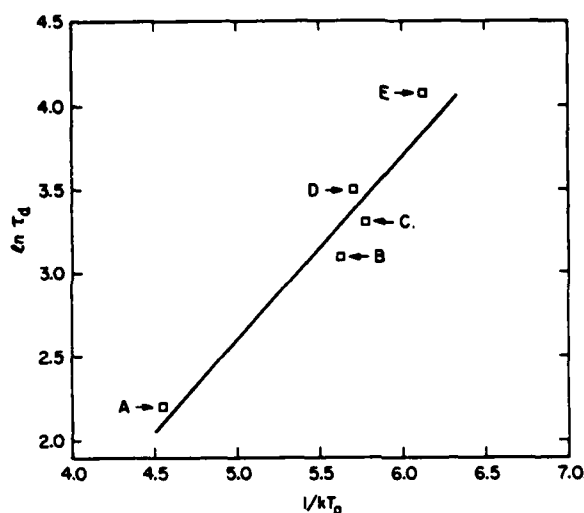


FIG. 7. A plot of $\ln \tau_d$ (the induction period) vs $1/kT_0$ for the 5 simulations of exothermic chem.

end of heating and a line through the data corresponding to the maximum slope in the kinetic energy vs time. This time we have associated with an induction time. Explosives exhibit such an effect. In Fig. 7 we have plotted the logarithm of the induction time vs $1/kT_0$. T_0 is the temperature at the end of heating. The data can be said to be consistent with a straight line which we take as evidence that the process of dissociation is thermally activated

The results of this and the previous section indicate, we believe, that method of MD can be usefully applied to the study of condensed matter chemistry, (The interested reader is referred to Ref 3 and 4 for greater details concerning the studies discussed in the previous two sections. The brief description presented here is intended for completeness).

SHOCK INITIATION OF DETONATION

With the results of the previous sections in hand we are encouraged to use this model in an attempt to simulate the initiation of a detonation wave with shock loading. Since the calculations presented in this section are extremely time consuming (computer time), it was important to us to choose parameters of the potential which would enhance the probability of success. In particular, the exothermicity parameter Q is of utmost importance. This is the parameter which controls the heat of reaction of the model. A chemical reaction which produces little

energy will of course never produce a detonation because the energy released will not be sufficient to allow the reaction zone to reinforce the shock front. For this reason we chose $Q = 32$. Another important factor is the strength of the shock loading. For reference (3) the velocity of sound in this material is measured to be ≈ 5.13 in units of $R_1(m/\epsilon)^{1/2}$. We have found that for values of U_p (Eq. 3) much lower than the sound velocity no chemistry is produced. For this reason we started the studies with a value of $U_p = 6$. The mechanism which controls whether a given shock loading will produce chemistry in this model is clear from the experience of the studies in the previous two sections. The shock wave heats the sample and promotes the initiation of chemistry, but it also compresses the sample thus increasing the $P\Delta V$ term in the activation energy Eq. 5 and this effect tends to quench chemistry. It is only when the heating effect overcomes the quenching effect that chemistry can occur.

Before starting the simulations, the system was equilibrated in its molecular form. The initial kinetic energy was $\approx 0.26\epsilon$ just below the threshold for spontaneous dissociation. The Z component of the mass average velocities was then changed from zero to $-U_p$ in a gradual manner according to the relation

$$U = \begin{cases} -(U_p/2)[1 - \cos(\pi\tau/\tau_0)] & \text{for } 0 \leq \tau \leq \tau_0 \\ -U_p & \text{for } \tau \geq \tau_0 \end{cases}$$

The column was thus caused to collide with its mirror image traveling with velocity $+U_p$ from the other side of the mirror. The collision caused the mass average velocity along the column progressively to come to a stop and this process generated a shock wave which propagated into the column.

We have obtained data for four values of U_p (6.0, 4.0, 3.75, 3.5) and in Fig. 8 we present the density (particle number per plane) for the case $U_p = 4.$, at a time $\tau = 22.8$ in units of $(mR_1^2/\epsilon)^{1/2}$ as a function of position along the filament expressed in N_a , the lattice plane number of the uncompressed lattice. This figure contains the total particle number per plane (squares), the particle number per plane of the material which are molecules (triangles) and the particle number per plane of reaction products (circles). The position of the shock front is located at the sharp rise of the total particle number per plane $N_a = 210$ lattice planes. Note that reaction does not occur immediately at the shock front but

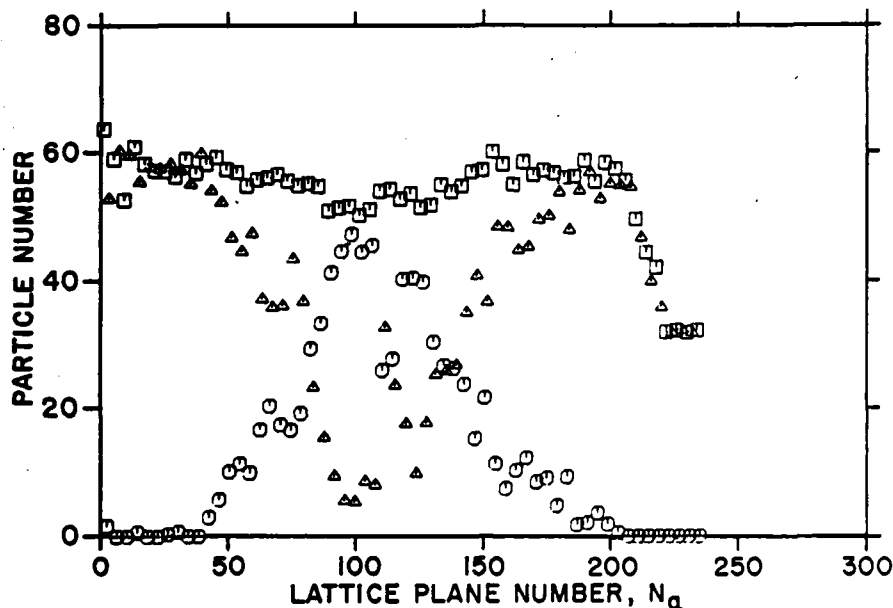


Fig. 8. The density as a function of position for $U_p = 4$. Total-squares, molecules-triangles and reaction products- circles.

rather approximately 35 lattice planes behind it. The reaction is almost complete at lattice plane 100 and then diminishes until there is very little at the mirror plane ($N_a=0$). The fact that there are no reaction products near the mirror can arise either from recombination or because this material never undergoes chemical reaction. The correct conclusion is immediately clear from inspection of Figs. 9a to 9d. In these Figures are plotted the particle number per plane of reaction products (free atoms) as a function of position along the filament for various times. Fig. 9b. presents the data for the case $U_p = 4$. Note that the material near the mirror has never undergone chemical reaction but that reaction started near $\tau = 8$. and at a distance of ≈ 50 lattice planes from the mirror. As time progressed the reaction quickly grew until almost complete reaction obtains behind the shock front. In addition the amount of material which has reacted is increasing so that the reaction zone grows but only in the direction of the shock front. It is not clear from the limited amount of data whether the reaction zone would grow fast enough to produce a steady detonation wave. Inspection of Fig. 9a ($U_p = 6.0$), however, clearly shows a steady detonation wave. Even in this case the material near the mirror has produced little chemistry.

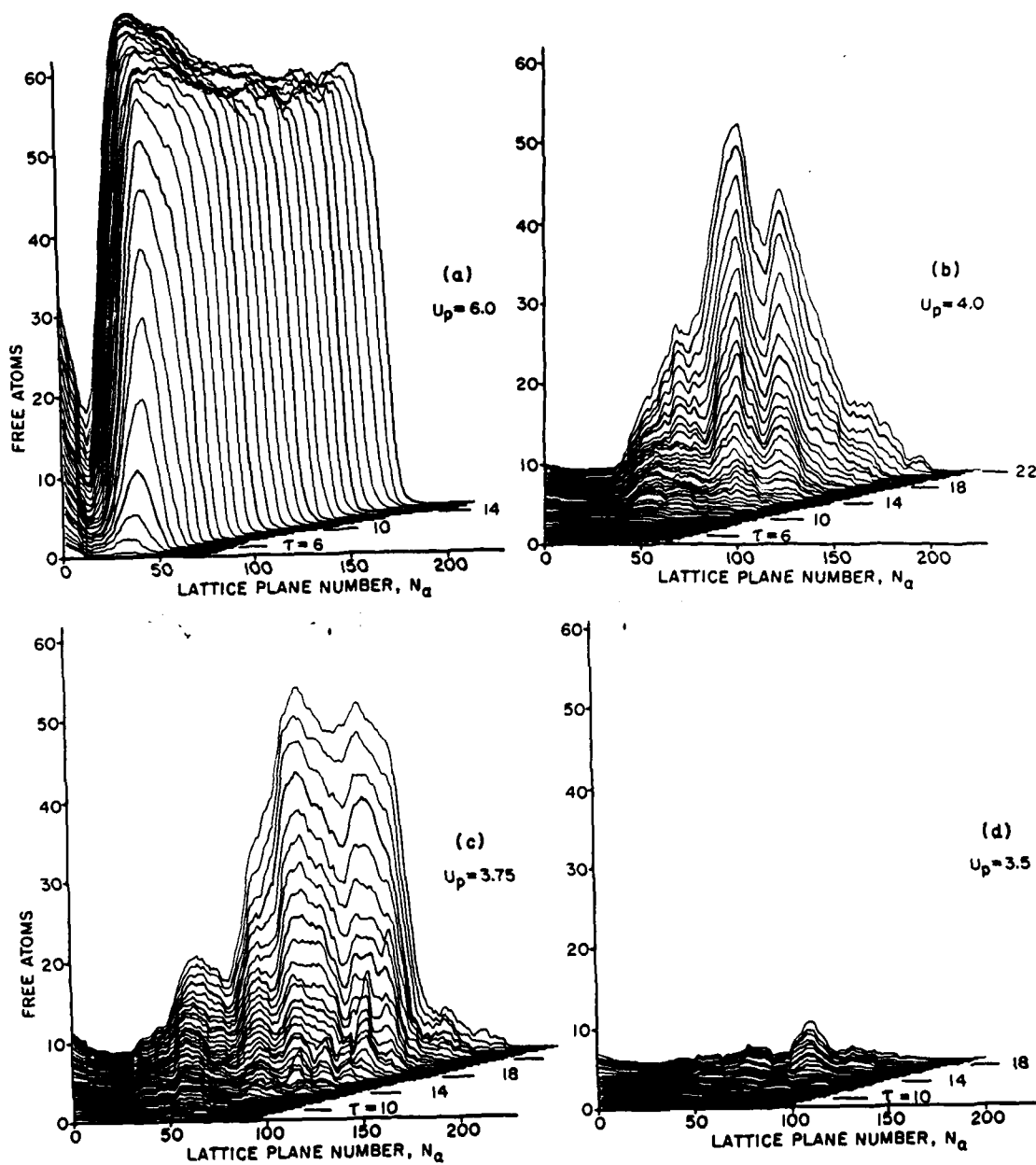


Fig. 9. The density of reaction products as a function of position for several times and the four values of U_p . Several times are noted with horizontal lines.

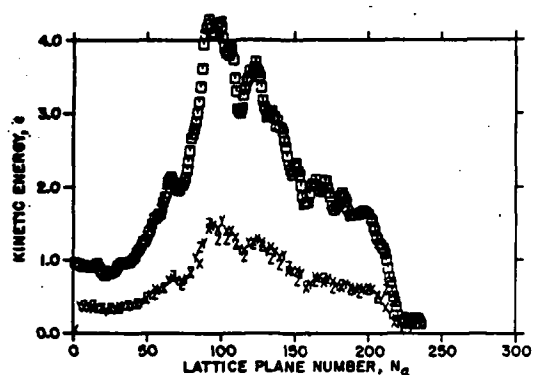


Fig. 10. The kinetic energy at time 22.8 for the case of $U_p = 4$. The components along the x y and z axis are drawn as x y and z respectively and the total (the sum) as squares.

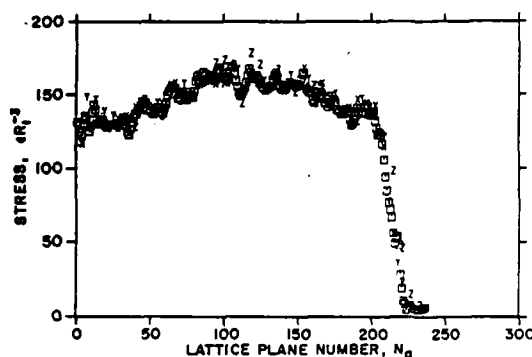


Fig. 11. The pressure for the conditions of Fig. 10. The stress in the x y and z directions are drawn as x y and z and the average as squares.

Table 3. The position (in lattice constants) and the time (in natural units) of the start of chemistry for the four cases studied of shock initiation.

U_p	Pos.	Time
6.0	33.	4.3
4.	49.	8.5
3.75	66.	9.0
3.5	105.	14.

Comparing the four cases in Fig. 9, one can see that the time and the position at which chemistry begins are clearly functions of the shock loading. Table 3 summarizes these results. The run for the lowest shock loading $U_p = 3.5$ has just begun to produce chemistry when the calculation was halted because of computer time considerations but it is useful for demonstrating the above mentioned effect.

Many other properties of the material have been measured. Among the more instructive are the kinetic energy and pressure. In Fig. 10, is presented the kinetic energy for the case $U_p = 4$, at a time of 22.8. Note that the initial temperature rise due to the shock wave is approximately 1.5 units of energy the shock wave front occurring at lattice plane 220 and its heating ending at lattice plane 180. The additional rise by an

amount 2.5 units of energy is due entirely to the energy of reaction this being the region in which the chemistry has occurred (see Fig 8). It is this very energy which causes the reaction zone to grow. Note also that the material near the mirror plane is quite cool in comparison to the region in the reaction zone. Another interesting observation is that the kinetic energy along the 3 directions X Y and Z are the same throughout the filament indicating that equipartition is quickly achieved. In Fig. 11. is presented the pressure for the same case. There is the initial rise due to the shock wave a subsequent rise in the reaction zone due to the chemical energy and a decrease to the mirror due to the fact that no chemistry has occurred. Again the X Y and Z components are nearly the same suggesting that stress equilibration is very efficient.

This amount of data, and that obtained on the response of the system to rapid heating (5), should serve as a useful starting point from which a comparison with hydrodynamic theories can be effected. It is our plan in the future to make this examination in order to improve the predictive capability of both methods.

CONCLUSION

We have shown in this work that the method of MD can be used successfully to model chemistry in the condensed state. The method is then used to obtain the properties of a detonation wave initiated by a shock wave and it is proposed that this data so obtained be used in a comparison with hydrodynamic theories of detonation waves.

REFERENCES

1. K. J. Laidler, *Theories of Chemical Reaction Rates* (McGraw-Hill), New York, 1969), Chapt. 6.
2. Linus Pauling, *The Nature of the Chemical Bond* (Cornell University Press, Ithaca, New York, 1960), Appendix VII.
3. D. H. Tsai and S. F. Trevino, *J. Chem. Phys.* **79**, 1684 (1983).
4. S. F. Trevino and D. H. Tsai, *J. Chem. Phys.* **81**, 248 (1984).
5. D. H. Tsai and S. F. Trevino, *J. Chem. Phys.* **81**, 5636 (1984)

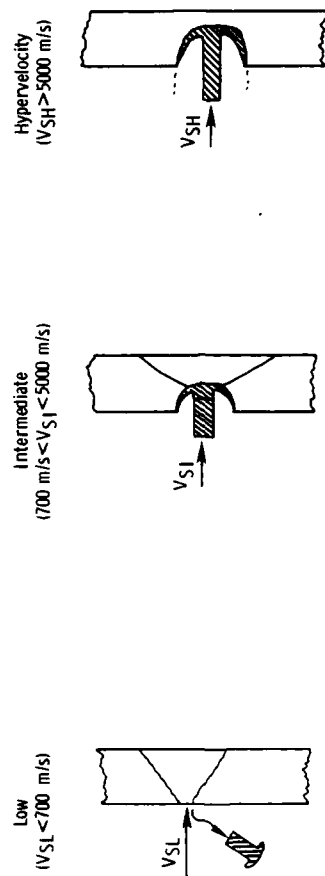
VIECHNICKI

FACTORS CONTROLLING THE BALLISTIC BEHAVIOR OF ARMOR CERAMICS

* DENNIS J. VIECHNICKI, DR
US ARMY MATERIALS TECHNOLOGY LABORATORY
WATERTOWN, MASSACHUSETTS 02172-0001

I. INTRODUCTION

Ceramic armor was developed in the late 1960's and found application in Vietnam as personnel body armor and aircraft armor on helicopters and fixed wing gunships. Weight reduction was the primary reason for its use in these cases. Interest in ceramic armor declined after the war, but was renewed in the late 1970's. This time the applications were for vehicular armor and again the primary reason was weight reduction. Currently, interest in ceramic armor is at a high level with many organizations involved in development, testing and manufacture of ceramic armor. Unfortunately with the exception of a few pioneering studies (1-6), ceramic armor technology has evolved to its current state of development and understanding using empirical cut-and-try methods, and there have been few recent attempts to find the basic mechanisms behind the defeat of ballistic threats by ceramic armor materials (7-10). This has resulted in a large amount of disparate and seemingly unrelated or contradictory information. It is the objective of this report to assess the state-of-understanding of ceramic armor materials response to ballistic impact, and to propose some basic defeat mechanisms that ceramic armor employs. Ceramic armor material response will be separated into three regimes dependent upon the velocity of the ballistic threat. This is an approach similar to one suggested by Fields and Hutchings (11) for water drop and solid particle impact upon materials. The regimes are simply low velocity, hypervelocity, and intermediate velocity (See Figure 1). The low velocity regime will be defined as ballistic threats below 700 m/s; the hypervelocity regime will be defined as ballistic threats above 5000 m/s; and the intermediate regime will fall between these two. These



$$V_{SL} < V_{SI} < V_{SH}$$

THREE VELOCITY REGIMES FOR CERAMIC ARMOR RESPONSE TO IMPACT

Figure 1

Table I. IMPORTANCE OF MATERIALS PROPERTIES IN THE DIFFERENT VELOCITY REGIMES DURING IMPACT OF CERAMIC ARMOR

* = VERY IMPORTANT, X = IMPORTANT, 0 = UNIMPORTANT

IMPORTANCE OF:	LOW ($V < 700$ m/s)	INTERMEDIATE ($700 \text{ m/s} < V < 5000$ m/s)	HYPERVELOCITY ($V > 5000$ m/s)
MECHANICAL PROPERTIES:			
COMPRESSIVE, SHEAR, TENSILE STRENGTHS, HARDNESS,	*	X	0
FRACTURE TOUGHNESS	*	0	0
ELASTIC PROPERTIES:	X	*	*
YOUNG'S, SHEAR, BULK MODULI, POISSON'S RATIO, SOUND SPEEDS			
DENSITY	0	*	X
MICROSTRUCTURE	*	*	0
POROSITY	*	*	X

boundaries may be somewhat imprecise, but they do relate to the changing characteristics of the projectile/armor interaction. The importance of materials properties in these different velocity regimes is outlined in Table I. At low velocity, $V_s < 700$ m/s, the bullet may be blunted but it is not shattered. Shock waves generated by the impact are not great enough to exceed projectile strength. The ceramic may be broken by the impact, but its compressive strength is great enough to defeat the projectile. Therefore, mechanical properties at low and moderate strain rates of the projectile and the ceramic armor control the penetration event. In the hypervelocity regime, materials behave as if they were liquids, and therefore mechanical properties are unimportant. Elastic properties, sound wave velocities, and material densities are the important factors. In the intermediate regime, velocities may be high enough on initial impact so that materials behave hydrodynamically, but the projectile quickly slows down to a point where mechanical properties at high strain rates of the projectile and the ceramic armor control the ballistic event. This report will discuss the ceramic armor materials response in terms of these three velocity regimes, and will expand upon the importance of the materials properties in the different velocity regimes as outlined in Table I.

II. CERAMIC ARMOR MATERIALS RESPONSE TO IMPACT

Ceramic armor materials response to impact will be divided into three velocity regimes:

- 1) Low Velocity ($V_s < 700$ m/s)
- 2) Hypervelocity ($V_s > 5000$ m/s)
- 3) Intermediate velocity (700 m/s $< V_s < 5000$ m/s)

1. Low Velocity ($V_s < 700$ m/s)

Impact in this velocity regime is characterized by blunting and deforming the projectile and fracturing of the ceramic armor. Shock waves generated during impact are not large enough or are rapidly attenuated so that the yield strength (Y) of the projectile is exceeded only near the site of the original impact. The magnitude of stress (σ) arising from shock waves generated by impact can be written as

$$\sigma = \rho C_o V_s \quad (\text{Equation 1})$$

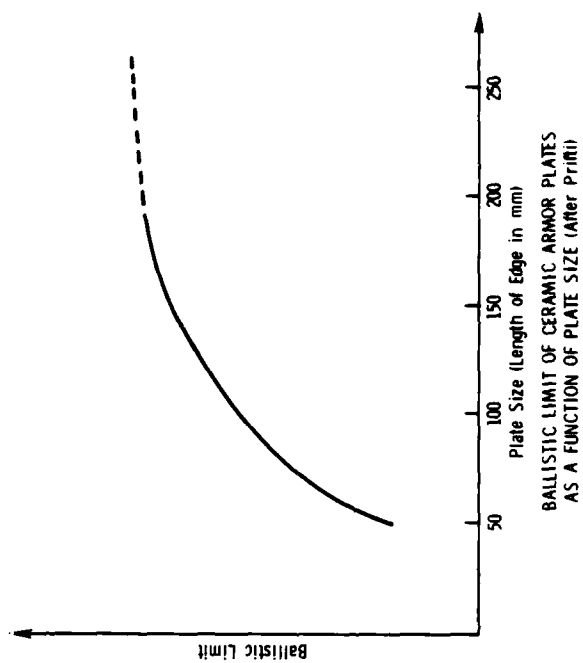
where ρ is material density, C_o is the elastic wave speed in the material, and V_s is the striking velocities. This leads to blunting and deformation of the projectile but not a complete shattering as is evident at higher velocities. The ceramic armor is fractured and pulverized near the original impact site as the compressive strength of the ceramic is exceeded. Hardness which relates to the incompressibility of the ceramic plays an important role. Fracture then occurs throughout the ceramic with a tensile crack forming at the back surface of the ceramic and then a Hertzian cone or conoid of fracture nucleating and growing from near the front surface as the shear strength is exceeded (6). The angle of the conoid is dependent upon the material as can be seen in flash X-ray photographs done by Wilkins et al (2). The angle defined by the normal to the surface of the ceramic plate and the fracture conoid surface is greater for B_4C than for BeO , and AD 85 alumina. The angle for B_4C was confirmed independently by the author on a ballistic target.

The consequences of low velocity impact being governed by the compressive (σ_c), tensile (σ_t) and shear strengths (σ_s), and hardness (KHN) of the ceramic is that since these properties are strongly dependent upon the microstructures of the ceramics and such things as grain size, second phases, microcrack populations, and porosity. This also leads to a ceramic plate size effect (12) of decreasing ballistic protection with decreasing ceramic plate size (See Figure 2). The length and width of the plate must be larger than the diameter of the fracture conoid. Formation of a partial fracture conoid because of intersection with a tile edge would require less energy and would result in a smaller piece of ceramic impeding the projectile.

2. Hypervelocity ($V_s > 5000$ m/s)

Hypervelocity impact is characterized by one liquid hitting another, i.e., the materials behave hydrodynamically. Material density (ρ) and elastic properties such as Young's Modulus (E), wave velocity (C_o), and impedance ($I = \rho C_o$) are important in this regime. Impedances of various armor and penetrator materials are seen in Table II. Penetration is governed by Bernouilli's Equation (13) for incompressible materials:

$$P_s = \frac{1}{2} \rho V_o^2 \quad (\text{Equation 2})$$



BALLISTIC LIMIT OF CERAMIC ARMOR PLATES
AS A FUNCTION OF PLATE SIZE (AFTER PRII)

Figure 2

Table II. IMPEDANCE OF ARMOR AND
PENETRATOR MATERIALS

MATERIAL	IMPEDANCE (kg/m ² sec) x 10 ⁷
W	7.88
DU	5.47
TiB ₂	5.00
Al ₂ O ₃	3.92-4.19
STEEL	4.06
SiC	3.65
B ₄ C	3.51
SODA-LIME SILICA GLASS	1.30
Al	1.29
KEVLAR	0.50

VIECHNICKI

where P_s is pressure, ρ is material density and V_0 is the initial impact velocity. From this equation Birkoff et al (14) derived a very useful equation:

$$P = L \sqrt{\rho_j / \rho_t} \quad (\text{Equation 3})$$

relating the distance penetrated into a target (P) to the length of the jet (L) and the densities of the jet (ρ_j) and the target (ρ_t).

Threats in this velocity regime are usually shape charge jets and explosively formed fragments (EFG's). They travel at or near the shock wave velocities in the materials they impact until slowed down during penetration. Defeat of these threats is generally done by perturbing the jet. The front end of the jet travels faster than the rear end, and there is a strong tendency for it to become a line of discrete particles rather than a continuous jet, thereby decreasing the penetrating power. The consequences of treating hypervelocity impact in a hydrodynamic mode is that ordinary mechanical properties of materials are unimportant. Also because the threats are traveling at or near the shock wave velocities, reflection of these waves from tile boundaries will not play a role in the penetration event, so there should be no effect of ceramic tile size on ballistic impact.

3. Intermediate Velocity ($700 \text{ m/s} < V_s < 5000 \text{ m/s}$)

This velocity regime is the most important one since most military ordinance lies here, from handgun bullets to tank long rod penetrators. It is the regime where ceramic armor plays its greatest role, since in other velocity regimes other armor technologies are cheaper and/or more effective. The intermediate regime is also the most complicated because more than one penetration mechanism occurs upon impact. During initial impact velocities and pressures are high enough for the materials to behave hydrodynamically. Some of the material is also vaporized. See Figure 3.1. Brittle ceramics do not flow like ductile metals. They fracture and are pulverized into very small particles which get out of the way of the penetrator by a combination of "granular flow" and high speed jetting (Figure 3.2) similar to the "water hammer effect" that occurs when high speed rain drops hit glass windshields. This effect is discussed in detail by Fields and Hutchings (11). Adams et al (15) used high speed photography to show the jets of ceramic particulates exiting the impact area and traveling back towards the gun at velocities greater than V_s . Very fine particles ($< 0.1 \mu\text{m}$) traveling at these high velocities could

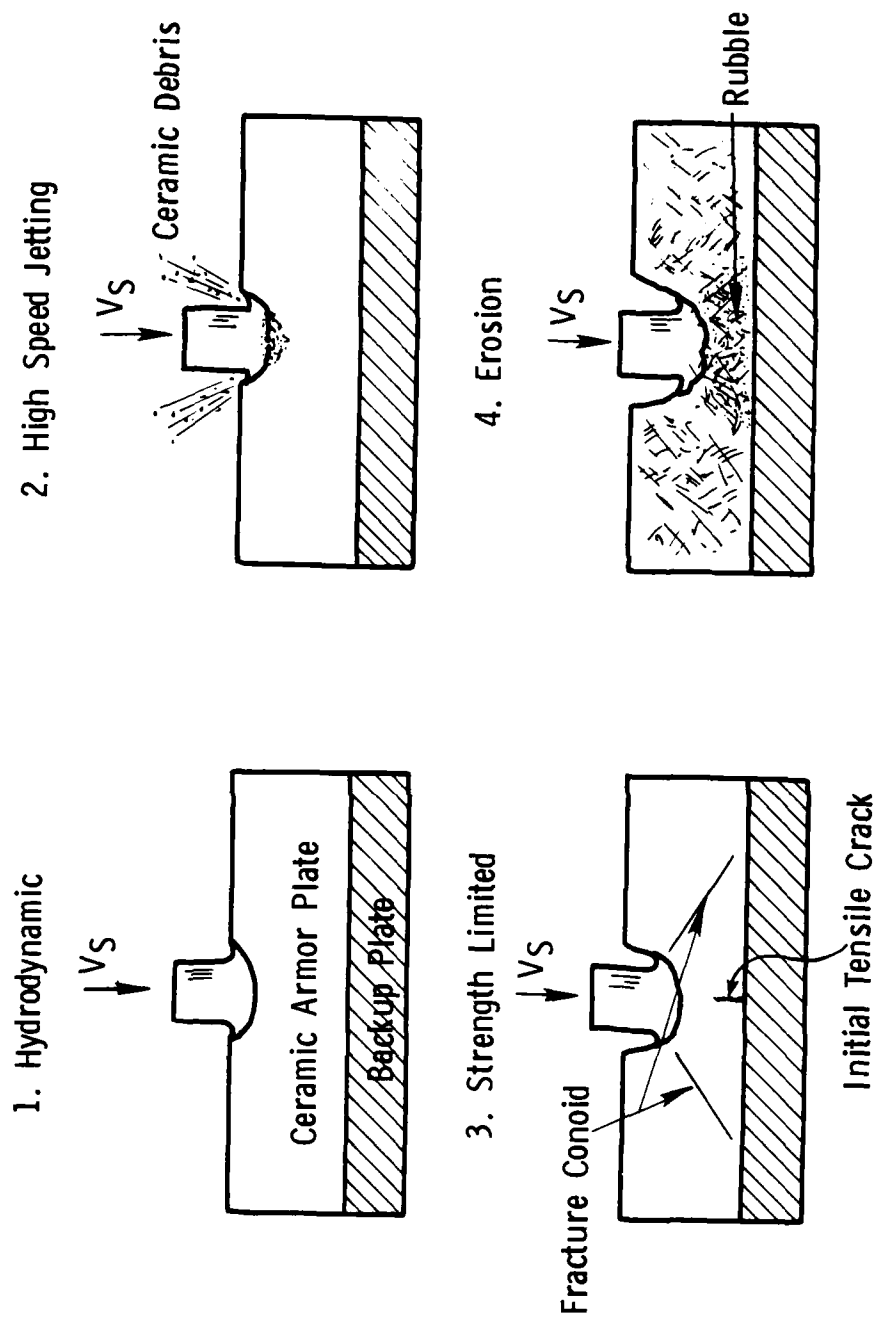


Figure 3 FOUR MECHANISMS RESIST PENETRATION OF A PROJECTILE INTO CERAMIC ARMOR

absorb a reasonable fraction ($> 10\%$) of the energy of the penetrator. The projectile is rapidly slowed down and mechanical properties at very high strain rates ($> 100,000/\text{s}$) are important. (Figure 3.3) High hardness and compressive strength resist penetration, while high tensile and shear strengths limit damage induced by the passage of the shock waves through the material. The projectile is vaporized, fractured, deformed, and eroded. The erosion is caused by the ceramic which has fractured into rubble but remains in the path of the projectile (Figure 3.4). The ceramic in the path of the projectile is vaporized, fractured, and pulverized. Ceramic not immediately in the path of the projectile is fractured because shock waves traveling ahead of the projectile interact with microcracks, pores, inclusions of other phases, and various imperfections in the ceramic causing secondary cracks to form well ahead of the primary cracks formed at the impact site. The mechanism of a damaged zone forming behind the shock wave front but ahead of the radial cracks was proposed by Hornemann et al (16) to explain phenomena they observed optically in glass targets. Their results show a zone of damaged material ahead of the projectile growing with a velocity greater than the radial crack velocity of the material ($0.4 - 0.5 C_0$) but less than the shock wave velocity (C_0). While this damaged zone will have lower strength than virgin material, the ceramic rubble will erode the projectile. The author determined the particle size distribution of rubble from several different armor ceramics after high velocity impact using sieves of different sizes. The distribution was independent of material and peaked at a fairly coarse particle size ($250 \mu\text{m} < d < 500 \mu\text{m}$). Calculations to determine how much energy was required to form these new surfaces during impact accounted for only 1% of the projectile energy. At the time this experiment was done, it was realized that the very fine particles could not be recovered. In fact recent electron microscopy photographs indicates that armor ceramics such as TiB_2 fracture into rubble particles $0.1 \mu\text{m}$ and smaller. The increased surface area created with these fine particles could absorb a lot more of the projectile energy, perhaps 10%. Precise calculations cannot be made at this time because the fraction of very fine particles is not known.

Since four mechanisms govern impact, all properties considered for the low and hypervelocity regimes must be considered for the intermediate velocity regime. These are density, elastic properties, sound velocities, hardness and compressive, tensile and shear strengths. Table III lists these properties for TiB_2 , SiC , B_4C and Al_2O_3 .

FIG. 4. PARTICLE SIZE OF CERAMICS AFTER BALLISTIC TESTING

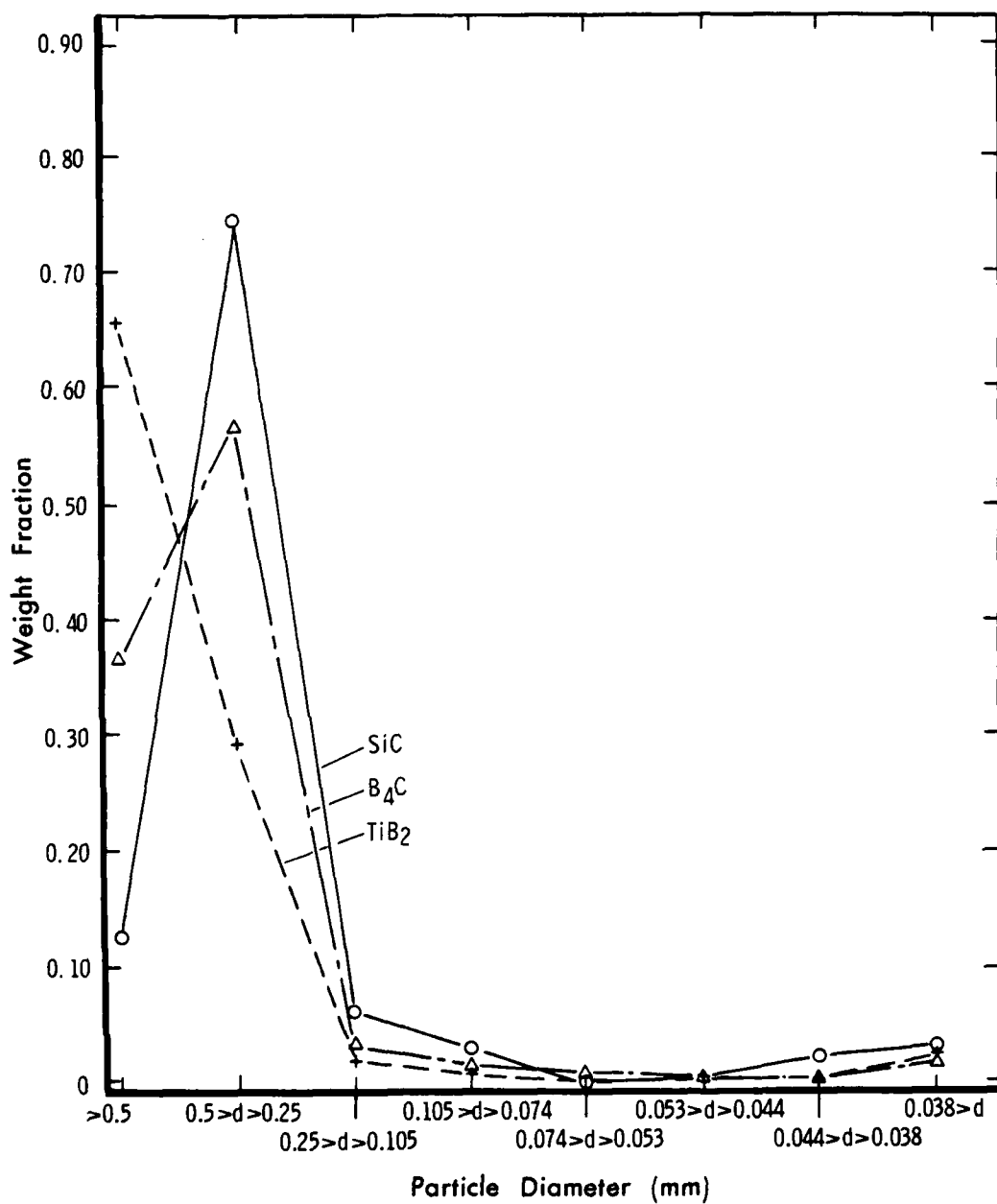


Table III. ELASTIC AND MECHANICAL PROPERTIES OF ARMOR CERAMICS

PROPERTY	TiB ₂	α -SiC	B ₄ C	Al ₂ O ₃
DENSITY (ρ) (kg/m ³ x 10 ³)	4.47	3.12	2.49	3.72
YOUNG'S MODULUS (E) (GPa)	548	402	457	364
SHEAR MODULUS (μ) (GPa)	245	174	195	131
BULK MODULUS (K) (GPa)	233	195	234	200
POISSON'S RATIO (ν)	0.108	0.158	0.175	0.22
TRANSVERSE SOUND VELOCITY (km/sec)	7.42	7.46	8.84	5.9
LONGITUDINAL SOUND VELOCITY (km/sec)	11.2	11.7	14.1	9.9
IMPEDANCE (kg/m ² sec x 10 ⁷)	5.00	3.65	3.51	3.68
HUGONIOT ELASTIC LIMIT (GPa)	8.9	8.2	9.9-15.51	8.3
COMPRESSIVE STRENGTH (GPa)	5.5	5.2	2.75	3.45
SHEAR STRENGTH (GPa)				
TENSILE STRENGTH (GPa)				0.193
BEND STRENGTH (GPa)	0.398	0.311	0.323-0.346	0.358
KNOOP HARDNESS (KHN) 0.98N LOAD (GPa)	26.0	29.0	27.5	19.6
FRACTURE TOUGHNESS (K _{IC}) (MN m ^{-3/2})	6.7	3.3	3.7	3.9

VIECHNICKI

Microstructure of the ceramics is important in the intermediate velocity regime because of the effect of microstructure on the strength and hardness of ceramics. Microstructure also affects elastic properties, such as Young's Modulus and sound velocities. Microcracks can attenuate shock waves and lower Young's Modulus (17). Porosity and second phases of lower Young's Modulus values can lower the modulus of the ceramic armor.

There is a tile size effect in the intermediate velocity regime (12). Since the shock waves travel appreciably faster than the projectile or the damage zone, regions in the path of the projectile experience shock waves that exceed the compressive strength of the ceramic. These regions are fractured into rubble. The amplitude of the shock waves diminish rapidly, but when they are reflected off a boundary, they become tensile waves which are still strong enough to cause fracture in the ceramic because the tensile strength of a ceramic is an order of magnitude lower than the compressive strength.

III. SUMMARY AND CONCLUSIONS

Ceramic armor materials response is dependent upon striking velocity, and three velocity regimes have been identified:

- 1) Low Velocity ($V_s < 700$ m/s)
- 2) Hypervelocity ($V_s > 5000$ m/s)
- 3) Intermediate (700 m/s $< V_s < 5000$ m/s)

In the velocity regime penetration is governed by the mechanical properties at moderately high strain rates of the ceramic.

In the hypervelocity regime penetration is governed by hydrodynamics and density and elastic properties are important. Mechanical properties of the ceramics are unimportant. Several mechanisms have been proposed to explain how ceramics defeat a charge jet, but no one mechanism accounts for all the phenomenon observed experimentally.

In the intermediate velocity regime penetration is most complex because more than one defeat mechanism is operating. On initial impact the materials behave hydrodynamically and density and elastic properties determine penetration. High velocity jetting of fractured ceramic rubble may absorb a sizeable fraction of the impact energy. Part way through the ceramic plate, the penetrator velocity is reduced and mechanical properties at high strain rates and resistance to erosion determine penetration.

VIECHNICKI

REFERENCES

1. Wilkins, M., Hanodel, C. and Sawle, D., "An Approach to the Study of Light Armor," Lawrence Radiation Laboratory, University of California, Livermore, CA 13 June 1967, UCRL-50284.
2. Wilkins, M.L., Cline, C.F., and Honodel, C.A., "Fourth Progress Report of Light Armor Program," Lawrence Radiation Laboratory, University of California, Livermore, CA 1969, UCRL-50694.
3. Wilkins, M.L., Landingham, R.L., and Honodel, C.A., "Fifth Progress Report of Light Armor Program, (U)" "Lawrence Radiation Laboratory, University of California, Livermore, CA January, 1971, UCRL-50980 (FOR OFFICIAL USE ONLY).
4. Landingham, R.L., and Casey, A.W., "Semiannual Progress Report of the Light Armor Materials Program," Lawrence Radiation Laboratory, University of California, Livermore, CA, 9 June 1971, UCRL-51066.
5. R. L. Landingham and Casey, A.W., "Final Report of the Light Armor Materials Program," Lawrence Livermore Laboratory, University of California/Livermore, 15 September 1972, UCRL-51269.
6. Wilkins, Mark L., "Computer Simulation of Penetration Phenomenon," in Ballistic Materials and Penetration Mechanics, edited by Roy C. Laible, Volume 5 of Methods and Phenomena: Their Application in Science and Technology, Elsevier Scientific Publishing Co., Amsterdam, 1980, pp. 225-252.
7. First Cater Mill Workshop(U), DARCOM/DARPA/DIA, Published by System Planning Corp., Arlington, VA 22209, 15-17 May 1979 (SECRET-NOFOREIGN).
8. Second Roof Point Program Workshop(U), Edited by Eugene T. Roecker, U.S. Army Armament Research and Development Command, Ballistic Research Laboratory, Aberdeen Proving Ground, MD, September 1980 (SECRET-NOFOREIGN).
9. Third Workshop on Ceramic Composite Armor (U), Edited by Dennis J. Viechnicki and Eugene Roekcer, US Army Materials and Mechanics Research Center, Watertown, MA 02172, February, 1982, AMMRC MS 82-1 (SECRET-NOFOREIGN).

VIECHNICKI

10. Armor/Anti-Armor Program Review (U), DARCOM/DARPA/DIA, Published by Systems Planning Corp., Arlington, VA 22209, 8-9 October 1981 (SECRET-NOFOREIGN).
11. Field, J.E., and Hutchings, J.M. "Impact Erosion Processes" Mechanical Properties at High Rates of Strain, 1984, Edited by J. Harding, Conference Series No. 70, The Institute of Physics, Bristol and London, 1984, p. 349.
12. Prifti, J., Private Communication, November, 1980.
13. Milne - Thompson, L.J., Theoretical Hydrodynamics, published by MacMillen Co., New York, 1960.
14. Birkoff, G., MacDougall, D.P., Pugh, E.M., and Taylor, G., "Explosives with Liquid Cavities", J. Appl. Phys., 19, (6) 563-82 (1948).
15. Adams, M., "Armor Development (U)", Published in Advanced Materials Technology Development Project, Progress in Structure and Armor Jet Propulsion Laboratory, 26 February 1985 (SECRET-NOFOREIGN).
16. Hornemann, U., Rothenhausler, H., Senf, H., Kaltoff, J.F., and Winkler, S., "Experimental Investigation of Wave and Fracture Propagation in Glass Slabs Loaded by Steel Cylinders at High Impact Velocities," in Mechanical Properties at High Rates of Strain, 1984, Edited by J. Harding, Conference Series, No. 70, The Institute of Physics, Bristol and London, 1984, p. 291.
17. Ferber, Matt, A., Becher, Paul F., and Finch, Cabell, B., "Effect of Microstructure on the Properties of TiB_2 Ceramics", Comm. Amer. Ceram. Soc. p. C-2, January, 1983.

WALTON

Dynamic Response of Armor Plate to Non-Penetrating Projectile Impact

W. Scott Walton
U.S. Army Combat Systems Test Activity
Aberdeen Proving Ground, MD 21005-5059

INTRODUCTION

A number of instrumentation related difficulties have been encountered during measurements of acceleration on armor plate subject to projectile impact. A classic example is a test done by Devost and O'Brasky (reference 1) of the Naval Ordnance Laboratory using the 5"/54 gun in 1972. In that test, only the accelerometers that were mechanically decoupled from the plate survived impact. Similar results have been observed by the U.S. Army Combat Systems Test Activity using smaller caliber projectiles.

To investigate these problems, and to characterize the ballistic shock environment, a controlled experiment was conducted. Figure 1 shows an RHA test plate .038 by .914 by .914 meters bolted to a rigid support structure.

The test plates were attached using 18 bolts on a .864 meter square. Assuming these bolts to be simple support, the lowest theoretical resonant frequency of this configuration is 249.6 Hz. The observed resonant frequencies of 4 different plates varied from 249 to 263 Hz.

INSTRUMENTATION

Figure 2 is a photograph of the instrumentation used to measure the acceleration, velocity, displacement, and strain response of the back of the plate. Measurements were made at positions 0, 100, 170, and 240 mm radially from the impact point.

Signal conditioning for all transducers was located in a box directly behind the support structure. This step was taken to obtain higher frequency response than is usually possible when transducers must drive long cables. A bridge conditioning electronics unit was fabricated for

WALTON

the accelerometers and strain gages to provide 100 KHz frequency response through 150 meters of RG-58 cable.

BALL BEARING IMPACT

The impact of a 50mm diameter steel ball bearing was used to check the instrumentation prior to firing projectiles. This impact is of interest because the momentum change and the impact duration are similar to projectile impact, and because this type of impact has been analyzed mathematically by several authors.

A computational technique used by Goldsmith (Reference 2) was used to analyze the lower modes of response of the armor plate to ball bearing impact. For a central transverse impact of a simply supported rectangular plate, the displacement in the Z direction of any point along the X axis of the plate can be calculated as a function of time.

Figure 3 compares the calculated and measured response of the plate to ball bearing impact. Although the plots do not agree perfectly, the measurements and the calculation demonstrate the same general trends.

Note how the half-sine shape of the forcing function dominates the measurements. The velocity and strain measurements at 0mm show a similar half-sine shape. As one would expect, the corresponding acceleration pulse is roughly a sine wave, passing through zero at the time when the velocity reaches its peak.

The strain signal is a tension pulse at the 0mm position and a compression pulse at the 170mm position. This transition from tension to compression was mentioned by Doyle (References 3 and 4) in his discussion of measuring the force vs. time of an impact by using strain signals. A resemblance to the half-sine shape of the forcing function clearly dominates both strain signals.

PROJECTILE IMPACT

Figure 4 shows some of the soft projectiles before and after impact. Figure 5 shows the three types of Fragment Simulating Projectiles (FSP) used in this experiment. These steel projectiles were fabricated according to MIL-P-46593A and hardened to a value of 30 on the Rockwell C scale. The projectile types and striking velocities are listed in Table 1.

Table 1. Types of Projectiles Fired

Bore	Type of Projectile	Projectile Mass In Grams	Nominal Striking Velocity in Meters/Sec (± 30)
.30 Caliber	Fragment Simulator (Steel)	2.85	335, 671, & 1006
.30 Caliber	Ball (Lead Antimony)	9.85	335 & 671
.50 Caliber	Fragment Simulator (Steel)	13.42	335, 671, & 1006
.50 Caliber	Ball (Lead Antimony)	45.88	335 & 671
20mm	Fragment Simulator (Steel)	53.79	335, 671, & 1006
20mm	Copper Slug	58.98	335 & 671
75mm	Aluminum Proof Slug	2348.0	335

The long term (90 millisecond) response of the plate is shown in Figure 6. A hammer impact (H4) is compared to a projectile impact (Round #28). The hammer impact lasted approximately 2 milliseconds and simply excites the 250 Hz resonance of the plate. Round 28 was a .30 caliber ball impact lasting approximately 120 microseconds, and excites much higher frequencies.

Note that the two displacement plots are similar in shape, and are dominated by the 250 Hz resonance of the plate. The two acceleration pulses are quite dissimilar. The acceleration from projectile impact is 2 orders of magnitude higher in amplitude and contains frequencies up to and above the 4 KHz limitation of the accelerometer used in channel 5.

During projectile impact, undamped accelerometers with high resonant frequencies indicated values as high as 200,000 g's and were destroyed. Yet damped accelerometers with low frequency response survived the same impact and indicated levels of only 200 g's, a discrepancy of 3 orders of magnitude!

WALTON

PEAK DISPLACEMENT

Because displacement response was dominated by the 250Hz resonance, peak displacement measurements are not seriously affected by instrumentation frequency response limitations. Hence peak displacement is one of the most accurate measurements made in the ballistic shock environment.

An equation for calculating peak displacement was developed by Westine (Reference 5) for rectangular plates with clamped supports. Westine's equation, as modified by the author for central impact of a simply supported square plate is:

$$Z_0 = \frac{M_0 V_0}{h^2 \sqrt{2.31 \rho E}}$$

Where Z_0 = Peak displacement at center of plate
 M_0 = Mass of striking projectile (.00985 Kg)
 V_0 = Velocity of striking projectile (335 meters/sec)
 h = Thickness of plate (.038 meters)
 ρ = Density of plate material (7833 Kg/meter³)
 E = Modules of elasticity of plate material
(2.07×10^{11} Newtons/meter²)

Hence a .30 caliber ball projectile (9.85 grams) striking a 38mm thick plate at 335 meters/second results in a peak displacement of 37.3 microns at the center of the plate. The spatial distribution of the displacement is assumed to be:

$$Z = Z_0 \left[\frac{3}{2} \left(\frac{x}{X} \right) - \frac{1}{2} \left(\frac{x}{X} \right)^3 \right] \left[\frac{3}{2} \left(\frac{y}{Y} \right) - \frac{1}{2} \left(\frac{y}{Y} \right)^3 \right]$$

Where Z_0 = Peak displacement at center of plate
 Z = Peak displacement at any point X, Y
 X = Distance from side edge of plate to center (.432 meters)
 x = Distance from side edge of plate to point of interest
(.332 meters)
 Y = Distance from top or bottom of plate to center
(.432 meters)
 y = Distance from top or bottom of plate to point of interest (.432 meters)

WALTON

Hence at a point on the central X axis of the plate, 100mm from the center of a .864 meter square, the peak displacement Z will be .926 of the peak displacement at the center of the plate. Thus, the predicted peak displacement at the 100mm position for a .30 caliber ball impact at 335 meters/second is 34.5 microns.

Figure 7 shows graphically the measured peak displacement values at the 100mm position for the various types of projectile impacts. Note that Westine's simple momentum prediction works well over a three order of magnitude variation in striking momentum.

CSTA VELOCITY GAGE

To rectify difficulties with surface velocity and acceleration measurements, a non-standard velocity measurement technique was used. A small pickup coil was epoxied directly to the armor plate and a magnet was suspended above the coil in a compliant casing as shown in Figure 8. Lacking any better name, and because the author did not think the idea would work, this arrangement was dubbed the "CSTA velocity gage".

A Hopkinson bar, instrumented as shown in Figure 9 was used to test the pseudo velocity gage. As discussed by Brown (Reference 6) and others, the strain gage can be used to measure the velocity of the free end of a Hopkinson bar according to the relationship:

$$V = 2ce$$

Where V = Velocity at the free end
c = Wave velocity in the bar material
e = Strain measured on bar

Hence the Hopkinson bar provides two independent measurements of velocity: one obtained from the strain gage, and another obtained by integrating the accelerometer signal. As shown in Figure 10, the CSTA velocity gage signal agreed well with these other two measurements of velocity.

FRAGMENT SIMULATING PROJECTILE IMPACT

Acceleration measurements were most difficult during FSP impact. The previously mentioned three order of magnitude discrepancy in peak acceleration values occurred during a .30 caliber FSP impact. To avoid destroying more accelerometers, no acceleration measurements were made during 20mm FSP impact.

The 20mm FSP impact was chosen by Quigley (Reference 7) for analysis using a finite element code normally used to predict armor penetration. A pseudo velocity gage measurement from a 20mm FSP making a central impact

WALTON

on a .038 by .305 by .305 meter RHA plate was made directly behind the projectile impact point.

A comparison of the CSTA velocity gage measurement with Quigley's prediction is shown in Figure 11. Note that the agreement is reasonably good.

Figure 11 also shows the differentiated CSTA velocity gage signal. Note that the observed peak acceleration values (1 to 3 million g's) agree reasonably well with Quigley's prediction of approximately 1 million g's.

The large magnitude (1 million g's) of the observed acceleration pulse is well beyond the range of any commercial accelerometer, and explain the loss of accelerometers observed during 20mm FSP impact. The short duration of the pulses (1 microsecond) is assumed to be responsible for the wide discrepancies in peak acceleration observed between accelerometers with different frequency response during lower level (.30 caliber FSP) impacts.

CONCLUSIONS

1. The ballistic shock environment is characterized by very little displacement (measured in microns) and very large acceleration (measured in millions of g's).
2. In a controlled environment (i.e., when a stable reference point is available), displacement can be measured readily. Peak displacement values can be adequately estimated using the momentum of the striking projectile.
3. The "CSTA velocity gage" provides an adequate surface velocity measurement in a 1 dimensional environment.
4. Direct measurement of acceleration with conventional accelerometers is impossible in the ballistic shock environment due to the high level (millions of g's) and short duration (microsecond) of the pulses present.

REFERENCES

1. DeVost, Val, and O'Brasky, James, "5"/54 Gun Projectile Armor Penetration Shock Measurement 1972", Presentation at the SNR Working Group Meeting on Standardization of Ballistic Shock Measuring Procedures, Data Evaluation Procedures, and Assessment, Aberdeen Proving Ground, MD, June 1983 (unpublished).
2. Goldsmith, Werner, Impact, Edward Arnold Publishers Ltd., London, Great Britain, 1960.

WALTON

3. Doyle, James F., "An Experimental Method for Determining the Dynamic Contact Law", Experimental Mechanics, Volume 24 - Society for Experimental Stress Analysis, Brookfield Center, Conn, March 1984, pp. 10-16.
4. Doyle, James F., "Further Developments in Determining the Dynamic Contact Law", Experimental Mechanics, Volume 24 - Number 4, Society for Experimental Mechanics, Brookfield Center, Conn, December 1984, pp. 265 - 270.
5. Westine, Peter S., et al, Ballistic Shock in Armored Vehicles Subjected to Impulsive Loads, R and D Center Laboratory Technical Report No. 12786, U.S. Army Tank - Automotive Command, Warren, Michigan, September 1983.
6. Brown, G. Wayne, "Accelerometer Calibration with the Hopkinson Pressure Bar", Instrument Society of America Preprint No. 49.3.63., 18th Annual ISA Conference and Exhibit, September 1963, Chicago, Illinois.
7. Private Communications from Ennis F. Ouigley, U.S. Army Ballistic Research Laboratory, May 1984.



Figure 1. (Left)
Photograph of RHA
test plate of rigid
support structure.
Note ball bearing,
suspended from two
wire pendulum, and
hammers, used to
check instrumenta-
tion prior to
projectile impact.

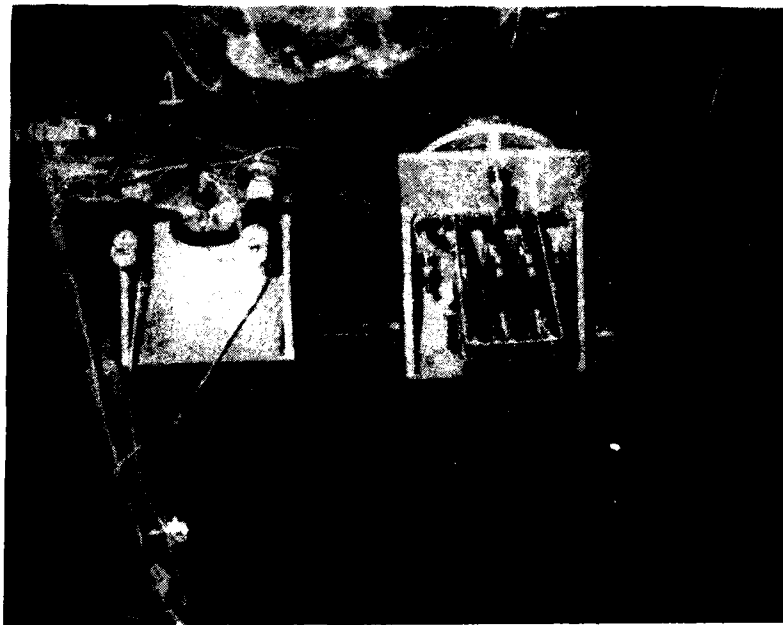


Figure 2. (Left)
Photograph of
instrumentation on
back of plate to
measure accelera-
tion, velocity,
displacement, and
strain. Device on
the right is a
non-contacting,
capacitive type
displacement sensor.

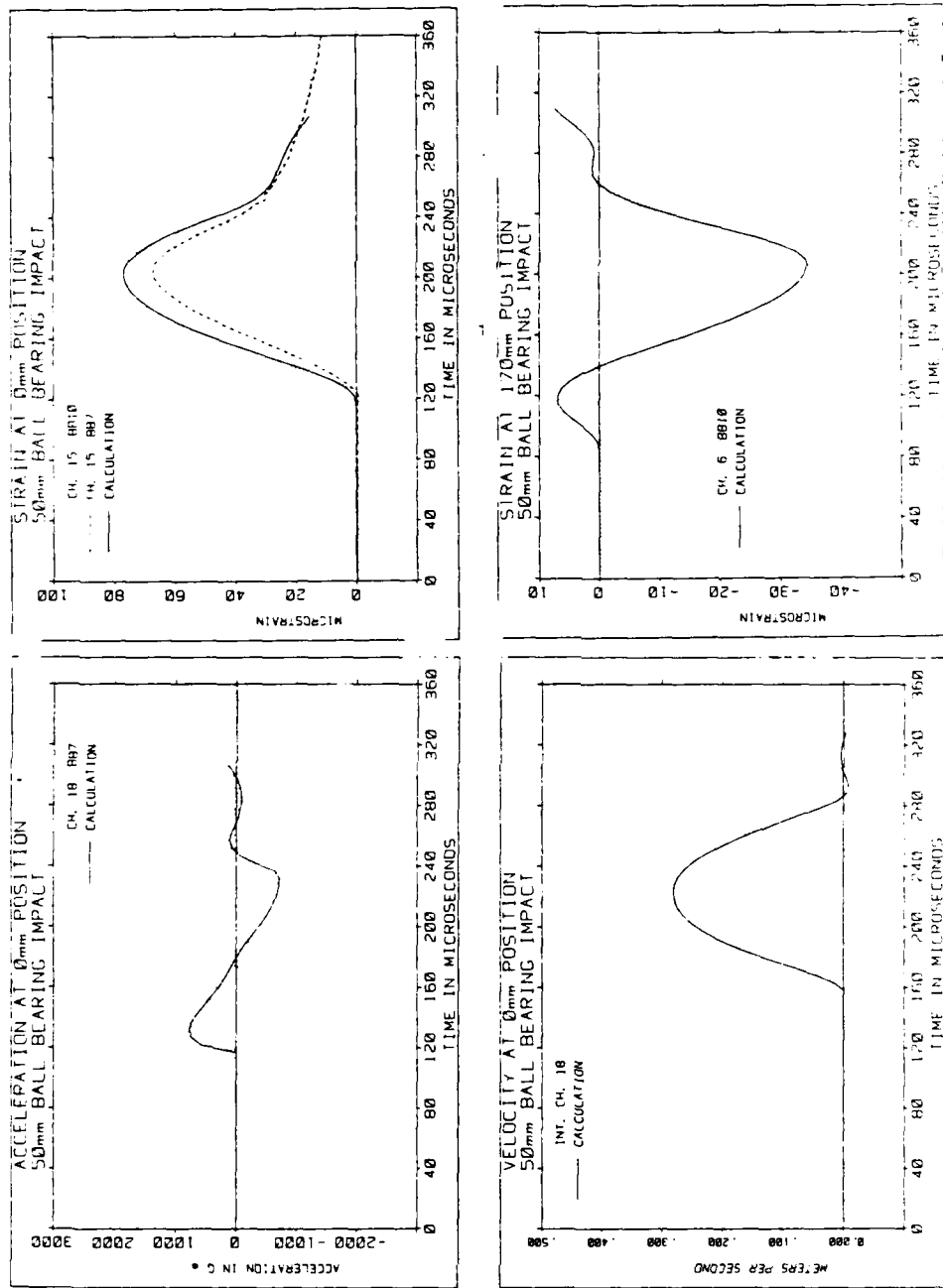


Figure 3. Measurements of Response of Plate to Ball Bearing Impact. Calculations Using Goldsmith (2) Technique.



Figure 4. Soft projectiles before and after impact at 335 meters/second. From left to right: .30 caliber ball,.50 caliber ball,20mm copper slug,and 75mm aluminum proof slug.

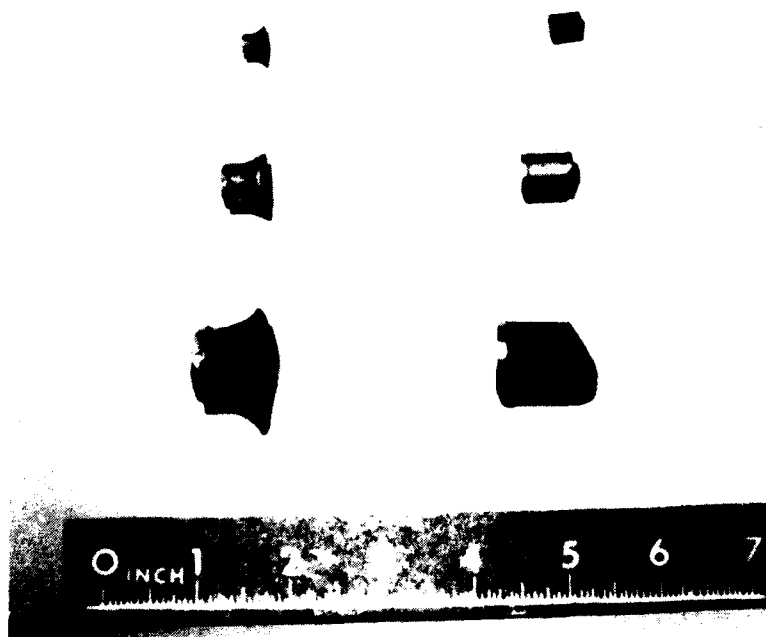


Figure 5.Fragment simulating projectiles,.30 caliber,.50 caliber,and 20mm.

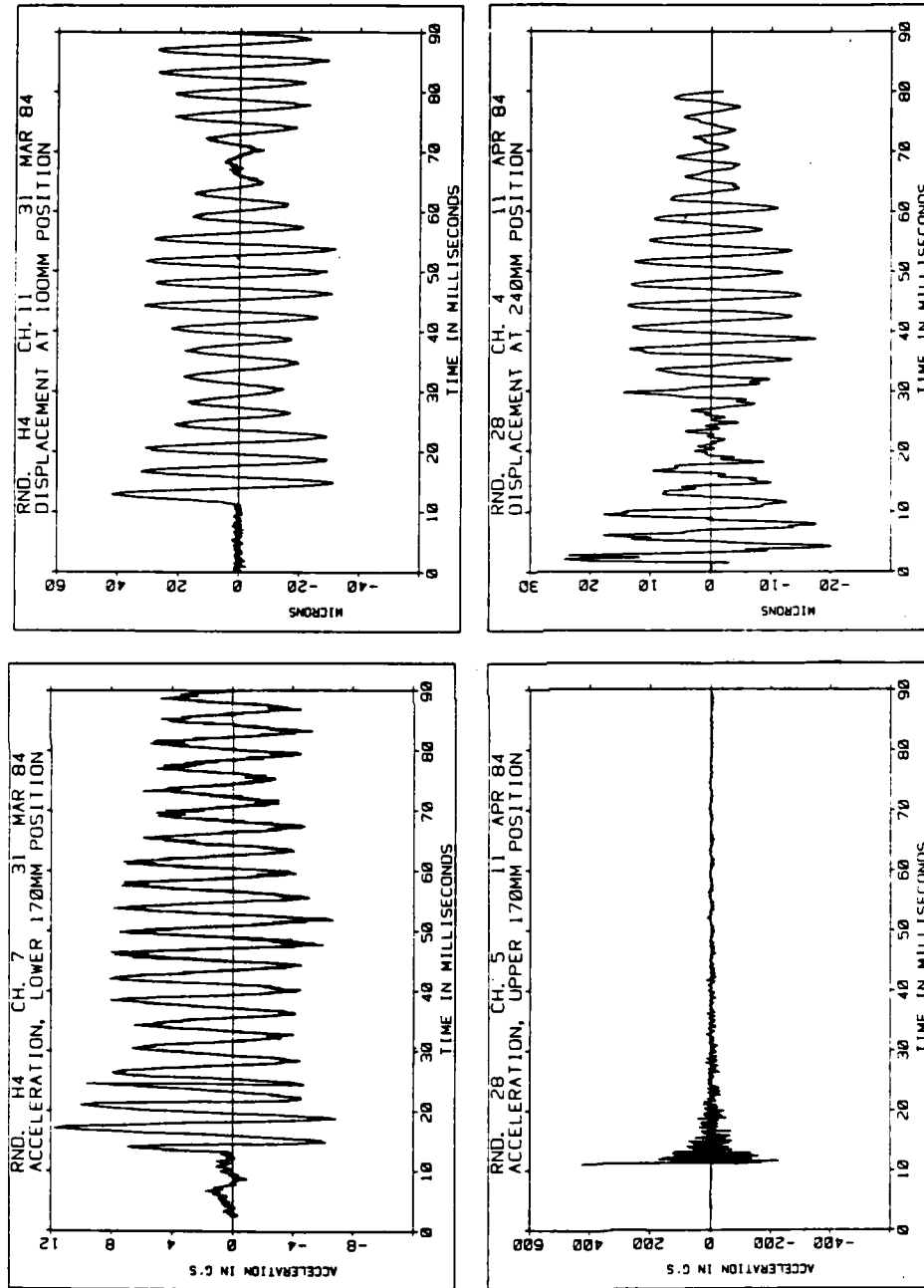


Figure 6. Long Term Response of Plate to Hammer Impact (H4) and .30 Caliber Ball Projectile Impact (Rd. 28).

WALTON

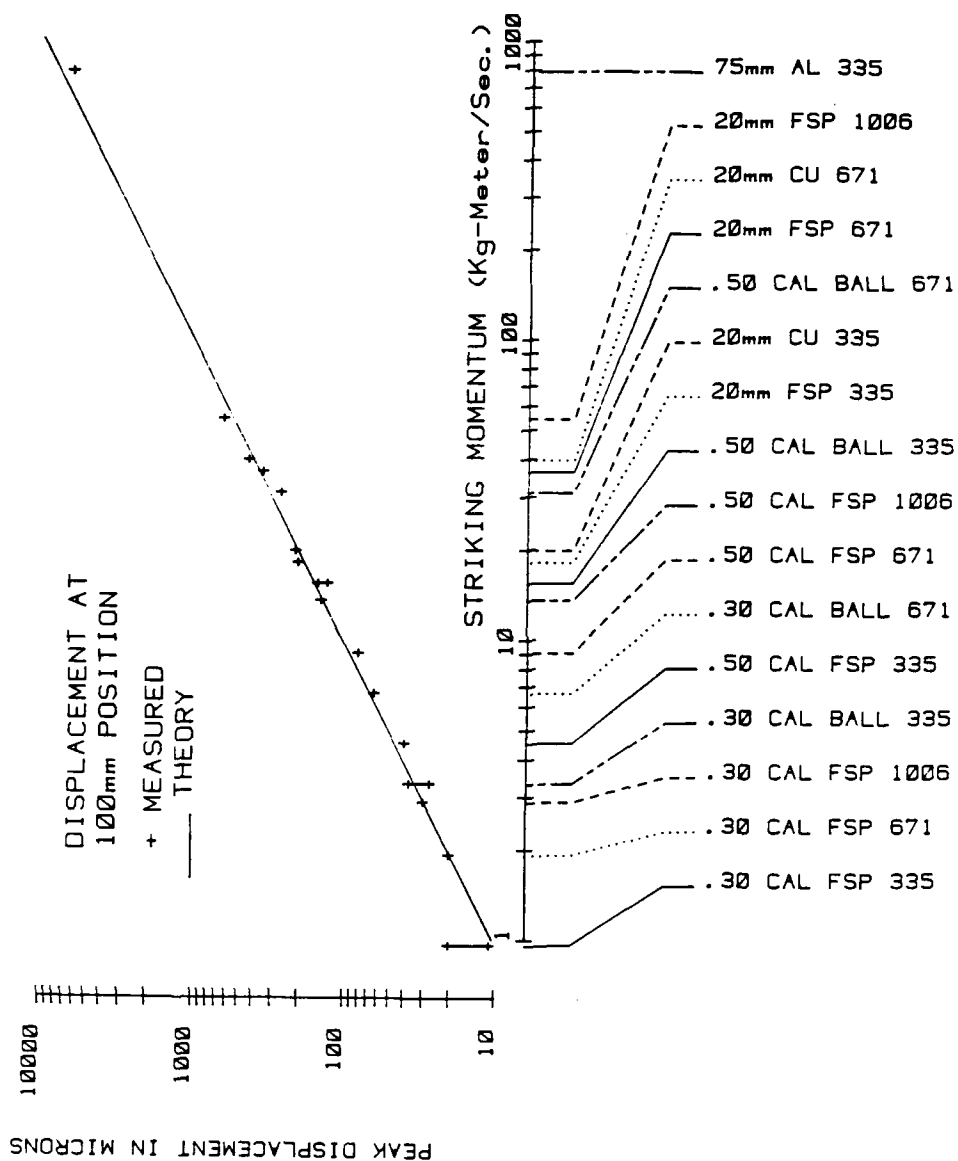


Figure 7. Correlation of Measured Peak Displacement with Momentum Prediction for Various Types of Projectiles.

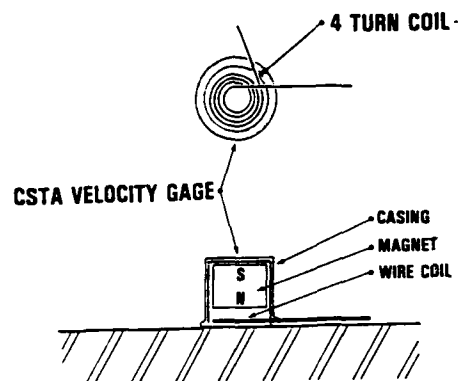


Figure 8. Schematic sketch of CSTA velocity gage. Casing is fabricated from compliant material, allowing magnet to remain stationary as coil on plate moves.

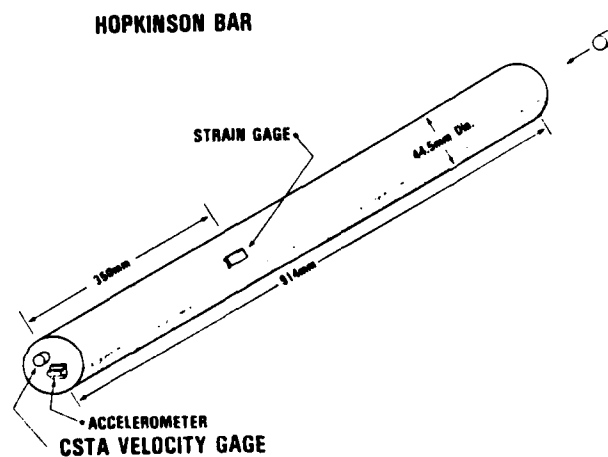


Figure 9. Sketch of instrumented Hopkinson Bar used to test CSTA velocity gage.

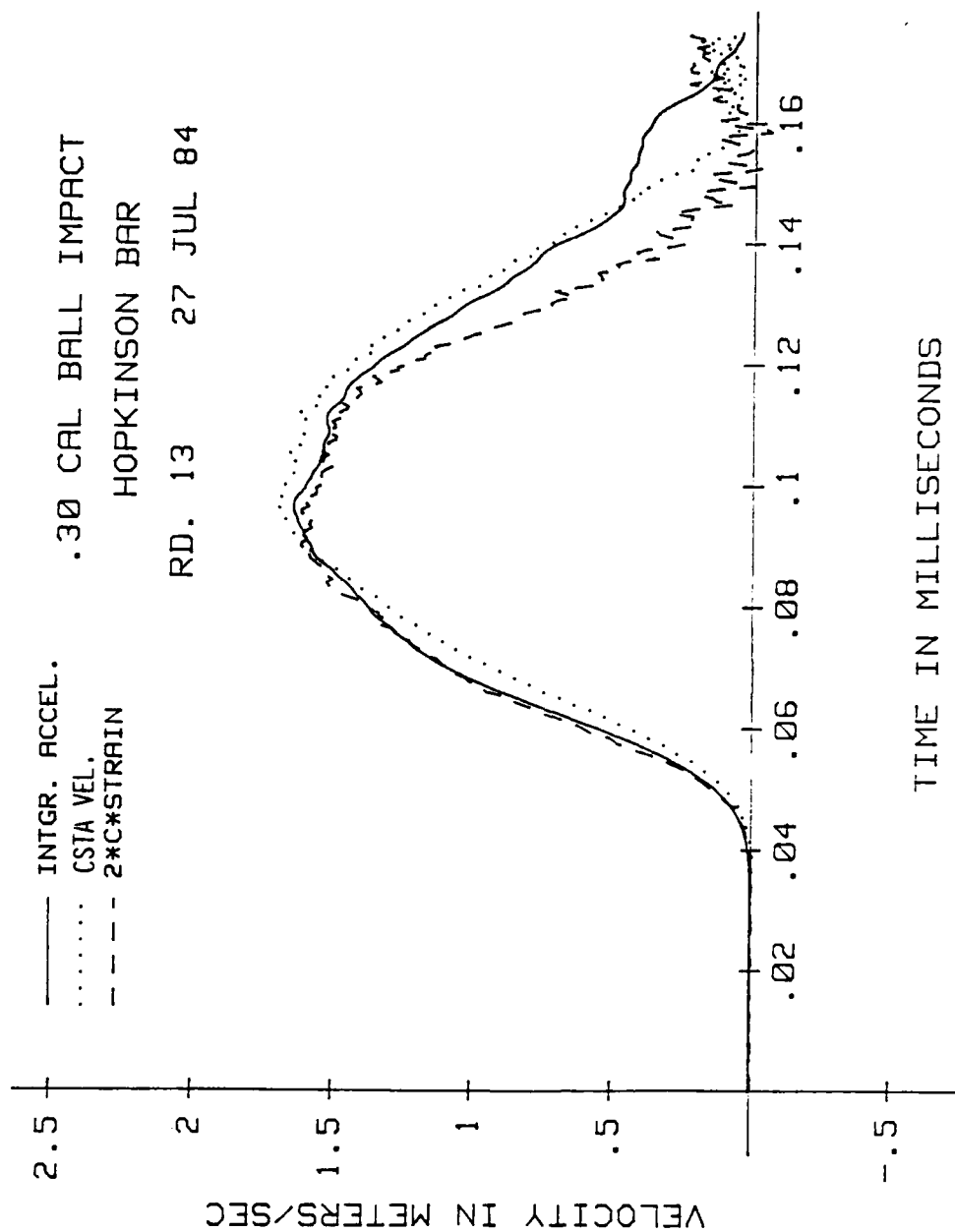


Figure 10. Comparison of CSTA velocity gage output with strain gage and integrated accelerometer measurements. Motion produced by impact of .30 caliber ball projectile (9.85 Gram) striking Hopkinson Bar at 335 meters/second.

WALTON

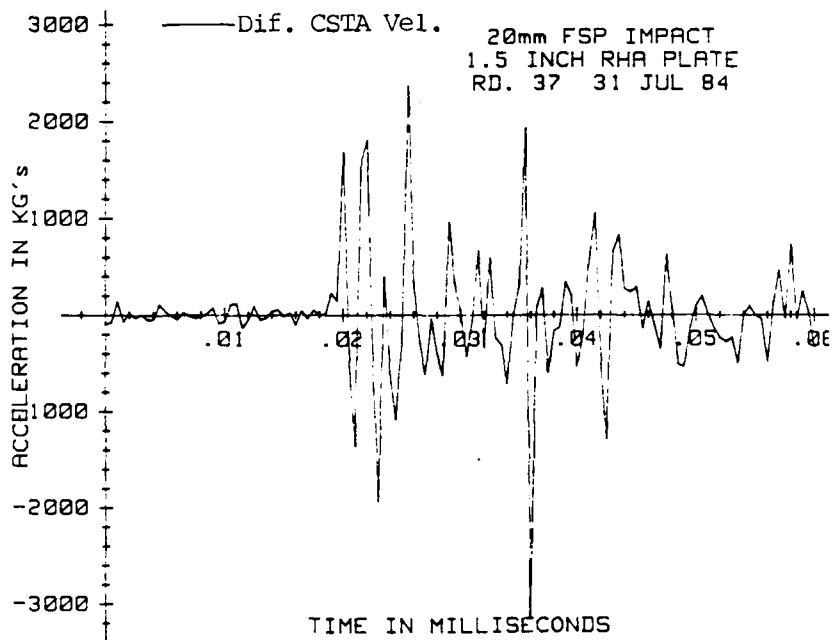
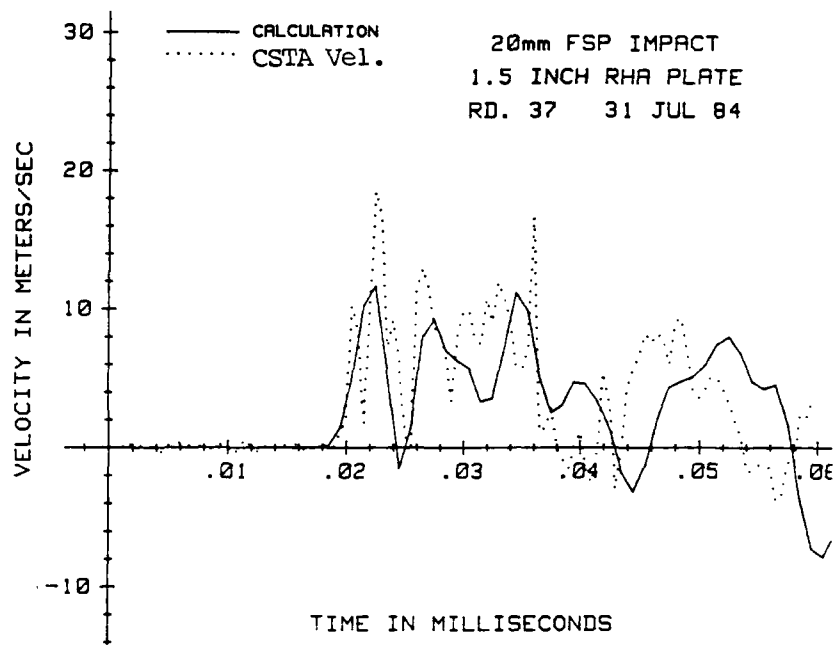


Figure 11. Velocity and acceleration measured directly behind impact point of 20mm FSP striking at 335 meters/second. Calculation performed by Quigley (7) using finite element code.

HI-TECH FIBERS FOR IMPROVED BALLISTIC PROTECTION (U)

*Janet E. Ward, Mrs. and Walter Koza, Mr.
U.S. Army Natick Research, Development and Engineering Center
Natick, Massachusetts 01760-5019

INTRODUCTION

Thousands of lives saved have proved that personnel body armor is effective in reducing combat casualties. Therefore, the Army continues to support research and development efforts to improve this type of ballistic protection for the individual soldier. Substantial gains in fragmentation protection were achieved when Kevlar[®], a high-strength aramid fiber, was identified as a superior ballistic-resistant material and replaced nylon as the state of the art in body armor.

However, to improve a soldier's mobility, lighter weight body armor systems are needed. Advances in weapons technology also require increased protection against multiple ballistic threats. Efforts to optimize the ballistic performance of Kevlar through systems engineering have potential for satisfying those needs in part. The achievement of another quantum leap in ballistic protection, like that seen in Kevlar over nylon, will most likely be accomplished through the development of hi-tech fibers.

Research groups, world wide, are pursuing the development of fibers with high strength, high tensile modulus, and high compressive modulus for the aerospace industry as well as for other low weight, high strength composite applications. Those fiber properties, essential for industrial needs, have also been shown through previous studies to be important in ballistic protective materials. Smith (1) stressed high strength, elongation, and work-to-break properties; while Laible, Figucia, and Ferguson (2) added high modulus and heat resistance to the desired properties for a better impact-resistance fiber.

Kevlar[®] is a registered trademark of E.I. duPont deNemours & Co., Inc.

By nature of the development criteria for the new hi-tech fibers, most would meet, at least in part, the physical properties for a "better" ballistic fiber. This does not automatically ensure, however, that the new materials will surpass the ballistic resistance capabilities of Kevlar. It is not known how to weight the relative importance of strength, modulus, elongation, heat resistance, and even denier per filament to ballistic resistance. This is especially true when the mechanical properties are known only for strain rates decades below those of interest. For this reason the body armor developer has a responsibility to conduct studies capable of identifying the more promising new fiber candidates.

Natick RD&E Center has developed a single yarn impact test to evaluate small amounts of fiber at ballistic speeds. This single yarn impact test and scanning electron microscopy (SEM) of the ballistically impacted yarns have been used to evaluate several new hi-tech fibers early in their development. The fiber samples were obtained through cooperative efforts with several fiber developers.

EXPERIMENTAL TEST METHOD

Single Yarn Impact Test

The Natick RD&E Center Single Yarn Impact Test has proven to be a useful method of evaluating the ballistic impact properties of textile yarn materials at an early stage in their development.

In this method, a single yarn is impacted in a crosswise direction by a speeding .22 caliber fragment simulating projectile (Figure 1) that elongates the yarn to rupture in microseconds time as illustrated in Figure 2 on the next page.



Figure 1. Fragment Simulating Projectile
.22 caliber (4.5X)

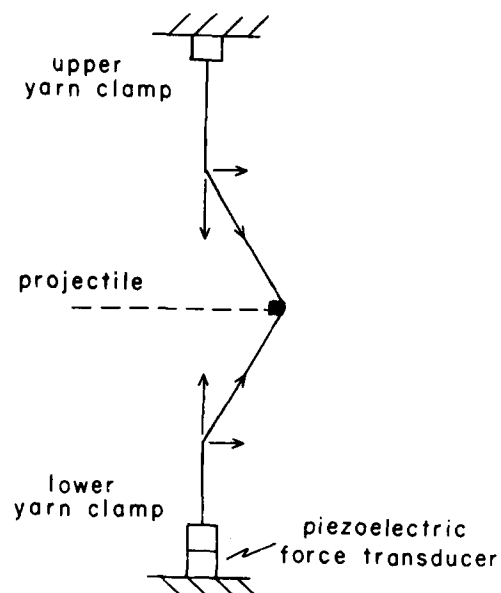


Figure 2. Schematic of Single Yarn Impact Test

During the impact process, the tensile force in the yarn is continuously measured and recorded with a piezoelectric force transducer and oscilloscope as shown in Figure 3.

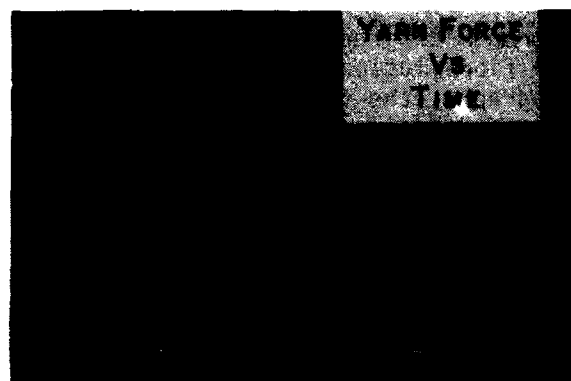


Figure 3. Oscilloscope trace showing Yarn Force vs. Time

At the same time, yarn elongation to rupture is periodically photographed by high frequency microflashes as seen in Figure 4 below. From these data, the ballistic properties of the yarn material are defined in terms of breaking tenacity, breaking elongation, time to break, initial tensile modulus, and strain wave velocity.

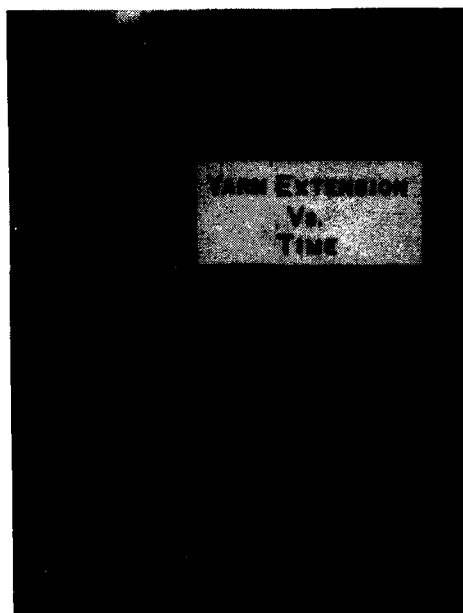


Figure 4. High Speed Photograph of Impacted Yarn
Used in Measurement of Yarn Extension vs. Time

Scanning Electron Micrographs

Scanning Electron Micrographs were used to analyze the mode of failure, melting or fibrillation, occurring in each fiber after rupture. To obtain the micrographs, the fractured ends of the impacted yarns were mounted on specimen studs using silver paint and single-faced adhesive aluminum tape. The samples were coated in a vacuum evaporator with a thin layer of gold palladium. The samples were coated for a total of 15 minutes with each being rotated approximately 120 degrees at 5-minute intervals to obtain a uniform and complete coating. The fracture patterns of the coated samples were observed in an AMR Model 1000A Scanning Electron Microscope using the secondary electron mode.

MATERIALS EVALUATED

Four new hi-tech fiber variants have been examined by the single yarn impact test and SEM procedures. The fibers were as follows:

PBT (polybenzthiazole), an experimental aromatic heterocyclic fiber developed in two forms by the U.S. Air Force -- As Spun (PBT/AS) and Heat Set (PBT/HS).

Spectra[®], an ultrahigh molecular weight polyethylene (gel spun) fiber developed by and commercially available in two forms from Allied Corporation -- Spectra 900 (S/900) and Spectra 1000 (S/1000).

Although exact methods for achieving the high modulus in the above fibers are not known, it is speculated that two separate methods were employed in achieving that property. It is our understanding that the approach taken by Allied in the production of Spectra is that of chain extension applied to a conventional polymer, in this case, polyethylene. On the other hand, the Air Force uses a different approach, that of processing liquid crystalline polymers using molecules that form thermotropic or lyotropic mesophases (3). Either method would result in extended chains and, in turn, high modulus and strength along the fiber axis.

Nylon 66 (T/728) and Kevlar 29 (K/29) yarns were also included in the evaluation as controls. Nylon was added to this evaluation for the failure mode analysis because of its low heat resistance. The acronyms in parenthesis will be used to designate fiber types in the following tables.

RESULTS AND DISCUSSION

The physical properties listed in Table 1 were obtained from static (low strain rate) tests completed by the fiber producers and are used here to illustrate the substantial improvements in physical properties of the hi-tech fibers over Kevlar and nylon. When compared directly, the properties of the four new materials are also different, especially in melting points. As shown in Table 1, the melting points of the polyethylenes are substantially lower than that of nylon.

Spectra[®] is a registered trademark of Allied Corporation.

Table 1. Physical Properties of Hi-Tech Fibers

Fiber Type	Fiber Density (g/cc)	Brkg. Ten'y (g/d)	Brkg. Elong. (%)	Initial Modulus (g/d)	Melting Point (°C)
PBT/HS	1.59	29.3	1.5	2000	370 ⁰
PBT/AS	1.58	25.4	1.8	1430	370 ⁰
S/1000	0.97	36.0	2.8	1900	147 ⁰
S/900	0.97	29.0	3.6	1400	147 ⁰
K/29	1.44	22.0	3.6	525	427 ⁰
T/728	1.14	9.8	18.2	45	254 ⁰

When the properties generated at ballistic speeds listed in Table 2 are compared to static properties of the same fibers in Table 1, significantly different values are seen. Differences between static properties and ballistic properties exist due to the added elements (cutting, flexing, and crushing) to which a specimen is exposed during ballistic testing. In this case as in most, the properties are generally lower for ballistic impact testing. More important, however, are the rates of change. In no case did the breaking tenacity or the initial modulus of the four hi-tech fibers fall below that of Kevlar. The levels of tenacities and moduli retained by the new fibers suggest the potential for substantial improvement over Kevlar in ballistic resistance capabilities.

Table 2. Ballistic Properties* of Hi-Tech Fibers

Fiber Type	Yarn Size (d)	Brkg. Ten'y (g/d)	Brkg. Elong. (%)	Initial Modulus (g/d)	Strain Wave Velocity (m/s)
PBT/HS	1808	19.6	1.4	1100	10,160
PBT/AS	1822	22.2	2.5	750	8,710
S/1000	645	24.6	2.2	840	8,710
S/900	1215	17.0	2.5	520	8,130
K/29	1502	11.2	2.6	475	6,770
T/728	1080	6.7	13.0	43	2,540

*Results of Single Yarn Impact Tests at 305 m/s.

Strain wave velocity is considered by many to be the most influential parameter in the ballistic performance of a material (4,5). It is the rapid propagation of stress away from the point of impact that incorporates more material into the impact resistance process. Strain wave velocities generated by the Single Yarn Impact Test on the four new hi-tech fibers are listed in Table 2 in descending order of expected ballistic performance. The strain wave velocities support the potential for improved ballistic performance in fabrics for all four of the new hi-tech fibers: PBT Heat Set, PBT As Spun, Spectra 1000, and Spectra 900.

Of notable interest is the earlier speculation that two different approaches were used in processing the new fibers. It appears from this preliminary analysis that either the chain extension method or the liquid crystalline method can achieve the property profile required for improved ballistic performance.

In addition to comparing the ballistic tensile properties of the evaluated fibers, the mode of failure that occurs in the new materials as a result of ballistic impact was determined. The response of PBT fibers, Heat Set and As Spun, appears to be very similar to that of Kevlar. Figures 5 and 6 illustrate the similarities of PBT As Spun and Kevlar with both demonstrating fibrillation as the form of failure.

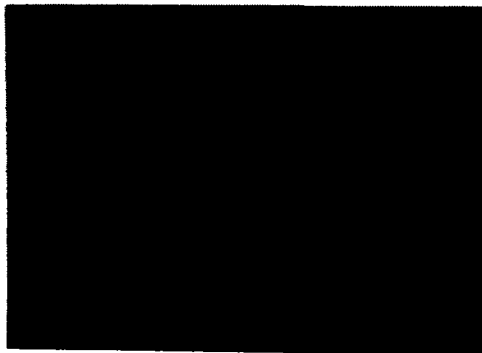


Figure 5. PBT As Spun



Figure 6. Kevlar 29

As shown in Figure 7, fusion from melting is extremely evident at the point of rupture on nylon fibers. That failure mechanism is commonly attributed to the low melting point of nylon. However, the other fiber of this group with an even lower melting point does not demonstrate the same failure trends as nylon. The polyethylene fiber, as seen in Figure 8, shows only slight evidence of fusion. Its high modulus to density ratio appears to increase its ability to respond quickly to high speed impact, thereby mitigating the extreme localized deformation (6). The high-modulus polyethylenes appear to have the capacity for plastic deformation which should be advantageous for improved ballistic behavior. Interpretation of results in Table 2 and the above SEM analysis shows that the low melting point of the polyethylene fiber has little effect on the ballistic resistance capabilities of that material.



Figure 7. Nylon 66



Figure 8. Spectra 900

As indicated earlier in this paper, the ballistic evaluations being reported are preliminary, but provide a reliable indication as to the ballistic performance potential of a new fiber. Conclusions drawn from the single yarn impact test and SEM analysis will determine when additional testing will be accomplished on the fiber in woven fabric and/or laminate form. For any new candidate ballistic fiber, the next phase of the evaluation would include the establishment of a V50 ballistic limit, the velocity at which 50% of a simulated threat completely penetrates a target material. Given satisfactory V50 results, a casualty reduction analysis would be conducted to validate the improved ballistic performance. The casualty reduction analysis is the final phase in the ballistic evaluation of a new material. The analysis provides an indication as to the relative percentages by which current and new materials reduce casualties in a given battlefield scenario.

It is well documented (7,8) that obtaining the maximized ballistic potential of a material in a fabric or non-woven form requires considerable research and development work in yarn geometry, fabric geometry, systems engineering, and surface modifications, as well as in other areas. The objective is to maximize filaments in the target impact cross-section. Improved theoretical models are being developed to help in the transitioning process.

CONCLUSIONS

There is a high priority requirement for lighter weight armor systems with improved protection against multiple ballistic threats.

A quantum leap in ballistic protection over that of Kevlar may be accomplished through new hi-tech fibers. The best source for such hi-tech fibers are the research and development efforts of producers of fiber products for use in aerospace and in low weight, high strength composite material applications.

Natick RD&E Center has developed a single yarn impact test to predict the ballistic potential of hi-tech fibers. Four new hi-tech fibers have been evaluated. Based on the single yarn impact test results, all four fibers, PBT As Spun, PBT Heat Set, Spectra 900 and Spectra 1000, have potential for substantial improvement in ballistic protection.

The next stage for these candidate materials includes V50 and casualty reduction analyses as well as studies in yarn geometry, fabric geometry, surface finishing, and systems engineering.

Natick RD&E Center will continue to maintain an awareness of new or emerging hi-tech fibers, evaluate their ballistic potential via our screening tests, and plan further ballistic evaluations as warranted.

ACKNOWLEDGEMENTS

Work reported here reflects a continuing research effort in ballistic fibers. The authors wish to acknowledge F. Figucia, B. Kirkwood, R.C. Laible, and C.R. Williams for their significant contributions in this area. The authors express their appreciation to M. Goode and C. Blouin for the excellent SEM Micrographs used in this report.

REFERENCES

1. Smith, Jack C. "Characterization of Textile Yarns for Use Under Ballistic Impact Conditions", Symposium on Personnel Armor, U.S. Naval Laboratory, Vol 1 (October 1961)
2. Laible, R.C., Figucia, F., and Ferguson, W. "The Application of High-Modulus Fibers to Ballistic Protection", J. Macromol. Sci. Chem. A7(1): 295-322 (1973)
3. Adams, W.W. "The Morphology of High-Modulus Fibers", Polymer Preprints 26(2) 306-7 (1985)
4. Figucia, F., Williams, C., Kirkwood, B., and Koza, W. "Mechanisms of Improved Ballistic Fabric Performance", Paper Presented at Gordon Conference on Fiber Science (1980)
5. Koza, W. "Experimental Method to Measure the Ballistic Properties of Textile Yarn Materials", U.S. Army Natick Research Development and Engineering Center, Unpublished Study at NRD&EC (STRNC-ITFR) (1980)
6. Laible, R.C., Figucia, F., and Kirkwood, B. "Scanning Electron Microscopy as Related to the Study of High-Speed Fiber Impact", TR73-58-CE, U.S. Army Natick Laboratories (October 1973) (AD 768 766)
7. Figucia, F. "The Effect of Kevlar Fabric Construction on Ballistic Resistance", TR75-103CE, U.S. Army Natick Development Center (April 1975)
8. Laible, R.C. (Ed.). Ballistic Materials and Penetration Mechanics. Vol 5 of Methods and Phenomena: Their Applications in Science and Technology, Elsevier Scientific Publishing Company, The Netherlands (1980)

SIMULATION OF THE SUPERSONIC FLOW ABOUT FINNED PROJECTILES (U)

PAUL WEINACHT, MR.* AND WALTER B. STUREK, DR.
US ARMY BALLISTIC RESEARCH LABORATORY
ABERDEEN PROVING GROUND, MARYLAND 21005-5066

I. INTRODUCTION:

The Aerodynamics Research Branch, Launch and Flight Division, has been actively developing the capability to predict the aerodynamics of US Army projectiles using Computational Fluid Dynamics (CFD) techniques. Successful prediction of the Magnus force for a spinning artillery projectile at supersonic velocities is a prime example of the powerful nature of these techniques (1,2). The eventual goal of CFD techniques is to allow the projectile designer to compute the flow field about projectiles accurately and efficiently resulting in improved performance of future projectile designs.

Currently under development is the capability to predict the supersonic aerodynamics of finned missiles such as kinetic energy (KE) penetrators (3,4). Kinetic energy penetrators are long length to diameter ratio finned projectiles which are used to defeat armored targets by punching holes through the armor. Their armor piercing capability results from the high speed (Mach 3 to Mach 5) of the high density rod housed inside the body. In contrast to conventional spin-stabilized shell configurations, KE penetrators rely on fins to remain aerodynamically stable.

The presence of the fins on these bodies and their long length presents a significant challenge to the researchers developing predictive capabilities. A shadowgraph of a KE penetrator in flight at Mach 4.3 is shown in Figure 1 and displays some of the relevant features of the flow field; a bow shock wave emanating from the nose of the projectile, expansion waves at the cone-cylinder junction, shocks at the leading edge of the fins, and a turbulent viscous boundary layer on the body which becomes quite thick as a result of the long body length. The ability to predict these features of the flow field is inherent to the development of a predictive capability for these projectiles.



Figure 1. Shadowgraph of KE Penetrator

Discussed here are computations for the supersonic flow about two finned configurations which resemble the M735 KE projectile. Computations have been performed over a range of supersonic Mach numbers and comparisons made with experimental range and wind tunnel measurements to assess the predictive capabilities.

Computations have been performed using several computational techniques; the parabolized Navier-Stokes (PNS) technique, the unsteady Navier-Stokes (UNS) technique, and two inviscid approaches. In each of these computational procedures, the governing partial differential equations are discretized using finite-difference methods and the resulting equations solved on a large scientific processor such as the CRAY X-MP supercomputer. Both the PNS and UNS techniques solve the thin-layer Navier-Stokes equations allowing viscous effects to be modeled, though they differ somewhat in their solution procedures. The inviscid approaches, while computationally more efficient than the PNS and UNS techniques, are limited in their range of applicability in that viscous components of drag and the surface heat transfer due to aerodynamic heating can not be obtained directly using these techniques. The application of these various techniques allows the capabilities and requirements of each of these approaches to be evaluated.

II. COMPUTATIONAL TECHNIQUES

Computation of the inviscid or viscous flow fields about the finned projectile configurations is accomplished by solving the Euler equations or the thin-layer Navier-Stokes equations using one of several numerical procedures. Discussion of the governing equations and the numerical techniques is provided below.

A. Euler and Thin-Layer Navier-Stokes Equations

The set of equations that describes three-dimensional compressible viscous flow is referred to as the Navier-Stokes equations. The Navier-Stokes equations express the conservation of mass, momentum and energy in

the three coordinate directions. This set of nonlinear partial differential equations is expressed below in conservative form.

$$\frac{\partial q}{\partial t} + \frac{\partial E}{\partial x} + \frac{\partial F}{\partial y} + \frac{\partial G}{\partial z} = \frac{\partial E_v}{\partial x} + \frac{\partial F_v}{\partial y} + \frac{\partial G_v}{\partial z} \quad (1)$$

Here, E , F and G are the inviscid flux vectors, and E_v , F_v and G_v are the viscous matrices, which are functions of the dependent variables represented by the vector, $q(\rho, \rho u, \rho v, \rho w, e)$ where ρ is the density, u , v , w , are the velocity components in the three spacial directions, x , y and z , and e is the total energy per unit volume. Closure of this set of equations is obtained by applying the ideal gas law, which allows the pressure to be related to the dependent variables.

Due to the complicated geometry of finned projectiles, the governing equations are transformed into generalized coordinates which allows the equations to be solved in a more uniform computational domain, as illustrated in Figure 2. The transformed governing equations are written below:

$$\frac{\partial}{\partial \xi} \left(\frac{q}{J} \right) + \frac{\partial}{\partial \eta} \left(\frac{\hat{E}}{J} \right) + \frac{\partial}{\partial \zeta} \left(\frac{\hat{F}}{J} \right) + \frac{\partial}{\partial \zeta} \left(\frac{\hat{G}}{J} \right) = \frac{\partial}{\partial \xi} \left(\frac{\hat{E}_v}{J} \right) + \frac{\partial}{\partial \eta} \left(\frac{\hat{F}_v}{J} \right) + \frac{\partial}{\partial \zeta} \left(\frac{\hat{G}_v}{J} \right) \quad (2)$$

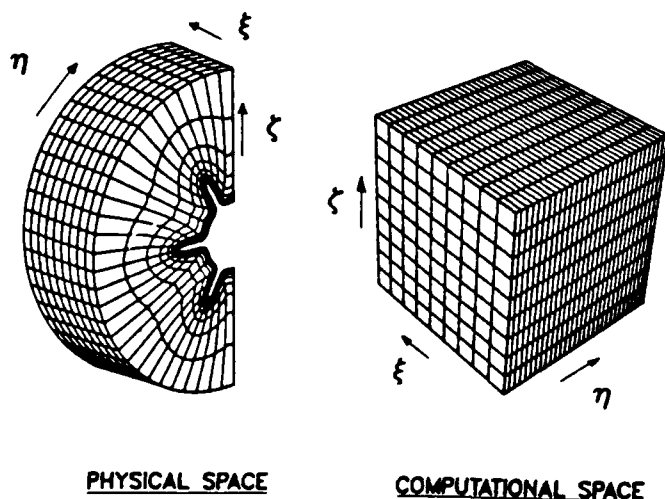


Figure 2. Schematic of Coordinate Transformation

where ξ , η , ζ are the generalized coordinate variables as displayed in Figure 2. The transformation results in additional terms, called metric terms, which describe the transformation from the complex physical space to the simpler computational space. While these metric terms complicate the governing equations to a small degree, they permit the governing equations to be applied to a variety of projectile shapes with little or no change to the basic numerical algorithms.

WEINACHT, STUREK

The thin-layer Navier-Stokes equations may be obtained from the more complete Navier-Stokes equations by retaining only the viscous terms in the direction normal to the body. For high Reynold's number flows, this is a valid approximation since these terms are usually large in relation to the other viscous terms. The governing thin-layer Navier-Stokes equations are expressed below

$$\frac{\partial}{\partial t} \left(\frac{q}{J} \right) + \frac{\partial}{\partial \xi} \left(\frac{\hat{E}}{J} \right) + \frac{\partial}{\partial \eta} \left(\frac{\hat{F}}{J} \right) + \frac{\partial}{\partial \zeta} \left(\frac{\hat{G}}{J} \right) = \frac{\partial}{\partial \zeta} \left(\frac{\hat{S}}{J} \right) \quad (3)$$

By invoking the thin-layer assumption, efficient implicit numerical algorithms can be developed to solve these equations.

The inviscid flow equations or Euler equations are obtained by eliminating the viscous terms entirely as shown below.

$$\frac{\partial}{\partial t} \left(\frac{q}{J} \right) + \frac{\partial}{\partial \xi} \left(\frac{\hat{E}}{J} \right) + \frac{\partial}{\partial \eta} \left(\frac{\hat{F}}{J} \right) + \frac{\partial}{\partial \zeta} \left(\frac{\hat{G}}{J} \right) = 0 \quad (4)$$

For non-separated, high Reynolds number flows, viscous effects are confined to a very thin region near the body, called the boundary layer. The bulk of the flow field can often be accurately predicted by ignoring the viscous effects in this region. From the inviscid flow field, many of the aerodynamic parameters of interest to the projectile designer can be determined. One such parameter is the pitching moment which influences the stability of a projectile. On the other hand, important parameters such as viscous drag and surface heat transfer can only be determined from a viscous flow field computation. Solution of the Euler equations can be performed in a more efficient manner compared with the thin-layer Navier-Stokes or complete Navier-Stokes equations. This is because (1) the complex viscous terms do not have to be calculated and (2) significantly fewer grid points are required since the thin viscous region near the body does not have to be resolved.

B. Finite-Difference Technique

The Euler equations and the thin-layer Navier-Stokes equations are coupled sets of nonlinear partial differential equations, which in general, can be solved only by approximate means. Currently, finite-difference methods are widely used for solving partial differential equations, such as the Euler and thin-layer Navier-Stokes equations. Using finite-difference methods, the governing partial differential equations are discretized on regular ordering of points throughout the flow field. This regular ordering of points is often referred to as a

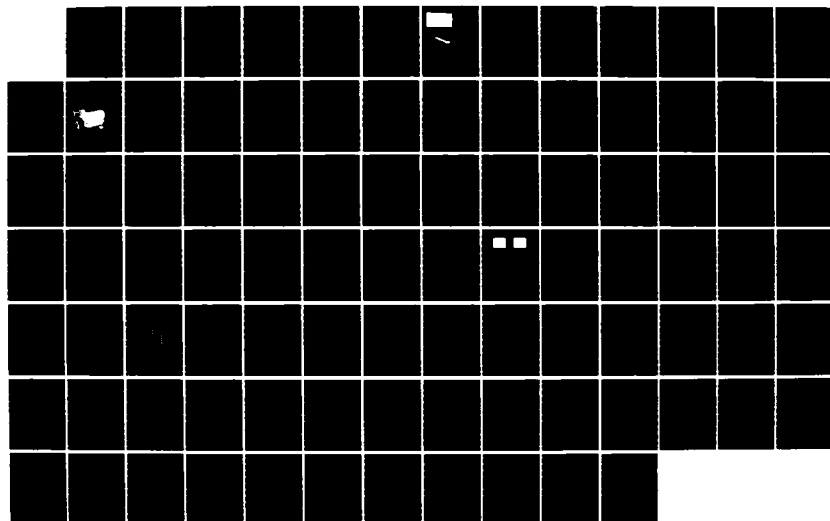
AD-A173 682

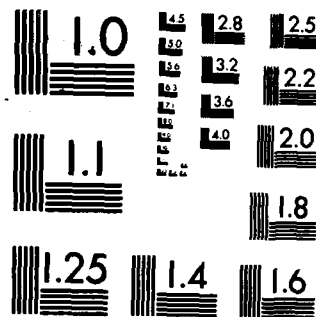
PROCEEDINGS OF THE ARMY SCIENCE CONFERENCE (15TH) HELD
IN WEST POINT NEW. (U) DEPUTY CHIEF OF STAFF FOR
RESEARCH DEVELOPMENT AND ACQUISITIO.. J SAHU ET AL.
20 JUN 86 F/G 5/2

4/84

UNCLASSIFIED

NL





MICROCOPY RESOLUTION TEST CHART
NATIONAL BUREAU OF STANDARDS-1963-A

computational mesh or grid. As a result of the discretization, the governing partial differential equations are transformed to a large set of algebraic equations, which are more readily solved on a large scientific processor, such as the Cray X-MP supercomputer.

C. Numerical Techniques

The development of predictive capabilities for projectiles has been focused on calculating the steady or time-independent flow. That is to say, each computation is performed for given projectile at a single fixed speed and attitude. To compute the steady flow over a body in the supersonic flight regime, there are two types of approaches that can be used: (1) space-marching techniques or (2) time-marching techniques.

Space-marching procedures, which are only applicable in the supersonic flight regime, solve the time-independent governing equations. The time-independent governing equations are obtained by simply dropping the dq/dt term in Equations 2-4. These equations are then solved starting near the nose of the projectile and the solution integrated or marched down the body, solving for the flow field at a single axial location at a time. The computation is complete when the flow field at the aft end of the projectile has been computed.

In contrast to space-marching techniques, time-marching or unsteady procedures involve marching the solution in time until a steady-state or time-independent (converged) solution is obtained. The unsteady technique is applicable to a larger class of problems than space-marching techniques, in that the requirements of supersonic external flow and no axial flow separation are removed. Additionally, effects such as upstream influence can be predicted using time-marching procedures. Time-marching procedures are, however, more computationally intensive than space-marching procedures in terms of both memory requirements and CPU time. Generally speaking, time-marching procedures require that the entire flow field be loaded into memory throughout the computation, while space-marching procedures require only two or three axial planes of data in main memory at any one time during the computation. Additionally, unsteady procedures require many iterations or sweeps through the grid until a converged solution is obtained, in contrast to space-marching techniques which require a single axial sweep through the grid.

In the results that are discussed in the paper a total of four computational procedures have been applied; consisting of three space-marching techniques and one time-marching technique. Each of these computational techniques are briefly discussed below.

D. Parabolized Navier-Stokes (PNS) Procedure

The Parabolized Navier-Stokes (PNS) technique of Schiff and Steger (5) is used to compute the supersonic viscous flow about many flight vehicles by solving the steady thin-layer Navier-Stokes equations using a spacing-marching procedure. Following the approach of Schiff and Steger (5), the governing equations are solved using a conservative, approximately factored, implicit finite-difference numerical algorithm as formulated by Beam and Warming (6).

E. Inviscid PNS Procedure

The numerical algorithm used to solve the PNS equations can also be applied to solve the steady Euler equations. Here, the viscous portion of the equations are simply set to zero and an inviscid flow surface boundary condition procedure applied at the body surface (7).

F. SWINT Inviscid Procedure

The SWINT code (8)- SWINT is an acronym for Supersonic Wing INlet Tail - solves the Euler equations using a space-marching procedure based on the explicit McCormack method. The procedure has the capability for computing the inviscid flow over bodies with fins and/or wings, and for the external flow about bodies with inlets. In contrast to the other numerical procedures examined here, treatment of the fin geometry is performed in a somewhat approximate manner, in that the surface grid does not conform to the fin geometry exactly. The code makes use of the thin-fin approximation, collapsing each fin along radial planes in the grid. The local slope of the fin geometry can be accounted for in the code by application of shock compression and Prandtl-Meyer expansion theories. The fin edges must be sharp and cannot extend beyond the bow shock.

G. Unsteady Thin-Layer Navier-Stokes Procedure (UNS)

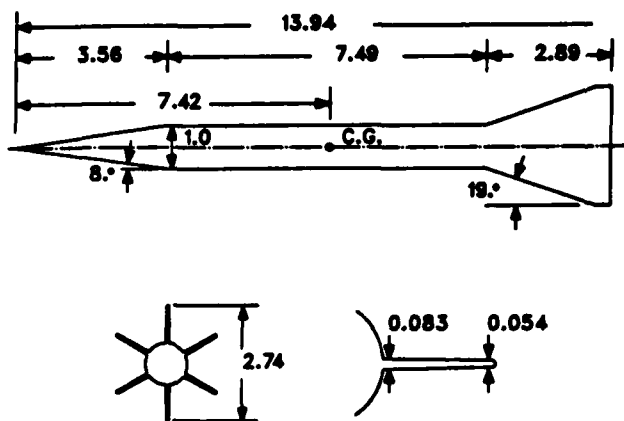
The time-marching approach used here is referred to as the UNS technique. In the UNS technique, the time-dependent thin-layer Navier-Stokes equations are solved using a conservative, approximately factored, implicit finite-difference numerical algorithm as formulated by Beam and Warming (6). Much of the initial development of the UNS technique was performed by Pulliam and Steger (9). The current version of the code has been improved by Rizk and others (10).

III. RESULTS

A. M735 Finned Projectile Configuration

The finned body configuration for which calculations have been performed resembles closely the M735 Army projectile. The modeled finned body configuration is characterized by a conical nose section joined to a smooth cylindrical main body with six symmetrical swept fins attached to the aft section of the projectile. Figure 3 displays the basic dimensions of this configuration. The actual projectile differs from the modeled projectile in that: (1) the actual projectile has circumferential grooves over much of the cylindrical portion of the body to prevent the sabot from sliding off the body in the gun tube; (2) fins which have a non-symmetrical sectional geometry to induce roll; and (3) a slightly rounded nose. Modeling the projectile with a sharp nose and symmetrical fin section are not the result of inherent limitations of the computational model, but rather a matter of convenience for these initial calculations. While modeling of the sabot grooves may be possible using surface blowing, wind tunnel results have shown that such grooves have almost no effect on the value of normal force and pitching moment. These grooves do, however, have a noticeable effect on drag, particularly at higher angles of attack (11).

Results were obtained for this finned configuration using the PNS, inviscid PNS, and SWINT numerical procedures. Results are presented here for Mach numbers 3, 4 and 5, and two degrees angle of attack. The PNS computations were run for atmospheric flight conditions and a turbulent



ALL DIMENSIONS IN CALIBERS (ONE CALIBER = 35.2 mm)

Figure 3. M735 Kinetic Energy Penetrator

boundary layer over the body. Calculations were made with two of the fins oriented vertically, enabling a half plane of symmetry to be applied.

Figure 4 shows the development of the normal force coefficient over the body as predicted by the PNS and SWINT codes. The normal force coefficient shows a moderate contribution due to the conical nose and cylindrical portion of the body and larger contribution due to the finned portion of body. Development of the normal force as predicted by the PNS and SWINT codes

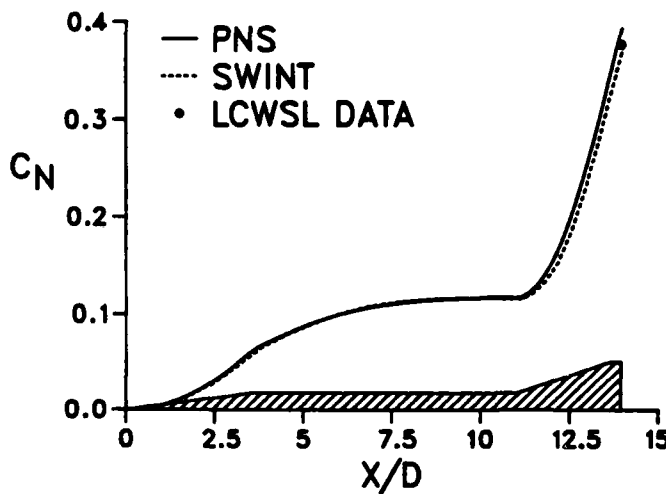


Figure 4. Development of Normal Force Coefficient, Mach 4, $\alpha = 2^\circ$

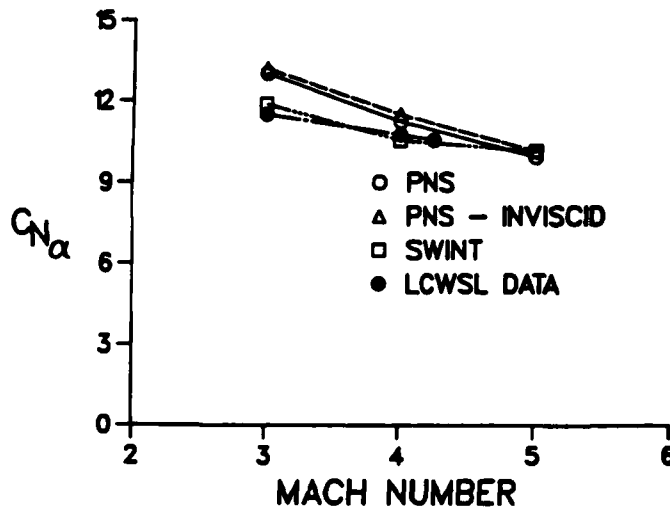


Figure 5. Slope of Normal Force Coefficient versus Mach Number

the center of gravity shown in Figure 3.) The predicted values from the PNS, inviscid PNS and SWINT codes are compared with values obtained from range firings. The PNS and inviscid PNS codes are seen to predict slightly larger values of normal force and pitching moment compared with the range data and SWINT code predictions at Mach 3 and 4. Good agreement between the predictions from each of the three techniques is seen at

compare well, particularly over the cone-cylinder portion of the body. For bodies with L/D 's greater than the current configuration, differences in the viscous (PNS) and inviscid (SWINT) code predictions can be expected due to viscous effects. (Previously obtained results (4) show little effect of Reynolds number at L/D 's less than about 12.) Over the finned portion of the body, slightly more lift is being predicted in PNS computation than in the SWINT result. Good agreement between the total value of normal force for both procedures is seen compared with the range data (12). Though not shown in this figure, very little difference in the predicted development of the normal force was observed using the PNS and inviscid PNS techniques.

The variation in the slope of the normal force and pitching moment coefficients with Mach number is shown in Figures 5 and 6. Pitching moment here has been referenced to

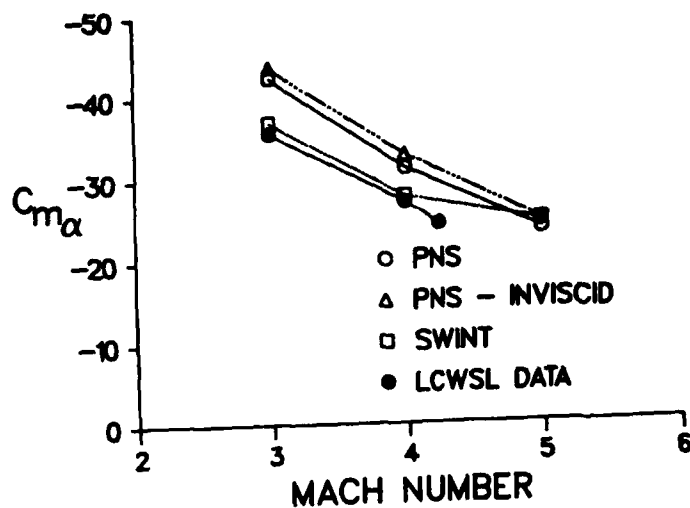
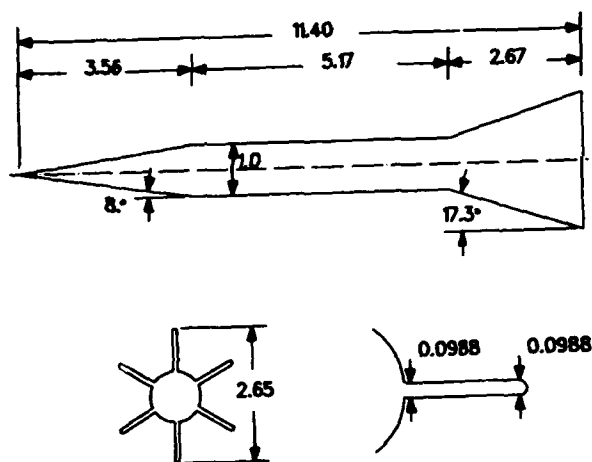


Figure 6. Slope of Pitching Moment Coefficient versus Mach Number

Mach 5. Differences in agreement between the PNS and inviscid PNS codes and the SWINT code predictions at Mach 3 and 4 occur almost entirely over the finned portion of the body and can be attributed to the differences in the computational modeling of the fin geometry. While a detailed implementation of the fin geometry is still required in each of the CFD codes, the basic capability for predicting the pitch-plane coefficients for finned bodies has been established.



ALL DIMENSIONS IN CALIBERS - ONE CALIBER = 10.2 CM

Figure 7. NYU Finned Configuration

B. NYU Finned Configuration

A second set of computational results has been obtained for a finned projectile configuration which is similar to the M735 projectile configuration in many respects. A schematic of the finned configuration is shown in Figure 7. Computations for the configuration have been performed using two computational techniques; the parabolized Navier-Stokes (PNS) technique and the unsteady Navier-Stokes (UNS) technique. Results have been obtained for a freestream Mach number of 6.3 and zero degrees angle of attack.

Wind tunnel tests (13) for this configuration are also currently under way at the New York University Antonio Ferri Laboratories and are being sponsored by the Army Research Office. The focus of the tests is to obtain pressure and heat transfer measurements and oil flow visualization in the vicinity of the fins. It is hoped that the data from these wind

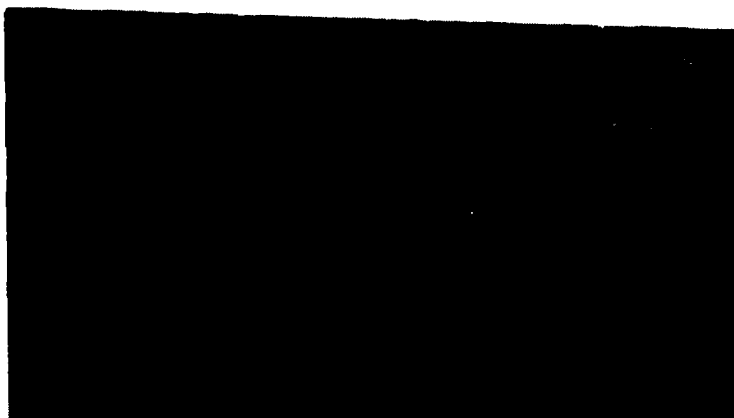


Figure 8a. Experimental Oil Flow Visualization

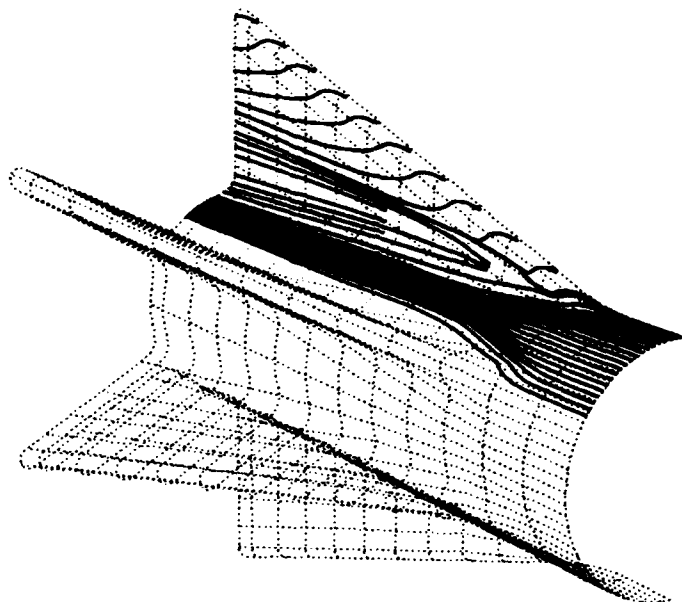


Figure 8b. Oil Flow Visualization from Computed Flow Field

particle paths on the body. Oil flow visualization from the computed PNS flow field has been performed and is shown in Figure 8b. The corresponding experimental oil flow patterns are seen in Figure 8a.

Distinct corner flow regions at the fin root-cylinder junctions are visible in both the experimental and computed oil flow visualizations.

tunnel tests can be used to help validate the previously discussed computer codes. At this time, the tests are still in progress. Some of the experimental data from this test are used here to compare with the computed results.

1. Flow Visualization

As was discussed above, oil flow visualizations were performed as part of the wind tunnel tests. Oil flow visualization is performed experimentally by placing small oil droplets on the projectile body, and then allowing the motion of the fluid near the body to move the droplets. After the test is complete the path of the droplets is visible on the projectile body. Oil flow visualization can also be simulated using the computed flow field. Massless particles are placed at various points on the body and, using the computed flow field near the body, the equations of motion of the particles are integrated to determine the

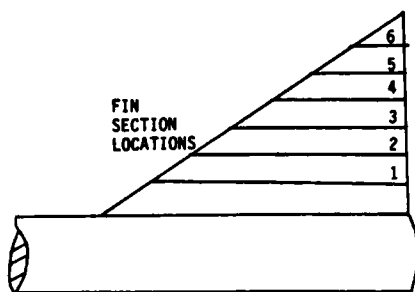


Figure 9. Fin Planform

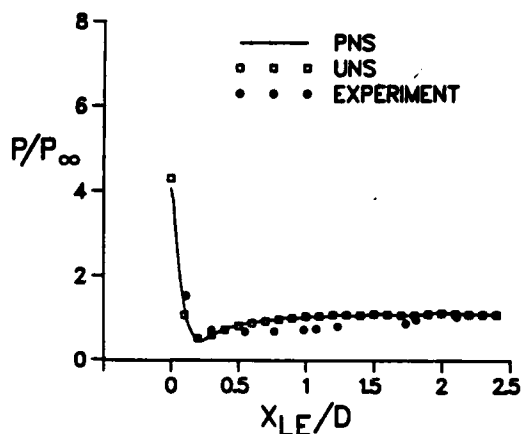


Figure 10a. Chordwise Pressure Distribution (Section 1)

Near the fin leading edges the flow appears to turn nearly normal to the fin leading edge as the flow expands around the leading edge. After passing the leading edge, the flow direction changes back to the main flow direction.

2. Surface Pressure

Surface pressure distributions in the vicinity of the fins have been obtained from the computed flow fields using both the PNS and UNS techniques and are compared with the available experimental pressure data. Figure 9 shows a planform view of the six chordwise locations of pressure taps.

Figures 10a, b, c display the experimental and computed chordwise pressure distributions at section 1, 3 and 5. High pressure due to the flow compression is seen at the leading edge, followed by a sharp drop as the flow expands around the leading edge.

Very good agreement is seen between the computed pressures using the PNS and UNS techniques. Only slight differences are evident in the computed results near the leading edge and in the region where the flow expands around the leading edge. The computed results seem to show only small deviations in the chordwise pressure distribution between sections 3 through 6, indicating the two-dimensional nature of the flow further away from the body. Section 1, appears to be within the thick boundary layer on the cylindrical portion of the body due to the lower leading edge pressure.

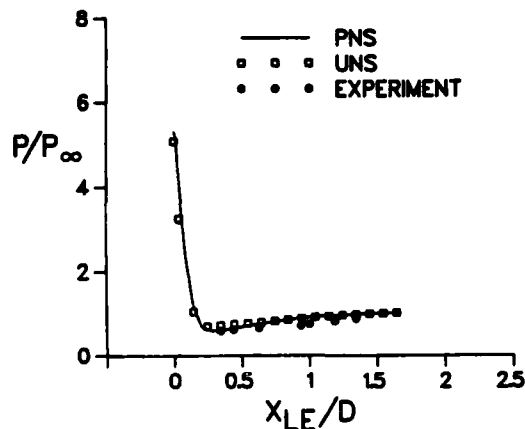


Figure 10b. Chordwise Pressure Distribution (Section 3)

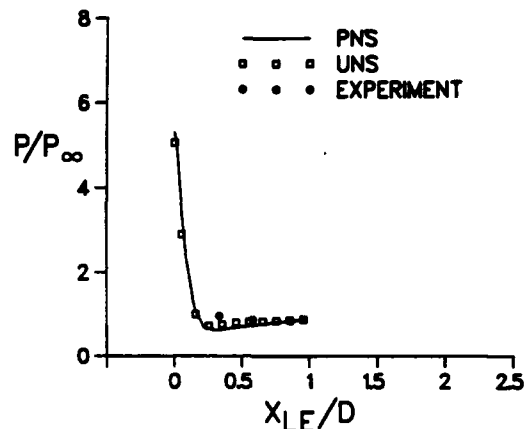


Figure 10c. Chordwise Pressure Distribution (Section 5)

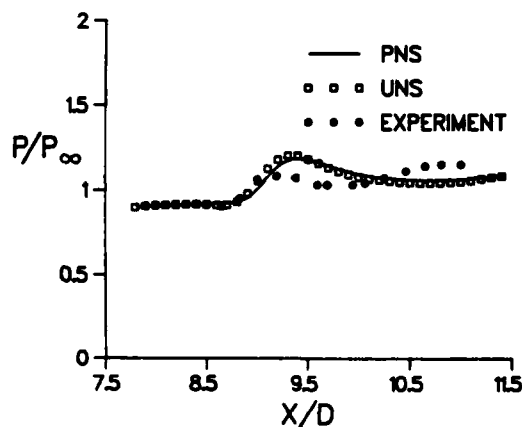


Figure 11. Axial Pressure Distribution on Cylinder Between Adjacent Fins

Good agreement between the computed and experimental chordwise pressure distributions are seen. Experimental leading edge pressures are not currently available, but will be at a future time. It should be emphasized that these tests are still in progress and additional data are expected.

The computed and experimentally determined axial pressure distribution on the cylinder body between two adjacent fins is shown in Figure 11. Upstream of the fins, the axial pressure gradient

is nearly zero. The pressure rises downstream of the location where the fins begin due to the interaction of the shocks from the adjacent fins. The computed pressure distributions agree very well, though the UNS computation predicts a rise in pressure slightly upstream of the PNS computation. This may be a result of the UNS technique's ability to predict upstream influence. The pressure jump due to the shocks is also shown in the preliminary experimental data.

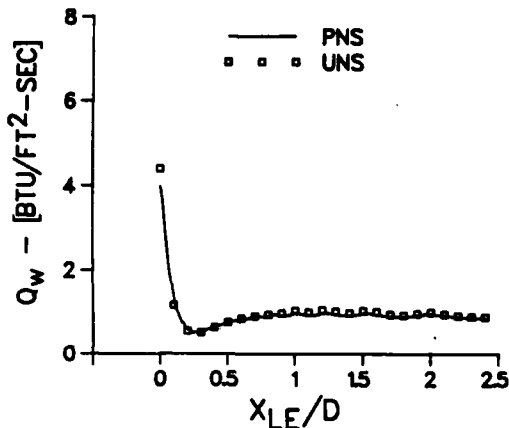


Figure 12a. Chordwise Heat Flux Distribution (Section 1)

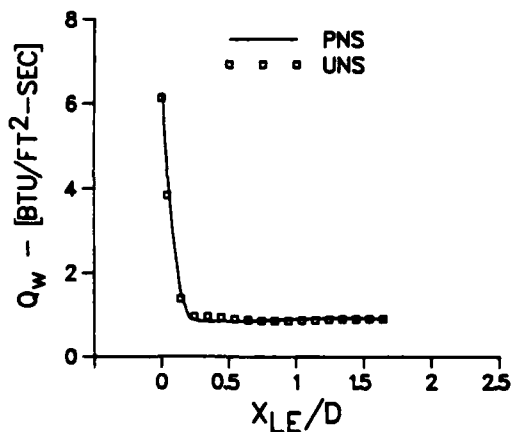


Figure 12b. Chordwise Heat Flux Distribution (Section 3)

3. Surface Heat Transfer

One of the parameters of interest to kinetic energy projectile designers is the surface heat transfer. It has been documented that kinetic energy penetrator fins occasionally experience melting during their flight trajectory due to inflight aerodynamic heating, inbore heating or a combination of both. These fins are particularly susceptible to melting because they are thin, made from aluminum which has a low melting temperature compared with other metals, and fly at high velocities. Determination of the surface heat transfer can provide the projectile designer with critical information for successful design.

From the computed viscous flow field it is possible to compute the heat transfer from the surrounding fluid to the projectile body by determining the fluid temperature gradient and the fluid conductivity, k , at the projectile surface. This is expressed below:

$$Q_w = k \frac{\partial T}{\partial n} \quad (5)$$

The surface heat transfer has been evaluated from both of the computed flow fields. Figures 12 a and b show the chordwise heat flux distribution at sections 1 and 3. High heat transfer rates are evident at the fin leading edges followed by a large drop as the flow expands around the fin leading edges. Excellent agreement between the heat transfer rates predicted by the PNS and UNS techniques is seen, to some degree validating both numerical approaches. Experimental heat transfer measurements are still in the process of being evaluated, and are not included here.

IV. SUMMARY AND CONCLUSIONS

CFD computations were presented for two finned configurations which resemble the US Army M735 kinetic energy penetrator projectile. In computing the flow fields over the finned configurations, a total of four different computational procedures were applied.

The first set of computational results presented were for a finned configurations which resembled the M735 projectile closely. From the computed flow field, the pitch-plane aerodynamic coefficients were determined and comparison was made with data available from range firings. Each of the computational procedures showed reasonable agreement with the range data. The PNS and inviscid PNS procedures yielded nearly identical agreement demonstrating the lack of viscous effects on the pitch-plane aerodynamic coefficients for length-to-diameter ratios less than 14.

The second set of computational results were obtained for a finned configuration for which wind tunnel tests are currently being performed. Experimental oil flow visualizations were compared with simulated oil flow visualizations from the flow field computed using the PNS technique. Both visualizations showed similar features. Computed surface pressures on the finned portion of the body showed good agreement with the available experimental data. Predictions of the surface heat transfer due to aerodynamic heating were presented. Very little difference between the PNS and UNS technique predictions of surface pressure and surface heat transfer were evident, providing validation of each of the two procedures. The PNS technique was significantly more efficient than the UNS procedure, with little difference in the overall accuracy noted. Within the range of applicability (supersonic flow and no streamwise separation), the PNS technique is the technique of choice for computing the viscous flow over finned projectiles.

Future research efforts will be directed towards developing a more accurate representation of the fin geometry including base region effects and towards obtaining results for increasing body lengths. However, the basic computational capability for finned projectiles is now well established and significant progress is anticipated when new supercomputer resources become available at the BRL.

REFERENCES

1. Sturek, W.B. and Schiff, L.B., "Numerical Simulation of Steady Supersonic Flow over Spinning Bodies of Revolution," AIAA Journal, Vol. 20, No. 12, December 1982, pp. 1724-1731.

WEINACHT, STUREK

2. Sturek, W.B. and Mylin, D.C., "Computational Parametric Study of the Magnus Effect on Boattailed Shell at Supersonic Speeds," AIAA Paper 81-1900, 8th Atmospheric Flight Mechanics Conference, August 1981.
3. Weinacht, P., Guidos, B.J. and Sturek, W.B., "PNS Computations for Spinning and Fin-Stabilized Projectiles at Supersonic Velocities," BRL Memorandum Report ARBRL-MR-03464, September 1985.
4. Weinacht, P., Guidos, B.J., Sturek, W.B. and Hodes, B.A., "PNS Computations for Spinning Shell at Moderate Angles of Attack and for Long L/D Finned Projectiles," AIAA Paper No. AIAA-85-0273, AIAA 23rd Aerospace Sciences Meeting, January 1985.
5. Schiff, L.B. and Steger, J.L., "Numerical Simulation of Steady Supersonic Viscous Flow," AIAA Journal, Vol. 18, No. 12, December 1980, jpp. 1421-1430.
6. Beam, R. and Warming, R.F., "An Implicit Factored Scheme for the Compressible Navier-Stokes Equations," AIAA Journal, Vol. 16, No. 4, 1978, pp. 85-129.
7. Rai, M.M. and Chaussee, D.S., "New Implicit Boundary Procedures: Theory and Applications," AIAA Paper No. 83-0123, 21st Aerospace Sciences Meeting, January 1983.
8. Wardlaw, A.B. Jr., Baltakis, F.P., Solomon, J.M. and Hackerman, L.B., "An Inviscid Computational Method for Tactical Missile Configurations," NSWC TR 81-457.
9. Pulliam, T.H. and Steger, J.L., "On Implicit Finite-Difference Simulations of Three-Dimensional Flows," AIAA Journal, Vol. 18, No. 2, February 1980, pp. 159-167.
10. Ryzk, Y.M. and Ben-shmuel, S., "Computations of the Viscous Flow Around the Shuttle Orbiter at Low Supersonic Speeds," AIAA Paper No. 85-0168, Reno, Nevada, January 1985.
11. Brandon, F., Private Communication, Unpublished Wind Tunnel Data, US Army Ballistic Research Laboratory, LABCOM.
12. Loeb, A., Private Communication, Unpublished Range Data, US Army Armament Research and Development Command, LCWSL.
13. Agnone, A., Private Communication, Unpublished Wind Tunnel Data, New York University Antonio Ferri Laboratories, Westbury, NY.

OPTICALLY ACTIVATED SWITCH TECHNOLOGY

*MAURICE WEINER, DR., LAWRENCE J. BOVINO, MR.,
TERENCE BURKE, MR., ROBERT J. YOUMANS, MR., &
MELVIN J. WADE, MR.,
U.S. Army Electronics Technology & Devices
Laboratory, LABCOM, Fort Monmouth, NJ 07703-5302

INTRODUCTION

Recent years have witnessed an acceleration in the investigation of photo-conductive devices in bulk semiconductors. In addition to the usual energy conversion and light detecting devices, a new class of high voltage semiconductor switches is emerging, which also relies on the photo-conductive phenomenon. The concept of this switch is shown in Fig. (1).

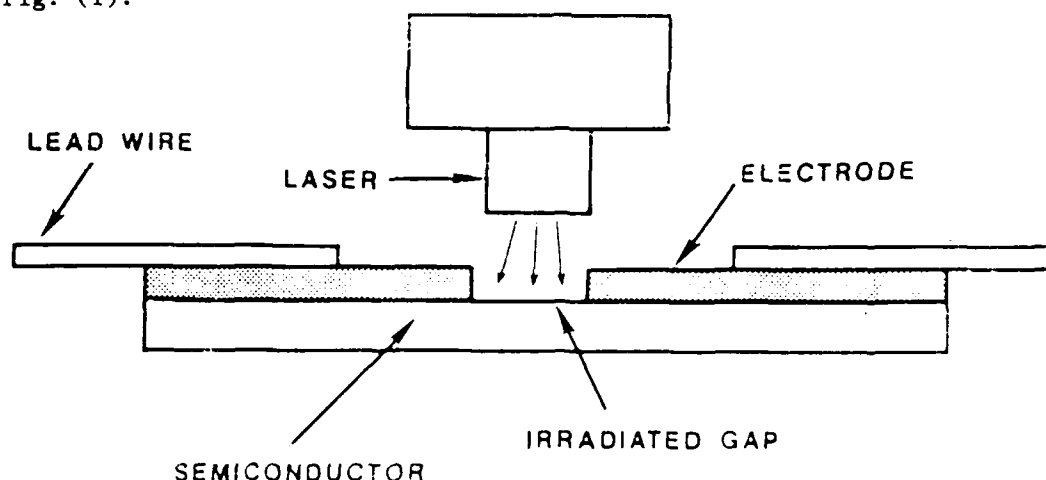


FIGURE 1: OPTICALLY ACTIVATED SEMICONDUCTOR SWITCH

The device consists of a block of high resistivity ($\geq 10^4 \Omega$ -cm) bulk semiconductor material upon which metal electrodes are evaporated. A voltage placed between the electrodes will not draw any appreciable current because of the inherently high resistivity of the semiconductor.

However, when the region between electrodes is flooded with radiation (usually from a laser or any other optical source) electron-hole pairs will be created which will increase the conductivity of the semiconductor, thereby producing current. The dynamics of the current response (rise-time, fall-time, amplitude, etc.) depend on numerous factors, several of which will be discussed in this paper.

The interest in the optical switch has its origin in certain unique properties which are briefly discussed. One of the major advantages of this device has to do with the fact that the optical signal, which controls the current, is completely isolated from the semiconductor circuit. This property is very advantageous in high voltage, high speed circuits where the introduction of the conventional drive signal into the circuit may cause problems in pulse fidelity. The drive circuitry must also be protected from high voltage transients, which adds to circuit complexity. Another advantage is the potential for picosecond switching speeds. If sufficient light energy is delivered to the inter-electrode region fast enough, then there is no transit time limitation, i.e., carriers throughout the semiconductor are instantaneously set into motion. Of course this places the burden of high speed response on the light source, so that for picosecond speeds, a mode locked laser is required to produce the desired picosecond current response. In the absence of a mode locked laser, nanosecond current responses maybe obtained with fast Q-switches or with light sources accompanied by high speed modulators. A corollary of the fast switching speed is the potential for low pulse jitter and the precise triggering of multiple semiconductor switches. If the same optical source (either a mode locked or Q-switched laser) is used, the light may be distributed among several switches for purposes of voltage or current multiplication. Another potential advantage deals with the scalability of the optical switch. In principle, since this is a bulk device, the voltage may be scaled upwards by increasing the gap length, and the current may be scaled by enlarging the cross-sectional area. Scalability is an appealing feature when designing higher power switching devices. Of course the higher power devices, in general, will require proportionately more light energy. In this connection, one should mention that the light energy requirement is probably the major disadvantage of this device, since the creation of photons with the correct wavelength is generally an inefficient process, and each photon produces only one carrier pair. The issue of efficient light sources will not be addressed here.

As outlined in the previous discussion, the application of optical switch technology, for generating kilovolt, nanosecond pulses, appears to have much potential. Depending on the light source and the semiconductor size, either large pulse energies (≥ 10 joules) or high pulse repetition frequencies (≥ 100 KHz) may be obtained. Such pulsers may be used as

modulators in laser and microwave transmitters.

In this paper two design approaches for the optically activated switch are discussed. The first is a high PRF low energy design which unites a fiber coupled, laser diode array with a GaAs semiconductor. The second design, the high energy version, couples a Q-switched Nd:YAG laser to a larger GaAs semiconductor. Experimental data for both configurations is presented and design considerations with anticipated operating ranges are discussed. A computer model which describes the transient conductivity and electric field profiles in the semiconductor is described.

DISCUSSION

Laser Diode Activation

The laser diode controlled switch couples a Laser Diode Laboratories model LDT-391 diode laser (Figure 2) to a Cr:GaAs switch. The LDT-391

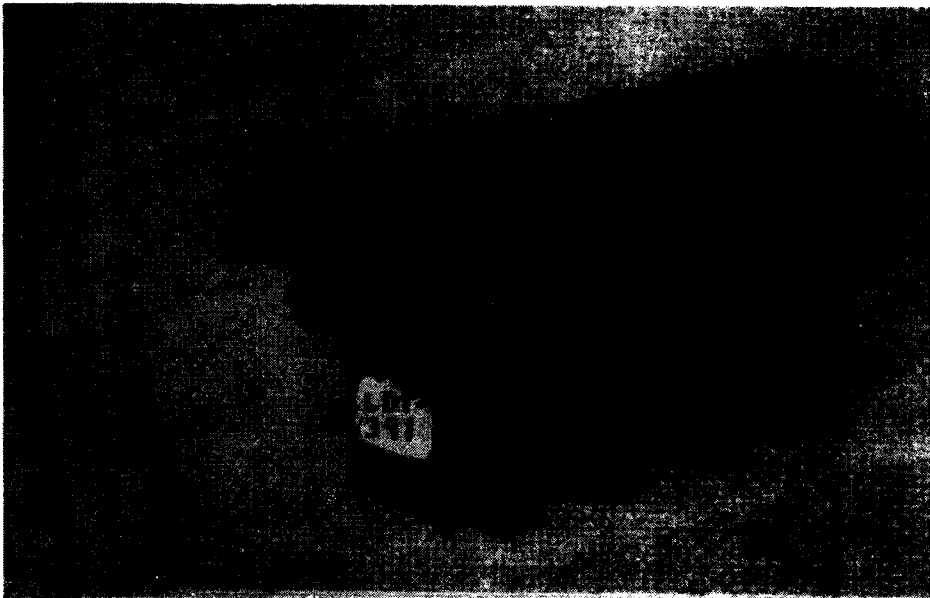


FIGURE 2: PHOTOGRAPH OF LDT-391 LASER DIODE ARRAY

consists of four separate LDT-350's. Each LDT-350 consists of any array of 12 single heterojunction GaAs laser diodes, emitting at a wavelength of 0.904 microns. Each diode is individually fiber coupled to the output of its LDT-350 and the light from the four LDT-350's is combined in a solid

glass integrator with an output aperture of approximately 0.5 mm by 0.5 mm. The specially designed "nosepiece", which houses the last inch or so of the integrator, extends the output aperture beyond the main frame of the laser, which is metallic. This extension provides the necessary high voltage isolation between the laser and the switch. The overall array is rated at 430 watts of optical power for a 200 ns pulse when driven with 40 amperes. At a 50 ns pulsewidth, the device can be driven with 60 amp peak currents and will provide a peak power of approximately 700 watts.

The switch (Fig. 3) is fabricated on a piece chromium doped GaAs

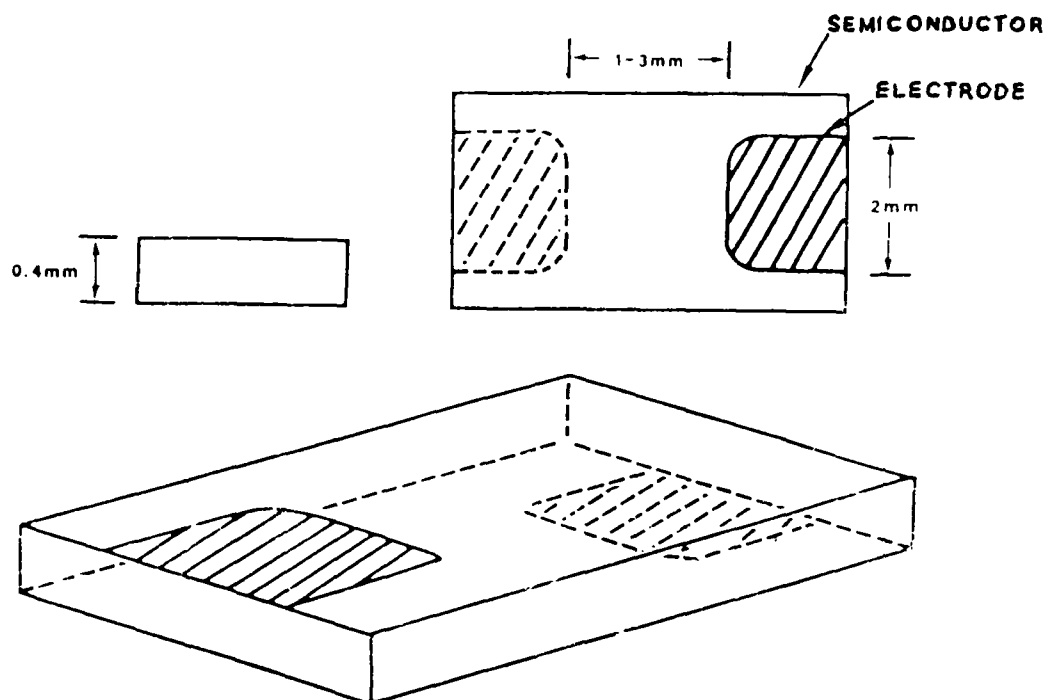


FIGURE 3: SWITCH DESIGN WITH ELECTRODES ON OPPOSITE SIDES OF WAFER, FOR USE WITH LASER DIODE ARRAY.

wafer approximately 5 mm wide by 10 mm long by 0.4 mm thick. The electrodes, 50 angstroms Ni, 450 Å Au, 200 Å Ge, 1000 Å Ag, capped with 4000 Å Au, are 2 mm wide and deposited on opposite sides of the chip as shown. The electrode separation ranges from 0.5 mm - 3.0 mm. Switches having this geometry provide DC voltage hold-off of up to 3 kV per millimeter of separation or "gap length" and have been observed to routinely

WEINER, BOVINO, BURKE, YOUNG, & WADE

and repetitively carry current pulses of up to 30 amperes. The carrier lifetime in Cr:GaAs or GaAs ranges from 1 - 30 ns.

Figure 4 shows the burst operation of the switch at 100 KHz, with a

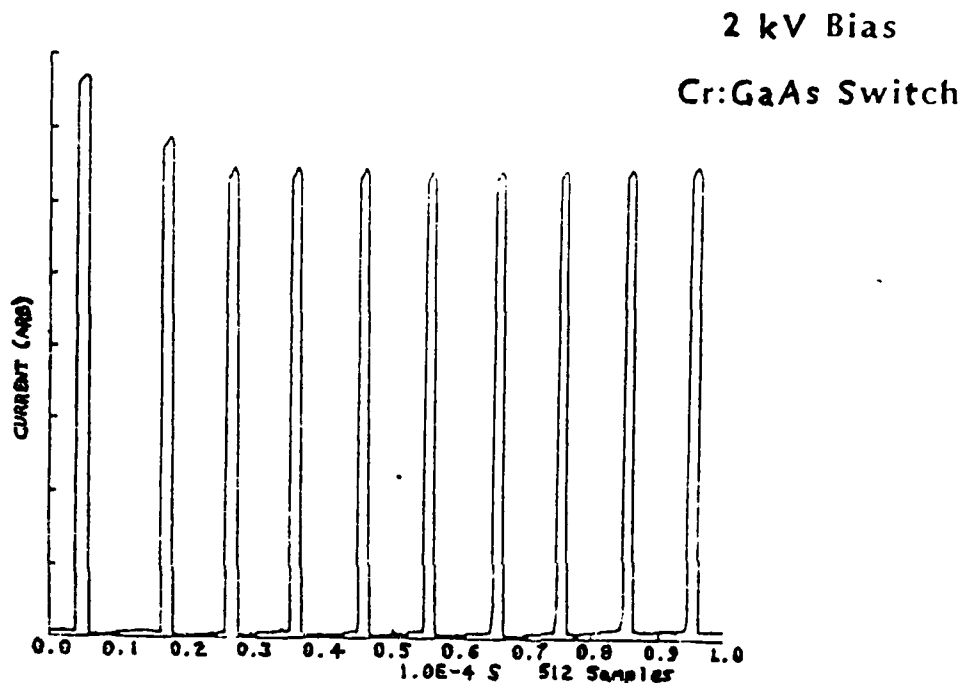


FIGURE 4: 100 KILOHERZ BURST OF PULSES USING THE SWITCH IN FIGURE 3. PULSE AMPLITUDE IS APPROXIMATELY 10 AMPS.

bias of 2 kV. Each pulse represents approximately a 10 ampere 50 ns wide pulse delivered into a 50Ω load. The waveforms were obtained with a Tektronix 7912 digitizer. Improvements in the design of the laser diode arrays, the laser drivers, as well as the switches themselves, should lead to kilovolt pulse generators with nanosecond risetimes, operating at PRF's of several hundred KHz.

Nd:YAG Laser Activation

In the high energy design, the Nd:YAG activated bulk semiconductor switch couples a Q-switched Nd:YAG laser (1.06 microns) to a GaAs switch of the design shown in Figure 5. The laser has a 50% pulse width of 25 ns

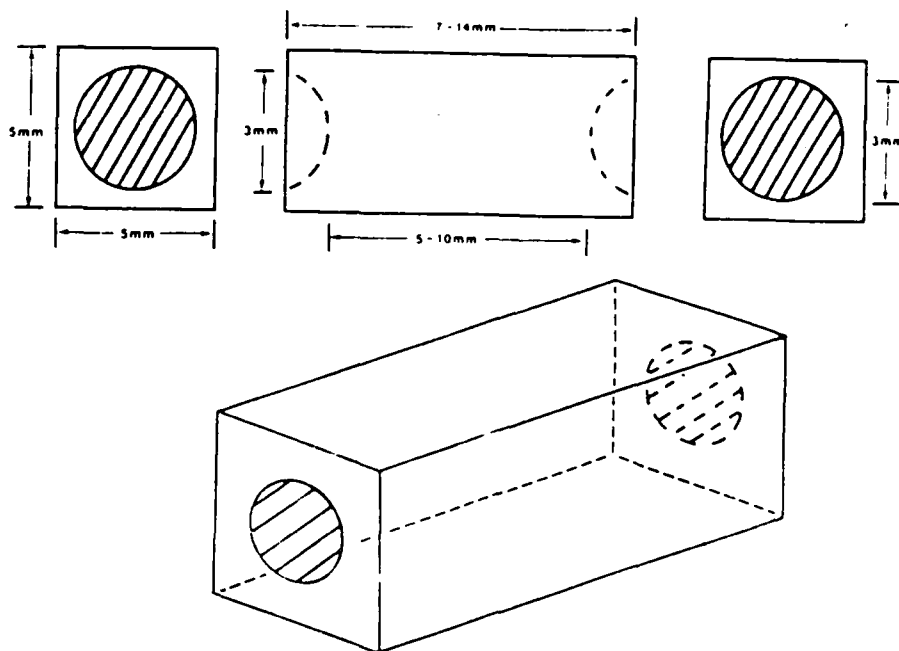


FIGURE 5: BAR TYPE DESIGN OF OPTICAL SWITCH, FOR USE WITH Nd:YAG LASER.

and a full power pulse energy of 150 millijoules. Usually, pulse energy is reduced to 20 millijoules using neutral density filters. The beam diameter is approximately 7 mm.

The switch is a rectangular bar of GaAs semiconductor with a square cross section of 5 mm by 5 mm. The contacts are of the same composition as those on the laser diode activated switch and are indented 2 mm into the square faces to help prevent surface breakdown. Switches with gaps of 5 mm and 10 mm have been tested. These switches provide DC voltage hold-off of up to 4 kV per millimeter of gap length. Because of their greater cross sectional area these targets have demonstrated a current carrying capability of up to 1000 amperes pulsed. At 20 millijoules per pulse, the Nd:YAG laser reduces the switch resistance less than 1 ohm in both the 5 mm and 10 mm.

Figure 6 shows a typical 1000 amp pulse delivered to a 10Ω load with a 5 mm switch. The optical pulse is 30 ns wide and the pulse-width of the pulse forming line is 50 ns. The time variation of the

5 mm Switch

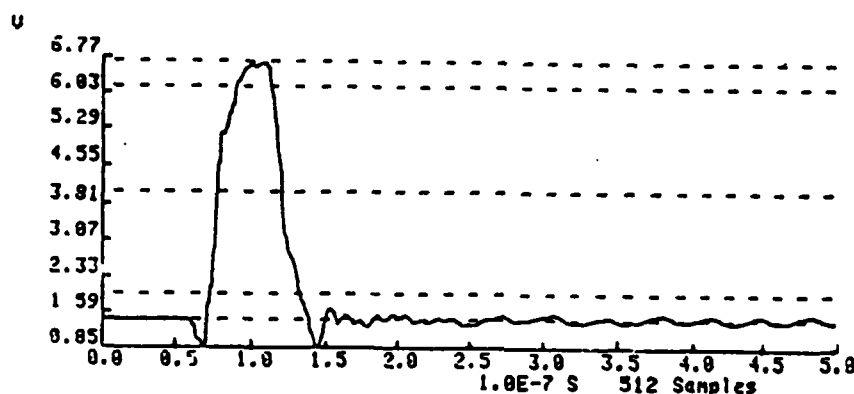
Volts x 10

20 kV Bias

20 Amps/Volt

10 ohm PFN & Load

1000 Amperes Peak



0% level: 1.43V
 10% level: 1.96V
 50% level: 4.07V
 90% level: 6.18V
 100% level: 6.70V

RISE TIME 1.751E-008S
 90% WIDTH 2.315E-008S
 50% WIDTH 4.362E-008S
 10% WIDTH 6.102E-008S
 FALL TIME 2.036E-008S

FIGURE 6: 1000 AMP, 10 KV PULSE USING BAR TYPE OPTICAL SWITCH.

current pulse is dependent on many factors, including the optical pulse shape, the pulse forming line, and the semiconductor properties. The low gap resistance is obtained in spite of the fact that the photon energy of the laser is substantially smaller than the gap energy in GaAs. Apparently the defects in GaAs are of sufficient number ($10^{16} - 10^{17} \text{ cm}^{-3}$) to produce intermediate energy levels capable of supplying the necessary carriers for efficient conduction.

Since a Nd:YAG laser can provide a great deal of energy per pulse, the switch element in this configuration can be almost indefinitely scaled in size to increase power handling capability. Previous experiments have demonstrated that Nd:YAG activated silicon switches of similar design (with length $\geq 2 \text{ cm}$) can be pulsed biased to 160 kV while carrying pulsed currents of up to 2 kA. The main advantage of GaAs over Si

switches is that they can be DC biased without the risk of thermal runaway and still draw less leakage current than a pulse biased Si switch. This greatly reduces the size and complexity of the charging circuit.

Computer Model

The conductivity and electric field profile in an optically controlled semiconductor is dependent on numerous factors. Several of the more important factors are listed:

1. Spatial/temporal variation of the light signal.
2. Contributions from hole as well as electron carriers (with different velocities for each type of carrier).
3. Carrier injection efficiency at the electrodes.
4. Space charge effects.
5. Transit time effects.
6. Displacement current (i.e., consideration of the semiconductor capacitance).
7. Carrier traps (including the effect of the immobile charge on the field).
8. Recombination of carriers.
9. Dependence of carrier velocity on field.
10. Geometry.
11. Effective carrier generation rate.

The complexities are such that the operation of the optical switch usually depends on several of these factors simultaneously. In addition to design considerations, there is also the more general problem in which carrying out an accurate comparison between theory and experiment is often impossible because various factors are neglected. Unfortunately no computer code exists which takes into account all factors. In order to address this situation, a calculational technique is being developed which deals with the majority of the issues. Following is a discussion of those items which are simplified or neglected in this technique:

In the case of geometry (factor 10) the problem is assumed to be one dimensional, i.e., there is no variation in the plane perpendicular to the carrier motion (variations in the direction of the carrier motion are, of course, allowed). Changes in the perpendicular plane may be caused, for example, by the exponential absorption of the light signal. In most cases, however, a simple modification of the one dimensional result is satisfactory to account for light penetration. In a related issue, the probability of generating a carrier pair with a given photon energy is assumed known. Direct recombination, for the present, is neglected. In silicon this assumption is fairly good. For the III-V compounds, the assumption is reasonably good provided the carrier densities are not too

large (carrier density $\lesssim 5 \times 10^{17} / \text{cm}^3$). If we neglect recombination, the dominant loss is trapping. To further simplify matters, the hole and electron transition frequencies for trapping are assumed constant. Trap filling effects are neglected. Finally, the most serious omission is considered, namely, the neglect of the carrier velocity dependence with field. Both hole and electron velocities are assumed constant. This assumption, together with the previous constraints, results in a complete linearization of the problem, allowing for simple closed form solutions. It should be mentioned, however, that these solutions provide a starting point from which the higher order nonlinear problem may be treated, including the velocity dependence on field.

The equations which must be solved are the particle conservation equation, the current continuity equation, and Poisson's equation. The light signal determines the particle densities, which in turn determines the current and field profiles. For simplicity it is assumed that the external circuit is purely resistive. Carrier current injection at each electrode is assumed to be determined by a constant factor which relates the injected carrier current at one terminal to the carrier current leaving the semiconductor at the other terminal.

As an example of the results of the analysis, the consequences of non-ohmic contacts is discussed. The results point out the importance of high injection efficiencies in order to prevent the build-up of large space charge fields in the semiconductor. As is well known, when the injection efficiency is perfect, the hole density exactly balances the electron density, and the space charge field is zero. However, if the injection efficiencies depart from unity by even a very small amount, large space charge fields may develop, particularly near the electrodes. Figure 7 shows the field profiles for various hole and electron injection efficiencies. Note the increased non-uniformity in the field as the injection is lowered. The profiles shown are for a uniform carrier pair generation rate of $1.25 \times 10^{22} / \text{cm}^3 - \text{sec}$. It should be pointed out that these large fields, particularly when they develop near the electrodes, probably cause the effective injection efficiency to increase. However the large fields may also trigger an avalanche or breakdown mechanism, before the contacts have an opportunity to become fully injecting. Further investigation is needed to clarify this issue.

Figure 8 shows a tentative comparison between the model and an experimental wave form of the current pulse. The GaAs target was illuminated with minimal light intensity, so as to keep the field variations to a minimum, thus supporting the linear assumptions of the model. An LDT-391 laser diode array was used to illuminate the 2 mm target. The light pulse is approximately 58 ns wide. The effective quantum efficiency, contained in the carrier generation rate, was adjusted so

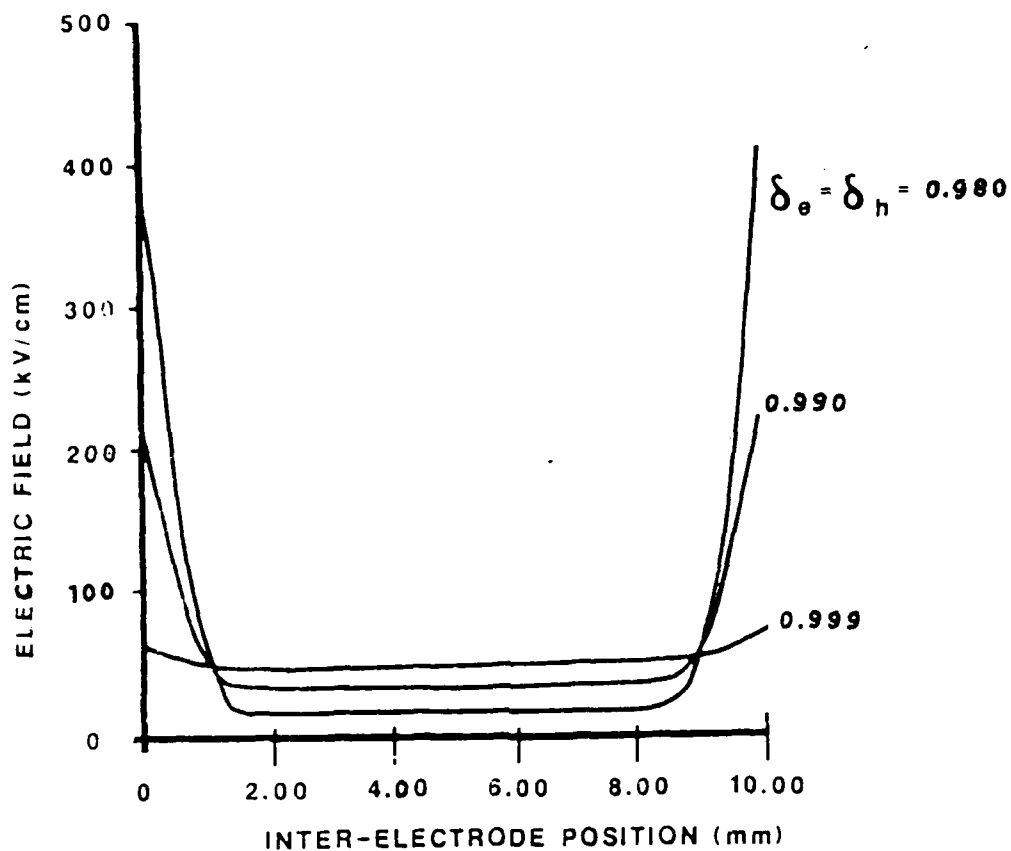


FIGURE 7: ELECTRIC FIELD PROFILES IN SEMICONDUCTOR FOR VARIOUS ELECTRON AND HOLE INJECTION EFFICIENCIES, δ_h AND δ_e .

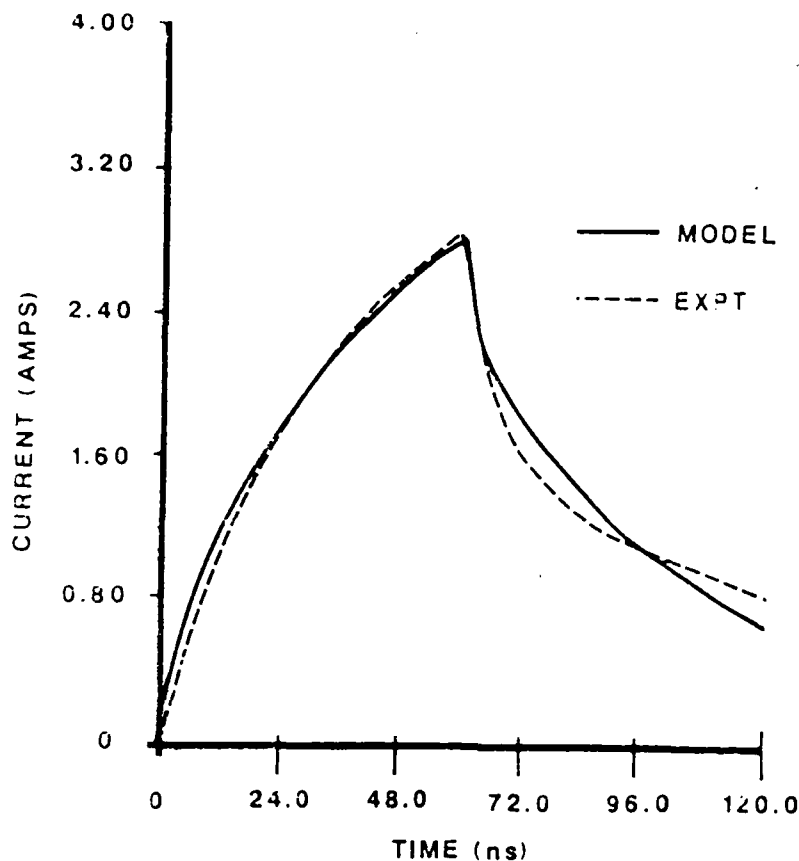


FIGURE 8: COMPARISON OF THEORETICAL AND EXPERIMENTAL CURRENT PULSES FOR 2 mm GaAs TARGET.

that the peak amplitudes of the theoretical and experimental were equal. Following the termination of the light pulse the current undergoes a fast initial recovery, followed by a slower decay. The model attributes this behavior to the longer trapping lifetime of the holes, compared to the electrons. Agreement between theory and experiment is reasonably good given the simple nature of the model. No attempt was made to "fine-tune" the comparison, since several factors have been omitted (such as trap filling), and a detailed comparison is best postponed until the model has been expanded.

CONCLUSIONS

Significant improvements in optically controlled switches have been achieved, using both laser diode arrays and Nd:YAG lasers as the light sources. The results indicate it is feasible to design a kilovolt, 100 KHz switch, at currents up to 100 amperes, using the laser diode array approach. The Nd:YAG controlled switch is suitable for applications involving much higher power. Q-switched lasers are available which supply sufficient energy to close a switch designed to hold off hundreds of kilovolts and switch tens of kiloamps. Development of a model which describes the transient conductivity and electric field profiles in the switch is progressing satisfactorily. The analysis has contributed to the understanding of the switch, particularly with regard to the effect of non-ohmic contacts.

Weisman, Zeballos, Johnson

**ACUTE STRENUOUS EXERCISE AT A SIMULATED ALTITUDE OF 2300m (7500 ft)
COMPARED TO SEA LEVEL IN INDIVIDUALS WITH SICKLE CELL TRAIT (SCT):
A CONTROLLED STUDY IN BASIC TRAINEES (U)**

*IDELLE M. WEISMAN, MAJ, MC
R. JORGE ZEBALLOS, M.D.
BRUCE D. JOHNSON, M.S.
WILLIAM BEAUMONT ARMY MEDICAL CENTER
EL PASO, TEXAS 79920-5001

INTRODUCTION

Sickle cell trait (SCT) is a heterozygous state characterized by the presence of hemoglobin (Hb)AS and is present in 7-9% of American blacks. Individuals with SCT are asymptomatic; therefore, SCT is generally regarded as a benign condition with limited proven morbidity (1). However, significant controversy persists regarding the risks assumed by individuals with SCT while engaged in military activities that would involve a greater likelihood of exposure to hypoxic environments and other stress situations (2).

The military has been particularly sensitized by anecdotal case reports of exercise-related morbidity in SCT as well as other anecdotal case reports of sudden unexplained death (SUD) in SCT individuals during strenuous exercise at altitude (3,4,5). An apparent substantiation of this greater risk for SUD in basic trainees has recently been reported (6). Past scientific investigations have been inconclusive in providing data upon which cogent statements regarding those risks could be made. The need for well designed, prospective, controlled studies is critical.

Therefore, in order to establish whether the physiologic changes associated with strenuous exercise at sea level and altitude (namely hypoxia, dehydration, and acidosis) may individually or in combination adversely affect similarly engaged individuals with SCT, a protocol was designed to investigate these factors. Phase I studies were conducted at WBAMC (Fort Bliss, Texas) at 1270m on healthy black male basic recruits with SCT (n=25) and controls (n=16) to evaluate the cardiopulmonary response to acute stressful exercise using an incremental and steady-state exercise protocol on a cycle ergometer before and after basic training. No discernible clinical or objectively determined cardiopulmonary response differences between the SCT and control groups were noted (7,8). Although sickling ($1.1 \pm 2 = \bar{x} + \text{SEM}$) was observed at rest in venous blood, no increase was noted immediately post-exercise. Furthermore, neither percent HbS nor percent sickling (measured at rest

and post-exercise) appeared to have any influence on acute stressful exercise performance at 1270m (9).

Having established an extensive cardiopulmonary and hematologic data base at 1270m, Phase II studies were performed in order to further evaluate the role of a greater hypoxic stimulus (simulated altitude of 2300m) on the interactions of HbS, sickling, and acute strenuous physical exertion in SCT volunteers.

MATERIALS AND METHODS

The following study was conducted in El Paso, Texas, at an altitude of 1270m, with a mean barometric pressure (P_B) of 656 mmHg, and temperature of 24°C.

Healthy, black, male, basic recruits, eleven with sickle cell trait (SCT, HbAS) and eleven without (controls, HbAA), with a minimum of 5 days' residence at 1270m participated, after signing informed written consent. The duration of the protocol was three days for each subject.

Screening for HbS was performed using a modified sickledex technique. On Day 1, sickledex positive individuals had a cellulose acetate electrophoresis (CAE) with HbS quantification (% total Hb) performed at the hemoglobin reference laboratory of Baylor University Medical Center, Dallas, Texas. Also on Day 1, a physical examination, chest x-ray, 12-lead resting ECG, and complete pulmonary functions, including spirometry and lung volumes (body plethysmograph, Gould 2800 Autobox) and single breath diffusing capacity of the lung (Collins DS 520) were performed. For PFTs, the equations published by the Intermountain Thoracic Society in Caucasians were used (10). An exercise cycle ergometer familiarization session was also performed.

During days 2 and 3, the effect of altitude on exercise performance was evaluated. Two conditions were simulated: sea level (SSL) was achieved by changing the fraction of the inspired oxygen (F_{I,O_2}) to 24% (hyperoxia) and 2300m (S2300m) using an F_{I,O_2} of 18% (hypoxia) while maintaining a constant barometric pressure (isobaric). The two respiratory gas mixtures were prepared by Scott Medical Products (Plumsteadville, Pennsylvania). The subjects equilibrated for two hours while breathing humidified gas through a respiratory gas mask (vital signs) with the inspiratory port connected to a 120L reservoir bag supplied from the gas cylinder and the expiratory port to room air. Prior to exercise, the subjects were changed over to a 2-way respiratory valve (Model 2700 Hans Rudolph) while continuing to breathe the same gas concentration until the completion of the exercise test.

The subjects undertook two types of exercise protocols on an electronically braked cycle ergometer (KEM 2): An incremental exercise test (IET) with the workload increasing at 25-watt intervals every minute until the subject's exhaustion, and a steady-state exercise test (SSET) which consisted of six minutes of constant power at 50% (SSI) and six minutes at 70% (SSII) of the maximum power achieved during IET.

Minute ventilation (\dot{V}_E), oxygen uptake ($\dot{V}O_2$), carbon dioxide production ($\dot{V}CO_2$), respiratory exchange ratio (R), and the ratio of physiologic dead space to tidal volume (V_D/V_T) were measured during exercise in a breath by breath fashion using a computerized system (Medical Graphics Corporation-2100) which integrated flow (pneumotachograph) with the respiratory gases measured continuously in the mouthpiece with a mass spectrometer (Perkin-Elmer). Heart rate (HR) and electrocardiography were monitored continuously during the exercise tests with an Anthrometric Electrocardiograph System (Model CC-103). Minute by minute automatic blood pressure determinations were obtained using a Puritan-Bennett Infrasonde D4000. SO_2 was monitored using a Hewlett Packard ear oximeter. Blood gases and SO_2 were analyzed in duplicate (Instrumentation Laboratories 1303 and IL CO-Oximeters 282). The predicted equations used for some of the human performance parameters (based on a Caucasian population) were for $\dot{V}O_2$ max, Bruce (obtained on a treadmill) modified by Hansen (11), and for HR and power, those published by Jones (12).

Venous blood for hemogram, P_{50} (hemox-analyzer, TCS Corp), and 2,3DPG (sigma kit - #665-PA enzymatic assay) was obtained after equilibration at simulated SL in all subjects. Haptoglobin (hapt) levels (Beckman, nephelometric technique) and SMA-20s were also obtained before and after exercise at SSL and S2300m in all subjects. Blood was collected anaerobically for venous blood gases (vBG) (PO_2 , PCO_2 , pH) and percent sickling after equilibration at each condition² (18% and 24%). Percent sickling (%S) was defined as the number of sickled cells expressed as a percent of 500 red cells counted on a wet mounted sealed slide of blood fixed in 1% gluteraldehyde phosphate buffer solution. Phase contrast photographs of these wet mount preparations were prepared and evaluated by two different observers.

On Day 2, two IETs were performed after equilibration with either 18% or 24% $F_{I}O_2$ randomly assigned and administered in a single blind fashion. A 2-hour rest period occurred between tests.

On Day 3, a radial arterial catheter was inserted prior to SSET to determine arterial blood gases and arterial saturation (SaO_2) at rest and during each of the last two minutes of SSI and SSII. Two SSETs were performed after the respective 2-hour equilibration period breathing either one of the respiratory gas mixtures ($F_{I}O_2$ =18% or 24%). The order of gas mixture administered was similar to Day 2's order. Again, a 2-hour rest period between SSETs occurred.

The Statistical Package for the Social Sciences (SPSS) was used to compute mean data, standard deviations, standard error of the means, student t-tests, analyses of variance, Pearson correlation coefficients, and linear regressions. A level of $p < 0.05$ was chosen for statistical significance.

RESULTS

Table 1 demonstrates that the SCT and control groups possessed com-

parable anthropometric characteristics and pulmonary functions. Both groups would be characterized as being young with normal weight and height. Pulmonary function data revealed that for spirometry, lung volumes, and diffusing capacity, there were no statistically significant differences between the two groups. However, for each of the two groups, forced vital capacity (FVC), forced expiratory volume in one second (FEV_1), and total lung capacity (TLC) were approximately 12% below published predicted values for Caucasians (13). The predicted values for \dot{V}_E for both groups was 82% of that for Caucasians. However, with the correction for alveolar volume, the values for \dot{V}_E/\dot{V}_A were comparable to predicted.

Baseline hematologic parameters (Table 2) and 2,3 DPG and P_{50} (Table 3) obtained at SSL conditions were within normal limits for each group without any significant differences

TABLE 1. ANTHROPOMETRIC CHARACTERISTICS AND PULMONARY FUNCTION MEASUREMENTS OF HEALTHY BLACK MALES WITH SCT (n=11) AND CONTROLS (n=11)

	Controls		SCT	
	mean \pm SEM	% Pred	mean \pm SEM	% Pred
Age (yrs)	18.5 \pm 0.3		18.7 \pm 0.3	
Wt (kg)	69.7 \pm 1.9		73.5 \pm 3.0	
Ht (cm)	174 \pm 2		178 \pm 2	
FVC (L)	4.73 \pm 0.22	88	4.87 \pm 0.18	86
FEV_1 (L)	4.06 \pm 0.21	89	4.16 \pm 0.14	88
TLC (L)	5.88 \pm 0.25	90	5.95 \pm 0.19	88
\dot{V}_E (L/min/mmHg)	34.2 \pm 1.4	81	36.2 \pm 1.4	83
\dot{V}_E/\dot{V}_A	6.10 \pm 0.19	95	6.32 \pm 0.33	98

PFT predicted values for Caucasians from Intermountain Thoracic Society, 2nd Edition (1984), Salt Lake City Utah

TABLE 2. BASELINE HEMATOLOGICAL PARAMETERS OF HEALTHY BLACK MALES WITH SCT AND CONTROLS AT SIMULATED SEA LEVEL (mean \pm SEM)

	Hb (g/dl)	Hct (%)	RBC (mill/u/l)	MCV (fl)	MCH (uug)	MCHC (%)	RDW (%)
Controls (n=11)	13.9 \pm .2	42.1 \pm .7	4.9 \pm .1	85.8 \pm 1.8	28.5 \pm .7	33.2 \pm .3	17 \pm 3
SCT (n=11)	13.8 \pm .3	41.9 \pm .8	4.8 \pm .1	86.5 \pm 1.4	28.5 \pm .4	32.9 \pm .2	22 \pm 2

TABLE 3. SPECIAL HEMATOLOGICAL TESTS PERFORMED AT REST IN HEALTHY BLACK MALES WITH SCT AND CONTROLS (SIMULATED SEA LEVEL)

	Controls			SCT		
	mean \pm SEM	Range	n	mean \pm SEM	Range	n
% HbS	-	-	-	41.7 \pm 1.0	34.7 - 47.4	11
2,3 DPG	2.6 \pm 0.1	2.2 - 3.2	10	2.5 \pm 0.1	1.9 - 2.8	9
P_{50}	26.3 \pm 0.4	23.5 - 27.5	9	26.5 \pm 0.3	25.0 - 27.5	11

TABLE 4. % SICKLING AND VENOUS BLOOD GASES AT REST DURING SIMULATED SEA LEVEL AND 2300m IN HEALTHY BLACK MALES WITH SCT (n=11) AND CONTROLS (n=11) (mean \pm SEM)

	Sea Level		Altitude	
	Controls	SCT	Controls	SCT
Sickling (%)	0 \pm 0*	1.3 \pm .3*	0 \pm 0*	1.7 \pm .3*
PvO_2 (mmHg)	36 \pm 4	31 \pm 2	32 \pm 2	30 \pm 3
SvO_2 (%)	56 \pm 7	46 \pm 5	52 \pm 4	42 \pm 6
$PvCO_2$ (mmHg)	50 \pm 2	51 \pm 1	47 \pm 1	48 \pm 2
pH	7.32 \pm .02	7.32 \pm .01	7.33 \pm .01	7.33 \pm .01

* Significant difference between groups at $p < 0.05$

TABLE 5. INDICES OF HEMOLYSIS BEFORE AND AFTER EXERCISE AT SIMULATED SEA LEVEL AND 2300m IN HEALTHY BLACK MALES WITH SCT (n=11) AND CONTROLS (n=11) (mean \pm SEM)

	Sea Level				2300m			
	Baseline		Post Exercise		Baseline		Post Exercise	
	Controls	SCT	Controls	SCT	Controls	SCT	Controls	SCT
Hapt (mg/dl)	96 \pm 16*	31 \pm 7*	100 \pm 15*	35 \pm 9*	95 \pm 16*	31 \pm 8*	107 \pm 16*	33 \pm 9*
Tot Bili (mg/dl)	.42 \pm .07#	.72 \pm .14#	.46 \pm .07#	.80 \pm .15#	.38 \pm .06*	.81 \pm .18*	.45 \pm .07#	.88 \pm .19
Ind Bili (mg/dl)	.35 \pm .06#	.61 \pm .12#	.40 \pm .06#	.66 \pm .14#	.31 \pm .05*	.67 \pm .16*	.36 \pm .06#	.73 \pm .18
SGOT (IU/L)	27 \pm 4	26 \pm 3	34 \pm 3	30 \pm 3	30 \pm 3	25 \pm 3	35 \pm 5	29 \pm 3
LDH (IU/L)	210 \pm 12	199 \pm 10	227 \pm 12	230 \pm 14	204 \pm 14	201 \pm 10	224 \pm 11	221 \pm 11
CK (IU/L)	375 \pm 99	363 \pm 104	397 \pm 97	376 \pm 135	361 \pm 91	295 \pm 82	397 \pm 97	350 \pm 99

* Significant difference between groups at $p < 0.05$ # $0.05 < p < 0.1$, between groups

noted between the two groups. The %HbS (\bar{x} ±SEM) was 41.7±1.0 (Table 3) with a range of 34.7-47.4. These values for %HbS in SCT are slightly higher than published series (14,15).

The %S and vBG data at rest for both groups appear in Table 4. SCT volunteers demonstrated a %S at SSL of 1.3±0.3 (\bar{x} ±SEM) which is consistent with that previously observed in the literature for SCT (16). The %S observed at S2300m in SCT volunteers was 1.7±0.3 (\bar{x} ±SEM) which was

slightly greater but not significantly different from that observed at SSL. Controls never demonstrated any sickling. vBG data failed to reveal any significant differences in PvO₂, PCO₂, SvO₂, and pH between the two groups at each of the simulated altitudes. It should be noted, however, that the range of observed values for PvO₂ and SvO₂ for both groups was large and overlapped considerably despite the differences in simulated altitudes.

A weak correlation between %S and PvO₂ was established ($r=-0.56$) with borderline significance ($.05 < p < .1$) at SSL; a stronger correlation ($r=-0.82$) which was significant ($p < .05$) at S2300m was observed. We have previously noted this correlation between %S and PvO₂ at 1270m (9). No correlation was demonstrated between %HbS and %S at SSL or S2300m.

TABLE 6. CARDIOPULMONARY RESPONSE TO INCREMENTAL EXERCISE IN HEALTHY BLACK MALES WITH SCT (n=11) AND CONTROLS (n=11) AT SIMULATED SEA LEVEL (mean \pm SEM)

	Rest		Peak Exercise			
	Controls	SCT	Controls	% Pred	SCT	% Pred
Power (W)			236 \pm 8	92	244 \pm 7	93
HR (bpm)	74 \pm 5	73 \pm 2	190 \pm 3	96	189 \pm 3	96
\dot{V}_E (L/min)	15.0 \pm 1.5	15.7 \pm 1.2	132 \pm 7		134 \pm 3	
$\dot{V}O_2$ (L/min)	.38 \pm .03	.40 \pm .03	3.09 \pm .10	91	3.07 \pm .10	88
$\dot{V}CO_2$ (L/min)	.34 \pm .03	.37 \pm .04	3.95 \pm .12		3.97 \pm .08	
R	.89 \pm .02	.90 \pm .03	1.28 \pm .01		1.29 \pm .02	
O ₂ Pulse (ml/beat)	5.3 \pm .5	5.5 \pm .4	16.2 \pm .5	95	16.2 \pm .6	92
AT ($\dot{V}O_2$ L/min)			1.69 \pm .08		1.65 \pm .08	

TABLE 7. CARDIOPULMONARY RESPONSE TO INCREMENTAL EXERCISE IN HEALTHY BLACK MALES WITH SCT (n=11) AND CONTROLS (n=11) AT SIMULATED 2300m (mean \pm SEM)

	Rest		Peak			
	Controls	SCT	Controls	% Pred	SCT	% Pred
Power (W)			217 \pm 9	85	226 \pm 6	86
HR (bpm)	76 \pm 4	79 \pm 3	187 \pm 4	94	189 \pm 3	95
\dot{V}_E (L/min)	15.4 \pm .6	16.7 \pm 1.1	128 \pm 6		136 \pm 4	
$\dot{V}O_2$ (L/min)	.41 \pm .02	.41 \pm .02	2.81 \pm .09	83	2.90 \pm .08	83
$\dot{V}CO_2$ (L/min)	.35 \pm .02	.37 \pm .03	3.45 \pm .13		3.57 \pm .09	
R	.85 \pm .02	.89 \pm .03	1.23 \pm .01		1.24 \pm .02	
O ₂ Pulse (ml/beat)	5.7 \pm .4	5.2 \pm .3	15.1 \pm .5	88	15.4 \pm .5	87
AT ($\dot{V}O_2$ L/min)			1.62 \pm .07		1.59 \pm .07	

Table 5 reveals that of the indices of hemolysis measured before and after exercise at both simulated altitudes, the hapt were significantly lower in the SCT group compared to the controls at all times. SCT volunteers consistently had hapt levels that were either below or at the lower limits of normal. The normal range for hapt measured in our laboratory is 30-270 mg/dl. The hapt levels for each group remained remarkably persistent despite exercise and altitude. All other measured indices of hemolysis were within normal limits for both groups. Although not significant in all the conditions, the higher levels of T. bilirubin and Ind. bilirubin in SCT volunteers compared to controls appear to trend consistently with the former's significantly lower hapt levels.

The cardiopulmonary response to IET for both groups at SSL is shown in Table 6. No significant differences were noted in the measured parameters between the SCT and control groups at rest and at peak exercise. Both groups achieved between 92 to 96% of the predicted values for power, HR, O_2 pulse, and around 90% for $\dot{V}O_2$ max at peak IET. The

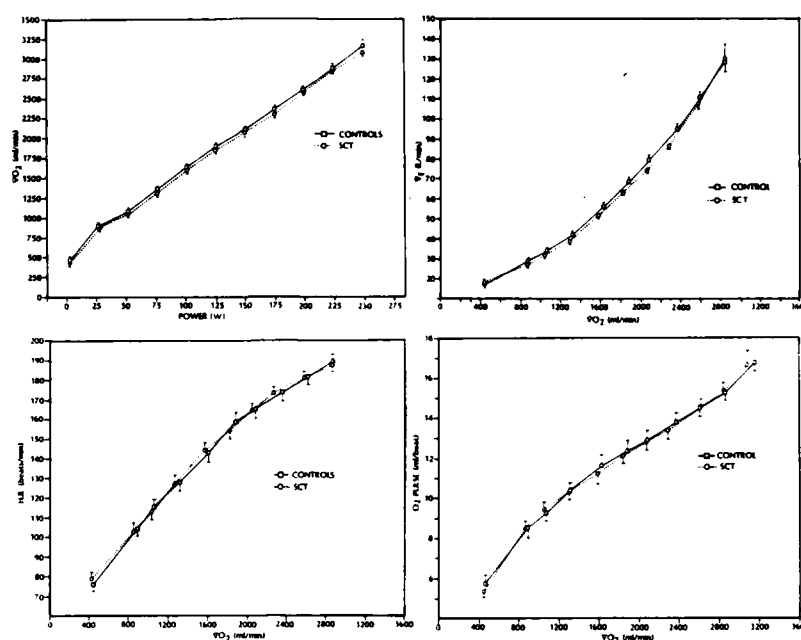


Fig. 1. Comparison of the relationship of $\dot{V}O_2$ with power and HR, $\dot{V}E$, and O_2 pulse with $\dot{V}O_2$ during incremental exercise in individuals with sickle cell trait (SCT) (n=11) and controls (n=11) at simulated 2300m. Plots represent mean \pm SEM data for each minute of exercise.

TABLE 8. GAS EXCHANGE DURING STEADY STATE EXERCISE AT SIMULATED SEA LEVEL IN HEALTHY BLACK MALES WITH SCT (n=11) AND CONTROLS (n=11) (mean \pm SEM)

	Rest		SSII	
	Controls	SCT	Controls	SCT
Power (W)			163 \pm 4	163 \pm 3
$\dot{V}O_2$ (L/min)	.35 \pm .02	.34 \pm .02	2.82 \pm .07	2.71 \pm .05
SaO ₂ (%)	97 \pm .2	97 \pm .1	97 \pm .3	97 \pm .2
PaO ₂ (mmHg)	104 \pm 1.6	106 \pm 1.8	105 \pm 2.4	107 \pm 1.8
PaCO ₂ (mmHg)	37 \pm .5	37 \pm .7	30 \pm .7	30 \pm .7
pH	7.39 \pm .00	7.39 \pm .01	7.32 \pm .01	7.32 \pm .01
P(A-a)O ₂ (mmHg)	2 \pm .9	3 \pm 1.2	14 \pm 1.8	12 \pm 1.4
$\dot{V}D/\dot{V}_T$ (%)	31 \pm 1.6	30 \pm 1.9	11 \pm .9	11 \pm 1.4

minute by minute cardiopulmonary data demonstrated a similar response in SCT and controls to IET at SSL. Likewise, Table 7 reveals no significant differences in the cardiopulmonary parameters measured at S2300m for rest and peak exercise between the two groups. The minute by minute cardiopulmonary data for the SCT and control groups reinforce the results of Table 7 (Fig 1).

The decrements in exercise performance at S2300m as reflected in reduced peak power and $\dot{V}O_2$ achieved when compared to SSL was comparable for both groups. Peak exercise at both simulated altitudes for both groups elicited comparable HR and \dot{V}_E responses despite reductions in peak power achieved at S2300m (Table 7).

The gas exchange data at rest and during SSET II at SSL (Table 8) reveals no significant differences in the measured parameters between SCT and control groups. These values were within normal limits for both groups. The heart rate (184 beats/min, 93% pred; 187 beats/min, 94% pred for the SCT and control groups, respectively) and $\dot{V}O_2$ achieved during SSET II ($\approx 90\%$ of peak $\dot{V}O_2$ during IET) indicate that a level of near maximal exercise was achieved.

Fig 2 graphically demonstrates the comparability of gas exchange results between both groups at SSL.

Table 9 demonstrates that at S2300m at rest and during SSET II, no significant differences in the measured parameters of gas exchange between the two groups were observed. The anticipated reductions in PaO_2 and SaO_2 and increase in pH were observed for both groups. During SSET II, the mean PaO_2 dropped slightly from baseline for both

TABLE 9. GAS EXCHANGE DURING STEADY STATE EXERCISE AT SIMULATED 2300m IN HEALTHY BLACK MALES WITH SCT (n=11) AND CONTROLS (n=11) (mean \pm SEM)

	Rest		SSII	
	Controls	SCT	Controls	SCT
Power (W)			160 \pm 4	165 \pm 3
$\dot{V}O_2$ (L/min)	.37 \pm .01	.39 \pm .02	2.73 \pm .07	2.68 \pm .06
SaO_2 (%)	93 \pm .4	93 \pm .4	90 \pm .9	90 \pm .5
PaO_2 (mmHg)	70 \pm 1.4	70 \pm 1.1	65 \pm 1.6	64 \pm 1.5
$PaCO_2$ (mmHg)	36 \pm .4	36 \pm .5	26 \pm .7	27 \pm .8
pH	7.41 \pm .00	7.41 \pm .01	7.35 \pm .01	7.36 \pm .01
$P(A-a)O_2$ (mmHg)	2 \pm .3	2 \pm .7	21 \pm 1.6	22 \pm 1.3
$\dot{V}O_2/\dot{V}_T$ (%)	28 \pm 1.1	27 \pm 1.4	11 \pm 0.9	12 \pm 1.4

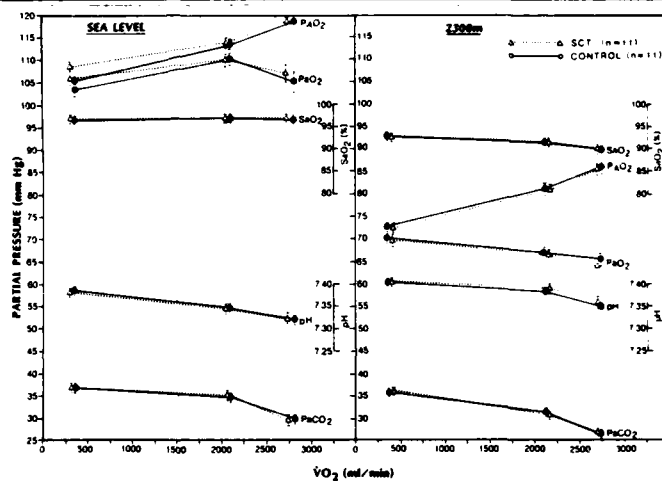


Fig. 2. Comparison of gas exchange between individuals with SCT (n=11) and controls (n=11) during rest and 2 levels of steady-state exercise at simulated sea level and 2300m.

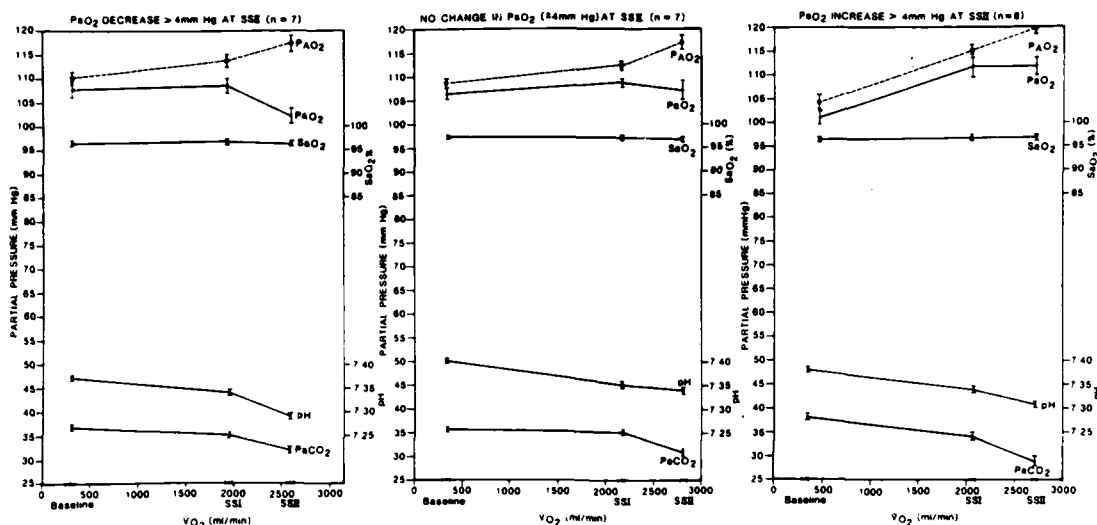


Fig. 3. Pooled gas exchange data (controls and SCT) categorized into 3 groups by changes in PaO_2 ($\pm 4\text{mmHg}$) between resting and steady-state exercise II at simulated SL. Plots represent mean \pm SEM.

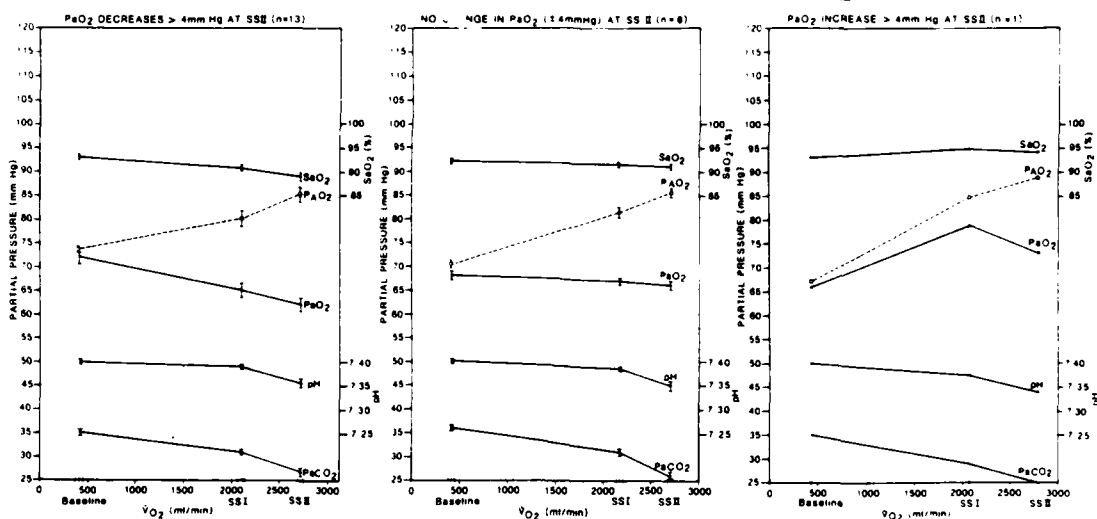


Fig. 4. Pooled gas exchange data (controls and SCT) categorized into 3 groups by changes in PaO_2 ($\pm 4\text{mmHg}$) between resting and steady-state exercise II at simulated 2300m. Plots represent mean \pm SEM.

groups. The $\text{P(A-a)}\text{O}_2$ response during SSET II at S2300m is of a magnitude that is noteworthy for both groups. Significant correlation was demonstrated between PaO_2 reduction and magnitude of $\text{P(A-a)}\text{O}_2$ ($r=-0.80, p<.05$). Again, near maximal exercise was achieved as evidenced by the VO_2 ($\approx 94\%$ of peak VO_2 during IET at S2300m) and heart rate (189 beats/min, 96% pred; 190 beats/min, 96% pred for SCT and control groups, respectively) responses. Fig 3 demonstrates the similarity of

gas exchange between both groups at S2300m.

Because no significant differences in parameters of cardio-pulmonary performance and gas exchange were noted between the SCT and control groups under both conditions, the gas exchange data were pooled ($n=22$) and are graphically displayed in Fig 3 and Fig 4 for SSL and S2300m, respectively.

Individual analysis of the data revealed that 59% of subjects dropped $PaO_2 > 4$ mmHg with exercise at S2300m versus only 23% at SSL. Only 5% increased $PaO_2 > 4$ mmHg at S2300m with exercise versus only 45% at SSL. No correlation was found between the drop in PaO_2 with exercise and $\dot{V}O_2$ peak achieved during IET.

Lastly, the relationship of quantitative HbS levels (%HbS) in SCT volunteers and the level of demonstrated aerobic performance as reflected in $\dot{V}O_2$ peak achieved during the IET at SSL and S2300m for $n=11$ subjects is shown in Fig 5. At SSL, %HbS weakly correlates with $\dot{V}O_2$ peak ($r=-0.60$, $p=0.05$) with borderline significance. However, at S2300m, no correlation was demonstrated with $\dot{V}O_2$ peak.

DISCUSSION

In view of the anecdotal case reports of SUD in basic trainees as well as a more recent apparent corroboration of that risk in the same population, our study subjects, by design, consisted of basic trainees for both our SCT and control populations (5,6). Appreciating that one of the criticisms of previous SCT investigations was inadequate or absent controls for various aspects being studied at the time, great emphasis was placed on utilizing a comparable control group for this study. The comparability of both our control and SCT groups as revealed in results is readily apparent. For both the SCT and control groups, the reduction in lung volumes was based on predicted values for Caucasians and has been described previously (13). Although \dot{V}_E/\dot{V}_T was in the lower limits of the normal range, when corrected for alveolar volume the values approximated 100% pred. A previous uncontrolled study in which \dot{V}_E/\dot{V}_T was performed in SCT subjects using a steady-state technique during exercise reported significant reductions; however, the available data was incomplete and alveolar volume corrections apparently were not made (15). This data has never been corroborated.

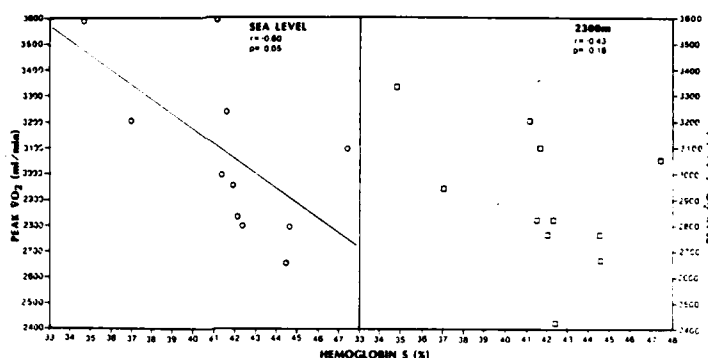


Fig. 5. Relationship of percent hemoglobin S with peak oxygen uptake ($\dot{V}O_2$) at simulated sea level and 2300m in individuals with sickle cell trait ($n=11$).

Careful characterization of the hemoglobinopathy was performed in order to avoid the criticism that sickle variants (sickle B-thal, SC, etc.) other than HbAS individuals were used as subjects (17). As would be expected for SCT, baseline hemograms were normal and comparable to the controls. As anticipated, the presence of HbS in the SCT group did not appear to affect SSL values for either P_{50} or 2,3 DPG which were comparable to those for the control group.

It should be noted that the values for %HbS obtained at SSL 41.7 ± 1.0 ($\bar{x} \pm \text{SEM}$) with an actual range of 34.7-47.4 are slightly higher than those reported in the literature (15,16); this most probably reflects methodologic differences related to obtaining higher yields for HbS. It has become apparent, however, that significant inter-laboratory variability for quantitative HbS levels exist without any "gold standard" reference being available. Therefore, the former practices, establishing an arbitrary level of HbS for the purposes of occupational disqualification seems even more questionable (18). The complex relationship between %HbS and exercise performance will be discussed subsequently.

The sickling that was noted during rest at SSL is consistent with published series (19). A similar magnitude of %S was seen at rest at 1270m (9). A slight increase in %S during rest at S2300m was observed; however, the increase was not significant. A reasonable explanation for the failure of %S to significantly increase with an increased hypoxic stimulus may be understood by appreciating that the only correlation of any consequence for %S was that with PvO_2 at SSL, the correlation was weak with only borderline significance ($r = -0.56$). However, a stronger correlation between %S and PvO_2 ($r = -0.82$, $p < 0.05$) was established at S2300m. Although PvO_2 did not change significantly between the 2 conditions, the range of observed values for PvO_2 was large and overlapped considerably despite the differences in simulated altitudes. It is, therefore, not surprising that since PvO_2 did not change significantly with altitude, neither would %S.

It should be noted that %S was measured in venous blood at rest but not during exercise; %S was measured in arterial blood during rest and exercise. The controls never demonstrated sickling under any condition. The SCT subjects never demonstrated sickling in arterial blood despite the presence of sickling in venous specimens at rest in the same individual obtained at concurrent times. The PO_2 in venous blood compared to arterial blood ($PvO_2 < PaO_2$) most likely explains the absence of %S in the latter. Since the occurrence of sickling in SCT subjects is reversible, the measurement of in vivo sickling during exercise should be performed from a venous effluent site from exercising muscles. That is because any stepwise increase in PvO_2 due to venous mixing from other sites would reverse the sickling.

Despite a commitment to meticulous sickling methodology, a shortcoming of this study was in not having obtained anaerobic venous effluent samples from exercising muscle. Most studies which have attempted

to evaluate %S and exercise have obtained post-exercise specimens, usually from far removed venous access sites (20). We are presently engaged in a study in which venous effluent blood from exercising muscles is being analyzed for %S *in vivo*.

A noteworthy observation in our SCT group that has not been previously described in asymptomatic, stable SCT subjects was that hapt levels (Table 2) were significantly lower under all conditions studied in the SCT group compared to control. It has been suggested that hapt levels may reflect an individual's level of fitness and/or general activity level (21). However, this does not appear to be the etiology of the reduced hapt presently since both the SCT and control groups demonstrated a comparable level of fitness. The failure to demonstrate reductions in hapt after exercise for both groups can most probably be explained on the basis of a relatively shorter duration of exercise performed by our subjects as has been previously described (21).

In addition, although T.bilirubin and Ind.bilirubin were well within normal limits for both groups, the slightly higher values under all conditions studied for individuals with SCT appear to trend consistently with the reduced hapt levels. Hapt may therefore be a very sensitive indicator of a chronic low-grade, sub-clinical hemolytic state in individuals with SCT. The clinical significance of this observation requires further study.

Although hypoxia, either alone or in combination with other factors (acidosis, dehydration, etc.), may be a potent stimulus in promoting intravascular sickling in subjects with SCT performing strenuous exercise, especially at altitude, we were unable to demonstrate it under these experimental conditions. On the contrary, what was clearly demonstrated in this study was that black male basic recruits with SCT had a cardiopulmonary response to acute strenuous exercise at altitudes simulating 2300m and SL similar to a control population.

Both groups could be characterized as having demonstrated an average-good level of fitness(22) (controls $\dot{V}O_2$ 44ml/Kg; SCT 43ml/Kg) and having achieved similar level of % predicted values for power, HR, \dot{V}_E , $\dot{V}O_2$, and O_2 pulse. The anticipated decrements in exercise performance noted² at S2300m were remarkably similar for both groups (Table 7) and comparable to those reported for Caucasians in the literature (23).

It should be noted, however, that this study does not preclude the possibility that during endurance exercise in which the other factors (acidosis, dehydration, temperature increases, etc.) become operative at either the same or greater hypoxic stimuli, exercise performance may be more greatly affected. Further investigative work must be done.

The similarity in arterial blood gases and gas exchange parameters between controls and SCT groups at SSL and S2300m would make more unlikely the possibility of significant pulmonary microcirculatory amputations due to sickling. However, it is appreciated that the PaO_2 , $P(A-a)O_2$, and VD/VT responses may not be sufficiently sensitive in

detecting mild microcirculatory abnormalities (24). Therefore, our data would suggest no clinically significant abnormalities in the pulmonary circulation in SCT subjects during acute exercise at altitudes up to S2300m.

When attempting to further characterize our population's gas exchange responses, individual analyses of the data were performed which revealed three different patterns of responses in PaO_2 with exercise, which are not in accordance with the current scientific knowledge. These patterns were observed in the same proportion in both SCT and control groups. Since no cardiopulmonary differences were determined between the groups, the data were pooled for further analysis.

A drop in PaO_2 with exercise has already been reported, but only in athletes under strenuous exercise conditions (25). Our data suggests that this phenomenon can also be observed in a significant proportion of non-athletic healthy young blacks during acute exercise. The significance of this observation for the establishment of critical criteria for normality in gas exchange during exercise is important.

Altitude may play a modulating role in this observation since the percent of individuals who show this characteristic increased significantly at S2300m. Arterial hypoxemia has been reported during exercise only at moderate and high altitude (26). However, we have consistently observed this phenomenon at SL and in our previous study at low altitude (1270m) (27).

Speculation regarding the etiology of this arterial hypoxemia during exercise requires consideration of multiple mechanisms which include an increase in the % of shunting, ventilation-perfusion (V/Q) abnormalities, diffusion limitations, and reduced mixed venous oxygen tensions due to increased oxygen extraction. In addition, an intriguing possibility is that of "relative hypoventilation" which is supported by the observation that the subjects who dropped their PaO_2 with exercise at SSL or S2300m were the ones who had the highest PaCO_2 compared to the subjects who improved their PaO_2 with exercise (Fig 3,4).

It should be noted that the role of the arterial hypoxemia in the level of exercise performance does not appear to be of significant importance at SSL or up to S2300m since no correlation was found between the drop in PaO_2 and VO_2 peak achieved.

For SCT subjects, the %HbS is one of the purported logical key determinants responsible for the occurrence of clinically significant sickling syndromes. It follows then that the higher the %HbS for a given set of adverse circumstances, the greater the amount of sickling and therefore clinical abnormality expected. It has been speculated that hypoxia either alone or in combination with other factors induced by exercise would influence sickling (5). What effect then would %HbS levels have on exercise performance? The data from this study would indicate that %HbS did not correlate with parameters of exercise performance at S2300m. The lack of correlation of acute exercise performance

to %HbS levels at 1270m in 25 subjects with SCT has previously been noted (9). It appears that neither %HbS nor %S play a critical role in the modulation of acute exercise performance at a level of hypoxia equivalent to 2300m.

The weak correlation with only borderline significance ($R=-0.56$, $p=0.05$) between %HbS and $\dot{V}O_2$ peak observed at SSL is of uncertain consequence. It would seem only logical that if HbS was to modulate exercise performance, it would have done so at 1270m and 2300m. Further studies with a greater number of individuals will be required to establish the significance of this observation at SSL and during endurance exercise protocols in order to elicit a greater contribution of the other factors.

In conclusion, although the presence of HbS may represent a theoretic potential hazard for SCT subjects under stressful environmental conditions, we were unable to detect differences in acute strenuous exercise performance with the control group utilizing current physiologic measurement tools at simulated SL and 2300m. Indeed, even if subclinical abnormalities were present, they were not of sufficient magnitude to affect the human performance of SCT subjects. Furthermore, within the SCT group, %HbS did not appear to play a critical role in the modulation of exercise performance at 2300m. The consistently lower haptoglobin levels observed in SCT subjects compared to controls may reflect a chronic low grade, sub-clinical hemolytic state in these individuals. These observations require further study in a larger controlled population. Significant arterial hypoxemia can be observed in healthy, young, black, non-athletes, both SCT and control, during exercise at conditions simulating SL and 2300m. Although present at SL, altitude appears to play an important role in this phenomenon. Further studies to evaluate the mechanism(s) responsible for this phenomenon are being performed.

Additional prospective studies will be necessary to assess what factor or combination of factors present at higher altitude (greater hypoxia equivalent to a $SAO_2 < 85\%$) and or during endurance exercise (increase temperature, dehydration, acidosis, hypoxia) may alter the circumstances under which the physiologic and hematologic changes associated with exercise may become more clinically important.

Acknowledgment

The authors gratefully acknowledge the excellent secretarial assistance of Ms. Wendy Smith.

REFERENCES

1. Sears DA. The morbidity of sickle cell trait - a review of the literature. Am J Med 1978; 64:1021-1036.

2. Diggs LW. The sickle cell trait in relation to the training and assignment of duties in the armed forces: 1. Policies, observations, and studies. *Aviat Space Environ Med* 1984; 55:180-5.
3. Koppes GM, Daly JJ, Coltmann CA, Butkus DE. Exertion induced rhabdomyolysis with acute renal failure and disseminated intravascular coagulation in sickle cell trait. *Am J Med* 1977; 63:313-317.
4. Helzlsoeur KJ, Haydn FG, Rogol AD. Severe metabolic complications in a cross country runner with SCT. *JAMA* 1983; 249:777-779.
5. Jones SR, Binder RA, Donowho EM Jr. Sudden death in sickle cell trait. *N Engl J Med* 1970; 282:323-325.
6. Posey DM, Kark JA, McMeekin RR, Schumacher HR. Sickle cell trait associated with sudden unexpected death in military basic trainees. *Aviat Space Environ Med* 1984; 55:459.
7. Weisman IM, Zeballos RJ, Johnson BD, Moreno AJ. The cardiopulmonary effects of stressful exercise at 4000 ft of individuals with sickle cell trait (SCT). *Am Rev Respir Dis* 1985; 131:A307.
8. Martin TW, Johnson BD, Weisman IM, Zeballos RJ. Effect of basic training on exercise performance in black recruits with and without sickle cell trait (SCT). *Med Sci Sports Exerc* (in press) 1986.
9. Weisman IM, Zeballos RJ, Johnson BD, Moreno AJ. Percent hemoglobin S (%HbS) and percent sickling (%S) as correlates for exercise performance at 4000 ft in individuals with sickle cell trait (SCT). *Fed Proc* 1985; 44:1012.
10. Morris AH, Kanner RE, Crapo RO, Gardner RM (eds). *Clinical pulmonary function testing*. 2nd ed. Salt Lake City: Intermountain Thoracic Society, 1984:101.
11. Hansen JE, Darryl YS, Wasserman K. Predicted values for clinical exercise testing. *Am Rev Respir Dis* 1984; 129: Suppl S81-S83.
12. Jones NL, Campbell EJM. *Clinical exercise testing*. 2nd Ed. Philadelphia: WB Saunders, 1982; 34,122.
13. Schoenberg JB, Beck GJ, Bouhuys A. Growth and decay of pulmonary function in healthy blacks and whites. *Respir Physiol* 1978; 33:367-393.
14. Goodman RL, Hazlet DR, Bergin JJ, Flannery EP, Schwartz M. Sickle cell trait and loss of pulmonary function at 5280 feet and sea level. In: Mammen EF, Anderson GF, Barnhart MI (eds). *Sickle cell disease. Transactions of the 20th annual symposium on blood*. Stuttgart Germany: FK Schattauer Verlag, 1973; 91-94.
15. Smith JA, Natta CL. The percentage of hemoglobin S in individuals with sickle cell trait. *Blood* 1981; 58:(Suppl 1) 64a.

Weisman, Zeballos, Johnson

16. Camëron BF, Smith DB, Cody B. Hemoglobin S levels in sickle cell trait individuals. *Am J Hematol* 1984; 16:123-127.
17. Sproule BJ, Halden RE, Miller WF. A study of cardiopulmonary alterations in patients with sickle cell disease and its variants. *J Clin Invest* 1958; 37:486-495.
18. Department of the Air Force, AFR 160-43, IMC 81-5, Interim Message Change to IMC 81-4, June 5, 1981.
19. Stryer L. *Biochemistry*. 2nd Ed. San Francisco: W.H. Freeman and Company, 1975:89.
20. Ramirez A, Hartley LH, Rhodes D, Abelman WH. Morphological features of red blood cells in subjects with sickle cell trait. Changes during exercise. *Arch Intern Med* 1976; 136:1064-1066.
21. Spitler DL, Alexander WC, Hoffler GW, Doerr DF, Buchanan P. Haptoglobin and serum enzymatic response to maximal exercise in relation to physical fitness. *Med Sci Sports Exerc* 1984; 16:366-370.
22. American Heart Association. Exercise testing and training of apparently healthy individuals: A handbook for physicians. Dallas: American Heart Association, 1972; 15.
23. Brooks GA, Fahey TD. Exercise physiology. Human bioenergetics and its applications. New York: John Wiley and Sons, 1984; 474-475.
24. Mohsenifar Z, Tashkin DP, Levy SE, Bjerke RD, Clements PJ, Furst D. Lack of sensitivity of measurements of V_D/V_T at rest and during exercise in detection of hemodynamically significant pulmonary vascular abnormalities in collagen vascular disease. *Am Rev Respir Dis* 1981; 123:508-512.
25. Dempsey JA, Hanson PG, Henderson KS. Exercise-induced arterial hypoxemia in healthy human subjects at sea level. *J Physiol* 1984; 355:161-175.
26. Tucker A, Stager JM, Cordain L. Arterial O_2 saturation and maximum O_2 consumption in moderate-altitude runners exposed to sea level and 3,050m. *JAMA* 1984; 252:2867-2871.
27. Zeballos RJ, Weisman IM, Johnson B, Moreno A. $P(A-a)O_2$ during exercise in healthy young blacks with sickle cell trait (SCT)² and controls. *Fed Proc* 1985; 44:1368.

WELLS

ACOUSTIC BIREFRINGENCE MEASUREMENTS IN ROLLED 5083 ALUMINUM PLATE (U)

FRANCINE S. WELLS, MS.
U.S. ARMY MATERIALS TECHNOLOGY LABORATORY
WATERTOWN, MA 02172-0001

Introduction

Ultrasonics offers a powerful and practical tool for the nondestructive measurement of stresses in a variety of Army structural materials. The acoustoelastic effect - the change in ultrasonic phase velocity with stress - gives us the opportunity to measure one or more components of the stress tensor σ_{ij} .

The Army's interest in internal stresses arises from the role they play in a variety of metal failures. Stress corrosion cracking is one such failure mode. Stress alone will react in ways well known in mechanical metallurgy such as creep, fatigue and tensile failure. Corrosion alone will react to produce characteristic dissolution reactions. However, the concomitant effects of tensile stress and a specific corrosion medium can sometimes produce disastrous results [1]. This is of particular concern for the soldier.

Residual Stresses

The stresses in Army structural materials such as aluminum and steel can be both residual and applied stresses. If we consider a metal bar deformed elastically in uniaxial tension, the applied stress is defined to be the applied force per unit area of cross-section. When the external force is removed, the stress disappears. However, there are a variety of operations that can leave a metal part in a stressed condition even after all external forces have been removed. Residual stress is the stress which exists in a metal part in the absence of external forces. Residual stress can be induced into metal parts by plastic deformation processes such as rolling, forging, machining or grinding.

Residual stresses induced in these deformation processes can consist of both microstresses and macrostresses. Micro-residual stresses vary from one grain to another or from one part of a grain to another on a microscopic scale. Residual stresses may be quite uniform over large distances - these are macro-residual stresses [2].

For a piece of material to be in equilibrium, the integrated macro-residual stresses through the thickness must equal zero. If this were not the case, the piece would be in motion! Thus, for a rolled plate with macro-residual stresses, the regions of tension must be balanced by the regions of compression. If V is the body's volume, then

$$\int \sigma_{ij}^{\text{macro.}} dV = 0 \quad (1)$$

The uniaxial residual stress distribution for macro-residual stresses induced in rolling are shown in Figure 1. Note that mechanical equilibrium is satisfied.

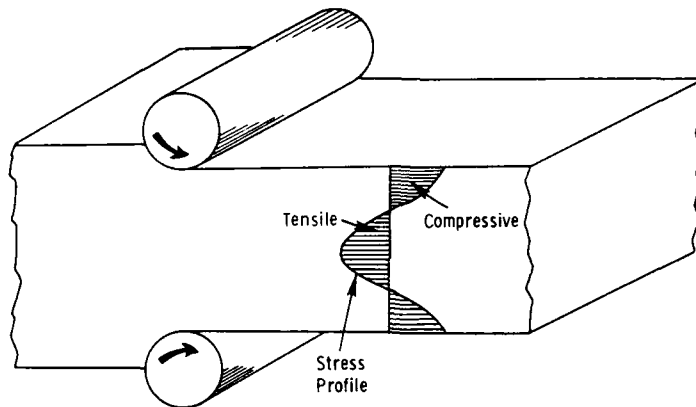


Figure 1. Stress distribution in a rolled plate

The service stress in any component is the sum of the applied stress due to the service load and any residual stress that may have been induced in manufacturing, i.e. before the service load was applied. When the service stress reaches dangerously high levels, failure occurs.

Texture Evolution During Deformation Processing

For purposes of analysing deformation processing operations such as rolling, material isotropy is generally assumed. Early theories developed for acoustoelastic stress measurement have treated polycrystalline materials as isotropic. However, it is well known that most, if not all, polycrystalline materials have some degree of preferred grain orientation or texture due to fabrication [3].

WELLS

Texture may be defined simply as a condition in which the distribution of crystal orientations is nonrandom. The texture that is produced by the forming process itself, such as plate or sheet rolling, is called a deformation texture. Deformation textures are due to the tendency of the grains in a polycrystalline material to rotate during plastic deformation. Each grain undergoes slip and rotation in a complex manner related to the force of the rollers and the interaction with adjoining grains [4].

It is clear that the influence of texture must be considered in the acoustoelastic measurement of residual stress induced in deformation processing. Ultrasonic wave propagation in an anisotropic medium is sensitive to both mechanical stresses and preferred grain orientation. In fact, the presence of texture can cause ultrasonic velocity changes of the same order of magnitude or greater than those due to stress [3].

Acoustoelastic Theory

Stress-Strain Relations [5]

For the case of a linear elastic anisotropic solid, the stress-strain relationship is

$$\sigma_{ij} = C_{ijkl} \epsilon_{kl} \quad (2)$$

where C_{ijkl} are the second-order elastic constants and ϵ_{kl} is the strain tensor. This is simply a statement of Hooke's Law. From the definition of strain which is defined in terms of displacements u_i we have:

$$\epsilon_{kl} = 1/2 [(\partial u_k / \partial x_l) + (\partial u_l / \partial x_k)] \quad (3)$$

The equations of motion can be rewritten as:

$$C_{ijkl} (\partial^2 u_k / \partial x_l \partial x_j) = \rho \ddot{u}_i \quad (4)$$

where ρ is the material density.

Let us assume a plane wave solution and rewrite the displacements as:

$$u_i(x_k, t) = A \alpha_i \exp i(\omega t - k_m x_m) \quad (5)$$

where A is the amplitude of the wave, ω is the angular frequency, t is the time, k_m are the components of the wave vector, α_i are the direction cosines of the particle displacements and x_k are the Cartesian coordinates.

We can rewrite the wave vector in terms of the direction cosines of the normal to the plane, $n_m = (l, m, n)$ as:

WELLS

$$k_m = (2\pi / \lambda) n_m = k n_m \quad (6)$$

where λ is the wavelength and k is the wavenumber. Therefore,

$$k_m x_m = k n_m x_m \quad (7)$$

The displacement may be rewritten as:

$$u_i = A \alpha_i \exp i(\omega t - k n_m x_m) \quad (8)$$

Differentiating and substituting into the equation of motion yields:

$$C_{ijkl} k^2 n_l n_j u_k = \rho \omega^2 u_i \quad (9)$$

$$\text{OR} \quad C_{ijkl} k^2 n_l n_j \alpha_k = \rho \omega^2 \alpha_i \quad (10)$$

This is equivalent to:

$$(C_{ijkl} n_l n_j - (\omega^2/k^2) \delta_{ik}) \alpha_k = 0 \quad (11)$$

$$\text{OR} \quad (C_{ijkl} n_l n_j - \rho V^2 \delta_{ik}) \alpha_k = 0 \quad (12)$$

where $V = \omega / k$ is the wave velocity, and δ_{ij} is the Kronecker delta function. This is known as the Christoffel equation.

In order to satisfy the Christoffel equation, the determinant of the coefficients of the α_k must be identically equal to zero.

$$\left| C_{ijkl} n_l n_j - \rho V^2 \delta_{ik} \right| = 0 \quad (13)$$

Solution of the equations of motion shows that three plane waves may be propagated in a linear elastic anisotropic solid. One such wave is a longitudinal or compressional wave. The other two are transverse or shear waves. The velocity of propagation V of each of these waves can be obtained by the determination of the eigenvalues and eigenvectors of the Christoffel equation [5].

The displacement vectors associated with each eigenvalue, ρV^2 , are mutually perpendicular. Thus, for a given direction of wave propagation, defined by the wave vector k , three waves are possible with mutually perpendicular displacement vectors but with different velocities. In general, these waves will not be pure longitudinal or pure transverse. For certain directions of propagation in a crystal lattice, however, the waves will be pure-mode. For a wave propagating in the short-transverse direction of rolled aluminum plate, the eigenvectors of the Christoffel equation give the particle displacement directions for pure-mode waves.

Rolled Plate Analysis

Consider a rolled plate in a plane stress state. For plane stress, there are only three non-zero components of the stress tensor σ_{ij} and $\sigma_{13} = \sigma_{23} = \sigma_{33} = 0$. For plane stress:

$$\sigma_{ij} = \begin{bmatrix} \sigma_{11} & \sigma_{12} & 0 \\ \sigma_{12} & \sigma_{22} & 0 \\ 0 & 0 & 0 \end{bmatrix}$$

The preferred orientation in the rolled plate can be considered to be orthotropically symmetric [6]. For an orthotropic plate, there will be three local two-fold symmetry axes. Due to rolling, one local two-fold axis is oriented normal to the plane of the plate. The rolling direction is also a two-fold symmetry axis as is the in-plane axis perpendicular to the rolling direction, i.e. the long transverse direction.

In the absence of either residual or applied stress, pure mode SH-waves can be propagated in the short-transverse direction, i.e. the plate thickness direction, with polarization directions along the two in-plane material symmetry axes. In general, in the absence of any stresses, the principal acoustic axes are coincident with the axes of material symmetry in the plate.

Due to the rolling process, the pure mode SH-waves will propagate at different acoustic velocities in the rolling and long-transverse directions. These are the "slow" and "fast" wave velocities respectively.

A coordinate system may be constructed in the plane of the plate to analyze shear-wave propagation through rolled 5083 aluminum plate [6]. This coordinate system is shown in Figure 2. The x_1 and x_2 axes are oriented along the plate's material symmetry directions. The shear-waves propagate through the plate's thickness, in the x_3 -direction. Consider the eigenvectors determined from the Christoffel equation which give the particle displacement directions for pure-mode SH-waves. Coordinate axes are drawn parallel to these eigenvectors. The slow acoustic wave propagates in the plate-thickness direction and is polarized along the "slow acoustic axis." Similarly, the fast acoustic wave propagates in the plate-thickness direction and is polarized along the "fast acoustic axis." In the unstressed state, these acoustic axes are designated S_0 and F_0 respectively.

The presence of stress causes the polarization directions for propagation of pure-mode SH-waves to rotate with respect to the initial unstressed acoustic axes [7]. The rotated "slow" and "fast" acoustic axes are designated S and F respectively. These rotated acoustic axes are referenced to

the unstressed acoustic axes by the angle ϕ . For a biaxial stress distribution with $\sigma_{33}=0$, σ_{11} and σ_{22} can be referenced to the unstressed "slow" acoustic axis by the angle θ .

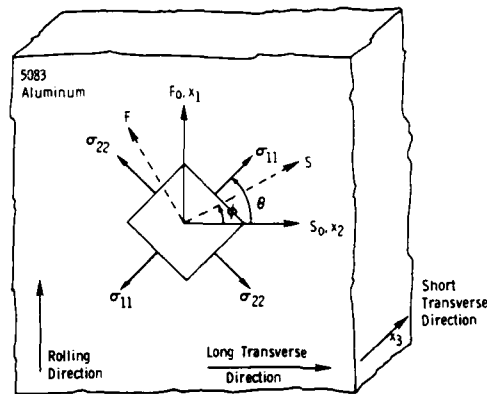


Figure 2. Coordinate system for analysis of shear waves propagating in rolled 5083 aluminum plate

The acoustic velocity of a SH-wave polarized along the rolling direction is slightly larger than that of a SH-wave polarized perpendicular to the rolling direction. By determining the phase velocities of orthogonally polarized shear waves in an anisotropic medium, we have a quick and inexpensive method of determining the rolling and long-transverse directions in a rolled plate product. The ΔV for orthogonally polarized shear waves also provides an estimate of the degree of anisotropy in the rolled product.

The splitting of a shear wave into two orthogonally polarized components, the "fast" and the "slow," is a phenomenon known as acoustic birefringence or double refraction. This is the acoustic analog of optical birefringence in photoelasticity.

The initial birefringence, B_0 , is defined as the normalized difference in acoustic velocities between the "fast" and "slow" waves in the absence of applied stress. This can be represented as:

$$B_0 = \frac{V_{f0} - V_{s0}}{1/2(V_{f0} + V_{s0})} \quad (14)$$

where V_{f0} is the phase velocity polarized along the "fast acoustic axis" and V_{s0} is the phase velocity polarized along the "slow acoustic axis." For an isotropic material, the two components of the shear wave degenerate into

WELLS

one. Therefore, the magnitude of the acoustic birefringence for an isotropic material in the absence of stress is equal to zero.

In the stressed state, the acoustic birefringence B is defined as:

$$B = \frac{V_f - V_s}{1/2 (V_f + V_s)} \quad (15)$$

where V_f and V_s are the acoustic wave velocities polarized along the "fast" and "slow" axes in the rotated coordinate system.

For plane stress, Okada derived an acoustic birefringence equation of the form [6,7]:

$$B = \left[B_0 + M_1 (\sigma_{11} + \sigma_{22}) + M_2 (\sigma_{11} - \sigma_{22}) \cos 2\theta \right]^2 + \left[M_3 (\sigma_{11} - \sigma_{22}) \sin 2\theta \right]^2 > 1/2 \quad (16)$$

where B_0 and B are as defined previously and M_i are acousto-elastic constants. The M_i are functions of the second- and third-order moduli of the material.

It can be shown from Okada's theory [7] that the angle ϕ between the initial unstressed acoustic axes and the rotated acoustic axes in the stressed state can be used to calculate the shear stress component σ_{12} , of the stress tensor for the case of plane stress.

$$\sigma_{12} = \frac{B \sin 2\theta}{2 M_3} \quad (17)$$

where B is the measured acoustic birefringence in the stressed state and M_3 is an acoustoelastic constant of the material.

Initial Acoustic Birefringence Parameter, B_0

Equation (16) is a nonlinear equation for the normalized difference in acoustic velocities of SH-waves propagating in a stressed orthotropic rolled plate in the x_3 - direction. To accurately determine the stress-acoustic response of rolled 5083 aluminum plate, the initial birefringence parameter B_0 must be used. This is, from equation (14), a function of the initial "fast" and "slow" acoustic velocities of pure-mode SH-waves.

One question naturally arises for the acoustoelastic measurement of stress. This is simply whether or not B_0 is a material constant, intrinsic to a

WELLS

given alloy. Okada's acoustic birefringence equation treats the initial birefringence parameter B_0 as a material constant. That is, when determining the acoustoelastic constants, M_i , for the material under investigation, a single value of B_0 is used. This initial birefringence parameter is inserted into the acoustic birefringence equation and a least squares fit performed to determine the M_i . This methodology does not account for the fact that B_0 may be inhomogeneous.

Due to the rolling process, the value of B_0 may vary from one position in a rolled plate to another. Similarly, the initial acoustic birefringence may vary for different thicknesses of rolled plates of the same alloy and temper. An error in B_0 will consequently result in errors in the magnitude of the M_i for a given material. This will, in turn, result in incorrect determination of the stress tensor components given the M_i and stressed acoustic birefringence measurements, B .

It is the purpose of this study to examine the variation in the initial acoustic birefringence parameter, B_0 , for various thicknesses of rolled aluminum plate of a single alloy and known deformation history.

Aluminum Considerations

For this investigation, the acoustoelastic properties of 5083 aluminum were studied. 5083 is one of the principal aluminum alloys used in the Bradley Fighting Vehicle and Armored Personnel Carrier.

To characterize the degree of homogeneity of the initial acoustic birefringence parameter B_0 for various thicknesses of 5083 rolled plate, a special lot of aluminum plate was fabricated. The chemical composition of this 5083 aluminum plate is shown in Figure 3. Four gauges of uniaxially rolled plate were fabricated, 1 inch, 3/4 inch, 5/8 inch, and 1/2 inch, originating from a single ingot. The relevant rolling conditions for the fabrication of the plates is shown in Figure 4.

CHEMICAL ANALYSIS OF ALUMINUM									
ALLOY	WEIGHT PERCENT								
	Si	Fe	Cu	Mn	Mg	Cr	Ni	Zn	OTHER
5083	0.1	0.27	0.069	0.69	4.45	0.1	0.002	0.03	0.01
5083*-NOMINAL	0.4	0.4	0.1	0.4- 1.0	4.0- 4.9	0.05- 0.25	-	0.25	

*NOMINAL COMPOSITION IN PERCENT MAXIMUM UNLESS SHOWN AS A RANGE

Figure 3.

ROLLING CONDITIONS - UNIAXIAL				
THICKNESS (Inches)	TEMPERATURE, °F	# OF ROLL PASSES	% REDUCTION/ ROLL PASS	% FINAL REDUCTION
(Start) 14.6	815			
4	830			72.6
1	750	5	15	93.15
3/4	624	1	25	94.86
5/8	523	1	20	95.89
1/2	515	1	16.67	96.58

Figure 4. Rolling Conditions employed for fabrication of 5083 aluminum plates

5xxx series aluminum-magnesium alloys are used in the strain-hardened (H) tempers. They do not gain significant strengthening from precipitation-hardening as do 7xxx series aluminum-zinc-magnesium and aluminum-zinc-magnesium-copper alloys [8].

For this investigation, the 5083 aluminum was manufactured in the F-temper. This indicates that the 5083 was "as fabricated" and there was no control over the amount of strain-hardening [8]. One of the consequences of cold working is the establishment of macro-residual stresses. These can be relieved through annealing [8]; for this acoustoelastic birefringence study no such stress-relieve was performed. Thus, the measured initial acoustic birefringence parameter B_0 represents the actual superimposed affects of deformation texture produced in uniaxial rolling and induced macro-residual stresses without subsequent annealing.

The fabricated rolled aluminum plate products were approximately four feet wide in the long-transverse direction. They were subsequently cut into two-feet X two-feet sections for analysis. Three plates in each of the four gauges were evaluated. Acoustoelastic birefringence data at 30 points per plate (360 total points) were collected. The initial acoustoelastic birefringence parameter was mapped as a function of position in the plates as shown in Figure 5. In addition, measurement of the position of the principal acoustic axes, i.e. directions of pure mode SH-waves, relative to the axes of material symmetry were made. Recall that rotation of the principal acoustic axes is an indicator of a shear stress component σ_{12} of the stress tensor under plane stress conditions. In order to systematically examine the effects of rolling reduction and position in a rolled plate upon the initial acoustoelastic birefringence parameter B_0 , a statistical analysis was performed.

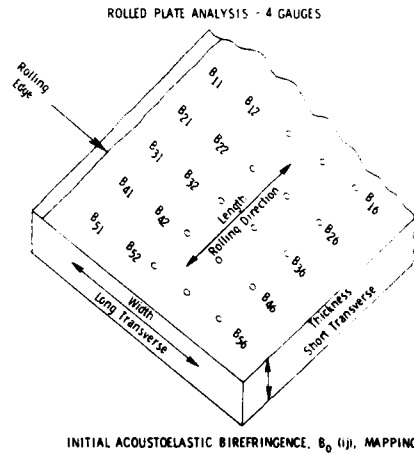


Figure 5

Experimental

Ultrasonic Measurements

Since acoustic birefringence is defined to be the normalized difference in acoustic velocities of orthogonally polarized shear waves, it suffices to measure the normalized difference in the wave transit times associated with these "fast" and "slow" SH-waves as they travel through the sample thickness. This is because at any one point, the thickness of the specimen is a constant. Thus, one of the valuable features of the acoustic birefringence technique is that absolute velocity measurements are not necessary.

For this investigation, a Panametrics 5050 Pulser-Receiver was used to generate short, large-amplitude electrical pulses of energy which, when applied to the ultrasonic transducer, were converted into energy of mechanical vibrations. A 5 MHz transducer was coupled to the aluminum plates through a viscous couplant. The shear wave transit times through the plate thickness were measured using a pulse-echo overlap technique. The transit times associated with the "fast" and "slow" SH-waves were measured using the delta-time feature of a Hewlett-Packard 1726A oscilloscope. The transit time for propagation of an ultrasonic wave can be determined by overlapping successive "back-echoes" of an echo train on an oscilloscope display. In the overlap mode, the CRT is used as a visual comparator for making accurate time-of-flight measurements. An echo train from the CRT display is shown in Figure 6. The overlap of two successive "back-echoes" from this display is shown in Figure 7. B_0 is calculated from Equation (14) where transit-time can be used in place of absolute velocities as discussed above.

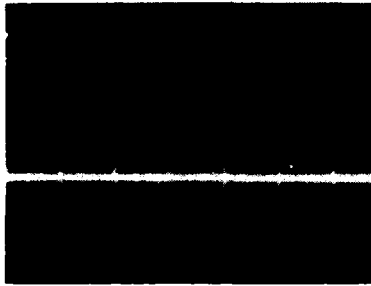


Figure 6.

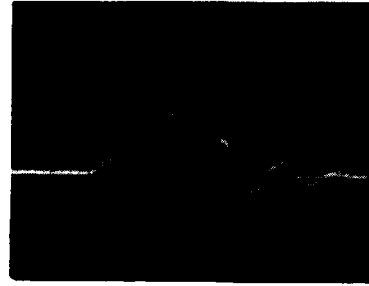


Figure 7.

The principal acoustic axes for propagation of pure-mode SH-waves were determined by examining the echo train as the transducer was rotated slowly through 360° . As a shear-wave transducer is rotated, the amplitudes of the reflected back-echoes, as displayed on the oscilloscope, exhibit maxima and minima. The "slow" and "fast" components of the orthogonally polarized SH-waves will interfere with each other and cause abnormal modulation of the pulse unless the transducer is polarized in a pure-mode direction [9]. By examining the modulation of the ultrasonic "back-echoes," it can be quickly determined if the pure-mode directions are coincident with the axes of material symmetry of the plate. In Figure 6, the transducer is polarized along a principal acoustic axes and hence, there is no abnormal modulation of the signals.

Statistical Analysis

An analysis of variance (ANOVA) was performed in order to examine the variation in the initial acoustoelastic birefringence parameter B_0 , as determined experimentally. ANOVA is a statistical procedure for investigating the change in a response (here, initial birefringence parameter, B_0) due to factors of interest [10]. In this investigation, the factors are the gauge and position within the rolled aluminum plates. Underlying the ANOVA model are the assumptions that the data are observations from a Gaussian distribution with constant unknown variance σ^2 and a mean μ which depends only on the levels of the factors under consideration. These parameters are estimated from the data. The estimate of σ^2 can be used to obtain confidence intervals within which the true unknown parameter value lies with prescribed probability. The hypothesis that the factors of interest have no effect on the response may be tested. A hypothesis of "no effect" is known as the null hypothesis [10].

The analyses of the initial birefringence data addressed three general questions. The first was to establish whether there was a statistically significant variation in B_0 within each 6x5 matrix corresponding to a "row" or "column" effect. The second was to assess whether the three 6x5 matrices per gauge demonstrated systematic variation. The last was to examine the

variation in the initial birefringence parameter for the four different gauges.

In order to establish whether the observed differences in the estimated level means can be attributed to randomness, the ratio of the between level variance is compared to the within level variance. This ratio is called an F-statistic [10]. Under the hypothesis that there is no effect due to the factor of interest, this F-statistic has a known tabulated distribution.

Comparison of the ratio as estimated from the data with the values from the F-statistic table determines how unlikely a ratio as large as the one observed is under the assumption of no effect due to the factor. If the probability is sufficiently low (conventionally less than .05), one says that the effect is "statistically significant" and the null hypothesis can not be accepted [10].

Results and Discussion

Analysis of the ultrasonically measured initial acoustic birefringence parameter B_0 for the four gauges of rolled 5083 aluminum showed that the data fit a Gaussian distribution quite well. This is illustrated in Figures 8 and 9.

The ANOVA showed no significant difference in the birefringence with respect to the longitudinal (rolling direction) of the plates. Since the probabilities associated with the "row" effects are greater than 0.05 for the initial acoustic birefringence data, these effects are not statistically significant and may be assumed to be zero.

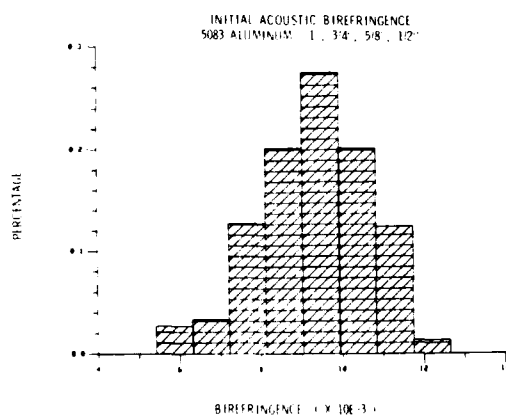


Figure 8.

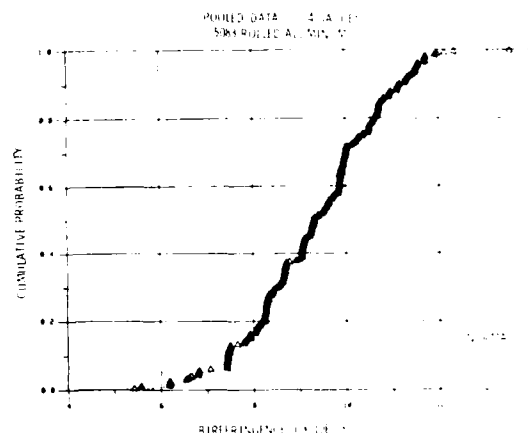


Figure 9.

The variation of the acoustic birefringence in the long transverse direction of the rolled plates was statistically significant, however. The ANOVA

WELLS

model was simplified to one in which there was a shift in the mean from "column" to "column" but not from "row" to "row." This "column" effect is equal to the difference between the average for each "column" and the overall mean. The initial acoustic birefringence as a function of transverse position in 5083 "as-fabricated" rolled plate is shown in Figure 10. Note that the abscissa corresponds to the $B_0(ij)$ for $j=1$ to 6 as shown in Figure 5. The "row" effect is not statistically significant. There was a strong effect on the initial acoustic birefringence parameter B_0 in the vicinity of the rolled edge and B_0 varies as a function of position.

In addition, there was marked variation in the direction of the principal acoustic axes with respect to the axes of material symmetry for propagation of pure-mode SH-waves for positions corresponding to the $B_0(i1)$ and the $B_0(ij)$ for $j=2$ to 6. For positions outside the vicinity of the rolled edge, the principal acoustic axes were generally coincident with the axes of material symmetry; the deviation of the S_0 and F_0 from the material symmetry axes was less than 5° . Near the rolling edge, however, there was consistently large deviation of the principal acoustic axes from the axes of material symmetry of the plates, on the order of 30° .

It is clear that the acoustoelastic properties at or near the rolling edge of the plates are markedly different from the properties of the rest of the plates. Visually inspecting the rolling edges of the plates in the "as-fabricated" condition confirms this acoustoelastic anomaly. There is substantial edge cracking on the plates and this region would not be commercially acceptable. In fact, this region near the rolled edge is cropped for commercial use. But from the standpoint of a technology demonstrator, the acoustoelastic properties of rolled plates are shown to be easily mapped using the birefringence technique; the magnitude of B_0 and the direction of the principal acoustic axes can be used as indicators for variation in properties locally due to deformation processing.

From Figure 10, it can also be seen that the magnitude of the acoustic birefringence for "column 6" at the cut edge is substantially lower than for other regions of the plate. One possible explanation for this is that there was a "stress-relief" due to cutting the plate that is "heard" in the vicinity of the cut edge. Recall that the 5083-F plates were originally four feet in width and were cut in half for this investigation. The directions of the principal acoustic axes did not vary markedly for measurements near the cut edge.

With data near the rolling edge removed, all four gauges showed the same systematic variation with respect to the long transverse direction of the plates. A 68% confidence interval for the initial birefringence parameter is about $\pm \sigma$ where σ is the standard deviation. This means that there is a 68% certainty that the true acoustoelastic birefringence parameter lies

within $\pm \sigma$ of the mean. For the population studied, this represents an uncertainty of between ± 11 and $\pm 20\%$. The estimated initial birefringence parameter $B_0(j) \times 10^{-3}$ and the respective means for the four gauges of interest are shown in Figure 11.

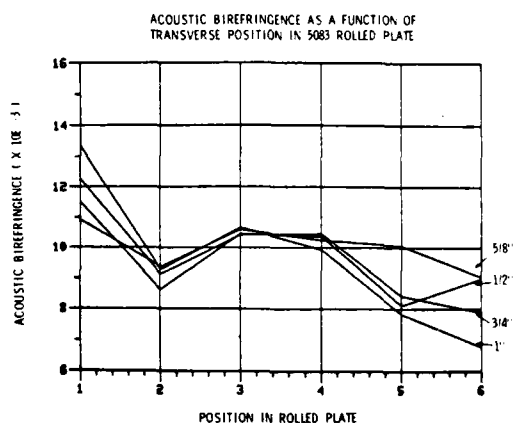


Figure 10

ESTIMATED INITIAL ACOUSTIC BIREFRINGENCE $B_0(j) \times 10^{-3}$

	COLUMN						
	1	2	3	4	5	6	MEAN
1							
F62	12.378	10.065	10.031	8.815	8.044	6.815	
G	13.570	8.009	11.492	11.717	7.052	7.423	
H	14.094	9.681	10.512	9.266	8.407	6.072	
POOLED	13.347	9.272	10.678	9.932	7.834	6.768	8.897
3/4							
F63	12.238	8.837	10.149	10.784	7.810	7.978	
G	13.104	9.759	11.210	10.695	8.246	6.415	
H	11.476	8.786	9.911	9.877	9.229	7.260	
POOLED	12.273	9.127	10.423	10.456	8.429	7.884	9.264
5/8							
E64	10.600	9.974	10.872	10.242	10.936	9.337	
G	11.862	8.131	10.104	9.823	8.699	8.482	
H	10.278	9.979	10.842	10.666	10.557	9.304	
POOLED	10.916	9.361	10.606	10.244	10.064	9.041	9.863
1/2							
E65	11.904	9.014	10.560	11.346	8.546	8.732	
G	11.928	7.878	10.208	9.568	7.715	9.166	
H	11.200	8.966	10.621	10.205	8.082	9.040	
POOLED	11.507	8.619	10.463	10.373	8.114	8.979	9.310

*ROLLING EDGE

Figure 11

One might expect different crystallographic texture distributions for rolled plates of different final reductions. Since texture has a strong effect on the acoustoelastic birefringence parameter, this explains why there is variation in B_0 for plates rolled from the same ingot to different final reductions. The largest mean B_0 value, 9.310×10^{-3} , was obtained for the 1/2" thick rolled plate and the smallest mean B_0 value, 8.897×10^{-3} , was obtained for the 1" thick rolled plate. Intuitively, this can be explained by the fact that the 1/2" thick plate received the greatest number of roll passes in deformation processing. The magnitude of the initial acoustic birefringence parameter, roughly 9 parts in 10^3 , is quite large. However, realizing that the aluminum plate was uniaxially rolled rather than cross-rolled would explain the large degree of preferred orientation that is observed in the B_0 values.

Conclusions

The inhomogeneity in the initial birefringence parameter B_0 for rolled plates has been previously alluded to in the literature but not formally studied. In this investigation, the variation of B_0 within plates of the same thickness and between plates of different thicknesses was studied for uniaxially rolled 5083 aluminum plate. It was shown that even for plates rolled to different final reductions from a single ingot, B_0 is not a constant. There was statistically significant variation in this parameter and the values of B_0 were normally distributed. Clearly, the acoustoelastic determination of residual stresses in rolled aluminum armor plate products will depend on the value of the initial birefringence parameter inserted

WELLS

into Okada's birefringence equation, Equation (16). Calibration of the acoustoelastic constants, M_i , will depend upon a "best fit" B_0 value. If one is to apply acoustoelasticity in the field, it is best to work with well-characterized materials. The rotation of the principal acoustic axes, referenced to the axes of material symmetry, gives an indication of relative stress-induced anisotropy. This can be qualitatively applied in the field.

Acknowledgements

The author wishes to thank ALCOA Davenport Works for fabricating the aluminum plate used in this study. She would additionally like to thank Messrs. Anil Govada and Robert Young from the ALCOA Technical Center for their technical support and suggestions and Mr. John Harrington who served as a liaison between ALCOA and the U.S. Army Materials Technology Laboratory (MTL). The author gratefully acknowledges the statistical work that was performed and the technical consultation provided by Mr. Mark Vangel of the Mechanics of Advanced Structures and Materials Branch at MTL. She would also like to thank Cadet Mark Waite of the U.S. Military Academy at West Point, who performed many of the acoustoelastic measurements described herein during his stay at MTL in 1985. The author acknowledges the support of Ms. Karen Pedrotti, and Mr. Harold Laye at MTL for the Figures contained in this report.

References

- 1 Fontana, M.G., Greene, N.D. Corrosion Engineering, McGraw-Hill Book Company, New York (1978)
- 2 Cullity, B.D. Elements of X-Ray Diffraction, Addison Wesley Publishing Company, Inc., Massachusetts (1978)
- 3 Clark, A.V., Mignogna, R.B., Sanford, R.J., Acoustoelastic Measurements of Stress and Stress Intensity Factors Around Crack Tips, Ultrasonics, 21 (1983) 57-64.
- 4 Backofen, W.A., Burke, J.J., Coffin, L.F. Jr., Reed, N.L., Weiss, V. Fundamentals of Deformation Processing, Proceedings of the 9th Sagamore Army Materials Research Conference, Syracuse University Press (1964)
- 5 Green, R.E., Ultrasonic Investigation of Mechanical Properties, Treatise on Materials Science and Technology, Volume 3, Academic Press, New York (1973)
- 6 Clark, A.V., Mignogna, R.B., A Comparison of Two Theories of Acoustoelasticity, Ultrasonics, 21 (1983), 217-225.
- 7 Okada, K., Acoustoelastic Determination of Stress in Slightly Orthotropic Materials, Experimental Mechanics, 21 (1981), 461-466
- 8 Hatch, J.E. Aluminum: Properties and Physical Metallurgy, American Society for Metals, Metals Park, Ohio (1984)
- 9 Hsu, N.N., Acoustic Birefringence and the Use of Ultrasonic Waves for Experimental Stress Analysis, Experimental Mechanics, 14(5) (1974), 169-176.
- 10 Box, G.E.P., Hunter, W.G., Hunter, J.S. Statistics for Experimenters, John Wiley and Sons, New York (1978)

WHITE, LEIPERTZ & BRITAN

THE ARMY'S KEY OPERATIONAL CAPABILITIES:
ANALYSIS OF C3 CONTRIBUTION (U)

JAMES L. WHITE, LTC
DONALD F. LEIPERTZ, MR.
RONNIE G. BRITAN, DR.

HEADQUARTERS, DEPARTMENT OF THE ARMY
OFFICE OF THE ASSISTANT CHIEF OF STAFF
FOR INFORMATION MANAGEMENT
PENTAGON, WASHINGTON, DC 20310-0700

I. INTRODUCTION

The Army's "Big 5" decision made in 1973 was designed to remedy the approaching obsolescence of the Army's primary mobility and firepower weapon systems. The "Big 5" program supported the development and fielding of the following systems: M-1 Tank, M-2 Infantry Fighting Vehicle, Advanced Attack Helicopter, Utility Tactical Transport Aircraft System, and Patriot Missile. The Army Staff completed a study in the Fall of 1985 to determine the merits of identifying a new program which would highlight a set of systems to focus Research, Development, and Acquisition Programs and Plans out to the year 2000. The Fall 1985 study found that the Army needs to focus on generic improvements that enhance the capabilities of major weapons systems which allow the execution of AirLand Battle doctrine against a projected threat instead of focusing on individual weapons systems. The five Key Operational Capabilities (KOC's) selected in 1985 were: Soldier and Unit Performance Enhancement; Command, Control and Communications (C3); Reconnaissance, Surveillance, and Target Acquisition; Battlefield Lethality; and Battlefield Sustainment. It was felt that the synergy of these five Key Operational Capabilities, working in consonance with the "Big 5" systems, would significantly increase warfighting capability.

Today's tremendous number of technological advancements offer alternate choices to enhance the Army's warfighting capabilities, especially in C3. Therefore, many candidate systems exist to compete for relatively scarce monies available for developing and procuring new or enhanced Army systems. Given this resource-constrained environment, it is critical for the Army to validate the relative battlefield

contributions of emerging C3 systems. This should be the basis for program prioritization, weighed in consonance with the correlated costs. Measuring the contribution of fighting systems is straightforward since contributions can be measured in terms of increased battlefield kills or deterrent kills. However, it is difficult to capture the battlefield impact of emerging information systems providing Command, Control, and Communications. With KOC as a backdrop, research was conducted on methodologies to quantify the combat measures of effectiveness (MOE) for C3 systems and determine if a measurable synergism is created by all five KOC's working in concert.

Other researchers have initiated efforts to quantify C3 measures of effectiveness (MOE) but no validated results are available. The research suggested new methods for combining existing models. Sample data are expected by late 1986. Spinoffs from suggested integration efforts may be more significant than the original intent of quantifying C3 value.

II. BACKGROUND

There are a wide variety of ways in which the importance of C3 systems can be demonstrated. When historians speak of the decisive role of the commander in battle, they state that the commander who has accurate information, timely communications, aids to enable wise decisions, and provides superior leadership attains a decisive advantage over his enemies.

Commanders and staff officers serving in today's Army who have served in a tactical operations center which has been out of communications, starved for intelligence, or drowning in a sea of knowledge intuitively know the value of Command, Control and Communications. These experienced soldiers, however, cannot quantify the difference C3 makes in a battle.

The most common method of measuring the value of C3 systems is by comparing their relative performance with similar C3 systems using established criteria, i.e., measures of performance (MOP) such as interoperability, resistance to jamming, reliability (mean time between failure), survivability, mobility, manpower reduction, functionality, range, throughput, etc. Mission Area Analysis (MAA) documents can be consulted to determine what MOPs are the most important to the Army based on established deficiencies and shortcomings. The C3 systems can be compared using techniques such as pairwise comparison to weigh each system's MOP with other MOPs. This multi-dimensional analysis can be fed into an existing software program, such as "Expert Choice" using a microcomputer to arrive at a single-dimensional comparison (3). C3

system capabilities can be quantified and graphically displayed; however, these results are based solely on the subjective assessments of experts in the C3 functional area. Cross functional comparisons may be subject to significant variation.

The MITRE Corporation has developed a, "Conceptual Framework for Evaluating and Comparing Command and Control Systems" (Figure 1) which allows for a more sophisticated framework for "...measuring the contribution of a C2 system to the command and control process it is intended to support" (6). This methodology allows the comparison of alternative C2 systems as well as organizational and procedural alternatives. If this suggested methodology can be validated, MITRE states it will allow tradeoffs at various system levels from component to architecture. Although timeliness and information utility are key measures of C3 system effectiveness, they should only be considered MOPs when comparing C3 systems with combat systems. This more sophisticated comparison, however, remains a subjective comparison.

Computer simulation models yield measures of performance (MOP) for C3 systems in a less subjective manner. Models designed to evaluate tactical communications networks usually measure such parameters as: average message delay, traffic handling capability, node storage, routing procedure and discipline, link channel capacity, and network topology in a jamming environment. Tactical automation systems, such as the Maneuver Control System and All Source Analysis System, are measured by less complex and somewhat more subjective criteria including deployability, pre-processing and speed of processing, communication efficiency as well as the ability to handle information surges.

There are many organizations now engaged in valuable modeling efforts to better quantify C3 MOPs. Major efforts were identified at TRADOC Systems Analysis Activity (TRASANA), Army Materiel Systems Analysis Activity (AMSAA), US Army Electronics Proving Ground (USAEPG), and the Electromagnetic Compatibility Analysis Center (ECAC). This analysis is valuable for determining performance degradation, network flow, and equipment tradeoffs. These studies enable C3 functional experts to gain a perspective of the strengths and weaknesses of the systems. When coupled with system cost, the models facilitate procurement prioritization. This perspective does not, however, enable the functional expert to articulate C3 system value to proponents of other functional areas since the C3 proponent has no measure other than his Army field experience from which to draw. For instance, the combat arms commander who is told that a communications system will allow his message to be received in less than 10 minutes or that an automation system will double message processing speed will probably say, "So What." He is rightfully interested in how these systems will help him "Fight

RELATIONSHIP AMONG SYSTEM MEASURES

MOE MOP	TIMELINESS	INFORMATION UTILITY
CONNECTIVITY	●	○
FLEXIBILITY	●	○
ACCURACY	◐	●
COMPLETENESS	◐	●
CURRENCY	◐	●
LEVEL OF AGGREGATION	○	●

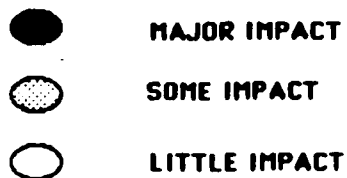


Figure 1

Out-Numbered and Win". He wants to know some measure of combat effectiveness.

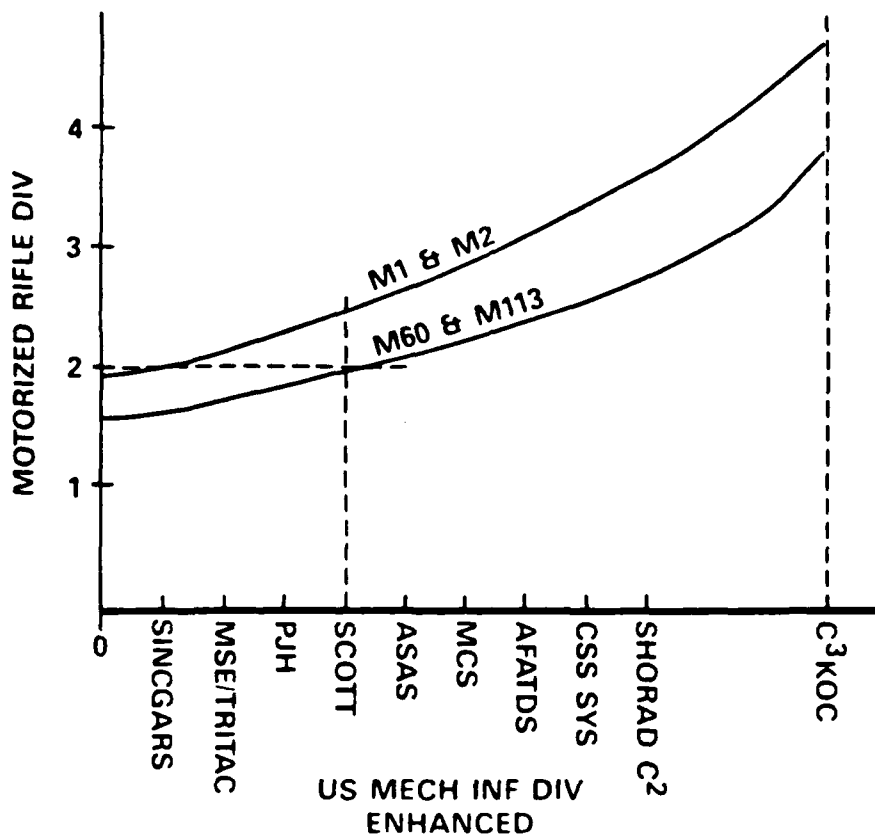
There are several combat models with resolution from Corps to Battalion that provide these measure of combat effectiveness (MOE) for weapons systems. Among the more popular are Vector II, VIC (VECTOR-IN-COMMANDER), CORDIVEM, FOURCE, CORBAN (formally QUICKSCREEN) and TACOS-II (7, 10, 11, 12). None of these models portray communications-electronics (C-E) as a dynamic model element. Communication is usually treated using tables of times for message delay from unknown sources. In some models the message preparation time including automated preparation is so much greater than the communications delay, the significance of the communications delay is overshadowed. As a consequence, the communications delays make little difference in model outcome, and to the uninitiated observer, communications is considered as unimportant (5). However, every commander can recall situations requiring the need for very rapid communications. Such situations include a call for air defense artillery, fire support, major troop commitment and battlefield air interdiction. Unfortunately, the environment requiring such communications when needed will be stressed by message congestion, enemy jamming, unit and node displacement, and attrition by enemy fires. These factors should all be important considerations in combat models but they currently are not.

III. DESIRABLE MODEL OUTCOME

An authentic representative of C3 in combat models can be achieved only by the integration of the best combat models and C3 models. The term C3 model will hereafter be used to include a collection of C-E and automation for Air Defense Artillery, Combat Service Support, Intelligence and Electronic Warfare, Fire Support, and Maneuver Control submodels. The C-E submodel will receive the most discussion because our research has determined it is the most difficult submodel to develop. The integrated model should be user friendly with new scenario turnaround time of one week for a coarse-grain analysis and two to three weeks for a detailed analysis. The analysis time must include setup, run, and sensitivity checks. To be useful to high level decision makers, results must be available in graphical form similar to Figure 2. Force-on-force comparisons should be made using several MOE criteria. Useful MOEs include attrition, mission accomplishment, ground gained or lost, and time to complete the mission.

Using scenarios such as SCORES V with selected MOEs, the results of a force-on-force engagement could be illustrated with both enhanced weapon systems and C3 systems. For example (Figure 2), a US Mechanized

U.S. (BLUE) DEFENDS/SOVIET (RED) ATTACKS



- SINGGARS (Single Channel Ground and Airborne Radio)
- MSE (Mobile Subscriber Equipment)
- TRITAC (The Joint Tactical Communications Program)
- PJH (Position Location Reporting System/Joint Tactical Information Distribution System/Hybrid)
- SCOTT (Single Channel Objective Tactical Terminal)
- ASAS (All Source Analysis System)
- MCS (Maneuver Control System)
- AFATDS (Advanced Field Artillery Tactical Data System)
- CSS SYS (Combat Service Support System)
- SHORAD C2 (Short Range Air Defense C2)
- C3KOC (Key Operational Capability "Objective Systems")

Figure 2

Infantry Division could be modeled against a Soviet Motorized Rifle Division. The established base case in a hypothetical scenario shows the US division in a standoff against 1.5 Soviet divisions. If the US division is enhanced with M1 Tanks and M2 Infantry Fighting Vehicles it may standoff two Soviet divisions. Incrementally enhancing the US division's C3 capabilities should also result in improved performance. At some point in this C3 enhancement process, the US division's performance capability should equal the performance capability with the M1 and M2 enhancement (Figure 2, SCOTT is at this enhanced C3 point, i.e., the performance capability of the US division with M60 and M113 plus SCOTT, PJH, MSE/TRITAC, and SINCGARS is hypothetically equivalent to the same US division with current C3 plus M1 and M2). This will enable some value judgments to be made between enhancing weapon systems versus C3. Similar comparisons could be made between other functional area systems and weapon systems. If there is a synergy between weapon systems and functional systems, the MOE curves should diverge as shown in Figure 2 with each incremental functional enhancement. Such a comparison could also provide valuable insight into preferred fielding sequence. For example, it may be preferable to enhance combat data communications before fielding ASAS and MCS as enhanced communications may improve automation system performance.

IV. ONGOING RESEARCH

Only two major research efforts were uncovered that might produce the desirable model outcome of integrated C3 and combat model. Both of these efforts, one at Bell Technical Operations Textron and the other at TRASANA, are still in the conceptual stage. The main reason this important work has not been studied more extensively is due to the complexity of current C-E models and the lack of meaningful parameters (sometimes called hooks) in combat models that can be dynamically modified by C-E model outputs.

Looking at the C-E model challenge we find that popular C-E models such as Communications-Electronics Operation Positioning System (CEOPS) and Environmental Interference Effects Model (EIEM) require large data bases containing detailed table of organization and equipment (TOE) data, X and Y coordinate locations for equipment on the battlefield, and detailed equipment technical characteristics. The model outputs are given in terms of technical communication parameters such as signal-to-noise ratios (SNR). These models have the advantage of assessing detailed performance at the equipment level as well as effects of terrain on specific communications links. The major disadvantages include: slow model run time; requirement for large computers with large data bases; difficulty of sensitivity analysis of network topology; and a well

trained staff to interpret outputs. These models are static and cannot handle new data dynamically. Therefore, it is extremely difficult to incorporate node movement and attrition. In addition, network capacity and time delays are not modeled. These are just a few of the reasons the current C-E models are not compatible with current combat models.

Bell Technical Operations Textron, under contract with the US Army Electronics Proving Ground, has studied the integrated model approach. Bell determined "...that explicit incorporation of detailed C-E phenomena into an existing large-scale tactical combat model was not a feasible near-term goal..." (4). Their study recommended development of a parametric interface between models. The communications model would receive battlefield information from the combat model and produce communications parameters that would be fed back to the combat model (Figure 3). Various forms of time delay were determined to be appropriate communications parameters. Bell indicated that the Vector-II corps-level combat model would be the preferred combat model because it is well documented, widely-used, and appears to be sensitive to communications effects. Bell did not discuss the potential model run time problems when linking to large models and the effect of attrition on a random routing network.

TRASANA has two independent modeling efforts whose integration may produce the desired model outcome. The model called Communications Model-Tactical (COMM-T) takes a much different approach than the large discrete event C-E models (11). This approach is aggregated network simulation and is built upon Kleinrock's, Prosser's, and Cooper's theorems of stochastic message flow queuing and delay in networks (5). COMM-T concentrates on network, nodal attributes and essential link system characteristics but also incorporates propagation, electronic counter measures (ECM) and network management algorithms. The model outputs are in the form used by most combat models which employ message delay, probability of node-to-node communications and effective link service rates. Message delays are given as a function of: network topology, nodal traffic loading, routing and capacity schemes, precedence levels and ECM effects. COMM-T's distinct advantage is that it can be made dynamic and interactive with most combat models because of its fast run time. To be dynamically integrable, a C-E model requires one-tenth the run time of the combat model to allow interruptible updates without significantly increasing the combat model's run time (12). COMM-T satisfies this criteria and would be controlled by the following combat states: jamming duty cycles, nodal attrition, nodal mobility, and nodal equipment reliability. COMM-T's current disadvantages include a difficulty in capturing performance of communication systems with similar characteristics and lack of traffic statistics using current software

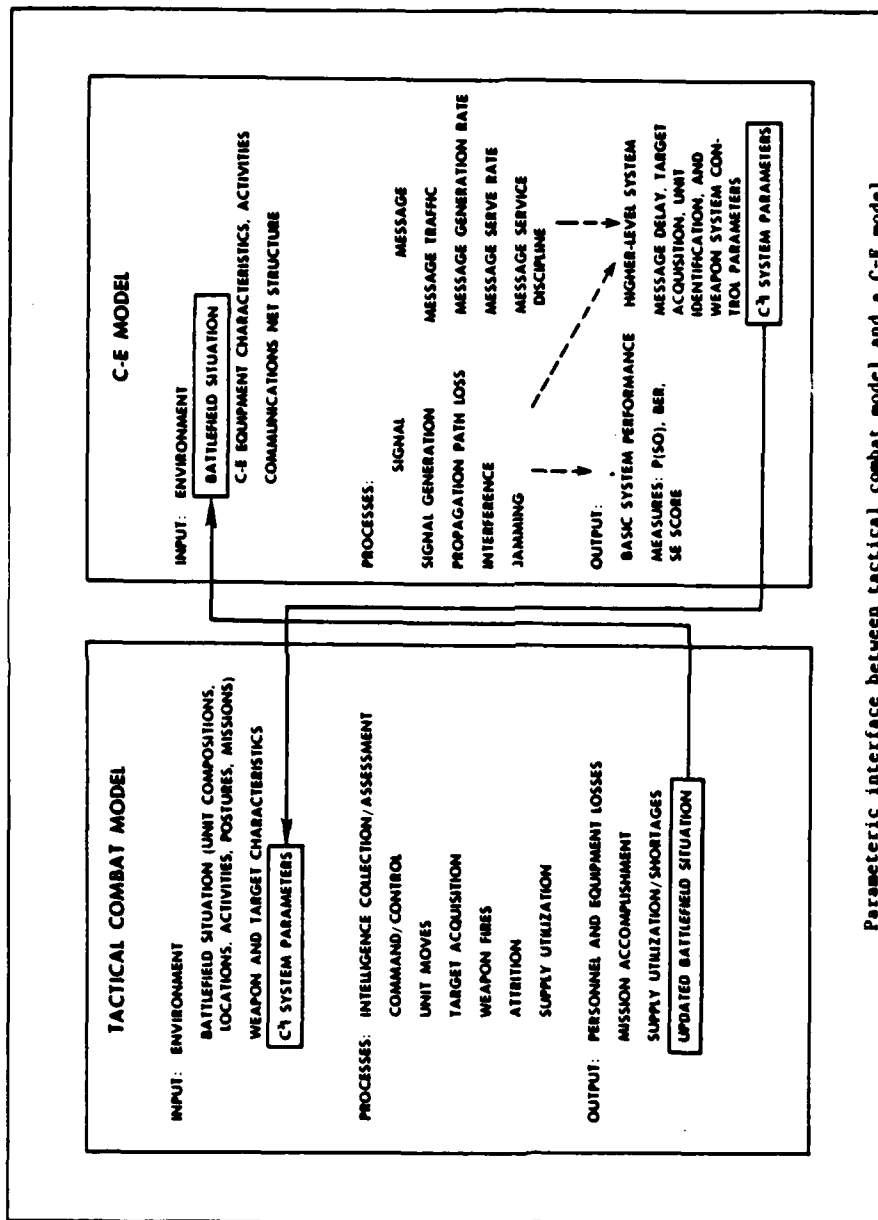


Figure 3

language. The first disadvantage results from the aggregated approach methodology. The second may be overcome in the future using SLAM II.

TRASANA's recently developed Vector-In-Commander (VIC) Corps level force-on-force model, which runs on a VAX-11/780, is well structured to allow the integration of C3 submodels such as C-E (12). The VIC architecture, data structures, input and output design, and decomposition of combat processes into submodels will support detailed representations of C3 systems and processes. VIC is currently being used to study Battlefield 90 for the German Army corps in Europe. This study, which is due to be completed within the next two months, should demonstrate VIC's validity for European scenarios. In November 1985 TRASANA began to build COMM-T features into VIC with completion of these modifications expected by late 1986. Initial test results look promising. Major modeling efforts planned by TRASANA using COMM-T integrated with VIC include an Air Force Forward Air Defense System (FADS) and a Joint Surveillance and Target Attack Radar Systems (JSTARS) simulation. The fact that this effort will dynamically model communication attrition, degradation, network loading and delays, for the first time is significant. The integration of COMM-T into VIC, when validated, may be of significant analytic value.

The BDM Corporation, sponsored by the Deep Attack Project Office of CACDA and the Defense Nuclear Agency, has developed the Corps Battlefield Analyzer (CORBAN). CORBAN is a Corps level force-on-force model which runs on a customized Apple II computer. Although not as sophisticated as VIC, it also appears to be well structured to allow integration of C3 models such as COMM-T. CORBAN provides quick turn around time using validated scenarios. It runs five days of combat in approximately 24 hours. CORBAN's usefulness was demonstrated in a study of MOEs for JSTARS. An MOE analysis was done using European scenarios to determine a value added for JSTARS. CORBAN parameters were changed to reflect JSTARS improved target locating error and extended range. Analysts were able to examine improved fire effects and determine how many systems were killed by deep fires and at what point in the battlefield JSTARS caused a decisive impact on the battle for the Corps. Users of CORBAN have indicated that it produces a good coarse grain analysis but that its hostile code sheet input and output mode is less mature than the simulation itself.

Working with an ongoing study sponsored by the Army Studies Office, Office of the Deputy Chief of Staff for Operations and Plans, we expect to obtain sample C3 MOEs using CORBAN. Man-in-the-loop CORBAN scenario runs will be periodically interrupted to update COMM-T. Updated time delays produced by COMM-T will be input into CORBAN. The plan calls for comparing battle results with communications equipment currently in the

Army inventory versus equipment expected in 1990 at Corps and below. Several time sensitive combat events, such as artillery fire requests, will be perturbed using the CORBAN model. Perturbations will represent time delays of a short and long duration to verify CORBAN's time sensitivity. Time is one of the parameters enhanced communications should favorably impact. Assuming CORBAN satisfies this test, COMM-T will be run using SINCGARS, PJH, and MSE data with selected CORBAN tactical scenarios. Results, similar to the combat effectiveness enhancement provided by JSTARS, are expected.

V. FUTURE ENHANCEMENTS

If the results of these manual CORBAN/COMM-T runs are valid, we will support the dynamic integration of these two models. This is similar to the VIC/COMM-T integration efforts at TRASANA. Assuming both CORBAN and VIC become COMM-T integrated, a comparison should be made between the two models running similar scenarios. Both models would be further validated by such scrutiny. The logical future enhancement to VIC and CORBAN is the integration of other C3 submodels: Air Defense Artillery, Fire Support, Maneuver Control, Intelligence and Electronic Warfare, and Combat Service Support. These functional areas are all being considered for battlefield automation. The integration would allow an assessment of increased MOEs by automating present manual functions. These totally integrated simulations could suggest doctrinal changes facilitating information flow and AirLand Battle decision making. For purposes of survivability and reconstitution, these simulations would help the architect of the Army Command and Control System (ACCS) design a battlefield information architecture optimizing information storage, retrieval, and interchange among the five functional systems. Also of significant benefit would be the upgrade of COMM-T with SLAM II software (11). An upgrade would provide an audit trail to determine why message delays occur significantly affecting battle outcome.

VI. SPINOFFS

Our research has disclosed many valuable spinoffs can result from a combat model that integrates C3 (C-E and the five functional areas). These spinoffs are in the areas of technological developments, training initiatives, and doctrinal studies.

New C-E systems are highly sophisticated, expensive, and take years to develop and field. Investigating these systems by modeling in a dynamic combat environment enhances the understanding of the physical systems enabling simplifying assumptions that were not possible when

examining individual links (5). During COMM-T test runs of MSE and PJH there was a message processing gain, even with significant network attrition, that had not been anticipated. Analysts discovered this gain results from a flexible random directory systems that will stand significant attrition and keep functioning. Although demonstrated mathematically by R. Prosser in 1962, it was now graphically demonstrable (5). Also, demonstrated have been the significant potential advantages of using communications relays in a jamming environment (1). Because of the large number of current relay candidates (unmanned aerial vehicles, manned airborne relay, mobile ground and fixed ground) and a high technology solution called a "Self-organizing Random Array Communications Relay" (9) not only MOPs but MOEs as well must be examined for cost effective solutions. Because these macro effects are not easily observed and quantified, the model provides a basis for comparing the value of added system capabilities that have significant battlefield impact. It may show that development dollars can be better spent on systems to kill enemy jammers than attempting to make communication systems almost totally robust. The value of increasing mobility and survivability to decrease attrition of information management systems may be shown to exceed the value of other enhancements.

The training value of these new models, if put into a user friendly package on mini and micro computers, can be invaluable for TRADOC schools and tactical units. In the next five years, the C-E officer is going to be faced with a highly complex array of communication networks that he must plan and control. If he is going to be expected to make smart decisions, he must realize the importance of his decisions to the communication network and to winning the "war". He can train in school on generic scenarios and in his assigned unit on specific scenarios. Such training will help the C-E officer anticipate and become proactive rather than reactive when it counts. Because current models and wargames essentially assume away the communications jamming and attrition problem, and jamming is not utilized to any extent in field training exercises, officers are not trained to react properly. Relays are not properly positioned, directional antennas and antenna terrain masking is not used, or alternate radio frequencies and alternate communications means selected. Our new communications equipment will function much better in jamming but is not jam proof. Models and wargames that realistically play communications will assist commanders and staffs to plan and optimize their communications capability.

Doctrinal changes may result from studies with fully integrated models. We may find that by automating the current five functional areas, functions may be combined for speed and efficiency. The perishability of information will become a reality in these models. Some rule of thumb or back of the envelope type equations may be developed as

command and staff decision aids--most general officers intuitively develop such rules of thumb from years of experience.

VII. SUMMARY AND CONCLUSIONS

Today's combat models do not adequately represent C3. They fail primarily by not dynamically representing attrition and message delay. C-E simulations present output in such unusable terms as signal-to-noise ratios, bit-error-rates and communications downtime. A model or models are urgently needed to compare tactics and equipment capabilities in terms of C3 (includes communications, data processing, and decision support systems) using the AirLand Battle concept.

We strongly suggest that work be continued at TRASANA to integrate COMM-T into VIC and are hopeful that off-line COMM-T inputs into CORBAN will demonstrate the feasibility of that integration as well as demonstrate the difference new C3 systems will make in battle outcome. It must be noted, however, many serious doubts exist that this is doable--the percent of variance that can be attributed to a given system may be less than measurement error or noise in the model. However, this cannot be determined until we test this in a model.

VIII. REFERENCES

1. Cook, Charles, "Optimum Deployment of Communications Relays in an Interference Environment", IEEE Transactions on Communications, Vol. Com. 28, No. 9, September 1980.
2. Force Control Model Background, TRASANA, Fort Leavenworth, Kansas, November 1985.
3. Forman, Ernest, Saaty, Thomas, Selly, Mary Ann, and Waldron, Rozann, "Expert Choice", Decision Support Software, Inc., McLean, Virginia, 1985.
4. Glover, Dennis and Caldwell, Gordon, "Dynamic Electromagnetic Systems Combat Effectiveness Model Computer Simulation Program Monte: Program Validation and Documentation, Bell Technical Operations Textron, Tucson, Arizona, January 1985.
5. Kleinrock, Leonard, "Communication Nets: Stochastic Message Flow and Delay", Dover Publications, Inc., New York, 1972.

WHITE, LEIPERTZ & BRITAN

6. Lindeman, William, "Conceptual Framework for Evaluating and Comparing Command and Control Systems", The MITRE Corporation, McLean, Virginia, 1985.
7. Parish, Randall, "FOURCE - Command, Control, Communications, and Combat Effectiveness", TRASANA, White Sands Missile Range, New Mexico, No Date.
8. Sweet, Ricki, Friedlander, Zitta, and Hamilton, Griffin, Hill, Linda, Holstein, Dennis, Hu, Richard, Ware, Hugh (Editor), "The 1984 Measures of Effectiveness (MOE) for C3I Evaluation Symposium: Proceedings and Analysis, Volume II, The MITRE Corporation, McLean, Virginia, October 1984.
9. Vespoli, Jorge, Haber, Fred, Berkowitz, Raymond, and Yavuz, Davras, "A Self-Organizing Random Array Communications Relay", IEEE Transactions on Communications, Vol. Com. 31, No. 4, April 1983.
10. White, James and Waylonis, Kenneth, CORBAN Workshop, Fort Leavenworth, Kansas, January 1986.
11. Yearley, Robert, COMM-T Model Methodology, TRASANA, White Sands Missile Range, New Mexico, February 1986.
12. Yearley, Robert, Vector-In-Commander Workshop, Washington, DC, February 1986.

LIQUID CRYSTALLINE SIDE CHAIN POLYMERS AS POTENTIAL DETECTION AGENTS FOR
CHEMICAL DEFENSE (U)

*Reginald A. Willingham, Dr., and Robert E. Singler, Dr.
U. S. Army Materials Technology Laboratory
Watertown, Massachusetts 02172-0001
Shekhar Manavalli, Dr.
Chemical Research and Development Center
Aberdeen Proving Grounds, Maryland 21010-5423

INTRODUCTION

The Army has a critical need for improved detection systems for chemical defense purposes. Ideal candidate materials should be capable of undergoing reversible transitions upon interaction with chemical agents and subsequent decontamination procedures. Liquid crystalline polymers are sensitive to physical-chemical changes in their environment, and thus may be suited for chemical defense applications.

Liquid crystalline polymers can be prepared in a variety of ways. Both main chain and side chain liquid crystalline polymers have been reported. Our approach has been to attach low molecular weight mesogenic molecules to the phosphazene (PN) backbone via a flexible spacer group (Figure 1). This concept of coupling a mesogenic group to a polymeric substrate has been demonstrated by Finkelmann and other workers (1). Phosphazenes offer a potential advantage in that a variety of different substituents can be readily attached to a common substrate to yield a wide range of materials with different properties (2). In our study, both cyclic phosphazenes and linear polymers are used as substrates, since the behavior of these systems is quite different. Cyclic phosphazenes serve mainly as model compounds, but they have some interesting properties of their own, and thus are included in this paper.

EXPERIMENTAL

Synthesis. The initial work was to prepare suitable side chain compounds (mesogens) Figure 2. Low molecular weight mesogens are rod-like molecules, such as biphenol or aromatic azo moieties. An additional requirement is a flexible spacer with a reactive end group to attach to the phosphazene substrate. The general synthetic procedures used in the preparation of the biphenol and aromatic azo compounds are given in Figures 3 and 4. Suitable yields of the final products were obtained in all cases. Nuclear magnetic resonance (NMR), mass spectrometry (MS) and elemental analysis confirmed identification of the desired compounds. Thin layer chromatography (TLC), capillary melting point determinations, differential scanning calorimetry (DSC), and elemental analysis were also used to ascertain the purity of the reaction products.

The general procedure to prepare the phosphazene derivatives is shown in Figure 5. Both hexachlorocyclotriphosphazene (I) and especially poly(dichlorophosphazene) (II) are reactive substrates. Sodium trifluoroethoxide ($\text{NaOCH}_2\text{CF}_3$) was often used in addition to the mesogenic moiety in order to insure complete replacement of chlorine from the phosphazene substrate.

The conversion of hexachlorocyclotriphosphazene to high molecular weight poly(dichlorophosphazene) has been studied extensively in our laboratory (3). The polymers used in this study were prepared by the bulk thermal polymerization route.

The cyclic phosphazenes (III) in Figure 3 were characterized using the same techniques mentioned for low molecular weight mesogens, as well as with high performance liquid chromatography (HPLC). Polymers (IV) were characterized by elemental analysis, DSC, HPLC, gel permeation chromatography (GPC) and with inherent viscosity, $[\eta]$, measurements. Polarized light microscopy with a hot stage attachment was used to study the liquid crystalline character of both the cyclic and polymeric phosphazenes.

RESULTS AND DISCUSSION

Table I gives the melting points for the intermediate phenols and alcohols used to prepare the substituted phosphazenes. None of the intermediates or chain extended compounds (mesogens) show liquid crystalline behavior; however, this is not entirely unexpected, since their behavior when attached to a polymeric backbone or other substrate could be quite different.

Table II lists the melting point determinations for several cyclic phosphazenes, including the starting material (1) for the synthesis. The cyclic phosphazenes (compounds 1 and 2) are previously reported compounds, and the melting points determined in this laboratory correspond to the literature values. Compounds 3 and 4 are new compounds which do not show any liquid crystalline character, but compound 5, which is also a new compound, shows a mesomorphic structure under the polarizing microscope.

Table III lists the viscosity and GPC molecular weight determinations for the polyphosphazenes prepared in this study. As previously stated, all substituted polymers are derived from a high molecular weight poly (dichlorophosphazene) intermediate. Both inherent viscosity and GPC molecular weight determinations confirm that the derived polymers retain the high molecular weight character of the preceeding polymer intermediate, and little, if any, degradation occurred during the substitution process.

Table IV gives the thermal analysis data for the polyphosphazenes listed in Table III. For polymer 1, values for the glass transition (T_g) and melting transition (T_m) are literature values (4). The low glass transition temperatures for polymers 1 and 2 are indicative of the high degree of flexibility in the phosphorus-nitrogen backbone. The trifluoroethoxy polymer 2 has a mesomorphic transition designated as $T(1)$ by workers in a previous study (5). This is a transition from a crystalline to a partially ordered state, but does not possess the smectic or nematic character normally associated with thermotropic liquid crystalline polymers. Polymer 4, on the other hand, does show an intermediate state of order which is nematic in character, as evidenced by its behavior under the optical microscope.

CONCLUSION

We have thus demonstrated that a thermotropic liquid crystalline side chain polymer based on a phosphorus-nitrogen chain has been prepared from poly (dichlorophosphazene) using an appropriate mesogenic molecule containing a flexible spacer unit. The analogous cyclic phosphazene also shows liquid crystalline character. Further work is in progress to fully ascertain the nature of the mesomorphic state. We also plan to expand the synthesis to other suitable mesogenic systems in order to prepare liquid crystalline polyphosphazenes for intended chemical defense purposes and other sensor applications.

ACKNOWLEDGEMENTS

The authors wish to thank Ms. Kathleen Harrington and Ms. Jane Brosseau (MTL) for assistance with DSC determinations and Professor Robert Lenz and Dr. Akira Furukawa (University of Massachusetts) for assistance with the optical microscopy studies.

REFERENCES

1. Finkelmann, H. "Polymer Liquid Crystals," Ciferri, A.; Krigbaum, W. R.; Meyer, R. B., Eds., Academic Press, New York, 1982, Chapt. 2.
2. Singler, R. E.; Schneider, N. S.; Hagnauer, G. L. Polym. Eng. and Sci. 1975, 15, 321.
3. Hagnauer, G. L. and Koulouris, T. N. "Liquid Chromatography of Polymers and Related Materials-III" Jack Cazes, Ed. Marcel Dekker, Inc. New York, 1981.
4. Allcock, H. R. and Arcus, R. A. Macromolecules 1979, 12, 1130.
5. Schneider, N. S.; Desper, C. R.; Singler, R. E. J. Appl. Polym. Sci. 1976, 20, 3087.

Table I Intermediates and Mesogens for Side Chain Substituents

<u>Compound^a</u>	<u>Melting Point °C</u>
CF ₃ CH ₂ OH	b
Ph-OCH ₂ CH ₂ OH	11-13
Ph-Ph-OH	165-167
Ph-Ph-OCH ₂ CH ₂ OH	118
Ph-N=N-Ph-OH	155-157
Ph-N=N-Ph-OCH ₂ CH ₂ OH	97
n-C ₄ H ₉ -Ph-N=N-Ph-OH	81
n-C ₄ H ₉ -Ph-N=N-Ph-OCH ₂ CH ₂ OH	99
CH ₃ O-Ph-Ph-OH	181
CH ₃ O-Ph-Ph-OCH ₂ CH ₂ OH	174

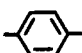

^aPh= ^bBoiling point 77-80°C

Table II Cyclic Phosphazenes $(R_2PN)_3$

#	Substituent R^a	$T_{lc}^{\circ}C$	$T_m^{\circ}C$
1	Cl-		112-114
2	CF_3CH_2O-		47-48
3	$Ph-OCH_2CH_2O-$		
4	$Ph-Ph-OCH_2CH_2O-$		
5	$n-C_4H_9-Ph-N=N-Ph-OCH_2CH_2O-$	132	191

 $^aPh =$ Table III Poly(organophosphazenes) $(R_2PN)_n$

#	Polymer ^a	$[n]$	MW (GPC)
1	$(Cl_2PN)_n$		$>10^6$
2	$[(CF_3CH_2O)_2PN]_n$	0.75	0.88×10^6
3	$[(Ph-Ph-OCH_2CH_2O)_y-(CF_3CH_2O)_yPN]_n$	0.57	0.98×10^6
4	$[(4-n-C_4H_9Ph-N=N-Ph-OCH_2CH_2O)_y-(CF_3CH_2O)_yPN]_n$	1.68	1.02×10^6

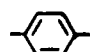

 $^aPh =$ 

Table IV Thermal Transitions (°C) for the Polyphosphazenes

#	Polymer ^a	<u>T_g</u>	<u>T(1)</u>	<u>T_{lc}</u>	<u>T_m</u>
1	[Cl ₂ PN] _n	-66			
2	[(CF ₃ CH ₂ O) ₂ PN] _n	-66	90		240
3	[(Ph-Ph-OCH ₂ CH ₂ O) _y - (CF ₃ CH ₂ O) _y PN] _n				130
4	[(4-n-C ₄ H ₉ -Ph-N=N-Ph-O) _y - (CF ₃ CH ₂ O) _y PN] _n			90	194

^aPh= 

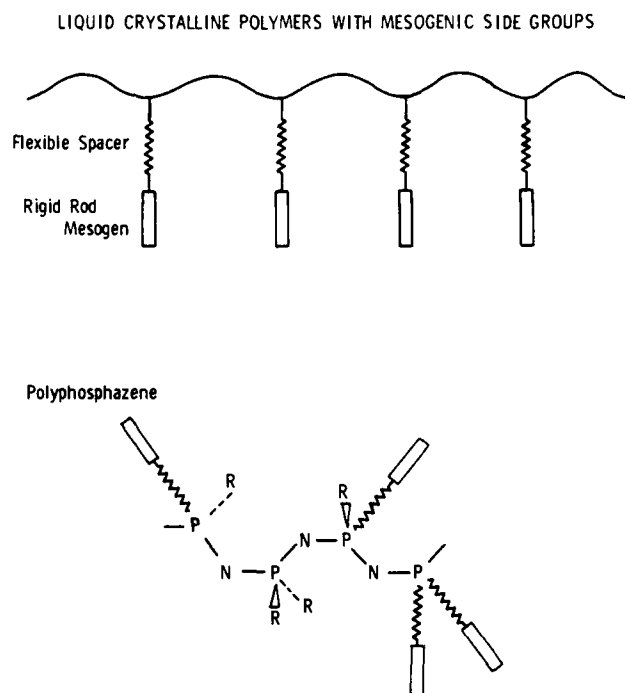
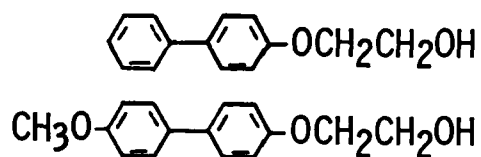


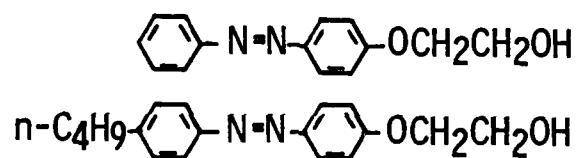
Figure 1. Liquid Crystalline Polymers With Mesogenic Side Groups

SIDE CHAIN COMPOUNDS

BIPHENYL



AROMATIC AZO



MODEL

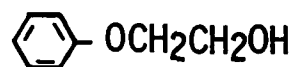


Figure 2. Side Chain Compounds

BIPHENYL COMPOUNDS

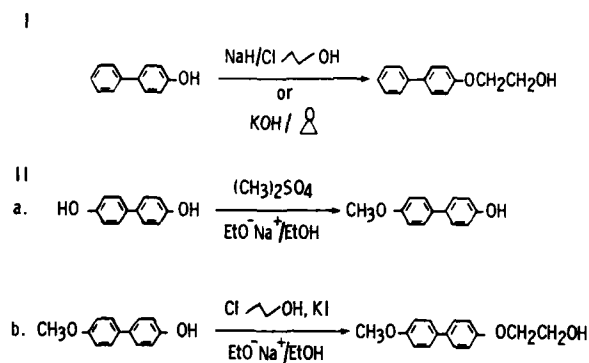


Figure 3. Synthesis of Biphenyl Compounds

AROMATIC AZO COMPOUNDS

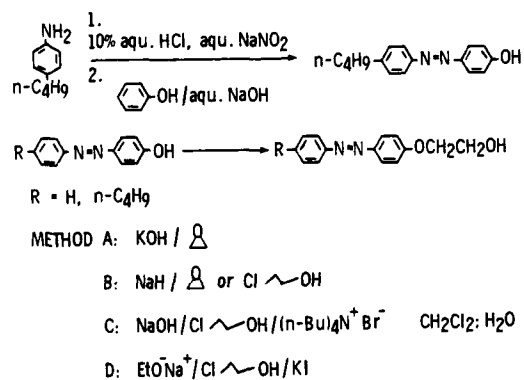


Figure 4. Synthesis of Azo Compounds

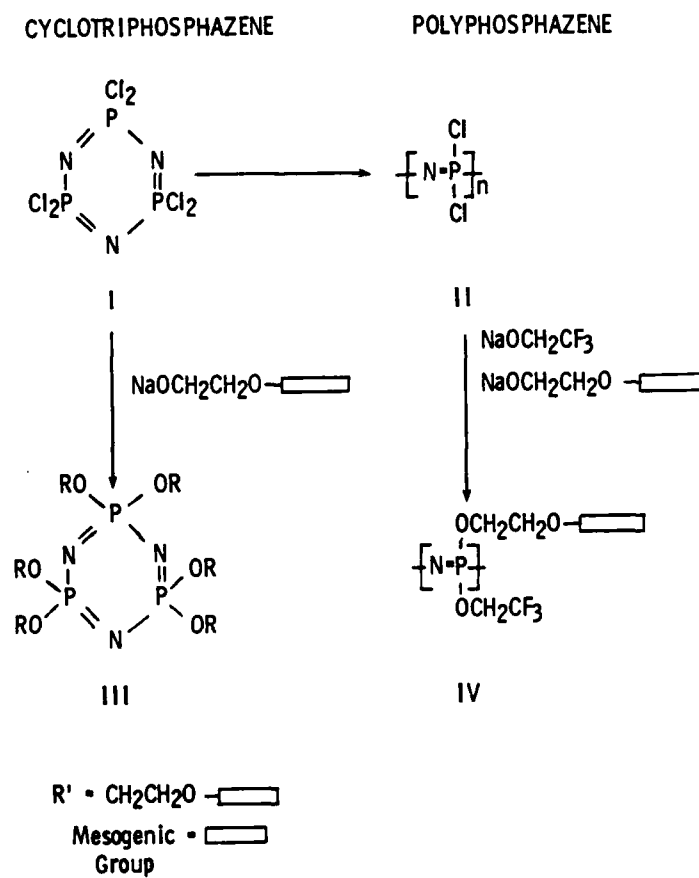


Figure 5. Phosphazene Synthesis

YALAMANCHILI, HOENIG & SCHICK

COOLING OF WEAPONS BY ELECTROSTATIC PHENOMENA (U)

* RAO YALAMANCHILI, PhD
Close Combat Armaments Center
US Army Armament Research and Development Center, Dover, NJ 07801-5001

STUART A. HOENIG, PhD AND MILTON J. SCHICK
University of Arizona, Tucson, AZ 85721

INTRODUCTION

The surface temperatures of a gun tube may reach 1500°F at the inner surface and 1000°F at the outer surface in a short period of time because of the high rate of fire. The outer surface of the gun tube is surrounded by ambient air which may be at a temperature between -60°F and 140°F and may move at a velocity between zero and 60 miles an hour. Since wind velocities help to cool the gun tube faster than free convection and radiation phenomena (still wind), thermal design of a gun tube may not include wind velocities. The free convection and radiation of a gun tube are found to be of the same order of magnitude when the surface temperature is about 450°F.

The unsteady heat transfer analysis for chosen ammunition, gun and firing schedule is quite complex. Since the result of sustained rapid firing is barrel overheating, a number of techniques have been used for cooling the barrels of automatic weapons, including natural convection and radiation cooling used by most weapons, cooling fins and liquid cooling. The problem of barrel overheating and excessive wear, and cookoff, however, is still of great concern to gun design engineers. The problem will, without any doubt, worsen since the trend is to higher performance weapons operating at higher pressures and generating higher temperatures. The need exists for improved methods to cool gun barrels, allowing higher firing rates and reduced wear and erosion in addition to safety of operating personnel.

An electrostatic field can induce the movement of air called the corona wind or electrical wind. The phenomenon involves one or more corona points that are operated at a high DC voltage with respect to ground. The corona points (needles) emit electrons which then attach

Copy available to DTIC does not
permit fully reliable reproduction

YALAMANCHILI, HOENIG & SCHICK

to oxygen molecules to form negative oxygen ions. These ions are pushed away from the corona points by the electrical field and collide with air (neutral) molecules thereby generating local wind velocities as high as 200 yards per minute. If the stagnant boundary layer that normally limits the rate of cooling by free convection is broken up by this mechanism, heat transfer is greatly increased.

The natural mode of heat transfer for a conventional weapon is herein analyzed by modeling free convection and radiation phenomena and by seeking a numerical solution of a system of nonlinear partial differential equations. This formed a basis for comparison of augmentation of heat transfer by electrostatic phenomena.

The test results on both model and full scale machine gun barrel systems indicated that electrostatic cooling can enhance the heat transfer from the barrel to the ambient environment. The power required to drive the electrostatic system is minute compared with the heat removed from the barrel, and high ambient dust levels or relative humidities do not interfere with the operation of the system.

Tests with electrical and mechanical primers indicate that there is no hazard of accidental detonation associated with the use of the electrostatic cooling system. The design of the system provides for personnel safety since there are no exposed high voltage components that might injure military personnel.

Results in the laboratory on scaled and full-scale models under steady state (constant temperature) conditions indicated that increases in convective heat transfer coefficient of 2.7 to 3 could be obtained with the electrostatic system. The standard .50 cal M2-ME machine gun was chosen for the full-scale firing test. The results from full-scale firing tests were complicated by the need to operate with an unsteady state (variable temperature) system. The variations in temperature with time and space (along the barrel) produced a significant flow of heat by conduction that tended to reduce the electrostatically induced convection cooling effects. A final conclusion is drawn with gut feelings based on assessment of its own merits.

FREE CONVECTION AND RADIATION

The normal mode of heat transfer from the gun tube to the ambient air is by free convection and radiation. The governing equations of unsteady free convection and radiation are a system of nonlinear partial differential equations of parabolic type with three independent variables and with variable linear and nonlinear (radiative) boundary conditions. For typical gun barrel conditions,

Copy available to DDC does not
permit fully legible reproduction

the Grashof number is 1.66956×10^6 whereas the Prandtl number is 0.964. The boundary layers which arise by free convection also change to turbulent flow when they reach a certain thickness. In air, this change occurs at a critical Grashof number (based on distance from origin) around one billion. This corresponds to a Reynolds number (based on velocity boundary layer thickness) of 550. The typical gun barrel example is still in the laminar range. Therefore, further work will be limited to the analysis of unsteady laminar boundary layers.

The governing equations of unsteady compressible laminar boundary layers due to free convection and radiation phenomena associated with a heated vertical flat plate or heated horizontal cylindrical tube are given below:

Continuity

$$\frac{\partial \rho}{\partial t} + \frac{\partial}{\partial x}(\rho u) + \frac{\partial(\rho v)}{\partial y} = 0 \quad [1]$$

$$\rho \frac{\partial u}{\partial t} + \rho u \frac{\partial u}{\partial x} + \rho v \frac{\partial u}{\partial y} = g(\rho_\infty - \rho) \sin \omega + \frac{\partial}{\partial y}(\mu \frac{\partial u}{\partial y}) \quad [2]$$

Energy

$$\rho C_p \frac{\partial \theta}{\partial t} + \rho C_p u \frac{\partial \theta}{\partial x} + \rho C_p v \frac{\partial \theta}{\partial y} + \rho C_p \theta \frac{\Delta T^1}{\Delta T} = \frac{\partial}{\partial y}(K \frac{\partial \theta}{\partial y}) - \frac{\partial q_r}{\partial y} \quad [3]$$

where u = velocity component along x-axis

v = velocity component along y-axis

$$\theta = \frac{T - T_\infty}{T_w - T_\infty} \quad \Delta T^1 = \frac{d(\Delta T)}{dt}$$

T = temperature

g = gravitational constant

t = time

ΔT = $T_w - T_\infty$ = difference in temperature between the hot wall and the ambient fluid

The symbol, ω , which is a function of x , is defined as the angle at that point between a tangent to the surface and a line perpendicular to the gravitational field. The boundary conditions are:

$$y = 0: u=0, v=0, \theta=1$$

$$y = \infty: u=0, \theta=0$$

[4]

In reality, the temperature boundary condition at the wall is unknown and varies with time, t . This can be taken into account by setting an energy balance at the wall (interface or compatible boundary condition)

$$\left(K \frac{\partial T}{\partial y} \right)_{y=0} = \left(K \frac{\partial T}{\partial y} \right)_{y=0} + -\epsilon \sigma (T_w^4 - T_\infty^4) \quad [5]$$

The ambient air may be considered as optically thin compared to the propellant gas inside the barrel. In this case the radiation term which is extremely complex is negligible compared to the other terms in the energy equation. Therefore, further analysis will be restricted to the solution of the governing equations without the radiative heat flux term. The details of the solution procedure are available in a technical report to be published and omitted here due to space limitations.

However, it is sufficient to say the following for conceptual design and evaluation of electrostatic cooling. The dependent variables such as velocity components and temperature as well as the independent variables are transformed into dimensionless form. The resulting equations are expressed in explicit finite-difference form. The stability criteria is established by Von Neumann and Dussinberre analysis. The difference equations are modified to make them unconditionally stable by the use of thermodynamic law. A comparison of the time-step calculated by the analytical stability criteria derived and the actual maximum time-step where the numerical computations are stable indicates that one can use a time-step over 40 percent larger than the step size allowed by the stability criteria. The thermal boundary layer in the upper half of the cylinder is much thicker than in the lower half of the cylinder. The thermal boundary layer thickness increases not only with the time but also with the position for large times. The velocity boundary layer thickness also grows with the time but not as fast as the growth of the thermal

YALAMANCHILI, HOENIG & SCHICK

boundary layer thickness. The dimensionless heat transfer is fairly uniform for small times and changes up to 50 percent over its maximum at that time. The convective and radiative (emissivity=0.5) heat losses are about 568 and 520 BTU/hr-ft respectively for a surface temperature of 500°F.

LABORATORY TESTS

The objective of this program is to demonstrate the feasibility of electrostatic cooling, to establish the optimum parameters, and to investigate the side effects, if any. Towards this goal, a commercial electrically driven heater rod was fitted with a thermocouple and a corona discharge electric wind generator. The technique involved driving the electrical heater with a known voltage and current to bring the thermocouple monitored area to a temperature of 360°C. When the temperature stabilized, the electrostatic cooling system (ECS) was activated and the increased power, to hold a constant temperature, was measured.

The results of the first study indicated that the power required to keep the heater at constant temperature, with the electrostatic system ON, was a factor of 3, larger than that required with the electric wind OFF. If we note that the rod was held at a constant temperature there was no change in radiation cooling; all the electrostatic effects involved enhanced convection cooling. The net increase in overall heat transfer coefficient was a factor of 3. This suggests that the normally laminar boundary layer around the rod was driven into the turbulent condition by the electrostatic wind.

Taking the ratio of heat removed to the power required to operate the electric wind system, leads to a value of 40. This shows a very high efficiency in terms of heat removed (in watts) per watt of electrical power to the corona system.

The results also indicate that the cooling was effective all along the rod even where the surface temperatures were low. For example, this is true at a location where the temperature is 200°C due to only heat conduction but not due to the electrical resistance heater.

Another question of some interest concerns the number of rows of corona points required at any given axial location for effective heat transfer. A number of corona points all around the circumference or concentrated heavily along the lower 75° arc of a heater or just one near the bottom of the heater produced almost the same results.

Copy sent to Mr. [illegible]
Printed copy [illegible]

YALAMANCHILI, HOENIG & SCHICK

Therefore, a single row of needles was chosen for a final design. Because of the desire to use as few corona points as possible, an optimum spacing from probe to probe was investigated. A test of this question indicated that a spacing of 25mm is the largest that can be used without sacrificing efficiency.

Further efforts were made to optimize the parameters in the electrostatic cooling system. To evaluate the minimum required distance between the corona needles and ground, the cooling effectiveness was measured as a function of needle to ground spacing. The results are shown in Figure 1. It is clear that there is no effect of spacing on efficiency as the distance changes from 12 to 23mm. Below 12mm arc-over effects precluded the development of any significant corona wind.

The effect of applied voltage was of interest and, in Figure 2, the variation in heat transfer is shown as a function of applied voltage at a constant needle to ground spacing. As expected, the higher the voltage the larger the cooling effect. Here again, the maximum voltage is limited by the formation of arcs. It is normal practice in industry to operate at a voltage about 10% below the point where arcing occurs.

The next experiments were conducted to answer two questions: Operation at high dust levels, and operation at 90% relative humidity (RH). For both studies the system was set up inside a one cubic meter box used earlier for other experiments. For the dust tests, AC Fine (Arizona Road Dust) was injected to a level of 25 g/cu m and the system was operated in the usual manner. There was no change in heat transfer rate from that observed without dust. There was evidence that the electrostatic wind "blew off" dust that would have otherwise collected on the heated rod.

For the humidity tests, humidified air was injected into the one cubic meter box until the RH level rose to 90% at a dry bulb temperature of 25°C. The system was operated as before, but no change in heat transfer characteristics could be observed.

The next part of the program involved testing the effects, if any, of the corona discharge on military primers. For the first study, 20-06 primers were exposed directly to the corona. The system was operated for two hours on several occasions. In no case was there any indication of cookoff of the primer. After the tests, the primers were tested in rifle firing pin systems and functionality was 100%.

YALAMANCHILI, HOENIG & SCHICK

The next study involved tests with electrical primers. For the first series of tests, four primers were each separately exposed to the corona discharge, at a 25.4 mm gap, for two hours. The voltage used was then lowered to 4mm from the rear of the primer and aligned on the center disk surrounded by the blue electrical insulator in the primer cup. The voltage was then pulsed to a high level to produce an intense arc-over to the primer to cause detonation. All four primers detonated. The previous two hour corona discharge bath did not detonate the primers nor were the primer's sensitivities affected.

Next, the rear of a primer was laid on a steel plate and a -30 kV arc-over was pulsed into the plate at a point 50.3 mm from the primer. This was done for a period of 10 minutes using two different primers. The two primers did not detonate. To test a third primer, the corona point was moved into the middle of the front of the primer. The point was 4mm from white material at the bottom of the cup. The voltage was raised to -30 kV, producing a constant arc-over. This level was maintained for 10 minutes without the primer detonating. Finally, these three primers were turned over for function firing; the three primers detonated indicating no loss in sensitivity.

The next series of tests involved a .50 caliber M2-HB barrel. The corona array and barrel were assembled as per Figure 3. Two Watlow, 12 inch, 1000 watt heaters were inserted into the barrel, one from each end to meet in the center of the corona array. The barrel was heated to a temperature of 350°C with the corona array OFF. With the corona array operating at -22kV at 1.6 mA, the electrical power input into the heaters had to be increased by a factor of three to maintain the temperature of 350°C. In all subsequent tests, the results with the .50 cal. M2-HB barrel exactly duplicated the results of the heater rod tests.

FIRING TESTS

The results in the laboratory under steady state (constant temperature) conditions indicated that increases in convective heat transfer coefficient by a factor of 2.7 to 3 could be obtained with the electrostatic cooling system. Because of this encouragement and lack of any side effects, a full-scale firing test was conducted by the use of a .50 cal. M2-HB machine gun with and without the electrostatic cooling system. 2000 rounds were fired. Only ambient winds, temperatures along the barrel, and relative humidity were measured. The intermittent winds ranged from 100 to 100 yards per

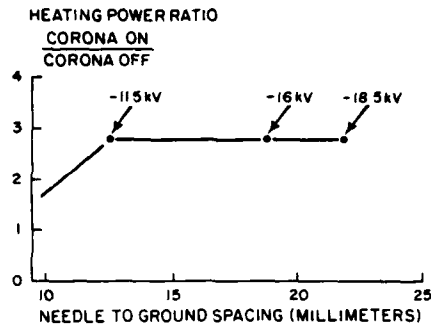


Figure 1. Effect of spacing between needle and ground

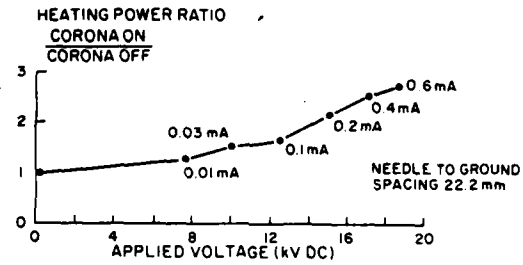


Figure 2. Effect of Voltage

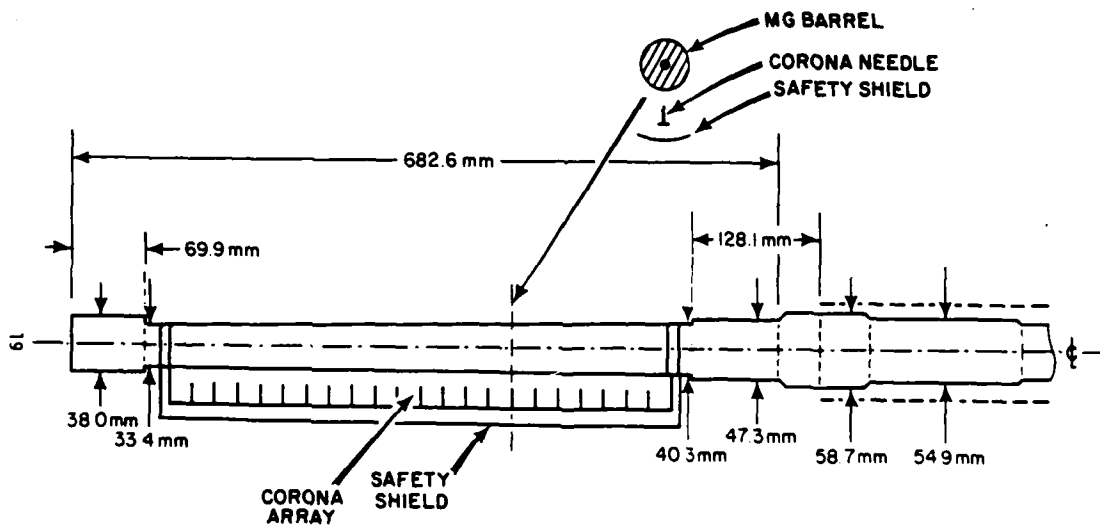


Figure 3. .50 Caliber M2-HB Browning Machine Gun with Electrostatic cooling system

YALAMANCHILI, HOENIG & SCHICK

minute. The temperature ranged from 37.3°F to 95°F. The firing rate was only approximate. Therefore, the interpretation of experimental data is qualitative due to limited instrumentation and approximate firing rates.

Test #1 involved normal firing (electrostatic cooling off) at 75 RPM for 4 minutes for a total of 300 rounds. The barrel was allowed to cool down to 68°C by free convection and radiation. The results are shown in Figures 4 and 5.

Test #2 was similar to test #1 except that the electrostatic cooling was actuated when firing ceased and was kept "ON" until the barrel cooled to 68°C. The results are shown in Figures 6 and 7.

The next test (#4) was similar to tests #1 and #2 except that the electrostatic cooling was "ON" during both firing and cool-down periods. The results are shown in Figures 8 and 9.

Test #5 involved a high rate of fire (100 RPM) with electrostatic cooling for 4 minutes for a total of 400 rounds. The results are shown in Figure 10.

From the observation of above results, it is interesting to note that during the firing cycles, the muzzle end of the barrel was always hotter than the center or the point where the barrel joined the chamber. It is apparent that the large mass of the chamber was acting as a "sink" for heat transferred by conduction from the barrel. This is an important point, in that as the barrel cooled down, the heat stored in the chamber "sink" was conducted back to the barrel and affected the electrostatic cooling process. It is concluded that this "source/sink effect" was the major reason that the field test results were not as encouraging as those obtained under steady state conditions in the laboratory.

Another indication of the fact that the chamber acted as a sink may be found in comparing Figure 4 (test #1, no electrostatic cooling) with that from Figure 3 (test #4 electrostatic cooling on). In Figure 4 where there was no electrostatic cooling, the muzzle end of the barrel was always hotter than the center of the barrel as might be expected if the only loss of heat was due to radiation, free convection, and conduction to the heavy chamber. In contrast, the data of Figure 3 where the electrostatic cooling was on show that the muzzle was always cooler than the center of the barrel as might be expected if the electrostatic system is adding forced convection cooling to the usual free convection, radiation, and conduction.

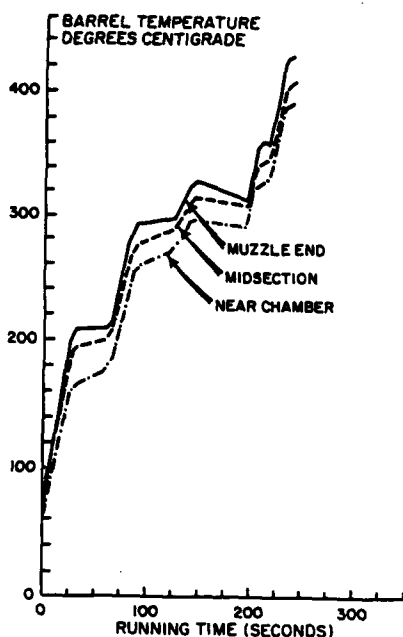


Figure 4. Barrel Temperature During Firing (Test #1)

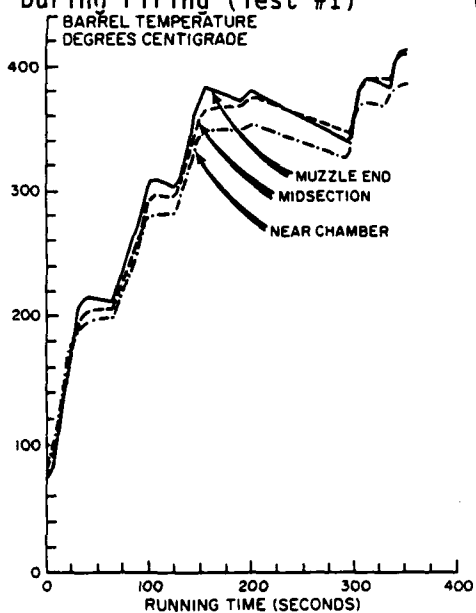


Figure 6. Barrel Temperatures During Firing (Test #2)

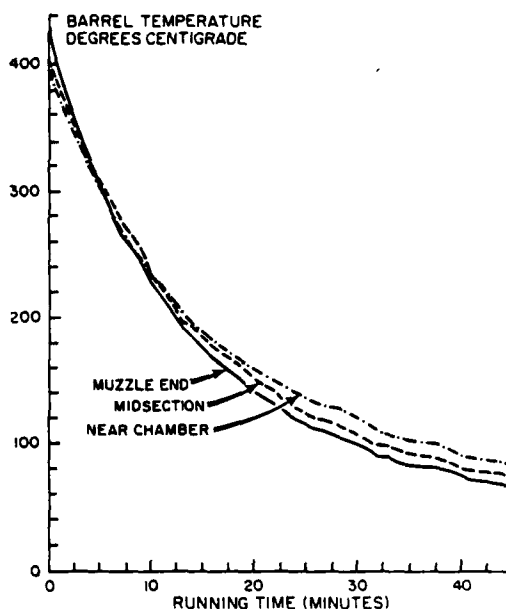


Figure 5. Barrel Temperatures During Cooling (Test #2)

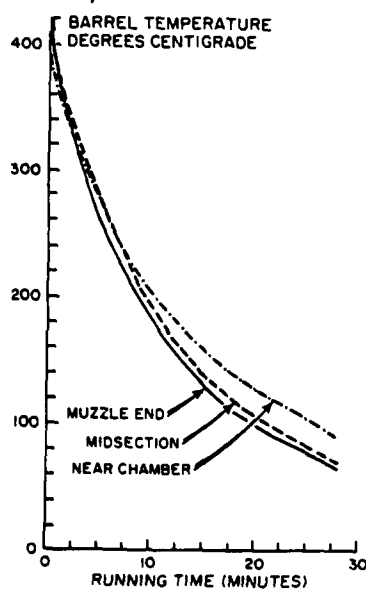


Figure 7. Barrel Temperatures During Cooling (Test #2)

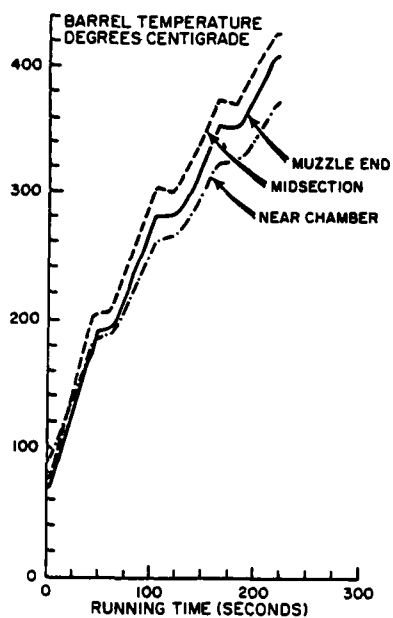


Figure 8. Barrel Temperatures During Firing (Test #4)

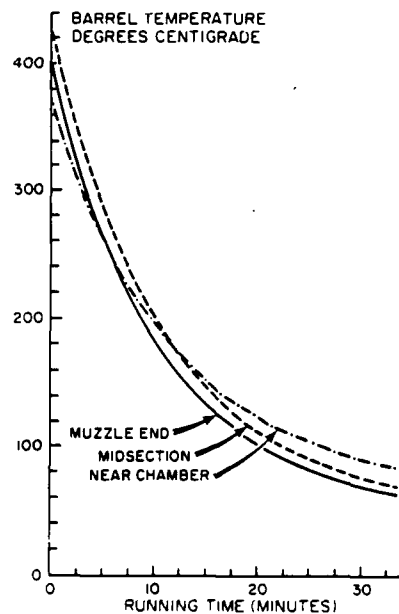


Figure 9. Barrel Temperatures During Cooling (Test #4)

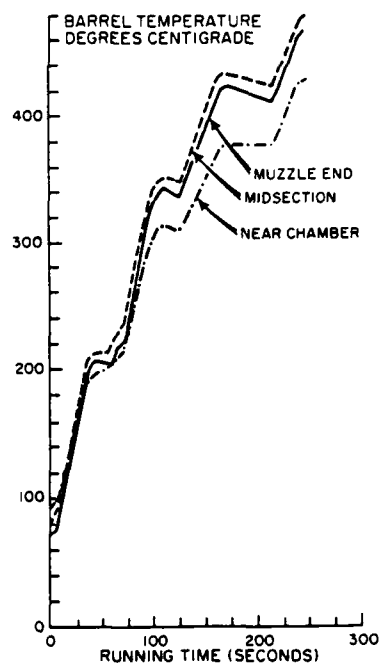


Figure 10. Barrel Temperatures During Firing (Test #5)

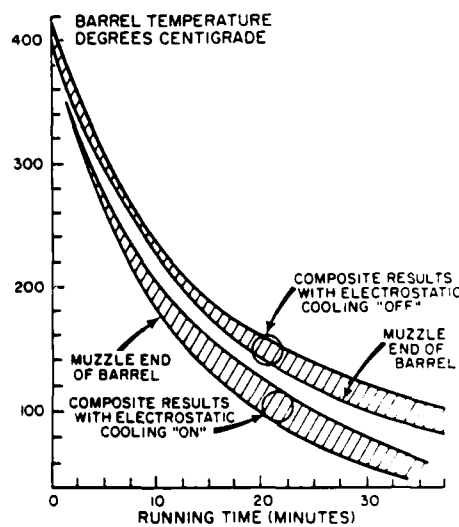


Figure 11. Composite Barrel Temperatures During Cooling

YALAMANCHILI, HOENIG & SCHICK

The same results can be observed during cooling by examining Figure 5 (test #1 electrostatic cooling off) and Figure 9 (test #4 electrostatic cooling on). In Figure 5, the muzzle was the hottest location when firing stopped, but as cooling proceeded, it reached a temperature significantly lower than that of the center or the chamber end of the barrel. The same effect is even more apparent in Figure 9 (test #4 electrostatic cooling on) in that not only was the end of the barrel cooler than the center where firing ceased, it continued to cool far more rapidly than the center or point near the chamber.

All of these results are in agreement with the statement above that the heavy chamber acted as a sink during the firing process and a source during the cool down. This tended to obscure the effects of the electrostatic cooling system over most of the barrel. This is more apparent when comparing the cooling of the whole barrel system with that of the muzzle only. Figure 11 shows the composite cooling curves for all three barrel locations with and without the electrostatic augmentation of heat transfer. There is a clear advantage to the use of the electrostatic system as barrel temperatures drop below 350°C.

The ratio of convective heat transfer coefficients with and without electrostatic cooling are computed based on results of Figure 11 and the heat transfer analysis. The ratios are shown in Table 1 for composite data and for the muzzle end of the barrel at various temperatures.

Table 1. Ratio of Convective heat transfer coefficients

Temperature, °C	Ratio of Convective heat transfer coefficients	
	Composite	Muzzle
100	1.71	1.73
150	1.59	1.58
200	1.34	1.40
250	1.20	1.40
300	1.09	1.40

YALAMANCHILI, HOENIG & SCHICK

The results show that electrostatic cooling is of marginal value when the whole barrel system is lumped together. This is due to the fact that the chamber acted as a sink during the firing part of the cycle and a source during the cool down process. The situation is somewhat improved in that the ratio of the corona "ON" to corona "OFF" is as high as 1.78 at 100°C. The values are significantly higher than those observed when the data for all three thermocouples was lumped together. However, the results are still far lower than those obtained in the laboratory under steady state conditions.

CONCLUSIONS AND RECOMMENDATIONS

The surface temperatures of a gun tube may reach 1500°F at the inner surface and 1000°F at the outer surface in a short period of time because of the high rate of fire. The cooling provided by free convection and radiation of conventional weapons is not adequate. The problems of barrel overheating and excessive wear and cook-off will, without any doubt, worsen since the trend is to higher performance weapons operating at higher pressures and generating higher temperatures.

The free convection and radiation around the gun tubes was analyzed by a new numerical scheme for the solution of a system of nonlinear partial differential equations with three independent variables. The free convection and radiation are found to be of the same order of magnitude when the surface temperature is about 450°F. The convective heat transfer coefficients are established.

An electrostatic wind generating system was utilized to cool the surface of a hot barrel. In laboratory tests the gun barrel was simulated as an electrical rod heater. The laboratory tests indicated that the power required to keep the heater at constant temperature, with the electrostatic system ON, was a factor of 3, larger than that required with the electric wind OFF. The net increase in overall heat transfer coefficient was a factor of 3. Taking the ratio of heat removed to the power required to operate the electric wind system, leads to a value of 40. This shows a very high efficiency in terms of heat removed (in watts) per watt of electrical power to the corona system.

The side effects of an electrostatic system applied to a gun, such as RF interference and corona discharge effects on mechanical and electric primers, were investigated and found to be insignificant. Also, dust and humidity did not affect the performance. Based on a

YALAMANCHILI, HOENIG & SCHICK

parametric analysis an electrostatic cooling system was designed for the .50 caliber M2-HB machine gun.

A 2000 round firing test was conducted with and without the electrostatic cooling system. The testing was complicated by the need to operate with an unsteady state (variable temperature) system. In addition to this problem, the large mass of the heavy chamber acted as a sink during firing and a source during the cooling phase. Even though, the results in the laboratory under steady state (constant temperature) conditions indicated that increases in convective heat transfer coefficients by a factor of 3 could be obtained due to electrostatic cooling phenomena, it is apparent that only up to a factor of 1.73 can be achieved in an actual live firing test. The wind conditions during firing also affected the results to a certain extent. It is not recommended, at this time, to transition to further development unless this factor can be increased to the value observed in the laboratory.

END

12-86

DTIC